Mechanical Response of Composites

Computational Methods in Applied Sciences

Volume 10

Series Editor

E. Oñate
International Center for Numerical Methods in Engineering (CIMNE)
Technical University of Catalunya (UPC)
Edificio C-1, Campus Norte UPC
Gran Capitán, s/n
08034 Barcelona, Spain
onate@cimne.upc.edu
www.cimne.com

For other titles published in this series, go to
www.springer.com/series/6899

Pedro P. Camanho • C.G. Dávila
S.T. Pinho • J.J.C. Remmers

Mechanical Response of Composites

Springer

Pedro P. Camanho
DEMEGI, Faculdade de Engenharia
Universidade do Porto
Rua Dr. Roberto Frias
4200-465 Porto
Portugal
pcamanho@fe.up.pt

Carlos G. Dávila
Durability, Damage Tolerance
and Reliability Branch
MS 188E NASA Langley Research Center
Hampton, VA 23681
U.S.A.
carlos.g.davalla@nasa.gov

Silvestre T. Pinho
Department of Aeronautics
Imperial College London
Prince Consort Road
London SW7 2AZ
United Kingdom
silvestre.pinho@imperial.ac.uk

Joris J.C. Remmers
Department of Mechanical Engineering
Eindhoven University of Technology
PO Box 513
5600 MB Eindhoven
The Netherlands
j.j.c.remmers@tue.nl

ISBN 978-1-4020-8583-3 e-ISBN 978-1-4020-8584-0

Library of Congress Control Number: 2008928687

Printed on acid-free paper

9 8 7 6 5 4 3 2 1

springer.com

Preface

The methodology for designing high-performance composite structures is still evolving. The complexity of the response of composite materials and the difficulties in predicting the composite material properties from the basic properties of the constituents result in the need for a well-planned and exhaustive test program. The recommended practice to mitigate the technological risks associated with advanced composite materials is to substantiate the performance and durability of the design in a sequence of steps known as the Building Block Approach. The Building Block Approach ensures that cost and performance objectives are met by testing greater numbers of smaller, less expensive specimens. In this way, technology risks are assessed early in the program. In addition, the knowledge acquired at a given level of structural complexity is built up before progressing to a level of increased complexity.

Achieving substantiation of structural performance by testing alone can be prohibitively expensive because of the number of specimens and components required to characterize all material systems, loading scenarios and boundary conditions. Building Block Approach programs can achieve significant cost reductions by seeking a synergy between testing and analysis. The more the development relies on analysis, the less expensive it becomes. The use of advanced computational models for the prediction of the mechanical response of composite structures can replace some of the mechanical tests and can significantly reduce the cost of designing with composites while providing to the engineers the information necessary to achieve an optimized design.

This book aims at bringing together the recent developments in the field of computational models for the design of advanced composite structures manufactured using both polymer and metal matrices. The book addresses latest developments relevant to virtual design of composite structures at different stages of the product development process, from manufacturing of the composite material to optimization of complex composite structures.

This book covers different types of composite materials, ranging from metal-matrix composites to polymer-matrix composites reinforced with fibers with different architectures, and it includes a chapter on the prediction of the thermo-elastic

properties of thermoplastic composites based on the simulation of the manufacturing process. New methods to predict the mechanical properties of textile-reinforced composites using advanced discretisation techniques and multiscale approaches are described. One particular topic that has deserved the attention of the scientific community is the prediction of crack initiation and propagation in composite structures, as these structures are very often strength-critical rather than stiffness-critical. Composite materials exhibit a complex mechanical response that renders the traditional design methods developed for metals unsuitable to predict the integrity of composite materials. This book includes contributions that provide detailed representations of the different failure mechanisms that occur in composite laminates, from distributed damage in the matrix, to ply-based failure mechanisms, delamination and their interactions. The computational models presented in the book use state-of-the-art technologies, such as the Domain Superposition Technique and the partition-of-unity concept. To take full advantage of the design tailorability of composite materials, optimization techniques should be used; therefore, an optimization strategy for complex composite structures is also presented in the book.

This book should be attractive to the entire scientific community interested in the use of advanced computational models to design composite materials and structures. The book is suitable to be used as a textbook in graduate courses on Mechanical, Civil, Aeronautical/Aerospace Engineering and Materials Science. In addition, the Editors envision that the book will also be relevant for the practitioners that need to be kept up-to-date with the recent developments on computational methods that support their activities in the optimal design of composite materials and structures.

The Editors would like to express their gratitude to all authors, who made valuable contributions to the book.

DEMEGI, Faculdade de Engenharia
Universidade do Porto, Portugal — *Pedro P. Camanho*

Department of Aeronautics, Imperial College London
United Kingdom — *Silvestre T. Pinho*

NASA Langley Research Center, United States — *Carlos G. Dávila*

Eindhoven University of Technology
The Netherlands — *Joris Remmers*

March 2008

Acknowledgements

The Editors of this volume would like to thank the European Community on Computational Methods in Applied Sciences and Engineering (ECCOMAS), the Portuguese Foundation of Science and Technology, the Portuguese Society for Applied and Computational Mechanics (APMTAC), the French Society for Composite Materials (AMAC), and the Faculty of Engineering of the University of Porto for their support to the First ECCOMAS Thematic Conference on the Mechanical Response of Composites.

A special acknowledgement is due to Professor Carlos Mota Soares from the Technical University of Lisbon, who first envisioned an ECCOMAS thematic conference on advanced composite materials, and to Mr. António Rui Melro for his outstanding support to the edition of this volume.

Contents

List of Contributors

René de Borst and Joris J.C. Remmers
Eindhoven University of Technology, Department of Mechanical Engineering, P.O. Box 513, 5600 MB Eindhoven, Netherlands,
e-mail: {r.d.borst,j.j.c.remmers}@tue.nl

Raimund Rolfes, Gerald Ernst, Matthias Vogler, and Christian Hühne
Institute for Structural Analysis, Leibniz University of Hannover, Appelstrae 9a, 30167 Hannover, Germany, e-mail: r.rolfes@isd.uni-hannover.de

Brian N. Cox
Teledyne Scientific Co., LLC, 1049 Camino Dos Rios, Thousand Oaks, CA 91360, United States of America, e-mail: bcox@teledyne.com

S. Mark Spearing
School of Engineering Sciences, University of Southampton, Southampton, SO17 1BJ, United Kingdom, e-mail: spearing@soton.ac.uk

Daniel R. Mumm
University of California, Irvine, California, United States of America,
e-mail: mumm@uci.edu

Albert Turon, Josep Costa, and Pere Maimí
AMADE, University of Girona, Spain,
e-mail: {albert.turon,josep.costa,pere.maimi}@udg.edu

Pedro P. Camanho
DEMEGI, Faculdade de Engenharia, Universidade do Porto, Rua Dr. Roberto Frias, 4200-465, Porto, Portugal, e-mail: pcamanho@fe.up.pt

Heinz E. Pettermann
Austrian Aeronautics Research (AAR)/Network for Materials and Engineering, Institute of Lightweight Design and Structural Biomechanics, Vienna University of Technology, Gusshausstrasse 2729/E317, 1040 Vienna, Austria,
e-mail: pettermann@ilsb.tuwien.ac.at

Clara Schuecker
NASA Postdoctoral Program, MS 188E NASA Langley Research Center, Hampton, VA 23681, United States of America, e-mail: schuecker@ilsb.tuwien.ac.at

Xavier Martínez and Sergio Oller
International Center of Numerical Methods in Engineering (CIMNE), c/Gran Capità s/n; 08034 Barcelona, Spain,
e-mail: xaviermg@cimne.upc.edu,sergio.oller@upc.edu

Ever Barbero
Mechanical and Aerospace Engineering, West Virginia University, P.O. Box 6106, Morgantown, WV 26505-6106, United States of America,
e-mail: ebarbero@wvu.edu

F.P. van der Meer and L.J. Sluys
Faculty of Civil Engineering and Geosciences, Delft University of Technology, P.O. Box 5048, 2600 GA Delft, The Netherlands, e-mail: f.p.vandermeer@tudelft.nl

Lucio Raimondo, Lorenzo Iannucci, Paul Robinson, and Silvestre T. Pinho
Imperial College London, Department of Aeronautics, South Kensington Campus, London SW7 2AZ, United Kingdom,
e-mail: {lucio.raimondo,lo.iannucci,p.robinson,silvestre.pinho}@imperial.ac.uk

N. Zobeiry, A. Forghani, C. McGregor, R. Vaziri, and A. Poursartip
Composites Group, Departments of Civil Engineering and Materials Engineering, The University of British Columbia, 6250 Applied Science Lane, Vancouver, BC, Canada, e-mail: reza.vaziri@ubc.ca

Ernest T.Y. Ng
Department of Mechanical Engineering, University of Victoria, British Columbia, Canada, e-mail: eng@me.uvic.ca

Afzal Suleman
Instituto de Engenharia Mecánica, Instituto Superior Técnico (IDMEC-IST), Instituto Superior Técnico, Lisbon, Portugal, e-mail: suleman@ist.utl.pt

J.A. Oliveira, J. Pinho-da-Cruz, and F. Teixeira-Dias
Departamento de Engenharia Mecânica, Universidade de Aveiro, Campus Universitário de Santiago, 3810-193 Aveiro, Portugal,
e-mail: {jalex,jpc,ftd}@ua.pt

Erik Lund and Leon S. Johansen
Department of Mechanical Engineering, Aalborg University, Pontoppidanstraede 101, DK-9220 Aalborg East, Denmark, e-mail: el@ime.aau.dk

M. Kästner, G. Haasemann, J. Brummund, and V. Ulbricht
Technische Universität Dresden, Institute of Solid Mechanics, D-01062 Dresden, Germany, e-mail: Markus.Kaestner@tu-dresden.de

Stephen R. Hallett and Michael R. Wisnom
Advanced Composites Centre for Innovation & Sciences,
Queens Building, University of Bristol, Bristol, BS8 1TR, United Kingdom,
e-mail: {stephen.hallett,m.wisnom}@bristol.ac.uk

Wen-Guang Jiang
Department of Engineering, University of Leicester, Leicester LE1 7RH,
United Kingdom, e-mail: wgj1@leicester.ac.uk

H. Miled, L. Silva, J.F. Agassant, and T. Coupez
Ecole des Mines de Paris; Centre de Mise en Forme des Matériaux, 1, Rue Claude
Daunesse, F-06904 Sophia Antipolis Cedex, UMR CNRS N° 7635, France, e-mail:
{fhoussem.miled,luisa.silva,jeanfrancois. agassant,thierry.coupezg}@ensmp.fr

Chapter 1
Computational Methods for Debonding in Composites

René de Borst and Joris J.C. Remmers

Abstract This contribution starts with a discussion of various phenomena in laminated composite structures that can lead to failure: matrix cracking, delamination between plies, and debonding and subsequent pull-out between fibres and the matrix material. The different scales are discussed at which the effect of these nonlinearities can be analysed. From these scales – the macro, meso and micro-levels – the meso-level is normally used for the analysis of delamination, which is the focus of this contribution. At this level, the plies are modelled as continua and interface elements between them conventionally serve as the framework to model delamination and debonding. After a a derivation of interface elements and a brief discussion of the cohesive–zone concept and its importance for the analysis of delamination, a particular finite element model for the plies is elaborated: the solid–like shell. Next, a more recent method to numerically model delamination is discussed, which exploits the partition–of–unity property of finite element shape functions. This approach offers advantages over interface elements, as will be discussed in detail.

1.1 Introduction

Failure in composites is governed by three mechanisms: matrix cracking, delamination, and fibre debonding and pull-out. Often, matrix cracking occurs first when loading a specimen. Together with the stress concentrations that occur near free edges and around holes, matrix cracks trigger delamination. Normally, delamination is defined as the separation of two plies of a laminated composite, although it has been observed that delamination not necessarily occurs exactly at the interface between two plies. For instance, in fibre-metal laminates delamination rather

R. de Borst and J.J.C. Remmers
Eindhoven University of Technology, Department of Mechanical Engineering, P.O. Box 513, 5600 MB Eindhoven, The Netherlands, e-mail: {r.d.borst,j.j.c.remmers}@tue.nl

resembles a matrix crack in the epoxy layer near and parallel to the aluminium-epoxy interface.

An important issue when modelling physical phenomena is the proper definition of the scale at which the (failure) mechanism under consideration is modelled. This holds a fortiori for composites, since the in-plane dimensions of a laminated composite structure exceed the length scale at which delamination, matrix cracking and fibre debonding take place by one to several orders of magnitude. This complicates an efficient, accurate and meaningful analysis. Typically, the in-plane dimensions of a laminated structure are in the order of meters, while its thickness can be just a few millimeters. Each ply is then less than a millimeter thick. Since, at least in conventional finite element analysis, each ply has to be modelled separately in order to capture delamination between two plies, and since the aspect ratio of finite elements is limited if one wishes to obtain a reliable stress prediction, the maximum in-plane dimension of a three-dimensional solid element will be around 1 cm. It is obvious that the number of elements that is needed to model each layer is already big, and the total number of elements required to model the entire structure, including possible holes and stiffened areas, can easily exceed computational capabilities when the analyst wishes to simulate nonlinear phenomena, such as delamination.

The same reasoning holds when considering matrix cracking. For most laminated composites, matrix cracks reach a saturation distance, which is in the order of the ply thickness. This implies that, when this phenomenon is to be included in the analysis in a truly discrete format – that is, matrix cracks are modelled individually and not smeared out over the plane – the in-plane discretisation must even be somewhat finer than for an analysis that includes delamination only, roughly one order of magnitude.

A further refinement of the discretisation of several orders of magnitude is required when individual fibres are to be modelled with the aim to include debonding and pull-out of individual fibres. It is evident, that such a type of modelling exceeds computational capabilities even of the most powerful computers nowadays available, if the analysis would consider the entire structure.

Multiscale approaches provide a paradigm to by-pass the problems outlined above. In these methods, the various aspects of the entire structural problem are considered at different levels of observation, each of them characterised by a well-defined *length scale*. The different levels at which analyses are carried out, are connected either through *length scale transitions*, in which the structural behaviour at a given level is homogenised to arrive at mechanical properties at a next higher level [12], or through (finite element) analyses which are conducted at two levels simultaneously and in which are connected by matching the boundary conditions at both levels [10]. In the former class of methods, the *Representative Volume Element* (*RVE*), the volume of heterogeneous material that can be considered as representative at a given level of observation and is therefore amenable to homogenisation, plays an important role.

This contribution will not address methods for length scale transition or approaches for carrying out multi-level finite element analyses. Instead, we shall focus on so-called meso-level approaches, in which delamination is assumed to

be the main degrading mechanism. For this purpose, the different levels of analysis – macro, meso and micro – are defined in the context of laminated composite structures. At the meso-level as well as at the micro-level, fracture along internal material boundaries, delamination and debonding, respectively, governs the failure behaviour. Most constitutive relations for such *interfaces* have in common that a so-called *work of separation* or *fracture energy* plays a central role. For this reason, a succinct discussion of cohesive-zone models, which are equipped with such a material parameter is included in the discussion.

Next, a solid-like shell elements will be introduced, which can be used to model the plies in a 3D-like manner, but allowing for much larger aspect ratios (up to 1,000) than standard solid elements would do. The second part of this contribution discusses a fairly recent development in numerical models for fracture, namely the partition-of-unity method. It exploits the partition-of-unity property of finite element shape functions and allows discontinuities to be inserted during a finite element analysis, either within a matrix, or, as used here, along interfaces between two materials. The concept will be elaborated for large displacement gradients, for the solid-like shell element discussed before and will be complemented by illustrative examples.

1.2 Levels of Observation

At the macroscopic or structural level the plies are normally modelled via a layered shell approach, where the different directions of the fibres in the layers are taken into account through an anisotropic elasticity model, Fig. 1.1. If this (anisotropic) elasticity model is augmented by a damage or plasticity model, degradation phenomena like matrix cracking, fibre pull-out or fibre breakage can also be taken into account,

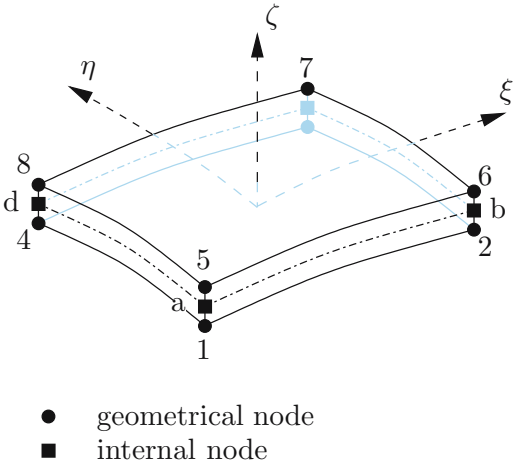

Fig. 1.1 Shell element for macroscopic analysis of a laminated composite structure

albeit in a smeared manner. At this level, the in-plane structural dimensions are the length scales that govern the boundary-value problem.

Indeed, discrete modelling of delamination, matrix cracking and debonding of fibres is not possible at this level. The level below, where the ply thickness becomes the governing length scale, allows for the modelling of delamination and matrix cracking. At this meso-level the plies are modelled as continua and can either be assumed to behave linearly elastically or can be degraded according to a damage law. In the approach suggested in [19, 20], elastic anisotropy and curing of composites are taken into account by including possible thermal and hygral effects, but eventual damage which can evolve in the plies is lumped into the interface. This approach is reasonable as long as the energy dissipation due to processes like matrix cracking is small compared to the energy needed for delamination growth, as for mode-I delaminations and for mixed-mode delaminations where the fibres are (almost) parallel to the intralaminar cracks. If this condition is not met, the interface delamination model must be supplemented by a damage model for the ply, which has been proposed in [3]. A drawback of existing damage approaches for modelling intralaminar cracks, fibre breakage and debonding is that no localisation limiter is incorporated, which renders the governing equations ill-posed at a generic stage in the loading process and can result in a severe dependence of the results on the spatial discretisation [7].

At the meso-level, delamination as a discrete process has conventionally been modelled as shown in Fig. 1.2, where the plies are considered as continua – and are discretised using standard finite elements – while the delamination is modelled in a discrete manner using special interface elements [1–3, 8, 19, 20]. Generalised plane-strain elements are often used to model free-edge delamination [19,20], while stacks of solid or shell elements and interface elements are applicable to cases of delamination near holes or other cases where a three-dimensional modelling is necessary (e.g. [22]).

The greatest level of detail is resolved in the analysis if the fibres are modelled individually. In such micro-level analyses the governing length scale is the fibre diameter. Possible debonding between fibre and matrix material is normally

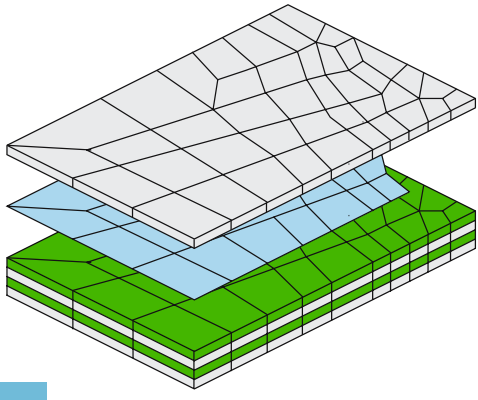

Fig. 1.2 Finite element model of a laminated composite. The individual layers are modelled with three-dimensional, generalised plane-strain or shell elements. Interface elements equipped with a cohesive-zone model are applied between the layers

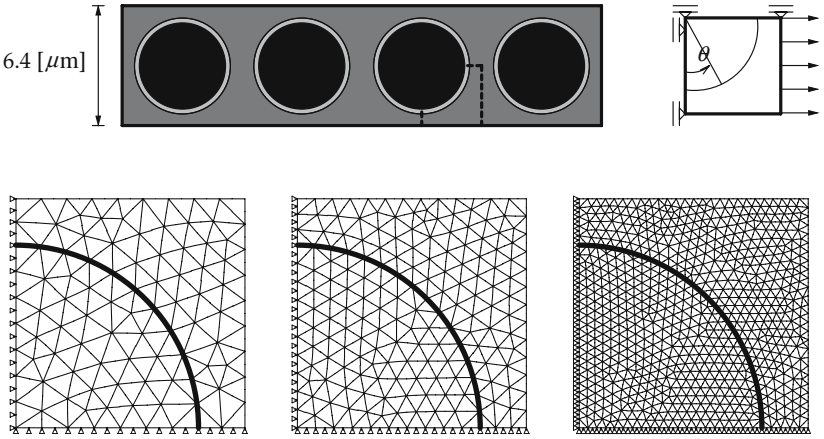

Fig. 1.3 Layer which is unidirectionally reinforced with long fibres (above) and finite element discretisations for three different levels of refinement of a representative volume element composed of a quarter of a fibre, the surrounding epoxy matrix and the interface between fibre and epoxy [21]

modelled via interface elements, equipped with cohesive-zone models, quite similar to models for delamination. An example is given in Fig. 1.3, which shows an epoxy layer, which has been reinforced uniaxially by long fibres, together with three levels of mesh refinement for a Representative Volume Element of the layer.

1.3 Zero-Thickness Interface Elements

The classical way to represent discontinuities in solids is to introduce zero-thickness interface elements between two neighbouring (solid) finite elements, e.g. Fig. 1.2 for a planar interface element. The governing kinematic quantities in interfaces are relative displacements: v_n, v_s, v_t for the normal and the two sliding modes, respectively. When collecting these relative displacements in a relative displacement vector $\mathbf{v}$, they can be related to the displacements at the upper $(+)$ and lower sides $(-)$ of the interface, $u_n^-, u_n^+, u_s^-, u_s^+, u_t^-, u_t^+$, by

$$\mathbf{v} = \mathbf{L}\mathbf{u} \tag{1.1}$$

with $\mathbf{u}^{\mathrm{T}} = (u_n^-, \ldots\ldots\ldots\ldots, u_t^+)$ and $\mathbf{L}$ an operator matrix:

$$\mathbf{L} = \begin{bmatrix} -1 & 0 & 0 \\ +1 & 0 & 0 \\ 0 & -1 & 0 \\ 0 & +1 & 0 \\ 0 & 0 & -1 \\ 0 & 0 & +1 \end{bmatrix} \tag{1.2}$$

The displacements contained in the array **u** are interpolated in a standard manner, as

$$\mathbf{u} = \mathbf{H}\mathbf{a} \tag{1.3}$$

where

$$\mathbf{H} = \text{diag}\left[\,\mathbf{h}\;\mathbf{h}\;\mathbf{h}\;\mathbf{h}\;\mathbf{h}\;\mathbf{h}\,\right] \tag{1.4}$$

with **h** a $1 \times N$ matrix containing the interpolation polynomials, and **a** the element nodal displacement array,

$$\mathbf{a} = \left(a_n^1, ..., a_n^N, a_s^1, ..., a_s^N, a_t^1, ..., a_t^N\right)^{\mathrm{T}} \tag{1.5}$$

with N the total number of nodes in the interface element. The relation between nodal displacements and relative displacements for interface elements is now derived from Eqs. (1.1) and (1.3) as:

$$\mathbf{v} = \mathbf{L}\mathbf{H}\mathbf{a} = \mathbf{B}_i\mathbf{a} \tag{1.6}$$

where the relative displacement-nodal displacement matrix $\mathbf{B}_i$ for the interface element reads:

$$\mathbf{B}_i = \begin{bmatrix} -\mathbf{h}\;\mathbf{h} & \mathbf{0}\;\mathbf{0} & \mathbf{0}\;\mathbf{0} \\ \mathbf{0}\;\mathbf{0} & -\mathbf{h}\;\mathbf{h} & \mathbf{0}\;\mathbf{0} \\ \mathbf{0}\;\mathbf{0} & \mathbf{0}\;\mathbf{0} & -\mathbf{h}\;\mathbf{h} \end{bmatrix} \tag{1.7}$$

For an arbitrarily oriented interface element the matrix $\mathbf{B}_i$ subsequently has to be transformed to the local coordinate system of the integration point or node-set.

For analyses of fracture propagation that exploit interface elements, cohesive-zone models [5, 9, 25] are used almost exclusively. In this class of fracture models, a discrete relation is adopted between the interface tractions $\mathbf{t}_i$ and the relative displacements **v**:

$$\mathbf{t}_i = \mathbf{t}_i(\mathbf{v}, \kappa) \tag{1.8}$$

with κ a history parameter. After linearisation, necessary to use a tangential stiffness matrix in an incremental-iterative solution procedure, one obtains:

$$\dot{\mathbf{t}}_i = \mathbf{T}\dot{\mathbf{v}} \tag{1.9}$$

with **T** the material tangent stiffness matrix of the discrete traction-separation law:

$$\mathbf{T} = \frac{\partial \mathbf{t}_i}{\partial \mathbf{v}} + \frac{\partial \mathbf{t}_i}{\partial \kappa}\,\frac{\partial \kappa}{\partial \mathbf{v}} \tag{1.10}$$

A key element is the presence of a work of separation or fracture energy, $\mathscr{G}_c$, which governs crack growth and enters the interface constitutive relation Eq. (1.8) in addition to the tensile strength f_t. It is defined as the work needed to create a unit area of fully developed crack:

$$\mathscr{G}_c = \int_{v_n=0}^{\infty} \sigma \mathrm{d}v_n \tag{1.11}$$

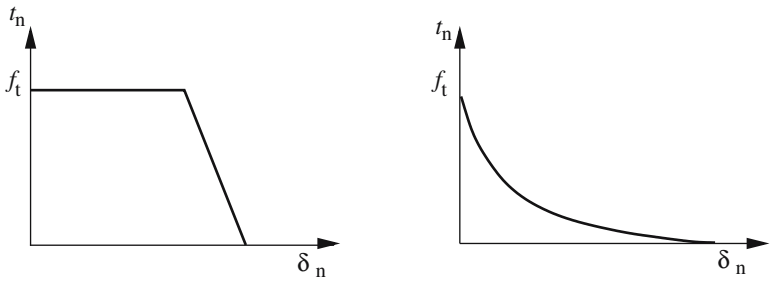

Fig. 1.4 Stress-displacement curves for ductile separation (*left*) and for quasi-brittle separation (*right*)

with σ the stress across the *fracture process zone*. It thus equals the area under the decohesion curves as shown in Fig. 1.4. Evidently, cohesive-zone models as defined above are equipped with an *internal length scale*, since the quotient $\mathscr{G}_c/E$, with E a stiffness modulus for the surrounding continuum, has the dimension of length.

Conventional interface elements have to be inserted in the finite element mesh at the beginning of the computation, and therefore, a finite stiffness must be assigned in the pre-cracking phase with at least the diagonal elements being non-zero. Prior to crack initiation, the stiffness matrix in the interface element therefore reads:

$$\mathbf{T} = \begin{bmatrix} d_n & 0 & 0 \\ 0 & d_s & 0 \\ 0 & 0 & d_t \end{bmatrix} \tag{1.12}$$

with d_n the stiffness normal to the interface and d_s and d_t the tangential stiffnesses. With the material tangent stiffness matrix $\mathbf{T}$, the element tangent stiffness matrix can be derived in a straightforward fashion, starting from the weak form of the equilibrium equations, as:

$$\mathbf{K} = \int_{\Gamma_i} \mathbf{B}_i^{\mathrm{T}} \mathbf{T} \mathbf{B}_i \mathrm{d}\Gamma \tag{1.13}$$

where the integration domain extends over the surface of the interface Γ_i. For comparison with methods that will be discussed in the remainder of this paper, we expand the stiffness matrix in the pre-cracking phase [18]:

$$\mathbf{K} = \begin{bmatrix} \mathbf{K}_n & \mathbf{0} & \mathbf{0} \\ \mathbf{0} & \mathbf{K}_s & \mathbf{0} \\ \mathbf{0} & \mathbf{0} & \mathbf{K}_t \end{bmatrix} \tag{1.14}$$

with the submatrices $\mathbf{K}_\pi$, $\pi = n,s,t$ defined as:

$$\mathbf{K}_\pi = d_\pi \begin{bmatrix} \mathbf{h}^{\mathrm{T}}\mathbf{h} & -\mathbf{h}^{\mathrm{T}}\mathbf{h} \\ -\mathbf{h}^{\mathrm{T}}\mathbf{h} & \mathbf{h}^{\mathrm{T}}\mathbf{h} \end{bmatrix} \tag{1.15}$$

with d_π the (dummy) stiffnesses in the interface prior to crack initiation.

An example where the potential of cohesive-zone models can be exploited fully using conventional discrete interface elements, is the analysis of delamination in layered composite materials [3, 19, 20]. Since the propagation of delaminations is restricted to the interfaces between the plies, inserting interface elements at these locations permits an exact simulation of the failure mode.

Due to mismatch of the Poisson effect between the layers of a laminated structure, caused by the different orientation of the fibres, interlaminar stresses will develop between the plies at the free edges. At a generic stage in the loading process, these edge stresses will lead to delamination. Depending on the stacking sequence of the laminate and the position of the delamination zone in the laminate, delamination occurs purely as mode-I delamination or as delamination due to a combination of several cracking modes, so-called mixed-mode delamination. For the three-dimensional example of Fig. 1.5, we will consider a lay-up that causes pure mode-I delamination, which is the dominant mode if delamination occurs in the mid-plane of a symmetric laminate. Consequently, only the upper (or equivalently, the lower) half of the laminate needs to be analysed. The interface delamination model was based on a damage formalism, see [22] for details.

The strip that has been analysed, has a laminate lay-up of $[25, -25, 90]_s$ and is manufactured of an AS-3501-06 graphite-epoxy. The specimen that has been analysed is depicted in Fig. 1.6 in more detail. The linear elastic ends of the specimen are a simplification of the real situation in an experiment and have been included in the analyses to limit the influence of the boundary conditions. Furthermore, to reduce the computation time, the radius of the transition zone has been taken fairly

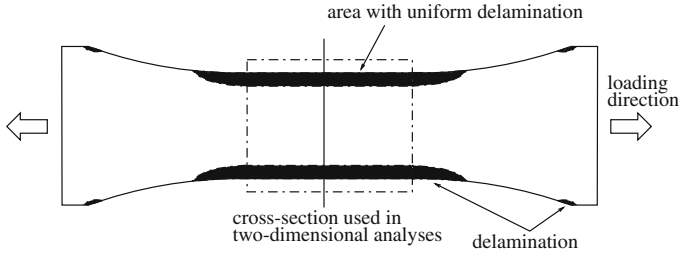

Fig. 1.5 T-bone shaped AS-3501-06 graphite-epoxy laminated strip subjected to uniaxial loading

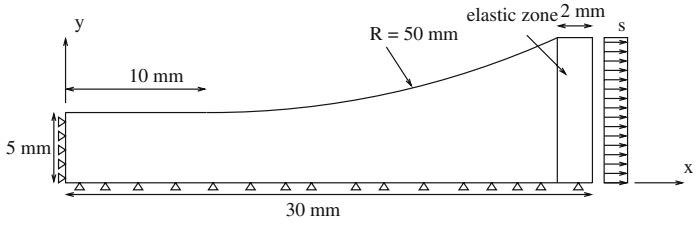

Fig. 1.6 Quarter of T-bone shaped laminated strip

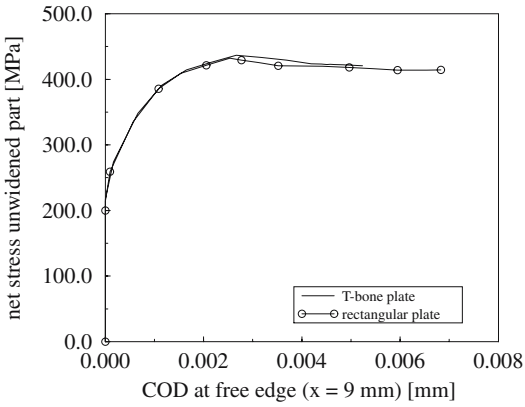

Fig. 1.7 COD *vs* axial stress for the full T-bone specimen and for an approximated 3D solution using the rectangular specimen of Fig. 1.8

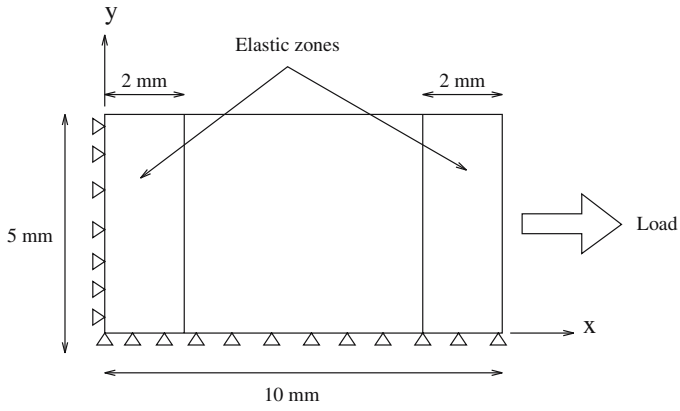

Fig. 1.8 Quarter of the rectangular specimen used in the approximate 3D solutions

small compared to data suggested in norms. The COD versus axial stress, measured as the average stress in the narrow part of the strip, is shown in Fig. 1.7.

Numerical solutions of boundary-value problems involving materials that show a descending branch after reaching a peak load level, can be highly mesh sensitive, e.g. [7]. However, in the present situation, where the degrading phenomena are limited to a discrete interface where the crack opening is controlled by a fracture energy (cohesive-zone approach), the boundary value problem remains well-posed and, consequently, no mesh sensitivity should be observed. This is confirmed in a mesh refinement study of a three-dimensional rectangular plate, Fig. 1.8, which is used to approximate the original T-bone specimen, but, because of its simpler geometry, is less expensive in mesh refinement studies. The load-displacement curves for the original T-bone specimen and the approximate 3D specimen are close, Fig. 1.7, justifying the approximation for the purpose of a mesh refinement study.

Three different meshes have been used in the calculations. The coarse mesh consisted of 20 elements over the width and 25 elements over the length of the plate.

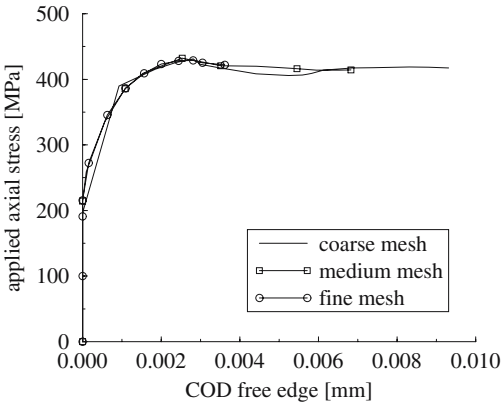

Fig. 1.9 Mesh sensitivity studies for the 3D rectangular specimen

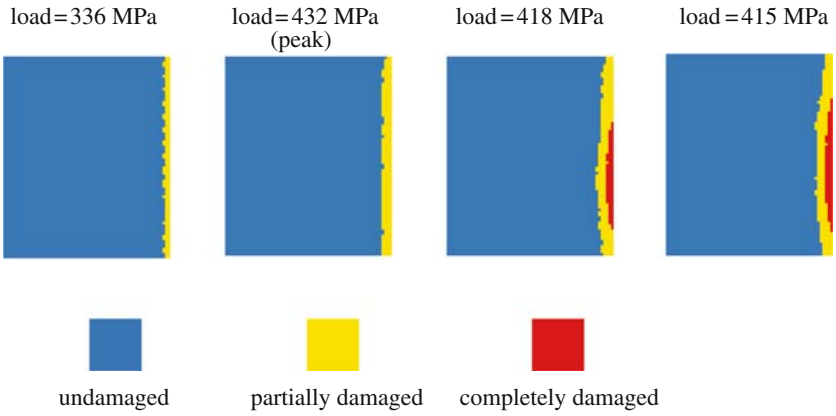

Fig. 1.10 Evolution of the delamination zone in simplified three-dimensional analysis

For the two finer meshes the element distribution over the width was not equidistant. For the 2.5 mm of the width of the plate closest to the free edge a finer mesh was used. This leads to 35 elements over the width and 25 elements over the length of the plate for the second mesh and to 70 elements over the width and 50 elements over the length of the place for the finest mesh. The crack opening displacement of a node near the centre of the free edge has been plotted versus the applied axial stress for all three meshes in Fig. 1.9. No mesh sensitivity can be noticed. In Fig. 1.10 the delamination zone of the plate is shown at several stages during the computation. Until the peak load the delamination is uniform, since the slight waviness is purely due to visualisation aspects. However, in the descending branch of Fig. 1.9 the delamination zone becomes more and more non-uniform.

Figure 1.11 shows an example of a uniaxially loaded laminate that fails under mixed-mode loading. Experimental and numerical results (which were obtained *before* the tests were carried out) show an excellent agreement, Fig. 1.11, which

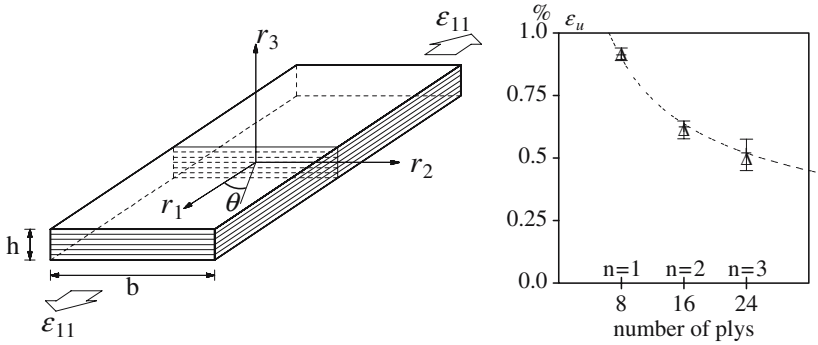

Fig. 1.11 *Left*: Uniaxially loaded laminated strip. *Right*: Computed and experimentally determined values for the ultimate strain ε_u as a function of the number of plies [20]. Results are shown for laminates consisting of 8 plies ($n = 1$), 16 plies ($n = 2$) and 24 plies ($n = 3$). The triangles, which denote the numerical results, are well within the band of experimental results. The dashed line represents the inverse dependence of the ultimate strain on the laminate thickness

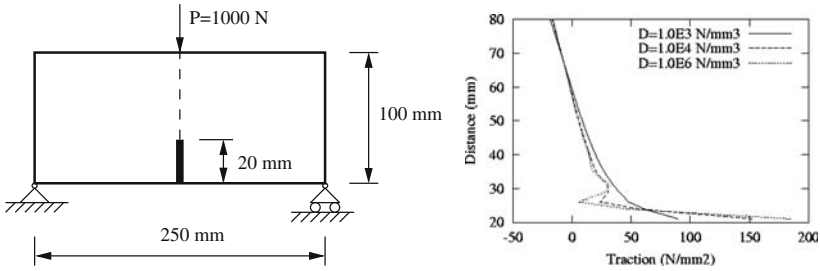

Fig. 1.12 *Left*: Geometry of symmetric, notched three-point bending beam. *Right*: Traction profiles ahead of the notch using linear interface elements with Gauss integration. Results are shown for different values of the 'dummy' stiffness $D = d_n$ in the pre-cracking phase [18]

gives the ultimate strain of the sample for different numbers of plies in the laminate [20]. A clear thickness (size) effect is obtained as a direct consequence of the inclusion of the fracture energy in the model.

As stipulated, conventional interface elements have to be inserted *a priori* in the finite element mesh. The undesired *elastic* deformations can be largely suppressed by choosing a high value for the stiffness d_n. However, the off-diagonal coupling terms of the submatrix $\mathbf{h}^T\mathbf{h}$ that enters the stiffness matrix of the interface elements, cf. Eq. (1.15), can lead to spurious traction oscillations in the pre-cracking phase for high stiffness values [18]. This, in turn, may cause erroneous crack patterns. An example of an oscillatory traction pattern ahead of a notch is given in Fig. 1.12. Moreover, when analysing dynamic fracture, spurious wave reflections can occur as a result of the introduction of such artificially high stiffness values prior to the onset of delamination. Thirdly, the necessity to align the mesh with the potential planes of delamination, restricts the modelling capabilities.

1.4 Solid-Like Shell Formulation

We consider the thick shell shown in Fig. 1.13. The position of a material point in the shell in the undeformed configuration can be written as a function of the three curvilinear coordinates $[\xi,\eta,\zeta]$:

$$\mathbf{X}(\xi,\eta,\zeta)=\mathbf{X}_0(\xi,\eta)+\zeta\mathbf{D}(\xi,\eta) \tag{1.16}$$

where $\mathbf{X}_0(\xi,\eta)$ is the projection of the point on the mid-surface of the shell and $\mathbf{D}(\xi,\eta)$ is the thickness director in this point:

$$\mathbf{X}_0(\xi,\eta)=\frac{1}{2}\left[\mathbf{X}_t(\xi,\eta)+\mathbf{X}_b(\xi,\eta)\right] \tag{1.17}$$

$$\mathbf{D}(\xi,\eta)=\frac{1}{2}\left[\mathbf{X}_t(\xi,\eta)-\mathbf{X}_b(\xi,\eta)\right] \tag{1.18}$$

The subscripts $(\cdot)_t$ and $(\cdot)_b$ denote the projections of the variable onto the top and bottom surface, respectively. The position of the material point in the deformed configuration $\mathbf{x}(\xi,\eta,\zeta)$ is related to $\mathbf{X}(\xi,\eta,\zeta)$ via the displacement field $\boldsymbol{\phi}(\xi,\eta,\zeta)$ according to:

$$\mathbf{x}(\xi,\eta,\zeta)=\mathbf{X}(\xi,\eta,\zeta)+\boldsymbol{\phi}(\xi,\eta,\zeta) \tag{1.19}$$

where:

$$\boldsymbol{\phi}(\xi,\eta,\zeta)=\mathbf{u}_0(\xi,\eta)+\zeta\mathbf{u}_1(\xi,\eta)+(1-\zeta^2)\mathbf{u}_2(\xi,\eta) \tag{1.20}$$

In this relation, $\mathbf{u}_0$ and $\mathbf{u}_1$ are the displacements of $\mathbf{X}_0$ on the shell mid-surface, and the thickness director $\mathbf{D}$, respectively:

$$\mathbf{u}_0(\xi,\eta)=\frac{1}{2}\left[\mathbf{u}_t(\xi,\eta)+\mathbf{u}_b(\xi,\eta)\right] \tag{1.21}$$

$$\mathbf{u}_1(\xi,\eta)=\frac{1}{2}\left[\mathbf{u}_t(\xi,\eta)-\mathbf{u}_b(\xi,\eta)\right] \tag{1.22}$$

and $\mathbf{u}_2(\xi,\eta)$ denotes the internal stretching of the element, which is colinear with the thickness director in the deformed configuration and is a function of an additional 'stretch' parameter w:

$$\mathbf{u}_2(\xi,\eta)=w(\xi,\eta)[\mathbf{D}+\mathbf{u}_1(\xi,\eta)] \tag{1.23}$$

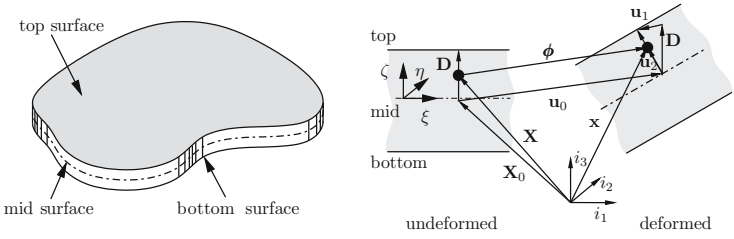

Fig. 1.13 Kinematic relations of the solid-like shell element

The displacement field $\boldsymbol{\phi}$ is considered as a function of two kinds of variables; the ordinary displacement field $\mathbf{u}$, which will be split in a displacement of the top and bottom surfaces $\mathbf{u}_t$ and $\mathbf{u}_b$, respectively, and the internal stretch parameter w:

$$\boldsymbol{\phi} = \boldsymbol{\phi}(\mathbf{u}_t, \mathbf{u}_b, w) \tag{1.24}$$

The derivation of the strains and the finite element formulation can be found in [15], or in [17].

Using the solid-like shell element, the behaviour of a Glare panel with a circular initial delamination and a sinusoidally shaped out-of-plane imperfection (with an amplitude of 0.003 mm) subject to a compressive load has been examined. The failure mechanism is slightly complicated, since the delaminated zone grows in a direction perpendicular to the main loading direction. As a result, the delaminated area transforms from a circular area into an ellipsoidal one. Consequently, the buckling mode will change as well, and some parts of the top layer will tend to move inwards. For this reason, the possibility of self-contact has been included and a contact algorithm has been activated.

The specimen of Fig. 1.14 consists of an aluminium layer with thickness $h_1 = 0.2$ mm and a Glare3 $0/90^\circ$ prepreg layer with a thickness $h_2 = 0.25$ mm. An initially circular delamination area with radius 8 mm is assumed. The layers are attached to

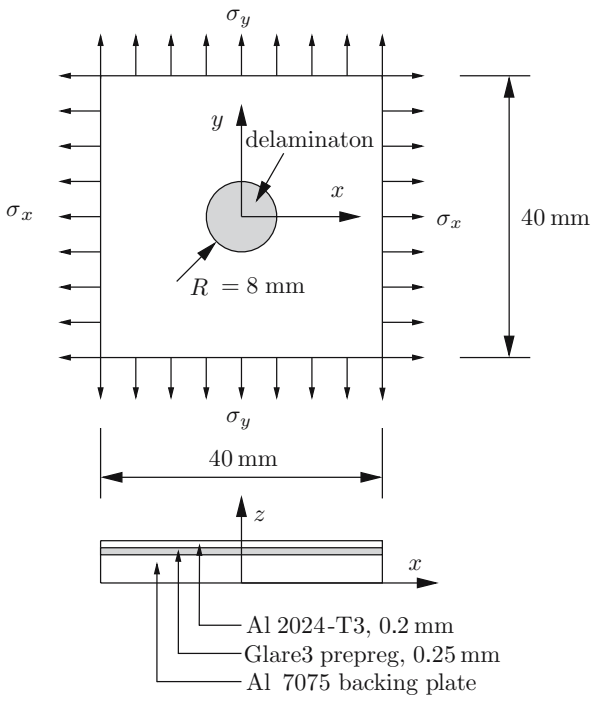

Fig. 1.14 Geometry of a Glare panel with a circular initial delamination

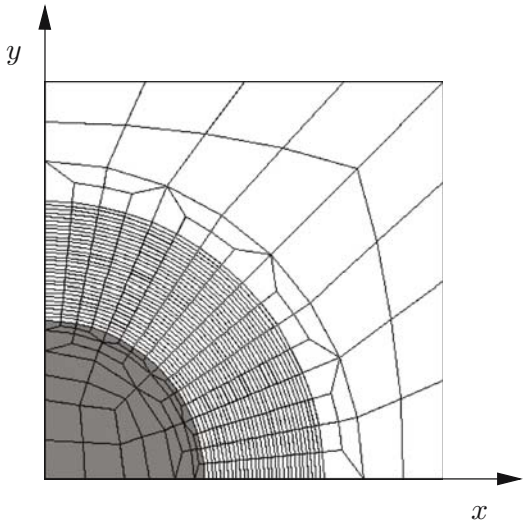

Fig. 1.15 Mesh used for the simulation of delamination growth in the Glare panel. The initial delamination is located at the darker elements. Note that just one quarter of the panel ($x > 0$, $y > 0$) has been modelled

Table 1.1 Material parameters for $0/90^\circ$ Glare3

E_{11} [MPa]	E_{22} [MPa]	E_{33} [MPa]	G_{12} [MPa]	G_{23} [MPa]	G_{13} [MPa]	ν_{12}	ν_{23}	ν_{13}
33,170	33,170	9,400	5,500	5,500	5,500	0.195	0.032	0.06

a thick backing plate in order to prevent global buckling. A uniaxial compressive loading in x-direction is considered ($\sigma_x = -\sigma_0$, $\sigma_y = 0.0$).

The finite element mesh is shown in Fig. 1.15. The material parameters for the Glare3 layer are taken from [11], see Table 1.1. The ultimate traction in normal direction in tension and compression are assumed to be $\bar{t}_n^t = 50\,\text{MPa}$ and $\bar{t}_n^c = 150\,\text{MPa}$, respectively, and the ultimate traction in the two transverse directions equals $\bar{t}_{s1} = \bar{t}_{s2} = 25\,\text{MPa}$. The work of separation is $\mathscr{G}_c = 1.1\,\text{N/mm}$. An initial stiffness of the interface elements of $d_n = 50{,}000\,\text{N/mm}^2$ has been assumed.

The analytical estimation for the local buckling load of a clamped unidirectional panel with thickness h_1 subjected to an axial compressive load σ_0 has been derived in [23]. For this configuration, the lowest critical buckling load is equal to $\sigma_0 = 113.2\,\text{MPa}$.

For the contact algorithm the penalty stiffness has been set equal to the initial stiffness of the interface elements with the delamination model, $d_{pen} = 50{,}000\,\text{MPa}$. The out-of-plane displacement of the centre point of the panel is shown in Fig. 1.16. The local buckling load is in agreement with an eigenvalue analysis [16]. Initial delamination growth does not start until a load level $\sigma_0 = 300\,\text{MPa}$, while progressive delamination begins at an external load level $\sigma_0 \approx 950\,\text{MPa}$. As this value is far beyond normal stress levels, the analysis suggests that delamination buckling is of little concern in uniaxially compressed Glare panels. As expected, the delamination extends in a direction perpendicular to the loading direction, Fig. 1.17.

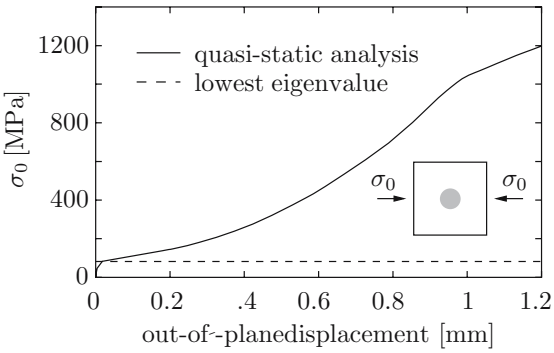

Fig. 1.16 Out-of-plane displacement of top layer versus applied axial compressive load σ_0. The dashed line corresponds to the critical buckling load obtained by an eigenvalue analysis [16]

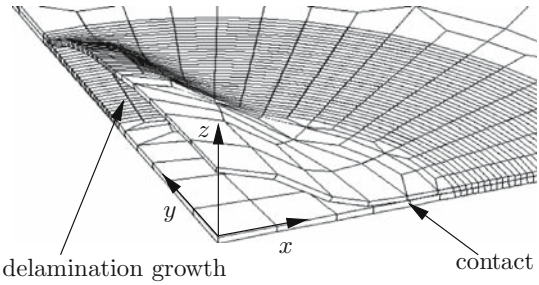

Fig. 1.17 Final deformation of the Glare laminate under uniaxial loading [16]

1.5 The Partition-of-Unity Concept

Recently, a method has emerged in which a discontinuity in the displacement field is captured exactly. It has the added benefit that it can be used advantageously at different scales, from microscopic to macroscopic analyses. The method exploits the partition-of-unity property of finite element shape functions [4]. A collection of functions ϕ_i, associated with nodes i, form a partition of unity if $\sum_{i=1}^{n} \phi_i(\mathbf{x}) = 1$ with n the number of discrete nodal points. For a set of functions ϕ_i that satisfy this property, a field u can be interpolated as follows:

$$u(\mathbf{x}) = \sum_{i=1}^{n} \phi_i(\mathbf{x}) \left(\bar{a}_i + \sum_{j=1}^{m} \psi_j(\mathbf{x}) \tilde{a}_{ij} \right) \tag{1.25}$$

with $\bar{a}_i$ the 'regular' nodal degrees-of-freedom, $\psi_j(\mathbf{x})$ the enhanced basis terms, and $\tilde{a}_{ij}$ the additional degrees-of-freedom at node i which represent the amplitudes of the jth enhanced basis term $\psi_j(\mathbf{x})$. In conventional finite element notation we can thus interpolate a displacement field as:

$$\mathbf{u} = \mathbf{N}(\bar{\mathbf{a}} + \tilde{\mathbf{N}}\tilde{\mathbf{a}}) \tag{1.26}$$

where $\mathbf{N}$ contains the standard shape functions, $\tilde{\mathbf{N}}$ the enhanced basis terms and $\bar{\mathbf{a}}$ and $\tilde{\mathbf{a}}$ collect the conventional and the additional nodal degrees-of-freedom,

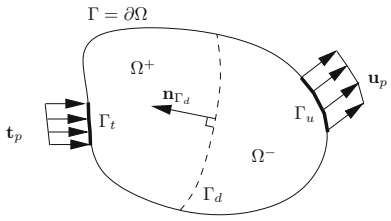

Fig. 1.18 Body composed of continuous displacement fields at each side of the discontinuity Γ_d

respectively. A displacement field that contains a single discontinuity, Fig. 1.18, can be represented by choosing [6, 14]:

$$\tilde{\mathbf{N}} = \mathscr{H}_{\Gamma_d}\mathbf{I} \tag{1.27}$$

where $\mathscr{H}_d$ is the Heaviside function which is equal to 1 when $\mathbf{x} \in \Omega^+$ and equal to 0 when $\mathbf{x} \in \Omega^-$.

Substitution into Eq. (1.26) gives

$$\mathbf{u} = \underbrace{\mathbf{N}\bar{\mathbf{a}}}_{\bar{\mathbf{u}}} + \mathscr{H}_{\Gamma_d}\underbrace{\mathbf{N}\tilde{\mathbf{a}}}_{\tilde{\mathbf{u}}} \tag{1.28}$$

Identifying $\bar{\mathbf{u}} = \mathbf{N}\bar{\mathbf{a}}$ and $\tilde{\mathbf{u}} = \mathbf{N}\tilde{\mathbf{a}}$ we observe that Eq. (1.28) exactly describes a displacement field that is crossed by a single discontinuity, but is otherwise continuous. Accordingly, the partition-of-unity property of finite element shape functions can be used in a straightforward fashion to incorporate discontinuities in a manner that preserves their discontinuous character.

We take the balance of momentum

$$\nabla \cdot \boldsymbol{\sigma} + \rho\mathbf{g} = \mathbf{0} \tag{1.29}$$

as point of departure and multiply this identity by test functions $\boldsymbol{w}$, taking them from the same space as the trial functions for $\mathbf{u}$,

$$\boldsymbol{w} = \bar{\boldsymbol{w}} + \mathscr{H}_{\Gamma_d}\tilde{\boldsymbol{w}} \tag{1.30}$$

Applying the divergence theorem and requiring that this identity holds for arbitrary $\bar{\boldsymbol{w}}$ and $\tilde{\boldsymbol{w}}$ yields the following set of coupled equations:

$$\int_\Omega \nabla^{\mathrm{sym}}\bar{\boldsymbol{w}} : \boldsymbol{\sigma}\mathrm{d}\Omega = \int_\Omega \bar{\boldsymbol{w}} \cdot \rho\mathbf{g}\mathrm{d}\Omega + \int_\Gamma \bar{\boldsymbol{w}} \cdot \mathbf{t}\mathrm{d}\Gamma \tag{1.31}$$

$$\int_{\Omega^+} \nabla^{\mathrm{sym}}\tilde{\boldsymbol{w}} : \boldsymbol{\sigma}\mathrm{d}\Omega + \int_{\Gamma_d} \tilde{\boldsymbol{w}} \cdot \mathbf{t}_i\mathrm{d}\Gamma = \int_{\Omega^+} \tilde{\boldsymbol{w}} \cdot \rho\mathbf{g}\mathrm{d}\Omega + \int_\Gamma \mathscr{H}_{\Gamma_d}\tilde{\boldsymbol{w}} \cdot \mathbf{t}\mathrm{d}\Gamma \tag{1.32}$$

where in the volume integrals the Heaviside function has been eliminated by a change of the integration domain from Ω to Ω^+. With the standard interpolation:

$$\begin{aligned} \bar{\mathbf{u}} &= \mathbf{N}\bar{\mathbf{a}}, \quad \tilde{\mathbf{u}} = \mathbf{N}\tilde{\mathbf{a}} \\ \bar{\boldsymbol{w}} &= \mathbf{N}\bar{\mathbf{w}}, \quad \tilde{\boldsymbol{w}} = \mathbf{N}\tilde{\mathbf{w}} \end{aligned} \tag{1.33}$$

and requiring that the resulting equations must hold for any admissible $\bar{\mathbf{w}}$ and $\tilde{\mathbf{w}}$, we obtain the discrete format:

$$\int_{\Omega} \mathbf{B}^{\mathrm{T}} \boldsymbol{\sigma} \mathrm{d}\Omega = \int_{\Omega} \rho \mathbf{B}^{\mathrm{T}} \mathbf{g} \mathrm{d}\Omega + \int_{\Gamma} \mathbf{N}^{\mathrm{T}} \mathbf{t} \mathrm{d}\Gamma \tag{1.34}$$

$$\int_{\Omega^+} \mathbf{B}^{\mathrm{T}} \boldsymbol{\sigma} \mathrm{d}\Omega + \int_{\Gamma_d} \mathbf{N}^{\mathrm{T}} \mathbf{t}_d \mathrm{d}\Gamma = \int_{\Omega^+} \rho \mathbf{B}^{\mathrm{T}} \mathbf{g} \mathrm{d}\Omega + \int_{\Gamma} \mathscr{H}_{\Gamma_d} \mathbf{N}^{\mathrm{T}} \mathbf{t} \mathrm{d}\Gamma \tag{1.35}$$

After linearisation, the following matrix-vector equation is obtained:

$$\begin{bmatrix} \mathbf{K}_{\bar{a}\bar{a}} & \mathbf{K}_{\bar{a}\tilde{a}} \\ \mathbf{K}_{\tilde{a}\bar{a}} & \mathbf{K}_{\tilde{a}\tilde{a}} \end{bmatrix} \begin{pmatrix} \mathrm{d}\bar{\mathbf{a}} \\ \mathrm{d}\tilde{\mathbf{a}} \end{pmatrix} = \begin{pmatrix} \mathbf{f}_{\bar{a}}^{ext} - \mathbf{f}_{\bar{a}}^{int} \\ \mathbf{f}_{\tilde{a}}^{ext} - \mathbf{f}_{\tilde{a}}^{int} \end{pmatrix} \tag{1.36}$$

with $\mathbf{f}_{\bar{a}}^{int}$, $\mathbf{f}_{\tilde{a}}^{int}$ given by the left-hand sides of Eqs. (1.31)–(1.32), $\mathbf{f}_{\bar{a}}^{ext}$, $\mathbf{f}_{\tilde{a}}^{ext}$ given by the right-hand sides of Eqs. (1.31)–(1.32) and

$$\mathbf{K}_{\bar{a}\bar{a}} = \int_{\Omega} \mathbf{B}^{\mathrm{T}} \mathbf{D} \mathbf{B} \mathrm{d}\Omega \tag{1.37}$$

$$\mathbf{K}_{\bar{a}\tilde{a}} = \int_{\Omega^+} \mathbf{B}^{\mathrm{T}} \mathbf{D} \mathbf{B} \mathrm{d}\Omega \tag{1.38}$$

$$\mathbf{K}_{\tilde{a}\bar{a}} = \int_{\Omega^+} \mathbf{B}^{\mathrm{T}} \mathbf{D} \mathbf{B} \mathrm{d}\Omega \tag{1.39}$$

$$\mathbf{K}_{\tilde{a}\tilde{a}} = \int_{\Omega^+} \mathbf{B}^{\mathrm{T}} \mathbf{D} \mathbf{B} \mathrm{d}\Omega + \int_{\Gamma_d} \mathbf{N}^{\mathrm{T}} \mathbf{T} \mathrm{d}\Gamma \tag{1.40}$$

If the material tangential stiffness matrices of the bulk and the interface, $\mathbf{D}$ and $\mathbf{T}$ respectively, are symmetric, the total tangential stiffness matrix remains symmetric. It is emphasised that in this concept, the additional degrees-of-freedom *cannot* be condensed at element level, because it is node-oriented and not element-oriented. It is this property which makes it possible to represent a discontinuity such that it is continuous at interelement boundaries.

The partition-of-unity property of finite element shape functions is a powerful method to introduce cohesive surfaces in continuum finite elements [13, 26, 27]. Using the interpolation of Eq. (1.28) the relative displacement at the discontinuity Γ_d is obtained as:

$$\mathbf{v} = \tilde{\mathbf{u}} \,|_{\mathbf{x} \in \Gamma_d} \tag{1.41}$$

and the tractions at the discontinuity are derived from Eq. (1.8). A key feature of the method is the possibility of extending a (cohesive) crack during the calculation in an arbitrary direction, independent of the structure of the underlying finite element mesh. It is also interesting to note that the field $\tilde{\mathbf{u}}$ does not have to be constant. The only requirement that is imposed is continuity.

When the discontinuity coincides with a side of the element, the traditional interface element formulation is retrieved. For this, we expand the term in $\mathbf{K}_{\tilde{a}\tilde{a}}$ which relates to the discontinuity as

$$\int_{\Gamma_i} \mathbf{H}^{\mathrm{T}}\mathbf{T}\mathbf{H}\mathrm{d}\Gamma = \begin{bmatrix} \mathbf{K}_n & \mathbf{0} & \mathbf{0} \\ \mathbf{0} & \mathbf{K}_s & \mathbf{0} \\ \mathbf{0} & \mathbf{0} & \mathbf{K}_t \end{bmatrix} \tag{1.42}$$

with $\mathbf{K}_\pi = d_\pi \mathbf{h}^{\mathrm{T}}\mathbf{h}$, cf. [24], which closely resembles Eqs. (1.14)–(1.15). Defining the sum of the nodal displacements $\bar{\mathbf{a}}$ and $\tilde{\mathbf{a}}$ as primary variable $\mathbf{a}$ on the + side of the interface and setting $\mathbf{a} = \bar{\mathbf{a}}$ at the – side and rearranging then leads to the standard interface formulation.

However, even though formally the matrices can coincide for the partition–of–unity based method and for the conventional interface formulation, both concepts are quite different. Indeed, simulations of delamination using the partition-of-unity property of finite element shape functions offer advantages. Because the discontinuity does not have to be inserted a priori, no (dummy) stiffness is needed in the elastic regime. Indeed, there does not have to be an elastic regime, since the discontinuity can be activated at the onset of cracking. Consequently, the issue of spurious traction oscillations in the elastic phase becomes irrelevant. Also, the lines of the potential delamination planes no longer have to coincide with element boundaries. They can lie at arbitrary locations inside elements and unstructured meshes can be used.

The above approach for capturing discontinuities can be generalised to large displacement gradients in a straightforward and consistent manner. To this end, one extends Eq. (1.28) as:

$$\mathbf{x} = \mathbf{X} + \bar{\mathbf{u}} + \mathscr{H}_{\Gamma_d^0}\tilde{\mathbf{u}} \tag{1.43}$$

with $\mathscr{H}_{\Gamma_d^0}$ the Heaviside function at the interface in the reference configuration, Γ_d^0. The deformation gradient follows by differentiation:

$$\mathbf{F} = \bar{\mathbf{F}} + \mathscr{H}_{\Gamma_d^0}\tilde{\mathbf{F}} + \delta_{\Gamma_d^0}(\tilde{\mathbf{u}} \otimes \mathbf{n}_{\Gamma_d^0}) \tag{1.44}$$

with $\bar{\mathbf{F}} = \boldsymbol{I} + \partial\bar{\mathbf{u}}/\partial\mathbf{X}$, $\tilde{\mathbf{F}} = \partial\tilde{\mathbf{u}}/\partial\mathbf{X}$ and $\delta_{\Gamma_d^0}$ the Dirac function at the interface in the reference configuration.

With aid of Nanson's relation for the normal $\mathbf{n}$ to a surface Γ:

$$\mathbf{n} = \det\mathbf{F}(\mathbf{F}^{-\mathrm{T}})\mathbf{n}_{\Gamma^0}\frac{\mathrm{d}\Gamma^0}{\mathrm{d}\Gamma} \tag{1.45}$$

the expressions for the normals at the $-$ side and at the $+$ side of the interface can be derived:

$$\mathbf{n}_{\Gamma_d^-} = \det\bar{\mathbf{F}}(\bar{\mathbf{F}}^{-\mathrm{T}})\mathbf{n}_{\Gamma_d^0}\frac{\mathrm{d}\Gamma_d^0}{\mathrm{d}\Gamma_d^-} \tag{1.46a}$$

$$\mathbf{n}_{\Gamma_d^+} = \det(\bar{\mathbf{F}} + \tilde{\mathbf{F}})(\bar{\mathbf{F}} + \tilde{\mathbf{F}})^{-\mathrm{T}}\mathbf{n}_{\Gamma_d^0}\frac{\mathrm{d}\Gamma_d^0}{\mathrm{d}\Gamma_d^+} \tag{1.46b}$$

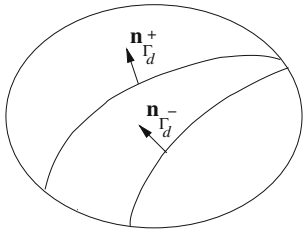

Fig. 1.19 Body crossed by a discontinuity Γ_d with normals $\mathbf{n}_{\Gamma_d^-}$ and $\mathbf{n}_{\Gamma_d^+}$ at both sides of the discontinuity

see Fig. 1.19. Distinction between $\mathbf{n}_{\Gamma_d^-}$ and $\mathbf{n}_{\Gamma_d^+}$ is possible because $\tilde{\mathbf{u}}$ is not spatially constant. In the cohesive-zone approach, interface tractions $\mathbf{t}_i$ are transmitted between Γ^- and Γ^+ with different normals $\mathbf{n}_{\Gamma_d^-}$ and $\mathbf{n}_{\Gamma_d^+}$. In a heuristic assumption, it has been assumed that an average normal can be defined for use within the cohesive-zone model [26]:

$$\mathbf{n}_{\Gamma_d^*} = \det(\bar{\mathbf{F}} + \frac{1}{2}\tilde{\mathbf{F}})(\bar{\mathbf{F}} + \frac{1}{2}\tilde{\mathbf{F}})^{-\mathrm{T}}\mathbf{n}_{\Gamma_d^0}\frac{\mathrm{d}\Gamma_d^0}{\mathrm{d}\Gamma_d^*} \tag{1.47}$$

We now recall the equilibrium equation in the current configuration, cf. Eq. (1.29):

$$\nabla_{\mathbf{x}} \cdot \boldsymbol{\sigma} + \rho\mathbf{g} = \mathbf{0}$$

In a Bubnov-Galerkin method the test functions $\boldsymbol{w}$ for a single discontinuity are given by:

$$\boldsymbol{w} = \bar{\boldsymbol{w}} + \mathscr{H}_{\Gamma_d^0}\tilde{\boldsymbol{w}} \tag{1.48}$$

Multiplying with this test function, integrating over the current domain Ω and requiring that the result holds for arbitrary $\bar{\boldsymbol{w}}$ and $\tilde{\boldsymbol{w}}$ yields:

$$\int_\Omega \nabla_{\mathbf{x}}\bar{\boldsymbol{w}} : \boldsymbol{\sigma}\mathrm{d}\Omega = \int_\Omega \bar{\boldsymbol{w}} \cdot \rho\mathbf{g}\mathrm{d}\Omega + \int_\Gamma \bar{\boldsymbol{w}} \cdot \mathbf{t}\mathrm{d}\Gamma \tag{1.49a}$$

$$\int_{\Omega^+} \nabla_{\mathbf{x}}\tilde{\boldsymbol{w}} : \boldsymbol{\sigma}\mathrm{d}\Omega + \int_{\Gamma_d} \tilde{\boldsymbol{w}} \cdot \mathbf{t}_i\mathrm{d}\Gamma = \int_{\Omega^+} \tilde{\boldsymbol{w}} \cdot \rho\mathbf{g}\mathrm{d}\Omega + \int_\Gamma \mathscr{H}_{\Gamma_d}\tilde{\boldsymbol{w}} \cdot \mathbf{t}\mathrm{d}\Gamma \tag{1.49b}$$

with the subscript $\mathbf{x}$ signifying differentiation with respect to the current configuration and $\mathbf{t}_d = \mathbf{n}_{\Gamma_d^*} \cdot \boldsymbol{\sigma}$ the traction at the discontinuity in the current configuration. With a standard interpolation:

$$\bar{\boldsymbol{w}} = \mathbf{N}\bar{\mathbf{w}}, \quad \tilde{\boldsymbol{w}} = \mathbf{N}\tilde{\mathbf{w}} \tag{1.50}$$

where $\mathbf{N}$ contains the interpolation polynomials and $\bar{\mathbf{w}}$ and $\tilde{\mathbf{w}}$ contain the discrete values for the test functions, the discrete format of Eqs. (1.49a)–(1.49b) reads:

$$\int_\Omega \mathbf{B}^{\mathrm{T}}\boldsymbol{\sigma}\mathrm{d}\Omega = \int_\Omega \rho\mathbf{B}^{\mathrm{T}}\mathbf{g}\mathrm{d}\Omega + \int_\Gamma \mathbf{N}^{\mathrm{T}}\mathbf{t}\mathrm{d}\Gamma \tag{1.51a}$$

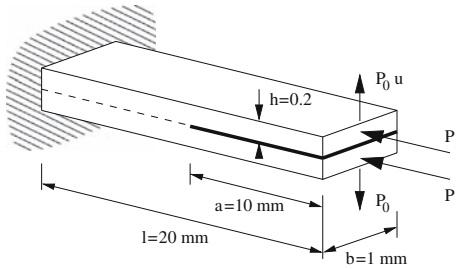

Fig. 1.20 Double cantilever beam with initial delamination under compression

$$\int_{\Omega^+} \mathbf{B}^{\mathrm{T}}\boldsymbol{\sigma}\mathrm{d}\Omega + \int_{\Gamma_d} \mathbf{N}^{\mathrm{T}}\mathbf{t}_i\mathrm{d}\Gamma = \int_{\Omega^+} \rho\mathbf{B}^{\mathrm{T}}\mathbf{g}\mathrm{d}\Omega + \int_{\Gamma} \mathscr{H}_{\Gamma_d}\mathbf{N}^{\mathrm{T}}\mathbf{t}\mathrm{d}\Gamma \tag{1.51b}$$

After substitution of the constitutive relations for the plies and that for the interface, and transforming back to the reference configuration, a nonlinear set of algebraic equations results, which can be solved in a standard manner using an incremental-iterative procedure. If a Newton-Raphson procedure is used, these equations have to be linearised in order to derive the structural tangential stiffness matrix [26].

To exemplify the possibilities of this approach to model the combined failure mode of delamination growth and local buckling we consider the double cantilever beam of Fig. 1.20 with an initial delamination length $a = 10$ mm. Both layers are made of the same material with Young's modulus $E = 135{,}000$ N/mm^2 and Poisson's ratio $\nu = 0.18$. Due to symmetry in the geometry of the model and the applied loading, delamination propagation can be modelled with an exponential mode-I decohesion law:

$$t^n_{\mathrm{dis}} = t_{\mathrm{ult}} \exp\left(-\frac{t_{\mathrm{ult}}}{\mathscr{G}_c} v^n_{\mathrm{dis}}\right) \tag{1.52}$$

where t^n_{dis} and v^n_{dis} are the normal traction and displacement jump respectively. The ultimate traction t_{ult} is equal to 50 N/mm^2, the work of separation is $\mathscr{G}_c = 0.8$ N/mm.

This case, in which failure is a consequence of a combination of delamination growth and structural instability, has been analysed using conventional interface elements in [2]. The beam is subjected to an axial compressive force $2P$, while two small perturbing forces P_0 are applied to trigger the buckling mode. Two finite element discretisations have been employed, a fine mesh with three elements over the thickness and 250 elements along the length of the beam, and a coarse mesh with only one (!) element over the thickness and 100 elements along the length. Fig. 1.21 shows that the calculation with the coarse mesh approaches the results for the fine mesh closely. For instance, the numerically calculated buckling load is in good agreement with the analytical solution. Steady-state delamination growth starts around a lateral displacement $u = 4$ mm. From this point onwards, delamination growth interacts with geometrical instability. Fig. 1.22 presents the deformed beam for the coarse mesh at a tip displacement $u = 6$ mm. Note that the displacements are plotted at true scale, but that the difference in displacement between the upper and

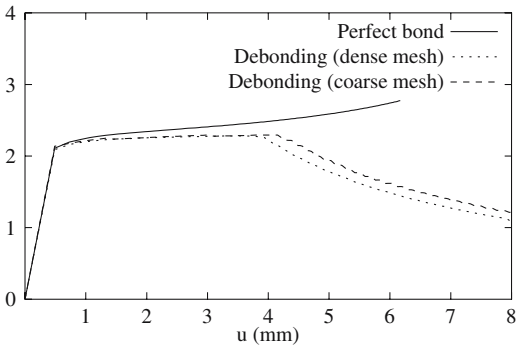

Fig. 1.21 Load-displacement curves for delamination-buckling test

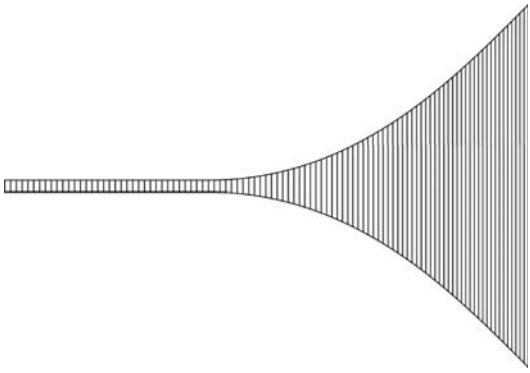

Fig. 1.22 Deformation of coarse mesh after buckling and delamination growth (true scale)

lower parts of the beam is for the major part due to the delamination and that the strains remain small.

1.6 Delamination in a Solid-Like Shell Element

The excellent results obtained in this example for the coarse discretisation have motivated the development of a layered plate/shell element in which delaminations can occur inside the element between each of the layers [17]. Because of the absence of rotational degrees-of-freedom, the solid-like shell element was taken as a point of departure. The shell of Fig. 1.23 is crossed by a discontinuity surface Γ_d^0 which is assumed to be parallel to the mid-surface of the thick shell. The displacement field $\boldsymbol{\phi}(\xi,\eta,\zeta)$ can now be regarded as a continuous regular field $\bar{\boldsymbol{\phi}}$ with an additional continuous field $\tilde{\boldsymbol{\phi}}$ that determines the magnitude of the displacement jump. The position of a material point in the deformed configuration can then be written as:

$$\mathbf{x} = \mathbf{X} + \bar{\boldsymbol{\phi}} + \mathscr{H}_{\Gamma_d^0}\tilde{\boldsymbol{\phi}} \tag{1.53}$$

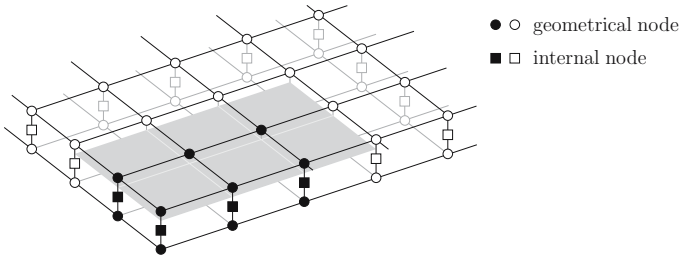

Fig. 1.23 Enhanced nodes (black) whose support contains a discontinuity (grey surface). The nodes on the edge of the discontinuity are not enhanced in order to ensure a zero delamination opening at the tip

Since the displacement field $\boldsymbol{\phi}$ is a function of the variables $\mathbf{u}_t$, $\mathbf{u}_b$ and w, we need to decompose these three terms as:

$$\begin{aligned} \mathbf{u}_t &= \bar{\mathbf{u}}_t + \mathscr{H}_{\Gamma_d^0}\tilde{\mathbf{u}}_t \\ \mathbf{u}_b &= \bar{\mathbf{u}}_b + \mathscr{H}_{\Gamma_d^0}\tilde{\mathbf{u}}_b \\ w &= \bar{w} + \mathscr{H}_{\Gamma_d^0}\tilde{w} \end{aligned} \tag{1.54}$$

Inserting Eq. (1.54) into Eqs. (1.21)–(1.23) gives:

$$\begin{aligned} \mathbf{u}_0 &= \bar{\mathbf{u}}_0 + \mathscr{H}_{\Gamma_d^0}\tilde{\mathbf{u}}_0 \\ \mathbf{u}_1 &= \bar{\mathbf{u}}_1 + \mathscr{H}_{\Gamma_d^0}\tilde{\mathbf{u}}_1 \\ \mathbf{u}_2 &= \bar{\mathbf{u}}_2 + \mathscr{H}_{\Gamma_d^0}\tilde{\mathbf{u}}_2 \end{aligned} \tag{1.55}$$

where:

$$\begin{aligned} \bar{\mathbf{u}}_0 &= \frac{1}{2}\left[\bar{\mathbf{u}}_t + \bar{\mathbf{u}}_b\right] \qquad & \tilde{\mathbf{u}}_0 &= \frac{1}{2}\left[\tilde{\mathbf{u}}_t + \tilde{\mathbf{u}}_b\right] \\ \bar{\mathbf{u}}_1 &= \frac{1}{2}\left[\bar{\mathbf{u}}_t - \bar{\mathbf{u}}_b\right] \qquad & \tilde{\mathbf{u}}_1 &= \frac{1}{2}\left[\tilde{\mathbf{u}}_t - \tilde{\mathbf{u}}_b\right] \\ \bar{\mathbf{u}}_2 &= \bar{w}\left[\mathbf{D} + \bar{\mathbf{u}}_1\right] \qquad & \tilde{\mathbf{u}}_2 &= \tilde{w}\left[\mathbf{D} + \bar{\mathbf{u}}_1 + \tilde{\mathbf{u}}_1\right] + \bar{w}\tilde{\mathbf{u}}_1 \end{aligned} \tag{1.56}$$

It is noted that the enhanced part of the internal stretch parameter $\mathbf{u}_2$, i.e. $\tilde{\mathbf{u}}_2$, contains regular variables as well as additional variables.

The magnitude of the displacement jump $\mathbf{v}$ at the internal discontinuity $\Gamma_{d,0}$ is equal to the magnitude of the additional displacement field at the discontinuity ζ_d. Neglecting terms that vary quadratically in the thickness direction, we obtain:

$$\mathbf{v} = \tilde{\mathbf{u}}_0 + \zeta_d \tilde{\mathbf{u}}_1 \tag{1.57}$$

The additional displacement field is described by an additional set of degrees-of-freedom which are added to the existing nodes of the model. Figure 1.23 shows

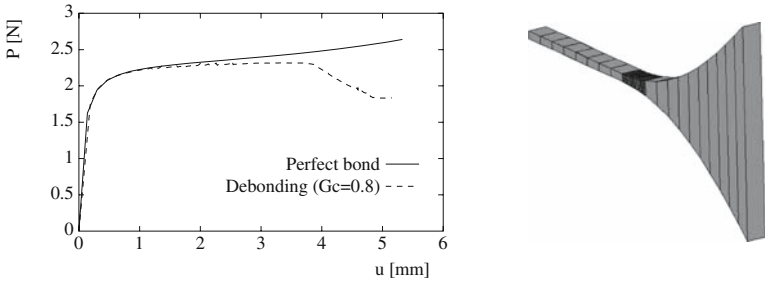

Fig. 1.24 Load-displacement curve and deformations of shell model after buckling and delamination growth (true scale) [17]

the activation of these additional sets of degrees of freedom for a given (static) delamination surface in the model. Both the geometrical and the internal nodes are enhanced when the corresponding element is crossed by the discontinuity. This implies that each geometrical node now contains three additional degrees-of-freedom next to the three regular ones, giving six degrees-of-freedom in total. Each internal node has one extra degree-of-freedom added to the single regular degree-of-freedom. As in the continuum elements, the discontinuity is assumed to always stretch through an entire element. This avoids the need for complicated algorithms to describe the stress state in the vicinity of a delamination front within an element. As a consequence, the discontinuity 'touches' the boundary of an element. The geometrical and internal nodes that support this boundary are not enhanced in order to assure a zero crack tip condition. The elaboration of the strains, the equilibrium equations and the linearisation follow standard lines [17].

The example of Fig. 1.20 has been reanalysed with a mesh composed of eight node enhanced solid-like shell elements [17]. Again, only one element in thickness direction has been used. In order to capture delamination growth correctly, the mesh has been refined locally. Figure 1.24 shows the lateral displacement u of the beam as a function of the external force P. The load-displacement response for a specimen with a perfect bond (no delamination growth) is given as a reference. The numerically calculated buckling load is in agreement with the analytical solution. Steady delamination growth starts around a lateral displacement $u \approx 4$ mm, which is in agreement with the previous simulations, e.g. [2].

1.7 Concluding Remarks

Numerical models with separate finite elements for interfaces and plies are a powerful tool to analyse delaminations in composite structures, but have some restrictions. Because the interface elements have to be inserted a priori, spurious elastic deformations will occur prior to delamination onset. These undesired deformations can be partially suppressed by assigning a high value to the normal stiffness modulus

in the elastic range, but this can result in traction oscillations ahead of the crack tip and in erroneous wave reflections when dynamic delaminations are analysed. Furthermore, this methodology restricts the freedom of the discretisation in the sense that element boundaries have to be aligned with surfaces of potential delamination.

Exploiting the partition-of-unity property of finite element shape functions enables placement of (cohesive) interfaces at arbitrary positions at the onset of delamination. Since interfaces are created at the moment when they are needed, the necessity of assigning an artificially high stiffness in the elastic regime no longer exists and traction oscillations or spurious wave reflections are no longer an issue. The fact that alignment of the discretisation with potential planes of delamination is no longer necessary, makes possible that unstructured meshes can be used. The versatility of the method is further enhanced by a consistent extension to large strains and by the incorporation in a solid-like shell element. It is the latter extension which enables large-scale computations of composite structures taking into account delaminations.

References

1. Alfano G, Crisfield MA (2001) Finite element interface models for the delamination analysis of laminated composites: mechanical and computational issues. Int J Numer Methods Eng 50:1701–1736
2. Allix O, Corigliano A (1999) Geometrical and interfacial non-linearities in the analysis of delamination in composites. Int J Solids Struct 36:2189–2216
3. Allix O, Ladevèze P (1992) Interlaminar interface modelling for the prediction of delamination. Compos Struct 22:235–242
4. Babuška I, Melenk JM (1997) The partition of unity method. Int J Numer Methods Eng 40:727–758
5. Barenblatt GI (1962) The mathematical theory of equilibrium cracks in brittle fracture. Adv Appl Mech 7:55–129
6. Belytschko T, Black T (1999) Elastic crack growth in finite elements with minimal remeshing. Int J Numer Methods Eng 45:601–620
7. de Borst R (2004) Damage, material instabilities, and failure. In: Stein E, de Borst R, Hughes TJR (ed) Encyclopedia of Computational Mechanics, Volume 2, Chapter 10. Wiley, Chichester
8. Corigliano A (1993) Formulation, identification and use of interface models in the numerical analysis of composite delamination. Int J Solids Struct 30:2779–2811
9. Dugdale DS (1960) Yielding of steel sheets containing slits. J Mech Phys Solids 8:100–108
10. Feyel F, Chaboche JL (2000) FE^2 multiscale approach for modelling the elastoviscoplastic behaviour of long fibre SiC/Ti composite materials. Comput Methods Appl Mech Eng 183:309–330
11. Hashagen F, de Borst R (2000) Numerical assessment of delamination in fibre metal laminates. Comput Methods Appl Mech Eng 185:141–159
12. Ladevèze P, Lubineau G (2002) An enhanced mesomodel for laminates based on micromechanics. Compos Sci Technol 62:533–541
13. Moës N, Belytschko T (2002) Extended finite element method for cohesive crack growth. Eng Fract Mech 69:813–833
14. Moës N, Dolbow J, Belytschko T (1999) A finite element method for crack growth without remeshing. Int J Numer Methods Eng 46:131–150
15. Parisch H (1995) A continuum-based shell theory for non-linear applications. Int J Numer Methods Eng 38:1855–1883

16. Remmers JJC, de Borst R (2002) Delamination buckling of Fibre-Metal Laminates under compressive and shear loadings. 43rd AIAA/ASME/ASCE/AHS/ASC Structures, Structural Dynamics and Materials Conference, Denver, CO, CD-ROM
17. Remmers JJC, Wells GN, de Borst R (2003) A solid–like shell element allowing for arbitrary delaminations. Int J Numer Methods Eng 58:2013–2040
18. Schellekens JCJ, de Borst R (1992) On the numerical integration of interface elements. Int J Numer Methods Eng 36:43–66
19. Schellekens JCJ, de Borst R (1993) A non-linear finite element approach for the analysis of mode-I free edge delamination in composites. Int J Solids Struct 30:1239–1253
20. Schellekens JCJ, de Borst R (1994) Free edge delamination in carbon-epoxy laminates: a novel numerical/experimental approach. Compos Struct 28:357–373
21. Schellekens JCJ, de Borst R (1994) The application of interface elements and enriched or rate-dependent continuum models to micro-mechanical analyses of fracture in composites. Comput Mech 14:68–83
22. Schipperen JHA, Lingen FJ (1999) Validation of two–dimensional calculations of free edge delamination in laminated composites. Compos Struct 45:233–240
23. Shivakumar K, Whitcomb J (1985) Buckling of a sublaminate in a quasi-isotropic composite laminate. J Compos Mater 19:2–18
24. Simone A (2004) Partition of unity–based discontinuous elements for interface phenomena: computational issues. Commun Numer Methods Eng 20:465–478
25. Turon A, Dávila CG, Camanho PP, Costa J (2007) An engineering solution for mesh size effects in the simulation of delamination using cohesive zone models. Eng Fract Mech 74:1665–1682
26. Wells GN, de Borst R, Sluys LJ (2002) A consistent geometrically non–linear approach for delamination. Int J Numer Methods Eng 54:1333–1355
27. Wells GN, Sluys LJ (2001) A new method for modeling cohesive cracks using finite elements. Int J Numer Methods Eng 50:2667–2682

Chapter 2
Material and Failure Models for Textile Composites

Raimund Rolfes, Gerald Ernst, Matthias Vogler, and Christian Hühne

Abstract The complex three-dimensional structure of textile composites makes the experimental determination of the material parameters very difficult. Not only the number of constants increases, but especially through-thickness parameters are hardly quantifiable. Therefore an information-passing multiscale approach for computation of textile composites is presented as an enhancement of tests, but also as an alternative to tests. The multiscale approach consists of three scales and includes unit cells on micro- and mesoscale. With the micromechanical unit cell stiffnesses and strengths of unidirectional fiber bundle material can be determined. The mesomechanical unit cell describes the fiber architecture of the textile composite and provides stiffnesses and strengths for computations on macroscale. By comparison of test data and results of numerical analysis the numerical models are validated.

To consider the special characteristics of epoxy resin and fiber bundles two material models are developed. Both materials exhibit load dependent yield behavior, especially under shear considerable plastic deformations occur. This non-linear hardening is considered via tabulated input, i.e. experimental test data is used directly without time consuming parameter identification. A quadratic criterion is used to detect damage initiation based on stresses. Thereafter softening is computed with a strain energy release rate formulation. To alleviate mesh-dependency this formulation is combined with the voxel-meshing approach.

Epoxy resin is modeled with the first, isotropic elastoplastic material model regarding a pressure dependency in the yield locus. As the assumption of constant volume under plastic flow does not hold for epoxy resin, a special plastic potential is chosen to account for volumetric plastic straining.

To describe the material behavior of the fiber bundles, the second, transversely isotropic, elastoplastic material model is developed. The constitutive equations for the description of anisotropy are formulated in the format of isotropic tensor

R. Rolfes, G. Ernst, M. Vogler, and C. Hühne
Institute for Structural Analysis, Leibniz University of Hannover, Appelstraße 9a, 30167 Hannover, Germany, e-mail: r.rolfes@isd.uni-hannover.de

functions by means of structural tensors. Opposed to the isotropic case the hardening curves are not obtained by experiment but by simulations performed done with the micromechanical model. So the hardening and softening curves from the micro model simulation, reflecting the homogenized material parameters from the micro model, are submitted to the next scale, the mesomechanical model.

2.1 Introduction

Composite materials have been successfully used since the 1960s for structural applications, because of their structural advantages of high specific strength and stiffness.

This first generation of materials are unidirectional composites, mostly based on prepreg materials. The prepreg composites are characterized by good quality, high stiffness and strength properties, but suffer from short storage life and high cost of the uncured material.

Textile composites describe the broad range of polymer composite materials with textile reinforcements, from woven and non-crimp commodity fabrics to three dimensional textiles. In a general manner textile composites are based on textile preforms manufactured by some textile processing technique and on some resin infiltration and consolidation technique. Examples of textile preforms are shown in Fig. 2.1. In contrast to prepreg materials the dry preform is infiltrated with a fluent resin. During the infiltration process the fibers are held in place by the textile structure of the preform. Whereas in a prepreg-composite fibers are dispersed relatively homogeneous, a textile composite has a more heterogeneous structure with epoxy resin pockets and fiber bundles, consisting of fibers and epoxy resin.

Textile composites are characterized by lower manufacturing costs and higher integrated parts compared to prepreg-composites. They are easy to handle, have a good to excellent drapability and hence are widely employed in aircraft, boat and defense industry.

In contrast to composites consisting of UD-lamina the geometry and structure of textile composites is much more complex. Orthotropic or even general anisotropic material behavior is observed due to through-thickness reinforcements instead of

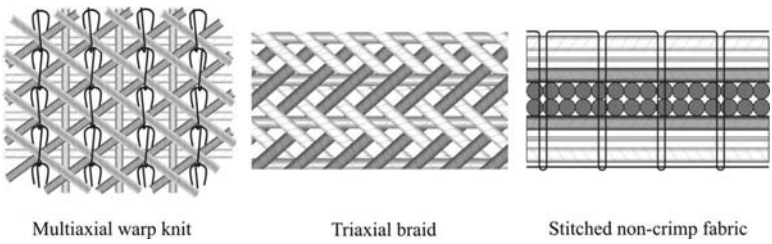

Fig. 2.1 Different preforms used in textile composites

transversely isotropic material behavior of UD-lamina. Fiber undulations reduce the in-plane mechanical performance depending on the specific textile architecture. The applicability of analytical methods to determine the stiffness and strength properties is limited.

Caused by the lack of analytical methods and the complex structure it is common to model the textile architecture with a representative volume element (RVE) using the finite element method to determine stiffness and strength properties. Cox et al. [2] proposed a binary model that describes the roving architecture with truss-elements. Due to the use of truss elements it is very efficient. This method was taken up by Haasemann et al. [8] and used for the homogenization of properties for a Cosserat continuum. There is also a number of approaches [7, 14, 15, 17, 22] which model the structure by volume elements and thus allow for consideration of different Poisson's ratios of fiber and matrix. Lomov et al. [17] developed a program to model various textile architectures and calculate stiffness of textile composites using the method of inclusions. Kim and Swan [15] describe a method to model a RVE for textile composites with an adaptive voxel method. Karkkainen and Sankar [14] use a RVE of the textile to compute the strengths of woven composites.

As mentioned before, textile lamina are orthotropic or general anisotropic, therefore well-known failure criteria for UD-lamina fall short in predicting failure of textile composites. Only textile composites with minimal fiber undulations and low 3D-reinforcement density can be described by failure criteria developed for UD-composites, such as e.g. the Tsai-Wu [11] or Puck [11] criterion. For other textile composites it is necessary to use appropriate failure criteria, that mostly are still to be developed. Juhasz et al. [13] developed a failure criterion for orthogonal 3D fiber reinforced plastics e.g. non-crimp fabrics.

Due to the orthotropic material behaviour, also strength parameters in the thickness direction are needed. To determine these parameters by tests, very thick specimens have to be manufactured which consist of several textile layers. To assure that the strength parameter of one textile layer is determined, the failure mode of specimen and single fabric layer has to be identical which can hardly be enforced through specimen geometry. Therefore, virtual tests are a very good alternative to experiments and are realized using a multiscale analysis.

To determine the material behavior of textile composites a multiscale analysis consisting of three levels is presented in Sect. 2.2. To account for the specific behavior of epoxy resin and fiber bundles two material models are given in Sect. 2.3. The numerical results in Sect. 2.4 focus on the microscale. They are validated by comparison to experimental data.

2.2 Multiscale Analysis

Mechanical properties of textile composites are influenced by several parameters and phenomena e.g. fiber architecture, undulations and plastic flow of epoxy resin. Each of these can influence the structural behavior, but can only be modelled on

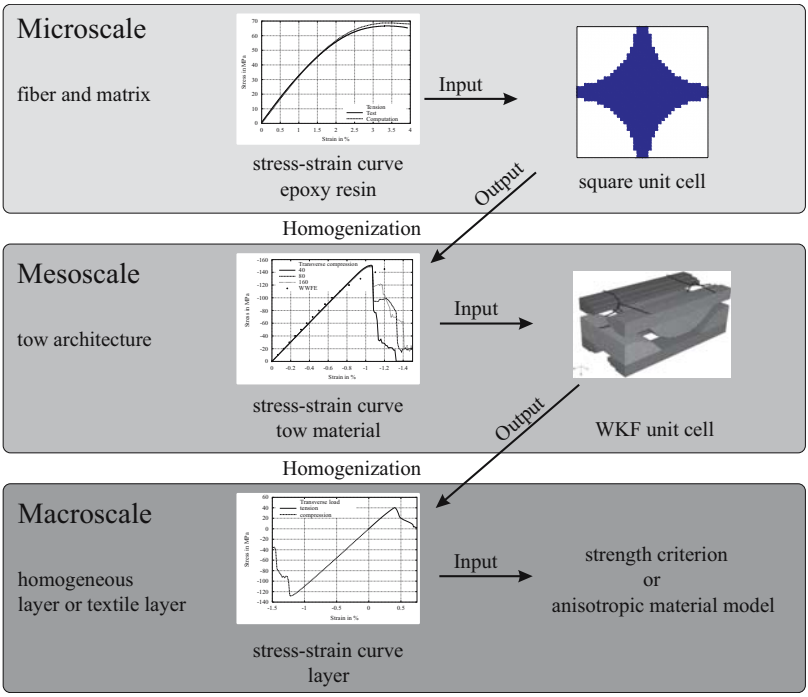

Fig. 2.2 Overview on multiscale-analysis

its specific length scale. For example fiber undulations in a woven lamina can not be discretized in the model of the whole structure, but on the mesoscale model. Therefore a multiscale analysis with a homogenization between scales is needed. In UD-composites the fibers are aligned, so that the homogenized parameters of the microscale are directly used on macroscale. The fiber architecture of textile composites is more complex due to undulations and reinforcements that have to be taken into account on a scale between micro- and macroscale: the mesoscale.

Figure 2.2 gives an overview of the three scales used consecutively, micro-, meso- and macroscale, between which homogenized material parameters are passed from the lower to the upper scale. The final objective of this multiscale analysis is to generate material parameters for the macroscale, on which structures are computed. The multiscale analysis starts on the microscale, where fiber and matrix are discretized. Material parameters of epoxy resin and fiber are well known and in case of nonlinear epoxy behavior, tabulated test data serve as input for the novel material model described in Sect. 2.3.1. The homogenized stress-strain curves of these unit-cell computations describe the transversely isotropic material behavior of the fiber bundles, consisting of fiber and matrix. In the mesomechanical unit cell, that models the fiber architecture of the textile composite, the fiber bundles are discretized as homogenized continua. Therefore, the stress-strain curves from the microscale are used as tabulated input data for the transversely isotropic material described in

Sect. 2.3.2. Finally the homogenized results of these unit cell computations serve as material parameters of a lamina on the macroscale, where laminate lay-up and the geometry of the structure are modelled.

2.2.1 Homogenization

Homogenization is used to simplify a heterogeneous material to an homogeneous one for reasons of numerical efficiency. It bridges the two length scales of heterogeneity of lower scale l and upper scale L. A representative volume element (RVE) is used to describe a representative part of the material with all relevant components and a statistical homogeneity, so that the properties of the RVE can be assumed to be the properties of the material. The statistical homogeneity requires the dimension of the RVE, a, to meet the criterion

$$l \ll a \ll L \tag{2.1}$$

In case the material has a regular substructure, the RVE consists only of this substructure. This special case of a RVE is called unit cell. It is usually much smaller than a RVE because it doesn't have to fulfill the requirement of statistical homogeneity, thus $l \approx a$. In this paper the statistical imperfections of the substructures at the micro- and meso-scale are neglected and unit cells are used.

The boundary conditions applied on the RVE or unit cell have great influence on the homogenization procedure. For an unit cell with its periodic substructure periodic boundary conditions give the exact solution, therefore they are chosen for the unit cells used here.

To determine all homogenized material parameter it is necessary to apply direct and shear load on the micro- and mesomechanical unit cells. The periodic boundary conditions for these load cases are shown in Fig. 2.3 for a x-y-z coordinate system. Depending on the load case, x, y and z are to be replaced by the directions of the layer, 1, 2 and 3.

Firstly periodic boundary conditions require opposing unit cell boundaries to remain parallel to each other and to have equal stresses. If load and unit cell are

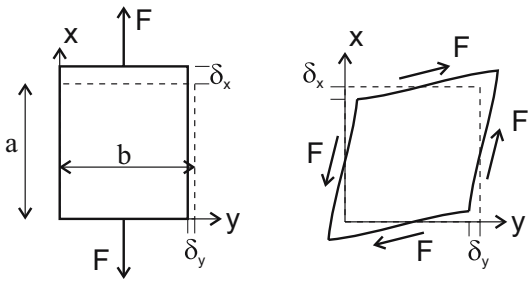

Fig. 2.3 Periodic boundary conditions

symmetric, which is the case for unit cells used here under direct loads, for reasons of symmetry the deformations have to be symmetric as well. Therefore, in case of direct load it has to be ensured that the boundaries remain plane. For most boundaries a deformation can be given

$$\begin{aligned} u(0,y,z) &= 0, \quad u(\mathrm{a},y,z) = \delta_x \\ v(x,0,z) &= 0 \\ w(x,y,0) &= 0 \end{aligned} \tag{2.2}$$

whereas other boundaries can deform but have to remain straight and orthogonal, which can be realized over a linear equation

$$\begin{aligned} v(x,\mathrm{b},z) &= const. = \delta_y \\ w(x,y,\mathrm{c}) &= const. = \delta_z \end{aligned} \tag{2.3}$$

Due to symmetry of unit cell and load it is only necessary to model one quarter of the micromechanical unit cell. Under shear load opposing boundaries of the unit cell have to remain parallel to each other:

$$\begin{aligned} u(0,y,z) &= u(\mathrm{a},y,z) \\ v(x,0,z) &= v(x,b,\mathrm{z}) \\ w(x,y,0) &= w(x,y,\mathrm{c}) = 0 \end{aligned} \tag{2.4}$$

but move in opposing directions:

$$\begin{aligned} u(x,0,z) &= -u(x,\mathrm{b},z) = -\delta_x \\ v(0,y,z) &= -v(\mathrm{a},y,z) = -\delta_y \end{aligned} \tag{2.5}$$

The forces F shown in Fig. 2.3 are the integrals over the stresses of the boundary and yield the homogenized stresses when divided by the corresponding boundary area. Deformations δ_i convert into homogenized unit cell strains and Poisson's ratios.

2.2.2 Voxel Mesh

Conventional modelling leads to a number of irregular elements, in particular for a mesomechanical unit cell of a textile composite, but also for the micromechanical unit cell. In combination with the strain energy based regularization irregular elements lead to a mesh-dependent solution, see [5], because the regularization requires elements with an aspect ratio of unity. To avoid this drawback of irregular elements, the unit cells shown here are meshed with voxel elements, meaning "volume pixel". They have an aspect ratio of one, hence the geometry can only be approximated because the mesh is regular.

Another advantage of the approximate meshing is that it simplifies the discretization of complicated geometries in the mesomechanical unit cell and the application of periodic boundary conditions. The geometry of fiber bundles has to be approximated anyway because it is irregular due to the manufacturing process. In addition the definition of clear boundaries between fiber bundle and epoxy is problematic as the fiber bundle itself contains epoxy. Therefore Gunnion [7] has shown that the voxel method is well suited to determine stiffnesses of textile composites.

2.2.3 Micromechanical Unit Cell

For transversely isotropic UD-material state of the art mixture rules give a good estimation of the elastic properties, but lack to predict inelastic properties such as strength and hardening of the fiber bundle. So, the micromechanical unit cell is needed to determine these parameters when experimental data is not available. This is often the case for textile composites, because the tests required cannot be done with the whole preform, but only with a part of it, the fiber bundles. Thus the specimens have to be produced especially for these tests.

A micrograph of unidirectional composite material is shown in Fig. 2.4a. It can be modelled with a representative volume element on the microscale that consists of fiber and matrix. Neglecting the random fiber distribution over the cross section, a regular square fiber arrangement, that can be reduced to the unit cell shown in Fig. 2.4b, is assumed. It has been shown previously [19], that this is a good approximation.

As mentioned above, the micromechanical unit cell consists only of one fibre, that can even be reduced to a quarter of a fiber, see Fig. 2.5 when a symmetric load is applied due to symmetry reasons.

In the examples given here glass fibres and epoxy matrix are used. Both are isotropic materials, whose material parameters are well known from test and are summarized in Table 2.1. Strength of the epoxy resin is neglected in fiber direction and therefore strength in fiber direction $R_{\parallel}^{t,c}$ can be computed analytically from the

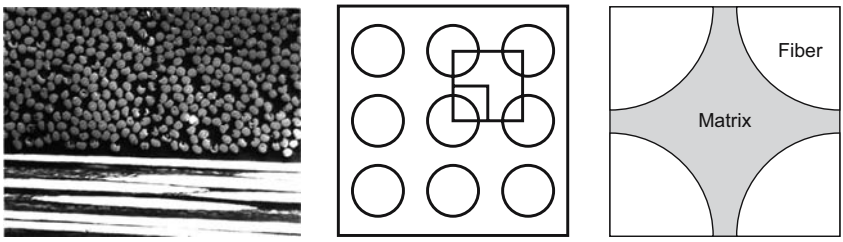

(a) Micrograph [3] (b) Square arrangement (c) Unit cell geometry

Fig. 2.4 Micromechanical unit cell

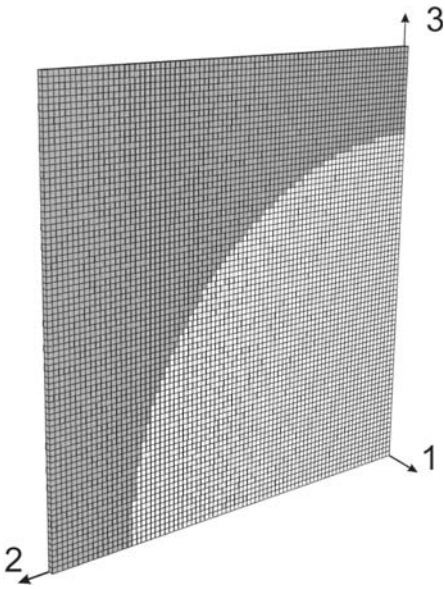

Fig. 2.5 Discretization of one quarter of micromechanical unit cell

Table 2.1 Material properties of fiber and matrix

Parameter	Unit	E-Glass	RIM 135	MY750/HY917/DY063
Young's modulus	GPa	74	3.35	3.35
Strength	MPa	2,150/1,450[a]	69/120/55[b]	80/120[a]
Failure strain	%	2.950/1.959[a]	3.4/4.2/22[b]	5./–[a]
Shear modulus	GPa	30.8	1.24	1.24
Poisson's ratio		0.2	0.35	0.35

[a] Tension/compression

[b] Tension/compression/shear

strength of the fiber $R^{t,c}_{\text{fiber}}$ and fiber volume fraction v_f

$$\mathrm{R}^{\mathrm{t,c}}_{\parallel} = R^{\mathrm{t,c}}_{\text{fiber}} * v_\text{f} \tag{2.6}$$

To determine strength parameters in other directions, four load cases summarized in Fig. 2.6 have to be computed: tension, shear and compression in transverse direction and in-plane shear.

2.2.4 Mesomechanical Unit Cell

The mesomechanical unit cell is used to model the fiber architecture and to determine material properties of one lamina on the macroscale. The number of layers

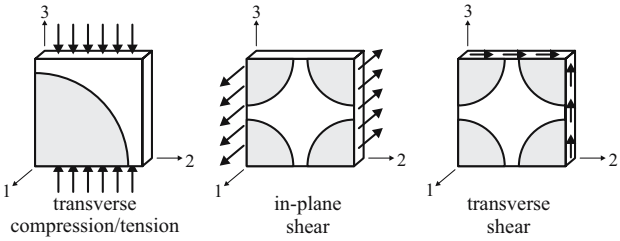

Fig. 2.6 Load cases for homogenization

homogenized in one lamina depends on the type of preform. In the following examples for a mesomechanical unit cell of a non-crimp fabric, see Fig. 2.1 and a weft-knitted fabric, see Fig. 2.9 are given. In the framework of this paper the models are shown to present a complete multiscale approach, but results of numerical analysis are focused on microscale simulations.

In general, cracks in a composite firstly evolve in the layers and secondly between layers. Thus, regarding progressive failure of the structure it is advantageous to model each layer in one separate lamina on the macroscale, because damage can be easily attributed and identified for each layer separately. For textile composites this means to neglect some effects of the fiber architecture, that connects the layers, on the material behavior. In case of the non-crimp fabric each layer is modelled separately, because through-thickness reinforcement density and influence are considerably low. Thus the advantage of modelling each layer in separate lamina prevails over the influence of the reinforcement. However, in case of the weft-knitted fabric the material inhomogeneity is so big, that it is only possible to identify single fiber bundles rather than separate layers. Therefore one lamina on the macroscale has to represent two fabrics at once. On macroscale both examples are treated as orthotropic textile layers, so nine elastic material constants and nine strengths have to be determined. Hence, compression, tension and shear are applied in each direction with periodic boundary conditions corresponding to Fig. 2.3.

Due to periodicity of stitching and knitting patterns an unit cell is used. The fiber bundles are modelled with transversely isotropic material described in Sect. 2.3.2, epoxy resin and yarn with isotropic material described in Sect. 2.3.1.

2.2.4.1 Non-Crimp Fabrics

Figure 2.7a shows a scan of a non-crimp fabric that shows the regular stitch pattern and the area of one unit cell. Of all textile fabrics the structure of the non-crimp fabric resembles UD-laminates most. Fiber layers can easily be identified and the disturbance through stitch yarns is comparatively low. Therefore it is logical to model each layer of the non-crimp fabric separately to identify the material parameters. Only the through-thickness part of the stitch yarn is taken into account, because it has a significant influence on the behavior of the unit cell. The in-plane part

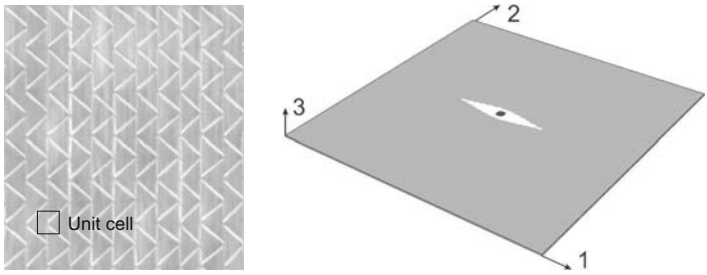

(a) Scan of NCF (b) Discretization

Fig. 2.7 Mesomechanical non-crimp fabric unit cell

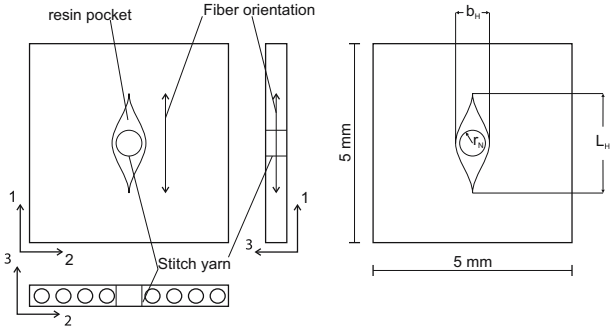

Fig. 2.8 Geometry of mesomechanical unit cell for non-crimp fabric

of the stitch yarn has no significant influence, because of its small diameter and minor material properties of the PES-yarn compared to the glass-fibers that lie in the same plane. The discretization of the unit cell is shown in Fig. 2.7b, it consists of $200 \times 200 \times 1$ elements. The fiber bundle structure in thickness direction is neglected, hence only one element is used in this direction. Figure 2.8 shows the different components, fiber bundle, epoxy resin pocket and stitching yarn, of the unit cell and their dimensions. The resin pocket is $L_H = 3.5\,\text{mm}$ long and $b_H = 0.3\,\text{mm}$ wide, the radius of the stitch yarn is $r_N = 0.054\,\text{mm}$.

2.2.4.2 Weft-Knitted Fabrics

Compared to the non-crimp fabric described above the yarn in weft-knitted fabrics presented here plays a bigger role, although still the yarn diameter is smaller than the fiber bundle diameter. Firstly the loops of the yarn are denser and secondly the yarn is stronger, because it consists of glass fibers instead of polyester and has a larger diameter. Secondly the material structure of the weft-knitted fabric is much more heterogeneous, the individual fiber bundles are clearly identifiable. Therefore in the draping process layers of weft-knitted fabric penetrate each other, as can be seen in Fig. 2.9. Thus the smallest unit cell of the weft-knitted fabric, see Fig. 2.9 includes

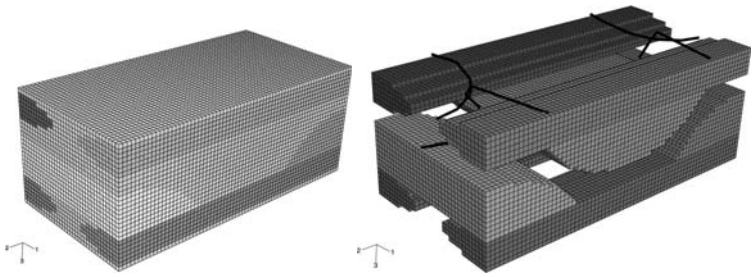

Fig. 2.9 Geometry of mesomechanical unit cell for two weft-knitted fabrics, epoxy resin is removed on right side

two fabrics. It consists of fiber bundles in warp- and fill-direction, the knitting yarn and the epoxy resin. The fiber bundles and epoxy resin are discretized with volume elements, whereas the knitting yarn, is modelled with truss elements, because of its lower diameter. On the right hand side of Fig. 2.9 the epoxy resin is removed to make the knitting yarn visible.

2.3 Material Models

In order to describe the specific phenomena of textile composites, special material models are developed on micro- and mesoscale. The fibers are represented by a linear elastic material model. For epoxy resin, an isotropic elastic-plastic material model with an isotropic damage formulation is presented in Sect. 2.3.1. Modelling the transversely isotropic behavior of the fiber bundles, a transversely isotropic elastic-plastic material model with damage is developed in Sect. 2.3.2.

2.3.1 Isotropic Elastic-Plastic Material Model for Epoxy Resin

Considering the micromechanical unit cell, epoxy resin turns out as the determining material concerning the overall mechanical behavior of the unit cell. Especially the plastic behavior and the fracture characteristic of epoxy resin prove to be the governing material parameters. Therefore, special care has to be taken to find a good representation of all experimentally observed characteristics of epoxy resin in the material model. An isotropic elastic-plastic material model with an isotropic damage formulation is considered as the best approach for modelling epoxy resin in the micromechanical unit cell.

2.3.1.1 Yield Surface

Generally, epoxy resin is a visco-elastic-plastic material, whereas the development of viscosity and plasticity varies depending on the type of epoxy resin and the

stress state. The main focus of the multi-scale analysis is the calculation of material strengths. Thus, quasi static loading is considered and viscous effects are neglected. To account for different yielding behavior under uniaxial tension, uniaxial compression and simple shear (see Fig. 2.11), a plasticity model with a pressure dependent yield surface is chosen [9]. In terms of the first two stress invariants pressure p and VON MISES stress σ_{vm}, the yield locus can be written as

$$f = \sigma_{\mathrm{vm}}^2 - a_0 - a_1\, p - a_2\, p^2 \tag{2.7}$$

whereby

$$p = \frac{1}{3}\sigma_{ii} \quad \text{and} \quad \sigma_{\mathrm{vm}} = \sqrt{\frac{3}{2} s_{ij} s_{ij}} \tag{2.8}$$

The term s_{ij} is the stress deviator tensor. This formulation of the yield locus allows to regard three material tests for modelling the epoxy resin. In this presentation, hardening curves from a uniaxial tensile test and a simple shear test are considered:

$$\begin{aligned} \sigma_{\mathrm{t}} &= \sigma_{\mathrm{t}}(\bar{\varepsilon}^{\mathrm{pl}}) = \text{tensile hardening curve} \\ \sigma_{\mathrm{s}} &= \sigma_{\mathrm{s}}(\bar{\varepsilon}^{\mathrm{pl}}) = \text{shear hardening curve} \end{aligned} \tag{2.9}$$

As a special feature of the material model, the hardening curves are scanned by the plasticity algorithm and the experimentally obtained test data are reproduced exactly in numerical simulations, see Sect. 2.3.1.3. As two material tests are regarded, the parameter a_2 in Eq. (2.7) is set to zero and the remaining parameters a_0 and a_1 are

$$\begin{aligned} a_0 &= 3\sigma_{\mathrm{s}}^2 \\ a_1 &= 3\frac{\sigma_{\mathrm{t}}^2 - 3\sigma_{\mathrm{s}}^2}{\sigma_{\mathrm{t}}} \end{aligned} \tag{2.10}$$

In every time step, the yield stresses σ_{s} and σ_{t} are readout of the hardening curves Eq. (2.9) in dependence of the accumulated plastic strain $\bar{\varepsilon}^{\mathrm{pl}}$. Hence, the experimentally measured yield stresses for uniaxial tension and pure shear are recovered exactly in the material model. Although only two hardening curves are considered, other stress states are properly regarded in the yield locus Eq. (2.7). For negative hydrostatic pressures p the material behaves stiffer than under positive pressure, see [6]. Further, in the range of biaxial to triaxial tensile stress states epoxy resin exhibits a lower strength, i.e. a lower yield and failure stress at these stress states [6]. Both effects are reflected in the yield surface Eq. (2.7). The lower strength at biaxial and triaxial stress states is due to the effect of crazing. Crazing goes along with initiation and evolution of micro pores, which results in a permanent increase in volume during plastic deformation. The yield surface Eq. (2.7) and the assumption of a non-associated flow rule with a plastic potential g (see Sect. 2.3.1.2) enables to control the volumetric plastic straining during plastification.

2.3.1.2 Flow Rule

Associated flow leads to plastic strain rate in terms of the normal vector to the yield surface. However, assuming an associated flow rule, the plastic Poisson ratio, defined as the ratio of transversal to longitudinal plastic strain rate, is not reflected in a correct way. In some cases there follow even physically nonsensical values for the plastic Poisson ratio. Further, there is no possibility to control the volumetric plastic straining. The assumption of a VON MISES plastic potential implies plastic flow under constant volume, which is equal to $\nu_{\mathrm{pl}} = 0.5$. This is not a correct assumption for epoxy resin. Experiments show that the plastic Poisson ratio depends on hydrostatic pressure and that there is in particular a different lateral behavior in tension and in compression, see [6]. Especially in the simulations of the micromechanical unit cell, the plastic Poisson ratio is of major importance. Assuming an associated flow rule, the volumetric plastic straining under pressure is overestimated. Although the hydrostatic pressure is negative, the associated flow rule yields to an increase in volume. That in turn results in a too stiff material behavior at compressive loading of the micromechanical model. To account for a realistic assumption for ν_{pl} and to control the lateral plastic straining in dependence on hydrostatic pressure, the plastic potential is assumed as (see [9]):

$$g = \sqrt{\sigma_{\mathrm{vm}}^2 + \alpha p^2} \tag{2.11}$$

The amount of dilatancy or compression, i.e. the increase or decrease in material volume due to yielding, can be controlled with the flow parameter α, whereas α correlates to the plastic poisson ratio ν_{pl} under uniaxial loading:

$$\nu_{\mathrm{pl}} = \frac{9 - 2\alpha}{18 + 2\alpha} \Rightarrow \alpha = \frac{9}{2}\frac{1 - 2\nu_{\mathrm{pl}}}{1 + \nu_{\mathrm{pl}}} \tag{2.12}$$

Plausible flow behavior means $0 \leq \nu_{\mathrm{pl}} \leq 0.5$ which is equal to $0 \leq \alpha \leq \frac{9}{2}$. If the flow parameter α is set to zero, there is no change in material volume when yielding occurs and the VON MISES plastic potential is recovered. So the VON MISES case is comprised as a special case in Eq. (2.11). The plastic potential is illustrated in Fig. 2.10.

2.3.1.3 Hardening Formulation

To describe the hardening behavior under plastic flow, a nonlinear isotropic hardening model is used. A special feature is the curve based input of hardening via tabulated data. That is, the hardening data obtained from uniaxial tensile, uniaxial compression and simple shear tests can directly be input in terms of load curves giving the yield stress as a function of the corresponding plastic strain. Consequently, the hardening is dependent on the state of stress and not only on the accumulated plastic strain. As the measurement results from material testing are

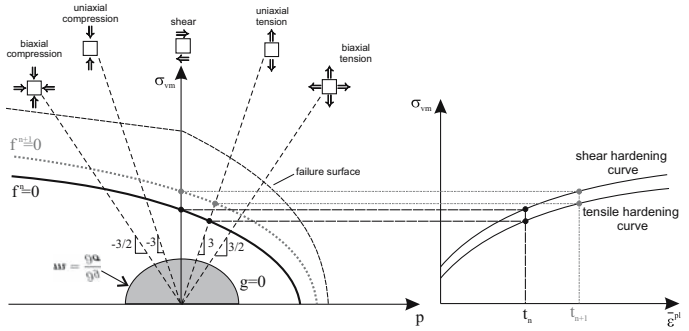

Fig. 2.10 Representation of plastic potential, yield surface and failure surface in σ_{vm}-p-invariant-plane

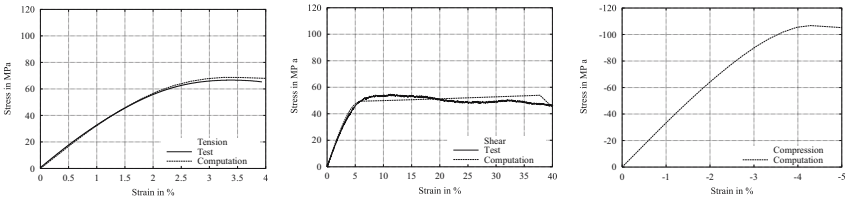

(a) Tension (b) Shear (c) Compression

Fig. 2.11 Stress-strain curves of epoxy matrix RIM 135 from tests and curves used in computation

commonly provided as true stresses over true total strains, the hardening curves must be prepared by subtracting the elastic part of the strains from the total strains:

$$\varepsilon_t^{pl} = \varepsilon_t - \frac{\sigma_t}{E}$$
$$\varepsilon_s^{pl} = \varepsilon_s - \frac{\sigma_s}{2G} \tag{2.13}$$

If the test results are given in engineering stresses and strains, a conversion into true stresses and true strains has to be done. The concept of tabulated input of hardening data allows for a straight forward treatment in computation. The test results, that are reflected in the load curves, are used exactly by the material model without fitting to any analytical expression. So there is no need of parameter identification. The load curves expected as input are briefly described in Fig. 2.12.

2.3.1.4 Damage Formulation

To describe the damage and failure behavior of epoxy resin, an isotropic damage model is implemented in the material model. At first, a damage initiation criterion is needed, which marks the location in stress space, when damage primarily occurs

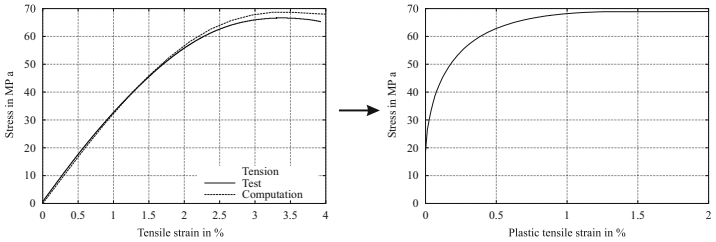

Fig. 2.12 Preparation of experimentally obtained hardening curves for input as tabulated data: Total strains has to be converted into plastic strains by Eq. (2.13)

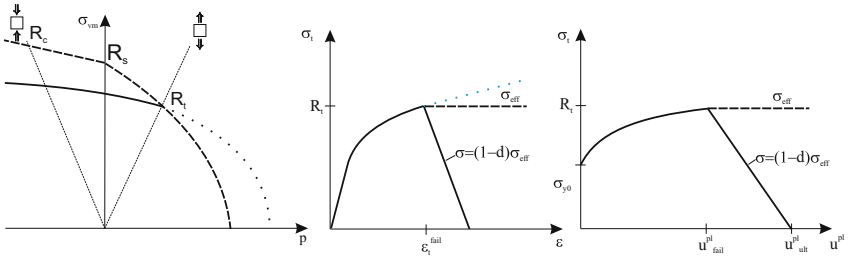

Fig. 2.13 Damage formulation

and stiffness degradation starts. Once, the failure surface is achieved at any point in stress space, i.e. the damage initiation criterion is active, stiffness degradation starts until the material finally collapses. The material stiffness degradation is controlled by a scalar damage parameter d. To avoid mesh dependency of numerical results, the fracture energy concept according to HILLERBORG (1976) is applied.

Failure Surface

In order to regard the material strengths from uniaxial tension, uniaxial compression and pure shear testings, the failure surface is split into two parts, as illustrated in Figures 2.13 and 2.10. In the region of positive pressures, the failure surface has a formulation in analogy to the yield surface:

$$r = \sigma_{\mathrm{vm}}^2 - b_0 - b_1 p \tag{2.14}$$

If $r = 0$, the failure criterion is active and stiffness degradation starts until the material finally fails. The parameters b_0 and b_1 are obtained in the same manner as the parameters a_0 and a_1 for the yield function Eq. (2.10). Therefore, the material strengths of uniaxial tension R_{t} and of shear R_{s} has to be inserted instead of the yield stresses in Eq. (2.10). In the region of negative pressures, a linear failure surface, connecting the uniaxial compressive strengths R_{c} and the shear strength R_{s} in the σ_{vm}-p-invariant-plane, is assumed (see Fig. 2.10).

Damage Evolution and Stiffness Degradation

The damage evolution law describes the rate of degradation of the material stiffness once the corresponding initiation criterion has been reached. A scalar damage variable d is introduced to control the stiffness degradation [16]. At any given time during the analysis, the stress tensor in the material is given by the scalar damage equation

$$\sigma = (1-d)\sigma_{\text{eff}} \tag{2.15}$$

where d is the overall damage variable and σ_{eff} is the effective, i.e. undamaged, stress tensor computed in the current increment. If the failure surface is achieved at any stress state, the yield surface is forced to remain constant by setting the hardening modulus to zero and stiffness degradation, controlled by the scalar damage variable d, starts until the material has lost its load-carrying capacity ($d = 1$), see Fig. 2.13. In numerical analysis, then the concerning elements are removed from the mesh.

Fracture Energy Concept

Softening material behavior, which results macroscopically in a loss of material stiffness with adjacent failure, is preceded by the initiation and accumulation of microscopical defects such as cracks, micro-pores, shear-bands or crazes [16]. The initiation and accumulation of such defects are a matter of local defects and are restricted to a local zone, whose size depends on the material [16]. Hence, softening response after damage initiation is governed by a stress-displacement response and not by a stress-strain response. Continuing to use a stress-strain relation introduces a strong mesh dependency based on strain localization, such that the energy dissipated decreases as the mesh is refined. HILLERBORG's fracture energy proposal [10] is used to reduce mesh dependency by creating a stress-displacement response after damage is initiated. Therefore, HILLERBORG defines the energy G_{f}, required to open a unit area of crack, and a characteristic internal length L_{i},which is a measurement of the size of the localized area, as material constants. The energy G_{f} required to open a unit area of crack, is

$$G_{\text{f}} = \int_{\bar{\varepsilon}^{\text{pl}}_{\text{fail}}}^{\bar{\varepsilon}^{\text{pl}}_{\text{ult}}} L_{\text{i}}\sigma_{\text{y}}\,\text{d}\bar{\varepsilon}^{\text{pl}} = \int_{\bar{u}^{\text{pl}}_{\text{fail}}}^{\bar{u}^{\text{pl}}_{\text{ult}}} \sigma_{\text{y}}\,\text{d}\bar{u}^{\text{pl}} \tag{2.16}$$

The implementation of this stress-displacement concept in a finite element model requires the definition of a characteristic element edge length L_{e} associated with an integration point. The fracture energy is then given as

$$G_{\text{f}} = \int_{\bar{\varepsilon}^{\text{pl}}_{\text{fail}}}^{\bar{\varepsilon}^{\text{pl}}_{\text{ult}}} L_{\text{e}}\sigma_{\text{y}}\,\text{d}\bar{\varepsilon}^{\text{pl}} = \int_{\bar{u}^{\text{pl}}_{\text{fail}}}^{\bar{u}^{\text{pl}}_{\text{ult}}} \sigma_{\text{y}}\,\text{d}\bar{u}^{\text{pl}} \tag{2.17}$$

This expression introduces the definition of the equivalent plastic displacement $\bar{u}_\mathrm{p}$ as the fracture work conjugate of the yield stress σ_y after the onset of damage:

$$\bar{u}^{\mathrm{pl}} = L_\mathrm{e}\bar{\varepsilon}^{\mathrm{pl}} \tag{2.18}$$

The definition of the characteristic length is based on the element geometry. For solid elements the cube root of the element volume is used. This definition of the characteristic length is chosen because the direction, in which fracture occurs, is not known in advance. Therefore, elements with large aspect ratios will have rather different behavior depending on the direction in which the crack evolves. This may lead to a mesh sensitivity of the simulation results. To avoid this problem, in the micro- and meso-models only voxel-elements are used with an aspect ratio of unity. The introduction of the characteristic element edge length L_e yields to a distribution of localized strains over the particular element width and enforces the fracture energy to be constant.

2.3.1.5 Numerical Treatment

The present model has been implemented as a user-defined material into ABAQUS implicit (user interface UMAT) and ABAQUS explicit (user interface VUMAT). Starting from the additive decomposition of the strain increment at time t_{n+1}

$$\Delta\varepsilon_{n+1} = \varepsilon_{n+1} - \varepsilon_n \tag{2.19}$$

the trial stress, assuming elastic behavior, is computed as

$$\sigma_{n+1}^{\mathrm{trial}} = \sigma_n + \mathbb{C}^{\mathrm{el}} : \Delta\varepsilon_{n+1} \tag{2.20}$$

Checking the yield surface

$$f = f(\sigma_{n+1}^{\mathrm{trial}}, \bar{\varepsilon}^{\mathrm{pl}}) \tag{2.21}$$

indicates elastic ($f \leq 0$) or plastic ($f > 0$) loading. In the case of plastic loading, a classical elastic-predictor plastic-corrector scheme is applied for stress integration, see [21] or [12]. The plastic strain increment can be written as

$$\Delta\bar{\varepsilon}_{n+1}^{\mathrm{pl}} = \bar{\varepsilon}_{n+1}^{\mathrm{pl}} - \bar{\varepsilon}_n^{\mathrm{pl}} = \Delta\lambda_{n+1}\mathsf{m}_{n+1} \tag{2.22}$$

where $\Delta\lambda$ is the sought plastic multiplier. The direction m of the plastic flow in the case of a non-associated flow rule is given by the derivation of the plastic potential g with respect to the stresses:

$$m_{n+1} = \partial g(\sigma_{n+1})/\partial\sigma_{n+1} \tag{2.23}$$

The increment of the equivalent plastic strain is obtained from

$$\Delta\bar{\varepsilon}_{n+1}^{\mathrm{pl}} = \Delta\lambda_{n+1}\,\|\mathsf{m}_{n+1}\| \tag{2.24}$$

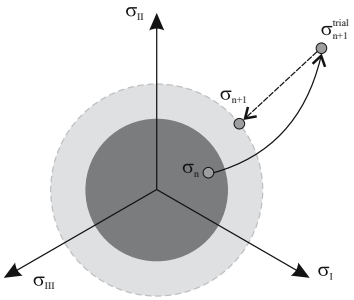

Fig. 2.14 Radial return algorithm

Hence, the stresses can be calculated through

$$\sigma_{n+1} = \sigma_{n+1}^{\text{trial}} - \Delta\lambda_{n+1}\mathbb{C}^{\text{el}} : \mathsf{m}_{n+1} \tag{2.25}$$

and the internal variable is updated by

$$\bar{\varepsilon}_{n+1}^{\text{pl}} = \bar{\varepsilon}_{n}^{\text{pl}} + \Delta\lambda_{n+1} \left\| \mathsf{m}_{n+1} \right\| \tag{2.26}$$

Inserting in the active yield surface Eq. (2.21) leads formally to a nonlinear equation in $\Delta\lambda_{n+1}$ which is solved by the Newton-Raphson method. Figure 2.14 shows an illustration of the applied integration algorithm.

2.3.2 Transversely Isotropic Elastic-Plastic Material Model for Fiber Bundles

Fiber bundles, as used in the mesomechanical unit cell, exhibit a transversely isotropic characteristic. Although plasticity is lower and the overall behavior is more brittle than pure resin, plasticity also occurs. Especially under transverse and in-plane shear stress states considerable plastic deformations can be observed, whereas under tensile and compressive loadings in fiber direction the fiber bundle exhibits an elastic-brittle behavior. That is, the material behavior can be approximated as nearly linear elastic until failure occurs and plasticity in fiber direction is neglected. Further, yielding behavior and material failure are dependent on hydrostatic pressure. Therefore, a transversely isotropic elastic-plastic material model with a pressure dependent C^1-continuous yield surface and a transversely isotropic damage formulation is developed. For the infinitesimal strain tensor, an additive decomposition is assumed:

$$\varepsilon = \varepsilon^{\text{el}} + \varepsilon^{\text{pl}} \tag{2.27}$$

For both the elastic and the plastic part of the transversally isotropic material model, the representation of the constitutive equations is carried out in the format of isotropic tensor functions by means of structural tensors. The structural tensor A, reflecting the materials intrinsic characteristic, is defined as the dyadic product of

the preferred direction **a**:

$$\mathsf{A} = \mathbf{a} \otimes \mathbf{a} \tag{2.28}$$

Transversal isotropy means, that the material response is invariant with respect to arbitrary rotations around this preferred direction **a**, to reflections at fiber parallel planes and to the reflection at that plane, whose normal is **a**. These are the group of symmetry transformations for transverse isotropy. For further description of invariant theory see [1]. In the sequel, constitutive equations for the elastic and the plastic part of the material model are derived.

2.3.2.1 Elastic Stress-Strain Relations

As only small elastic deformations are considered, the assumption of HOOKE's linear elasticity law $\sigma = \hat{\sigma}(\varepsilon^{\mathrm{el}})$ is justified. Postulating hyperelasticity, the first derivative of the free energy function $\hat{\Psi}$ with respect to the strains $\varepsilon^{\mathrm{el}}$ delivers the stresses σ and the second derivation with respect to the strains $\varepsilon^{\mathrm{el}}$ gives the elasticity tensor $\mathbb{C}^{\mathrm{el}}$. In case of transverse isotropy, the free energy function is formulated in isotropic invariants of the strain tensor $\varepsilon^{\mathrm{el}}$ and the structural tensor A. To derive a representation of $\hat{\Psi}$ and the infinitesimal stress tensor σ as isotropic tensor-functions, the functional basis of the two symmetric second order tensorial arguments σ and A is needed. Assuming the stresses to be a linear function of the strains and providing a stress free undistorted initial configuration, i.e. $\sigma(\varepsilon = 0) = 0$, terms are neglected, which are linear or cubic in the strains. This enforces the elasticity tensor $\mathbb{C}^{\mathrm{el}}$ to be constant and yields to a formulation of the free energy function with five elasticity constants λ, α, μ_L, μ_T and β, describing the transversely isotropic material behavior:

$$\begin{aligned}\hat{\Psi}(\varepsilon^{\mathrm{el}}, \mathsf{A}) := \frac{1}{2}\lambda(\operatorname{tr}\varepsilon^{\mathrm{el}})^2 + \mu_T \operatorname{tr}(\varepsilon^{\mathrm{el}})^2 + \alpha(\mathbf{a}^{\mathrm{T}}\varepsilon^{\mathrm{el}}\mathbf{a}) \operatorname{tr}\varepsilon^{\mathrm{el}} \\ + 2(\mu_L - \mu_T)(\mathbf{a}^{\mathrm{T}}(\varepsilon^{\mathrm{el}})^2\mathbf{a}) + \frac{1}{2}\beta(\mathbf{a}^{\mathrm{T}}\varepsilon^{\mathrm{el}}\mathbf{a})^2\end{aligned} \tag{2.29}$$

For the stresses we obtain

$$\begin{aligned}\sigma = \lambda(\operatorname{tr}\varepsilon^{\mathrm{el}})1 + 2\mu_T\varepsilon^{\mathrm{el}} + \alpha(\mathbf{a}^{\mathrm{T}}\varepsilon^{\mathrm{el}}\mathbf{a}1 + \operatorname{tr}\varepsilon^{\mathrm{el}}\mathsf{A}) \\ + 2(\mu_L - \mu_T)(\mathsf{A}\varepsilon^{\mathrm{el}} + \varepsilon^{\mathrm{el}}\mathsf{A}) + \beta\mathbf{a}^{\mathrm{T}}\varepsilon^{\mathrm{el}}\mathbf{a}\mathsf{A}\end{aligned} \tag{2.30}$$

and the elasticity tensor is

$$\begin{aligned}\mathbb{C}^{\mathrm{el}} = \lambda 1 \otimes 1 + 2\mu_T\mathbb{I} + \alpha(\mathsf{A} \otimes 1 + 1 \otimes \mathsf{A}) \\ + 2(\mu_L - \mu_T)\mathbb{I}_{\mathsf{A}} + \beta\mathsf{A} \otimes \mathsf{A}\end{aligned} \tag{2.31}$$

Hereby, the fourth order tensor $\mathbb{I}_{\mathbf{A}}$ in index notation reads $A_{im}\mathbb{I}_{jmkl} + A_{jm}\mathbb{I}_{mikl}$. In matrix notation, the fourth order elasticity tensor of transversal isotropy for a preferred X_1-direction in a Cartesian coordinate system, i.e. $\mathbf{a} = [1,0,0]^T$, reads:

Table 2.2 Elasticity constants for transversely isotropic elasticity

Symmetry of the elasticity tensor:

$$\frac{\nu_{12}}{E_{22}} = \frac{\nu_{21}}{E_{11}};\ \frac{\nu_{13}}{E_{33}} = \frac{\nu_{31}}{E_{11}};\ \frac{\nu_{23}}{E_{33}} = \frac{\nu_{32}}{E_{22}}$$

Constants of invariant formulation:

$$\begin{aligned}
\lambda &= E_{22}(\nu_{23} + \nu_{31}\nu_{13})/D \\
\alpha &= E_{22}[\nu_{31}(1 + \nu_{32} - \nu_{13}) - \nu_{32}]/D \\
\beta &= E_{11}(1 - \nu_{32}\nu_{23})/D - E_{22}[\nu_{23} + \nu_{13}\nu_{31}]/D - 4\mu_{12} \\
\mu_l &= \mu_{12} \\
\mu_t &= \mu_{23} \\
D &= 1 - \nu_{32}^2 - 2\nu_{13}\nu_{31} - 2\nu_{32}\nu_{31}\nu_{13}
\end{aligned}$$

Engineering constants:

$$\begin{aligned}
E_{22} &= E_{33}, \quad \nu_{23} = \nu_{32}, \quad \nu_{12} = \nu_{13}, \quad \nu_{21} = \nu_{31}, \quad \mu_{12} = \mu_{13} \\
E_{11} &= -(\lambda\mu_t - 4\lambda\mu_l - \lambda\beta - 2\alpha\mu_t + 2\mu_t^2 - \beta\mu_t - 2\alpha\mu_t - 4\mu_l\mu_t + \alpha^2)/(\lambda + \mu_t) \\
E_{22} &= -4\mu_t(\lambda\mu_t - 4\mu_l\lambda - \beta\lambda + 2\mu_t^2 - \beta\mu_t - 2\alpha\mu_t - 4\mu_t\mu_l + \alpha^2)/D_t \\
\nu_{12} &= 2\mu_t(\lambda + \alpha)/D_t \\
\nu_{21} &= (\lambda + \alpha)/(2\lambda + 2\mu_t) \\
\nu_{23} &= -(\alpha^2 + 2\lambda\mu_t - \beta\lambda - 4\mu_l\lambda)/D_t \\
\mu_{12} &= \mu_l \\
\mu_{23} &= \mu_t \\
D_t &= 4\mu_l\lambda + \beta\lambda - 4\mu_t^2 + 4\mu_t\alpha + 2\beta\mu_t + 8\mu_l\mu_t - \alpha^2
\end{aligned}$$

$$\mathbb{C}^{\mathrm{el}} = \begin{bmatrix}
\lambda + 2\alpha + \beta + 4\mu_L - 2\mu_T & \lambda + \alpha & \lambda + \alpha & 0 & 0 & 0 \\
\lambda + \alpha & \lambda + 2\mu_T & \lambda & 0 & 0 & 0 \\
\lambda + \alpha & \lambda & \lambda + 2\mu_T & 0 & 0 & 0 \\
0 & 0 & 0 & \mu_L & 0 & 0 \\
0 & 0 & 0 & 0 & \mu_L & 0 \\
0 & 0 & 0 & 0 & 0 & \mu_T
\end{bmatrix} \tag{2.32}$$

The transformation from engineering constants to those of the invariant representation an vice versa are listed in Table 2.2.

2.3.2.2 Transversely Isotropic Yield Surface

Our proposal of a transversely isotropic yield surface is an extension of a yield function following [1] and [18] and its numerical treatment in [20] and [4]. Four invariants I_1, I_2, I_3 and I_4 are introduced for the construction of the yield surface. The first two invariants I_1 and I_2 are chosen according to [20]. Therefore, a decomposition of the stress tensor into an extra stress tensor σ^{pind}, inducing plastic yielding, and a remaining reaction stress tensor σ^{reac} is assumed:

$$\sigma = \sigma^{\mathrm{pind}} + \sigma^{\mathrm{reac}} \tag{2.33}$$

where the stress components σ^{reac} and σ^{pind} are:

$$\begin{aligned}\sigma^{\text{reac}} &= \underbrace{\frac{1}{2}(\operatorname{tr}\sigma - \mathbf{a}^T\sigma\mathbf{a})}_{p}\,1\,\underbrace{-\frac{1}{2}(\operatorname{tr}\sigma - 3\mathbf{a}^T\sigma\mathbf{a})}_{T_a}\,\mathsf{A}\\ \sigma^{\text{pind}} &= \sigma - \frac{1}{2}(\operatorname{tr}\sigma - \mathbf{a}^T\sigma\mathbf{a})1 + \frac{1}{2}(\operatorname{tr}\sigma - 3\mathbf{a}^T\sigma\mathbf{a})\mathsf{A}\end{aligned} \tag{2.34}$$

The term T_a can be interpreted as a fiber overstress, exceeding the hydrostatical part of the stress tensor and p represents the hydrostatical pressure. In order to account for plastification in fiber direction, the projection of the deviatoric part of the reaction stress tensor σ^{reac} onto $\mathbf{a}$ can be regarded:

$$\mathbf{a}^T(\operatorname{dev}\sigma^{\text{reac}})\mathbf{a} = \mathbf{a}^T T_a(\operatorname{dev}\mathsf{A})\mathbf{a} = T_a\,\mathbf{a}^T(\mathsf{A} - \frac{1}{3}1)\mathbf{a} = \frac{2}{3}T_a \tag{2.35}$$

The yield condition can be composed of the basic invariants of the related stresses and the structural tensor. The invariants I_1 and I_2 are formulated with σ^{pind}, see [1], [18] and [20]:

$$\begin{aligned}I_1 &:= \frac{1}{2}\operatorname{tr}(\sigma^{\text{pind}})^2 - \mathbf{a}^T(\sigma^{\text{pind}})^2\mathbf{a}\\ I_2 &:= \mathbf{a}^T(\sigma^{\text{pind}})^2\mathbf{a}\\ I_3 &:= \operatorname{tr}\sigma - \mathbf{a}^T\sigma\mathbf{a}\\ I_4 &:= \tfrac{3}{2}\mathbf{a}^T\sigma^{\text{dev}}\mathbf{a} = T_a\end{aligned} \tag{2.36}$$

The invariant I_3 represents the hydrostatical pressure and thus accounts for a pressure dependency of the yield locus. The invariant I_4 is chosen to regard plastification in fiber direction. The yield function as a function of the introduced invariants is formulated as

$$f = \alpha_1 I_1 + \alpha_2 I_2 + \alpha_3 I_3 + \alpha_{32} I_3^2 + \alpha_4 I_4^2 - 1 \tag{2.37}$$

with the flow parameters α_1, α_2, α_3, α_{32} and α_4. The first and second derivative of the yield locus Eq. (2.37) are:

$$\begin{aligned}\partial_\sigma f &= \partial_{I_i} f\,\partial_\sigma I_i f\\ &= \alpha_1\sigma^{\text{pind}} + (\alpha_2 - \alpha_1)(\mathsf{A}\sigma^{\text{pind}} + \sigma^{\text{pind}}\mathsf{A}) + \alpha_3(1-\mathsf{A})\\ &\quad + 2\alpha_{32}I_3(1-\mathsf{A})\alpha_4(3I_4\mathsf{A}^{\text{dev}}) \;=:\; \mathbb{A}:\sigma + \mathsf{B}\\ \partial^2_{\sigma\sigma} f &= \alpha_1\mathbb{P}^{\text{pind}} + (\alpha_2 - \alpha_1)\mathbb{P}^{\text{pind}}_{\mathsf{A}} + 2\alpha_{32}(1-\mathsf{A})\otimes(1-\mathsf{A})\\ &\quad + \alpha_3(1-\mathsf{A})\frac{9}{2}\alpha_4\mathsf{A}^{\text{dev}}\otimes\mathsf{A}^{\text{dev}} \;=:\; \mathbb{A}\end{aligned} \tag{2.38}$$

with the projection tensor

$$\mathbb{P}^{\text{pind}} := \partial_\sigma\sigma^{\text{pind}} = \mathbb{I} - \frac{1}{2}(1\otimes 1) + \frac{1}{2}(\mathsf{A}\otimes 1 + 1\otimes\mathsf{A}) - \frac{3}{2}(\mathsf{A}\otimes\mathsf{A}) \tag{2.39}$$

and $(\mathbb{P}^{\text{pind}}_{\mathsf{A}})_{ijkl} := A_{im}\mathbb{P}^{\text{pind}}_{mjkl} + A_{mj}\mathbb{P}^{\text{pind}}_{imkl}$.

A^{dev} is the deviator of the structural tensor A, $\mathbb{A}$ is the constant bending tensor and B is the first derivative of the linear terms in σ of the quadratic yield locus. This enables us to state the yield function Eq. (2.37) in the more general form:

$$f = \frac{1}{2}\sigma : \mathbb{A} : \sigma + \mathsf{B} : \sigma - 1 \tag{2.40}$$

2.3.2.3 Parameter Identification

To determine the five material parameters α_1, α_2, α_3, α_{32} and α_4 of the yield function, material simulations of the micromechanical unit cell are used. As already explained, in fiber direction yielding is not assumed, because the strength in the preferred direction is determined by the strength of the fibers. So the parameter α_4 is set to zero and there remain four parameters to be determined by means of four virtual material tests done with the micro model. The material tests and there representation in stress space are:

1. Simple shear in the plane perpendicular to the fiber (transverse shear)

$$\sigma = \operatorname{dev}\sigma = \sigma^{\text{pind}} = \begin{bmatrix} 0 & y_{\perp\perp} & 0 \\ y_{\perp\perp} & 0 & 0 \\ 0 & 0 & 0 \end{bmatrix}, \qquad \mathbf{a} = \begin{bmatrix} 0 \\ 0 \\ 1 \end{bmatrix}$$

$$I_1 = (y_{\perp\perp})^2, \qquad I_2 = 0, \qquad I_3 = 0, \qquad I_4 = 0$$

$$\rightsquigarrow \qquad f = \alpha_1 (y_{\perp\perp})^2 - 1 = 0$$

$$\boxed{\alpha_1 := 1/(y_{\perp\perp})^2} \tag{2.41}$$

2. Simple shear in the fiber plane (in-plane shear)

$$\sigma = \operatorname{dev}\sigma = \sigma^{\text{pind}} = \begin{bmatrix} 0 & y_{\perp\parallel} & 0 \\ y_{\perp\parallel} & 0 & 0 \\ 0 & 0 & 0 \end{bmatrix}, \qquad \mathbf{a} = \begin{bmatrix} 1 \\ 0 \\ 0 \end{bmatrix}$$

$$I_1 = 0, \qquad I_2 = (y_{\perp\parallel})^2, \qquad I_3 = 0, \qquad I_4 = 0$$

$$\rightsquigarrow \qquad f = \alpha_2 (y_{\perp\parallel})^2 - 1 = 0$$

$$\boxed{\alpha_2 := 1/(y_{\perp\parallel})^2} \tag{2.42}$$

3. Uniaxial tension and uniaxial compression perpendicular to the fiber

$$\sigma = \begin{bmatrix} 0 & 0 & 0 \\ 0 & 0 & 0 \\ 0 & 0 & y_{\perp} \end{bmatrix}, \qquad \mathbf{a} = \begin{bmatrix} 1 \\ 0 \\ 0 \end{bmatrix}$$

$$I_1 = \frac{(y_\perp)^2}{4}, \qquad I_2 = 0, \qquad I_3 = y_\perp, \qquad I_4 = 0$$

$$\rightsquigarrow \qquad f = \alpha_1 \frac{(y_\perp)^2}{4} + \alpha_3 y_\perp + \alpha_{32} (y_\perp)^2 - 1 = 0 \tag{2.43}$$

Inserting $y_\perp^t$ firstly and $y_\perp^c$ secondly into Eq. (2.43) leads to a system of equations which yields the parameters

$$\boxed{\alpha_{32} := \frac{\frac{1}{y_\perp^t} - \frac{1}{y_\perp^c} - \frac{\alpha_1}{4}(y_\perp^t - y_\perp^c)}{y_\perp^t - y_\perp^c}} \tag{2.44}$$

$$\boxed{\alpha_3 := \frac{1}{y_\perp^t} - \frac{\alpha_1}{4} y_\perp^t - \alpha_{32} y_\perp^t} \tag{2.45}$$

In contrast to transverse and in-plane shear tests, where pronounced plasticity can be observed until failure occurs (see Fig. 2.19), the stress-strain curves from uniaxial loadings of the micro-mechanical model are nearly elastic-brittle, that is, damage in this case is initiated without significant plastic deformation. Consequently, plasticity can be neglected in the case of uniaxial loading. However, to handle the stiffness degradation in the material model, the uniaxial stress-strain curves are first considered as linear-elastic ideal-plastic as the material strengths from uniaxial micro-simulations are considered as the "yield" stresses $y_\perp^t$ and $y_\perp^c$ in uniaxial tension and compression. The stiffness degradation starts immediately, when the "yield" stress in tension or compression, i.e. the particular strength in tension and in compression, is reached. The ideal plastic stresses are the undamaged stresses σ_{eff} and σ is the reduced stress tensor, see Sect. 2.3.1.4. Modelling the plastic behavior of the transverse and in-plane shear tests, the same approach is followed as already demonstrated for the isotropic epoxy resin model. The hardening curve are input via tabulated data giving the yield stress as a function of the corresponding plastic strains. The simulation results from the micro model, that are reflected in the hardening curves, will be used exactly by the material model without any parameter fitting. In analogy for the σ_{vm}-p-invariant-plane for the isotropic yield locus, the transversely isotropic yield locus can be illustrated in an invariant plane respecting the first and third invariant I_1 and I_3. For convenience and for a better comparability with the invariant plane for the isotropic model, the abscissa is the third invariant I_3 and the ordinate is the square root of the first invariant I_1, see Fig. 2.15. To clarify this representation, the stress states for uniaxial, biaxial and pure shear loadings are indicated in Fig. 2.15. Triaxial stress states are not represented in this invariant plane, because stresses in fiber direction are assumed to not induce yielding and so the projections of the stress tensor onto the preferred direction are not reflected in the invariants I_1 and I_3. As illustrated in Fig. 2.15, the ordinate corresponds to a pure transversal shear stress state, the abscissa represents biaxial stress states and the two

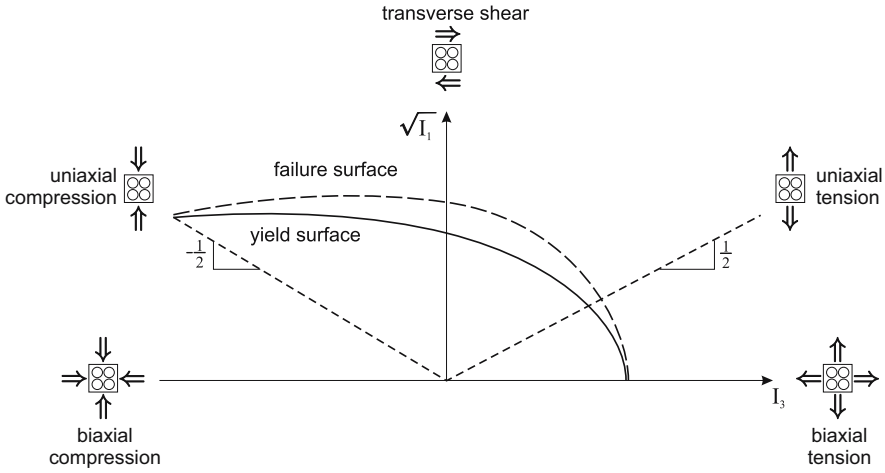

Fig. 2.15 Yield and failure surface of the transversely isotropic material model in $\sqrt{I_1}$-I_3-invariant-plane

graphs with a slope of 0.5 and -0.5 mark uniaxial tension and compression loading states. The stress states and their representation in the I_3-$\sqrt{I_1}$-plane are:

- Transverse shear loading:

$$I_1 = y_{\perp\perp}^2, \qquad I_3 = 0$$

- Uniaxial loading:

$$I_1 = \frac{(y_\perp)^2}{4}, \qquad I_3 = y_\perp$$

- Biaxial loading:

$$I_1 = 0, \qquad I_3 = 2y_{\text{biax}}$$

2.3.3 Transversely Isotropic Damage Formulation

In order to model damage and failure of the fiber bundle, two damage initiation criterions are introduced. The first one, the fiber failure criterion, only accounts for the stress resistance in fiber direction, whereas the second one, the inter-fiber failure criterion, regards stress states caused by shear stresses and loadings perpendicular to the fiber direction. Stiffness degradation and element failure occur in a similar way as already described in the isotropic material model, see Sect. 2.3.1.4. However, if the inter-fiber failure criterion is active, the stresses in fiber direction are not effected, whereas, if the fiber failure criterion is achieved, the material collapses and the affected elements are removed from the mesh.

2.3.3.1 Fiber Failure Criterion

It is assumed, that the strength in fiber direction is mainly governed by the strength of the fibers. Thus, in the material model a fiber tensile strength $R_{\parallel}^{t}$ and a compressive strength $R_{\parallel}^{c}$, representing the resistance of the fiber bundle under uniaxial tension and compression in fiber direction, are needed as input data. Theses ultimate stresses are obtained from experiment [11]. If one of these strengths is achieved, the material fails and there is no remaining load carrying capacity. The failure criterion for fiber failure is:

$$\frac{\mathbf{a}^{T}\sigma\mathbf{a}}{R_{\parallel}} = 1 \tag{2.46}$$

The term $\mathbf{a}^{T}\sigma\mathbf{a}$ is the projection of the stress tensor onto the preferred direction and $R_{\parallel}$ is the resistance of the fiber bundle in fiber direction in tension ($R_{\parallel} = R_{\parallel}^{t}$) and in compression ($R_{\parallel} = R_{\parallel}^{c}$) respectively.

2.3.3.2 Inter-Fiber Failure Criterion

To consider stress states out of the fiber direction, a further damage criterion is introduced. This inter-fiber failure criterion is formulated in the format of the yield locus in the $\sqrt{I_1}$-I_3-invariant-plane, as illustrated in Fig. 2.15. The failure surface is:

$$r = \beta_1 I_1 + \beta_2 I_2 + \beta_3 I_3 + \beta_{32} I_3^2 + \beta_4 I_4^2 - 1 \tag{2.47}$$

The failure criterion is active, when $r = 0$. The parameters β_1, β_3 and β_{32} are obtained in the same manner as the parameters α_1, α_3 and α_{32} for the yield function Eq. (2.37). Therefore, the material strengths of uniaxial tension $R_{\perp}^{t}$ and compression $R_{\perp}^{c}$ perpendicular to the fiber and the material strength of transverse shear $R_{\perp\perp}$ and in-plane shear $R_{\parallel\perp}$ has to be inserted instead of the yield stresses in Eq. (2.37). The required strengths $R_{\perp}^{t}$, $R_{\perp}^{c}$, $R_{\perp\perp}$ and $R_{\parallel\perp}$ are obtained from simulations with the micromechanical unit cell. If the inter-fiber failure criterion is reached, stiffness degradation is initiated and controlled by a scalar damage variable d, es already described in Sect. 2.3.1.4 for the isotropic model. The damage variable d does not effect the stresses in fiber direction.

2.4 Results of Micromechanical Unit Cell Computations

The convergence of the presented material in combination with the voxel mesh is very good as seen in Fig. 2.16. It shows stress-strain curves from computations on the micromechanical unit cell under compression and shear with different mesh refinements (40×40, 80×80 and 160×160 elements).

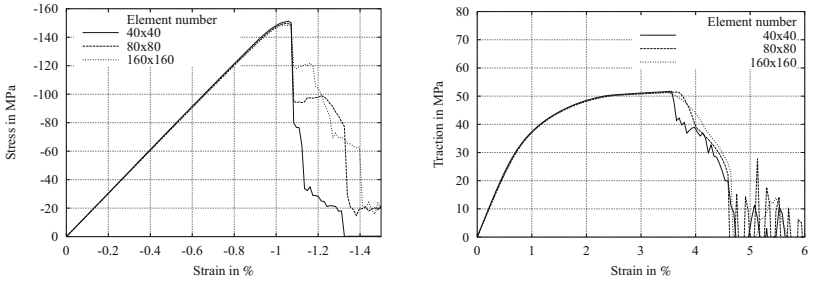

(a) Transverse compression (b) In-plane shear

Fig. 2.16 Stress-strain curves of micromechanical unit cell computations with different element number

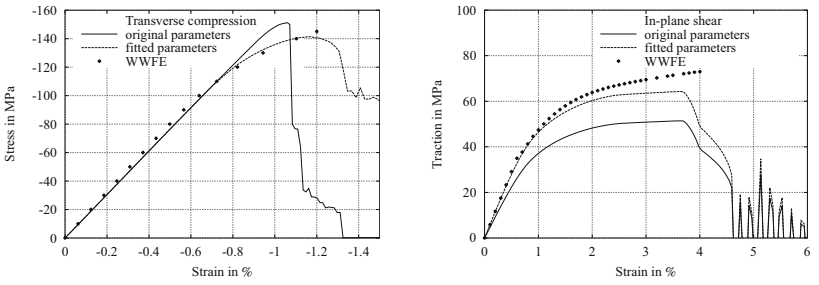

(a) Transverse compression (b) In-plane shear

Fig. 2.17 Stress-strain curves of micromechanical unit cell computations compared with test results from WWFE

2.4.1 Comparison with Test Results from WWFE

To validate the presented model, test results on unidirectional lamina from the World-Wide Failure Exercise [11] were compared with results from the micromechanical unit cell. Test results are given for transverse compression and in-plane shear of unidirectional lamina comprised of E-Glass fibers and epoxy resin MY750/HY917/DY063 with a volume fraction $v_f = 60\%$. The material parameters given in the WWFE are summarized in Table 2.1. Unfortunately these are not all parameters needed for the material model used here Therefore the plastic hardening curves of epoxy resin RIM135 given in Fig. 2.11 are used for this resin as well as shear strength and failure strains. Table 2.1 shows that these two resin systems are very similar. In the WWFE a strain energy release rate $G_{Ic} = 0.165 \frac{\mathrm{N}}{\mathrm{mm}}$ is given for the lamina and taken for the resin here.

Stress-strain curves of the micromechanical unit cell computations are shown in Fig. 2.17 compared to test results from the WWFE. First of all, both curves do describe the main characteristics of the experimental results very well due to the material formulation. In principle the strength of the unit cell is dependent on the strength of the epoxy matrix, which is the weaker of the two constituents. Therefore

an apparently implausible result of the computation is that the strength under compression is higher than the one given for the epoxy resin in Table 2.1, which but is the strength under uniaxial compression. However, in the micromechanical unit cell a three-dimensional stress state occurs. It is caused by different Young's modulus and Poisson's ratio of fiber and matrix and the fact that the unit cell is built of volume elements and under plain strain conditions. In Sect. 2.3.1 it can be seen, that the stress triaxiality has a considerable influence on the strength. Multiaxial stresses under compression increase the strength, under tension the strength decreases. This is the reason why under compression the strength of the unit cell is higher than that of epoxy under uniaxial compression and why under tension the strength of the unit cell is very small.

Thus, under compression the results are in good agreement with the test curves, although the nonlinearity is not modelled very well. It is captured better when lowering the strength to 100 MPa and increasing the strain energy release rate to $G_{Ic} = 0.330$ N/mm, see Fig. 2.17a. Under shear the test results are much stiffer, about 25%, than the unit cell computations. However, Hinton states in the WWFE that the experimental determination of shear and compression properties is particularly difficult and material data given might be inaccurate. Therefore, by increasing shear modulus and hardening curve by 25% test results and computation agree very well, see Fig. 2.17b.

Figure 2.18 shows the evolution of the crack path through the 40×40 elements unit cell. Under in-plane shear a damage is initiated on the interface between fiber and matrix and then localizes in a straight crack band through the unit cell. Under compression the crack is not initiated on the interface but in the upper left corner were the highest strains are in the matrix, but the crack then evolves along the interface, where large shear deformations occur.

The in-plane shear strength calculated here is a little lower than the shear strength of the epoxy $51.74 < 55.0$ MPa. This result is reasonable because the crack runs through the epoxy matrix, see Fig. 2.18b and therefore the unit cell strength cannot exceed the epoxy strength. Actually it is a little smaller due to the inhomogeneous stress distribution.

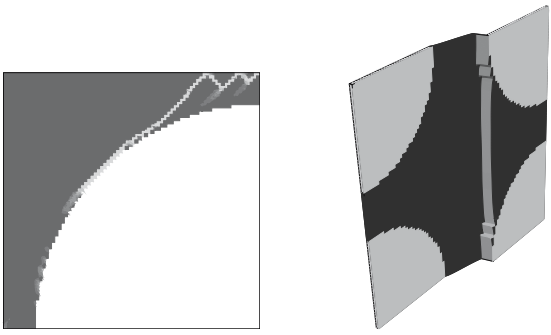

(a) Transverse compression (b) In-plane shear

Fig. 2.18 Damage evolution in micromechanical unit cell

2.4.2 Results of Micromechanical Unit Cell for Homogenization

For a complete set of parameters for the transversely isotropic fiber bundle material four virtual tests are needed. The homogenized stress-strain curves given in Fig. 2.19 were determined for fiber bundles comprising of e-glass fibers and epoxy resin RIM 135 with a volume fraction $v_f = 50\%$. Material parameters are given in Table 2.1, the plastic hardening curves are shown in Fig. 2.11 and the strain energy release rate $G_{Ic} = 0.165$ N/mm is taken from the similar material of the WWFE.

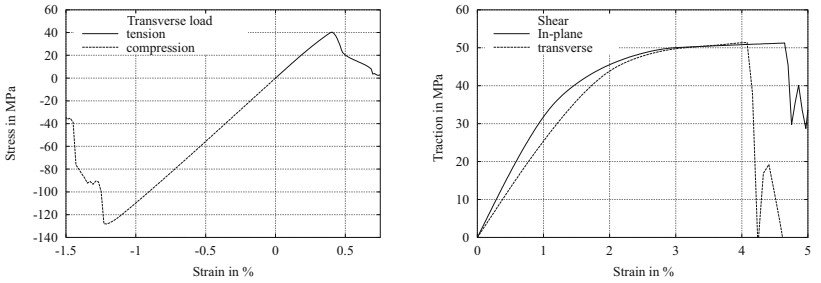

(a) Transverse compression (b) In-plane shear

Fig. 2.19 Stress-strain curves of micromechanical unit cell computations for use in mesomechanical unit cells

Table 2.3 Mechanical properties WWFE (E-Glass/MY750/HY917/DY063-epoxy) and E-Glass/RIM135 lamina

Properties	Unit	Test results WWFE	Micro. unit cell	
			WWFE	E-Glass/ RIM 135
Longitudinal modulus[a] $E_{\parallel}$	GPa	45.6	45.7	38.7
Longitudinal tensile strength $R^t_{\parallel}$	MPa	1280	1308	1075
Longitudinal tensile failure strain $\varepsilon^t_{\parallel}$	%	2.807	2.807	2.807
Transverse modulus[a] $E_{\perp}$	GPa	16.2	15.06	11.07
Transverse compressive strength $R^c_{\perp}$	MPa	145	149.5	128.5
Transverse compressive failure strain $\varepsilon^c_{\perp}$	%	1.2	1.05	1.21
Transverse tensile strength $R^t_{\perp}$	MPa	45	38.3	40.3
Transverse tensile failure strain $\varepsilon^c_{\perp}$	%	0.25	0.3	0.4
In-plane Shear Modulus[a] $G_{\parallel\perp}$	GPa	5.83	4.66	3.51
In-plane Poisson's ratio $\upsilon_{\parallel\perp}$		0.278	0.256	0.264
In-plane Shear strength $R_{\parallel\perp}$	MPa	73	51.7	51.2
In-plane Shear failure strain $\upsilon_{\parallel\perp u}$	%	4	3.42	4.64
Transverse Shear modulus[a] $G_{\perp\perp}$	GPa	–	3.3	2.63
Transverse Poisson's ratio $\upsilon_{\perp\perp}$		0.4	0.262	0.32
Transverse Shear strength $R_{\perp\perp}$	MPa	–	51.04	51.4
Transverse Shear failure strain $\upsilon_{\perp\perp u}$	%	–	3.17	4.08

[a] Initial modulus

Table 2.3 sums up homogenized material parameters of these computations and compared to test results of the WWFE and micromechanical unit cell computations given in Sect. 2.4.1.

2.5 Conclusion

A multiscale analysis for the determination of stiffnesses and strengths of textile composites has been presented. It consists of unit cells on micro- and mesoscale to describe the behavior of unidirectional fiber bundle material and the textile fabric architecture, respectively. Novel material formulations for isotropic epoxy resin and transversely isotropic fiber bundle material have been developed that allow for load dependent plastic hardening. The hardening curves are input as tabulated data directly from tests or computations. Results of micromechanical unit cell computations have been compared to experimental results of the WWFE and show the capabilities of the presented material model and multiscale analysis.

Acknowledgements Part of this work was funded by the German Research Council (DFG). This support within the framework of SPP-1123 "Textile composite design and manufacturing technologies for lightweight structures in mechanical and vehicle engineering" is highly appreciated.

References

1. Boehler JP (ed) (1987) Applications of Tensor Functions in Solid Mechanics. CISM No. 292, Springer, Wien
2. Cox BN, Carter WC, Fleck NA (1994) A binary model of textile composites - I. Formulation. Acta Metall Mater 42:3463–3479
3. Ehrenstein GW (2006) Faserverbund-Kunststoffe. Hanser Fachbuch, München
4. Eidel B (2004) Anisotropic Inelasticity - Modelling, Simulation, Validation. Ph.D. thesis, Technische Universität Darmstadt
5. Ernst G, Hühne C, Rolfes R. (2006) Micromechanical voxel unit cell for strength analysis of fiber reinforced plastics. Proceedings of the CDCM06
6. Fiedler B, Hojo M, Ochiai S, Schulte K, Ando M (2001) Failure behavior of an epoxy matrix under different kinds of static loading. Compos Sci Technol 61:1615–1624
7. Gunnion AJ (2004) Analytical assessment of fibre misalignment in advanced composite materials. Ph.D. thesis, RMIT University
8. Haasemann G, Ulbricht V (2006) On the simulation of textile reinforced composites and structures. Proc Appl Math Mech 6:479–480
9. Haufe A, Du Bois PA, Kolling S, Feucht M. (2005) A semi-analytical model for polymers subjected to high strain rates. In: 5th European LS-DYNA Users' Conference, Birmingham, ARUP, UK
10. Hillerborg A, Modeer M, Petersson PE (1976) Analysis of crack formation and crack growth in concrete by means of fracture mechanics and finite elements. Cem Concr Res 6:773–782
11. Hinton MJ, Kaddour AS, Soden PD (eds) (2004) Failure Criteria in Fibre Reinforced Polymer composites: The World-Wide Failure Exercise. Elsevier Science, Oxford

12. Hughes TJR (2003) Efficient and simple algorithms for the integration of general classes of inelastic constitutive equations including damage and rate effects. In: Hughes TJR, Belytschko T (eds) Nonlinear Finite Element Analysis Course Notes, Zace Services Ltd., Lausanne
13. Juhasz TJ, Rolfes R, Rohwer K (2001) A new strength model for application of a physically based failure criterion to orthogonal 3D fiber reinforced plastics. Compos Sci Technol 61:1821–1832
14. Karkkainen RL, Sankar BV (2006) A direct micromechanics method for analysis of failure initiation of plain weave textile composites. Compos Sci Technol 66:137–150
15. Kim HJ, Swan CC (2003) Voxel-based meshing and unit-cell analysis of textile composites. Int J Numer Methods Eng 56:977–1006
16. Lemaitre J, Chaboche JL (1988) Mécanique des matériaux solides. Dunod
17. Lomov SV, Belov EB, Bischoff T et al. (2002) Carbon composites based on multiaxial multiply stitched preforms. Part I - Geometry of the preform. Compos Part A 33:1171–1183
18. Rogers TG (1987) Yield criteria, flow rules and hardening in anisotropic plasticity. In: Boehler JP (ed) Yielding, Damage and Failure of Anisotropic Solids, Volume 5, pages 53–79. EGF Publication, Mechanical Engineering Pubns Ltd., Bury St. Edmunds
19. Rolfes R, Ernst G, Hartung D, Teßmer J (2006) Strength of textile composites - A voxel based continuum damage mechanics approach. In: Mota Soares CA, Martins JAC, Rodrigues HC, Ambrosio JAC (eds) Computational Mechanics - Solids, Structures and Coupled Problems, pages 497–520. Springer, Lisbon
20. Schröder J (1995) Theoretische und algorithmische Konzepte zur phänomenologischen Beschreibung anisotropen Materialverhaltens. Ph.D. thesis, Universität Hannover
21. Simo JC, Hughes TJR (1998) Computational Inelasticity. Springer, New York
22. Takano N, Uetsuji Y, Kashiwagi Y, Zako M (1999) Hierarchical modelling of textile composite materials and structures by the homogenization method. Model Simul Mater Sci Eng 7: 207–231

Chapter 3
Practical Challenges in Formulating Virtual Tests for Structural Composites

Brian N. Cox, S. Mark Spearing, and Daniel R. Mumm

Abstract Taking advantage of major recent advances in computational methods and the conceptual representation of failure mechanisms, the modeling community is building increasingly realistic models of damage evolution in structural composites. The goal of virtual tests appears to be reachable, in which most (but not all) real experimental tests can be replaced by high fidelity computer simulations. The payoff in reduced cycle time and costs for designing and certifying composite structures is very attractive; and the possibility also arises of considering material configurations that are too complex to certify by purely empirical methods. However, major challenges remain, the foremost being the formal linking of the many disciplines that must be involved in creating a functioning virtual test. Far more than being merely a computational simulation, a virtual test must be a system of hierarchical models, engineering tests, and specialized laboratory experiments, organized to address the assurance of fidelity by applications of information science, model-based statistical analysis, and decision theory. The virtual test must be structured so that it can function usefully at current levels of knowledge, while continually evolving as new theories and experimental methods enable more refined depictions of damage.

To achieve the first generation of a virtual test system, we must pay special attention to unresolved questions relating to the linking of theory and experiment: how can we assure that damage models address all important mechanisms, how can we calibrate the material properties embedded in the models, and what constitutes sufficient validation of model predictions? The virtual test definition must include real tests that are designed in such a way as to be rich in the information needed to

B.N. Cox
Teledyne Scientific Co., LLC, 1049 Camino Dos Rios, Thousand Oaks, CA 91360, United States of America, e-mail: bcox@teledyne.com

S.M. Spearing
School of Engineering Sciences, University of Southampton, Southampton, SO17 1BJ, United Kingdom, e-mail: spearing@soton.ac.uk

D.R. Mumm
University of California, Irvine, CA, United States of America, e-mail: mumm@uci.edu

inform models; and model-based analyses of the tests are required to mine the information. To date these compelling issues have been greatly underserved by both the modeling and experimental communities. Model-based analysis of tests has been undertaken only in terms of very simple (linear or continuum) engineering concepts; information-rich tests for more complex damage mechanisms have not been defined; and in fact the information in which experiments need to be rich has not been stated. Specific challenges in designing experiments for informing virtual tests and some promising experimental methods are summarized here.

3.1 Introduction – The Concept of a Virtual Test

The process of qualifying and certifying composite materials and structures for strength, fatigue life, fracture resistance, and damage tolerance remains almost entirely empirical. Coupon tests are conducted for all material types (layups), under all stress states that are anticipated in the structure, and covering monotonic loading, fatigue, impact, and long-duration environmental exposure. Coupon tests are followed by tests of large substructures and structures subjected to service conditions. In the case of airframes, the cost of testing to prove safety is immense: a typical large airframe, for example, currently requires $\sim 10^4$ tests of components and structures up to entire tails, wing boxes, and fuselages, to achieve safety certification [27].

While laminar stress analysis is an excellent tool for predicting the distribution of loads throughout a composite structure when its behavior is linear-elastic, once damage begins prediction is much more difficult. Damage in composites involves extremely complicated nonlinear processes acting from the atomic scale (molecular bond rupture, fiber-matrix debonding), through the microscale (microcracking, crazing, kink band formation), and on up to the scale of the structure itself (large delamination cracks and other cracks and buckling modes). Nevertheless, advances in modeling concepts and computational methods, including the refinement of cohesive models of fracture and the formulation of mixed stress-strain and traction-displacement models that combine continuum (spatially averaged) and discrete damage representations in a single calculation, have led to damage simulations of increasing realism. Emerging hierarchical formulations add the potential of tracing the damage mechanisms down through all scales to the atomic. As the fidelity of modeling increases, the possibility is approached of using simulations as virtual tests, replacing perhaps the majority of the real tests currently needed for design and system certification.

To serve as a virtual test, a simulation need not necessarily re-create every last detail of damage, right down to molecular processes, but it must be a satisfactory replication of a real test in certain engineering aspects. Just which real test results must be replicated will depend on the application. The minimum requirements will commonly include (1) correct predictions of the nonlinear relation between load and far-field displacement (the compliance of the part); (2) the ultimate strength of the

part if the magnitude of the load in a particular loading configuration continues to rise; (3) its strength if the loading configuration is switched to a different load type after damage has already occurred in the first configuration; and (4) changes in part strength under cyclic loading or environmental exposure. The last two requirements are usually the most demanding of fidelity, because they depend on accurate prediction of the type and spatial distribution of damage, resolved down to some material gauge length. The question of how small that gauge length must be is one of the most critical in defining a valid virtual test.

This definition of a virtual test drives the formulation to a top-down, rather than bottom-up model. A top-down model begins with a macroscopic engineering model, which is progressively augmented by incorporating just those successive levels of detail that are necessary to account for features of engineering tests. Since the model is always calibrated against engineering tests, predictions are available to designers at any stage of model augmentation, subject to some current set of restrictions. The process of continually validating predictions against tests rapidly distinguishes those mechanisms, or those parameters incorporated in models of mechanisms, that have an important effect on engineering performance from those that are irrelevant. A bottom-up model, in contrast, seeks to simulate failure by building up detailed models of atomic and molecular processes using quantum mechanics and classical molecular dynamics [1, 2, 6, 8, 9, 30, 32, 41]. The difficulty with the bottom-up method in the context of virtual tests is that the intervals of time and the size of the material that can be modeled remain many orders of magnitude below the duration of a test and the size of a structural test coupon, let alone a structure; therefore, the mechanisms that may be revealed by the model during a simulation (rather than written into the model explicitly) cannot be guaranteed to be exhaustive of those that arise in large-scale or long-duration experiments. While a top-down model may well reach down to include an atomic scale model in representing a particular mechanism, attempts to build complete simulations from the bottom up continue to fall well short of satisfying the requirements of virtual tests of engineering materials.

The utility of a virtual test will be as an accurate interpolator between relatively sparse engineering data accumulated by conventional, real tests. The interpolation could, for example, span deviations from the real test matrix in ply layup, stress state, or the shape of stress concentrators such as cutouts. There are also large benefits associated with reducing the need for long duration testing or tests of coupled environmental and mechanical effects, whose strong interactions necessitate complicated and expensive test matrices for accurate failure mapping. A realistic goal might be to substitute for 90% of the test matrix currently required for component design and certification, using the remaining 10% of the real test matrix to anchor the virtual tests and establish their validity.

In this vision of a virtual test, the link between model and experiment is central; it defines the virtual test. Experimental limitations on our ability to witness damage mechanisms and quantify the material behavior that controls them impose a rigid bound upon what is achievable in a virtual test.

3.2 The Structure of a Virtual Test – Formalizing the Link Between Experiment and Theory

Figure 3.1 introduces a schematic of the structure and components of a virtual test in the vision presented in this paper. (The reader is also referred to an excellent paper by Ashby on how to construct a model for more general materials problems than considered here [3].) The central column shows a typical choice of the hierarchical separation of modeling scales in a multi-scale simulation. The formalism of multi-scale methods binds the hierarchy together. The separation into scales, the phenomena modeled, and the idealizations used at each scale are chosen in response to the physics discovered by many types of experiments that are usually complicated and conducted in specialized laboratories (right hand column). The left column shows classes of engineering tests used in the field, with links to the level of detail required in the top-down modeling strategy for their simulation. The engineering tests provide data against which the choice of model formulations can be assessed and validated via sensitivity tests. The engineering tests also provide the primary data from which model calibration can be carried out via inverse problem methods. The specialized laboratory experiments (right column) may have a supplementary role in model calibration, provided standards of easy repeatability can be satisfied. The arrows in the schematic show some of the obvious links between engineering tests, specialized experiments, and theory; others can also be imagined.

The initial process of choosing a model that is an apt representation of an observed mechanism is qualitative and subjective. The modeler will refer to the accumulated wisdom of the literature, examine the best evidence available from experimental sources, and choose a theoretical formulation of the features of observations that are perceived to be most important and satisfy personal biases. In a top-down strategy, the modeler will also choose which mechanisms and modeling idealizations should be allocated to different levels in the model hierarchy. For example, the highest level (simplest) representation of a composite laminate may include only calculations of stress and strain in the elastic regime; the next level of detail might include continuum damage representations of nonlinearity; the next level might include principal crack systems (delaminations, splitting cracks, etc.), the next level a discrete representation of microcracks, the next level failure processes on the scale of individual fibers, etc. (Fig. 3.1). Or some other partitioning of the hierarchy might be preferred. There is no unique outcome of this decision-making process.

However, once the initial choices have been made, a formal strategy of refining and testing the fidelity of the model must be found. One method of posing this problem is to study influence functions [31,44] that quantify the degree to which an engineering observable (ultimate strength, crack size at some point in the loading history, etc.) depends on the choice of the most detailed hierarchical level that is included, which particular mechanisms are included, the functional form of a model that represents a particular mechanism, or the values of parameters in models of mechanisms. One should expect to discover that certain engineering properties can

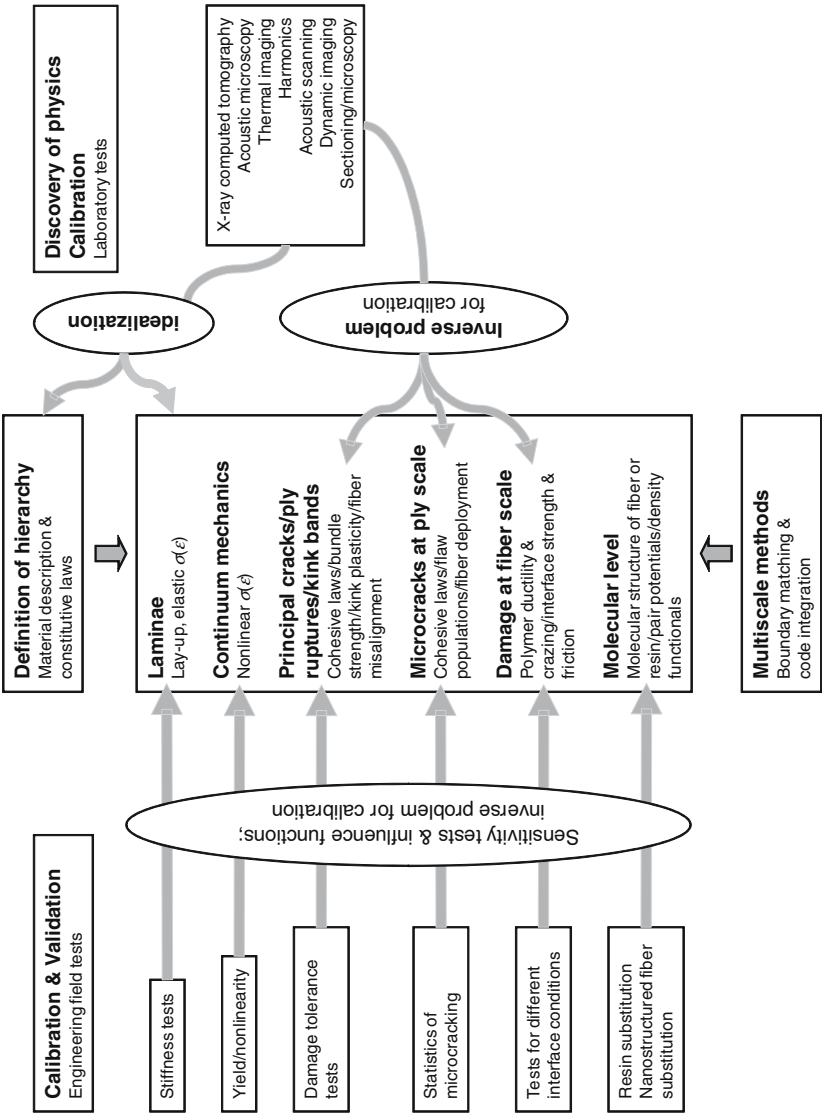

Fig. 3.1 Structure of a virtual test

be successfully predicted with a high level (simple) simulation, while others require that increasing levels of detail be included. For each level of complexity chosen for the simulation, some mechanisms will prove irrelevant to certain engineering properties and critical to others. Curiously, this exercise of systematically relating model complexity and mechanisms to the fidelity of engineering predictions seems never to have been undertaken in the context of composite damage simulations; yet it is an essential step towards a verified virtual test.

The study of influence functions should not be conducted as a theoretical exercise exclusively within the community of modelers (a regrettably common paradigm!). Experimental confirmation of an identified strong influence should always be sought, e.g., by varying the ply lay-up or resin in such a way that the simulations predict a significant change in the value or variance of an observable. The ability of a simulation to match the values of different engineering observables simultaneously (e.g., monotonic strength and fatigue lifetime) and to predict the variance in observables should be tested. The internal elements of the simulation, whether models of mechanisms or parameters within models of mechanisms, that have the greatest impact on predicted properties and their variance need to be identified.

A formal approach should also be followed for seeking the optimal values of model parameters via experimental calibration. Simple curve fitting (e.g., minimizing deviance) may not be sufficient; a preferable method is often to infer a model parameter from experimental data by solving an inverse problem [39, 47, 54]. In principle, the kernel of the model simulation of an experiment, whose inverse maps data onto inferred quantities, can always be derived, although this may be a substantial undertaking for a complex, nonlinear experiment. The labor is ultimately justified because such a model-based approach to deducing parameters from experiments ought to be the most accurate available (provided the simulation is based on the correct physics!). The inverse problem approach commonly includes regularization to treat the effects of noise and ill-posedness in the parameter evaluation. The outcome of the regularization calculation is a quantitative estimation of the degree to which the parameter can be determined. (Illustrations of the use of inverse methods to assess the level of detail deducible for single-mode cohesive laws from fracture data can be found in [17, 43].) Thus this formal analysis has the important virtue of quantifying the degree to which mechanisms and parameters have an influence on experiments; if the parameters cannot be determined because of noise and ill-posedness, the measurable outcome of the experiment has no information in it that determines the parameter. In other words, the parameter is not relevant to the engineering property being measured.

3.3 The System Management Challenge

Figure 3.2 presents the composition of a virtual test in terms of disciplines, in approximately one-to-one correspondence with the schematic of Fig. 3.1. At least six distinct disciplines can be identified, peopled by researchers and engineers who

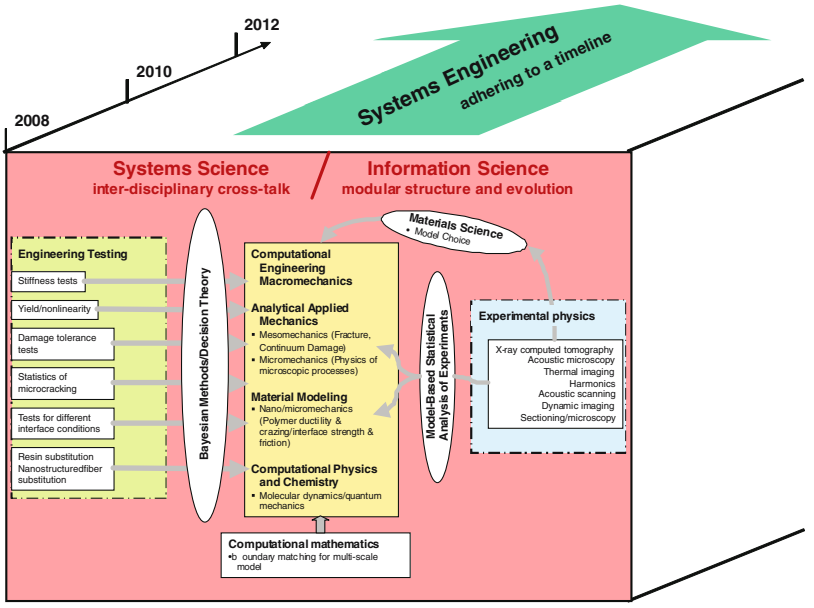

Fig. 3.2 Disciplinary composition of a virtual test. The general layout corresponds to that of Fig. 3.1

have little tradition of joint work. The framework that embraces these disciplines comprises two distinguishable activities, namely Systems Engineering and Systems Science. Systems Engineering governs the functional definition of the virtual test, coordination of people working on its development, adhesion to timelines in development work, and assuring the quality of the final product. Systems Science deals with coupling the scientific details that are involved in work performed in different disciplines.

A number of theoretical disciplines contribute to the formulation of the multi-scale simulations (central column in Fig. 3.2), ranging from engineering fracture mechanics and damage mechanics for modeling at the coarser scales, through applied mechanics for modeling micromechanisms using continuum mechanics, down ultimately to computational physics and chemistry for molecular dynamics simulations (either classical or quantum based) and the analysis of inter-atomic bonds. The boundary matching problems of linking models operating at vastly different time and length scales have been addressed by a newly evolving branch of mathematics, distinct from any of the specialties used in modeling a single scale [7, 29, 46, 57, 58].

The column headed "experimental physics" spans the traditional disciplines of non-destructive evaluation (acoustics, X-radiography, electromagnetic methods, thermal wave analysis), as well as computed tomography for retrieving three-dimensional images, which has been developed furthest in the medical community. But it also extends now to emerging areas of physics, especially the generation of

high fluxes of coherent, short pulse radiation (X-rays, terahertz radiation) or particles (neutrons, positrons) generated using femtosecond laser pulses [12, 22, 56, 61]. Interesting challenges arise for materials modelers in mining relevant information from new experiments based on these sources. A new role also exists for nanoscale materials synthesis: can multifunctional materials be devised that enhance the sensitivity of new experiments by interacting with the probing radiation or particle fluxes?

The column headed "engineering testing" refers specifically to the discipline of field engineers versed in the definition and use of standardized tests for structural performance and reliability. This discipline includes the members of standards committees (e.g., within the American Society for Testing and Materials) and certifying agencies (e.g., the U. S. Federal Aviation Authority).

Between models and engineering tests or models and experimental physics fall mathematicians and statisticians. The techniques of model-based analysis of experiments, inverse problem theory, decision theory, and Bayesian methods of predicting distributions (e.g., for remaining life) given the condition of an experimental result all have important roles in maximizing the flow of information from experiments into models.

The last discipline in the virtual test paradigm is information science, which contributes modular structures and protocols for linking disparate computational, statistical and interfacing software. Information science addresses challenges that are crucial to maximizing the benefit of investing in a virtual test system: how can a virtual test system be constructed so that it can easily expand to incorporate new levels of modeling or new classes of experimental data; and how can the system be assured of continuing as a growing entity after the first generation of experts who have created it have moved away to other projects? Part of the answer to these challenges must come from business success: a virtual test system will grow and survive if it is profitable. But the practical issues of constructing the system in such a way that data can flow freely among different disciplines, and modules can be easily revised or added, must also be dealt with.

3.4 Experiments That Guide Model Formulations

Much of the taxonomy of damage mechanisms in polymer composite laminates is well known through many decades of testing and post-mortem analysis. For the task of identifying mechanisms, destructive sectioning prior to ultimate failure is often acceptable, after which optical and electron microscopy will reveal details down to submicron scales. Identified mechanisms include delamination cracking, large splitting cracks running in the loading direction within aligned plies, diffuse transverse microcracking within off-axis plies, the microbuckling (kinking) of aligned fibers under compression, ply buckling, global buckling, matrix crazing leading to hackle cracks, matrix shear bands emanating from stress concentrators, debonding of the fiber/matrix interface, fiber rupture, and fiber collapse in compression.

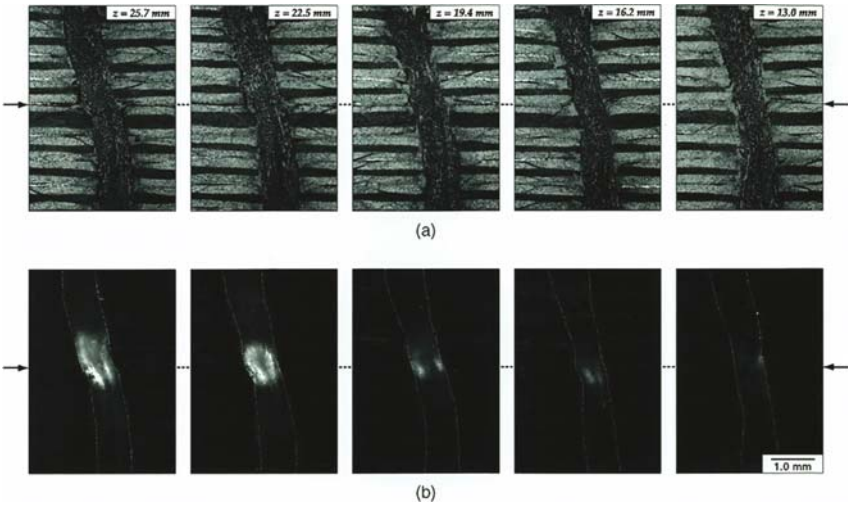

Fig. 3.3 Images of stitches reinforcing a carbon/epoxy laminate at marked distances z behind a mode II delamination crack tip: (**a**) optical images; (**b**) polarized reflected light images

An unusual example of information detectable on sections is shown in Fig. 3.3. A mode II delamination crack has been grown through a carbon/epoxy laminate reinforced by stitching. The specimen has then been fixed in a bath of resin, sectioned while still under load (specimen and grips together), and polished on a section that passes through a series of individual stitches. The stitches seen in the figure are at increasing distances from the delamination crack tip (which is out of frame to the right) and the series therefore shows how the state of deformation varies as the crack sliding displacement increases (from right to left). The deformation is revealed by polarized reflected light microscopy, which picks up changes in the refractive index of the polymer due to irreversible damage (crazing, etc.). Thus the light regions show concentrations of pseudo-plasticity in the material. The plasticity is confined mostly to the stitches themselves at these small crack sliding displacements; less sensitive observations reported elsewhere show that the laminate also deforms at larger sliding displacements, as the stitches press into it laterally [43, 55]. These images of the distribution of plasticity in stitched composites provided essential guidance to the formulation of models of the mechanics of the bridging supplied by the stitches. They show that, in contrast to the case of stitches that bridge mode I cracks, models of the mode II stitch movement and pullout that treat the stitch as elastic could not be correct [15, 16]. Similar images of other zones of stress concentration in composites would be very enlightening.

Information from imaged sections is nevertheless limited. In particular, a section provides almost no information about the disposition of damage in three dimensions and therefore limited information on the shape of cracks or interactions between different damage mechanisms. A three-dimensional image can be built up by serial sectioning or progressive polishing, but this is very expensive,

provides poor information about any damage entities that lie almost parallel to the exposed surface, and causes concern over possible changes in the damage state during material removal. A much more satisfactory experiment probes the interior of the composite without sectioning.

Early experiments to probe a material's interior predominantly used X-rays and acoustic imaging. Figure 3.4 shows damage mechanisms in a carbon/epoxy laminate

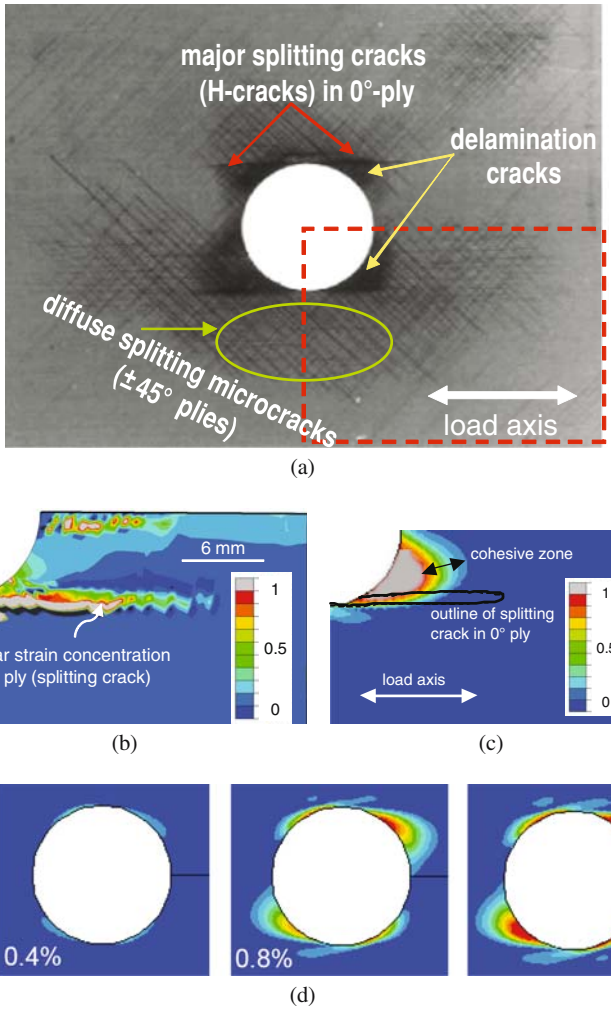

Fig. 3.4 **(a)** X-radiography images of a quasi-isotropic laminate with a circular hole loaded in tension [13] show splitting cracks, delaminations, and diffuse microcracking occurring predominantly in the 45° plies. **(b)** Computed continuum damage distribution in 0° ply (blue undamaged; gray is completely failed material) showing shear strain concentration that forms splitting crack. **(c)** Computed damage in cohesive zone between 0° and 45° plies (blue is undamaged; gray is completely failed material). **(d)** Initiation and evolution of damage in cohesive zone between 0° and 45° plies at marked applied strains (blue is undamaged material; red is completely failed (traction-free)) [20]

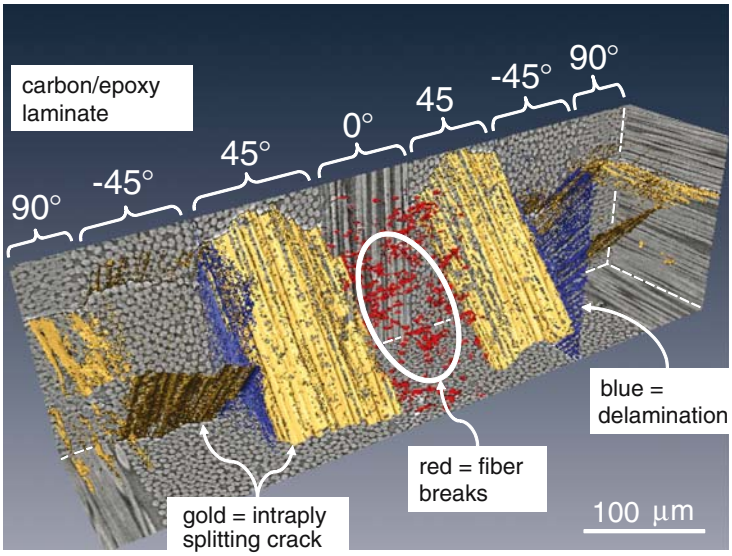

Fig. 3.5 X-ray computed tomography image of damage in a quasi-isotropic carbon/epoxy laminate (Ian Sinclair, University of Southampton, UK, 2007) (Reproduced by kind permission)

loaded in tension-tension fatigue, revealed by X-ray radiography. The image is a projection through the thickness of the laminate and therefore does not resolve depth through the laminate, but the cracking systems are well defined and can be correlated with plies by other means (although this would be more difficult in field applications or for complex, thicker layups). This imaging is however destructive, in that the material is significantly perturbed: the cracks are visible only if they are first filled with a dye penetrant, which could modify any further crack or damage development if the test were continued.

Continuing advances in X-ray computed tomography have recently led to very exciting demonstrations of the possibilities for imaging internal damage nondestructively. Figure 3.5 shows microcracking and fiber breakage in a cuboidal volume within a quasi-isotropic carbon/epoxy laminate loaded in tension along the 0° fiber direction. This image was reconstructed from data taken at the European Synchrotron Radiation Facility facility in Grenoble, using a high flux X-ray beam line. The gray contrast in the image shows the fiber (light gray) and matrix (dark gray) positions on the three planes furthest from the viewer that bound the image domain. The orientations of the plies can be inferred from the shapes of the individual fibers on these planes (either circles, ellipses, or lines). The colored features show damage within the interior of the cuboid. A complex system of interacting fiber breaks (red), delamination cracks (blue), and intraply transverse microcracks (gold) is revealed. The spatial resolution of the damage imaging in this image is approximately 0.7 µm, which is an order of magnitude better than achieved in current medical imaging or laboratory systems. The value of three-dimensional imaging is clear: the relation between the spatial distribution of different damage mechanisms is revealed.

For example, a correlation is evident between the fiber breaks in the 0° ply and the splitting cracks on neighboring plies, the former falling approximately on the same plane as the splitting cracks.

3.5 Challenges in Observing Mechanisms

While the computed tomography represented by Fig. 3.5 offers a breakthrough in the clarity with which damage mechanisms can be imaged, the depiction of damage initiation and evolution remains far from complete. Consider, for example, the onset of diffuse transverse microcracking in off-axis plies, e.g., a 90° ply. These cracks are bounded in one direction by the ply thickness, but extend infinitely (or to the edges of the component) in the fiber direction. Observations of analogous cracks in thin films, where the growth process can be relatively stable due to ductility in either the film or the substrate, suggests that extension in the fiber direction will occur via the so-called tunneling crack mechanism (Fig. 3.6) [19, 23, 35, 36, 40, 53]. However, direct observation of the tunneling mode of propagation has not been made for transverse microcracks in laminates.

The experimental challenges increase as microcrack initiation is considered at finer scales: prior to tunneling propagation, an earlier phase of growth is necessary to create a microcrack that has the tunneling configuration, i.e., that extends across the thickness of the ply. This first phase begins with damage at a critical defect within the ply, either an imperfection of the resin or a variation in the deployment of fibers that creates a local stress concentration in the resin. The first observable matrix microcrack will have a length similar to the spacing between two fibers ($\sim$1 μm in a carbon fiber composite). Theoretical studies suggest some surprising possibilities. When the composite is loaded in tension with the stress axis perpendicular to the fiber direction, the highest stress concentrations between fibers do not necessarily trigger microcracks in planes normal to the load axis. Depending on local fiber separations, the magnitude of residual stresses, and the integrity of the fiber-matrix interface, the microcracks may actually initiate on planes parallel to the load axis (Fig. 3.6c). This counter-intuitive prediction is corroborated by experiments on a composite of large (150 μm) SiC fibers in a low-ductility Ti_3Al matrix [42]. (The predicted stress variations are independent of the scale of the fibers in a linear material system.) Subsequent growth and coalescence of microcracks results in a transverse crack that is usually approximately normal to the load axis over scales comparable to the ply thickness; but to understand the initiation process, the possibility of non-normal cracks must be considered. A definitive experiment for carbon/epoxy composites, where the scale is a factor of 20 finer than in the SiC/Ti_3Al composites, remains to be performed. Until that has been achieved, modelers cannot be sure that they are describing the details of transverse ply crack initiation correctly. Revealing experiments require spatial resolution inferior to the spacing between fibers.

Similar experimental challenges confront those probing the interaction of delamination cracks with transverse microcracks, the development of kink band

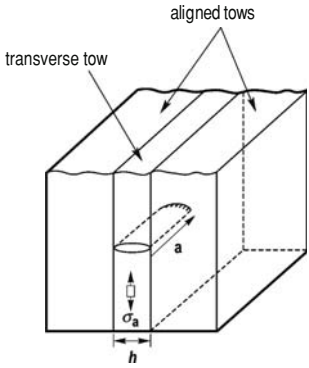

(a) Schematic of a tunneling crack in a transverse ply

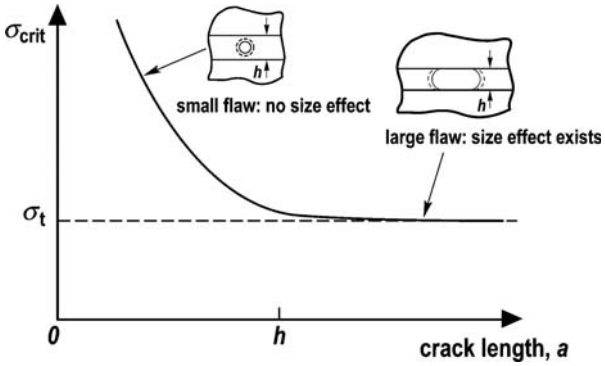

(b) Putative relation of the critical stress to the crack size during evolution from initiation to the tunneling phase

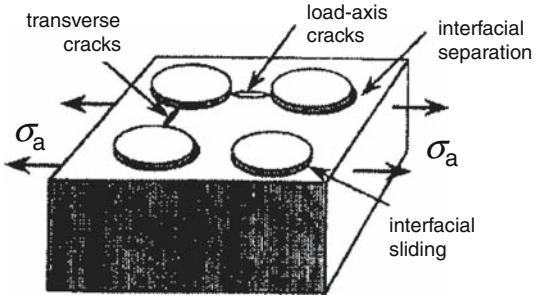

(c) Microcrack possibilities observed in composites of SiC monofilaments (150 μm diameter) in a low-ductility Ti3Al alloy matrix [42]

Fig. 3.6 A typical challenge problem for experimental and modeling analysis of damage initiation in a composite

failures in compression within the interior of a laminate, the initiation of delaminations at free edges, etc. No direct observations have been reported in the literature for any of these phenomena. A critical contribution to the development of virtual tests is therefore the expansion of experimental imaging capabilities.

High resolution X-ray tomography such as that used to obtain the images in Fig. 3.5 has the resolution required to resolve microcracks and even to measure strain fields, if marker features can be identified or introduced (see [37]). However, approximately 30 minutes are currently required to acquire images of the necessary fidelity. Acquisition times several orders of magnitude lower than this would open the possibility of monitoring damage evolution in real time during a test. Furthermore the high resolution illustrated in Fig. 3.5 is only possible on specimens of limited cross-section, currently $1\,\text{mm} \times 1\,\text{mm}$, which is insufficient for most structural details of interest. Resolution can be traded for large field of view, but this would limit the calibration data for models at the micromechanics scale. New high flux, coherent X-ray sources, e.g., generated using high intensity femtosecond laser pulses, might one day improve conditions to the point of permitting the scanning of structural subcomponents, either in laboratory testing or for field inspection.

Other full-field techniques are available to image damage and strain fields at larger scales, including thermoelastic stress analysis (e.g. [25]) and digital image correlation (e.g. [34]), although these are both inherently surface imaging techniques. There may be scope for embedding optical fibres (e.g. [21]) or using Raman spectroscopy on carbon-containing fibers (e.g. [33]) to infer local strain distributions and damage extent in composite test structures. It is also worth noting the increasing interest in multiple embedded sensors for structural health monitoring or in situ non-destructive inspection, which offer data-rich paths to model calibration and validation.

The projection that resolution and speed will continue to increase in the future implies a continuing improvement in the quantification of damage mechanisms, which will enable advances in the level of detail that can be incorporated in a material model. A successful formulation of a virtual test must recognize this through a model structure that can accommodate continual embellishment and refinement.

Furthermore, no single experimental technique will prove to be sufficient for informing, calibrating, and validating models. The best route forward is to employ multiple experimental techniques across a range of length scales in a complementary fashion. Learning to exploit the information from qualitatively different experiments by formal coupling to a comprehensive damage model represents a crucial challenge in realizing the vision of a virtual test.

3.6 The Cycle of Calibration and Validation

Decisions about which mechanisms are important and what idealizations of them are physically reasonable are subjective rather than quantitative; and they can be supported by images that are imperfect or not amenable to quantification. For

example, to see a crack even fuzzily is enough to recognize that a damage simulation should permit fracture as a possibility. In contrast, calibration and validation demand quantitative data. Therefore special experimental and theoretical challenges arise in calibrating the physical models of damage that are embedded in a virtual test.

Consider as an illustration the problem of calibrating the material constitutive laws that represent the nonlinear failure processes depicted in Fig. 3.4a, including diffuse microcracks, delaminations, and splitting cracks. Good qualitative simulations of the evolution of these interacting mechanisms have been demonstrated using hybrid stress-strain and traction-displacement models, in which two forms of constitutive relation are used. When spatially continuous changes arise in the material, the deformation is represented by a constitutive relation between the stress and strain tensors, $\bar{\sigma}(\bar{\varepsilon})$ (including dependence on time, history, etc.), i.e., by continuum damage mechanics. This is a useful approximation for diffuse microcracking in defining a top-down model that possesses the lowest order of detail in representing microcracks. The second form of constitutive law depicts a discontinuity (or very large gradient) in the material displacement as a localized damage band, which is a mathematically generalized crack across which stresses may continue to be transmitted by partially failed material. As the crack opens, vector tractions, $\mathbf{p}$, applied to the crack surfaces equilibrate stresses in the bulk material. The needed constitutive law is the relation $\mathbf{p}(\mathbf{u})$ between $\mathbf{p}$ and the displacement discontinuity, $2\mathbf{u}$. This relationship is often called a cohesive model. Cohesive models are useful for modeling the development of delaminations and other primary cracks (Fig. 3.1b–d) [5, 10, 11, 14, 20, 24, 26, 45, 48–50, 59, 60].

The qualitatively successful predictions of delamination crack shapes shown in Fig. 3.4 and in [20, 60] was obtained using nonlinear constitutive laws $\mathbf{p}(\mathbf{u})$ and $\bar{\sigma}(\bar{\varepsilon})$, whose shape was guessed from prior work on polymer adhesives and micromechanical models; for quantitatively validated virtual tests, new calibration of the laws appropriate for composites is essential. The cohesive law is especially challenging, since it refers in polymer composites to nonlinear zones that are $\sim$1 mm or less in size. The inference of $\mathbf{p}(\mathbf{u})$ from nonlinearity in load-deflection data, which works well for materials possessing larger cohesive zones $\sim$10 mm [43, 51], is problematic for a 1 mm zone because specimen deflections are small during the zone's development. Once the crack is relatively large (well developed damage zone), its behavior contains no information about $\mathbf{p}(\mathbf{u})$ other than $\int p_i du_i$ (the work of fracture) [4, 18, 28, 52]. Alternative experiments that infer $\mathbf{p}(\mathbf{u})$ from crack profiles in plane specimens such as the short shear beam or cantilever beam [17, 43] would need to resolve displacements around cracks that are barely discernible. Thus none of the common methods in the literature appear immediately workable.

This particular calibration problem is complicated by the fact that the cohesive law must be considered a vector (mixed-mode) relation. Simulations such as those of Fig. 3.4 demonstrate very strong variations of the mode ratio both around a delamination crack front and with crack size. The problem of determining mixed-mode cohesive laws for delamination cracks has not even been addressed to date, to our knowledge. (Tests that determine the critical energy release rate for a long

mixed-mode crack are not enough.) A map of the vector displacement field around an initiating crack would in principle be a sufficient measurement, but the questions of how to make such a measurement and the accuracy required of it remain very much open. New experimental methods for measuring very small crack displacements, e.g., with high-resolution x-ray tomography, are very promising; however, data acquisition and analysis for such experiments are challenging and yet to be demonstrated. A simpler prospect may be to use the evolution of the macroscopic crack shape as the calibrating information, since Fig. 3.4 and similar figures in [13, 20, 38, 60] suggest that this is an information-rich experiment for determining p(u). Current research continues to seek a calibration method, validated by testing the accuracy to which ensuing predictions match fracture experiments.

3.7 Concluding Remarks

A functioning virtual test is a system of theoretical models, specialized laboratory tests, and engineering field tests, linked by statistical and decision theory tools, which only when taken in its entirety can satisfy the goal of substituting simulations for a large fraction of real tests in a material design or material certification procedure. The virtual test is a rich and complex system, requiring Systems Engineering and Systems Science governance of activities in a number of disparate research and engineering disciplines. Prior efforts to develop virtual tests for composite materials (or other engineering or biological materials) appear not to have addressed the assembly of the complete structure. Advances in modeling, computation and experimental techniques over the past two decades make the development of a virtual test a realistic goal; the major new challenge is achieving the integration of the necessary disciplines.

This challenge should not be mistaken as merely the need for more experiments or more modeling. The greatest gaps in the technology of virtual tests lie where models and experiments should be unified. In particular, theorists are challenged by (1) the need to participate in the design of new experiments that will yield the information they need to inform and calibrate models and (2) the need for model-based methods of inferring data from tests. Experimentalists are challenged by designing experiments that yield the correct type of information for extending the scope of models. Higher spatial and temporal resolution and three-dimensional imaging are of course very useful, but more specifically experiments must be devised that probe those aspects of materials damage that are critical to formulating and quantifying models. The skill sets needed to meet these challenges are not necessarily to be found among current modeling and experimental communities. Other disciplines, especially statistics, decision theory, and physics, must be brought into the effort.

A virtual test should be a living, continually evolving system. Therefore a key challenge is to create a structure that can support its maintenance. Both systems engineering and systems science aspects exist in this challenge, with the whole integrated by the tools of information science.

Acknowledgements Brian N. Cox supported by the Army Research Office, Agreement No. W911NF-05-C-0073. S. Mark Spearing partially funded by a Royal Society-Wolfson Research Merit Award and EPSRC grant EP/E003427/1.

References

1. Abraham FF (2003) How fast can cracks move? A research adventure in materials failure using millions of atoms and big computers. Adv Phys 52:727–790
2. Abraham FF, Walkup R, Gao H et al. (2002) Simulating materials failure by using up to one billion atoms and the world's fastest computer: brittle fracture. Proc Natl Acad Sci USA 99:5777–5782
3. Ashby MF (1992) Physical modelling or materials problems. Mat Sci Technol 8:102–111
4. Bao G, Suo Z (1992) Remarks on crack-bridging concepts. Appl Mech Rev 24:355–366
5. de Borst R (2003) Numerical aspects of cohesive-zone models. Eng Fract Mech 70:1743–1757
6. Buehler MJ (2006) Nature designs tough collagen: Explaining the nanostructure of collagen fibrils. Proc Natl Acad Sci USA 103:12285–12290
7. Buehler MJ (2006) Large-scale hierarchical modeling of nanoscale, natural and biological materials. J Comput Theor Nanosci 3:603–623
8. Buehler MJ, Gao H (2005) Ultra large scale atomistic simulations of dynamic fracture. In: Rieth M, Schommers W (eds) Handbook of Theoretical Computational Nanotechnology, Volume X, pp 1–41, American Scientific Publishers Ranch, CA
9. Cai W, Bulatov VV, Chang J et al. (2004) Dislocation core effects on mobility. In: Nabarro FNR, Hirth JP (eds) Dislocations in Solids, Volume 12, Chapter 64, Elsevier, Amsterdam
10. Camanho PP, Dávila CG, Pinho ST (2004) Fracture analysis of composite co-cured structural joints using decohesion elements. Fatigue Fract Eng Mat Struct 27:745–757
11. Carpinteri A (ed) (1999) Nonlinear Crack Models for Nonmetallic Materials. Kluwer, Dordrecht, The Netherlands
12. Carroll FE, Mendenhall MH, Traeger RH, Brau C et al. (2003) Pulsed tunable monochromatic X-ray beams from a compact source: New opportunities. Am J Roentgenol 181:1197–1202
13. Case SW, Reifsnider KL (1999) Mrlife12 theory manual – a strength and life prediction code for laminated composite materials. Technical report, Materials Response Group, Virginia Polytechnic Institute and State University
14. Corigliano A (1993) Formulation, identification and use of interface models in the numerical analysis of composite delamination. Int J Solids Struct 30:2779–2811
15. Cox BN (1999) Constitutive model for a fiber tow bridging a delamination crack. Mech Compos Mat Struct 6:117–138
16. Cox BN (2005) Snubbing effects in the pullout of a fibrous rod from a laminate. Mech Adv Mat Struct 12:85–98
17. Cox BN, Marshall DB (1991) The determination of crack bridging forces. Int J Fract 49: 159–176
18. Cox BN, Marshall DB (1994) Concepts for bridged cracks in fracture and fatigue. Acta Metall Mater 42:341–363
19. Cox BN, Marshall DB (1996) Crack initiation in brittle fiber reinforced laminates. J Am Ceram Soc 79:1181–1188
20. Cox BN, Yang QD (2006) In quest of virtual tests for structural composites. Science 314:1102–1107
21. Dawood TA, Shenoi RA, Sahin M (2007) A procedure to embed fibre Bragg grating strain sensors into GFRP sandwich structures. Compos Part A 38:217–226
22. Dobashi K, Fukuasawa A, Uesaka M et al. (2005) Design of compact monochromatic tunable hard X-ray source based on X-band linac. Jpn J Appl Phys 44:1999–2005
23. Dvorak GJ, Laws N (1987) Analysis of progressive matrix cracking in composite laminates. II - First ply failure. J Compos Mat 21:309–329

24. Elices M, Guinea GV, Gomez J et al. (2002) The cohesive zone model: Advantages, limitations and challenges. Eng Fract Mech 69:137–163
25. Emery T, Dulieu-Barton JM, Cunnigham PR (2005) Identification of damage in composite structures using thermoelastic stress analysis. Key Eng Mat 293–294:583–590
26. Falk ML, Needleman A, Rice JR (2001) A critical evaluation of cohesive zone models of dynamic fracture. J de Phys IV 11:43–50
27. Fawcett A, Trostle J, Ward S (1997) 777 empennage certification approach. In: Scott ML (ed) 11th International Conference on Composite Materials, Gold Coast, Australia. Technomic Publishing, Lancaster, PA
28. Francis Rose LR (1987) Crack reinforcement by distributed springs. J Mech Phys Solids 35:383–405
29. González C, Llorca J (2006) Multiscale modeling of fracture in fiber-reinforced composites. Acta Mater 54:4171–4181
30. Gumbsch P (2001) Brittle fracture and the breaking of atomic bonds. In: The Society for Materials Science, Osaka, Japan (JSMS) (ed) Materials Science for the 21st Century, Volume A, pp 50–58
31. Hampel FR, Ronchetti EM, Rousseeuw PJ et al. (2005) Robust Statistics: The Approach Based on Influence Functions. Wiley, New York
32. Thompson JB, Kindt JH, Drake B, Hansma HG, Morse DE, Hansma PK (2001) Bone indentation recovery time correlates with bond reforming time. Nature 414:773–776
33. vanden Heuvel PWJ, Peijs T, Young RJ (1997) Failure phenomena in two-dimensional multi-fibre microcomposites, 2. A raman spectroscopic study of the influence of inter-fibre spacing on stress concentrations. Compos Sci Technol 57:899–911
34. Hild F, Roux S (2006) Digital image correlation: from displacement measurement to identification of elastic properties - a review. Strain 42:69–80
35. Ho S, Suo Z (1992) Microcracks tunneling in brittle matrix composites driven by thermal expansion mismatch. Acta Metall Mater 40:1685–1690
36. Ho S, Suo Z (1993) Tunneling cracks in constrained layers. J Appl Mech 60:890–894
37. Khor KH, Buffiere JY, Ludwig W et al. (2004) In situ high resolution synchrotron X-ray tomography of fatigue crack closure mechanisms. J Phys Condens Matter 16:S3511–S3515
38. Kortschot MT, Beaumont PWR (1990) Damage mechanics of composite materials: I - Measurements of damage and strength. Compos Sci Technol 39:289–301
39. Kozhanov AI (1999) Composite Type Equations and Inverse Problems. VSP, Utrecht, The Netherlands
40. Liang J, Huang R, Prevost JH, Suo Z (2002) Thin film cracking modulated by underlayer creep. Experimental Mechanics
41. Marder M (1999) Molecular dynamics of cracks. Comput Sci Eng 1:48–55
42. Marshall DB, Morris WL, Cox BN et al. (1994) Transverse strengths and failure mechanisms in ti3al matrix composites. Acta Metall Mater 42:2657–2673
43. Massabò R, Mumm DR, Cox BN (1998) Characterizing mode II delamination cracks in stitched composites. Int J Fract 92:1–38
44. Melnikov Y (1998) Influence Functions and Matrices. CRC Press, West Palm Beach, FL
45. Mohammed I, Lechti M (2000) Cohesive zone modeling of crack nucleation at bimaterial corners. J Mech Phys Solids 48:735–764
46. Park HS (2005) Three-dimensional bridging scale analysis of dynamic fracture. J Comput Phys 207:588–609
47. Prilepko AI, Orlovsky DG, Vasin IA (1999) Methods for Solving Inverse Problems in Mathematical Physics. Dekker, New York
48. Remmers JJC, de Borst R, Needleman A (2003) A cohesive segments method for the simulation of crack growth. Comput Mech 31:69–77
49. Schellekens JCJ, de Borst R (1996) On the numerical modeling of edge delamination in composites. Key Eng Mater 121–122:131–60
50. Shahwan KW, Waas AM (1997) Non-self-similar decohesion along a finite interface of unilaterally constrained delaminations. Proc Royal Soc Lond A 453:515–550

51. Stigh U (1988) Damage and crack growth analysis of the double cantilever beam specimen. Int J Fract 37:R13–R18
52. Suo Z, Bao G, Fan B (1992) Delamination R-curve phenomena due to damage. J Mech Phys Solids 40:1–16
53. Suo Z, Prevost JH, Liang J (2003) Kinetics of crack initiation and growth in organic-containing integrated structures. J Mech Phys Solids 51:2169–2190
54. Tarantola A (2004) Inverse Problem Theory and Model Parameter Estimation. SIAM, Philadelphia, PA
55. Turrettini A (1996) Ph.D. thesis, University of California, Santa Barbara, CA
56. Vlieks AE, Caryotakis G, Martin D et al. (2004) Compton X-ray source. In: EPAC 2004, pp 2837–2839, Lucerne, Switzerland
57. Wagner GJ, Liu WK (2003) Coupling of atomistic and continuum simulations using a bridging scale decomposition. J Comput Phys 190:249–274
58. Weinan E, Engquist B, Li X et al. (2007) Heterogeneous multiscale methods: A review. Commun Comput Phys 2:367–450
59. Wisnom MR, Chang FK (2000) Modelling of splitting and delamination in notched cross-ply laminates. Compos Sci Technol 60:2849–2856
60. Yang QD, Cox BN (2005) Cohesive models for damage evolution in laminated composites. Int J Fract 133:107–137
61. Yorozu M, Yang J, Okada Y, Yanagida T (2001) Short-pulse X-ray generation via Thomson scattering in 0 and 90 interactions. Jpn J Appl Phys 40:4228–4232

Chapter 4
Analytical and Numerical Investigation of the Length of the Cohesive Zone in Delaminated Composite Materials

Albert Turon, Josep Costa, Pedro P. Camanho, and Pere Maimí

Abstract An accurate prediction of the length of the cohesive zone ahead of a crack tip is fundamental for the correct simulation of delamination in composite materials under both quasi-static and fatigue loading. To ensure a correct dissipation of energy during delamination propagation, several cohesive finite elements have to span the cohesive zone. The length of the cohesive zone depends on the material properties, the geometry/size of the structure, and on the loading mode. This chapter presents new expressions to estimate the length of the cohesive zone under general mixed-mode loading conditions and for finite-sized geometries. The analytical model is validated by comparing its predictions with numerical results based on cohesive-zone models. The relevance of the proposed analytical solutions to the effective simulation of delamination is demonstrated by simulating delamination growth under mixed-mode loading using meshes with the length of the elements greater than the cohesive zone length.

4.1 Introduction

Cohesive zone models provide an ideal representation of the delamination process of advanced composite materials. The excellent performance of cohesive zone models in the simulation of delamination is due to the accurate kinematic representation of the fracture process, based on a strong discontinuity in the displacement field, and to the possibility to use constitutive models that correctly account for the the different loading modes [19].

A. Turon, J. Costa, and P. Maimí
AMADE, University of Girona, Spain, e-mail: {albert.turon, josep.costa, pere.maimi}@udg.edu

P.P. Camanho
DEMEGI, Faculdade de Engenharia, Universidade do Porto, Rua Dr. Roberto Frias, 4200-465, Portugal, e-mail: pcamanho@fe.up.pt

However, cohesive zone models require an accurate representation of the stress field ahead of a crack tip. This means that several finite elements are required in the cohesive zone ahead of a crack tip. The authors have previously developed a methodology that enables the use of coarse meshes ahead of a crack tip [21]. This methodology relies upon the accurate estimation of the length of the cohesive zone ahead of a crack tip.

The cohesive zone models developed for quasi-static loading conditions have been recently enhanced to predict the propagation of delamination under fatigue loading [20]. The accurate simulation of delamination growth under fatigue loading also requires the accurate prediction of the length of the cohesive zone.

There are models able to predict the dimension of cohesive zones for isotropic materials with infinite sizes loaded in pure mode I or mode II. However, no reliable models are available for the general case of non-isotropic materials with finite dimensions under mixed-mode loading. Therefore, the objective of this work is to propose a new analytical model to calculate the length of the cohesive zone in a delaminated composite material under general loading conditions. A summary of the models developed for infinite-size isotropic materials is presented. These models are generalized to predict the length of cohesive zones of orthotropic materials, and a new analytical model accounting for the effects of finite-sized geometries and mixed-mode loading is presented. The analytical solutions are compared with the numerical results obtained using a cohesive zone model implemented in a finite element code [19].

4.2 Length of the Cohesive Zone for Isotropic Materials

There are several approaches for the determination of the size of the cohesive zone ahead of a crack tip. One approach derives from the Dugdale's model [7]. By linear superposition of the crack tip stress intensity factors produced by the external loads and by the internal cohesive tractions along the crack tip wake, the length of the cohesive zone, l_{cz}^{∞}, is computed assuming that the total stress intensity factor at the crack tip is equal to zero [5]. Using this approach, the length of a cohesive zone subjected to constant tractions of an infinite specimen under remote loading is:

$$l_{cz}^{\infty} = \frac{\pi}{8} \frac{K_{Ic}^2}{(\tau^o)^2} \tag{4.1}$$

where K_{Ic} is the critical stress intensity factor, and τ^o is the maximum traction in the cohesive zone, i.e., the interface strength.

Another approach to estimate the size of the cohesive zone in a ductile solid is the Irwin's model [13]. The generalization of the Irwin's model for softening, quasi-brittle materials was proposed by Bažant et al. [2]. In the Irwin/Bažant model, the traction profile in the inelastic zone ahead of the crack tip follows a general expression:

$$\tau = \tau^o \left(\frac{x}{l_{cz}} \right)^n \tag{4.2}$$

where n is a material parameter.

In the elastic zone, the traction profile follows the expression given by the Linear Elastic Fracture Mechanics (LEFM) solution:

$$\tau = \frac{K_I}{\sqrt{2\pi\,(x - r_1)}} \tag{4.3}$$

The size of the inelastic zone, l_{cz}, also called cohesive zone or fracture process zone, is obtained by assuming that the traction given by Eqs. (4.2) and (4.3) must be equal at $x = l_{cz}$, and that the areas A_1 and A_2 represented in Fig. 4.1 are equal [2]. Assuming that there are no size effects, the crack propagates when the stress intensity factor K_I equals to the critical value K_{Ic}. Therefore, the size of the cohesive zone when the crack is propagating in a self-similar way can be solved using the previous equations, resulting in:

$$l_{cz}^{\infty} = \frac{n+1}{\pi} \frac{K_{Ic}^2}{(\tau^o)^2} \tag{4.4}$$

Cox and Marshall [5] proposed an alternative approach to predict the length of the cohesive zone. The Cox and Marshall [5] model is based on the concept of a bridged crack, where the length of the bridging zone is calculated by imposing two

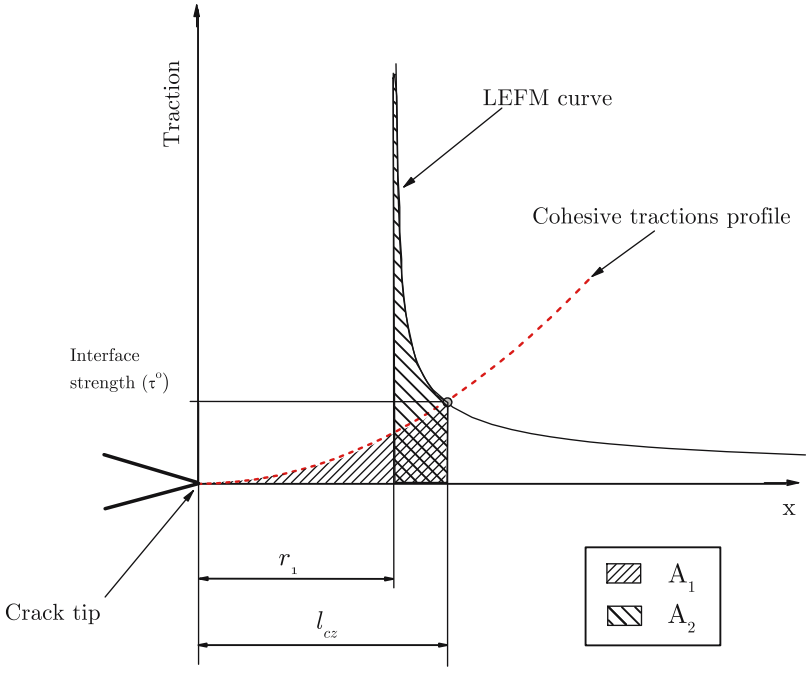

Fig. 4.1 Stress profile ahead of the crack tip

Table 4.1 Length of the cohesive zone and equivalent value of the parameter M

	M
Hui et al. [12]	$\frac{2}{3\pi} = 0.21$
Irwin [13]	$\frac{1}{\pi} = 0.31$
Bažant et al. [2]	$\frac{n+1}{\pi}$
Dugdale [7], Barenblatt [1]	$\frac{\pi}{8} = 0.39$
Cox and Marhall [5]	$\frac{\pi}{4} = 0.785$
Rice [16], Falk et al. [8]	$\frac{9\pi}{32} = 0.88$

conditions: the stress intensity factor at the crack tip must be equal to the critical value for crack propagation, and the crack opening at the beginning of the cohesive zone must be equal to its critical value. Using these two conditions the length of the cohesive zone is given as [5]:

$$l_{cz}^{\infty} = \frac{\pi}{4} \frac{K_{Ic}^2}{(\tau^o)^2} \tag{4.5}$$

The prediction of the cohesive length using all the approaches previously described may be generalized by the following equation:

$$l_{cz}^{\infty} = M \frac{K_{Ic}^2}{(\tau^o)^2} \tag{4.6}$$

where M is a factor that depends on the model used and/or the constitutive relation of the material. Some of the different values of M given from different authors are summarized in Table 4.1. The quantity $\frac{K_{Ic}^2}{(\tau^o)^2}$ is the characteristic length of the material introduced by Hillerborg [11].

4.3 Length of the Cohesive Zone for Orthotropic Materials

Assuming that Linear-Elastic Fracture Mechanics applies, Irwin's model relates the energy release rate, G_I, to the stress intensity factor, K_I, as:

$$G_I = \frac{K_I^2}{E'} \tag{4.7}$$

where E' is an elastic modulus that depends on the state of stress. Under plane stress, E' is the Young modulus of the material, while under plane strain $E' = \frac{E}{1-\nu^2}$.

Therefore, the length of the cohesive zone under mode I loading for isotropic materials can be written as a function of the fracture toughness of the material G_{Ic}:

$$l_{cz}^{\infty} = M\frac{E'G_{Ic}}{(\tau^o)^2} \tag{4.8}$$

For orthotropic materials under mode I or mode II loading, the relation between the energy release rate and the stress intensity factor can be written as [9]:

$$G_I = K_I^2\left(\frac{a_{11}a_{22}}{2}\right)^{\frac{1}{2}}\left[\left(\frac{a_{22}}{a_{11}}\right)^{\frac{1}{2}} + \frac{2a_{12}+a_{66}}{2a_{11}}\right]^{\frac{1}{2}} \tag{4.9}$$

$$G_{II} = K_{II}^2\frac{a_{11}}{\sqrt{2}}\left[\left(\frac{a_{22}}{a_{11}}\right)^{\frac{1}{2}} + \frac{2a_{12}+a_{66}}{2a_{11}}\right]^{\frac{1}{2}} \tag{4.10}$$

where a_{11}, a_{22}, a_{12} and a_{66} are the components of the compliance matrix.

Therefore, the length of the cohesive zone for orthotropic materials under pure mode I or mode II loading can be written as:

$$l_{Icz}^{\infty} = M_I\frac{E_I'G_{Ic}}{(\tau_3^o)} \tag{4.11}$$

$$l_{IIcz}^{\infty} = M_{II}\frac{E_{II}'G_{IIc}}{(\tau_{shear}^o)} \tag{4.12}$$

where E_I' and E_{II}' are obtained from Eqs. (4.9) and (4.10) as:

$$E_I' = \left(\frac{a_{11}a_{22}}{2}\right)^{-\frac{1}{2}}\left[\left(\frac{a_{22}}{a_{11}}\right)^{\frac{1}{2}} + \frac{2a_{12}+a_{66}}{2a_{11}}\right]^{-\frac{1}{2}} \tag{4.13}$$

$$E_{II}' = \left(\frac{a_{11}}{\sqrt{2}}\right)^{-1}\left[\left(\frac{a_{22}}{a_{11}}\right)^{\frac{1}{2}} + \frac{2a_{12}+a_{66}}{2a_{11}}\right]^{-\frac{1}{2}} \tag{4.14}$$

Under plane stress, $a_{11} = \frac{1}{E_{11}}$, $a_{22} = \frac{1}{E_{22}}$, $a_{12} = -\frac{\nu_{12}}{E_{22}}$ and $a_{66} = \frac{1}{G_{12}}$. Therefore, Eqs. (4.13) and (4.14) can be written for plane stress problems as:

$$E_I' = \left(\frac{E_{22}}{Q}\right) \tag{4.15}$$

$$E_{II}' = \frac{E_{22}}{Q}\left(\frac{E_{11}}{E_{22}}\right)^{\frac{1}{2}} \tag{4.16}$$

where:

$$Q = \frac{1}{2}\sqrt{2\left[\left(\frac{E_{22}}{E_{11}}\right)^{\frac{1}{2}} - \nu_{21}\right] + \frac{E_{22}}{G_{12}}} \tag{4.17}$$

Under plane strain, the variables a_{11}, a_{22}, a_{12} and a_{66} in equations (4.13) and (4.14) are: $a_{11} = \frac{1}{E_{11}} - \frac{\nu_{31}^2}{E_{33}}$, $a_{22} = \frac{1}{E_{22}} - \frac{\nu_{32}^2}{E_{33}}$, $a_{12} = -\frac{\nu_{12}}{E_{11}} - \frac{\nu_{31}\nu_{32}}{E_{33}}$ and $a_{66} = \frac{1}{G_{12}}$.

4.3.1 Length of the Cohesive Zone Under Mixed–Mode Loading

Under mixed mode loading, the mixed–mode traction vector is defined as [19]:

$$\tau^2 = \tau_3^2 + \tau_{shear}^2 \tag{4.18}$$

where τ_3 and τ_{shear} are respectively the normal and shear components of the traction vector. Using Eq. (4.3), an equivalent mixed-mode stress intensity factor is defined as:

$$K^2 = K_I^2 + K_{II}^2 \tag{4.19}$$

where the mixed-mode stress intensity factor reads:

$$K^2 = GE_m \tag{4.20}$$

G is the mixed mode energy release rate and E_m is an equivalent mixed-mode Young modulus. The mixed mode energy release rate G can be written as:

$$E_m G = E_I G_I + E_{II} G_{II} \tag{4.21}$$

Defining the mode ratio, B, as:

$$B = \frac{G_{II}}{G_I + G_{II}} \tag{4.22}$$

with $G = G_I + G_{II}$. Using Eqs. (4.21) and (4.22), the equivalent mixed-mode Young modulus reads:

$$E_m = E_I(1 - B) + E_{II}B \tag{4.23}$$

Using the same approaches that for pure mode loading, the length of the cohesive zone under mixed-mode ratio reads:

$$l_{cz}^{\infty} = ME_m \frac{G_c}{(\tau^o)^2} \tag{4.24}$$

where G_c is the mixed-mode fracture toughness of the material and τ^o is the equivalent interface strength under mixed-mode loading. The mixed-mode fracture

toughness can be obtained from the pure mode fracture toughness of the material using the expression proposed by Benzeggagh and Kenane [3]:

$$G_c = G_{Ic} + (G_{IIc} - G_{Ic})B^{\eta} \tag{4.25}$$

where η is a mixed-mode interaction parameter. The equivalent interface strength under mixed-mode loading, τ^o, can be related to the pure mode interface strengths using the expression [19]:

$$(\tau^o)^2 = (\tau_3^o)^2 + \left[(\tau_{shear}^o)^2 - (\tau_3^o)^2\right] B^{\eta} \tag{4.26}$$

where τ_3^o and τ_{shear}^o are the interface strengths under mode I and shear mode loading, respectively.

4.4 Generalization of the Length of the Cohesive Zone for Finite-Sized Geometries

The models used for the estimation of the cohesive length outlined in Sect. 4.2 assume that the crack propagates unstably when the applied energy release rate is equal to the fracture toughness of the material, G_c. However, depending on the specimen geometry, unstable crack propagation occurs before the maximum value of the fracture toughness is attained. The alternative method proposed here to predict the length of the cohesive zone under mode I loading is based on the relation between this length and the size effect experienced by the structure.

Schematically representing the R-curve, Fig. 4.2, it is observed that the applied energy release rate that produces unstable propagation, G_{Iu} is equal to the value where the R-curve and the G_I curve are tangent.

The applied energy release rate is a function of the geometry:

$$G_I(a,h) = \frac{1}{E'}\sigma_N^2 h k(a,h)^2 \tag{4.27}$$

where σ_N is a nominal stress [2], h is a geometry-dependent quantity, and $k(a,h)$ is the shape factor for K_I. For a double-cantilever beam (DCB) specimen, taking h as the thickness of the specimen arm and B the width of the specimen, the applied energy release rate reads:

$$G_I(a,h) = \frac{12P^2a^2}{E'B^2h^2} \tag{4.28}$$

By comparing Eqs. (4.27) and (4.28) the nominal stress σ_N and the shape factor $k(a,h)$ used in Eq. (4.27) are given as:

$$\sigma_N = \frac{P}{bh} \tag{4.29}$$

$$k(a,h) = 2\sqrt{3}\frac{a}{h} \tag{4.30}$$

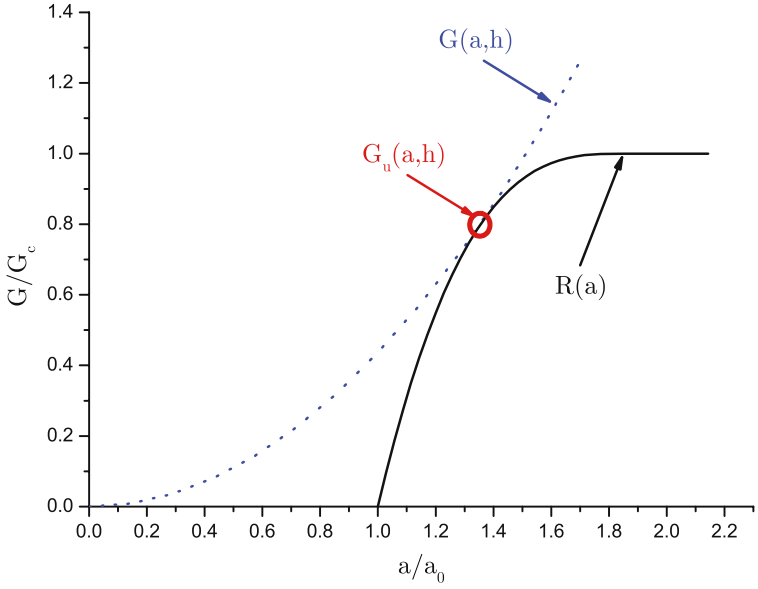

Fig. 4.2 Stress profile ahead of the crack tip

The applied energy release rate at the point where the R-curve and the G-curve are tangent is:

$$G_{Iu}(a,h) = \frac{1}{E'}\sigma_{Nu}^2 hk(a,h)^2 \tag{4.31}$$

where σ_{Nu} is the ultimate nominal stress that depends on the specimen geometry. It is assumed here that Bažant's size effect law [2] holds, i.e.,

$$\sigma_{Nu} = \frac{Bf_t'}{\sqrt{1+\dfrac{h}{h_I}}} \tag{4.32}$$

where h_I is a characteristic length that depends on the material and on the structure [2]. The parameter Bf_t' is related to the fracture toughness of the material as:

$$Bf_t' = \sqrt{\frac{G_{Ic}E'}{h_I k(a_0,h)^2}} \tag{4.33}$$

Using Eqs. (4.32) and (4.33) in Eq. (4.31), the applied energy release rate for unstable propagation reads:

$$G_{Iu}(a,h) = \frac{G_{Ic}}{\left(1+\dfrac{h}{h_I}\right)}\frac{h}{h_I}\left(\frac{k(a,h)}{k(a_0,h)}\right)^2 \tag{4.34}$$

For brittle materials, such as carbon-epoxy composites, the length of the cohesive zone is small. Therefore, the shape factor of the specimen with the initial crack length, $k(a_0,h)$, and the shape factor when unstable crack growth occurs are similar, and the ratio between the shape factor of the initial crack length and the shape factor when unstable crack growth starts can be assumed to be approximately equal to 1:

$$\frac{k(a,h)}{k(a_0,h)} \approx 1 \tag{4.35}$$

Using Eq. (4.35) in Eq. (4.34), the energy release rate required for unstable propagation is:

$$G_{Iu}(h) = \frac{G_{Ic}h}{(h+h_I)} \tag{4.36}$$

Therefore, since unstable crack propagation for finite-sized geometries occurs at an applied energy release rate smaller than the fracture toughness of the material, the length of the cohesive zone for finite-sized geometries is smaller than for infinite-sized geometries and reads:

$$l_{Icz}(h) = M_I \frac{G_{Iu}(h)E'}{\left(\tau_3^o\right)^2} = \frac{h}{(h+h_I)} M_I \frac{G_{Ic}E'}{(\tau_3^o)^2} = \frac{h}{(h+h_I)} l_{Icz}^{\infty} \tag{4.37}$$

4.4.1 Mode II

Using an approach similar to that presented for mode I loading, the energy release rate for unstable propagation under mode II loading is obtained replacing G_{Iu} and G_{Ic} by G_{IIu} and G_{IIc} in Eqs. (4.33) and (4.34). Therefore, G_{IIu} reads:

$$G_{IIu}(a,h) = \frac{G_{IIc}}{\left(1+\dfrac{h}{h_{II}}\right)} \frac{h}{h_{II}} \left(\frac{k(a,h)}{k(a_0,h)}\right)^2 \tag{4.38}$$

For the end-notched flexure (ENF) test, the shape factor $k(a,h)$ is given as:

$$k(a,h) = \frac{3\sqrt{2}}{2} \frac{2L-a}{\sqrt{h}} \tag{4.39}$$

where L is the specimen length.

Assuming that the length of the cohesive zone is small, compared to the initial crack length, that is $\frac{k(a,h)}{k(a_0,h)} \approx 1$, the energy release rate required for unstable propagation is:

$$G_{IIu}(h) = \frac{G_{IIc}h}{(h+h_{II})} \tag{4.40}$$

Therefore, the length of the cohesive zone for finite-sized geometries under mode II loading is smaller than for infinite-sized geometries and reads:

$$l_{IIcz}(h) = \frac{h}{(h+h_{II})} M_{II} \frac{G_{IIc} E'}{(\tau^o_{shear})^2} = \frac{h}{h+h_{II}} l^{\infty}_{IIcz} \tag{4.41}$$

4.4.2 Mixed-Mode I and II

Using the same hypothesis and conditions as those used for mode I and mode II loading, the length of the cohesive zone for finite-sized geometries under mixed-mode loading conditions can be estimated using the equation

$$l_{cz}(h) = \frac{h}{(h+h_0)} l^{\infty}_{cz} \tag{4.42}$$

where h_0 is a characteristic length under mixed-mode loading conditions. h_0 is related to the pure mode quantities h_I and h_{II}. Equation (4.42) is a general expression for the prediction of the cohesive zone of finite-sized geometries under any general loading conditions.

4.5 Validation of the Model

4.5.1 Numerical Model

The proposed analytical solutions for the length of the cohesive zone are compared with numerical predictions. The cohesive zone models previously developed by the authors [4,19] are used in the predictions of the length of cohesive zones for different geometries and loading modes.

The constitutive behavior of cohesive elements is implemented using a cohesive damage zone model that relates the tractions, τ, to the displacement jumps, Δ, at the interfaces where crack propagation occurs. Damage initiation is related to the interfacial strength of the material, τ^o. When the energy dissipated is equal to the fracture toughness of the material, G_c, the traction is reduced to zero and new crack surfaces are formed.

The constitutive law used in this work is a bilinear relation between the tractions and the displacement jumps [4, 19]. The bilinear cohesive law uses an initial linear elastic response before damage initiation, as shown in Fig. 4.3. This linear elastic part is defined using a penalty stiffness parameter, K, that ensures a stiff connection between the surfaces before crack propagation. The interfacial strength and the penalty stiffness define an onset displacement jump, Δ^o, related to the initiation of damage.

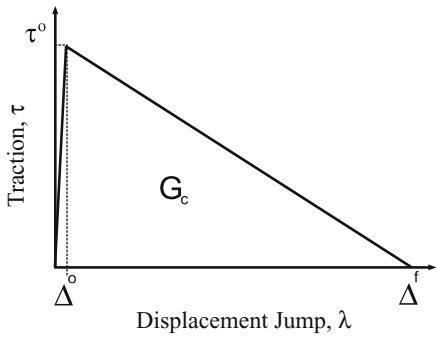

Fig. 4.3 Bilinear constitutive law used for quasi-static loading

The displacement jump across the interface $[\![u_i]\!]$, is obtained from the displacements of the points located on the top and bottom sides of the interface, u_i^+ and u_i^-, respectively:

$$[\![u_i]\!] = u_i^+ - u_i^- \tag{4.43}$$

where $u_i^{\pm}$ are the displacements with respect to a fixed Cartesian coordinate system. The components of the displacement jump vector in the local coordinate system on the deformed interface, Δ_m, are expressed in terms of the displacement field in global coordinates:

$$\Delta_m = \Theta_{mi}\,[\![u_i]\!] \tag{4.44}$$

where Θ_{mi} is the rotation tensor, defined in [4, 19]. The constitutive operator of the interface, D_{ji}, relates the tractions, τ_j, to the displacement jumps, Δ_i:

$$\tau_j = D_{ji}\Delta_i \tag{4.45}$$

The damage model simulates delamination onset and delamination propagation using a single scalar variable, d, to track the damage at the interface under general loading conditions. An initiation criterion that results from the Benzeggagh-Kenane fracture criterion [3] (B-K) ensures that the model accounts for changes in the loading mode in a thermodynamically consistent way and avoids restoration of the cohesive state. The constitutive model prevents interpenetration of the faces of the crack during closing, and a Fracture Mechanics-based criterion is used to predict crack propagation. The norm of the displacement jump tensor, λ, is used to compare different stages of the displacement jump state. The equivalent displacement jump is a non-negative and continuous function, defined as:

$$\lambda = \sqrt{\langle \Delta_3 \rangle^2 + (\Delta_{shear})^2} \tag{4.46}$$

where $\langle\cdot\rangle$ is the MacAuley bracket defined as $\langle x\rangle = \frac{1}{2}(x + |x|)$.

The displacement jump in mode I, i.e., normal to midplane is Δ_3. The displacement jump tangent to the midplane, Δ_{shear}, is computed with the Euclidean norm of

the displacement jump in mode II and mode III:

$$\Delta_{shear} = \sqrt{(\Delta_1)^2 + (\Delta_2)^2} \tag{4.47}$$

A bilinear cohesive law for mixed-mode delamination can be constructed by determining the initial damage threshold Δ^o from the criterion for damage initiation and the final displacement jump, Δ^f, from the formulation of the propagation surface or propagation criterion [19]. For the B-K fracture criterion, the mixed-mode displacement jump for damage initiation is [19] is

$$\Delta^o = \sqrt{\left(\Delta_3^o\right)^2 + \left[\left(\Delta_{shear}^o\right)^2 - \left(\Delta_3^o\right)^2\right] B^\eta} \tag{4.48}$$

where the B-K parameter η is obtained by curve-fitting the fracture toughness of mixed-mode tests.

The displacement jump for final fracture is also obtained from the critical displacement jumps as

$$\Delta^f = \frac{\Delta_3^o \Delta_3^f + \left(\Delta_{shear}^o \Delta_{shear}^f - \Delta_3^o \Delta_3^f\right) B^\eta}{\Delta^o} \tag{4.49}$$

During overload, the state of damage d is a function of the current equivalent displacement jump λ:

$$\mathsf{d} = \frac{\Delta^f (\lambda - \Delta^o)}{\lambda (\Delta^f - \Delta^o)} \tag{4.50}$$

The corresponding tractions can be written as

$$\tau_i = \delta_{ij} K \left[1 - \mathsf{d}\left(1 + \delta_{3j} \frac{\langle -\Delta_j \rangle}{\Delta_j}\right)\right] \tag{4.51}$$

where the Kronecker δ_{3j} is used to prevent the interpenetration of the surfaces of a damaged element when contact occurs [19]. In summary, by assuming that toughnesses and strengths in modes II and III are equal to each other, it is shown that the mixed-mode constitutive equations of a cohesive element are defined by five material properties and three displacement jumps: G_{Ic}, G_{IIc}, τ_3^o, τ_{shear}^o, K, Δ_1, Δ_2, and Δ_3. This formulation of the damage model allows an explicit integration of the constitutive model and ensures consistency in the evolution of damage during loading, unloading, and changes in mode mixity. The derivation and implementation of the cohesive damage model is described in [18, 19] and the reader is referred to those sources for further details.

4.5.2 Mode I loading

Several simulations of the Double Cantilever test (DCB) for different heights of the arms were performed to measure the length of the cohesive zone predicted by the

numerical model. The cohesive damage model presented in previous section was implemented in ABAQUS [10] by means of a user element subroutine [18, 19]. The finite element model is composed of four-node plane strain elements for the arms, which are connected by four-node cohesive elements representing the interface. A very refined mesh has been selected in order to correctly capture the tractions's profile ahead of the crack tip. The length of the cohesive elements is 0.01 mm. Sixteen elements are used through the thickness of each arm.

The following material properties have been used in the numerical simulations.

A set of simulations of the DCB test for a range of the specimen arm heights between 1.55 and 12.4 mm and an aspect ratio of $\frac{a_0}{h} = 23$ were carried out. The simulations were repeated with an aspect ratio of $\frac{a_0}{h} = 13$. The load-displacement curves for three of the specimens simulated with $\frac{a_0}{h} = 13$ are shown in Fig. 4.4.

The length of the cohesive zone is obtained from the FE simulations, measuring the length that span the cohesive elements with a damage $\mathsf{d} \in (0, 1)$, i.e., the damaged elements that are not completely open. As shown in Fig. 4.5, the length of the cohesive length was found to be independent of the aspect ratio of the specimen, but dependent on the height of the arms of the specimen.

The constants for h_I and M_I were calculated by a nonlinear regression of the numerical data. The values obtained are $h_I = 2.5$ and $M_I = 0.66$. The analytical prediction of the cohesive zone length given by Eq. (4.37) with $M_I = 0.66$ and $h_I = 2.5$ is also plotted in Fig. 4.5. It is worth noticing that the parameter M_I obtained is approximately equal to the value obtained using Bažant's model with $n = 1$, i.e.,

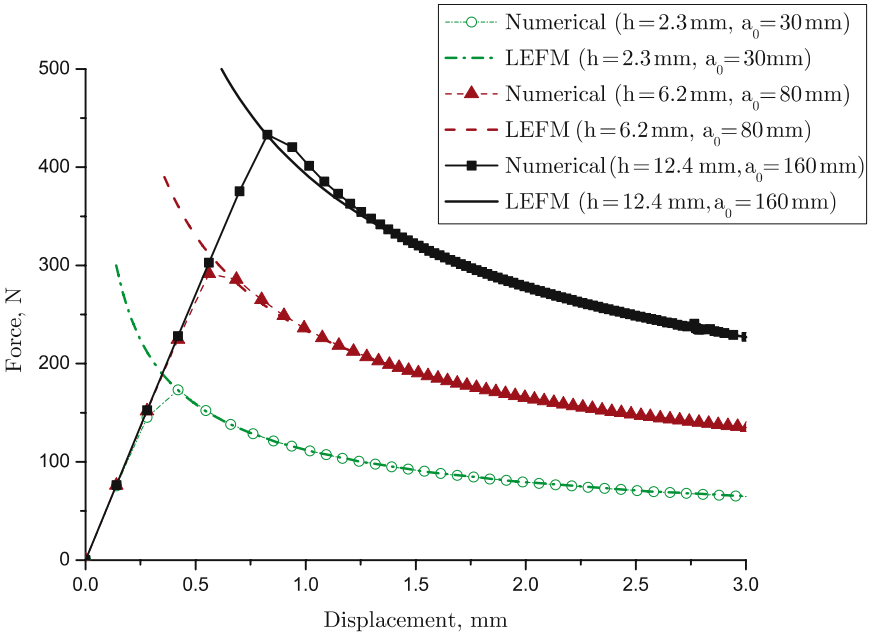

Fig. 4.4 Load-displacement curves obtained for some of the different specimens simulated

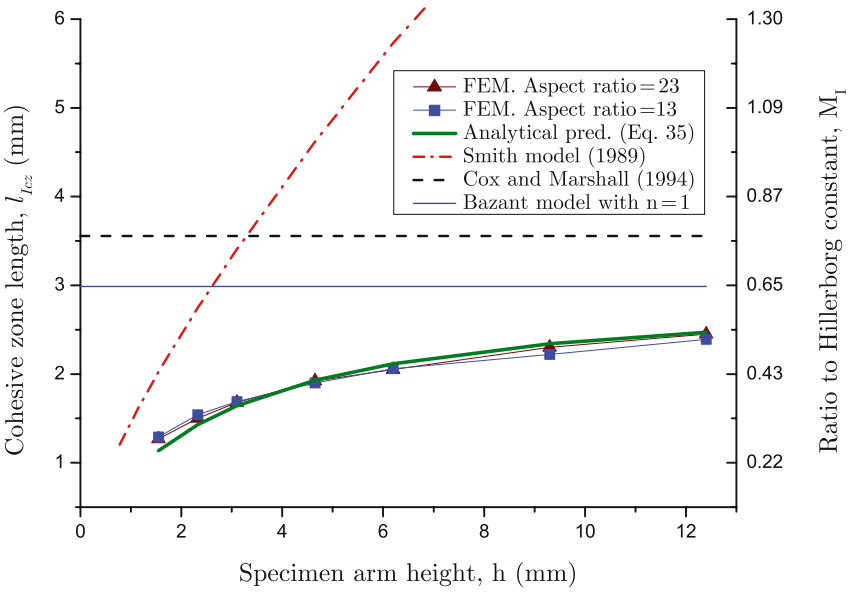

Fig. 4.5 Length of the cohesive zone under mode I loading for different specimen's arm thickness

assuming a linear distribution of tractions ahead of the crack tip. The length of the cohesive zone for finite-sized specimens under mode I loading can also be estimated using the model proposed by Smith [17] and later adopted by Yang and Cox [22], which is based on the following expression:

$$l_{Icz}(h) = \left(\frac{G_{Ic}E'}{(\tau_3^o)^2}\right)^{\frac{1}{3}} h^{\frac{3}{4}} \tag{4.52}$$

Figure 4.5 shows that the analytical expression proposed here accurately predicts the length of the cohesive zone as a function of the thickness of the arm of the DCB specimen. It is also observed in Fig. 4.5 that the prediction of the length of the cohesive zone using Eq. (4.52) is less accurate, specially for thicker specimens.

4.5.3 Mode II Loading

Several simulations of the Four-Point End Notched Flexure test (4-ENF) for different heights of the arms were performed to measure the length of the cohesive zone. The length of the cohesive elements used is 0.04 mm. Eight elements are used through the thickness of each arm. A coarser mesh than for mode I simulations is used to reduce the computation time. However, this change in the mesh does not

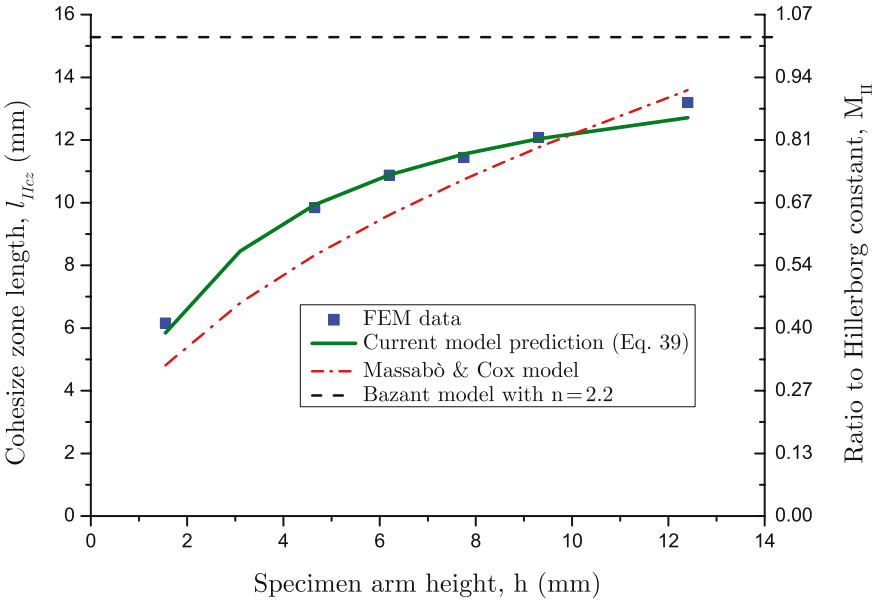

Fig. 4.6 Length of the cohesive zone under mode II loading for different specimen's arm thickness

affect the results since the mesh is still very refined, being the length of the cohesive elements much smaller than the length of the cohesive zone.

The results obtained from the FEM simulations are shown in Fig. 4.6. The prediction of the length of the cohesive zone using Eq. (4.41) with $M_{II} = 1.03$ and $h_{II} = 2.5$ mm is also plotted together with the prediction of the length of the cohesive zone using the model presented by Massabò and Cox [14], where the length of the cohesive zone for finite-sized geometries is predicted using the following equation:

$$l_{IIcz}(h) = \sqrt{\left(\frac{G_{IIc}E'}{(\tau_3^o)^2}\right)h} \tag{4.53}$$

A good agreement between the length of the cohesive zone obtained from the FEM simulation and the prediction using Eq. (4.41) is observed. The prediction using Massabò and Cox model, Eq. (4.53), provides a reasonable approximation but it is less accurate than the model proposed here.

4.5.4 Mixed-Mode Loading

Several simulations of the Mixed Mode Bending test (MMB) for different heights of the arms were performed to measure numerically the length of the cohesive zone.

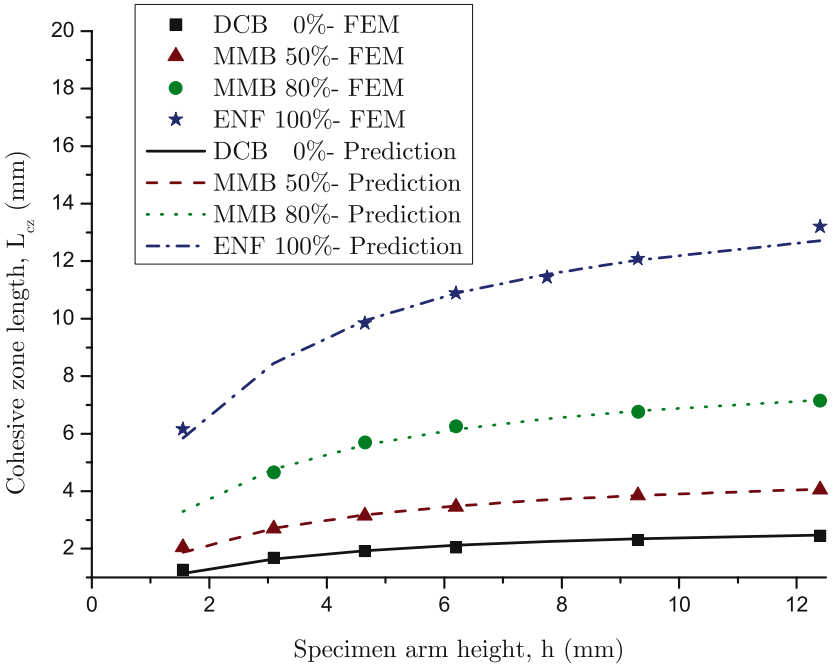

Fig. 4.7 Length of the cohesive zone under mixed-mode loading for different specimen's arm thickness

The finite element mesh is the same as that used for the 4ENF test simulations. Two different mixed mode ratios, $B = 50\%$ and $B = 80\%$ were simulated. The measure of the length of the cohesive length obtained from the FEM simulations is shown in Fig. 4.7 for mode I, mode II and mixed-mode loading. The numerical prediction using Equation (4.42) with the parameters M given in Table 4.3 and $h_0 = 2.5$ is represented together with the FEM data in Fig. 4.7. A good agreement between predicted and measured lengths of the cohesive length is observed for the different mixed-mode ratios.

It is observed that the parameter M that defines the ratio between the length of the cohesive zone and the Hillerborg's material constant, varies with the mode ratio. This variation of the parameter M with the mixed-mode ratio can be related to the pure mode values, M_I and M_{II}, and the mixed-mode ratio B using the expression:

$$M = M_I - \eta' B + (M_{II} - M_I + \eta')B^2 \tag{4.54}$$

where η' is a mixed-mode interaction parameter. The parameter η' used here is $\eta' = 1.14$.

4.6 Updated Engineering Solution to Use Coarse Meshes

In order to obtain accurate numerical results using cohesive zone models, the tractions in the cohesive zone must be accurately represented by the finite element spatial discretization [21]. The number of elements in the cohesive zone is:

$$N_e = \frac{l_{cz}}{l_e} \tag{4.55}$$

where l_e is the mesh size in the direction of crack propagation. When the cohesive zone is discretized by too few elements, the distribution of tractions ahead of the crack tip is not represented accurately. Therefore, a minimum number of elements, N_e, is needed in the cohesive zone to get successful numerical results.

One of the drawbacks in the use of cohesive zone models is that very fine meshes are needed to assure a reasonable number of elements in the cohesive zone. The length of the cohesive zone given by Eq. (4.8) is proportional to the fracture energy release rate (G_c) and to the inverse of the square of the interfacial strength τ^o. For typical graphite-epoxy or glass-epoxy composite materials, the length of the cohesive zone is smaller than one or two millimeters. Therefore, according to Eq. (4.55), the mesh size required in order to have more than three elements in the cohesive zone should be smaller than a millimeter. The computational requirements needed to analyze a large structure with these mesh sizes may render most practical problems intractable.

An alternative to using fine meshes of cohesive elements was proposed by Turon et al. [21]. The approach consists in reducing the strengths τ_3^o and τ_{shear}^o such that the length of the cohesive zone increases to cover at least three elements. The propagation of an existing delamination can be considered to be driven by the energy release rate, which is calculated more accurately when the damage zone is elongated. Results presented in [6, 15, 21], show that using this approach the computational cost of the simulations is reduced considerably and render the analysis of large structures possible to be handled.

The approach proposed in [21] can be generalized for specimens with finite dimensions under mixed–mode loading by using an equivalent strength, τ^o, reduced by a factor f_r given by:

$$f_r = \frac{\tau^o}{\sqrt{\dfrac{Mh}{h+h_0}\dfrac{E_m G_C}{N_e l_e}}} \tag{4.56}$$

It is worth noticing that the reduction factor f_r can be computed directly using the mixed-mode ratio B and pure mode quantities, since the parameters E_m, G_c, τ^o, and M can be expressed as a function of the pure mode quantities using Eqs. (4.23), (4.25), (4.26), and (4.54), respectively.

Having defined the reduction factor f_r, the modified mode I and mode II strengths to be introduced in the FEM model are calculated from the damage activation function as:

$$\tau_3^o = \min\left(\tau_3^o, f_r \tau_3^o\right) \tag{4.57}$$

$$\tau_{shear}^o = \min\left(\tau_{shear}^o, f_r \tau_{shear}^o\right) \tag{4.58}$$

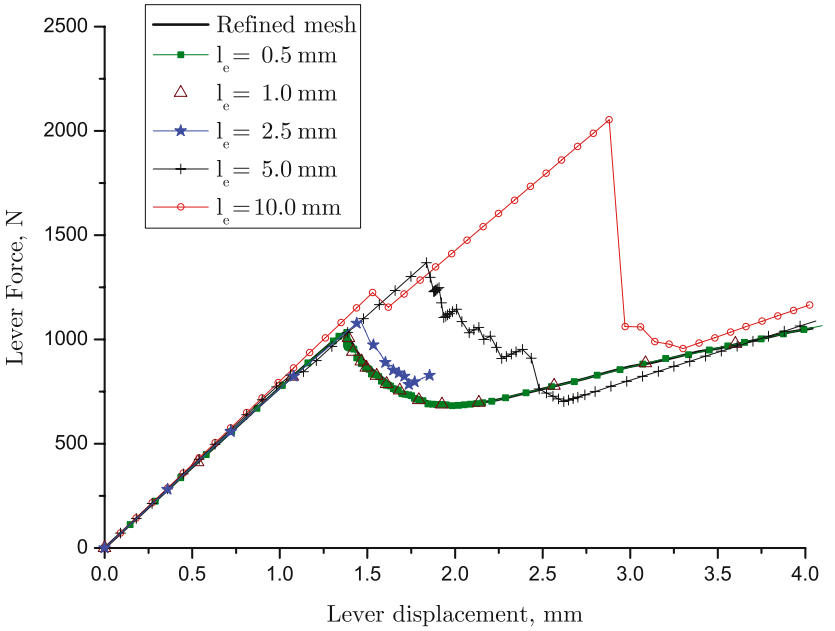

Fig. 4.8 Load-displacement curve of the lever point for different length of the elements ahead of the crack tip

Table 4.2 Interface and elastic properties used

E_{11}(GPa)	$E_{33} = E_{22}$(GPa)	$G_{12} = G_{13}$(GPa)	G_{23}(GPa)	$\nu_{12} = \nu_{13}$	ν_{23}
120	10.5	5.2	5.25	0.3	0.51
G_{Ic}(kJ/m^2)	G_{IIc}(kJ/m^2)	$\tau_2^0 = \tau_1^0$(MPa)	τ_3^0(MPa)	K (N/mm^3)	η
0.26	1.002	30	45	10^6	1.45

The MMB test with a mixed-mode ratio of 50% and an arm height of 12.4 mm was simulated for different mesh sizes. The load-displacement curve at lever point obtained are shown in Fig. 4.8. It is observed that the FEM results for mesh sizes larger than 1 mm do not converge to the solution obtained using the refined mesh.

To obtain converged results with coarse meshes, the procedure presented in this section was used. The mode I and mode II interface strengths, 30 and 45 MPa respectively, for the FEM models with $l_e = 2.5$, 5 and 10 mm, were reduced according to Eq. (4.58) where the material properties used are given in Tables 4.2 and 4.3. Five element were chosen to span the cohesive zone ($N_e = 5$). The results obtained are shown in Fig. 4.9. It is observed that load-displacement curves obtained using the reduced strengths are significantly different to those obtained with the original properties (Fig. 4.8), and converge to the solution obtained using the refined mesh.

Table 4.3 Values of the parameter M

M_I	$M_{50\%}$	$M_{80\%}$	M_{II}
0.66	0.51	0.66	1.03

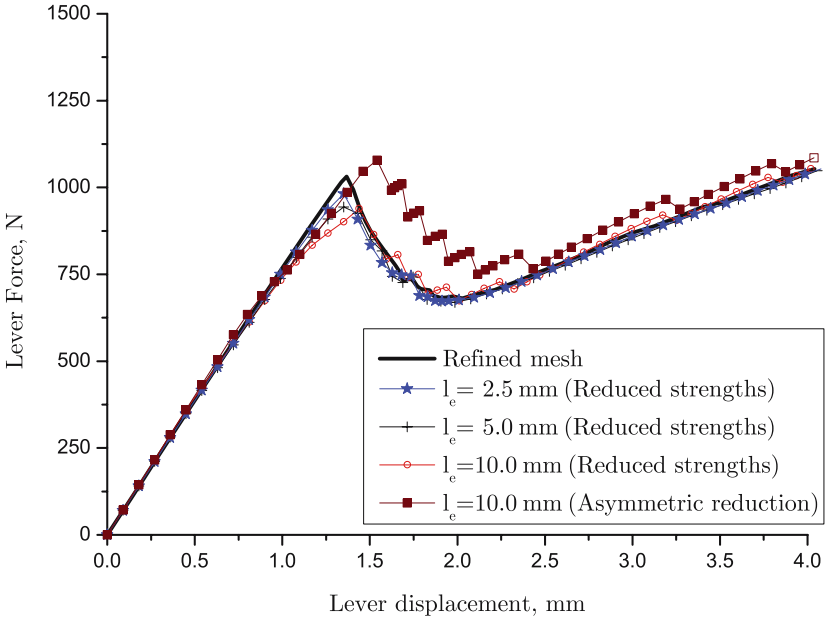

Fig. 4.9 Load-displacement curve of the lever point for different lengths of the elements ahead of the crack tip, reducing interface strengths

Another simulation was done to demonstrate that the reduction factor f_r needs to be computed for a unique mode-ratio, and that the mode I and mode II strengths must be reduced by the same factor f_r. The mode I and mode II strengths were lowered independently, computing a reduction factor for mode I, $f_{rI} = 0.22$, and another for mode II, $f_{rII} = 0.51$, using in both cases the pure mode loading values and $N_e = 5$. The resulting load-displacement curve was added to Fig. 4.9 (with the label *asymmetric reduction*). It can be observed that the load-displacement curve obtained with the asymmetrical reduction of the interface strengths does not converge to the correct solution. If the pure mode interface strengths are lowered by a different factor, the shape of the initiation surface changes and, therefore, the results of the simulation become inaccurate, specially if the mode ratio changes during the simulation.

Usually, the length of the cohesive zone is smaller for mode I than for other loading modes. Therefore, in problems where the mixed-mode ratio is not known or may change during the propagation of delamination, the reduction factor f_r can be computed using the pure mode I properties.

4.7 Conclusions

An investigation of the length of the cohesive zone in delaminated composite materials was presented. It was shown that the length of the cohesive zone depends on the material properties, the geometry/size of the structure, and on the loading mode. New expressions to estimate the length of the cohesive zone of finite-sized specimens under general loading conditions were derived.

The accuracy of the model was assessed by comparing its predictions with numerical results obtained in simulations of test specimens loaded in pure mode I, pure mode II, and mixed-mode I and II. The numerical simulations were performed using a cohesive zone model previously developed by the authors and implemented in ABAQUS as a user-written subroutine. A good agreement between predictions and experiments was obtained for all loading situations and sizes of the test specimens.

Finally, the model presented was used to simulate delamination propagation in composites using coarse meshes. A methodology previously developed by the authors to simulate delamination using coarse meshes has been updated to be used under any general loading situation and specimen geometry. The results obtained using this methodology yield converged solutions even for elements that are ten time larger than the nominal length of the cohesive zone.

References

1. Barenblatt G (1962) The mathematical theory of equilibrium cracks in brittle fracture. Adv Appl Mech 7:55–129
2. Bažant ZP, Planas J (1998) Fracture and Size Effect in Concrete and Other Quasibrittle Materials. CRC Press, West Palm Beach, FL
3. Benzeggagh ML, Kenane M (1996) Measurement of mixed-mode delamination fracture toughness of unidirectional glass/epoxy composites with mixed-mode bending apparatus. Compos Sci Technol 49:439–49
4. Camanho PP, Dávila CG, de Moura MF (2003) Numerical simulation of mixed-mode progressive delamination in composite materials. J Compos Mater 37:1415–1438
5. Cox BN, Marshall DB (1994) Concepts for bridged cracks in fracture and fatigue. Acta Metall Mater 42:341–363
6. Dávila CG, Camanho PP, Turon A (2008) Effective simulation of delamination in aeronautical structures using shells and cohesive elements. J Aircraft 45:663–672
7. Dugdale DS (1960) Yielding of steel sheets containing slits. J Mech Phys Solids 8:100–104
8. Falk ML, Needleman A, Rice JR (2001) A critical evaluation of cohesive zone models of dynamic fracture. J Phys IV, Proc:543–550
9. Gdoutos EE (1990) Fracture Mechanis Criteria and Applications. Kluwer, Dordrecht, The Netherlands
10. Hibbitt D, Karlsson B, Sorensen P (2005) ABAQUS 6.5 Users's Manuals, Pawtucket, RI
11. Hillerborg A, Modéer M, Petersson PE (1976) Analysis of crack formation and crack growth in concrete by means of fracture mechanics and finite elements. Cem Concr Res 6:773–782
12. Hui CY, Jagota A, Bennison SJ, Londono JD (2003) Crack blunting and the strength of soft elastic solids. Proc Royal Soc Lond A 459:1489–1516

13. Irwin GR (1960) Plastic zone near a crack and fracture toughness. In: Proceedings of the Seventh Sagamore Ordnance Materials Conference, Volume IV, pp. 63–78, Syracuse University, New York
14. Massabò R, Cox BN (1999) Concepts for bridged Mode II delamination cracks. J Mech Phys Solids 47:1265–1300
15. Overgaard LCT, Camanho PP, Lund E (2006) Structural response of Vestas V45 wind turbine blade. In: Camanho PP, Wisnom MR, Pierron F (eds) Proceedings of the Composite Test and Model Identification Conference - CompTest 2006, Porto, Portugal
16. Rice JR (1980) The mechanics of earthquake rupture. Phys Earth's Interior. In: Dziewonski AM, Boschhi E (eds) Proc Int Sch Phys "Enrico Fermi", Course 78), Italian Physical Society and North-Holland Publishing, New York, pp. 555–649
17. Smith E (1989) The size of the fully developed softening zone associated with a crack in a strain-softening material - II. A crack in a double-cantilever-beam specimen. Int J Eng Sci 27:309–314
18. Turon A (2006) Simulation of delamination in composites under quasi-static and fatigue loading using cohesive zone models. Ph.D. thesis, University of Girona, Spain
19. Turon A, Camanho PP, Costa J, Dávila CG (2006) A damage model for the simulation of delamination in advanced composites under variable-mode loading. Mech Mater 38:1079–1089
20. Turon A, Costa J, Camanho PP, Dávila CG (2007) Simulation of delamination in composites under high-cycle fatigue. Compos Part A 38:2270–2282
21. Turon A, Dávila CG, Camanho PP, Costa J (2007) An engineering solution for solving mesh size effects in the simulation of delamination with cohesive zone models. Eng Fract Mech 74:1665–1682
22. Yang Q and Cox BN (2005) Cohesive models for damage evolution in laminated composites, Int J Fract 133:107–137

Chapter 5
Combining Elastic Brittle Damage with Plasticity to Model the Non-linear Behavior of Fiber Reinforced Laminates

Clara Schuecker and Heinz E. Pettermann

Abstract The present work is concerned with modeling the non-linear behavior of continuous fiber reinforced laminates with a special emphasis on loading conditions that lead to high ply shear stresses. Typically, the modeling of non-linear laminate behavior focuses on damage mechanics approaches and assumes that the non-linearity is caused by brittle matrix cracking. Based on the correlation of experimental data and modeling results, this assumption seems to hold true for load cases in which layers experience mainly tensile stresses. Under shear dominated loads, however, it has been found that the agreement between tests and model predictions is less satisfactory. Additionally, considerable permanent strains develop under such loading conditions that cannot be explained by brittle mechanisms alone.

Here, a model is presented that combines damage mechanics with a plasticity law to capture both degradation of stiffness due to cracking and residual strains accumulated under shear loads. It is assumed that damage starts to develop close to the first ply failure load and any non-linear behavior prior to the onset of damage is attributed to plastic shear strains. Predictions of the model are compared to experimental data and are shown to give improved correlation to experiments under shear dominated loading. By taking residual stresses into account, the model is also able to explain discrepancies in the shear behavior derived from two different test methods. Furthermore, the combined damage/plasticity model captures the accumulation of residual strains, the non-linear behavior observed in uniaxial transverse compression tests, and the influence of transverse normal stress on the non-linear shear behavior reported in the literature.

C. Schuecker
NASA Postdoctoral Program, MS 188E NASA Langley Research Center, Hampton, VA 23681, United States of America, e-mail: schuecker@ilsb.tuwien.ac.at

H.E. Pettermann
Austrian Aeronautics Research (AAR)/Network for Materials and Engineering, Institute of Lightweight Design and Structural Biomechanics, Vienna University of Technology, Gusshausstrasse 27–29/E317, 1040 Vienna, Austria, e-mail: pettermann@ilsb.tuwien.ac.at

5.1 Introduction

The present work is concerned with modeling the non-linear behavior of continuous fiber reinforced laminates made of polymer matrix composite (PMC) plies. The modeling of non-linearity in such laminates has been a topic of active research over the past decades. Owing to the typically brittle behavior of polymers used in PMCs for structural applications, it is usually assumed that the non-linear behavior is a result of brittle cracking inside the matrix material (or at the fiber/matrix interface) leading to a degradation of ply and laminate stiffness. Therefore, previous modeling efforts have been focused on continuum damage mechanics [13,21]. Within this framework, cracks are treated in a homogenized manner to predict reduced stiffnesses of the material. Many continuum damage models for plane stress states have been presented in the literature [1, 2, 4, 6, 12, 20, 24, 25, 27]. These models have proven to be very successful in predicting the non-linear behavior under monotonic loading if the damaged plies experience primarily tensile stresses normal to the fibers. Under shear dominated loading, however, comparisons between model predictions and experimental data have been less satisfactory. The main difference between the behavior of a single PMC ply or uni-directional (UD) laminate under transverse tension and under shear is that there is almost no non-linearity in the tension case but a severe non-linearity in shear tests. Similarly, the behavior of a ply embedded in a laminate shows much greater non-linearity under shear loading than under transverse tension.

Recent research implies that the mechanisms leading to the non-linear behavior under shear dominated loading cannot be attributed to brittle damage alone. Varna et al. [29] studied the damage behavior of multi-directional laminates containing off-axis plies and found that when the off-axis plies are subjected to high shear stresses they show a highly non-linear load response but no observable cracks. For laminates where the off-axis plies are experiencing high transverse tensile stresses, on the other hand, the increasing non-linearity correlates with increasing crack density. A similar observation was made for out-of-plane shear behavior of a carbon fiber/epoxy material [16] where the load response was clearly non-linear but it was not possible to detect cracks, neither in the matrix nor the fiber/matrix interface. Finally, another study [28] has shown that significant residual strains remain after unloading of specimens tested under shear dominated loading. The shear stress – shear strain behavior of a symmetric ± 45 laminate tested under uniaxial tension is given in [28] (see Fig. 5.1). Several unloading/reloading loops are performed during the test which reveal that the non-linearity at first is related to considerable residual strains and the stiffness (indicated by dash-dotted lines) only changes at higher loads. The residual strains are not likely to be caused by crack face friction since transverse ply stresses in a ± 45 laminate under uniaxial tension are tensile, which would cause any existing cracks to open.

A possible source of the observed non-linear behavior under shear is plasticity in the matrix constituent. The polymers normally used in PMCs for structural applications, such as epoxy resins or PEEK, are known for their brittle behavior in tensile tests. However, it has been reported that plastic or visco-plastic behavior

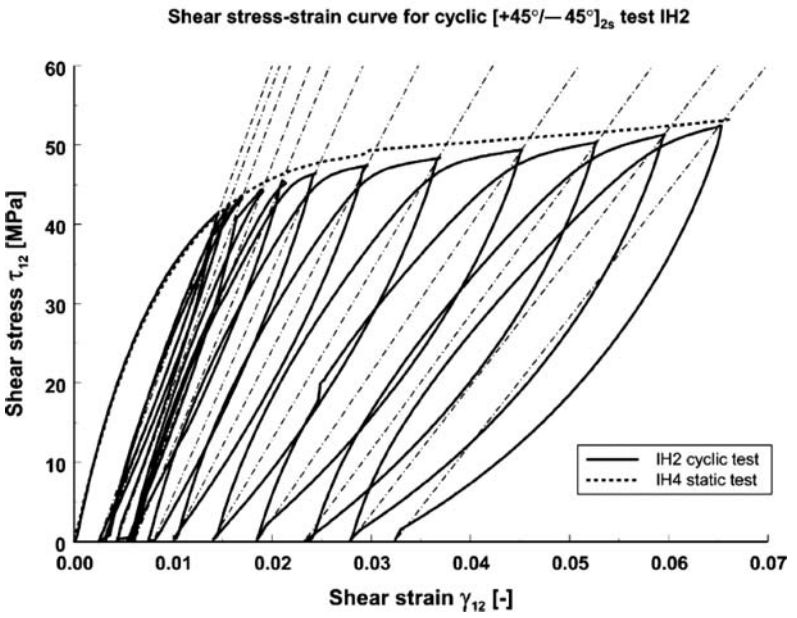

Fig. 5.1 Shear stress–shear strain response of a symmetric ± 45 laminate under uniaxial tension including unloading/reloading loops showing the evolution of shear modulus and residual strains [28]

can be observed under shear loading [8, 10, 30]. Furthermore, it has been found that fiber reinforced epoxy under transverse compression fails in an inclined plane due to shear stresses and that shear bands form in these planes prior to cracking [3]. Therefore, it is likely that the residual strains are a result of matrix plasticity. Irrespective of the actual mechanisms behind the residual strains, it is clear that an approach other than elastic/brittle damage mechanics is necessary to capture these strains in a model.

In the present work, a ply-level plasticity model for plane stress states that is able to capture the residual strains is presented. The plasticity model is combined with a damage model for brittle matrix failure that has previously been proposed by the authors [22, 24, 25]. Based on available experimental data, the combined damage/plasticity model assumes that stiffness degradation due to damage is related to the onset of matrix cracking at first ply failure (FPF). Consequently, damage accumulation only occurs in plies embedded in a multi-axial laminate close to the FPF load. The non-linearity of embedded plies prior to damage onset and all non-linearity in a single ply or UD laminate is due to plastic shear strains predicted by the proposed plasticity model.

Note that the objective of the combined damage/plasticity model is to predict residual strains and stiffness degradation. Hysteresis loops like the ones shown in Fig. 5.1 during unloading and reloading, which could be the result of viscous effects, are neglected in this study.

5.2 Plasticity Model

The plasticity model proposed here is a phenomenological approach based on the assumption that plastic deformation occurs in the form of shear bands with a specific orientation. As mentioned previously, experimental results of a study into the micromechanics of PMC failure mechanisms suggest that the shear bands are precursors of later cracks [3]. It is therefore assumed further that the shear bands develop in planes that have the same orientation as the fracture plane which is predicted here by Puck's action plane failure criterion for plane stress states (Puck 2D) [17, 20, 23].

According to Puck, fracture occurs in a plane that is parallel to the fiber orientation and defined by a fracture plane angle, θ_{fp}, as depicted in Fig. 5.2, left. The fracture plane is perpendicular to the laminate plane (i.e. $\theta_{\mathrm{fp}} = 0$) in the case of combined transverse tensile stresses and in-plane shear (mode A) or moderate transverse compression with in-plane shear (mode B). For combinations of high transverse compressive stresses with shear, the fracture plane angle is non-zero (mode C) and can be computed analytically [17,20,23]. For example, uniaxial transverse compression of epoxy matrix composites typically leads to a predicted fracture plane angle of approximately $\theta_{\mathrm{fp}} = 50^\circ - 56^\circ$, which agrees well with experimental findings [3,17,20] and results of micromechanical models [9]. In light of the considerations put forth above, the plasticity law is formulated with respect to the predicted fracture plane.

5.2.1 Plastic Strain for $\theta_{\mathrm{fp}} = 0$ (Puck Modes A and B)

In a perpendicular plane, $\theta_{\mathrm{fp}} = 0$, the only shear stress component under plane stress conditions is σ_{12}. The relation of shear stress and plastic shear strain for in-plane simple shear, $\gamma_{12}^{\mathrm{pl}}(\sigma_{12}, \sigma_{22} = 0)$, can be derived from experimental data and described by any suitable analytical expression. Here, a power law,

$$\gamma_{12} = \gamma_{12}^{\mathrm{el}} + \gamma_{12}^{\mathrm{pl}} = \frac{\sigma_{12}}{G_{12}} + \left(\frac{\sigma_{12}}{k}\right)^n \tag{5.1}$$

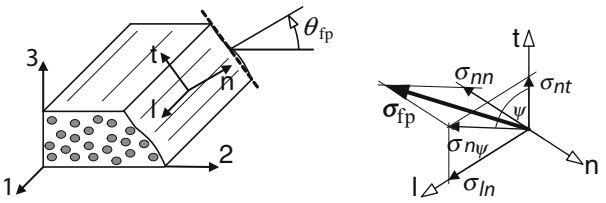

Fig. 5.2 Definition of fracture plane and corresponding coordinate system, l-n-t, with regard to the ply coordinate system, 1-2-3, by fracture plane angle, θ_{fp} (*left*); tractions on the fracture plane for $\theta_{\mathrm{fp}} \neq 0$ (*right*)

with plasticity parameters, k and n, is used which has been found to yield a good description of the non-linear response of a UD laminate under in-plane simple shear.

It has been previously reported in the literature that experimental tests typically show an influence of transverse tensile stress on the non-linear shear response [17, 19, 20]. In order to reflect this effect, a linear influence of transverse normal stress by a factor μ_{12}^{pl} is assumed leading to an equivalent shear stress, $\sigma_{12}^{\mathrm{eq}}$, given by

$$\sigma_{12}^{\mathrm{eq}} = |\sigma_{12}| + \mu_{12}^{\mathrm{pl}} \sigma_{22} \tag{5.2}$$

The plastic shear strain for perpendicular fracture planes (mode A or mode B stress states) under combined shear and normal stresses is then computed from the equivalent stress by employing the relation in Eq. (5.1) as

$$\gamma_{12}^{\mathrm{pl}}(\sigma_{12}, \sigma_{22} \neq 0) = \left(\frac{\sigma_{12}^{\mathrm{eq}}}{k} \right)^n \tag{5.3}$$

5.2.2 *Plastic Strain for $\theta_{\mathrm{fp}} \neq 0$ (Puck Mode C)*

If the fracture plane is inclined at an angle $\theta_{\mathrm{fp}} \neq 0$, the traction vector of the fracture plane, σ_{fp}, in general, has two shear components, σ_{nl} and σ_{nt} (see Fig. 5.2, right). For plane stress states, the component σ_{nl} is related to in-plane shear, σ_{12}, whereas σ_{nt} is the result of in-plane transverse compressive stresses, σ_{22}. Assuming transversely isotropic symmetry of the ply material, the material response due to shear stress in fiber direction, σ_{nl}, is the same as that for in-plane shear. Therefore, the same influence of normal stress given in Eq. (5.2) can be applied to the inclined fracture plane as

$$\sigma_{\mathsf{nl}}^{\mathrm{eq}} = |\sigma_{\mathsf{nl}}| + \mu_{12}^{\mathrm{pl}} \sigma_{\mathsf{nn}} \tag{5.4}$$

A similar relation is assumed for the transverse shear component, σ_{nt}, but with a different influence factor, μ_{23}^{pl}, to account for the different effect of the layer's micro-geometry in the direction transverse to the fibers which yields

$$\sigma_{\mathsf{nt}}^{\mathrm{eq}} = |\sigma_{\mathsf{nt}}| + \mu_{23}^{\mathrm{pl}} \sigma_{\mathsf{nn}} \tag{5.5}$$

To account for the interaction of the two shear components, the plasticity law given in Eq. (5.3) is applied to the total shear stress of the fracture plane, $\sigma_{\mathsf{n}\psi}$, analogously to Eqs. (5.2) and (5.3) as

$$\sigma_{\mathsf{n}\psi}^{\mathrm{eq}} = \left|\sigma_{\mathsf{n}\psi}\right| + \mu_{\mathsf{n}\psi}^{\mathrm{pl}} \sigma_{\mathsf{nn}} \quad \text{and} \quad \gamma_{\mathsf{n}\psi}^{\mathrm{pl}} = \left(\frac{\sigma_{\mathsf{n}\psi}^{\mathrm{eq}}}{k} \right)^n \tag{5.6}$$

where $\sigma_{\mathsf{n}\psi} = \sqrt{\sigma_{\mathsf{nl}}^2 + \sigma_{\mathsf{nt}}^2}$ is the projection of the traction vector, σ_{fp}, onto the fracture plane (Fig. 5.2, right), ψ is the angle between the directions of σ_{nt} and

$\sigma_{n\psi}$, and $\mu^{pl}_{n\psi}$ is interpolated from μ^{pl}_{12} and μ^{pl}_{23} as

$$\mu^{pl}_{n\psi} = \mu^{pl}_{12}\sin^2(\psi) + \mu^{pl}_{23}\cos^2(\psi) \tag{5.7}$$

The general form of the plasticity law is assumed to be the same for all combinations of fracture plane shear stresses, so n and k of Eq. (5.6) are the same as in Eqs. (5.1) and (5.3).

To compute the plastic strain tensor in ply coordinates, the plastic strain $\gamma^{pl}_{n\psi}$ is split into its two components and the plastic strain tensor referenced to the inclined fracture plane, $\bar{\boldsymbol{\varepsilon}}^{pl} = (0,0,0,\gamma^{pl}_{nl},0,\gamma^{pl}_{nt})^T$ (in Nye-notation), is transformed to ply coordinates. Since the value of γ^{pl}_{nt} is generally non-zero for inclined fracture planes, the transformation leads to plastic normal strains, ε^{pl}_{22} and $\varepsilon^{pl}_{33} = -\varepsilon^{pl}_{22}$, as well as out-of-plane shear strains, γ^{pl}_{23}. The latter, however, cancel each other out if an equal accumulation of plastic shear strains γ^{pl}_{nt} in planes oriented at $+\theta_{fp}$ and $-\theta_{fp}$ is assumed.

Finally, the plastic strain tensor in ply coordinates is given by

$$\boldsymbol{\varepsilon}^{pl} = \begin{cases} (0,0,0,\gamma^{pl}_{12},0,0)^T & \texttt{mode A,B} \\ (0,\varepsilon^{pl}_{22},\varepsilon^{pl}_{33},\gamma^{pl}_{12},0,0)^T & \texttt{mode C} \end{cases} \tag{5.8}$$

5.2.3 *Identification of Parameters for the Plasticity Model*

There are four parameters which need to be identified in order to fully define the plasticity model described above, i.e. n and k for the plasticity law under in-plane simple shear (Eq. 5.1), as well as μ^{pl}_{12} and μ^{pl}_{23} for the influence of normal stress (Eqs. 5.2 and 5.5, respectively). To identify these parameters it is convenient to use data from tests on UD laminates because then all non-linearity is related to plasticity, according to the model assumptions.

The plasticity parameters, n and k, can be derived from experimental data of shear tests on a UD laminate following Eq. (5.1). Ideally, n and k are determined by curve fitting if the shear stress–shear strain curve is known. If the complete stress–strain data is not available for a given ply material, approximations can be obtained by choosing n in the range of $n = 5-7$ and computing k from the stress and strain values at failure. As an example, the shear stress vs. plastic shear strain curve for a glass fiber/epoxy material (see Table 5.1 for material data) is shown in Fig. 5.3, left, using experimental data of a test on a hoop wound tube taken from [11]. The best fit using Eq. (5.1) is obtained with parameters $n = 7.2$ and $k = 120.7$ MPa (solid line). As indicated by the dashed line for the lowest suggested value of $n = 5$ (resulting in $k = 150.6$ MPa), a lower value of n only affects the curvature of the graph but passes through the same end point and still yields reasonable agreement with the experimental data.

Table 5.1 Material data [11, 26] and parameters for the damage/plasticity model of glass fiber/epoxy UD-layer E-glass/MY750 [18]

Elastic constants				
E_1 (GPa)	$E_2 = E_3$ (GPa)	$G_{12} = G_{13}$ (GPa)	$\nu_{12} = \nu_{13}$	ν_{23}
45.6	16.2	5.5	0.278	0.4

Strength data					
	R_{11} (MPa)	R_{22} (MPa)	R_{12} (MPa)	p_{12}	p_{23}
tension $()^t$	1280	40	73	0.3[a]	0.3[a]
compression $()^c$	520	145	73	0.25[a]	0.206[a]

Damage and plasticity parameters							
κ	e_n	ξ^{sat}	μ_D	n	k	μ_{12}^{pl}	μ_{23}^{pl}
0.05	0.0144	0.2	11	7.2	120.7 MPa	0.25	0.2

[a] Following Puck's guidelines for glass fiber materials

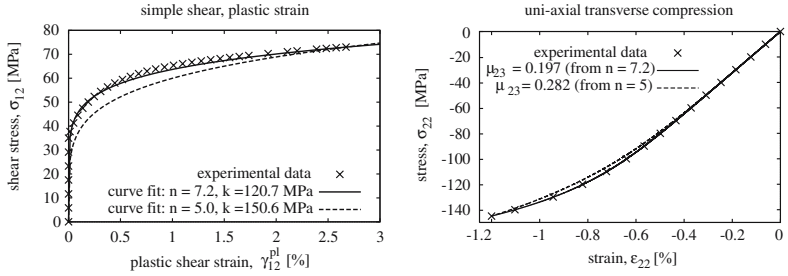

Fig. 5.3 Identification of plasticity model parameters for E-glass/MY750 glass fiber/epoxy material; plastic strain under simple shear (*left*); non-linear behavior under uniaxial transverse compression (*right*) (Experimental data from [11, 26])

Once the relation for simple shear is known, μ_{23}^{pl} can be computed from the failure stress and strain under uniaxial transverse compression based on Eqs. (5.5), (5.6), and (5.7). The transverse compression curve for the glass fiber/epoxy material is shown in Fig. 5.3, right, displaying experimental data [26] and model results for both curve fits $n = 7.2$ and $n = 5$ leading to $\mu_{23}^{pl} = 0.197$ and $\mu_{23}^{pl} = 0.282$, respectively.

The factor μ_{12}^{pl} for the influence of transverse stresses on γ_{12} (or γ_{nl}) should be derived from experimental data of tests with various stress ratios σ_{22}/σ_{12}. Since this data is often unavailable, a method to estimate μ_{12}^{pl} (and μ_{23}^{pl}) is suggested here. It has been found that typical values for μ_{23}^{pl} are similar to the values of the slope parameter p_{23}^{c} used in Puck's failure criterion to account for the shear-strengthening effect due to transverse compression [17, 20, 23]. Assuming that the influence of

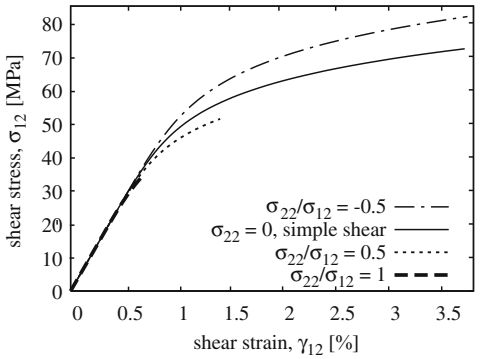

Fig. 5.4 Influence of transverse normal stress on the shear response of glass fiber/epoxy material E-glass/MY750 predicted by the plasticity model (perpendicular fracture plane)

transverse normal stress on shear regarding failure and plasticity is a result of similar mechanisms, it is suggested to estimate μ_{12}^{pl} and μ_{23}^{pl} as the corresponding values of slope parameters of the Puck criterion $\mu_{12}^{\mathrm{pl}} = p_{12}^{\mathrm{c}}$ and $\mu_{23}^{\mathrm{pl}} = p_{23}^{\mathrm{c}}$ when experimental data is not available. Guidelines for the choice of p_{12}^{c} and p_{23}^{c} are given in [18]. For the glass fiber/epoxy material, the values obtained using Puck's recommendation amount to $\mu_{12}^{\mathrm{pl}} = p_{12}^{\mathrm{c}} = 0.3$ and $\mu_{23}^{\mathrm{pl}} = p_{23}^{\mathrm{c}} = 0.206$.

The predicted effect of additional transverse normal stress on the shear stress–shear strain relation of a UD laminate based on the values identified for the glass fiber/epoxy material is shown in Fig. 5.4. Since a UD laminate is considered, the curves terminate at FPF predicted by the Puck criterion. All stress ratios shown in this figure result in a perpendicular fracture plane (mode A or B). Therefore, the influence of transverse stress is a result of the chosen value of μ_{12}^{pl}, only (for $\mu_{12}^{\mathrm{pl}} = 0$ there would be no effect of transverse stresses on the plastic behavior). Qualitatively, the predictions shown in Fig. 5.4 are consistent with trends reported in the literature for other materials [17, 19, 20].

5.2.4 Lamina Response for Mode C

The interaction of non-linearities due to transverse compression and in-plane shear in UD laminates has been studied in [30] for the material AS4/PEEK (see material data in Table 5.2). Experimental data from this study for radial loading paths of various stress ratios, σ_{22}/σ_{12}, are shown in Figs. 5.5 and 5.6 in comparison to predictions of the proposed plasticity model. The parameters for the plasticity model are identified as outlined in Sect. 5.2.3. Parameters for Eq. (5.1) are determined from the test data of simple shear as $n = 6.25$ and $k = 144\,\mathrm{MPa}$. The value of μ_{23}^{pl} is computed from the FPF stress and strain under uniaxial transverse compression as $\mu_{23}^{\mathrm{pl}} = 0.322$. Since there is only little difference between the simple shear curve and

Table 5.2 Material data and parameters for the plasticity model of AS4/PEEK UD-layer [30]

Elastic constants				
E_1 (GPa)	$E_2 = E_3$ (GPa)	$G_{12} = G_{13}$ (GPa)	$\nu_{12} = \nu_{13}$	ν_{23}
130	11.2	5.3	0.306	0.48

Strength data					
	R_{11} (MPa)	R_{22} (MPa)	R_{12} (MPa)	p_{12}	p_{23}
tension $()^t$	2,100	80	79.5	0.35[a]	0.35[a]
compression $()^c$	1,100	241.3	79.5	0.25[a]	0.3[a]

Plasticity law parameters			
n	k	μ_{12}^{pl}	μ_{23}^{pl}
6.25	144 MPa	0.05	0.322

[a] Following Puck's guidelines for carbon fiber materials [18]

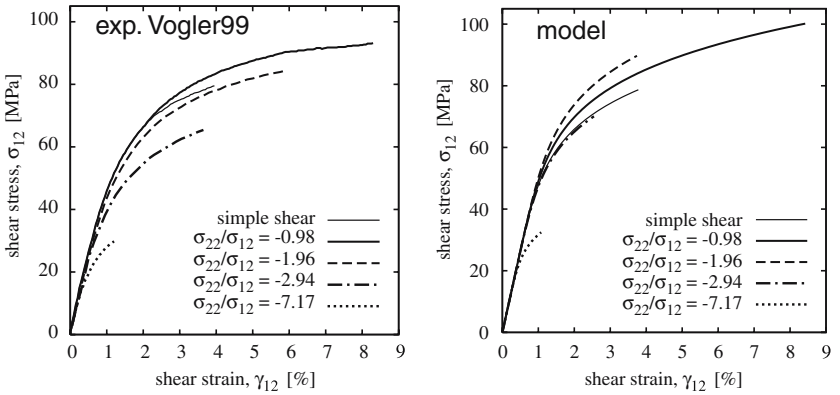

Fig. 5.5 Non-linear shear response for AS4/PEEK UD laminates under various stress ratios σ_{22}/σ_{12} (Experimental data from [30] (*left*); model prediction (*right*))

the one for stress ratio $\sigma_{22}/\sigma_{12} = -0.98$ (Fig. 5.5, left), it can be inferred that the value of μ_{12}^{pl} has to be rather small. Its value is chosen as $\mu_{12}^{pl} = 0.05$ which gives good correlation between predictions of the plasticity model and experimental data for the shear stress–shear strain curve of stress ratio $\sigma_{22}/\sigma_{12} = -0.98$.

According to the proposed plasticity model, all stress ratios of the given test cases, except for the simple shear case, correspond to inclined fracture planes. For this reason, the $\sigma_{22} - \varepsilon_{22}$ relation is predicted to be non-linear in all test cases and the additional in-plane shear stress has an influence on the non-linearity (see Fig. 5.6, right). If one of the stress ratios had led to a perpendicular fracture plane (mode B), the $\sigma_{22} - \varepsilon_{22}$ relation would be linear according to the proposed plasticity model,

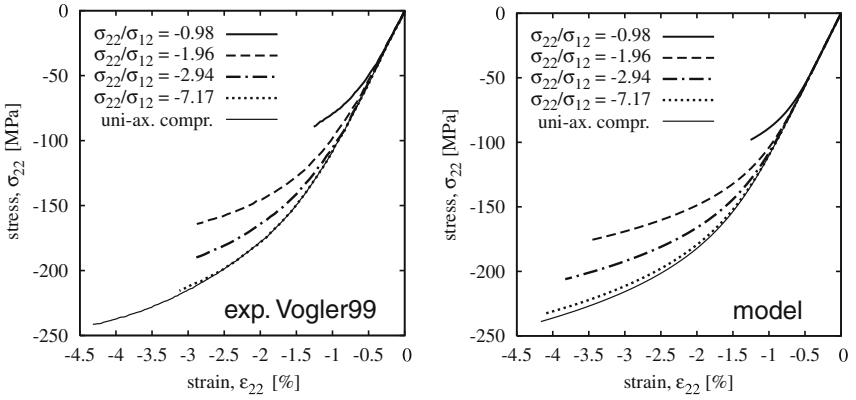

Fig. 5.6 Non-linear compressive response of AS4/PEEK UD laminates under various stress ratios σ_{22}/σ_{12} (Experimental data from [30] (*left*); model prediction (*right*))

irrespective of the amount of superimposed shear stress, and the stress ratio would only have an effect on compressive strength.

The overall correlation of experimental data and model predictions is very good, especially for the influence of shear stresses on the transverse compressive behavior (Fig. 5.6). The effect of compression on shear behavior (Fig. 5.5) is captured qualitatively. For stress ratio $\lambda = -0.98$, strength and onset of non-linearity are shifted to higher stresses. With further increase of compression, this trend is reversed and the curves shift to lower stresses. Quantitatively, the correlation between model and experiments is good for test cases $\lambda = -0.98$ and $\lambda = -7.17$. For stress ratios $\lambda = -1.96$ and $\lambda = -2.94$ the plastic shear strains at failure are underestimated by 37% and 31%, respectively. The prediction of failure stresses, on the other hand, is excellent for all load cases considered.

5.3 Combination with Damage Model

If a ply is embedded in a laminate, the first crack does not cause immediate laminate failure. Therefore, non-linearity in a multi-axial laminate can have two contributions: plasticity and damage. To model the stiffness degradation of an embedded ply due to progressive damage in addition to the accumulation of plastic strains, the plasticity model is combined with a damage model previously proposed by the authors [22, 24, 25]. The relation between layer stresses, $\boldsymbol{\sigma}$, and total strains, $\boldsymbol{\varepsilon}$, for the combined damage/plasticity model is expressed by the equation

$$\boldsymbol{\sigma} = \boldsymbol{E}^{\mathrm{d}} \left(\boldsymbol{\varepsilon} - \boldsymbol{\varepsilon}^{\mathrm{pl}} \right) \tag{5.9}$$

where $\boldsymbol{\varepsilon}^{\mathrm{pl}}$ is the plastic strain tensor as defined by the plasticity model and $\boldsymbol{E}^{\mathrm{d}}$ is the elasticity tensor of a damaged layer reflecting the material degradation due to damage. Both of these tensors can contribute to the non-linear behavior.

The elasticity tensor $\boldsymbol{E}^{\mathrm{d}}$ is predicted by the damage model as follows. First, the ply stress state is evaluated by the factor of effort, f_{E}, which is defined from

$$\boldsymbol{\sigma}^{\mathrm{FPF}} f_{\mathrm{E}} = \boldsymbol{\sigma} \tag{5.10}$$

where $\boldsymbol{\sigma}$ is the given stress state and $\boldsymbol{\sigma}^{\mathrm{FPF}}$ is the corresponding failure stress state determined from the Puck 2D failure criterion. The amount of damage in a composite ply is quantified by a scalar damage state variable, ξ, and is related to the factor of effort by an evolution law of the form

$$\frac{\xi}{\xi^{\mathrm{sat}}} = \begin{cases} 0 & \text{for} \quad f_{\mathrm{E}} \leq \dfrac{1}{1+\kappa} \\ 1 - \exp - \dfrac{(f_{\mathrm{E}}(1+\kappa)-1)^2}{2\kappa^2} & \text{for} \quad f_{\mathrm{E}} \geq \dfrac{1}{1+\kappa} \end{cases} \tag{5.11}$$

with damage evolution parameter κ. The maximum amount of damage that can be reached in a ply is given by the damage state variable at saturation, ξ^{sat}, which is typically set to $\xi^{\mathrm{sat}} = 0.2$. The general shape of the evolution law function is chosen based on experimental observations regarding the increasing crack density with load (e.g. [15,20]). The evolution parameter κ determines the damage onset load and how quickly damage progresses with an increase of load. Typical values are in the range of $\kappa = 0.01 - 0.05$ such that damage onset, given by $f_{\mathrm{E}}^{\mathrm{onset}} = \frac{1}{1+\kappa}$, occurs close to the FPF load. For $\kappa \to 0$, the evolution law converges to the step function, i.e. the damage state grows from zero to the final damage state, $\xi = \xi^{\mathrm{sat}}$, instantly at FPF. Note that unlike the originally proposed damage model, the combined damage/plasticity model uses a constant evolution parameter $\kappa = \kappa_{22}$ that is independent of the stress state [22, 24].

The elasticity tensor $\boldsymbol{E}^{\mathrm{d}}$ for a given damage state, ξ, is computed by the Mori-Tanaka approach [14] using penny-shaped inclusions aligned with the fracture plane predicted by Puck 2D and having a constant aspect ratio e_{n}. Note that the inclusions are not intended to model actual cracks in the material, rather they are used to derive a full triaxial elasticity tensor of the damaged material in a thermodynamically consistent way. This way, the anisotropic effect of damage is captured qualitatively, while quantification is provided by parameter identification from experimental data as described in [24]. The material properties assigned to the inclusions depend on the stress state. If the normal stress on the corresponding fracture plane, σ_{nn}, is tensile such that cracks would be open, the inclusions become voids with zero stiffness. For compressive normal stress, the inclusions' properties are the same as those of the initial (undamaged) ply material except for reduced shear moduli in the fracture plane, $G_{\mathrm{nl}}^{\mathrm{incl}}$ and $G_{\mathrm{nt}}^{\mathrm{incl}}$. These are computed as

$$G_{\mathrm{nl}}^{\mathrm{incl}} = G_{\mathrm{nt}}^{\mathrm{incl}} = \mu_{\mathrm{D}} |\sigma_{\mathrm{nn}}| \tag{5.12}$$

where the factor μ_{D} is a material parameter accounting for shear stiffness recovery attributed to frictional forces at the crack faces. For a detailed discussion of the

damage model assumptions, the exact formulation of the constitutive equations as well as identification procedures for the model parameters see [22, 24, 25].

5.4 Laminate Behavior

In order to apply the combined damage/plasticity model to the analysis of multi-directional laminates, the model is implemented in combination with classical lamination theory extended for plastic strains (e.g. [5]). In the following, model predictions are compared to experimental data to assess the model's capabilities of capturing laminate behavior under various loading conditions.

5.4.1 Influence of Curing Stresses on Shear Behavior

In this section, the combined damage/plasticity model is used to investigate the effect of curing stresses on the shear response derived from two different experimental test methods reported in [11]. One method is a torsion test of a hoop-wound tube which yields the shear stress–shear strain relation of a UD laminate under in-plane simple shear. The other method is to derive the non-linear shear response via lamination theory from tests on ± 45 laminates under stress ratio $\sigma_{xx}/\sigma_{yy} = -1$ leading to in-plane simple shear in each layer. Since the individual plies experience only shear stresses in both experiments, there should be no difference between the non-linear shear responses derived by either test method. Both of these methods were used in [11] to determine the shear response of the glass fiber/epoxy material E-glass/MY750 (see Table 5.1). The experimental results are shown in Fig. 5.7 denoted as 'exp. UD' and 'exp. laminate'. One difference between the two curves is related to the fracture process. Fracture of the UD specimen is the result of a single matrix crack, while a laminate can continue to carry load well after the individual plies have cracked. But also prior to cracking, the non-linear behavior is not the same as the curves from the laminate tests exhibit significantly higher strains beyond $\sigma_{12} \approx 40\,\text{MPa}$. A possible explanation for this discrepancy are residual curing stresses due to the production process which are expected to exist in the ± 45 laminate but not in the UD specimens.

The results of analyses employing the proposed damage/plasticity model are also displayed in Fig. 5.7. Damage parameters for the glass fiber/epoxy material have been identified previously in [24] and are listed with the other material data in Table 5.1. The non-linearity predicted for a UD laminate is caused by plasticity only and the corresponding curve is labeled as 'model UD' in Fig. 5.7. It is a perfect fit to the corresponding experimental curve, since the experimental data is the same as that used for parameter identification in Fig. 5.3, left. The curve predicted for the biaxial laminate test without consideration of residual stresses ('model laminate') also follows the same curve up to the onset of damage and then continues with an

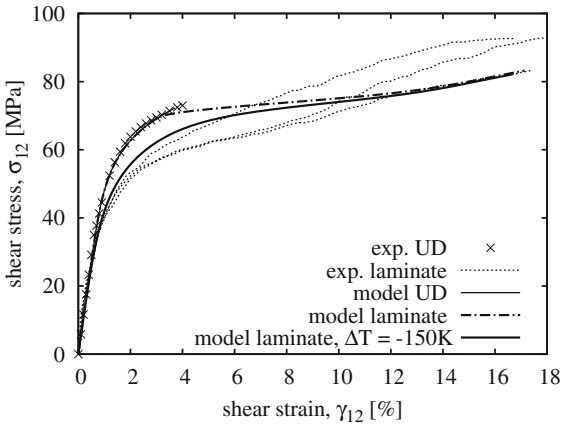

Fig. 5.7 Effect of curing stresses on the shear stress–shear strain curve determined by two different test methods, torsion of a hoop-wound tube and biaxial testing of a ±45 laminate (Experimental data from [11])

almost horizontal tangent as damage is increasing in addition to further accumulation of plastic strain. To account for curing stresses in the simulation of the laminate test, a temperature change of $\Delta T = -150\,\mathrm{K}$ from a stress-free state is prescribed. The result of this analysis is shown by a thick solid line in Fig. 5.7. It can be seen that the effect of residual stresses predicted by the combined model for the laminate test leads to a similar change in shear response as observed in the experiments. Note that the effect of fiber rotation related to the high amount of shear strain is not taken into account in the model. This potentially leads to the higher tangent stiffness in the experimental data compared to model predictions at higher strain.

The same comparison has also been performed previously using the original formulation of the damage model without taking shear plasticity into account [22]. There, it was found that the discrepancy between the two test methods cannot be explained if non-linearity is attributed only to brittle damage since residual stresses are released due to the stiffness degradation when damage starts to develop. Consequently, the results of the combined damage/plasticity model shown in Fig. 5.7 represent a significant improvement over predictions of the original brittle damage model.

5.4.2 Accumulation of Plastic Strain

To study the accumulation of plastic strain under shear dominated loading, a series of uniaxial tensile tests on symmetric angle ply laminates, $(\pm\beta)_{2s}$, with varying layup-angle, β, has been carried out (experimental data courtesy of *PCCL – Polymer Competence Center Leoben*, Austria). The tests were conducted on flat coupons of carbon fiber/epoxy with a nominal cross-sectional area $A = 25\ \mathrm{mm}^2$

Table 5.3 Material data and parameters for the damage/plasticity model of a carbon fiber/epoxy UD-layer [18]

Elastic constants				
E_1 (GPa)	$E_2 = E_3$ (GPa)	$G_{12} = G_{13}$ (GPa)	$\nu_{12} = \nu_{13}$	ν_{23}
140	8.5	4.5	0.35	0.4

Strength data					
	R_{11} (MPa)	R_{22} (MPa)	R_{12} (MPa)	p_{12}	p_{23}
tension $()^t$	2,376	60	108	0.35[a]	0.35[a]
compression $()^c$	1,420	200[b]	108	0.3[a]	0.23[a]

Damage and plasticity law parameters							
κ	e_n	ξ^{sat}	μ_D	n	k	μ_{12}^{pl}	μ_{23}^{pl}
0.01	0.012	0.2	15	5.88	145.6 MPa	0.3	0.23

[a] Following Puck's guidelines for carbon fiber materials

[b] Estimated value

(see Table 5.3 for material data). During some tests, several unload/reload loops were performed to investigate the amount of accumulated residual strain. Experimental results for laminates with angles $\beta = 25°, 45°, 55°$, and $65°$ are shown in Fig. 5.8, with 'exp.stat' denoting monotonic loading and 'exp.loop' denoting tests with unload/reload loops. These four layup angles give rise to ply stress ratios $\sigma_{22}/\sigma_{12} = -0.88$, 0.15, 0.76, and 1.6, respectively, for the linear elastic range.

Predictions by the combined damage/plasticity model for these tests including unloading paths are also shown in Fig. 5.8. The damage parameters for the model are chosen the same as those of a comparable material that has been identified previously [22,25] (see Table 5.3). It is noted, however, that the progression of damage plays a minor role in most of the test cases shown here since damage onset under shear dominated loads occurs very late in the loading history.

Due to the lack of experimental data on the shear behavior of UD specimens, the shear plasticity parameters are deduced from data of the monotonic test of a ± 45 laminate. For this layup, the ply stress state is close to in-plane simple shear ($\sigma_{22}/\sigma_{12} = 0.15$ in the linear elastic range). Since data on the compressive response and the influence of transverse normal stresses on the shear response is also not available, the influence parameters for normal stresses are chosen as suggested in Sect. 5.2.3 as $\mu_{12}^{pl} = p_{12}^{c} = 0.3$ and $\mu_{23}^{pl} = p_{23}^{c} = 0.23$. It is noted that effects of curing stresses, fiber rotation due to large shear strains, and increased strength of thin plies (in-situ effect, see e.g. [7]) are not accounted for in the present analyses.

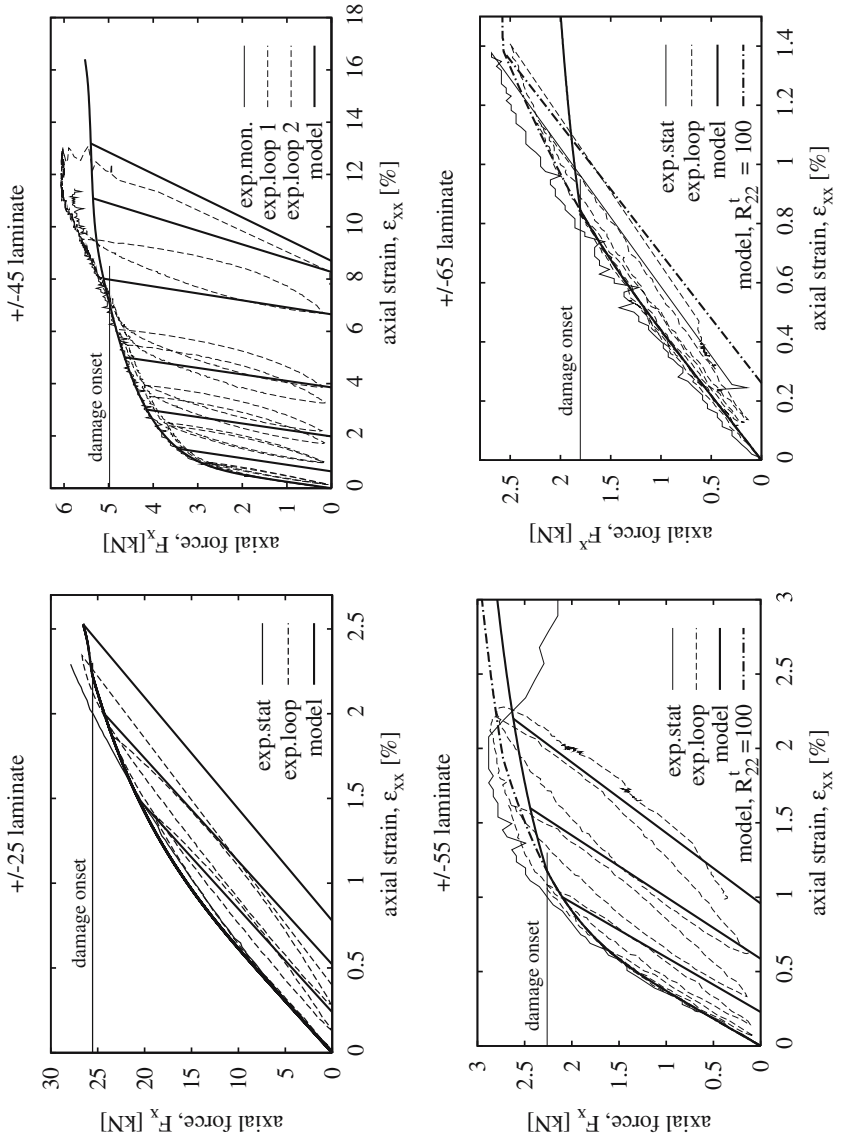

Fig. 5.8 Experimental results and model predictions of axial force–strain plots of tensile tests on various angle-ply laminates including unload/reload loops (cross-sectional area of coupons $A = 25\,\text{mm}^2$ (Experimental data courtesy of PCCL, Leoben))

As the results in Fig. 5.8 indicate, the agreement between model predictions and experiments, in general, is quite satisfactory for all four laminates regarding the non-linear response as well as accumulated residual strain.

In the ± 25 laminate (Fig. 5.8, top left), the induced ply stress state leads to an inclined fracture plane (mode C). The predicted fracture plane angle starts out at

$\theta_{fp} = 33°$ and increases with the accumulation of plastic strain and damage to reach $\theta_{fp} = 43°$ at failure. Due to the model formulation, the plastic strain tensor and the elasticity tensor of a damaged ply implicitly depend on the fracture plane angle. In the current implementation, the fracture plane angle corresponding to a given load increment is used for computing the plastic strain tensor and the elasticity tensor at that load. Although this is not strictly correct, the error is expected to be small for this example since the initial fracture plane angle of $\theta_{fp} = 33°$ is already relatively large.

Prior to damage onset, the unloading path follows the initial axial stiffness of the laminate, which correlates fairly well with the experimental data. Note that the load of damage onset and ultimate failure predicted for the ± 25 laminate is predominantly influenced by the transverse compressive strength R^c_{22}, which was not available for this material. Typical values for carbon fiber/epoxy materials are on the order of $R^c_{22} = 200-250\,\text{MPa}$. In Fig. 5.8, top left, an estimated value of $R^c_{22} = 200\,\text{MPa}$ is used. A higher compressive strength would shift the damage onset and ultimate failure stresses to higher values but it would have little influence on the non-linear behavior below damage onset. The choice of R^c_{22} does not have any influence on the predicted behavior of the other layups considered here.

The monotonic test of a ± 45 laminate (Fig. 5.8, top right) is used for identification of the plasticity parameters. Therefore, the model prediction is a perfect fit to this curve below damage onset which occurs at $F_x = 4.93\,\text{kN}$ (i.e. 1% below the FPF stress due to the chosen value of $\kappa = 0.01$). After the onset of damage, the predicted curve is lower than the experimental ones. This is most likely due to the neglected stiffening effect of fiber rotation and the fact that the ± 45 laminate test was used to identify the plasticity parameters rather than a test of a UD laminate. While plastic strains continue to increase after damage onset, the accumulation of damage additionally leads to a degradation of the axial stiffness. Fairly good agreement is found by comparing the predicted unloading paths to the experimental unload/reload loops with only a small underestimation of stiffness degradation by the model. It seems that a small reduction of stiffness occurs in the experiments already at the start of loading. However, most of the non-linearity prior to FPF is related to residual strains as it is assumed in the proposed model.

Similar observations can be made for the ± 55 laminate (Fig. 5.8, bottom left). The overall agreement between model and experiments is good, showing only a slight underestimation of stiffness degradation. It is interesting to note that strain softening can be observed in the experimental data of the monotonic test. The source of this effect is not clear but it is conceivable that additional failure mechanisms, such as delamination between the laminate layers, come into play which are not included in the present model. The tests with unloading/reloading loops were terminated before a reduction of force was noticed.

In the ± 65 laminate tests (Fig. 5.8, bottom right), the ratio of transverse normal stress over shear stress is the highest of all tests considered here ($\sigma_{22}/\sigma_{12} = 1.6$). Consequently, only a minor amount of non-linearity is observed in the experiments which is also predicted correctly by the model. Although the experimental data is not that clear since the non-linearity is very small, it seems that most of the

non-linearity is related to residual strains. All specimens tested fail very abruptly at a stress of approximately 100 MPa. Subsequent inspection of the specimens led to the conclusion that the onset of damage in one ply instantly triggers fiber failure in the neighboring plies due to a concentration of shear stresses at the location of the matrix crack. Therefore, the onset of damage in the model should be considered as ultimate failure in this case. However, the predicted FPF load is significantly lower than the laminate failure load in the experimental tests. The reason for this discrepancy is most likely a result of a higher tensile strength due to the 'in situ' effect [7]. If the FPF strength for transverse tension is increased to $R_{22}^{t} = 100\,\text{MPa}$ such that the predicted failure load agrees with the experimental data, the amount of plastic strain predicted by the simulation shows very good agreement with the experiment.

The effect that a higher transverse tensile strength has on the predicted response of the ± 55 laminate is shown in Fig. 5.8, bottom left, by the dash-dotted line. For the other two laminates, there would be almost no change due to the increased tensile strength in the case of the ± 45 and no change for the ± 25 layup according to the proposed model.

5.5 Conclusions

In the present work, a model combining elastic brittle damage mechanics with plasticity is presented to predict the non-linear load response of fiber reinforced polymer laminates under plane stress states. Although continuum damage mechanics is typically used to model non-linearity of laminate plies, it has been found that not all of the non-linear effects observed experimentally can be explained by brittle damage. For example, it is reported in the literature that residual strains occur in experiments under shear-dominated loading conditions. To capture these strains, a formulation for plastic shear strains is proposed and combined with a damage model developed previously by the authors. The combined damage/plasticity model is able to capture the non-linear ply behavior accounting for stiffness degradation due to matrix cracking as well as residual strains caused by plastic shear deformation. Comparisons to experimental data show that taking plastic shear strains into account leads to significant improvements in the predictive capabilities. Additionally, the combined model reflects the accumulation of residual strains, the non-linear response observed in uniaxial transverse compression tests, and the influence of transverse normal stress on the non-linear shear behavior. This influence of transverse stress, furthermore, is able to explain discrepancies between the shear behavior derived from tests on a UD laminate compared to biaxial tests on a multi-directional laminate attributed to residual curing stresses. Another advantage of the proposed model is the relatively small amount of material parameters. The identification of parameters for the plasticity model by standard test methods is also discussed in this work.

Acknowledgements The funding of the Austrian Aeronautics Research (AAR)/Network for Materials and Engineering by the Austrian Federal Ministry of Economics and Labor is gratefully acknowledged. Part of the research was supported by the NASA Postdoctoral Program at the Langley Research Center, administered by Oak Ridge Associated Universities. The authors would also like to thank Gerald Pinter of PCCL – Polymer Competence Center Leoben, Austria, for providing experimental data.

References

1. Allen DH (1994) Damage evolution in laminates. In: Talreja R (ed) Damage Mechanics of Composite Materials, Volume 9 of Composite Materials Series, Chapter 3. Elsevier Science, Oxford, UK
2. Allix O, Daudeville L, Ladevèze P (1991) Delamination and damage mechanics. In: Baptiste D (ed) Mechanics and Mechanisms of Damage in Composites and Multi-Materials, pp 143–158. Mechanical Engineering Publications Limited, London, UK
3. Aragonés D (2007) Fracture micromechanisms in C/epoxy composites under transverse compression. Master's thesis, Universidad Politécnica de Madrid, Spain
4. Barbero EJ, Lonetti P (2002) An inelastic damage model for fiber reinforced laminates. J Compos Mater 36:941–962
5. Bednarcyk BA (2002) A fully coupled micro/macro theory for thermo-electro-magneto-elasto-plastic composite laminates. Technical Report NASA/CR—2002-211468, NASA
6. Camanho PP, Dávila CG, Maimí P, Mayugo JA (2005) A continuum damage model to predict ultimate failure of composite structures. In: Proc. of 15th International Conference on Composite Materials (ICCM 15), June 27–July 1, 2005, Durban, South Africa. Paper P-07f
7. Camanho PP, Dávila CG, Pinho ST et al. (2006) Prediction of in situ strengths and matrix cracking in composites under transverse tension and in-plane shear. Compos Part A 37: 165–176
8. Gilat A, Goldberg RK, Roberts GD (2005) Strain rate sensitivity of epoxy resin in tensile and shear loading. Technical Report TM-2005-213595, NASA
9. GonzálezC, Llorca J (2007) Mechanical behavior of unidirectional fiber-reinforced polymers under transverse compression: microscopic mechanisms and modeling. Compos Sci Technol 67:2795–2806
10. G'Sell C, Jacques D, Favre JP (1990) Plastic behaviour under simple shear of thermosetting resins for fibre composite matrices. J Mater Sci 25:2004–2010
11. Kaddour AS, Hinton MJ, Soden PD (2003) Behaviour of $\pm 45^\circ$ glass/epoxy filament wound composite tubes under quasi-static equal biaxial tension–compression loading: experimental results. Compos Part B 34:689–704
12. Ladevèze P (1991) On a damage mechanics approach. In: Baptiste D (ed) Mechanics and Mechanisms of Damage in Composites and Multi-Materials, pp 119–142. Mechanical Engineering Publications Limited, London, UK
13. Lemaitre J (1992) A Course on Damage Mechanics. Springer, Berlin/Heidelberg, Germany
14. Mori T, Tanaka K (1973) Average stress in the matrix and average elastic energy of materials with misfitting inclusions. Acta Metall 21:571–574
15. Nairn JA, Hu S (1994) Matrix microcracking. In: Talreja R (ed) Damage Mechanics of Composite Materials, Volume 9 of Composite Materials Series, Chapter 6. Elsevier Science, Oxford, UK
16. Pettersson K (2005) The inclined double notch shear test for determination of interlaminar shear properties of composite laminates. Ph.D. thesis, Royal Institute of Technology, Solid Mechanics, Stockholm, Sweden
17. Puck A (1996) Festigkeitsanalyse von Faser-Matrix-Laminaten. Carl Hanser Verlag, München Wien, Germany

18. Puck A, Kopp J, Knops M (2002) Guidelines for the determination of the parameters in Puck's action plane strength criterion. Compos Sci Technol 62:371–378
19. Puck A, Mannigel M (2007) Physically based non-linear stress–strain relations for the inter-fibre fracture analysis of FRP laminates. Compos Sci Technol 67:1955–1964
20. Puck A, Schürmann H (1998) Failure analysis of FRP laminates by means of physically based phenomenological models. Compos Sci Technol 58:1045–1067
21. Rabotnov JN (1969) Creep Problems in Structural Members, Volume 7 of North-Holland series in Applied Mathematics and Mechanics. North-Holland, Amsterdam, The Netherlands
22. Schuecker C (2005) Mechanism based modeling of damage and failure in fiber reinforced polymer laminates. Ph.D. thesis, Institute of Lightweight Design and Structural Biomechanics, Vienna University of Technology, Vienna, Austria (also published in: VDI Fortschritt-Berichte VDI Reihe 18 Nr. 303, VDI-Verlag, Düsseldorf)
23. Schuecker C, Pahr DH, Pettermann HE (2006) Accounting for residual stresses in FEM analyses of laminated structures using the Puck criterion for three-axial stress states. Compos Sci Technol 66:2054–2062
24. Schuecker C, Pettermann HE (2006) A continuum damage model for fiber reinforced laminates based on ply failure mechanisms. Compos Struct 76:162–173
25. Schuecker C, Pettermann HE (2007) Constitutive ply damage modeling, FEM implementation, and analyses of laminated structures. Comput Struct, doi:10.1016/j.compstruc.2007.04.021
26. Soden PD, Hinton MJ, Kaddour AS (1998) Lamina properties, lay-up configurations and loading conditions for a range of fibre-reinforced composite laminates. Compos Sci Technol 58:1011–1022
27. Talreja R, Yalvac S, Yats LD, Wetters DG (1992) Transverse cracking and stiffness reduction in cross ply laminates of different matrix toughness. J Compos Mater 26:1644–1663
28. Van Paepegem W, De Baere I, Degrieck J (2006) Modelling the nonlinear shear stress–strain response of glass fibre-reinfroced composites. Part I: Experimental results. Compos Sci Technol 66:1455–1464
29. Varna J, Joffe R, Akshantala NV, Talreja R (1999) Damage in composite laminates with off-axis plies. Compos Sci Technol 59:2139–2147
30. Vogler TJ, Kyriakides S (1999) Inelastic behavior of an AS4/PEEK composite under combined transverse compression and shear. Part I: experiments. Int J Plast 15:783–806

Chapter 6
Study of Delamination in Composites by Using the Serial/Parallel Mixing Theory and a Damage Formulation

Xavier Martínez, Sergio Oller, and Ever Barbero

Abstract This work presents a new procedure to deal with the delamination problem found in laminated composites, based in a continuum mechanics formulation. The procedure proposed obtains the composite constitutive performance with the Serial/Parallel mixing theory, developed by F. Rastellini. This theory characterizes composite materials by coupling the constitutive behaviour of the composite components, imposing an iso–strain relation among the components in the fibre (or parallel) direction and an iso–stress relation in the remaining directions (serial directions). The proposed procedure also uses a damage formulation to characterize the constitutive behaviour of matrix component in order to obtain the stress–strain performance of this material.

With these two formulations, the delamination phenomenon is characterized naturally by the numerical simulation, being unnecessary the definition of special elements or computationally expensive techniques like the definition of contact elements or mesh separation. Matrix failure, as a result of the stress state found in it, leads to a reduction of the stiffness and strength capacity of the composite in its serial direction. This reduction provides a composite performance equivalent to what is found in a delaminated material.

To prove the ability of the formulation proposed to solve delamination problems, the End Notch Failure test is numerically simulated and the results obtained are compared with experimental ones. The agreement found in the results with both simulations, numerical and experimental, validate the proposed methodology to solve the delamination problem.

X. Martínez and S. Oller
International Center of Numerical Methods in Engineering (CIMNE), c/Gran Capità s/n; 08034 Barcelona, Spain, e-mail: xaviermg@cimne.upc.edu, e-mail: sergio.oller@upc.edu

E. Barbero
Mechanical and Aerospace Engineering, West Virginia University, P.O. Box 6106, Morgantown, WV 26505-6106, United States of America, e-mail: ebarbero@wvu.edu

6.1 Introduction

The use of new materials in structural applications implies dealing with new failure processes, not existing in traditional materials. One of these is the delamination phenomenon found in laminated composites. The lost of adherence between the different layers of the composite leads to a reduction of the section strength and stiffness that can finish in a structural failure.

The importance of this phenomenon is demonstrated by the amount of authors that have developed theories and formulations to deal with it. All authors that have studied the problem agree that the delamination process is characterized by two main phenomenons, the crack initiation and its propagation along the composite. Crack initiation can be obtained by comparing the strain–stress state of the material, in the region where delamination takes place, with a critical one [1, 4, 6, 15] or in terms of the traction versus relative displacement [2, 3, 12]. And the delamination propagation is usually treated opening the mesh to simulate the crack effect where it takes place. To open the mesh different procedures are proposed. One of them is the virtual crack closure technique (VCCT) [8], based on the assumption that when a crack is extended, the energy required to open the crack is the same required to close it. Another procedure, each time more used, is the use of a cohesive zone model [4]. The cohesion elements are placed in the interface of the layers that can suffer delamination and its propagation is obtained with damage or plastic formulations applied to those elements.

Besides the differences in the existing formulations found in literature to simulate the delamination phenomenon, all of them agree in dividing the mesh where the crack is developed. This procedure is computationally very expensive, as it requires contact formulations to avoid the interpenetration of one body into the other. And, also, all of them require an special formulation where the delamination will occur, with interface elements [1], cohesive zones [2] or with coincident nodes, not connected to allow the mesh opening, as it is done with the VCCT [8]. In contrast to the scope used by these authors to solve the delamination problem, this work uses the continuum mechanics to simulate the delamination initiation and propagation, without making any distinction of the elements in which delamination takes place.

In this work, the Serial/Parallel (S/P) mixing theory developed by Rastellini [13], is used to obtain the composite performance and to simulate the delamination process. This theory is based on the definition of some compatibility equations between the strain–stress states of the composite constituent materials. In the case of a composite made of fibre and matrix, what the Serial/Parallel mixing theory does is to impose an iso–strain condition on the parallel direction, usually the fibre direction, and a iso–stress condition on the serial direction, usually the remaining directions of the stress and strain tensors. With this scope, if the matrix structural capacity is lost, the S/P mixing theory will reduce the structural capacity of fibre material in the serial directions due to the iso–stress condition. Thus, it will be impossible for the composite layer to develop shear or transversal stresses, less to transmit them to the surroundings elements. The structural performance of a material in which serial

stresses are zero is similar, as it will be proved in this work, to the performance shown by a delaminated material.

To obtain this structural behaviour, the matrix material has to loose its strength for a certain stress state. This lost of strength must be permanent in order to simulate the real crack produced by delamination in the material. This is achieved with a damage formulation based on the fracture energy of the material.

A detailed description of the different formulations required to simulate the delamination process: the S/P mixing theory and the damage formulation used in matrix material, are described in the following section. Afterwards, to prove the validity of the scope used to simulate the delamination phenomenon, as well as the ability of the formulations proposed to simulate it, this work compares the results obtained from the experimental test made to obtain the mode II fracture energy of a composite with the results obtained from a numerical simulation of the same model. The experimental test is the End Notch Flexure (ENF) test defined by the *European Structural Integrity Society* (ESIS). The agreement between experimental and numerical results will prove the ability of the S/P mixing theory, together with the damage formulation used, to simulate delamination processes.

6.2 Formulation

The formulation shown in this work to simulate the delamination effect in composite materials made of laminates of fibre reinforced polymers is the following one: The composite behaviour is obtained from its constituent materials with the serial/parallel mixing theory developed by Rastellini [13]. This theory is described in Sect. 6.2.1. To obtain a good convergence ratio in the process and, in most cases, to be able to obtain convergence, it is necessary to use a tangent constitutive tensor. This tensor can be obtained analytically for some constitutive equations but not for the damage formulation used in the presented simulation. To solve this problem, the tangent constitutive tensor is obtained performing a numerical derivation with a perturbation method. This methodology is exposed in Sect. 6.2.2. Finally, the delamination process is obtained as a lost of strength and stiffness in matrix material. This effect is characterized using a damage formulation, which is described in Sect. 6.2.3.

6.2.1 Serial/Parallel Mixing Theory

The serial/parallel mixing theory considers that in a certain direction (or directions) the compounding materials behave in parallel, while their behaviour is serial in the remaining directions. For this reason it is necessary to define, and split, the serial and parallel parts of the strain and stress tensors. This is done with two complementary fourth order projector tensors, one corresponding to the serial direction (P_S) and the

other to the parallel direction (P_P). These tensors are defined from the fibre axial direction in the composite. Thus,

$$\begin{aligned} \boldsymbol{\varepsilon} &= \varepsilon_P + \varepsilon_S \\ &\text{with} \quad \varepsilon_P = P_P : \boldsymbol{\varepsilon} \quad \text{and} \quad \varepsilon_S = P_S : \boldsymbol{\varepsilon} \end{aligned} \tag{6.1}$$

where,

$$N_P = e_1 \otimes e_1; \quad P_P = N_P \otimes N_P \quad \text{and} \quad P_S = I - P_P \tag{6.2}$$

Being e_1, the director vector that determines the parallel behaviour (fibre direction), and I the identity. The stress state may be split analogously, finding its parallel and serial parts using also the fourth order tensors P_P and P_S:

$$\begin{aligned} \boldsymbol{\sigma} &= \sigma_P + \sigma_S \\ &\text{with} \quad \sigma_P = P_P : \boldsymbol{\sigma} \quad \text{and} \quad \sigma_S = P_S : \boldsymbol{\sigma} \end{aligned} \tag{6.3}$$

6.2.1.1 Hypothesis for the Numerical Modeling

The numerical model developed to take into account this strain-stress state is based on the following hypothesis:

1. The composite is composed by only two components: fibre and matrix.
2. Component materials have the same strain in parallel (fibre) direction.
3. Component materials have the same stress in serial direction.
4. Composite material response is in direct relation with the volume fractions of compounding materials.
5. Homogeneous distribution of phases is considered in the composite.
6. Perfect bonding between components is also considered.

6.2.1.2 Constitutive Equations of Component Materials

Each composite component material is computed with its own constitutive equation. However, since the materials will be modeled with a damage formulation, the description of the formulation is done considering the particular case of isotropic damage. So, the stresses in matrix and fibre materials are obtained using:

$$\begin{aligned} {}^m\boldsymbol{\sigma} &= (1 - {}^m d) \cdot {}^m\mathbb{C} : {}^m\boldsymbol{\varepsilon} \\ {}^f\boldsymbol{\sigma} &= (1 - {}^f d) \cdot {}^f\mathbb{C} : {}^f\boldsymbol{\varepsilon} \end{aligned} \tag{6.4}$$

being ${}^m\mathbb{C}$ and ${}^f\mathbb{C}$ the matrix and fibre stiffness tensors, respectively.

These equations can be rewritten taking into account the serial and parallel split of strain and stress tensors (Eqs. 6.1 and 6.3), obtaining:

$$\begin{bmatrix} {}^{i}\sigma_P \\ {}^{i}\sigma_S \end{bmatrix} = (1 - {}^{i}d) \cdot \begin{bmatrix} {}^{i}\mathbb{C}_{PP} & {}^{i}\mathbb{C}_{PS} \\ {}^{i}\mathbb{C}_{SP} & {}^{i}\mathbb{C}_{SS} \end{bmatrix} : \begin{bmatrix} {}^{i}\varepsilon_P \\ {}^{i}\varepsilon_S \end{bmatrix} \tag{6.5}$$

where

$$\begin{cases} {}^{i}\mathbb{C}_{PP} = P_P : {}^{i}\mathbb{C} : P_P \\ {}^{i}\mathbb{C}_{PS} = P_P : {}^{i}\mathbb{C} : P_S \\ {}^{i}\mathbb{C}_{SP} = P_S : {}^{i}\mathbb{C} : P_P \\ {}^{i}\mathbb{C}_{SS} = P_S : {}^{i}\mathbb{C} : P_S \end{cases} \quad \text{with} \quad i = m, f \tag{6.6}$$

6.2.1.3 Equilibrium and Compatibility Equations

The equations that define the stress equilibrium and establish the stain compatibility between components arise from the analysis of the hypotheses previously exposed,

$$\text{Parallel behaviour:} \quad \begin{aligned} {}^{c}\varepsilon_P &= {}^{m}\varepsilon_P = {}^{f}\varepsilon_P \\ {}^{c}\sigma_P &= {}^{m}k^{m}\sigma_P + {}^{f}k^{f}\sigma_P \end{aligned} \tag{6.7}$$

$$\text{Serial behaviour:} \quad \begin{aligned} {}^{c}\varepsilon_S &= {}^{m}k^{m}\varepsilon_S + {}^{f}k^{f}\varepsilon_S \\ {}^{c}\sigma_S &= {}^{m}\sigma_S = {}^{f}\sigma_S \end{aligned} \tag{6.8}$$

where superscripts ^{c}, ^{m} and ^{f} stand for composite, matrix and fibre, respectively and ${}^{i}k$ corresponds to the volume fraction coefficient of each constituent in the composite.

6.2.1.4 Serial/parallel Rule of Mixtures Algorithm

The known variable that enters the algorithm is the strain state ${}^{c}\varepsilon$ of the composite material at time $t + \Delta t$. From this variable, the serial/parallel rule of mixtures algorithm has to find the strain and stress state of each component that fulfils the equilibrium, the compatibility and the constitutive equations and the evolution of the internal variables.

The first thing done by the algorithm is to split the strain tensor into its parallel and its serial parts, in order to compute the strain state in the matrix and the fibre. The parallel strain component is, according to Eq. (6.7), the same for both materials and for the composite. On the other hand, the serial strain component requires a prediction of the strains expected in one of the composite components. If this prediction is done for the matrix, the increment of its serial strains can be computed as

$$\begin{aligned} \left[{}^{m}\Delta\varepsilon_S\right]^{0} = \mathbb{A} : \big[& {}^{f}\mathbb{C}_{SS} : {}^{c}\Delta\varepsilon_S + \\ & {}^{f}k \left({}^{f}\mathbb{C}_{SP} - {}^{m}\mathbb{C}_{SP} \right) : {}^{c}\Delta\varepsilon_P \big] \end{aligned} \tag{6.9}$$

with $\mathbb{A} = \left({}^{m}k^{f}\mathbb{C}_{SS} + {}^{f}k^{m}\mathbb{C}_{SS} \right)^{-1}$ and ${}^{m}\Delta\varepsilon_S = {}^{t+\Delta t}\left[{}^{c}\varepsilon_S\right] - {}^{t}\left[{}^{c}\varepsilon_S\right]$.

The initial prediction of matrix serial strains, proposed by Rastellini [13] and described in Eq. (6.1), is obtained considering that the distribution of the total strain, in its parallel and serial parts, is done in function of the composite tangent stiffness obtained in previous time step. With the prediction of the matrix serial strains, the fibre serial strains can be computed, in the iteration step n, according to Eq. (6.8),

$$ {}^{t+\Delta t}\left[{}^{f}\Delta\varepsilon_S\right]^n = \frac{1}{{}^{f}k}\,{}^{t+\Delta t}\left[{}^{c}\varepsilon_S\right] - \frac{{}^{m}k}{{}^{f}k}\,{}^{t+\Delta t}\left[{}^{m}\varepsilon_S\right]^n \tag{6.10} $$

where ${}^{t+\Delta t}\left[{}^{m}\varepsilon_S\right]^n = {}^{t}\left[{}^{m}\varepsilon_S\right] + \left[{}^{m}\Delta\varepsilon_S\right]^n$.

Regrouping again the serial and parallel components of the strain tensor (Eq. 6.3), the constitutive equations can be applied to the predicted strains to obtain the stress tensor for both materials and the update of their internal variables. Fibre and matrix are modeled, each one, with their own constitutive law. If both materials are described with an additive plasticity formulation, the stress vector for each one is obtained using Eq. (6.4). The stresses obtained must fulfill the following equation:

$$ \left[\Delta\sigma_S\right]^n = {}^{t+\Delta t}\left[{}^{m}\sigma_S\right]^n - {}^{t+\Delta t}\left[{}^{f}\sigma_S\right]^n \leq \text{tolerance} \tag{6.11} $$

If the residual stress is smaller than the tolerance, the computed strains and stresses are considered to be correct and the structural calculation can continue. However, if Eq. (6.11) is not fulfilled, the initial prediction of the matrix strain tensor has to be corrected. This correction is performed using a Newton-Raphson scheme, in which the update is made using the Jacobian of the residual forces. It is obtained deriving the residue function with respect to the unknown. According to Rastellini [14], the expression for the Jacobian is given as follows:

$$ \mathbb{J} = \left.\frac{\partial\Delta\sigma_S}{\partial{}^{m}\varepsilon_S}\right|_{{}^{m}\varepsilon_S = {}^{t+\Delta t}\left[{}^{m}\varepsilon_S\right]^n} = \left[{}^{m}\mathbb{C}_{SS}\right]^n + \frac{{}^{m}k}{{}^{f}k}\left[{}^{f}\mathbb{C}_{SS}\right]^n \tag{6.12} $$

and, the correction of the matrix serial strains becomes

$$ {}^{t+\Delta t}\left[{}^{m}\varepsilon_S\right]^{n+1} = {}^{t+\Delta t}\left[{}^{m}\varepsilon_S\right]^n - \mathbb{J}^{-1} : \left[\Delta\sigma_S\right]^n \tag{6.13} $$

To obtain quadratic convergence in the S/P mixing theory, the Jacobian must be obtained using the tangent constitutive tensors for the fibres and the matrix. Depending on the constitutive equation defined for each material, the constitutive tensor cannot be obtained analytically. Thus, in order to obtain a reliable algorithm, the expression of the tangent tensor is obtained numerically.

6.2.2 Tangent Constitutive Tensor

The tangent constitutive tensor, $\mathbb{C}^t$, is obtained numerically for each component material of the composite using a perturbation method. The definition of the tangent

constitutive tensor is,

$$\dot{\boldsymbol{\sigma}} = \mathbb{C}^t : \dot{\boldsymbol{\varepsilon}} \tag{6.14}$$

This definition of the tangent constitutive tensor can be written for isotropic and orthotropic materials, using the reduction of tensors to their matrix description as:

$$\begin{bmatrix} \dot{\sigma}_1 \\ \vdots \\ \dot{\sigma}_n \end{bmatrix} = \begin{bmatrix} c^t_{11} & \dots & c^t_{1n} \\ \vdots & \ddots & \vdots \\ c^t_{n1} & \dots & c^t_{nn} \end{bmatrix} \cdot \begin{bmatrix} \dot{\varepsilon}_1 \\ \vdots \\ \dot{\varepsilon}_n \end{bmatrix} \tag{6.15}$$

The stress vector rate of Eq. (6.15) can be obtained as the sum of n stress vectors, resultants from the product of the j component of the strain vector rate by the j column of the tangent stiffness tensor; this is:

$$\dot{\boldsymbol{\sigma}} = \sum_{j=1}^{n} \delta^j \dot{\sigma} = \sum_{j=1}^{n} \boldsymbol{c}^t_j \cdot \dot{\varepsilon}_j \tag{6.16}$$

with,

$$\boldsymbol{c}^t_j = \left[c^t_{1j}\, c^t_{2j} \dots c^t_{nj} \right]^T \tag{6.17}$$

Thus, the j column of the tangent stiffness tensor, which is unknown, can be obtained from Eq. (6.16), as:

$$\boldsymbol{c}^t_j = \frac{{}^j\dot{\boldsymbol{\sigma}}}{\dot{\varepsilon}_j} \equiv \frac{\delta^j \boldsymbol{\sigma}}{\delta \varepsilon_j} \tag{6.18}$$

The perturbation method consist on defining n small variations, or perturbations, of the strain vector $\delta\varepsilon_j$, to obtain n stress vectors $\delta^j\boldsymbol{\sigma}$, that will be used in Eq. (6.18) to obtain the numerical expression of the tangent constitutive tensor.

6.2.2.1 Numerical Implementation of the Tangent Constitutive Tensor

In a finite element code, the material constitutive law provides the stress tensor $\boldsymbol{\sigma}$ and the internal variables q associated to a defined strain tensor $\boldsymbol{\varepsilon}$. With the strain and stress vectors resulting from the constitutive equation, a small perturbation is applied to the strain vector to obtain its associated stress tensor. The obtained stresses, together with the perturbation defined, will be used to compute the tangent constitutive matrix using Eq. (6.18).

In the procedure defined, the smaller the perturbation value is, the better will be the approximation computed for the tangent constitutive tensor. With this consideration in mind, the perturbation value defined for each component of the strain tensor is obtained by the following procedure:

$$\begin{aligned} &\text{if} \quad \varepsilon_j \neq 0 \rightarrow \delta\varepsilon_j = \varepsilon_j \cdot 10^{-5} \\ &\text{if} \quad \varepsilon_j = 0 \rightarrow \delta\varepsilon_j = \min\{\varepsilon_k\} \cdot 10^{-5} \qquad \forall k = 1, n \end{aligned} \tag{6.19}$$

Selecting the perturbation value in this way, the strain increment will be always small enough to ensure that the stress variation is close to the computed value. However, this procedure can deal with perturbation values near to zero (i.e. when one of the strain values is nearly zero). This will lead to an indetermination in Eq. (6.18). To avoid such a situation, a new condition must be imposed in order to assure a perturbation value large enough. This condition is

$$\delta\varepsilon_j > \max\{\varepsilon_k\} \cdot 10^{-10} \qquad \forall k = 1, n \tag{6.20}$$

This procedure allows obtaining an accurate approximation to the tangent constitutive tensor for any constitutive law used and any yield surface, ensuring the convergence of the numerical process.

6.2.3 Isotropic Continuum Damage Formulation

The material degradation in a continuum solid, due to a fracture process, can be simulated with a damage formulation. This formulation takes into account the reduction of the effective area of the material by a reduction of its stiffness properties. To simulate the delamination phenomenon in composites, the formulation that will be used in this work to predict the constitutive behaviour of matrix material is the isotropic continuum damage formulation defined by Oller in [10]. This formulation is based on the theory of continuum damage first developed by Kachanov [7]. In this section, the main aspects of the isotropic continuum damage formulation to be used are exposed.

6.2.3.1 Isotropic Damage Model

A damage process can be simulated, in the context of continuum mechanics, by the introduction of a material internal variable, $\boldsymbol{M}$, representing the amount of damage found in it. This variable transforms the real stress tensor, $\boldsymbol{\sigma}$ into an effective stress tensor $\boldsymbol{\sigma_0}$. This is:

$$\boldsymbol{\sigma}_0 = \boldsymbol{M}^{-1} : \boldsymbol{\sigma} \tag{6.21}$$

In the case of an isotropic damage, all directions of the stress tensor suffer the same degradation. This consideration allows defining the damage internal variable in function of an scalar variable and the damage equation becomes:

$$\boldsymbol{\sigma}_0 = [(1-d)\boldsymbol{I}]^{-1} : \boldsymbol{\sigma} = \frac{1}{(1-d)}\boldsymbol{\sigma} \tag{6.22}$$

Being d the damage scalar internal variable. Its value is limited by 0 and 1. When the material is not damaged, the value of the damage variable is 0 while, when the

material is completely damaged, $d = 1$. The effective stresses, shown in Eq. (6.22), correspond to the stresses that would be obtained in the material if it is not damaged:

$$\boldsymbol{\sigma}_0 = \mathbb{C}_0 : \boldsymbol{\varepsilon} \tag{6.23}$$

And the real stress tensor can be obtained, from the strain state of the material, by coupling Eqs. (6.22) and (6.23).

$$\boldsymbol{\sigma} = (1-d)\boldsymbol{\sigma}_0 = (1-d)\mathbb{C}_0 : \boldsymbol{\varepsilon} \tag{6.24}$$

6.2.3.2 Damage Criterion

The damage criterion predicts when the damage process begins to take place in the material, this is: when the material elastic behaviour is lost as a result of the degradation. This criterion is used to represent different material behaviours, and it depends on the stress tensor and on the value of the internal variables found in the material point under study. Its expression is:

$$\mathbb{F}(\boldsymbol{\sigma}_0, \boldsymbol{q}) = f(\boldsymbol{\sigma}_0) - c(d) \leq 0 \qquad \text{with} \quad \boldsymbol{q} \equiv \{d\} \tag{6.25}$$

where $c(d)$ is a function defining the damage limit value and $f(\boldsymbol{\sigma}_0)$ defines the damage surface. Damage will start the first time that $f(\boldsymbol{\sigma}_0)$ value is equal or larger than $c(d)$. Usually, instead of working with Eq. (6.25), the damage criterion is converted to an equivalent one by using a scalar function G which is positive and with its derivative positive, monotonously increasing and invertible:

$$\mathbb{F}^*(\boldsymbol{\sigma}_0, d) = G[f(\boldsymbol{\sigma}_0)] - G[c(d)] \leq 0 \tag{6.26}$$

The damage surface to be used with this formulation can be any of the existing in literature (i.e. Von-Mises, Mohr-Coulomb, etc.) and its election will depend on the material to be modeled. In the present work, the damage surface that will be used for matrix material corresponds to the one defined by norm of principal stresses, weighted according to the compression–tension proportion found in the principal stress tensor. This damage surface can be written as:

$$f(\boldsymbol{\sigma}_0) = \rho \cdot \|\boldsymbol{\sigma}_{\boldsymbol{I}}\| \tag{6.27}$$

being $\boldsymbol{\sigma}_{\boldsymbol{I}}$ the principal stress tensor and ρ the compression–tension weight function, defined as:

$$\rho = r_0 N + (1 - r_0) \tag{6.28}$$

where $N = \sigma_c^{max} / \sigma_t^{max}$ is the material ratio between the maximum accepted compressive strength/tensile strength. And r_0 is a scalar function that defines the relation

between the compression and the tension state of the stress tensor. This last function is defined with the following expression:

$$r_0 = \frac{\sum_{I=1}^{3} < \sigma_I >}{\sum_{I=1}^{3} |\sigma_I|} \tag{6.29}$$

with $< x >= 0.5\,[x + |x|]$ the McAully function.

The compression–tension weight function has been defined to obtain a damage surface to be compared with a compression stress. Hence, when using this damage criterion, the value of $c(d)$ must be referred to compression stresses.

6.2.3.3 Evolution of the Damage Variable: Softening Behaviour

In the mechanical problems where the internal variables appear, it is necessary to define their evolution law. In the damage problem, the law that defines the evolution of the damage variable is [10]:

$$\dot{d} = \dot{\mu}\frac{\partial \mathbb{F}^*(\boldsymbol{\sigma}_0, d)}{f(\boldsymbol{\sigma}_0)} \equiv \dot{\mu}\frac{G[f(\boldsymbol{\sigma}_0)]}{f(\boldsymbol{\sigma}_0)} \tag{6.30}$$

being μ a non-negative scalar called damage consistency parameter. This parameter is used to define the load, unload and reload Kuhn–Tucker conditions:

$$\dot{\mu} \geq 0; \quad \mathbb{F}^*(\boldsymbol{\sigma}_0, d) \leq 0; \quad \dot{\mu} \cdot \mathbb{F}^*(\boldsymbol{\sigma}_0, d) = 0 \tag{6.31}$$

The Kuhn–Tucker condition tells that if the damage criterion is lower than zero, then $\dot{\mu} = 0$ and there is no damage evolution. And, when the damage criterion is equal to zero, which means that the stress tensor is on the damage surface, the damage consistency parameter is larger than one and there is damage evolution. Making use of the consistency condition, $\dot{\mathbb{F}}^*(\boldsymbol{\sigma}_0, \boldsymbol{q}) = 0$, it can be proved [11] that the final expression of the damage parameter can be defined as:

$$d = G[f(\boldsymbol{\sigma}_0)] \tag{6.32}$$

So, the evolution of the damage parameter depends on how the function G is defined. Two different definitions of the G function are exposed below. Both of them correspond to a material with a softening behaviour.

Linear softening: The evolution of the damage parameter, in case of considering a linear softening, is defined by the following expression of the G function:

$$d = G[f(\boldsymbol{\sigma}_0)] = \frac{1 - \frac{\boldsymbol{\tau}^0}{f(\boldsymbol{\sigma}_0)}}{1 + A} \tag{6.33}$$

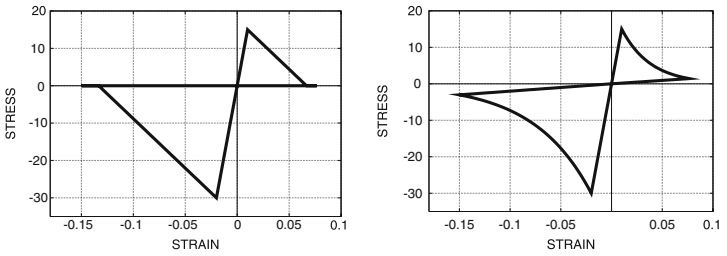

(a) (b)

Fig. 6.1 Stress–strain graph obtained with the damage formulation. In (**a**) is represented a material with linear softening while (**b**) shows a material with exponential softening

Exponential softening: This function was first proposed by Oliver et al. [9], to obtain an exponential softening in the material. The expression of the damage parameter is:

$$d = G[f(\boldsymbol{\sigma}_0)] = 1 - \frac{\boldsymbol{\tau}^0}{f(\boldsymbol{\sigma}_0)} e^{A\left(1 - \frac{f(\boldsymbol{\sigma}_0)}{\boldsymbol{\tau}^0}\right)} \tag{6.34}$$

The parameter A depends of the fracture energy of the material. Its expression is defined in the following section. And, the value $\boldsymbol{\tau}^0$, corresponds to the limit elastic stress that can be found in the material. When using the damage surface based on the norm of the principal stresses, differentiating between the compression and tension states, the limit stress to be defined is the one corresponding to the compression case, σ_c^{max}.

Figure 6.1 a shows the stress-strain relation obtained for a material with a linear softening; and Fig. 6.1b shows the evolution of the same material when an exponential softening is applied to it. In both cases the relation defined between the compression strength and the tension strength is: $N = 2$.

6.2.3.4 Parameter *A*

The parameter A, appearing in Eqs. (6.33) and (6.34), is obtained from the dissipation equation of the material, considering an uniaxial process under a monotonous increasing load. The parameter deduction can be obtained from [11] and their expression is,

$$\begin{aligned} &\text{Linear softening:} && A = -\frac{1}{2}\frac{(\boldsymbol{\tau}^0)^2}{g_c C_0} \\ &\text{Exponential softening:} && A = +\frac{1}{\frac{g_c C_0}{(\boldsymbol{\tau}^0)^2} - \frac{1}{2}} \end{aligned} \tag{6.35}$$

where C_0 is the uniaxial stiffness of the material and g_c corresponds to the maximum energy per unit volume that can dissipate the point under consideration in a compression case.

Classical fracture mechanics defines the fracture energy of a material as the energy that has to be dissipated to open a fracture in an unitary area of the material. This energy is defined as:

$$G_f = \frac{W_f}{A_f} \tag{6.36}$$

where W_f is the energy dissipated by the fracture at the end of the process and A_f is the area of the surface fractured. When coupling the fracture mechanics theory with the continuum mechanics, the relation defined to relate W_f with g_f is:

$$W_f = G_f \cdot A_f \equiv \int_{V_f} g_f \, dV \tag{6.37}$$

And the relation between the fracture energy defined as a material property, G_f, and the maximum energy per unit volume required by the damage formulation, g_f, becomes:

$$g_f = \frac{W_f}{V_f} = \frac{W_f}{A_f l_f} = \frac{G_f}{l_f} \tag{6.38}$$

Thus, the fracture energy per unit volume is obtained as the fracture energy defined for the material divided by the fracture length. This fracture length corresponds to the length, perpendicular to the fracture area, considered to be damaged. If this theory is applied to a finite element code, in which a continuum formulation is transformed into a discrete formulation, the fracture will have to be transformed from the continuum to a discrete space. So, the fracture length will not be zero, which corresponds to a fracture in a plane, but will have a minimum length size. This minimum length correspond to consider that the fracture is extended along the whole gauss point section. Figure 6.2 shows a representation of this fracture length.

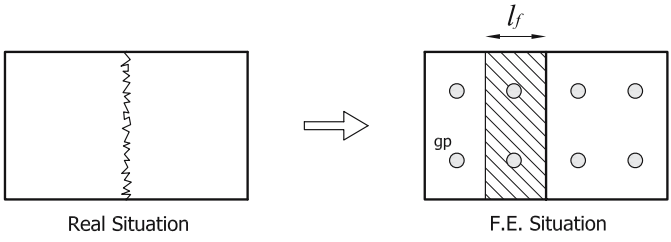

Fig. 6.2 Fracture in a real body and in its finite element discretization. Fracture length description

6.3 End Notch Flexure (ENF) Test Simulation

To prove the ability of the formulation developed to simulate delamination processes, this work shows the numerical result obtained from the simulation of the *End Notch Flexure* (ENF) test, defined by the *European Structural Integrity Society* (ESIS). This test seeks to obtain the toughness for crack propagation in mode II, corresponding to a shear crack, in unidirectional fibre reinforced polymer composites (FRPC).

The experimental results have been obtained from the tests made by CIMEP (Centre per a la Innovació en Materials, Estructures i Processos) and the Univerity of Girona for the project GRINCOMP (ref. MAT2003-09768-C03) [5].

6.3.1 Experimental Test Description

The End Notch Flexure test is based in the flexure of a beam with an initial crack in one of its ends. The test has been applied to a composite made of carbon fibres with an epoxi polymeric matrix. Fibres are oriented in the longitudinal direction of the beam and the initial crack is created introducing an insert in the laminate during its fabrication. The width of the gap generated by this insert must be smaller than 50 μm. The span of the beam is 100 mm and it is loaded with a concentrated load at its mid–span. The test is made with a displacement controlled mechanism. Three different series (GRIN006, GRIN015 and GRIN024), each one containing five different samples, where tested during the experimental campaign. To perform the numerical simulation, the first sample of serie GRIN006 has been considered (beam 3M101, according to the notation used in the tests). The dimensions of this sample, as well as the dimensions considered for the numerical simulation, are shown in Fig. 6.3.

The experimental test applies a vertical displacement to the beam, as shown in Fig. 6.3, until the initial crack starts its propagation. The imposed displacement is applied until the crack progression stops and the beam recovers its linear behaviour. At this point, the sample is unloaded. Main results obtained from this test are two: The force–displacement graph, which shows the structural performance of the

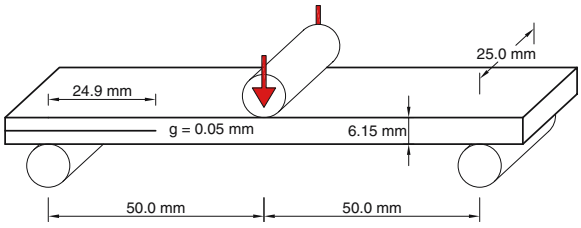

Fig. 6.3 Sample geometry used for the ENF test

Table 6.1 Composite components mechanical properties

Matrix properties		Fibre Properties	
Tensile strength	120.66 MPa	Tensile strength	4,278 MPa
Tensile modulus	4.67 GPa	Tensile modulus	228 GPa
Poisson modulus	0.30	Poisson modulus	0.0
Mode I fracture energy	0.68 kJ/m^2	Volume content	57.4%
Volume content	42.6%		

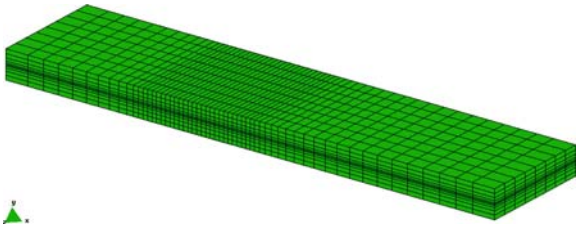

Fig. 6.4 Three dimensional model developed. Mesh description

composite beam, and the final length of the initial crack. These two results are the ones that will be compared with the numerical model developed.

The exact properties of the composite material used in the experimental simulations were unknown when the experimental tests were performed [5]. However, the composite is known to be made of carbon fibres and an epoxy polymeric matrix from Hexcel composites. For the numerical simulation, the mechanical values considered to define the composite are the ones described in Table 6.1, obtained form Hexcel Product data description. The fibre (AS4) and matrix considered are the ones found in HexPly 8552 UD carbon prepegs.

6.3.2 Numerical Model Description

Two different numerical models have been developed to simulate the End Notch Flexure Test. One using a plain stress two dimensional formulation and a second one using a three dimensional formulation. The 2D model has been defined with 627 linear quadrilateral elements while the 3D model has 5016 linear brick elements. The mesh defined for the three dimensional model is shown in Fig. 6.4.

Two different materials have been defined in the numerical simulation. One corresponding to the composite material and another one corresponding to the insert material. The composite material is defined by the properties of the epoxy matrix and the carbon fibres shown in Table 6.1. Fibre material is defined as an elastic material. Matrix material is characterized by a damage law, like the one defined on Sect. 6.2.3 of present document.

Table 6.2 Insert material mechanical properties

Insert material properties	
Tensile modulus	1,000 GPa
Shear modulus	10^{-9} GPa
Poisson modulus	0.0
Volume content	100%

The damage model used requires knowing the relation between the compression strength and the tension strength of the material in order to obtain the correct damage evolution. As these parameters are unknown, what is done in the present document is to consider that both strengths the same and to define the fracture energy of the material as the mode II fracture energy obtained from the experimental results. The value of this energy, for the 3M101 beam, is: $G_{II} = 1.02\,\mathrm{kJ/m^2}$.

The definition of the insert material properties has been done taking into account its structural performance. The main effect of this material in the beam is allowing the sliding of the section found above the insert along the section found below it. To do so, a material with a shear modulus nearly zero has been defined (it has not been defined as strictly zero to avoid numerical instabilities during the simulation). On the other hand, the longitudinal and transversal elastic modulus have been defined with a high value to avoid the penetration of the section above the insert into the section below it. This material has been defined as an elastic material. Its main mechanical properties are described in Table 6.2.

6.3.3 Comparison Between the Numerical and the Experimental Results

The numerical and the experimental results are compared with the force–displacement graph obtained for both cases. The displacement represented corresponds to the vertical deflection of the point where the load is applied. This graph is shown in Fig. 6.5, in which the results for the 2D and 3D numerical simulations and the experimental test are represented.

Figure 6.5 shows that the two dimensional simulation provides exactly the same results as the three dimensional one, thus, for these kind of problems, 2D simulations are preferable, as the computer cost is much lower. However, the most important result shown in Fig. 6.5 is the agreement between the numerical and the experimental results. The beam initial elastic stiffness obtained in the numerical simulation is nearly the same that is obtained from the experimental test. And this agreement between results is even better when comparing the beam maximum load capacity or failure point. The only result that differs in the numerical simulation is the final beam stiffness, when the crack has reached its maximum length. In this case, the

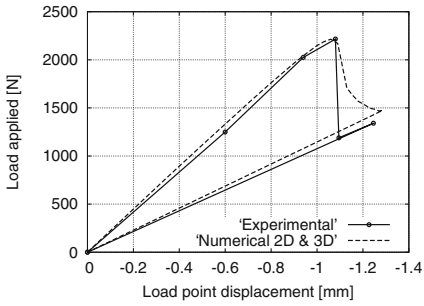

Fig. 6.5 Force–displacement graph obtained for the different models

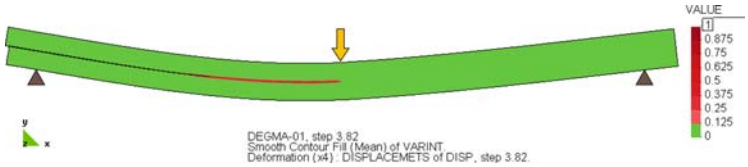

Fig. 6.6 Damage in matrix material when the maximum deflection has been reached

numerical beam is a 6% stiffer than the experimental one (the stiffness obtained in each case is, respectively, 1,146 N/mm and 1,076 N/mm).

The other result to be compared is the final crack length. The experimental values obtained for this final crack length for the sample being compared (3M101) is of 50.34 mm, and the mean value of the crack length for all the GRIN006 serie is around 49.0 mm; this is, a bit less than half the beam.

In the numerical simulation, the crack points correspond to those in which the damage parameter, in matrix material, is equal to one. These points have a matrix stiffness equal to zero. This implies that the composite serial stiffness is also zero, due to the iso–stress condition imposed by the Serial/Parallel mixing theory. Those points with matrix completely damaged cannot develop any shear strength. Hence, the final crack length can by obtained by finding the point, closer to the beam mid–span, with a value of the damage parameter, in matrix material, equal to one. Figure 6.6 shows the damage parameter in matrix in the load step in which the beam reaches its maximum deflection. In this figure can be seen that the crack length obtained with the numerical simulation also nearly reaches the mid–span section.

The exact value of the damage parameter is shown, for the points represented in Fig. 6.7a, in Fig. 6.7b. In this figure can be seen that point 13 (corresponding to mid–span) reaches a damage value of 0.6, while the value of point 12 is approximately 0.98. Considering this last value close enough to one and thus, the section completely broken, the numerical crack length obtained is of 48 mm. The point found at 49 mm of the support has a damage value in matrix material of 0.89, which is also close enough to one to consider that the numerical results are exactly the same as the experimental ones.

In this last figure is also represented the force–displacement graph (with the force value divided by 2,500 N, to fit into the figure). It can be seen that the main crack

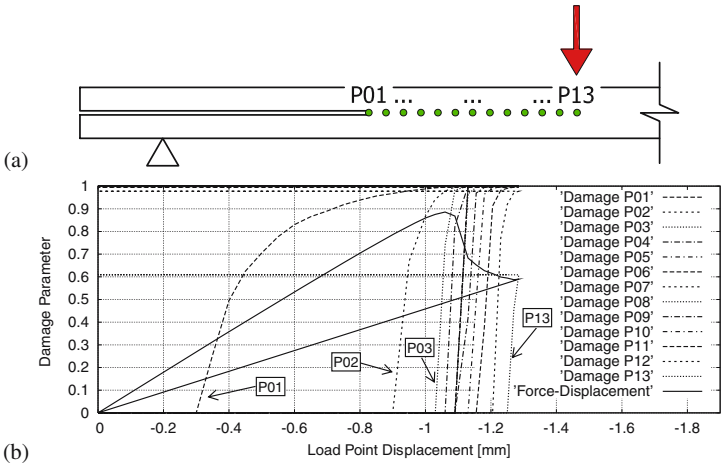

Fig. 6.7 Evolution of the damage parameter in the beam

is developed just after the beam reaches its maximum strength capacity. The lost of stiffness suffered by the beam due to the crack propagation is stabilized as the crack reaches the mid–span section because the crack cannot pass trough it. The sign of the shear stresses is reversed at mid–span and, just in it, shear stresses are zero; so, there are no efforts to damage the mid-span section.

6.3.4 Detailed Study of the Numerical Results

According to the force–displacement graph obtained for the beam (Fig. 6.5), the results obtained with the three dimensional simulation match exactly with the results obtained with the two dimensional simulation. Thus, for the sake of simplicity, the detailed study of the numerical results is preformed using only the two dimensional simulation.

The first thing to study of the results obtained from the numerical simulations is if the supposition made to define the insert material is accomplished, this is: that it will allow the sliding between the section above and below it, by reducing to nearly zero its shear stiffness. To verify that this is the behaviour found in the insert material, the horizontal gap that appears between the upper and lower nodes (nodes A and B respectively in Fig. 6.8a) has been represented in Fig. 6.8b. This figure shows a linear increment of the gap between both nodes for the first load steps. This gap increment proves the validity of the material defined, as it shows that the section above the insert of the beam slides over the section below it. This gap increment remains linear until the displacement of the load point is a bit larger than 1.0 mm, at this point the gap increases exponentially doubling its size. This point corresponds to the load for which the crack propagation begins and it ends when the crack has reached the

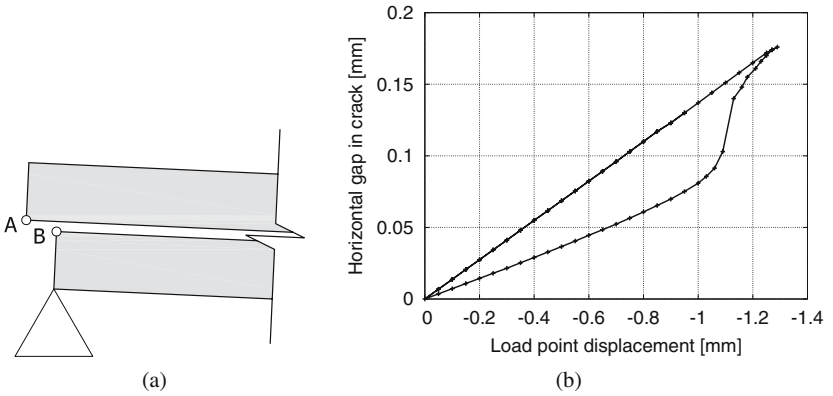

(a) (b)

Fig. 6.8 Evolution of the damage parameter in the beam

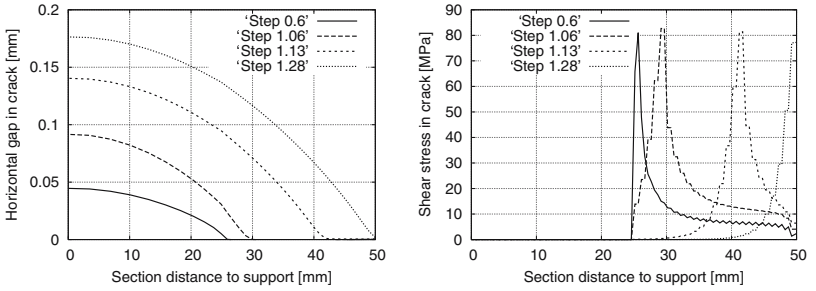

(a) (b)

Fig. 6.9 Evolution of the horizontal gap (**a**) and the shear stresses (**b**) along the beam mid–width for different load steps

section at mid–span. Afterwards, when unloading the beam, the horizontal gap size recovers the linear behaviour found before the crack propagation.

A better comprehension of the process that takes place in the beam can be obtained studying the evolution of the horizontal gap along the beam longitudinal axis, and the evolution of the shear stresses in the same region. Both parameters are displayed in Fig. 6.9 for different load steps. Each load step represented corresponds to a displacement of the load point of the same magnitude (i.e. step 1.06 corresponds to a load point displacement of 1.06 mm). Figure 6.9 show that for the load step 0.60, when the crack propagation has not begin, the only gap found is in the sections where the insert is applied and that all shear stresses are concentrated at the first section without insert (point P01 of Fig. 6.7a). However, when the crack begins its propagation, the gap initiation, as well as the shear stresses peak, move towards the beam mid–span. The final step represented, step 1.28, corresponds to the load step in which the crack has reached the mid–span section. Figure 6.9 also shows that the behaviour of the composite, when matrix is completely damaged, is

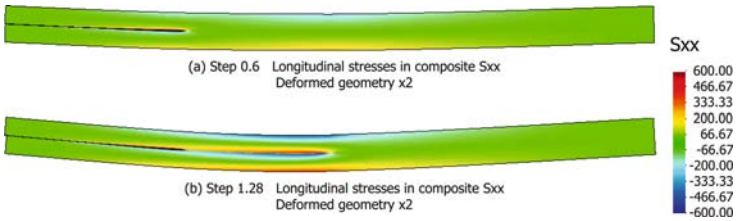

Fig. 6.10 Longitudinal stresses in the composite for two different load steps

the same found in the insert material. So, as damage in matrix increases and its stiffness is reduced, the composite cannot develop shear stresses and the section above the mid–width plane slides freely over the section below.

The effect of the crack propagation on the beam can also be seen by studying the longitudinal stresses in the composite (Fig. 6.10). The contour map of the longitudinal stresses shown in Fig. 6.10a corresponds to step 0.6, when crack propagation has not started. This figure shows that the distribution of longitudinal stresses in the sections with the insert corresponds to the case of having two beams, one disposed over the other, while the complete section (i.e. at mid–span) behave like just one beam: the bending effort compresses the top of the beam section while the bottom is in tension. On the other hand, when the crack has reached the mid–span section (Fig. 6.10b), the two beams behaviour is extended to all the cracked sections, as it can be seen along the whole left side of the beam.

The composite performance is obtained using the Serial/Parallel mixing theory, which imposes an iso–strain condition in the fibre direction and an iso–stress condition in the remaining directions. As the shear stresses are developed in the direction in which the iso–stress condition is applied, when matrix is completely damaged and cannot develop more shear stresses, the same happens with the rest of composite components (fibre, in this case). This is the reason because the shear stress of the composite, shown in Fig. 6.9b, is zero although fibre is an elastic material and still has the capacity to develop stresses.

Finally, a last numerical test has been performed to validate the fracture length parameter, required by the damage formulation used to simulate matrix material. According to what has been explained in Sect. 6.2.3, the fracture length represents the distance, perpendicular to the fracture surface, in which the fracture will be developed in the finite element formulation. The mesh used in the finite element simulation has a single element beside the gap opened by the insert, as it is shown in Fig. 6.11. This figure also shows the gauss points found in a finite element.

With the gauss point distribution shown in Fig. 6.11, the fracture length to be defined is half the gap size, as this is the gauss point length perpendicular to the fracture plane. Three different simulations have been performed with different gap sizes and fracture lengths. Model *Delam-2D-g20* has a gap size of 20 µm and a fracture length of 10 µm, model *Delam-2D-g50* has a gap size of 50 µm and a fracture length of 25 µm and, finally, model *Delam-2D-g80* has a gap size of 80 µm and a fracture length of 40 µm. The force–displacement graph obtained for these models

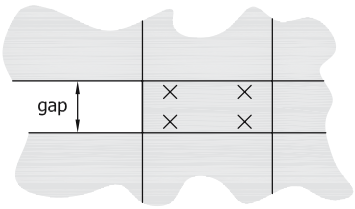

Fig. 6.11 Finite elements and gauss points found around the gap opened by the insert in the beam

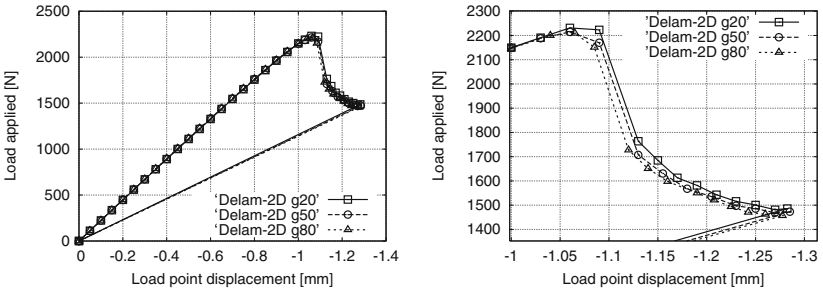

Fig. 6.12 Force–displacement graph obtained for three different gap size models. General view and detail of the crack propagation zone

is displayed in Fig. 6.12a, and a detail of this same graph in 6.12b. This figure shows that the results are practically the same for all cases and that only few differences are found in the crack propagation zone. This agreement among the different models allows considering the formulation defined, and the fracture length considered, correct.

6.4 Conclusions

The current work has shown that the Serial/Parallel mixing theory is able to simulate a delamination process by using the appropriate constitutive equations to predict the material behaviour of the composite components. No other help or formulation is needed. This affirmation has been proved with the simulation of the End Notch Flexure (ENF) test. The results obtained with the numerical simulation are practically identical to the results obtained from the experimental tests.

The structural behaviour of the materials, obtained from the numerical simulation, shows that the delamination phenomenon occurs as a result of the lost of stiffness in matrix material due to the damage produced by the shear stresses in it. This lost of stiffness in matrix material implies that no other component material can develop serial stresses, due to the iso–stress condition of the Serial/Parallel mixing theory in the serial direction. This is translated in a lost of stiffness of the composite in all serial directions. In the case considered, the serial directions are all

directions non coincident with fibre orientation. Thus, the composite is unable to avoid the shear deformations produced by the external loads. This situation is the same defined by the insert material, which has been proved to allow a perfect sliding between the materials found above and below it.

This procedure to deal with the delamination phenomenon provides an almost perfect simulation of the phenomenon without making any material distinction of the section expected to delaminate. All beam has been modeled with the same material properties. Thus, the formulation becomes a good tool to study problems in which the delamination is known to occur but it is not known in which structural component or section will happen. Also, with the procedure developed, no remeshing formulation, neither contact, is needed to obtain the delamination effects on the structure; which reduces significatively the computational cost of the simulation.

The simulation performed has proved, also, that the damage formulation developed to simulate the matrix material constitutive behaviour requires knowing the properties of the mesh generated to perform the simulation, as the fracture energy that can be developed by the model depends on the fracture length of it. This fracture length corresponds to the dimension perpendicular to the fracture surface. However, once knowing this dimensional parameter, the results obtained are mesh independent.

Finally, results obtained have shown that there is no difference in the results, for the case considered, between performing a two dimensional simulation or a three dimensional one, although the computational cost of the three dimensional simulation is considerably more expensive. This shows that the Serial/Parallel mixing theory, together with the damage formulation proposed, can deal with the delamination phenomenons with both simulations: 2D and 3D.

Acknowledgements This work has been supported by CEE–FP6 (LESSLOSS project, reference FP6-50544(GOCE)) and by the Spanish Goverment through the Ministerio de Ciencia y Tecnología (RECOMP project, ref. BIA2005-06952 and DECOMAR project, ref. MAT2003-08700-C03-02) and the Ministerio de Fomento (project "Retrofitting and reinforcement of reinforced concrete structures with composite materials. Numerical and experimental developments applied to joint of bars and composites anchorage proposal"). The fellowship of X. Martinez has been provided by CIMNE (International Centre for Numerical Methods in Engineering). All these supports are gratefully acknowledged.

References

1. Balzani C, Wagner W (2007) An interface element for the simulation of delamination in unidirectional fiber–reinforced composite laminates. Eng Fract Mech, doi: 10.1016/j.engfracmech.2007.03.013
2. Borg R, Nilsson L, Simonsson K (2002) Modeling of delamination using a discretized cohesive zone and damage formulation. Compos Sci Technol 62:1299–1314
3. Borg R, Nilsson L, Simonsson K (2004) Simulating DCB, ENF and MMB experiments using shell elements and cohesive zone model. Compos Sci Technol 64:269–278
4. Camanho PP, Dávila CG (2002) Mixed-mode decohesion finite elements for the simulation of delamination in composite materials. Technical Report TM-2002-211737, NASA

5. Corbella B, Vicens J, Costa J (2004) Informe de los resultados de los ensayos de propagación de grieta en modo II del "round robin test" del proyecto grincomp (mat2003-09768-c03). Technical Report 2004-CYT-01-IT01, CIMEP
6. Jansson N, Larsson R (2001) A damage model for simulation of mixed–mode delamination growth. Compos Struct 53:409–417
7. Kachanov L (1986) Introduction to continuum damage mechanics, mechanics of elastic stability. Martinus Nijhoff, Dordrecht, The Netherlands
8. Krueger P (2004) Virtual crack closure technique: history, approach and applications. Appl Mech Rev 57:109–143
9. Oliver J, Cervera M, Oller S, Lubliner J (1990) Isotropic damage models and smeared crack analysis of concrete. In: Mang H, Bicánić N (eds) Second internaltional conference on computer aided analysis and design of concrete structures, Zell am See, Austria, 945–958
10. Oller S (2001) Fractura mecánica. Un enfoque global. Centro Internacional de Métodos Numéricos en Ingeniería, Barcelona, Spain
11. Oller S (2002) Dinámica no–lineal. Centro Internacional de Métodos Numéricos en Ingeniería, Barcelona, Spain
12. Pinho ST, Iannucci L, Robinson P (2006) Formulation and implementation of decohesion elements in an explicit finite element code. Compos Part A: Appl Sci Manuf 37:778–789
13. Rastellini F, Oller S, Salomon O, Oñate E (2007) Composite materials non-linear modelling for long fibre reinforced laminates: continuum basis, computational aspects and validations. Comput Struct, doi:10.1016/j.compstruc.2007.04.009
14. Salomon O, Rastellini F, Oller S, Oñate E (2005) Fatigue prediction for composite materials and structures. In: NATO Research and Technology Organisation (RTO) (eds) Air Vehicle Technology: AVT-121. Symposium on the evaluation, control and prevention of high cycle fatigue, Granada, Spain
15. Turon A, Camanho PP, Costa J, Dávila CG (2006) A damage model for the simulation of delamination in advanced composites under variable-mode loading. Mech Mater 38:1072–1089

Chapter 7
Interaction Between Intraply and Interply Failure in Laminates

F.P. van der Meer and L.J. Sluys

Abstract A mesoscale model for finite element analysis of failure in laminates is presented. The model consists of separate parts for failure inside a ply (intraply) and failure between plies (interply). Both parts offer a description from onset of failure to complete local failure, thus allowing for progressive failure analysis. Intraply failure is simulated with a softening plasticity model based on a Tsai-Wu criterion with viscoplastic regularization. Details are presented on the implementation of the softening law for orthotropic materials in finite element computation. Interply failure is modeled using interface elements with a damage law for mixed mode delamination. The performance of the model is illustrated by means of an analysis of a laminate with a sharp internal notch – a case in which different modes of ply failure successively take place and interact with failure between the plies.

7.1 Introduction

Failure of laminated composites is generally analyzed on the mesolevel, i.e. the laminate is modeled as a stack of homogeneous plies, each with its own orthotropic properties that depend on the fiber direction (see e.g. [6, 10] and references therein). With this approach, two distinct failure mechanisms may occur in the laminate: failure inside a ply (intraply) and failure between the plies (interply). The first of these can be connected to different underlying micromechanical failure modes, such as fiber fracture, fiber buckling, matrix cracking and fiber/matrix debonding. The second is referred to as delamination. Ultimate failure of a laminate is often preceded by both failure mechanisms. Therefore, simulation of failure in laminated composites requires a model which includes both intraply and interply failure as well as interaction. In this paper, such a model is presented. For both failure mechanisms,

F.P. van der Meer and L.J. Sluys
Faculty of Civil Engineering and Geosciences, Delft University of Technology, P.O. Box 5048, 2600 GA Delft, The Netherlands, e-mail: f.p.vandermeer@tudelft.nl

constitutive models are incorporated that give a complete description of the local process from initial elastic behavior to complete loss of integrity.

For intraply failure, numerous theories exist that provide criteria to evaluate the stresses inside a ply, either based on the different failure modes [7, 9, 17] or defined as polynomial interaction between stress components [11, 24]. However, not much is known on what happens inside a ply after such a criterion has been violated, even though this information is necessary to predict redistribution of stresses and ultimate failure of the laminate. We have used an interactive criterion and extended it with a new softening plasticity model for the simulation of progressive failure.

For interply failure, models for the nonlinear material behavior are available in literature. The interface can be modeled with interface (or decohesion) elements [4, 12, 14, 21, 25, 30], thin volume elements [27], or embedded discontinuities incorporated through the partition of unity method [18]. Here, we have used interface elements with a constitutive law developed by Turon et al. [25] to capture the onset and growth of delamination cracks.

The outline of this paper is as follows. First, the softening orthotropic material model for intraply failure is presented. Next, the delamination model is described. And finally, the performance of the framework combining the two models is exemplified.

7.2 Softening Orthotropic Plasticity

The single expression failure criteria for orthotropic materials by Hoffman [11] and Tsai and Wu [24] may be written in tensor notation (cf. [19]):

$$f(\sigma) = \frac{1}{2}\sigma \cdot \mathsf{P}\sigma + \sigma \cdot \mathbf{p} - 1 \tag{7.1}$$

where σ is the stress in Voigt notation, and the components of matrix P and vector $\mathbf{p}$ are computed from the uniaxial strength parameters. Every stress state for which $f \leq 0$ is considered admissible. For the generalized Von Mises version of the Tsai Wu criterion, P and $\mathbf{p}$ are defined as

$$\mathsf{P} = \begin{bmatrix} \frac{2}{F_{1t}F_{1c}} & -\frac{1}{\sqrt{F_{1t}F_{1c}F_{2t}F_{2c}}} & -\frac{1}{\sqrt{F_{1t}F_{1c}F_{2t}F_{2c}}} & 0 & 0 & 0 \\ -\frac{1}{\sqrt{F_{1t}F_{1c}F_{2t}F_{2c}}} & \frac{2}{F_{2t}F_{2c}} & -\frac{1}{F_{2t}F_{2c}} & 0 & 0 & 0 \\ -\frac{1}{\sqrt{F_{1t}F_{1c}F_{2t}F_{2c}}} & -\frac{1}{F_{2t}F_{2c}} & \frac{2}{F_{2t}F_{2c}} & 0 & 0 & 0 \\ 0 & 0 & 0 & \frac{1}{F_4^2} & 0 & 0 \\ 0 & 0 & 0 & 0 & \frac{1}{F_6^2} & 0 \\ 0 & 0 & 0 & 0 & 0 & \frac{1}{F_6^2} \end{bmatrix} \tag{7.2}$$

and

$$\mathbf{p} = \begin{bmatrix} \frac{1}{F_{1t}} - \frac{1}{F_{1c}} \\ \frac{1}{F_{2t}} - \frac{1}{F_{2c}} \\ \frac{1}{F_{2t}} - \frac{1}{F_{2c}} \\ 0 \\ 0 \\ 0 \end{bmatrix} \tag{7.3}$$

where F_{1t}, F_{1c}, F_{2t}, F_{2c}, and F_6 are the five independent strength parameters of a transversely isotropic material, representing the longitudinal tensile and compressive strength, the transverse tensile and compressive strength and the longitudinal shear strength, respectively. F_4 is the transverse shear strength, which is, for transverse isotropy, a dependent quantity according to

$$F_4 = \sqrt{\frac{F_{2t}F_{2c}}{3}} \tag{7.4}$$

The simplest way to introduce softening behavior in a plastic material with a yield criterion in the form of Eq. (7.1), is to define a scalar softening variable κ which determines the degradation of all strength parameters. If the evolution of all strength parameters is given by $F_i(\kappa) = F_i^0 h(\kappa)$ with an isotropic softening function $h(\kappa)$, ranging from 1 to 0, criterion 7.1 may be rewritten as

$$f(\sigma, \kappa) = \frac{1}{2}\sigma \cdot \mathsf{P}(\kappa)\sigma + \sigma \cdot \mathbf{p}(\kappa) - 1 \tag{7.5}$$

with

$$\mathsf{P}(\kappa) = \frac{1}{(h(\kappa))^2}\mathsf{P}^0 \tag{7.6}$$
$$\mathbf{p}(\kappa) = \frac{1}{h(\kappa)}\mathbf{p}^0$$

where P^0 and $\mathbf{p}^0$ are constructed from the initial strength parameters, F_i^0, as in Eq. (7.2)–(7.3). In this case, the yield surface shrinks upon softening to the origin of the stress space (see Fig. 7.1).

An evolution law for the softening variable is needed. A convenient choice is to couple softening variable κ to the equivalent plastic strain in incremental format, according to

$$\Delta\kappa = \sqrt{\Delta\varepsilon^{\mathrm{p}} \cdot \mathsf{Q}\Delta\varepsilon^{\mathrm{p}}} \tag{7.7}$$

where ε^{p} is the plastic strain and

$$\mathsf{Q} = \mathrm{diag}\left[1, 1, 1, \frac{1}{2}, \frac{1}{2}, \frac{1}{2}\right] \tag{7.8}$$

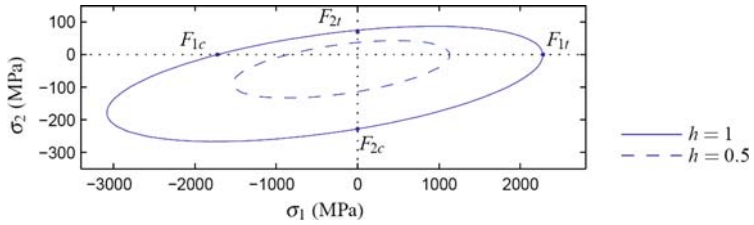

Fig. 7.1 Softening Tsai Wu failure criterion in plane stress space ($F_{1t} = 2{,}280$ MPa, $F_{1c} = 1{,}725$ MPa, $F_{2t} = 70$ MPa, $F_{2c} = 228$ MPa)

It would be more realistic to have an anisotropic softening law, because degradation is typically not isotropic (e.g. matrix cracking due to transverse tension hardly reduces the tensile strength in longitudinal direction). But implementation of an orthotropic softening law is significantly more complicated. For each failure mode a state variable will be needed (i.e. a vector $\boldsymbol{\kappa}$, instead of scalar κ), each with its own evolution law depending on the strain history. And for each strength parameter, a law to compute the degradation from the state variables will be needed (i.e. a vector $\mathbf{h}$ instead of scalar h). Many extra material parameters or assumptions will be needed. A possible danger of the softening of individual strength parameters, is that combinations of strength parameters may occur for which the yield surface is no longer convex, as a consequence of which uniqueness in the stress return mapping is lost. Another problem is that softening or hardening in one direction will have opposite effects in another direction [3, 13].

7.2.1 Viscoplastic Regularization

Softening material models, such as the one described above, suffer severe mesh dependency [22]. Localization of deformations will occur in one row of elements, as a consequence of which the dissipated energy will depend on the element size, approaching zero for infinitesimal element size. The most straightforward method to solve this problem is the fracture energy approach, in which the local stress strain behavior depends on the element size [2]. However, this does not solve the mesh sensitivity problem completely. Moreover, in the case of non-localized material degradation, which may occur in laminates as distributed transverse matrix cracking [16], this approach causes an opposite mesh-dependency, i.e. a smaller element size causes an increase of the dissipated energy.

Three better options for regularization are non-local models [1], gradient plasticity [15] and viscoplasticity [22]. Viscoplasticity is chosen here, for its relatively easy implementation. The consistency model formulation, introduced by Wang et al. [28], is used. The basic concept of this formulation is that the yield surface expands for nonzero plastic strain rate. In our current model, this comes down to the introduction of a dependency on $\dot{\kappa}$ in the softening function h. We choose a

softening law that is linear in both κ and $\dot{\kappa}$:

$$h(\kappa, \dot{\kappa}) = 1 + H\kappa + V\dot{\kappa} \tag{7.9}$$

in which softening modulus H typically is negative and viscoplastic modulus V typically is positive. The softening function h is not allowed to become smaller than $h_{\min} = 0.01$. After this value has been reached once, h is fixed, so that recovery of strength after failure is impossible.

Note that, upon the assumption that the plastic strain rate is constant over the time step (i.e. $\dot{\kappa} = \Delta\kappa/\Delta t$), both κ and $\dot{\kappa}$ depend on one single unknown, $\Delta\kappa$, inside each time step Δt. Therefore, Eq. (7.9) may be rewritten as

$$h(\Delta\kappa) = 1 + H\kappa_0 + \left(H + \frac{V}{\Delta t}\right)\Delta\kappa \tag{7.10}$$

where κ_0 is the value of κ at the end of the previous time step.

7.2.2 Stress Evaluation

The stress evaluation is executed with a return mapping algorithm. The unknown variables in the stress evaluation for time step n are σ_n and $\Delta\kappa_n$. As long as the material is in the plastic state, these variables should satisfy the yield criterion

$$f = \frac{1}{2}\sigma_n \cdot \mathsf{P}(\Delta\kappa_n)\sigma_n + \sigma_n \cdot \mathbf{p}(\Delta\kappa_n) - 1 = 0 \tag{7.11}$$

and the constitutive relation

$$\mathbf{g} = \sigma_n - \mathsf{D}(\varepsilon_n - \varepsilon^{\mathrm{p}}_{n-1}) + \Delta\lambda(\sigma_n, \Delta\kappa_n)\mathsf{D}\mathbf{m}(\sigma_n, \Delta\kappa_n) = \mathbf{0} \tag{7.12}$$

in which the plastic multiplier $\Delta\lambda$ and the direction of plastic flow $\mathbf{m}$ are secondary variables, which are computed from $\Delta\kappa_n$ and σ_n, and D is the elastic stiffness matrix. Equation 7.12 is based on fully implicit Euler backward integration of the plastic flow rule

$$\Delta\varepsilon^{\mathrm{p}}_n = \Delta\lambda_n \mathbf{m}_n \tag{7.13}$$

For clarity, the index n is dropped in the remainder of this section – all quantities refer to time step n, unless indicated otherwise.

We assume associative flow:

$$\mathbf{m} = \frac{\partial f}{\partial \sigma} \tag{7.14}$$

An expression for $\Delta\lambda$ is obtained by combining Eq. (7.13) and (7.7).

$$\Delta\lambda = \frac{\Delta\kappa}{\sqrt{\mathbf{m} \cdot \mathsf{Q}\mathbf{m}}} \tag{7.15}$$

The derivatives of f and $\mathbf{g}$ with respect to $\Delta\kappa$ and σ read:

$$\frac{\partial f}{\partial \Delta\kappa} = -\frac{1}{h}\frac{\partial h}{\partial \Delta\kappa}\left(\sigma \cdot \mathsf{P}\sigma + \sigma \cdot \mathbf{p}\right) \tag{7.16}$$

$$\frac{\partial f}{\partial \sigma} = \mathsf{P}\sigma + \mathbf{p} \tag{7.17}$$

$$\frac{\partial \mathbf{g}}{\partial \Delta\kappa} = \mathsf{D}\mathbf{m}\frac{\partial \Delta\lambda}{\partial \Delta\kappa} + \Delta\lambda\,\mathsf{D}\frac{\partial \mathbf{m}}{\partial \Delta\kappa} \tag{7.18}$$

$$\frac{\partial \mathbf{g}}{\partial \sigma} = \mathsf{I} + \mathsf{D}\mathbf{m} \otimes \frac{\partial \Delta\lambda}{\partial \sigma} + \Delta\lambda\,\mathsf{D}\frac{\partial \mathbf{m}}{\partial \sigma} \tag{7.19}$$

with

$$\frac{\partial h}{\partial \Delta\kappa} = H + \frac{V}{\Delta t} \tag{7.20}$$

$$\frac{\partial \mathbf{m}}{\partial \sigma} = \mathsf{P} \tag{7.21}$$

$$\frac{\partial m}{\partial \Delta\kappa} = -\frac{1}{h}\frac{\partial h}{\partial \Delta\kappa}\left(2\mathsf{P}\sigma + \mathbf{p}\right) \tag{7.22}$$

$$\frac{\partial \Delta\lambda}{\partial \sigma} = \frac{\partial \Delta\lambda}{\partial \mathbf{m}}\frac{\partial \mathbf{m}}{\partial \sigma} \tag{7.23}$$

$$\frac{\partial \Delta\lambda}{\partial \Delta\kappa} = \frac{1}{\sqrt{\mathbf{m} \cdot \mathsf{Q}\mathbf{m}}} + \frac{\partial \Delta\lambda}{\partial \mathbf{m}} \cdot \frac{\partial \mathbf{m}}{\partial \Delta\kappa} \tag{7.24}$$

$$\frac{\partial \Delta\lambda}{\partial \mathbf{m}} = -\frac{\Delta\kappa \mathsf{Q}\mathbf{m}}{\left(\mathbf{m} \cdot \mathsf{Q}\mathbf{m}\right)^{3/2}} \tag{7.25}$$

The return mapping algorithm is presented in Fig. 7.2, in which B is a matrix containing the partial derivatives of f and $\mathbf{g}$ with respect to $\Delta\kappa$ and σ

$$\mathsf{B} = \begin{bmatrix} \dfrac{\partial f}{\partial \Delta\kappa} & \dfrac{\partial f}{\partial \sigma} \\ \dfrac{\partial \mathbf{g}}{\partial \Delta\kappa} & \dfrac{\partial \mathbf{g}}{\partial \sigma} \end{bmatrix} \tag{7.26}$$

and D^{con} is the consistent tangent (for derivation, see Sect. 7.2.3).

In the algorithm, $\Delta\kappa$ is initialized at a nonzero value. For this purpose the value for $\dot{\kappa}$ is stored for each integration point, additional to the state variable κ. In order to improve the stability of the return mapping algorithm, the Newton Raphson loop that solves for $\Delta\kappa$ and σ is reformulated in a form analogous to Heun's method.

When the strength approaches zero, this algorithm may fail, due to the singularity of f for $h = 0$. When the first algorithm fails, another return mapping scheme is entered. In this algorithm, there is a double iteration loop. The outer loop searches for the correct value of $\Delta\kappa$, while the inner loop solves the plasticity equations for

(1) Initialize $\sigma^0 = \mathsf{D}(\varepsilon - \varepsilon^{\mathrm{p}}_{n-1})$, $\Delta\kappa^0 = 0$

(2) If $f(\sigma^0, \Delta\kappa^0) < 0$: exit with $\mathsf{D}^{\mathrm{con}} = \mathsf{D}$, $\sigma_n = \sigma^0$, $\kappa_n = \kappa_{n-1}$, $\dot{\kappa}_n = 0$ otherwise continue with (3)

(3) Initialize: $\Delta\kappa^0 = \Delta t\, \dot{\kappa}_{n-1}$, $j = 0$

(4) Return mapping iteration: $j = j + 1$

(5) Evaluate $f = f(\Delta\kappa^{j-1}, \sigma^{j-1})$ and $\mathbf{g} = \mathbf{g}(\Delta\kappa^{j-1}, \sigma^{j-1})$

(6) Evaluate derivatives of f and $\mathbf{g}$ with respect to $\Delta\kappa$ and σ (see 7.16–7.19)

(7) Compute first increment $\begin{bmatrix} \mathrm{d}\Delta\kappa \\ \mathrm{d}\sigma \end{bmatrix}_1 = -\left[\mathsf{B}(\Delta\kappa^{j-1}, \sigma^{j-1})\right]^{-1} \begin{bmatrix} f \\ \mathbf{g} \end{bmatrix}$

(8) Update unknowns: $\begin{bmatrix} \Delta\tilde{\kappa}^j \\ \tilde{\sigma}^j \end{bmatrix} = \begin{bmatrix} \Delta\kappa^{j-1} \\ \sigma^{j-1} \end{bmatrix} + \begin{bmatrix} \mathrm{d}\Delta\kappa \\ \mathrm{d}\sigma \end{bmatrix}_1$

(9) Re-evaluate derivatives with updated unknowns

(10) Compute second increment $\begin{bmatrix} \mathrm{d}\Delta\kappa \\ \mathrm{d}\sigma \end{bmatrix}_2 = -\left[\mathsf{B}(\Delta\tilde{\kappa}^j, \tilde{\sigma}^j)\right]^{-1} \begin{bmatrix} f \\ \mathbf{g} \end{bmatrix}$

(11) Update unknowns $\begin{bmatrix} \Delta\kappa^j \\ \sigma^j \end{bmatrix} = \begin{bmatrix} \Delta\kappa^{j-1} \\ \sigma^{j-1} \end{bmatrix} + \frac{1}{2}\left(\begin{bmatrix} \mathrm{d}\Delta\kappa \\ \mathrm{d}\sigma \end{bmatrix}_1 + \begin{bmatrix} \mathrm{d}\Delta\kappa \\ \mathrm{d}\sigma \end{bmatrix}_2 \right)$ go to (4)

(12) If converged go to (13), otherwise go to (4)

(13) Store $\kappa_n = \kappa_{n-1} + \Delta\kappa^j$, $\sigma_n = \sigma^j$, $\dot{\kappa}_n = \dfrac{\Delta\kappa^j}{\Delta t_n}$ and compute $\mathsf{D}^{\mathrm{con}}$ with Eq. (7.57)

Fig. 7.2 Return mapping algorithm for rate dependent orthotropic plasticity with softening

ideal plasticity with given $\Delta\kappa$ (see Fig. 7.3). Derivatives of f and $\mathbf{g}$ to unknowns $\Delta\lambda$ and σ can be computed much simpler when $\Delta\kappa$ is fixed (cf. Eq. (7.16)–(7.25)):

$$\frac{\partial f}{\partial \Delta\lambda} = 0 \tag{7.27}$$

$$\frac{\partial f}{\partial \sigma} = \mathsf{P}\sigma \tag{7.28}$$

$$\frac{\partial g}{\partial \Delta\lambda} = \mathsf{D}\mathbf{m} \tag{7.29}$$

$$\frac{\partial g}{\partial \sigma} = \mathsf{I} + \Delta\lambda\, \mathsf{D}\mathsf{P} \tag{7.30}$$

In each outer iteration there is an input value $\Delta\kappa^{\mathrm{in}}$, which determines the strength, and an output value $\Delta\kappa^{\mathrm{out}}$, which is obtained from the magnitude of the plastic strain increment for this strength. When $\Delta\kappa^{\mathrm{out}} = \Delta\kappa^{\mathrm{in}}$, the correct value of $\Delta\kappa$ has been found.

As long as $\partial h / \partial \Delta\kappa > 0$ (which is necessary for a regularizing effect of the rate dependent term) the yield surface expands as $\Delta\kappa^{\mathrm{in}}$ increases, and therefore the

(1) Initialize: $\sigma^0 = \mathsf{D}(\varepsilon - \varepsilon^{\mathrm{p}}_{n-1})$, $\Delta\lambda^0 = 0$, $k = 0$, $j = 0$

(2) Outer iteration: $k = k + 1$

(3) Give estimate for $\Delta\kappa$ with

$$\Delta\kappa^{\mathrm{in}}_k = \begin{cases} \dfrac{h(\kappa_{n-1}, \dot{\kappa}_{n-1}) - h(\kappa_{n-1}, 0)}{\partial h / \partial \Delta\kappa} & k = 1 \\ \max\left(0, \dfrac{h(\kappa_{n-1}, \dot{\kappa}_{n-1}) - h_{\min}}{\partial h / \partial \Delta\kappa}, \Delta\kappa^{\mathrm{out}}_1\right) & k = 2 \\ \Delta\kappa^{\mathrm{in}}_{k-1} + \Delta\kappa^{\mathrm{in}}_{k-1} - \Delta\kappa^{\mathrm{in}}_{k-2} \dfrac{\delta\kappa_{k-1}}{\delta\kappa_{k-2} - \delta\kappa_{k-1}} & k > 2 \end{cases}$$

(4) Inner iteration: $j = j + 1$

(5) Evaluate $f(\Delta\kappa^{\mathrm{in}}_k, \sigma^{j-1})$ and $\mathbf{g}(\Delta\kappa^{\mathrm{in}}_k, \Delta\lambda^{j-1}, \sigma^{j-1})$

(6) Compute derivatives of f and $\mathbf{g}$ with respect to $\Delta\lambda$ and σ (see 7.27–7.30)

(7) Update unknowns $\begin{bmatrix} \Delta\lambda^j \\ \sigma^j \end{bmatrix} = \begin{bmatrix} \Delta\lambda^{j-1} \\ \sigma^{j-1} \end{bmatrix} - \left[\mathsf{B}(\Delta\lambda^{j-1}, \sigma^{j-1})\right]^{-1} \begin{bmatrix} f \\ \mathbf{g} \end{bmatrix}$

(8) Inner loop: If converged go to (9), otherwise go to (4)

(9) Outer loop: Check whether $\Delta\kappa^{\mathrm{in}}$ is compatible with obtained plastic flow
$\Delta\kappa^{\mathrm{out}}_k = \sqrt{\Delta\varepsilon^{\mathrm{p}} \cdot \mathsf{Q}\Delta\varepsilon^{\mathrm{p}}}$, $\delta\kappa_k = \Delta\kappa^{\mathrm{out}}_k - \Delta\kappa^{\mathrm{in}}_k$
If $\delta\kappa_k <$ tolerance, or ($h = h_{\min}$ and $\delta\kappa_k < 0$) go to (10), otherwise go to (3)

(10) Store $\kappa_n = \kappa_{n-1} + \Delta\kappa^{\mathrm{out}}_k$, $\sigma_n = \sigma^j$, $\dot{\kappa}_n = \dfrac{\Delta\kappa^{\mathrm{out}}_k}{\Delta t}$
and compute $\mathsf{D}^{\mathrm{con}}$ with Eq. (7.57)

Fig. 7.3 Stable return mapping algorithm for rate dependent orthotropic plasticity with softening in case the origin in the stress space is approached

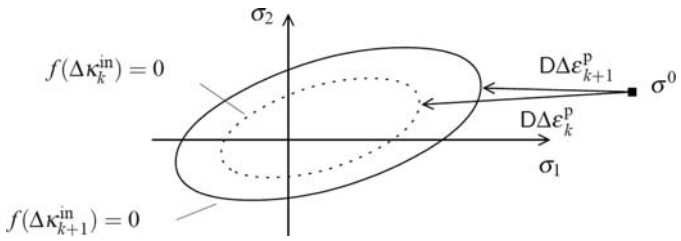

Fig. 7.4 Relation between $\Delta\kappa^{\mathrm{in}}_k$ and $\Delta\kappa^{\mathrm{out}}_k$. An increase in trial value $\Delta\kappa^{\mathrm{in}}_{k+1} > \Delta\kappa^{\mathrm{in}}_k$ results in a decrease in the amount of plastic strain and consequently in $\Delta\kappa^{\mathrm{out}}_{k+1} < \Delta\kappa^{\mathrm{out}}_k$

plastic strain increment $\Delta\varepsilon^{\mathrm{p}}$ and, consequently, $\Delta\kappa^{\mathrm{out}}$ become smaller, as illustrated in Fig. 7.4. So we postulate

$$\frac{\partial\Delta\kappa^{\mathrm{out}}}{\partial\Delta\kappa^{\mathrm{in}}} < 0 \quad \forall \quad \Delta\kappa^{\mathrm{in}} > 0 \tag{7.31}$$

In the first two outer iterations, bounds for $\Delta\kappa$ are determined, and from the third iteration on, the estimate for $\Delta\kappa$ is repeatedly improved with linear interpolation or extrapolation based on the $\Delta\kappa^{\mathrm{in}}$ and $\Delta\kappa^{\mathrm{out}}$ values from the previous two iterations.

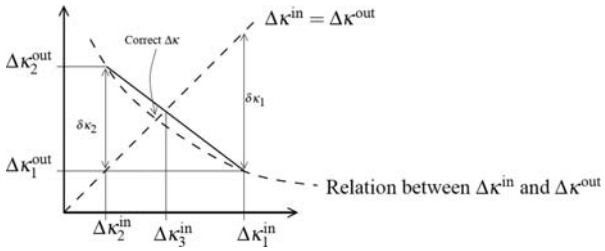

Fig. 7.5 Update of $\Delta\kappa^{in}$ through linear interpolation

The first estimate is obtained assuming

$$h(\kappa_n, \dot{\kappa}_n) = h(\kappa_{n-1}, \dot{\kappa}_{n-1}) \tag{7.32}$$

From Eq. (7.31), it follows that if $\Delta\kappa^{in}$ is higher than the correct value of $\Delta\kappa$, $\Delta\kappa^{out}$ is lower than that value, and vice versa. So if we set

$$\Delta\kappa_2^{in} = \Delta\kappa_1^{out} \tag{7.33}$$

it is secured that the correct value of $\Delta\kappa$ lies between $\Delta\kappa_1^{in}$ and $\Delta\kappa_2^{in}$. And if we add the two conditions

$$\Delta\kappa_2^{in} \geq 0 \tag{7.34}$$

$$h(\Delta\kappa_2^{in}) \geq h_{min} \tag{7.35}$$

the search for the true $\Delta\kappa$ must converge when the next estimate for $\Delta\kappa_k^{in}$ is each time computed from linear interpolation (see Fig. 7.5), except when $h(\Delta\kappa_2^{in}) = h_{min}$ and $h(\Delta\kappa_2^{out}) < h_{min}$. In that case the material point has failed and h is fixed at h_{min} and the stress obtained with $h(\Delta\kappa^{in}) = h_{min}$ is the correct stress.

7.2.3 Consistent Linearization

For proper convergence of the model, it is of great importance that a consistent tangent is used. The derivation of the consistent tangent is given below.

We start with expanding the constitutive law 7.12 around a small variation:

$$\delta\mathbf{g} = \mathbf{0} \quad \Leftrightarrow \quad \delta\sigma = \mathsf{D}\,\delta\varepsilon - \mathsf{D}\mathbf{m}\,\delta\lambda - \Delta\lambda\,\mathsf{D}\,\delta\mathbf{m} \tag{7.36}$$

The expression for $\delta\mathbf{m}$ is:

$$\delta\mathbf{m} = \frac{\partial\mathbf{m}}{\partial\sigma}\,\delta\sigma + \frac{\partial\mathbf{m}}{\partial\kappa}\,\delta\Delta\kappa \tag{7.37}$$

with

$$\delta\Delta\kappa = \frac{\partial\Delta\kappa}{\partial\lambda}\,\delta\lambda + \frac{\partial\Delta\kappa}{\partial\mathbf{m}}\cdot\delta\mathbf{m} \tag{7.38}$$

and

$$\frac{\partial\mathbf{m}}{\partial\sigma} = \mathsf{P} \tag{7.39}$$

$$\frac{\partial\mathbf{m}}{\partial\Delta\kappa} = \frac{\partial\mathsf{P}}{\partial\Delta\kappa}\sigma + \frac{\partial\mathbf{p}}{\partial\Delta\kappa} \tag{7.40}$$

$$\frac{\partial\Delta\kappa}{\partial\mathbf{m}} = \Delta\lambda\frac{\mathsf{Q}\mathbf{m}}{\sqrt{\mathbf{m}\cdot\mathsf{Q}\mathbf{m}}} \tag{7.41}$$

$$\frac{\partial\Delta\kappa}{\partial\lambda} = \sqrt{\mathbf{m}\cdot\mathsf{Q}\mathbf{m}} \tag{7.42}$$

Equation 7.37 is solved for $\delta\mathbf{m}$, after substitution of Eq. (7.38), resulting in

$$\delta\mathbf{m} = \mathsf{E}^{-1}\frac{\partial\mathbf{m}}{\partial\sigma}\,\delta\sigma + \mathsf{E}^{-1}\frac{\partial\mathbf{m}}{\partial\Delta\kappa}\frac{\partial\Delta\kappa}{\partial\lambda}\,\delta\lambda \tag{7.43}$$

with

$$\mathsf{E} = \mathsf{I} - \frac{\partial\mathbf{m}}{\partial\Delta\kappa}\otimes\frac{\partial\Delta\kappa}{\partial\mathbf{m}} \tag{7.44}$$

With Eq. (7.6), we have

$$\frac{\partial\mathsf{P}}{\partial\Delta\kappa} = -\frac{2}{h^3}\frac{\partial h}{\partial\Delta\kappa}\mathsf{P}^0 = -\frac{2}{h}\frac{\partial h}{\partial\Delta\kappa}\mathsf{P} \tag{7.45}$$

$$\frac{\partial\mathbf{p}}{\partial\Delta\kappa} = -\frac{1}{h^2}\frac{\partial h}{\partial\Delta\kappa}\mathbf{p}^0 = -\frac{1}{h}\frac{\partial h}{\partial\Delta\kappa}\mathbf{p} \tag{7.46}$$

Using Eqs. (7.45) and (7.46), (7.40) may be rewritten into

$$\frac{\partial\mathbf{m}}{\partial\Delta\kappa} = -\frac{1}{h}\frac{\partial h}{\partial\Delta\kappa}\left(2\mathsf{P}\sigma + \mathbf{p}\right) \tag{7.47}$$

Substitution of Eq. (7.43) into Eq. (7.36) gives

$$\mathsf{A}\,\delta\sigma = \mathsf{D}\,\delta\varepsilon - \mathsf{D}\bar{\mathbf{m}}\,\delta\lambda \tag{7.48}$$

with

$$\mathsf{A} = \mathsf{I} + \Delta\lambda\,\mathsf{D}\mathsf{E}^{-1}\frac{\partial\mathbf{m}}{\partial\sigma} \tag{7.49}$$

$$\bar{\mathbf{m}} = \mathbf{m} + \Delta\lambda\,\mathsf{E}^{-1}\frac{\partial\mathbf{m}}{\partial\Delta\kappa}\frac{\partial\Delta\kappa}{\partial\lambda} \tag{7.50}$$

Next, we eliminate $\delta\lambda$. For this purpose δf is expanded:

$$\begin{aligned}\delta f &= \frac{\partial f}{\partial \sigma}\cdot\delta\sigma + \frac{\partial f}{\partial \Delta\kappa}\delta\Delta\kappa \\ &= \mathbf{m}\cdot\delta\sigma + \frac{\partial f}{\partial \Delta\kappa}\left(\frac{\partial \Delta\kappa}{\partial \lambda}\delta\lambda + \frac{\partial \Delta\kappa}{\partial \mathbf{m}}\delta\mathbf{m}\right)\end{aligned} \tag{7.51}$$

Substitution of Eq. (7.43) into Eq. (7.51), with the condition $\delta f = 0$, gives

$$\delta\lambda = \frac{1}{\eta}\bar{\mathbf{n}}\cdot\delta\sigma \tag{7.52}$$

with

$$\bar{\mathbf{n}} = \mathbf{m} + \frac{\partial f}{\partial \Delta\kappa}\frac{\partial \Delta\kappa}{\partial \mathbf{m}}\cdot\mathsf{E}^{-1}\frac{\partial \mathbf{m}}{\partial \sigma} \tag{7.53}$$

$$\eta = -\frac{\partial f}{\partial \Delta\kappa}\frac{\partial \Delta\kappa}{\partial \lambda}\left(1 + \frac{\partial \Delta\kappa}{\partial \mathbf{m}}\cdot\mathsf{E}^{-1}\frac{\partial \mathbf{m}}{\partial \Delta\kappa}\right) \tag{7.54}$$

Substitution of Eq. (7.52) into Eq. (7.48) gives:

$$\delta\varepsilon = \left[\mathsf{H}^{-1} + \frac{1}{\eta}\bar{\mathbf{n}}\otimes\bar{\mathbf{m}}\right]\delta\sigma \tag{7.55}$$

with

$$\mathsf{H} = \mathsf{A}^{-1}\mathsf{D} \tag{7.56}$$

The compliance matrix in Eq. (7.55) is inverted with the Sherman–Morrison formula [8] to arrive at the consistent tangent:

$$\mathsf{D}^{\text{con}} = \mathsf{H} - \frac{(\mathsf{H}\bar{\mathbf{m}})\otimes(\bar{\mathbf{n}}\cdot\mathsf{H})}{\eta + \bar{\mathbf{n}}\cdot\mathsf{H}\bar{\mathbf{m}}} \tag{7.57}$$

The consistent tangent is not necessarily symmetric, even when associative flow is assumed.

Note that the derivation above holds for any differentiable hardening or softening function $h(\Delta\kappa)$, with or without rate dependent term.

7.2.4 Convergence Issue

Although a consistent tangent is used, difficulties may arise in the first iteration of the global Newton–Raphson loop. The problem is that the converged solution from the previous time step is not an equilibrium solution for the current time step. Thus, the Newton–Raphson loop starts with an unbalance. This results in instabilities comparable to what happens in a nonlinear analysis with too large time steps, but here, the problem cannot be solved by reducing the time step size.

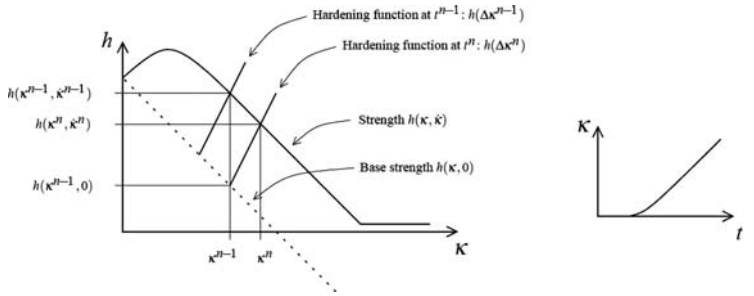

Fig. 7.6 Typical strength evolution for rate dependent model (*left*), with corresponding evolution of κ (*right*). Within each time step in the plastic regime, there is a hardening relation between κ and h (i.e. between plastic strain and strength), whereas the relation from one time step to the other may be a softening relation

The problem can be illustrated as follows. In standard (rate independent) finite element calculations the internal force vector is a function of displacements only $f_{\text{int}}(\mathbf{u})$. But upon the introduction of rate dependency, we get $f_{\text{int}}(\mathbf{u},\dot{\mathbf{u}})$. Within every time step it is possible to reformulate the internal force vector to $f_{\text{int}}(\Delta\mathbf{u})$, similar as in rate independent analysis. But an important difference is, that now $f_{\text{int}}(\Delta\mathbf{u}=\mathbf{0}) \neq 0$. This is related to the behavior of the hardening function h (see Fig. 7.6). In each time step, there is a function $h(\Delta\kappa)$, but in each time step it is a different one, and if $\Delta\kappa_{n-1} \neq 0$, the strength in case of an elastic increment in time step n is not equal to the equilibrium strength from the previous time step

$$h(\Delta\kappa_n = 0) \neq h(\kappa_{n-1},\dot{\kappa}_{n-1}) \tag{7.58}$$

A better starting point is obtained with $\Delta\mathbf{u}^n = \Delta\mathbf{u}^{n-1}$, or, in the more general case in which the time step size may vary

$$\Delta\mathbf{u}^n = \Delta\mathbf{u}^{n-1}\frac{\Delta t^n}{\Delta t^{n-1}} \tag{7.59}$$

In that case, the internal force vector $f_{\text{int}}^{t+\Delta t}(\Delta\mathbf{u}^t)$ does approach zero upon time step size reduction.

7.2.5 Associativity Versus Non-associativity

A problem with the use of associative plasticity and a smooth yield surface for strongly orthotropic materials, is that the direction of plastic flow tends to display a pronounced orientation in the weak direction, even when the material is loaded in the strong direction. Moreover, the direction of plastic flow when loading in the strong

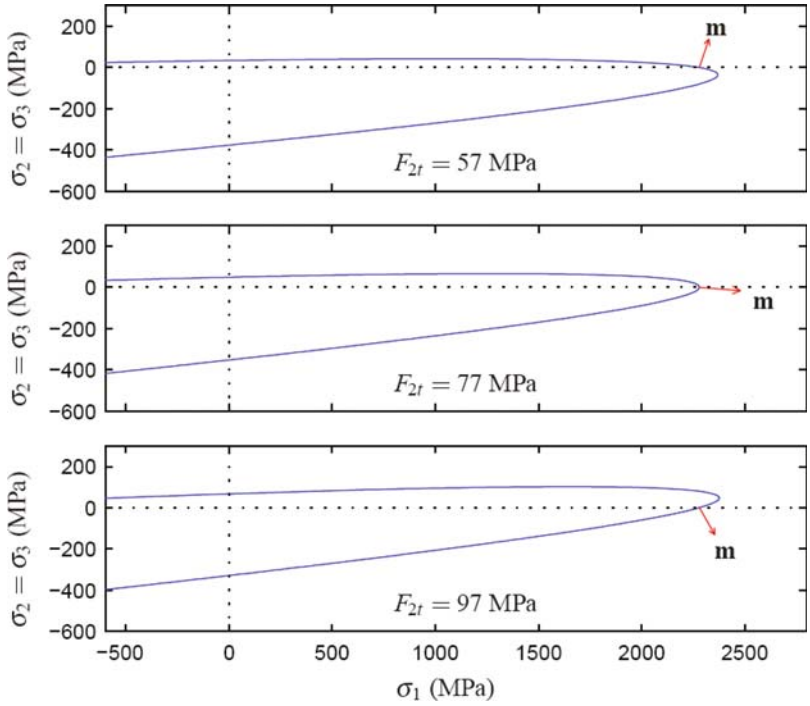

Fig. 7.7 Sensitivity of plastic flow direction in uniaxial tensile test in strong direction to tensile strength in weak direction ($F_{1t} = 2{,}280$ MPa, $F_{1c} = 1{,}725$ MPa, $F_{2c} = 228$ MPa)

direction is very sensitive to the transverse strength parameters. This sensitivity is illustrated in Fig. 7.7, in which the direction of plastic flow ($\mathbf{m} = \partial f / \partial \sigma$) in case of uniaxial tensile loading in the strong (fiber) direction is shown for three different values of the transverse tensile strength.

As a consequence, unrealistically large transverse deformations may dominate the structural response in the simulation of a test with fiber failure. The transverse strains influence the softening rate and possibly accelerate delamination. This problem cannot be solved easily by abandoning the associative plasticity assumption, because this endangers the stability of the stress evaluation. For most sets of experimental data, an artificial increase of the transverse tensile strength may be applied, such that the direction of plastic flow in uniaxial tensile loading in fiber direction is approximately parallel to the load direction. An increase in this value can be justified because the in situ transverse strength can be expected to be higher than the experimental value for the isolated ply [5, 7, 23]. But still, it would be a mere coincidence if the value for the in situ transverse strength is equal to the value for which spurious transverse strains are suppressed.

7.3 Delamination

For the modeling of delamination, plane interface elements are used (see Fig. 7.8). The elements are constructed from two quadrilateral planes, that are initially on top of each other and connected with a high dummy stiffness K. An orthonormal frame $\{s,t,n\}$ is defined with the n-axis normal to the interface plane. To avoid spurious oscillations in the traction distribution, a Newton-Cotes integration scheme is used, as proposed by Schellekens and De Borst [20].

Several different material models for the analysis of delamination with interface elements have been proposed. We use the model developed by Camanho et al. [4] in the improved version of Turon et al. [25]. With this constitutive model, mixed mode delamination with varying mode ratio can be analyzed. Two modes are distinguished: shear failure $(\cdot)_r$ and normal failure $(\cdot)_n$. In both modes the relation between traction and crack opening is bilinear (see Fig. 7.9). For normal compression, the interface behaves elastically to prevent interpenetration. Input parameters are single mode fracture toughness G_{Ic} and G_{IIc}, single mode strength $t_n^{\max}$ and $t_r^{\max}$, interaction parameter η, and initial stiffness K.

The values of the displacement jump for onset and propagation in single mode opening are calculated from the input parameters with

$$\delta_n^0 = \frac{t_n^{\max}}{K}, \qquad \delta_n^f = \frac{2G_{Ic}}{t_n^{\max}} \tag{7.60}$$

$$\delta_r^0 = \frac{t_r^{\max}}{K}, \qquad \delta_r^f = \frac{2G_{IIc}}{t_r^{\max}} \tag{7.61}$$

where index 0 refers to onset of damage and index f to propagation.

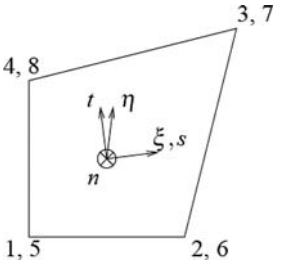

Fig. 7.8 Definition of 8-node interface element with isoparametric axes $\{\xi,\eta\}$ and local orthogonal frame $\{s,t,n\}$

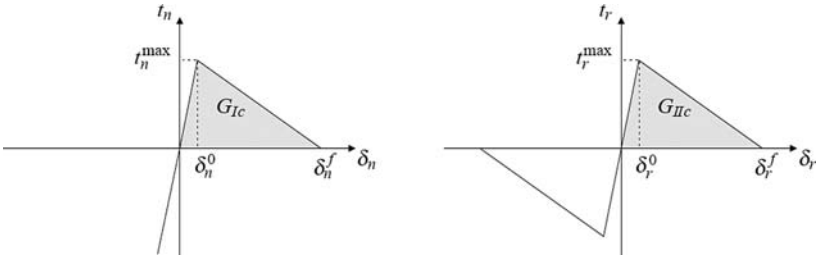

Fig. 7.9 Relation between traction and relative displacement

For the evaluation of the traction, the equivalent displacement jump is calculated via

$$\delta_b = \sqrt{\langle \delta_n \rangle^2 + \delta_r^2} \tag{7.62}$$

where subscript b refers to the current mixed mode and δ_r is defined as the total shear displacement jump: $\delta_r^2 = \delta_s^2 + \delta_t^2$. Normal relative displacements only contribute when positive, hence the use of the MacAuley operator, which is defined as $\langle x \rangle = (x + |x|)/2$.

The mixed mode ratio β and the related variable B are computed according to

$$\beta = \frac{\delta_r}{\delta_r + \langle \delta_n \rangle} \tag{7.63}$$

$$B = \frac{\beta^2}{1 + 2\beta^2 - 2\beta} \tag{7.64}$$

The onset criterion and the propagation criterion for the current mixed mode ratio are

$$\delta_b^0 = \sqrt{(\delta_n^0)^2 + \left((\delta_r^0)^2 - (\delta_n^0)^2\right) B^\eta} \tag{7.65}$$

and

$$\delta_b^f = \frac{\delta_n^0 \delta_n^f + \left(\delta_r^0 \delta_r^f - \delta_n^0 \delta_n^f\right) B^\eta}{\delta_b^0} \tag{7.66}$$

respectively, where η is a material parameter that is to be obtained from experimental data and is related to mode interaction.

With this, the bilinear constitutive law for the current mixed mode ratio is complete and the damage variable can be updated. Upon monotonic loading, the damage variable, d, is calculated with

$$d = \frac{\delta_b^f \left(\delta_b - \delta_b^0\right)}{\delta_b \left(\delta_b^f - \delta_b^0\right)}, \qquad d \in [0, 1] \tag{7.67}$$

To obtain the correct loading-unloading-reloading behavior, the following condition is added

$$\dot{d} \geq 0 \tag{7.68}$$

which demands storage of d as history variable at each integration point, similar to the description by Jiang et al. [12], which is different from the description by Turon et al. [25], where the maximum total displacement jump, δ_b, is stored as history variable and substituted into Eq. (7.67).

Tractions in the local coordinate frame are calculated by means of the secant tangent

$$D_{ij} = \bar{\delta}_{ij} K \left(1 - d \left[1 + \bar{\delta}_{3j} \frac{\langle -\delta_n \rangle}{\delta_n} \right] \right) \tag{7.69}$$

where $\bar{\delta}_{ij}$ is the Kronecker delta, barred to distinguish it from the relative displacements; i and j range from 1 to 3, where 3 is the normal direction. The term within square brackets is included to cancel the contribution from d in the normal direction in case of a negative displacement jump in normal direction.

When d does not grow, the consistent tangent is equal to the secant tangent, otherwise it is defined as

$$D_{ij}^{\text{con}} = D_{ij} - K \left[1 + \bar{\delta}_{3i} \frac{\langle -\delta_n \rangle}{\delta_n} \right] \left[1 + \bar{\delta}_{3j} \frac{\langle -\delta_n \rangle}{\delta_n} \right] S \delta_i \delta_j \tag{7.70}$$

with

$$S = \frac{\delta_b^f \delta_b^0}{\left(\delta_b^f - \delta_b^0 \right) (\delta_b)^3} \tag{7.71}$$

7.4 Numerical Example

As an example of the possibilities of the mesoscale model with both intraply and interply failure, we consider a rectangular plate with an interior notch (see Fig. 7.10, cf. [29, 30]). A $[0/90]_s$ laminate is considered, of which only the upper two plies are modeled, due to symmetry. The two in-plane axes of symmetry are also used to reduce the size of the model. Each ply is modeled with a single layer of brick elements. The plies are connected with interface elements. The material parameters are:

- Elastic lamina properties: $E_1 = 140 \cdot 10^3$ MPa $E_2 = 10 \cdot 10^3$ MPa, $\nu_{12} = \nu_{23} = 0.21$, $G_{12} = 5 \cdot 10^3$ MPa, in which E_1 and E_2 are the longitudinal and transverse Young's modulus, ν_{12} and ν_{23} are the longitudinal and transverse Poisson's ratio and G_{12} is the longitudinal shear modulus.
- Lamina strength properties: $F_{1t} = 2{,}280$ MPa, $F_{1c} = 1{,}725$ MPa, $F_{2t} = 57$ MPa, $F_{2c} = 228$ MPa, $F_6 = 76$ MPa.

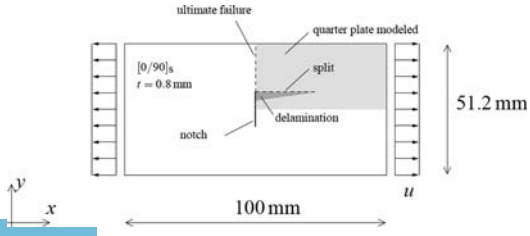

Fig. 7.10 Notched laminate

- Lamina softening properties: $H = -0.8$, $V = 0.1$/s, loading rate: 0.5 mm/s (1%/s).
- Interface properties: $K = 50 \cdot 10^3$ N/mm^3, $t_n^{\max} = 10$ MPa, $t_r^{\max} = 6$ MPa, $G_{Ic} = 0.35$ N/mm, $G_{IIc} = 0.70$ N/mm, $\eta = 1$.

The values for the elastic properties of a unidirectional lamina and the interface properties are those given by Yang and Cox for a carbon/epoxy laminate [30]. However, the interface strength parameters are reduced, as proposed by Turon et al. [26] to allow for the use of a relatively coarse mesh (this reduction leads to an increase in the length of the cohesive zone). The lamina strength properties are those provided by Daniel and Ishai [6] for a unidirectional carbon/epoxy lamina.

A similar analysis has been executed by Wisnom and Chang [29] and by Yang and Cox [30]. The former used stacked plane stress elements connected with springs, the latter used volume elements. In both references, not only the interply failure, but also the intraply failure was modeled with interface elements. In experiments it has been observed that a splitting crack grows from the notch tip in the 0-layers. This crack has been modeled in [29] and [30] by inserting interface elements where the crack is expected. The orthotropic plasticity model used here is more general, since the crack path need not be specified beforehand. Moreover, it allows for the modeling of ultimate failure of the laminate.

The evolution of plasticity in the ply with fibers in loading direction is shown in Fig. 7.11. It can be observed that the split grows as long as the load increases. In the continuum approach, the splitting mechanism is necessarily represented by a band with localized deformation. This band is parallel to the fiber direction, which is in correspondence with the experimental observations. Then tensile failure initiates at the notch tip and propagates throughout the cross section. Eventually, the band with tensile failure deviates from the plane of symmetry, after which the assumption of a symmetric response is no longer realistic. Viscoplastic regularization preserves the mesh objectivity of the results.

The final size of the delamination area due to the growth of the splitting crack is shown in Fig. 7.12. This figure displays the state at peak load level. After this, the triangular delamination area that accommodates the splitting crack in the 0-layer does not grow any further. In the post peak part of the simulation, some delamination in the vicinity of the tensile failure has been observed.

Figure 7.13 shows part of the deformed mesh, shaded where softening in the plies occurs. The two areas of plastic strain, corresponding with the different failure mechanisms, can be distinguished. The sliding between the two plies is also visible.

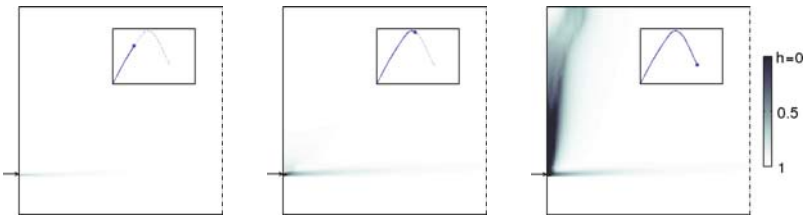

Fig. 7.11 Evolution of softening variable h in 0-ply. The arrow indicates the notch tip

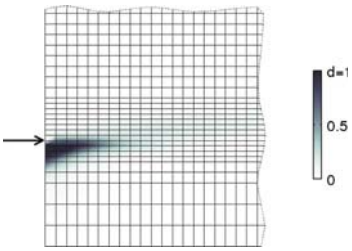

Fig. 7.12 Interface damage near the notch tip at peak load level. The arrow indicates the notch tip. Part of the mesh is shown, the arrow is scaled accordingly (cf. Fig. 7.11)

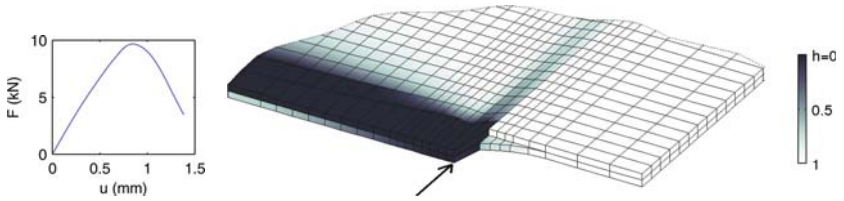

Fig. 7.13 Load displacement diagram and zoom of final deformed mesh (displacements in load direction only). The arrow indicates the notch tip. Part of the mesh is shown, the arrow is scaled accordingly (cf. Fig. 7.11)

7.5 Discussion

A model for mesoscale analysis of failure in composite laminates has been presented. An existing model for delamination has been combined with a new softening plasticity model for lamina failure. The combined model is robust, due to a carefully designed stress evaluation algorithm and the use of a consistent tangent operator. The simulation of failure processes in laminates that involve both interply and intraply processes and their interaction is possible with this model. In the analysis of a notched laminate a sequence of interacting failure events is simulated: the growth of a splitting crack in one of the plies, which is accommodated by delamination between this ply and its neighbor, and subsequently the tensile failure in all plies, which constitutes final failure of the laminate.

In developing the softening model, several non-trivial choices had to be made. Firstly for the failure criterion. An interactive criterion has been chosen for reasons of computational efficiency and robustness, in spite of the appealing physical motivation of failure mode based criteria. Secondly for the degradation law. The simplest possible formulation with which complete local failure can be simulated has been chosen, with the motivation to keep the computation robust and to limit the number of input parameters.

Some drawbacks of the softening model in its current form are that the direction of plastic strain is often unrealistic resulting in spurious transverse strains, and that viscoplastic regularization is a method that is not clearly linked to physical phenomena. Furthermore, it would be ideal if fracture energy values measured in different uniaxial tests would be direct input parameters for the material model, which is currently not the case.

Both the delamination model and the softening plasticity model, put a serious restriction on the maximum element size in the regions where failure occurs. The cohesive zone in delamination and the localization band in intraply failure have to be spanned by more than one element. In the already relatively costly three dimensional framework, which is necessary to cover all possible failure events, this means that there is a limit to the size of the structure that can be analyzed without excessive growth of computation time.

Acknowledgements This research is supported by the Technology Foundation STW (under grant DCB.6623) and the Ministry of Public Works and Water Management, The Netherlands.

References

1. Bazant ZP, Pijaudier-Cabot G (1989) J Eng Mech 115:755–767
2. Bazant ZP, Oh B (1983) Crack band theory for fracture of concrete. Mater Struct 16:155–177
3. Bićanić N, Pearce CJ, Owen DRJ (1994) Failure predictions of concrete like materials using softening Hoffman plasticity model. In: Mang H, Bićanić N, de Borst R (eds) Proceedings of EURO-C 1994. Pineridge Press, Swansea
4. Camanho PP, Dávila CG, de Moura MF (2003) Numerical simulation of mixed-mode progressive delamination in composite materials. J Compos Mater 37:1415–1438
5. Camanho PP, Dávila CG, Pinho ST et al. (2006) Prediction of in situ strengths and matrix cracking in composites under transverse tension and in-plane shear. Compos Part A 37:165–176
6. Daniel IM, Ishai O (2006) Engineering Mechanics of Composite Materials. Oxford university press, New York
7. Dávila CG, Camanho PP, Rose CA (2005) Failure criteria for FRP laminates. J Compos Mater 39:323–345
8. Hager WW (1988) Applied Numerical Linear Algebra. Prentice–Hall, Englewood Cliffs, NJ
9. Hashin Z (1980) Failure Criteria for Unidirectional Fiber Composites. J Appl Mech 47: 329–334
10. Hinton MJ, Soden PD (1998) Predicting failure in composite laminates: the background to the exercise. Compos Sci Tech 58:1001–1010
11. Hoffman O (1967) The Brittle Strength of orthotropic materials. J Compos Mater 1:200–206
12. Jiang WG, Hallett SR, Green BG, Wisnom MR (2007) A concise interface constitutive law for analysis of delamination and splitting in composite materials and its application to scaled notched tensile specimens. Int J Numer Methods Eng 69:1982–1995
13. Li X, Duxbury PG, Lyons P (1994) Considerations for the application and numerical implementation of strain hardening with the Hoffman yield criterion. Comput Struct 52:633–644
14. Mi Y, Crisfield A, Hellweg HB, Davies GAO (1998) Progressive delamination using interface elements. J Compos Mater 32:1246–1272
15. Muhlhaus HB, Aifantis EC (1991) A variational principle for gradient plasticity. Int J Solids Struct 28:845–858
16. Nairn JA, Hu S (1994) Matrix microcracking. In: Talreja R (ed) Damage Mechanics of Composite Materials. Elsevier science, Amsterdam
17. Puck A, Schürmann H (1998) Failure analysis of FRP laminates by means of physically based phenomenological models. Compos Sci Technol 58:1045–1067
18. Remmers JJC, Wells GN, de Borst R (2003) A solid-like shell element allowing for arbitrary delaminations. Int J Numer Method Eng 58:2013–2040
19. Schellekens JCJ, de Borst R (1990) The use of the Hoffman yield criterion in finite element analysis of anisotropic composites. Comput Struct 37:1087–1096

20. Schellekens JCJ, de Borst R (1993) On the numerical integration of interface elements. Int J Numer Method Eng 36:43–66
21. Schellekens JCJ, de Borst R (1994) Free edge delamination in carbon-epoxy laminates: a novel numerical/experimental approach. Compos Struct 28:357–373
22. Sluys LJ (1992) Wave propagation, localisation and dispersion in softening solids. Ph.D. thesis, Delft University of Technology
23. Sun CT, Tao J (1998) Prediction of failure envelopes and stress/strain behaviour of composite laminates. Compos Sci Technol 58:1125–1136
24. Tsai SW, Wu EM (1971) A general theory of strength for anisotropic materials. J Compos Mater 5:58–80
25. Turon A, Camanho PP, Costa J, Dávila CG (2006) A damage model for the simulation of delamination in advanced composites under variable-mode loading. Mech Mater 38:1072–1089
26. Turon A, Dávila CG, Camanho PP, Costa J (2007) An engineering solution for mesh size effects in the simulation of delamination using cohesive zone models. Eng Fract Mech 74:1665–1682
27. Wagner W, Gruttmann F, Sprenger W (2001) A finite element formulation for the simulation of propagating delaminations in layered composite structures. Int J Numer Method Eng 51:1337–1359
28. Wang WM, Sluys LJ, de Borst R (1997) Viscoplasticity for instabilities due to strain softening and strain-rate softening. Int J Numer Method Eng 40:3839–3864
29. Wisnom MR, Chang FK (2000) Modelling of splitting and delamination in notched cross-ply laminates. Compos Sci Technol 60:2849–2856
30. Yang QD, Cox BN (2005) Cohesive models for damage evolution in laminated composites. Int J Fract 133:107–137

Chapter 8
A Numerical Material Model for Predicting the High Velocity Impact Behaviour of Polymer Composites

Lucio Raimondo, Lorenzo Iannucci, Paul Robinson, and Silvestre T. Pinho

Abstract This paper describes key features of an advanced, physically-based, numerical material model for predicting the static and dynamic, failure and damage, response of polymer matrix composites with fibrous UD plies. The model has been implemented into the explicit Finite Element code LS-DYNA3D for solid brick elements with one integration point.

A comprehensive test programme was conducted for characterising the high velocity impact response of a class of NCF/Epoxy composites. The impact tests were conducted for varying impact conditions and parameters such as: impact angle, coupon thickness, laminate lay-up and projectile material. Data from these tests was reduced in the form of ballistic curves, mass of target debris generated upon complete penetration, and (C-Scan) impact damage areas. This data was used for validation of the proposed model.

General conclusions from this work indicate that physically-based modelling approaches can improve considerably the predictive capabilities of current FE codes for structural analysis applications.

8.1 Introduction

There are four main different strategies that have been employed for predicting composite impact damage within the low and medium velocity regime [6]:

1. A failure criteria approach (which can be based on the equivalent stress or strain)
2. A fracture mechanics approach (based on energy release rates)
3. A plasticity or yield surface approach
4. A damage mechanics approach

L. Raimondo, L. Iannucci, P. Robinson, and S.T. Pinho
Imperial College London, Department of Aeronautics, South Kensington Campus, London SW7 2AZ, United Kingdom,
e-mail: {lucio.raimondo, lo.iannucci, p.robinson, silvestre.pinho}@imperial.ac.uk

Published works can be found in the open literature on composites for high velocity impact modelling. The approaches used for high velocity impact modelling typically fall in one or more of the categories listed above. The good results obtained from application of the model in [16] indicate that "hybrid approaches" can be particularly effective. An attractive failure and damage modelling strategy was proposed in [9, 10] based on the simultaneous application of the strategies (1), (2) and (4) that were listed above: phenomenological failure criteria were applied to predict damage initiation, a DM (Damage Mechanics) approach based on fracture mechanics was applied for predicting damage evolution. Such hybrid techniques proved to be accurate in predicting the low-velocity impact response of polymer composites [3].

In this work, a damage model is proposed for high velocity impact modelling based on the combined application of different modelling strategies, i.e. the application of plasticity, failure, damage mechanics and fracture mechanics. This work is an enhanced version of a model previously implemented in LS-DYNA3D [9, 10].

8.2 A Phenomenological Model for Predicting Material Non-linear Effects in UD Plies Under Compressive/Shear Loading Conditions

8.2.1 Premise

In UD polymer plies, compressive failure is ultimately driven by shear mechanisms. This is evident from visual examination of failed composite specimens: the fracture plane orientation for the case of transverse compressive failure is inclined to the loading directions and principal material symmetry axes. The non-linear behaviour of composites under loading conditions that promote matrix deformation indicates that failure is, for these loading cases, a progressive and continuous process. The term "progressive failure", or "damage", can be used in a macro-mechanical framework to define the physical processes that result in degradation of composites mechanical properties, such as plasticity, matrix micro-cracking or a combination of both. In the present work, "progressive failure" is assumed to be driven by shear mechanisms.

8.2.2 Outline of the Modelling Approach

In [11], Puck and Schurmann discuss an adaptation of the Mohr-Coulomb failure criterion for predicting composite failure in the transverse matrix compressive/shear:

$$f_{mc} = \left(\frac{\tau_T}{S_T - \mu_T \sigma_n}\right)^2 + \left(\frac{\tau_L}{S_L - \mu_L \sigma_n}\right)^2 \tag{8.1}$$

In this equation the traction components τ_T, τ_L and σ_n on the potential fracture plane are computed from stress rotation in the (bc) plane. The (abc) reference is defined as proposed in [9]. S_T and S_L are the traction strength on the fracture plane, μ_T and μ_L are the friction coefficients. This criterion was later adopted in [9] where orthotropic friction coefficients are derived for a composite lamina.

In [2, 10] this failure criterion was expressed for 2D and 3D applications, respectively. Since the orientation of the potential fracture plane cannot be known a priori for the generic multi-axial case, the definition of "potential fracture plane" was proposed in [2], and successfully implemented in FE for numerical applications in [10]. The tractions calculated on this plane are those that maximise the functional part of Eq. (8.1). For a specimen failed in transverse compression, it can be assumed that the plane in which cracking and plasticity primarily occur is coincident with the fracture plane. This implies that the "potential fracture plane" can be used to define the orientation of a plane on which progressive failure is likely to accumulate in a composite volume under generic loading conditions. Thus, the plane of progressive failure is here defined as:

$$\begin{cases} f_{cr}(\phi) = \left(\dfrac{\tau_T(\phi)}{S_T - \mu_T \sigma_n(\phi)}\right)^2 + \left(\dfrac{\tau_L(\phi)}{S_L - \mu_L \sigma_n(\phi)}\right)^2 \\ \overline{\phi} : f_{cr}\left(\overline{\phi}\right) > f_{cr}(\phi) \forall \phi \in [0, \pi[\end{cases} \tag{8.2}$$

In the framework of progressive failure modelling, the plane of micro-damage development is the potential plane defined by Eq. (8.2). However, Eq. (8.2) does not predict whether micro-damage has or has not yet initiated, and progressive failure can be predicted only when further data is available. The required information is obtained from pure shear loading data. Compressive stress acting perpendicularly to the progressive failure plane is assumed to delay damage propagation, and the approach to model these effects will be discussed in the later Sect. 8.2.4 of this paper.

8.2.3 Shear Non-linear Stress-Strain Behaviour

Non-linear shear stress-strain functions are used for modelling material non-linearity in the generic loading case. The non-linear shear stress-strain curves in the (ab), (bc) and (ac) planes are required by the model. For the accurate modelling of unloading situations, data will also be required from cyclic loading-unloading shear testing. The generic non-linear shear stress-strain curve is modelled using incremental calculation as follows:

$$\begin{aligned} \Delta\tau^{el} &= G_0 \Delta\gamma \\ \tau^{n+1} &= \tau^n + f(\gamma^n)\Delta\tau^{el} \end{aligned} \tag{8.3}$$

With:

$$f(\gamma^n) = \frac{\Delta\left(\sum_{k=1}^{N} a_k (\gamma^n)^k\right)}{G_0 \Delta\gamma} = \frac{\sum_{k=1}^{N} k a_k (\gamma^n)^{k-1}}{G_0} \tag{8.4}$$

Where the a_k coefficients are derived from polynomial data fitting of (τ, γ) experimental data points. The function $f(\gamma)$ defines the relationship between the tangent shear stiffness normalised to the initial stiffness and the shear strain. The unloading path from an arbitrary state is predicted assuming no hysteresis but shear stiffness reduction with strain. The current strain upon unloading is defined as the additive sum of a permanent strain γ_P, and an elastic strain γ_{el}:

$$\gamma^n = \gamma_{el}^n + \gamma^{n_p} \tag{8.5}$$

When the elastic strain has been fully recovered, at which point the shear stress has reduced to zero, if the shear strain continues to decrease it is also assumed that this occurs with no internal stress generated in the material:

$$\begin{aligned} &\Delta\tau^{el} = G_0 \Delta\gamma \\ &\left|\gamma_p^{\overline{n}}\right| < |\gamma| < \left|\gamma^{\overline{n}}\right| \rightarrow \tau_{un}^{n+1} = \tau^n + \left(d_0 + d_1\gamma^{\overline{n}}\right)\Delta\tau^{el} \\ &|\gamma| < \left|\gamma_p^{\overline{n}}\right| \rightarrow \tau_{un}^{n+1} = \tau^n \equiv 0 \\ &|\gamma| > \left|\gamma^{\overline{n}}\right| \rightarrow \tau^{n+1} = \tau^n + f(\gamma^n)\Delta\tau^{el} \end{aligned} \tag{8.6}$$

In this Eq. (8.6), $\overline{n}$ is the step of the analysis at which the unloading process begins; $\gamma_p^{\overline{n}}$ is the permanent strain measured upon complete recovery of the elastic strain ($\gamma_p^{\overline{n}}$ is defined for $\tau^{\overline{n}} = 0$ upon unloading). This formulation ensures that the numerical damage process is irreversible. The d_0 and d_1 parameters are characterised by measuring the gradual shear stiffness reduction in cyclic loading-unloading shear testing as discussed in [12]. Figure 8.1 shows a comparison between the model prediction and experimental results published in [8].

8.2.4 Modelling Effects of Mechanical (or "Internal") Friction on Progressive Failure Development

The initiation of fracture in loaded composites is inhibited for superimposed hydrostatic pressure confinement [15], which results in compressive strength increase. It is assumed here that also progressive failure is affected by friction effects. In the open literature, composites have been defined as "brittle", e.g. [2,9,11], or "plastic", e.g. [1]. It is worth noting that in Eq. (8.1) two "mechanical" friction coefficients are defined, whose use is strictly meaningful for modelling brittle behaviour. Ward [18] defined an "internal stress" for polymers which represents the resistance to molecular flow during inelastic straining. In previously published works that have used the Mohr-Coulomb theory [2, 9, 11], the values for the (mechanical) friction coefficients were computed from measured compressive strength values and geometry arguments, i.e. not from tribology arguments. Thus there is no evidence of whether the friction coefficients used within this theory, when applied to polymer composites, are a representation of mechanical friction effects or of "internal" friction effects. An "internal friction parameter" η_ε is thus defined here, which is used to

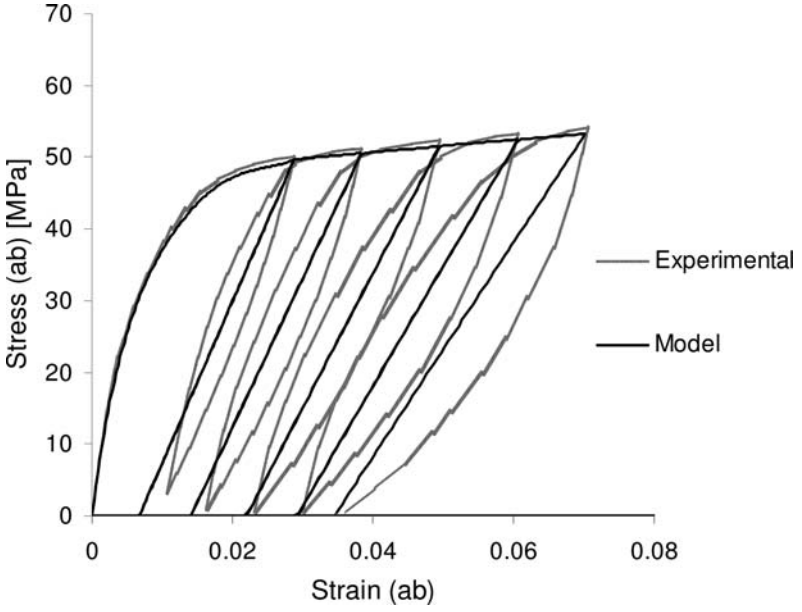

Fig. 8.1 Model prediction vs. experimental results, these are from [8]

scale the amount of progressive failure that develops under confinement for combined compressive/shear loading conditions. The proposed interpretation can justify the modelling of a damaging plastic material with a Mohr-Coulomb theory based approach. For ease of implementation the parameter η_ε is here defined in the strain space as:

$$\begin{aligned} \varepsilon_V < 0 &\rightarrow \gamma_{eff} = \langle |\gamma_{el}| + \eta_\varepsilon \varepsilon_V \rangle \\ \varepsilon_V > 0 &\rightarrow \gamma_{eff} = |\gamma_{el}| \end{aligned} \tag{8.7}$$

Where $\langle\ \rangle$ are McCauley brackets and the volumetric strain ε_V is defined as the sum of the three extensional strains:

$$\varepsilon_V = \varepsilon_a + \varepsilon_b + \varepsilon_c \tag{8.8}$$

A definition for η_ε such as in Eq. (8.7) is a practical solution. For instance, the coupling between the hydrostatic stress and the deviatoric stress field is not explicitly accounted for when adopting such a definition. Other definitions are possible and experimental studies are needed for developing a model of a more fundamental nature. The function $f(\gamma^n)$, Eq. (8.4), can be applied to predict shear driven progressive failure in a compressed material as:

$$f(\gamma) = \frac{\sum_{k=1}^{N} a_k \left(\langle \gamma_{eff} \rangle \right)^{k-1}}{G_0} \tag{8.9}$$

And the shear stress update procedure takes the following form:

$$\tau^{n+1} = \tau^n + f\left(\gamma_{eff}^n\right) \Delta\tau^{el} \tag{8.10}$$

The predicted $\left(\tau, \gamma_{eff}\right)$ behaviour reduces to the characterised shear stress-strain curve for the pure shear loading case, in which case $\varepsilon_V = 0$.

8.2.5 Modelling Progressive Failure in Matrix Dominated Modes

The linear elastic vector stress increment at the current time of analysis is defined as:

$$\{\Delta\sigma\}_{abc} = [C]\{\Delta\varepsilon\}_{abc}\{\Delta\sigma_a \;\; \Delta\sigma_b \;\; \Delta\sigma_c \;\; \Delta\tau_{ab} \;\; \Delta\tau_{bc} \;\; \Delta\tau_{ac}\}^T \tag{8.11}$$

In which $[C]$ is the orthotropic stiffness matrix and the notation $\{\ \}_{abc}$ is used to define a vector in (abc) material axes. Assuming small time increments (time-steps) and noting that Eq. (8.2) is a function of solely total quantities, and when using a limited number of trial angles [2, 10] the orientation of the plane of cracks nucleation at the current time of analysis can be assumed to be the same orientation that was predicted at the end of the previous time-step, i.e. $\overline{\phi}^n \cong \overline{\phi}^{n-1}$. Providing that the time steps are small, as it is the case in explicit FE models, this is an acceptable approximation. The linear elastic vector stress increment $\{\Delta\sigma\}_{abc}$ is rotated to the coordinate system $(ab'c')$, which is defined by a rotation of the (abc) reference around the a axis of the angle $\overline{\phi}^{n-1}$:

$$\begin{aligned} &\{\Delta\sigma\}_{abc} \xrightarrow{\phi^{n-1}} \{\Delta\sigma\}_{ab'c'} \\ &\{\Delta\sigma\}_{ab'c'} = \{\Delta\sigma_a \;\; \Delta\sigma_{b'} \;\; \Delta\sigma_{c'} \;\; \Delta\tau_{ab'} \;\; \Delta\tau_{b'c'} \;\; \Delta\tau_{ac'}\} \end{aligned} \tag{8.12}$$

In a similar fashion the current vector strain increment is defined in principal material axes (abc) as:

$$\{\Delta\varepsilon\}_{abc} = \{\Delta\varepsilon_a \;\; \Delta\varepsilon_b \;\; \Delta\varepsilon_c \;\; \Delta\gamma_{ab} \;\; \Delta\gamma_{bc} \;\; \Delta\gamma_{ac}\} \tag{8.13}$$

and it is rotated to the plane of progressive failure:

$$\begin{aligned} &\{\Delta\varepsilon\}_{abc} \xrightarrow{\phi^{n-1}} \{\Delta\varepsilon\}_{ab'c'} \\ &\{\varepsilon\}_{ab'c'}^n = \{\varepsilon\}_{ab'c'}^{n-1} + \{\Delta\varepsilon\}_{ab'c'} \end{aligned} \tag{8.14}$$

The non-linear effects are modelled in the rotated reference frame by updating the relevant numerical shear functions:

$$\begin{aligned}
&\{\Delta\widetilde{\sigma}\}_{ab'c'} = \{\Delta\sigma_a \;\; \Delta\sigma_{b'} \;\; \Delta\sigma_{c'} \;\; \Delta\widetilde{\tau}_{ab'} \;\; \Delta\widetilde{\tau}_{b'c'} \;\; \Delta\widetilde{\tau}_{ac'}\} \\
&\Delta\widetilde{\tau}_{ab'} = f\left(\gamma^{n_{ab',\,eff}}\right)\Delta\tau^{el}_{ab'} \\
&\Delta\widetilde{\tau}_{b'c'} = f\left(\gamma^{n_{b'c',\,eff}}\right)\Delta\tau^{el}_{b'c'} \\
&\Delta\widetilde{\tau}_{ac'} = f\left(\gamma^{n_{ac',\,eff}}\right)\Delta\tau^{el}_{ac'}
\end{aligned} \tag{8.15}$$

The incremental stress state is defined upon unloading as:

$$\begin{aligned}
&\{\Delta\widetilde{\sigma}\}_{ab'c'} = \{\Delta\sigma_a \;\; \Delta\sigma_{b'} \;\; \Delta\sigma_{c'} \;\; \Delta\widetilde{\tau}_{ab'} \;\; \Delta\widetilde{\tau}_{b'c'} \;\; \Delta\widetilde{\tau}_{ac'}\} \\
&\Delta\widetilde{\tau}_{b'c'} = f\left(d_{0,bc} + d_{1,bc}\gamma^{\overline{n}}_{b'c',\,eff}\right)\Delta\tau^{el}_{b'c'} \\
&\Delta\widetilde{\tau}_{ab'} = f\left(d_{0,ab} + d_{1,ab}\gamma^{\overline{n}}_{ab',\,eff}\right)\Delta\tau^{el}_{ab'} \\
&\Delta\widetilde{\tau}_{ac'} = f\left(d_{0,ac} + d_{1,ac}\gamma^{\overline{n}}_{ac',\,eff}\right)\Delta\tau^{el}_{ac'}
\end{aligned} \tag{8.16}$$

The coefficients for the empirical functions $f(\gamma)$, and the parameters d_0 and d_1 are determined from experimental data fitting. Equations 8.15 and 8.16 define the "damaged" vector stress increment $\{\Delta\widetilde{\sigma}\}_{ab'c'}$ (function of the "damaged" shear stress increments $\Delta\widetilde{\tau}_{b'c'}$, $\Delta\widetilde{\tau}_{ab'}$ and $\Delta\widetilde{\tau}_{ac'}$), which is rotated back to principal material axes (abc):

$$\{\Delta\widetilde{\sigma}\}_{ab'c'} \xrightarrow{-\phi^{n-1}} \{\Delta\widetilde{\sigma}\}_{abc} \tag{8.17}$$

The "damaged" stress increment $\{\Delta\widetilde{\sigma}\}_{abc}$ is finally used to update the total stress state:

$$\{\sigma\}^{n+1}_{abc} = \{\sigma\}^{n}_{abc} + \{\Delta\widetilde{\sigma}\}_{abc} \tag{8.18}$$

As a result of the back-rotation Eq. (8.17) the incremental stress vector $\{\Delta\widetilde{\sigma}\}_{abc}$ has five components that are affected by the non-linear effects: component in direction b and c and all three shear components. The model requires a value for the internal friction parameter η_ε before it can be applied in the generic case. In this work this will be done by predicting the uni-directional transverse compressive behaviour of the composite for different assigned values of η_ε, iteratively, until a best match between the numerical and the experimental curves is achieved.

8.2.6 Validation of the 3D Plasticity Model

Comparison between experimental and numerical results is presented in Fig. 8.2 for the case of a T300/914 CFRP UD composite under transverse compression (transverse shear and transverse compressive experimental stress-strain data for this material is published in [7]).

The most interesting capability of the model is that it can predict realistic unloading paths in the stress-strain space for the transverse compressive mode, with associated stiffness reduction.

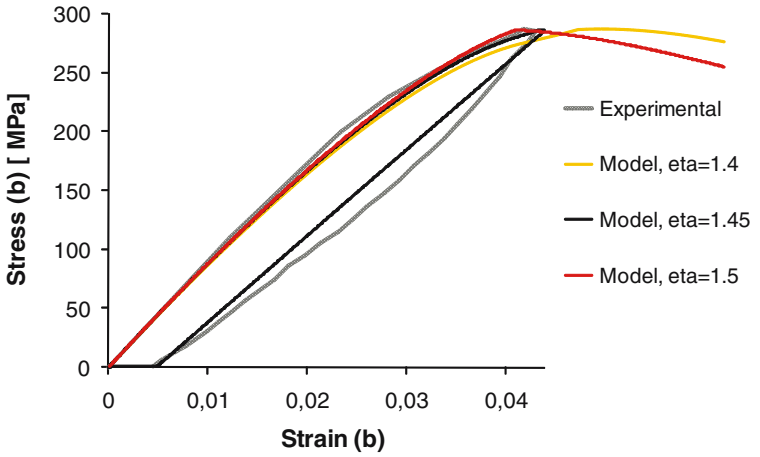

Fig. 8.2 Transverse compressive stress-strain behaviour of a T300/914 CFRP UD composite, experimental curve from [7] and numerical prediction

8.3 Modelling Strain Rate Effects in Compression

8.3.1 Premise and Outline Modelling Approach

Matrix dominated mechanical properties of polymer composites are rate sensitive, and the pure shear mode appears the most strain rate sensitive mode of deformation in laminated composites, e.g. [13]. Thus, it can be argued that strain rate sensitivity in modes other than shear is a 3D effect, due to the fact that the planes of maximum shear stress are at an angle to the principal planes of material symmetry. For example, strain rate induced hardening in metals can be explained by the theory of dislocations. The motion and slipping of dislocations is governed by shear forces at the lattice scale, e.g. [17]. When the (shear) loading rate increases and overcomes the rate of recovery, more dislocations are generated and entangle, which is the reason for strain rate material hardening experimentally observed for these materials. A similar interpretation is typically given for polymers: their micro-structure is composed of molecular chains which flow with deformation [18].

8.3.2 Shear Strain Rate Dependent Behaviour

Non-linear strain rate dependent functions are used only for the pure shear stress-strain behaviour when modelling material non-linear strain rate dependent response in 3D. For applicability of the 3D model, all the three shear stress-strain behaviours in the (*ab*), (*bc*) and (*ac*) planes, would need characterising under static and dynamic loading. However this data is seldom available; thus it is here assumed the composite has same shear strain rate sensitivity when deformed in either (*ab*), (*bc*) or (*ac*)

shear. The generic strain rate dependent shear law is modelled by using a scaling function, $T(\dot{\gamma}^n)$, and incremental calculation as follows:

$$\tau^{n+1} = \tau^n + T(\dot{\gamma}^n) f(\gamma^{n\,eff}) \Delta\tau \tag{8.19}$$

where $f(\gamma^{n\,eff})$ is defined in Sect. 8.2.4. $\dot{\gamma}^n$ is the current shear strain rate, which is defined as:

$$\dot{\gamma}^n = \frac{\Delta\gamma}{\Delta t} \tag{8.20}$$

In which $\Delta\gamma$ is the shear strain increment at the current time step, Δt and $T(\dot{\gamma})$ is a scaling function of shear strain rate, which is characterised using pure longitudinal static and dynamic stress-strain data, as shown in [12].

8.3.3 Modelling Strain Rate Effects in Matrix Dominated Modes of Deformation

Strain rate effects are modelled on the plane of maximum shear stress (with friction) interaction as:

$$\begin{aligned}
\{\Delta\tilde{\sigma}\}_{ab'c'} &= \left\{\Delta\sigma_a \;\; \Delta\sigma_{b'} \;\; \Delta\sigma_{c'} \;\; \Delta\bar{\bar{\tau}}_{ab'} \;\; \Delta\bar{\bar{\tau}}_{b'c'} \;\; \Delta\bar{\bar{\tau}}_{ac'}\right\} \\
\Delta\bar{\bar{\tau}}_{b'c'} &= T(\dot{\gamma}^n_{b'c'}) f\left(\gamma^n_{b'c',\,eff}\right) \Delta\tau_{b'c'} \\
\Delta\bar{\bar{\tau}}_{ab'} &= T(\dot{\gamma}^n_{ab'}) f\left(\gamma^n_{ab',\,eff}\right) \Delta\tau_{ab'} \\
\Delta\bar{\bar{\tau}}_{ac'} &= T(\dot{\gamma}^n_{ac'}) f\left(\gamma^n_{ac',\,eff}\right) \Delta\tau_{ac'}
\end{aligned} \tag{8.21}$$

Upon unloading the constitutive law is assumed as follows:

$$\begin{aligned}
\{\Delta\tilde{\sigma}\}_{ab'c'} &= \left\{\Delta\sigma_a \;\; \Delta\sigma_{b'} \;\; \Delta\sigma_{c'} \;\; \Delta\bar{\bar{\tau}}_{ab'} \;\; \Delta\bar{\bar{\tau}}_{b'c'} \;\; \Delta\bar{\bar{\tau}}_{ac'}\right\} \\
\Delta\bar{\bar{\tau}}_{b'c'} &= \left(d_{0,bc} + d_{1,bc}\gamma^{\bar{n}}_{b'c'},\; eff\right) T(\dot{\gamma}^n_{b'c'}) \Delta\tau_{b'c'} \\
\Delta\bar{\bar{\tau}}_{ab'} &= \left(d_{0,ab} + d_{1,ab}\gamma^{\bar{n}}_{ab'},\; eff\right) T(\dot{\gamma}^n_{ab'}) \Delta\tau_{ab'} \\
\Delta\bar{\bar{\tau}}_{ac'} &= \left(d_{0,ac} + d_{1,ac}\gamma^{\bar{n}}_{ac'},\; eff\right) T(\dot{\gamma}^n_{ac'}) \Delta\tau_{ac'}
\end{aligned} \tag{8.22}$$

The stress increment vector is then rotated back to material principal axes. The 3D rotation results in more components of the stress increment vector that are strain rate dependent.

8.3.4 Validation of the 3D Strain-Rate Dependent Plasticity Model

Single solid element simulations are conducted at constant strain rate and the numerical results are compared with the experimental data available in the open literature, Hsiao et al. [5]. They investigated the effect of strain rate on the mechanical

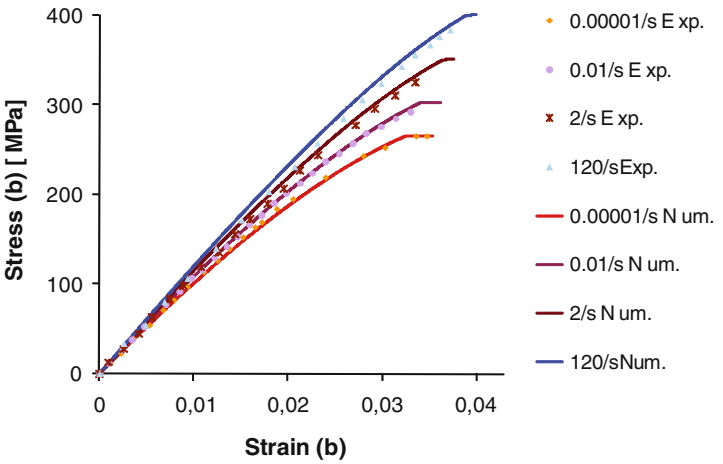

Fig. 8.3 Transverse compressive stress-strain numerical and experimental curves for UD IM6G/3501-6 carbon/epoxy under quasi-static and dynamic loading

compressive properties of IM6G/3501-6 Carbon/Epoxy thick laminates. A comparison between the predicted and the experimental stress-strain curves is shown in Fig. 8.3.

It is important to note that in this case, both the polynomial coefficients for the non-linear transverse shear behaviour and the internal friction parameter were assumed. The results however show that very good match of the experimental transverse compressive behaviour of the composite at different strain rates can be obtained. Realistic shear (*bc*) behaviour was assumed. Despite the proved capability of the formulation in predicting 3D strain-rate effects with no extensive need for data fitting, further detailed testing is deemed necessary for the rigorous validation of the model.

8.4 Strain-Rate Dependent Energy-Based Damage Mechanics Approach

A 3D energy based damage formulation was proposed and implemented in LS-DYNA3D [10] for a composite with non-linear in-plane shear behaviour. The material model here developed simulates non-linear strain-rate-dependent material behaviour in 3D. Thus, the approach for matrix damage propagation described in [10] is reformulated to account for 3D non-linear and strain-rate dependent material response. The dynamic matrix failure criteria, which are used in the present work to predict onset of matrix damage, are fully discussed in [14].

The orientation of the fracture plane at matrix failure onset is $\overline{\phi}^0$. The linear elastic vector stress increment $\{\Delta\sigma\}_{abc}$ is rotated to the coordinate system $(ab'c')$, which is defined by a rotation of the (abc) reference around the a axis of the angle $\overline{\phi}^0$:

$$\begin{aligned} &\{\Delta\sigma\}_{abc} \xrightarrow{\overline{\phi}^0} \{\Delta\sigma\}_{ab'c'} \\ &\{\Delta\sigma\}_{ab'c'} = \{\Delta\sigma_a \;\; \Delta\sigma_{b'} \;\; \Delta\sigma_{c'} \;\; \Delta\tau_{ab'} \;\; \Delta\tau_{b'c'} \;\; \Delta\tau_{ac'}\} \end{aligned} \tag{8.23}$$

When the criterion for matrix failure is met, the tractions have exceeded the traction strengths on the potential fracture plane. It was noted in [10] that at onset of matrix failure, while the energy absorbed due to the non-linear shear behaviour is proportional to the volume of the specimen, the energy absorbed by the fracture process is proportional to the area created. Thus only the elastic internal energy in the element at onset of failure contributes to the matrix fracture process. Stress increments are then computed for loading as:

$$f_m = 1 \rightarrow \begin{cases} \{\Delta\widetilde{\sigma}\}_{ab'c'} = \{\Delta\sigma_a \;\; \Delta\sigma_{b'} \;\; \Delta\sigma_{c'} \;\; \Delta\widetilde{\tau}_{ab'} \;\; \Delta\widetilde{\tau}_{b'c'} \;\; \Delta\widetilde{\tau}_{ac'}\} \\ \Delta\widetilde{\tau}_{ab'} = f\left(\gamma^n_{ab',\,eff}\right)\Delta\tau^{el}_{ab'} \\ \Delta\widetilde{\tau}_{b'c'} = f\left(\gamma^n_{b'c',\,eff}\right)\Delta\tau^{el}_{b'c'} \\ \Delta\widetilde{\tau}_{ac'} = f\left(\gamma^n_{ac',\,eff}\right)\Delta\tau^{el}_{ac'} \end{cases} \tag{8.24}$$

And for unloading as:

$$f_m = 1 \rightarrow \begin{cases} \{\Delta\widetilde{\sigma}\}_{ab'c'} = \{\Delta\sigma_a \;\; \Delta\sigma_{b'} \;\; \Delta\sigma_{c'} \;\; \Delta\widetilde{\tau}_{ab'} \;\; \Delta\widetilde{\tau}_{b'c'} \;\; \Delta\widetilde{\tau}_{ac'}\} \\ \Delta\widetilde{\tau}_{ab'} = T\left(\dot{\gamma}_{ab'}\right)\left(d_{0,ab} + d_{1,ab}\gamma^0_{ab',\,eff}\right)\Delta\tau^{el}_{ab'} \\ \Delta\widetilde{\tau}_{b'c'} = T\left(\dot{\gamma}_{b'c'}\right)\left(d_{0,bc} + d_{1,bc}\gamma^0_{b'c',\,eff}\right)\Delta\tau^{el}_{b'c'} \\ \Delta\widetilde{\tau}_{ac'} = T\left(\dot{\gamma}_{ac'}\right)\left(d_{0,ac} + d_{1,ac}\gamma^0_{ac',\,eff}\right)\Delta\tau^{el}_{ac'} \end{cases} \tag{8.25}$$

Where $f_m = 1$ indicates that the failure criterion for matrix compressive failure is met. The matrix damage driving strain, ε_{mat}, is here defined as:

$$\varepsilon_{mat} = \frac{\left\langle \sigma^n_{b'} \right\rangle}{\sigma^n_{b'}}\varepsilon^{el}_{b'}\sin\omega + \left|\gamma^{el}_{b'c'}\cos\lambda + \gamma^{el}_{ab'}\sin\lambda\right| \tag{8.26}$$

In which $\langle\,\rangle$ are McCauley brackets, the angles ω and λ are defined in Fig. 8.4 in [10] and:

$$\begin{aligned} \varepsilon^{el}_{b'} &= \frac{1}{2}\left[(\varepsilon_b + \varepsilon_c) + (\varepsilon_b - \varepsilon_c)\cos\left(2\overline{\phi}^0\right) + \gamma^{el}_{bc,eff}\sin\left(2\overline{\phi}^0\right)\right] \\ \gamma^{el}_{b'c'} &= \frac{\tau^n_{b'c'}}{\left(d_{0,b'c'} + d_{1,b'c'}\gamma^0_{b'c',\,eff}\right)G_{b'c'}} \\ \gamma^{el}_{ab'} &= \frac{\tau^n_{ab'}}{\left(d_{0,ab'} + d_{1,ab'}\gamma^0_{ab',\,eff}\right)G_{ab'}} \end{aligned} \tag{8.27}$$

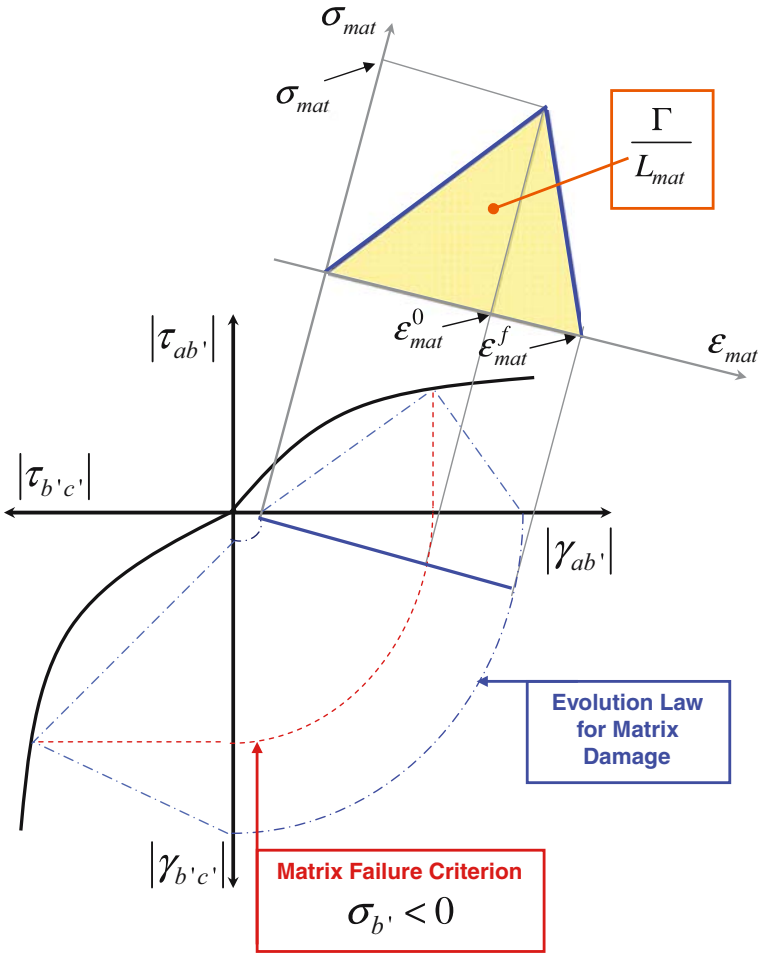

Fig. 8.4 Non-linear Damage Mechanics approach for matrix compressive failure (static loading)

With:

$$\gamma^{el}_{bc,\,eff} = \frac{\tau^0_{bc}}{G_{bc}\left(d_{0,bc} + d_{1,bc}\gamma^0_{bc,\,eff}\right)} \tag{8.28}$$

In which $\gamma^0_{bc,eff}$ is obtained from rotation of the strain vector from the plane of fracture propagation to the principal material axes.

The matrix damage evolution law is defined as proposed in [10]:

$$d_{mat} = \max\left\{0, \min\left\{1, \varepsilon^f_{mat}\frac{\varepsilon_{mat} - \varepsilon^0_{mat}}{\varepsilon_{mat}\left(\varepsilon^f_{mat} - \varepsilon^0_{mat}\right)}\right\}\right\} \tag{8.29}$$

In which ε_{mat}^{f} is defined as:

$$\varepsilon_{mat}^{f} = \frac{2\overline{\Gamma}}{\sigma_{mat}^{0} L_{mat}} \tag{8.30}$$

The driving stress at the onset of matrix failure, σ_{mat}^{0}, is defined as [10]:

$$\sigma_{mat}^{0} = \sqrt{\left(\sigma_{b'}^{n}\right)^{2} + \left(\tau_{b'c'}^{n}\right)^{2} + \left(\tau_{ab'}^{n}\right)^{2}} \tag{8.31}$$

Equation 8.30 indirectly depends on strain rate through the "dynamic matrix fracture toughness" $\overline{\Gamma}$. This is a function of strain rate defined by assuming that a relationship of direct proportionality exists between shear traction strengths and fracture toughness: the same scaling function that was used for predicting the enhancement of shear strength with strain rate is used for scaling fracture toughness with strain rate:

$$\overline{\Gamma} = \Gamma_{b} \left\langle \frac{\sigma_{b'}^{0}}{\sigma_{mat}^{0}} \right\rangle^{2} + z\left(\dot{\gamma}_{b'c'}\right) \Gamma_{b'c'} \left\langle \frac{\tau_{b'c'}^{0}}{\sigma_{mat}^{0}} \right\rangle^{2} + z\left(\dot{\gamma}_{ab'}\right) \Gamma_{ab'} \left\langle \frac{\tau_{ab'}^{0}}{\sigma_{mat}^{0}} \right\rangle^{2} \tag{8.32}$$

This is a simplification and dynamic fracture energies should be experimentally characterised. However, the formulation proposed here can be used with an arbitrary scaling function.

The stress vector is then updated on the fracture plane as follows:

$$\{\widetilde{\sigma}\}_{ab'c'}^{n+1} = \{\sigma_{a} \;\; \sigma_{b'} \;\; \sigma_{c'} \;\; \widetilde{\tau}_{ab'} \;\; \widetilde{\tau}_{b'c'} \;\; \widetilde{\tau}_{ac'}\}^{n+1} = \{\widetilde{\sigma}\}_{ab'c'}^{n} + \{\Delta\widetilde{\sigma}\}_{ab'c'} \tag{8.33}$$

And the relevant stresses are degraded on this plane:

$$\begin{aligned}
\left(\sigma_{a}^{n+1}\right)^{d_{mat}} &= \sigma_{a}^{n+1} \\
\left(\sigma_{b'}^{n+1}\right)^{d_{mat}} &= \left(1 - d_{mat}^{inst} \frac{\left\langle \sigma_{b'}^{n+1} \right\rangle}{\widetilde{\sigma}_{b'}^{n+1}}\right) \sigma_{b'}^{n+1} \\
\left(\sigma_{c'}^{n+1}\right)^{d_{mat}} &= \sigma_{c'}^{n+1} \\
\left(\widetilde{\tau}_{ab'}^{n+1}\right)^{d_{mat}} &= \left(1 - d_{mat}^{inst}\right) \widetilde{\tau}_{ab'}^{n+1} \\
\left(\widetilde{\tau}_{b'c'}^{n+1}\right)^{d_{mat}} &= \left(1 - d_{mat}^{inst}\right) \widetilde{\tau}_{b'c'}^{n+1} \\
\left(\widetilde{\tau}_{ac'}^{n+1}\right)^{d_{mat}} &= \widetilde{\tau}_{ac'}^{n+1}
\end{aligned} \tag{8.34}$$

$\left\{\widetilde{\sigma}^{n+1}\right\}^{d}_{ab'c'}$, the damaged stress vector defined on the plane of fracture propagation, is finally rotated back to the lamina axis:

$$\left\{\widetilde{\sigma}^{n+1}\right\}^{d}_{ab'c'} \xrightarrow{-\overline{\phi}^{0}} \left\{\sigma^{n+1}\right\}_{abc} \tag{8.35}$$

In Fig. 8.4, the DM approach for a non-linear material model is illustrated for the case of static compressive matrix failure.

8.5 Validation of the Impact Damage Model

Experimental impact tests were conducted with a gas-gun on carbon NCF/RTM6 Reduced Size (RS) composite coupons (and effects of target thickness, lay-up, impact angle and projectile density were investigated). The full set of data generated, instrumentation used and details of specimen geometry and boundary conditions during the tests are available in [12]. Numerical simulations of the impact tests were conducted with LS-DYNA3D. Both target and impactor are simulated using single-point integration solid elements available in LS-DYNA [4]. The impactor is simulated as a rigid body and each individual ply of the composite target is simulated using the damage model with features which have been described in this paper. The definition of a strategy for elements erosion is necessary for successfully simulating ballistic penetration using Lagrangian FE approaches. Distorted elements must be eliminated for two main reasons, i.e. (1) Experimental evidence: composite fragments are driven off the target during penetration; (2) Stability of the numerical analysis: the Lagrangian local reference frame is fixed to the base of a solid element and is oriented depending on the base nodes numbering and their relative position. If the elements distort severely and the nodes undergo relative movement the Lagrangian approach becomes inaccurate [4]. Thus, elements that are too distorted, rather than elements that have "failed", should be deleted from the mesh. The criterion for element erosion takes the following form:

$$f_{erosion} = \min\left(f_{ft}, \max\left(\gamma_{ab}, \gamma_{bc}, \gamma_{ac}\right) - \Omega\right) = 0 \tag{8.36}$$

In which Ω is a user-defined parameter, i.e. $\Omega = 1.25$ for the current simulations. Figures 8.5, 8.6 and 8.7 show a selection of results from the impact tests and simulations using the proposed model. Very good correlation is obtained between experimental and numerical ballistic curves. All the composite impact test coupons were weighed before and after impact. The numerical debris mass loss was computed based on the number, volume and density of the eroded elements and compared against the mass loss which was characterized experimentally, see Fig. 8.7. No effects of lay-up were evident from both tests and simulations for both the $\sim$2 and $\sim$4 mm thick coupons.

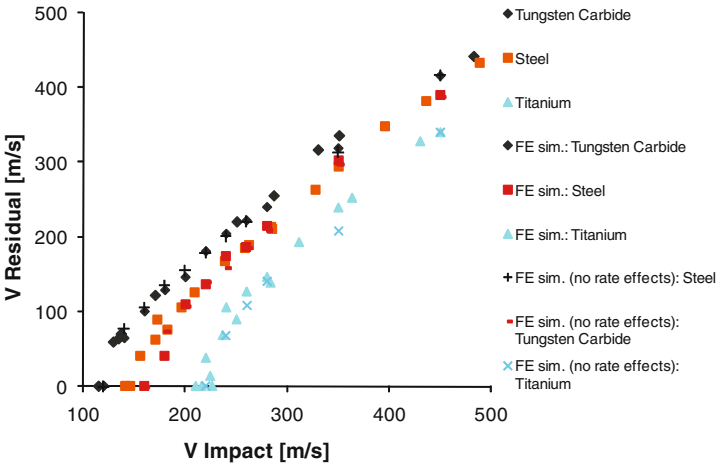

Fig. 8.5 Ballistic tests data and numerical results: effects of projectile density

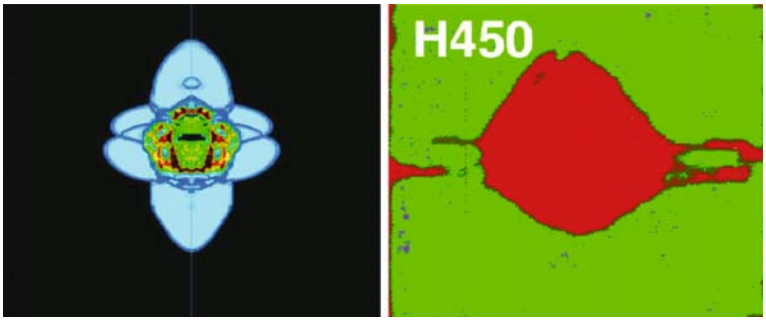

Fig. 8.6 Comparison of numerical (*left*) and experimental (*right*) impact damage areas for an impact at 260 m/s at 40° incidence

8.6 Conclusions

This paper has described the main features and the applicability of a numerical composite material model suitable for predicting the high velocity impact behaviour of polymer composites made with UD carbon fibrous reinforcement. The numerical results from over 70 simulations were reduced in the form of ballistic curves. A series of conclusions can be drawn:

- A good correlation is obtained between the numerical and the experimental ballistic curves for varying target thickness, impact angle, projectile material and target lay-up.
- The energy absorbed through ballistic penetration does not appear to be affected by strain-rate effects (Fig. 8.5), but the use of a strain-rate dependent failure

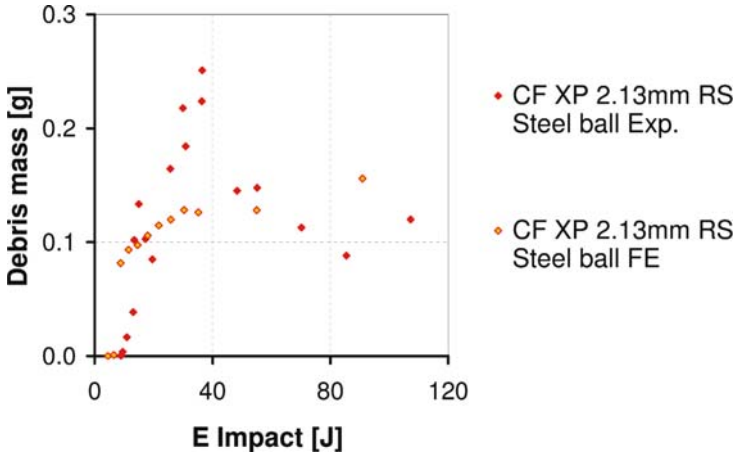

Fig. 8.7 Experimental and numerical debris mass variation with impact energy for CF cross-ply (XP) 2 mm RS coupons impacted by a steel ball at normal incidence

and damage formulation can improve the correlation between numerical and experimental damage areas, especially for higher impact velocities.

- The correlation between the numerical and the experimental matrix damage area is however not always satisfactory. The experimental damage area is underestimated by the model and this is found more evident for thicker specimens. This is because the smeared formulation applied here cannot predict fibre splitting and thus the lifting mechanism of split and broken fibres of the inner layers pushing on the rear-face ply of the target upon projectile penetration.
- Further numerical simulations could use interface elements.
- The results are strongly dependent on the strategy adopted for element erosion. However, the results presented in Fig. 8.7 would further validate the strategy adopted here.
- Meshless methods, such as SPH or partition of unity methods, which do not require a strategy for element erosion, would improve the performances of energy based damage models in which failure is predicted by the application of "directional" (or "modal") failure criteria.
- Experimental work should be conducted for characterisation of the dynamic fracture toughness of the composite in the failure modes predicted by the failure criteria that were applied.

Acknowledgements The authors would like to acknowledge the support from DSTL and the funding from the UK MoD. Professor P.T. Curtis and Dr. G.M. Wells are gratefully acknowledged for the useful discussions on any aspect of the research carried out in this work.

References

1. Chen JK, Allahdadi FA, Sun CT (1997) A quadratic yield function for fiber-reinforced composites. J Compos Mater 31:788–811
2. Dávila CG, Camanho PP, Rose CA (2005) Failure criteria for FRP laminates. J Compos Mater 39:323–346
3. Donadon MV (2005) The structural behaviour of composite laminates manufactured using resin infusion under flexible tooling. Ph.D. thesis, Imperial College London, UK
4. Hallquist JO (1998) LS-DYNA theorethical manual, version 970
5. Hsiao HM, Daniel IM, Cordes RD (1998) Dynamic compressive behavior of thick composite materials. Exp Mech 38:172–180
6. Iannucci L, Ankersen J (2006) An energy based damage model for thin laminated composites. Compos Sci Technol 66:934–951
7. Mesopoulet S (1999) Through-thickness test methods for laminated composite materials. Ph.D. thesis, Imperial College London, UK
8. vanPaepegem W, deBaere I, Degrieck J (2006) Modelling the nonlinear shear stress-strain response of glass fibre-reinforced composites. Part I: Experimental results. Compos Sci Technol 66:1455–1464
9. Pinho ST, Iannucci L, Robinson P (2006) Physically-based failure models and criteria for laminated fibre-reinforced composites with emphasis on fibre kinking. Part I: Development. Compos Part A 37:63–73
10. Pinho ST, Iannucci L, Robinson P (2006) Physically-based failure models and criteria for laminated fibre-reinforced composites with emphasis on fibre kinking. Part II: FE implementation. Compos Part A 37:766–777
11. Puck A, Schurmann H (2002) Failure analysis of FRP laminates by means of physically based phenomenological models. Compos Sci Technol 62:1633–1662
12. Raimondo L (2007) Predicting the dynamic behaviour of polymer composites. Ph.D. thesis, Imperial College London, UK
13. Raimondo L, Iannucci L, Robinson P et al. (2006) Investigating the strain rate effects on the mechanical properties of polymer composites: a review. Compos Sci Technol, paper Submitted for publication, 2006.
14. Raimondo L, Iannucci L, Robinson P et al. (2007) Predicting the dynamic behaviour of polymer composites. In: 16th International Conference on Composite Materials, Kyoto, Japan
15. Rhee KY, Pae KD (1995) Effects of hydrostatic pressure on the compressive properties of laminated, 0 unidirectional, graphite fiber/epoxy matrix thick-composite. J Compos Mater 29:1295–1307
16. Riedel W, Harwick W, White DM et al (2003) Adammo advanced material damage models for numerical simulation codes. Final report. Technical report, EMI
17. Smoluchowsky R (1957) Dislocation in solids. In: Goldman JE (ed) The science of engineering materials. John Wiley and Sons, New York
18. Ward IM (1982) Mechanical properties of solid polymers. Wiley, New York

Chapter 9
Progressive Damage Modeling of Composite Materials Under Both Tensile and Compressive Loading Regimes

N. Zobeiry, A. Forghani, C. McGregor, R. Vaziri, and A. Poursartip

Abstract A constitutive model is presented for the complete in-plane response of composite materials within the framework of a previously developed continuum damage mechanics model, CODAM. While the previous CODAM formulation was primarily developed to simulate the progression of damage under tensile loading, the proposed extension is guided by a mechanical analogue model that accounts for the initiation and propagation of damage mechanisms under both tension and compression. Calibration of the tensile damage parameters of the model using the over-height compact tension test (OCT) is presented. Simulations of notched panels under quasi-static in-plane tension and compression loading are used to demonstrate the effectiveness of the model in predicting the load-displacement response as well as the overall damage zone size. Finally, limitations of local smeared crack models are discussed and the preliminary results of a non-local approach to simulating damage progression that overcomes such limitations are presented.

9.1 Introduction

As composite materials are being increasingly used in industrial applications, the ability to confidently predict their response to various types of loading is becoming ever more important. Whether the interest is to assess the structural integrity of composites or to quantify their energy absorption capability, it is very desirable to have predictive analysis tools that capture the physics of the damage mechanisms and their propagation under general loading conditions including both tensile and compressive loads.

N. Zobeiry, A. Forghani, C. McGregor, R. Vaziri, and A. Poursartip
Composites Group, Departments of Civil Engineering and Materials Engineering, The University of British Columbia, 6250 Applied Science Lane, Vancouver, BC, Canada,
e-mail: reza.vaziri@ubc.ca

There are several issues related to the behaviour of composite materials that need to be addressed. One important problem is the prediction of failure and damage propagation from an imperfection under tension or compression loading. Composite components are likely to contain many discontinuities acting as stress raiser sites introduced either intentionally, e.g. cutouts and fastener holes, or unintentionally, e.g. fabrication defects and imperfections, mismatch between layers of different fibre orientations, misalignment of fibres and accidental damage. These defects can act as potential sites for the development and subsequent propagation of cracks.

There are some primary differences between the failure mechanisms in tension and compression. Tensile failure is most commonly due to fibre breakage and matrix cracking or yielding. However, depending on the laminate lay-up, failure can also involve delamination. For compressive failure the primary failure mechanism is kink banding, which is the formation of matrix cracking or yielding and fibre rotation in plies having their reinforcement aligned with the loading direction. This mechanism, along with delamination and off-axis matrix cracking, is most likely to occur in failure of composites under compression [24, 25].

The reduction of the mechanical properties of composite components caused by defects and the resulting reduction in their compressive load carrying capacity have received relatively little attention. Many researchers have undertaken studies to improve our understanding of compressive failure in composite materials. It is well recognized that there are two main sources responsible for compressive failure of composites: weak matrix properties and misalignment of fibres. These two sources can contribute to a number of different mechanisms as Fleck [7] presented in his comprehensive study on compressive failure mechanisms of unidirectional and notched multidirectional composite laminates. In his study, he categorized the main mechanisms of compressive failure for unidirectional composites as: elastic microbuckling, fibre crushing, splitting, buckle delamination, shear band formation and plastic micro-buckling or kinking. Bazant et al. [2] showed that the two distinct failure mechanisms in compressive failure of unidirectional laminates are delamination and kinking.

Recently, various micromechanical studies of the kinking failure as the main compressive failure mechanism of unidirectional composites have appeared in the literature. Based on the studies of Sutcliffe and Fleck [30] and Fleck et al. [8], a good understanding of the fracture mechanics aspects of kinking has been gained. These studies revealed the crack like behaviour of the kink band which was confirmed by Moran et al. [19] who discovered the phenomenon of band broadening whereby the damage zone grows under a constant remote stress.

As Shih and Moran [23] observed, there is little evidence of fibre breakage during the formation of the kink band. Fibre breakage in compression was observed after the formation of the first kink band during the band broadening process [26] when the damage zone, under further application of displacement, propagates into the undamaged interior materials. On the overall stress-strain response, this broadening of the kink band combined with fibre breakage and splitting results in a plateau stress after the softening. The various stages in the kinking process recorded by a video camera [19] are shown schematically in Fig. 9.1.

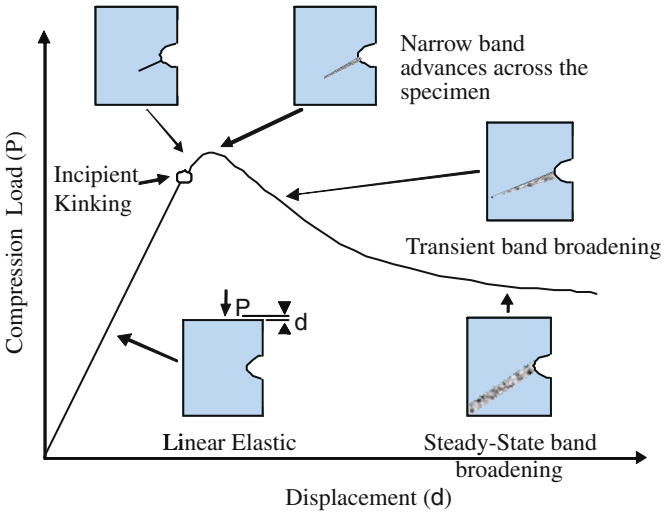

Fig. 9.1 Various stages of kink band formation (Reproduced from [19])

A few studies have focused on the micromechanics of damage propagation in multidirectional composites in compression [24, 25, 28, 29]. Sivashanker [24] presented a detailed account of micromechanical behaviour of three different multi-directional lay-ups of carbon-fibre epoxy composites. He identified the compressive failure process as one that emanates from out of plane micro-buckling of the 0° layers, off-axis layer damage and interface delamination between layers. He observed that micro-buckling in multidirectional laminates is accompanied by delamination in the vicinity of the micro-buckled zone. He also reported a similar behaviour for failure of unidirectional laminates including strain-softening response and kink-band broadening stage under a constant stress. For this band broadening stage, he reported a growth of delamination combined with the growth of kink band height. The constant plateau stress during band broadening stage was also observed and measured. This constant stress was mainly attributed to the steady state band broadening in the 0° layers and steady state delamination crack growth.

A brief review of the literature reveals the lack of a consistent description for composite materials failure under compression and tension. Only a few comprehensive models capable of simulating the mechanical behaviour of composite materials during the compressive and tensile failure exist (see for example [13, 14]). While it has been shown that the energy dissipated during the band broadening stage plays an important role in the response [32], band broadening phenomena and corresponding plateau stress in compression have been rarely formulated and implemented in commercial finite element codes. It is known that for a specific geometry and loading condition, the lay-up of the laminate plays an important role in the damage propagation process, formation of kink band, the plateau stress level and consequently energy dissipated during this process. All these aspects present challenges

for constructing a comprehensive model capable of capturing the true behaviour of composite materials under both compression and tension.

Rather than modeling the fracture as a discrete entity, a formidable computational task when there are a multitude of fracture planes, one can represent fracture in a smeared manner using continuum damage mechanics (CDM) models. In this manner fracture can be assumed to be damage propagating within a specific zone of a representative volume element (RVE) of the material resulting in a reduction of its stiffness and an overall strain-softening constitutive behaviour (i.e. stress reduction with increasing strain). Perhaps the best advantage of this method is its ease of implementation in commercial finite element codes.

It is well known that CDM based constitutive models when implemented in finite element codes result in numerical solutions that are not objective. In other words, with successive mesh refinement, damage localizes into a zone of zero volume and the numerical results fail to converge to a unique solution. To remedy this problem in a simple and computationally effective way, Bazant and Oh [3, 4] proposed the crack band theory according to which the product of the area under the stress-strain curve (in the softening regime) and the characteristic size of the RVE corresponds to the fracture energy, G_f. This fracture energy is assumed to be a material constant. Therefore, regardless of the choice of the mesh, which is a subjective aspect of numerical analyses, the overall energy dissipation due to damage and hence G_f must remain constant.

According to the crack band approach, damage localizes into a zone that is one element in height. This requires one to know the crack path a priori and design a mesh accordingly. Also the crack band method is applicable when the crack actually localizes, e.g. in quasi-static loading of notched specimens. In situations where a well-defined path for the crack propagation does not exist, e.g. in scenarios involving dynamic loading or quasi-static loading of un-notched specimens, where the damage pattern is rather diffused the crack band concept ceases to apply [1]. In such cases a non-local approach is generally recommended. Non-local methods can address the mesh size dependency problem as well as improve the unrealistic mesh orientation dependency of the classical smeared crack methods.

In this study, a constitutive model is presented for the complete in-plane response of composite materials within the framework of a previously developed continuum damage mechanics model, CODAM [31]. While the previous CODAM formulation was primarily developed to simulate the progression of damage under tensile loading, the proposed extension is guided by a mechanical analogue model that accounts for the initiation and propagation of damage mechanisms under both tension and compression, and load reversals (unloading) in each mode of loading.

The layout of this paper is as follows. Section 9.2 presents a descriptive outline of the analogue model that forms the physical basis for the new CODAM constitutive formulation. Section 9.3 briefly describes the over-height compact tension test (OCT) used to calibrate the tensile damage parameters of the model. Simulations of notched panels under tension and compression that are used for model validation are presented in Sect. 9.4. Section 9.5 outlines the limitations of local

smeared crack models and offers the preliminary results of a non-local approach to simulating damage progression that overcomes such limitations.

9.2 Description of the CODAM Model

To help with the development of the constitutive model, notably to account for the mechanisms under compression, a physically meaningful "analogue model" capable of simulating the behaviour of composite materials during the failure process in tension, compression and possible load reversals in each of these modes of loading is presented. This model consists of simple basic elements such as springs, fuses, gaps and sliders. The springs simulate the material stiffness which when combined with the fuses, can represent the failure of a RVE of composite under tension or compression. On the other hand, gaps and sliders in series with springs simulate the band broadening stage under compression. The proposed analogue model is shown in Fig. 9.2.

The model consists of an infinite number of gaps and springs (left part of Fig. 9.2a), which are in series with a slider element. This collection of elements is also in parallel with an infinite number of springs and fuses in series (right part of Fig. 9.2a). These elements are divided into two groups of elements (sub-models), namely, the Laminate and Rubble sub-models as shown in Fig. 9.2b.

A summary of the analogue model elements is presented here while more details can be found in references [17, 32, 33]. The laminate sub-model simulates the behaviour of the intact laminate in the process of damage propagation and represents the strain-softening behaviour of the composite material under tensile and compressive loads.

As damage progresses in the laminate, its overall strain-softening response is different under tension and compression. Under a tensile load, the softening is a consequence of the reduction in effective area due to fibre and matrix cracking.

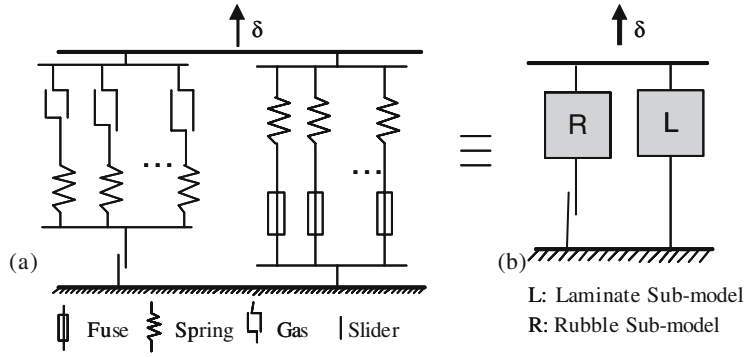

Fig. 9.2 (**a**) A schematic of the analogue model showing arrangement of basic elements, (**b**) a schematic of the analogue model showing the laminate and rubble sub-models

In compression, on the other hand, this softening occurs due to matrix cracking or yielding and fibre instability. In addition, the instability and rotation of the fibres combined with fibre breakage and splitting contribute to the overall softening behaviour under compression. In fact, in compression, matrix cracking leads to the instability of fibres which is not the case in tension.

The overall reduction in the laminate tangential stiffness, which leads to the softening behaviour, has been modeled using fuses and springs. Fuses fail sequentially upon application of a remote displacement to the laminate sub-model. This results in the overall stiffness reduction of the laminate sub-model and an ensuing softening behaviour similar to the composite response under tension.

The rubble sub-model represents the behaviour of the damaged material in compression. Upon reaching the damage initiation strain under compressive loads, the matrix starts to crack or yield resulting in the formation of multiple cracked surfaces or rubble. With further damage growth under compression, the friction between the newly cracked surfaces results in an increase in the load carrying capacity of the material. This damaged material can continue to carry compressive loads.

The behaviour of the rubble sub-model can be represented with an analogue model consisting of gap and spring elements to model the compressive load carrying response with an increasing stiffness. The gap element is inactive (open) before damage initiation. After damage initiates, new surfaces form resulting in an increased stiffness of the damaged material. This is modeled by sequential closure of the varying sized gaps in compression. By virtue of the gaps remaining open, the rubble sub-model cannot carry any load in tension.

The slider simulates the damage band (kink band) propagation. The yield strain is assumed to coincide with the saturation strain of the rubble sub-model. At the instant of final gap closure, the slider activates, indicating progressive specimen end shortening (damage zone broadening) under a constant applied load. This results in the damage propagation into the undamaged interior material and an increasing damage height for compressive failure.

Together, the Laminate and Rubble sub-models represent the overall response of the composite in the force-displacement space during progressive damage growth in tension or compression. Figure 9.3 shows a schematic example of the response of a RVE under controlled displacement loading based on the analogue model. First displacement is applied in the tensile mode until fibre and matrix damage occurs in the RVE. Subsequently the RVE is unloaded and then reloaded in the compressive regime. In this case, the initial reduced modulus (dashed line) compared to the undamaged modulus (solid curve) is due to the previous damage incurred in tension. After reaching a saturation state of matrix damage in the RVE, upon further application of displacement, the damage broadens into the undamaged material resulting in the band broadening phenomena and the corresponding plateau stress. The band broadening then continues up to the point of complete failure (fibre damage saturation).

The analogue model described above has been used to extend the compression modeling capabilities of a continuum damage mechanics model (CODAM) previously developed by Williams et al. [31] for gross damage development in polymeric

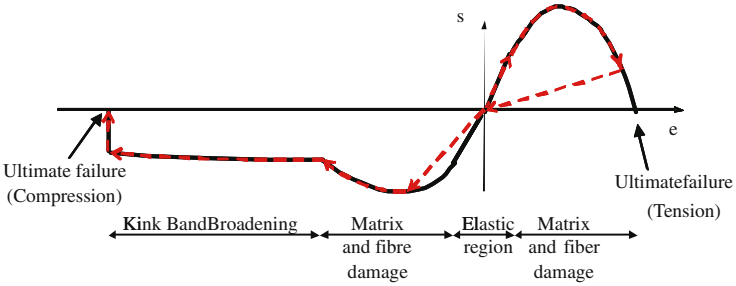

Fig. 9.3 An example of the constitutive response obtained from the proposed analogue model

matrix composites. CODAM is a phenomenological model that smears the material response (stress-strain behaviour) over a finite RVE of the laminate made up of a repeating unit or sub-laminate through the thickness and a characteristic size, *hc*, in the plane of the laminate. The construction of the model at this scale ensures that: (1) by considering a sub-laminate the lamina interactions in terms of damage initiation and evolution are implicitly taken into account, and (2) the characteristic planar length provides a measure of the inherent toughness (or brittleness) of the material (the smaller the *hc* the more brittle the material). The latter is also related to the size of the fully developed fracture process zone (i.e. the height of the damage zone ahead of a crack in a test configuration that leads to a stable crack growth). In formulating CODAM two sets of curves are defined: one relating the damage variables to an effective strain, and the other relating modulus reduction to the damage variables. This results in a strain-softening type stress-strain curve for the characteristic RVE. Damage variables are defined for each of the principal orthotropic directions as well as in shear loading, and the damage growth and modulus reduction curves are unique in each case and sensitive to differences in tension and compression. The CODAM approach has been designed to be computationally oriented, conceptually simple and easy to characterize.

The model has been implemented as a user material model in the commercial finite element code, LS-DYNA, and combined with a modified crack band scheme to address mesh sensitivity. Its ability to predict the response of composites under a variety of loading scenarios has been demonstrated elsewhere [16, 17, 31–33]. A simplified version of CODAM has also been successfully implemented in the commercial implicit finite element code, ABAQUS.

9.3 Model Calibration

For its characterization, the CODAM constitutive model requires some basic input parameters such as the amount of fracture energies under compression and tension, the plateau stress and peak stresses in addition to the standard elastic constants. To obtain some of these parameters, results from experiments such as the over-height

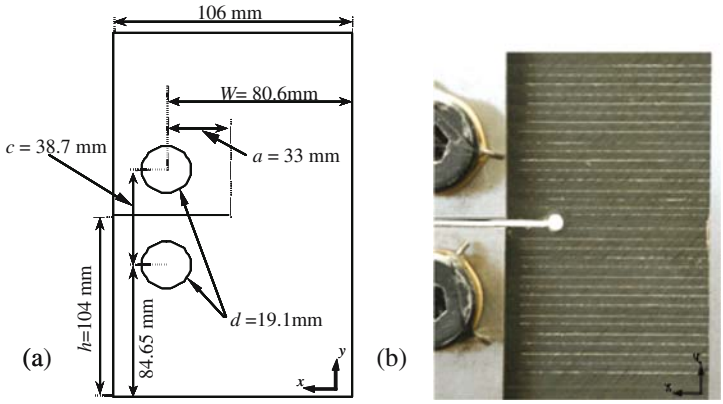

Fig. 9.4 (**a**) Configuration of OCT test and (**b**) scribed lines for the line analysis [18]

compact tension (OCT) [9,18] test are required. Further details on model calibration can be found in [16, 17, 31–33] while here we focus on the OCT test.

The OCT test, developed by Kongshavn and Poursartip [9], is based on a modified version of the standard Compact Tension (CT) test. This test, which leads to a stable growth of damage, has been mainly used to determine the intralaminar damage and fracture characteristics of composite materials. Figure 9.4a shows a schematic setup of an OCT specimen.

In order to extract the fracture energy $\left(G_f\right)$, the position of the crack tip and hence the crack length need to be measured from these tests. A line analysis technique has previously been employed [9, 18] to obtain the profile of crack opening displacement along the crack. Accordingly, a series of horizontal lines that are scribed on the specimen parallel to the notch plane (as shown in Fig. 9.4b) are used as references for measuring the displacement profile using photographs taken during the test. By comparing the coordinates of points on the drawn lines during the test to their initial values, and hence measuring the relative local displacements, the crack opening displacement (COD) profile can be traced. This in turn is used to find the instantaneous position of the crack tip and thus a measure of the crack length.

During the stable crack growth, the average value of the energy release rate is the dissipated energy (energy absorbed in the damage process) divided by the projected area of the crack given by:

$$G_f = \frac{U^*}{Ba} \tag{9.1}$$

where U^* is the portion of the external work absorbed in the damage process, B is the thickness of the specimen and a is the crack length.

Obtaining the above fracture energy release rate along with the height that the damage grows into (via sectioning) from the OCT test allows one to quantify some of the CODAM parameters. Since the damage model is associated with a characteristic size (height, hc) of the RVE, the CODAM parameters are determined such that the resulting peak stress (obtained independently from a simple tension or preferably

a 4 point bend test) and absorbed energy during the damage process are consistent with the measured quantities from the OCT test.

Recently, an advanced image processing technique has been used to extract the crack length and damage height information from the OCT tests in a more accurate and less invasive manner. In this method, the specimen is treated with a speckle pattern and several images of the specimen are recorded during the test using a camera. These images are then processed by a computer software which produces the displacement and strain fields as output. This method enables the quantification of the local displacement/strain fields in the critical positions such as the damage zone. Figure 9.5 shows an example of the strain field contours that can be extracted from an OCT test using the image analysis software [12].

Figure 9.6 shows the strain profiles at a section close to the notch tip and perpendicular to the crack line. The strain profiles for two different levels of pin opening

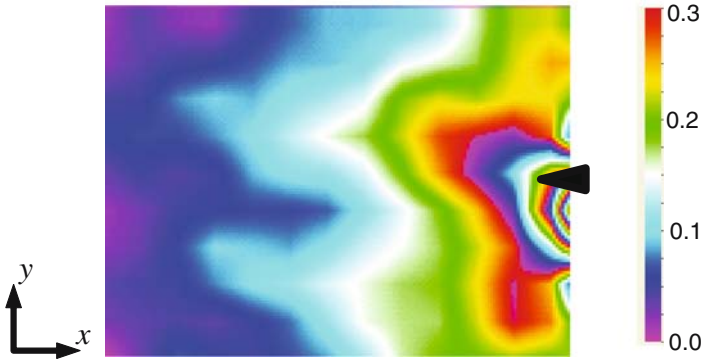

Fig. 9.5 An example of the strain field calculated by the image processing software, DaVis [12]. The arrow shows the position of the initial notch in the OCT test [15]

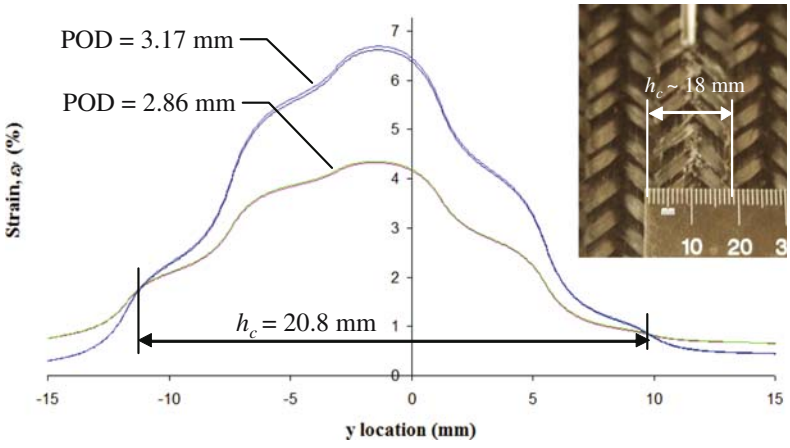

Fig. 9.6 Longitudinal strain profiles at two different levels of pin opening displacement (POD) along a vertical line through the damage zone in an OCT test specimen using the image analysis software, DaVis [12]

displacement (POD) are shown. Localization of the strains into a zone with a height of approximately 20.8 mm can be easily identified from this graph as the distance between the two intersection points. These intersection points differentiate the zone in which the strains are increasing (damage localization) from the zones in which the strains are decreasing (unloading in undamaged material). This allows for an estimate of the height of damage without the need for time consuming sectioning. The height of damage serves as a key parameter for determining the size of the zone used for non-local regularization in the numerical simulations (see Sect. 9.5.2).

9.4 Model Validation

9.4.1 Simulation of OCT Test

The OCT test that was used for characterizing some of the model parameters was also used to validate the performance of CODAM in predicting the behaviour of a composite structure undergoing damage and fracture under tensile loading. Finite element simulations of the OCT test were carried out using both the LS-DYNA and ABAQUS implementations of CODAM. Figure 9.7 compares the predictions of the applied force versus crack mouth opening displacement (CMOD) with the corresponding test results for a class of carbon fibre reinforced plastic (CFRP) laminates with a $[45/-45/0_2/90/0_2/-45/45]_6$ layup [18]. In this model, the sub-laminate elastic properties used are: $E_x = 75.0$ GPa, $E_y = 32.0$ GPa, $\nu_{xy} = 0.161$ and $G_{xy} = 17.1$ GPa. Also, the peak stress as measured from a 4 pt bend test is 460 MPa and the fracture energy release rate $G_f = 80$ kJ/m^2 based on the findings of

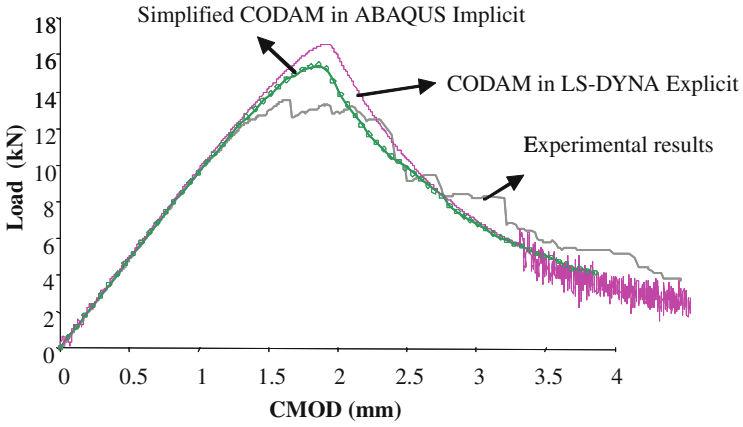

Fig. 9.7 Longitudinal strain profiles at two different levels of pin opening displacement (POD) along a vertical line through the damage zone in an OCT test specimen using the image analysis software, DaVis [12]

the OCT experiment. According to this figure, the numerical predictions agree well with the experimental results. Simulation results in the form of predicted damage patterns will be presented in Sect. 9.5.2 within the context of non-local models.

9.4.2 Simulation of Open Hole Plates Under Compression

Soutis and Spearing [29] presented an investigation into the compressive strength of CFRP laminates. They performed quasi-static compressive tests on panels with different specimen and notch sizes. In their study they used specimen sizes of 50×50 mm and notch diameters ranged from 2.5 to 25 mm resulting in hole-diameter/width ratios of 0.05 to 0.5.

The material used in this experiment was a quasi-isotropic $[(\pm 45/0/90)_3]_s$ CFRP laminate with an approximately 3 mm thickness and elastic properties $E_x = E_y = 63$ GPa, $\nu_{xy} = 0.315$ and $G_{xy} = 24$ GPa.

To use CODAM in modeling these experiments, first we need to derive the damage parameters in compression. The damage initiation strain is the strain at which matrix cracking; fibre rotation and delamination start to propagate. In the experiments by Soutis and Spearing [29] on notched specimens, this strain was measured to be around 80% of the strain at the peak stress point. The average strain at peak stress was reported to be almost 1.0%. Therefore, the damage initiation strain can be estimated to be -0.008 (negative sign implies compression). This value is taken to be the damage initiation strain for both the fibre and the matrix due to the fact that matrix cracking and fibre rotation initiate at the same strain level in the kinking process.

The compressive fracture toughness for a variety of lay-ups for T800 carbon fibres embedded in Ciba-Geigy BSL 924C epoxy resin was measured by Soutis et al. [28] to be 40 MPa $m^{1/2}$. Here we use the same value of fracture toughness for these panels. This yields a fracture energy of 25.4 kJ/m^2.

Sivashanker [24] has performed an experimental study on the compressive response of the same lay-up and material as in [29], except that he used T300 carbon fibres in his study. We can reasonably ignore this difference in the fibre type as the damage mechanism in these panels is driven mainly by the matrix properties. In Sivashanker's work, the plateau stress was reported to be in the range of 100–133 MPa. Here we use a plateau stress of 100 MPa.

Figure 9.8 shows a comparison between the experimental results and the predicted compressive strengths of notched laminates using the new implementation of CODAM in LS-DYNA. It can be seen that using the above parameters the predictions lie well within the experimental bounds. Sensitivities of the strength predictions to variations in some of the key constitutive parameters in the compression regime, such as the plateau stress and fracture energy have been carried out and reported in [32].

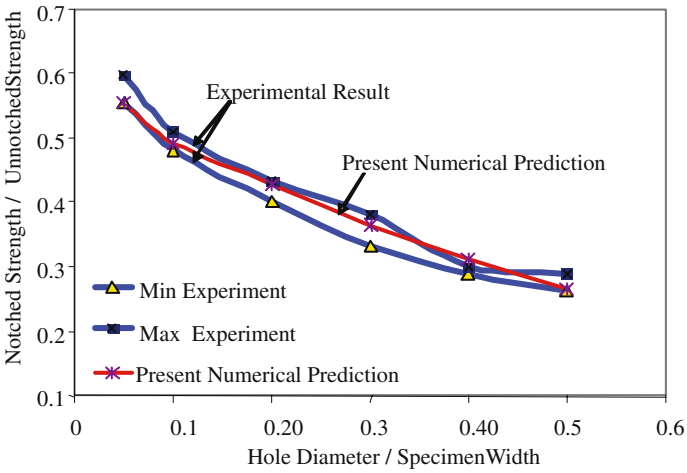

Fig. 9.8 Comparison of experimental [29] and present numerical strength predictions of open hole panels under uniaxial compression

9.5 Non-local Approach

9.5.1 Limitations of Local Damage Models

As stated earlier (see Sect. 9.1) the Bazant's crack band approach used in conjunction with the local damage model, CODAM, is only applicable to a limited class of problems. The following are a list of some of these limitations:

- The crack band method is based on the premise that the damage localizes into a zone with a certain height. This is valid only in quasi-static loading of notched specimens; otherwise the scaling concept used in the crack band approach does not apply.
- Crack and damage tend to grow parallel to the mesh orientation. In other words, the results of the FE simulation using the local crack band formulation leads to mesh orientation dependent results. As a result, this method can practically be used only when the crack path is known in advance.
- To achieve more realistic results in terms of local displacements, strain and stress fields, the height of elements should be close to the actual height of damage observed in the experiments. For example, using elements that are much coarser than the damage height result in under-prediction of strain and stress gradients in the vicinity of the notch. Conversely, by virtue of the required scaling of the softening portion of the stress-strain curve used in the crack band approach, finer elements lead to unrealistically large strains in damaged elements.

To overcome the above limitations, other numerical approaches that address the localization problem, such as non-local regularization, need to be adopted.

9.5.2 Non-local Regularization

It is well-known that the local equations governing the behaviour of a strain softening solid system are ill-posed [1, 5, 22]. As a result, the finite element simulation of strain-softening materials is not objective and suffers from the so called spurious localization problem leading to mesh size dependency of the numerical predictions. Various remedies have been proposed in the literature to address this problem. The non-local approach (e.g. [22]), explicit and implicit gradient formulations [21], Cosserat continuum (e.g. [6]) and visco-plastic regularization (e.g. [20, 27]) are among the techniques that render the numerical simulation objective and are known as localization limiters [10]. Introduction of a length scale and consequently prevention of localization to a zero-width band are common in all the proposed remedies.

The advantage of the non-local regularization (e.g. [1]) compared with other techniques is that the introduced length scale is explicitly adjustable. Furthermore, it is relatively easy to implement this method in finite element codes (specially the integral form of non-local regularization).

In the integral form of the non-local regularization, the damage parameter (d) is a function of the average of an appropriate variable over a finite neighbourhood of a point. It has been shown by Jirasek [10] that the inelastic (damage) strain given by Eq. (9.2) is a suitable variable for averaging. This results in the damage parameter being a function of the non-local inelastic strain (Eq. (9.3)):

$$\overline{\varepsilon}_d(X) = \int_{\Omega_X} \varepsilon_d(X)\, w(X-x)\, d\Omega \tag{9.2}$$

$$d(X) = d\left(\overline{\varepsilon}(X)\right) \tag{9.3}$$

where w is the weight function. Averaging is performed around point X over a finite neighbourhood (Ω_X) and x represents all the points within the domain Ω_X. Gauss distribution or other bell shaped functions are usually assumed for w.

The following is an example of the weight function that is used in the non-local averaging scheme in LS-DYNA:

$$w(x) = \left[1 + \left(\frac{x}{l}\right)^p\right]^{-q} \tag{9.4}$$

The parameter l is the actual length scale introduced to the model while p and q alter the distribution shape. The size of the averaging area directly depends on l and consequently the predicted height of damage is a function of l. Observations of OCT test in terms of height of damage (h_c), can be used to determine an appropriate length scale (l) for the non-local averaging. It is important to choose the strain-to-failure (saturation strain) such that the total energy dissipated in the damage process is consistent with the value of fracture energy release rate, G_f measured from the OCT test. In a non-local model the latter can be written in the form of Eq. (9.5) [11].

$$G_f = c l g_f \tag{9.5}$$

where g_f is the energy release rate density which is the area under the stress-strain curve, and c is the multiplier which represents the relation between the height of damage (h_c) and the length parameter (l) and is roughly equal to h_c/l. The value of c mainly depends on the definition of the weight function and for the function defined in Eq. (9.4), it ranges between 2 to 2.5.

Numerical simulations that are based on non-local averaging not only resolve the mesh size dependency problem but lead to more realistic prediction of the local strain/stress fields including the size of the damage zone. An added benefit of the non-local approach is that it improves the mesh orientation bias for damage propagation direction [1].

The LS-DYNA software provides non-local averaging capability for a select number of built-in material models. Unfortunately, this tool is currently not available for either built-in anisotropic damage models or user-defined damage models. Therefore, in the presented analyses the MAT_PLASTICITY_WITH_DAMAGE material model which uses a scalar damage model (SDM) for isotropic materials is adopted.

Figure 9.9 shows the longitudinal strain contours in an OCT simulation of a $[0/\pm 45]_4$ braided composite material [15] using an effective isotropic Young's modulus of 12.5 GPa, peak stress of 110 MPa, and a fracture energy release rate (G_f) of 45 kJ/m^2. It can be seen that the height of the zone with localized strain defining the damage zone is almost constant during the analysis. By changing the length parameter (l), the predicted height of damage can be adjusted to fit the experimental measurements.

To illustrate the mesh orientation dependency of local damage models and the resulting improvement using a non-local damage approach, an example of the OCT simulation is carried out with an inclined mesh introduced ahead of the notch.

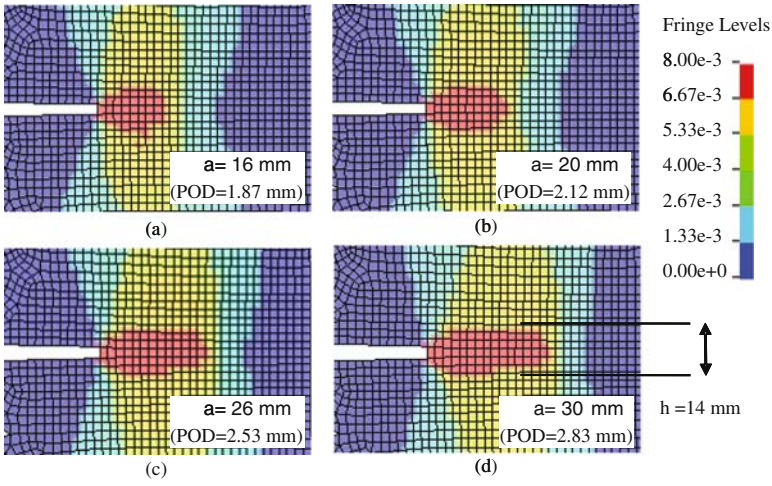

Fig. 9.9 Predicted longitudinal strain (ε_y) contours and crack length values, Δa, in the OCT simulation of a $[0/\pm 45]_4$ braided CFRP at various levels of pin opening displacement (POD)

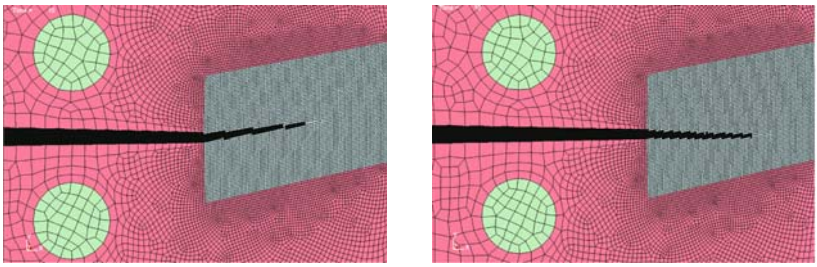

(a) Using local scalar damage formulation

(b) Using non-local scalar damage formulation

Fig. 9.10 Predicted damage/crack pattern in an OCT test

Figures 9.10a, b show the predicted damage/crack pattern in local and non-local simulations, respectively. It is seen that the non-local averaging can significantly improve the dependency of the FE predictions on mesh orientation as the crack follows the expected path (i.e. along the axis of the notch).

9.6 Conclusions

A previously developed continuum damage mechanics based constitutive model, CODAM, has been further modified to account for the distinct damage mechanisms that occur under compressive loading of fibre reinforced composite materials. The proposed extension has been guided by the development of a simple mechanical analogue model that through special arrangement of basic elements describes the one-dimensional non-linear response of composite laminates under both in-plane tension and compression loading.

The calibration of the tensile damage parameters of the model using an Overheight Compact Tension (OCT) test setup have been discussed. Results presented here show the efficacy of the model in predicting the overall damage zone size and force-displacement response of quasi-statically loaded OCT and open hole compression test panels.

Finally, the limitations of local smeared crack (crack band) approaches in modeling damage propagation and its numerical implications have been discussed. It is shown that a non-local integral approach is an efficient remedy for problems stemming from the so-called localization and mesh orientation bias that local approaches suffer from.

Acknowledgements The authors would like to acknowledge the financial support provided by the Natural Sciences and Engineering Research Council (NSERC) of Canada. The contributions made to this work by many of the past members of the Composites Group at UBC are also gratefully acknowledged.

References

1. Bazant ZP, Jirasek M (2002) Nonlocal integral formulations of plasticity and damage: Survey of progress. J Eng Mech 128:1119–1149
2. Bazant ZP, Kim JH, Daniel IM et al. (1999) Size effect on compression strength of fibre composites failing by kink band propagation. Int J Fract 95:103–141
3. Bazant ZP, Oh BH (1983) Crack Band Theory for Fracture of Concrete. Materiaux et Constructions. Mater Struct 16:155–177
4. Bazant ZP, Oh BH (1984) Rock fracture via strain-softening finite elements. J Eng Mech 110:1015–1035
5. Belytschko T, Bazant ZP, Hyun YW, Chang TP (1986) Strain-softening materials and finite element solutions. Comput Struct 23:163–180
6. de Borst R (1991) Simulation of Strain Localization: A reappraisal of Cosserat continuum. Eng Comput 8:317–332
7. Fleck NA (1997) Compressive failure of fibre composites. Adv Appl Mech 33:43–113
8. Fleck NA, Deng L, Budiansky B (1995) Prediction of kink width in compressed fibre composites. J Appl Mech 62:329–337
9. Kongshavn I, Poursartip A (1999) Experimental investigation of a strain softening approach to predicting failure in notched fibre reinforced composite laminates. Compos Sci Technol 59:29–40
10. Jirasek M (1998) Nonlocal models for damage and fracture. Int J Solids Struct 35:4133–4145
11. Jirasek M, Rolshoven S, Grassl P (2004) Size effect on energy induced by non-locality. Int J Numer Anal Methods in Geomech 28:653–670
12. LaVision StrainMaster Brochure (2007)
13. Maimí PP, Camanho PP, Mayugo JA, Dávila CG (2007a) A continuum damage model for composite laminates: Part I - Constitutive model. Mech Mater 39:897–908
14. Maimí PP, Camanho PP, Mayugo JA, Dávila CG (2007b) A continuum damage model for composite laminates: Part II - Computational implementation and validation. Mech Mater 39:909–919
15. McGregor C, Vaziri R, Poursartip A (2007) Investigation into the Tensile Behaviour of Notched Braided Laminates: Experimental and Numerical. Report submitted to General Motors Corporation under NSERC CRD File No: CRCPJ306287–04, The University of British Columbia
16. McGregor C, Vaziri R, Poursartip A, Xiao X (2007) Simulation of progressive damage development in braided composite tubes under axial compression. Compos Part A, doi: 10.1016/j.compositesa.2006.10.007
17. McGregor C, Zobeiry N, Vaziri R, Poursartip A (2007) A Constitutive Model for Progressive Compressive Failure of Composites. To be submitted
18. McLennan SA (2004) Crack growth and damage modeling of fibre reinforced polymer composites. M.A.Sc. thesis, Department of Materials Engineering, The University of British Columbia, Vancouver, BC, Canada
19. Moran PM, Liu XH, Shih CF (1995) Kink band formation and band broadening in fire composites under compressive loading. Acta Metall Mater 43:2943–2958
20. Needleman A (1987) Material rate dependence and mesh sensitivity in localization problems, Comput Methods Appl Mech Eng 67:69–85
21. Peerlings RHJ, de Borst R, Brekelmans WAM, Geers MGD (2002) Localization issues in local and nonlocal continuum approaches to fracture. Eur J Mech Solids, 21:175–189
22. Pijaudier-Cabot G, Bazant ZP (1987) Nonlocal Damage Theory. J Eng Mech 113:1512–1543
23. Shih CF, Moran PM (1998) Kink band propagation and broadening in ductile matrix fibre composites: Experiments and analysis. Int J Solids Struct 35:1709–1722
24. Sivashanker S (2001) Damage propagation in multidirectional composites subjected to compressive loading. Metall Mater Trans A: Phys Metall Mater Sci 32:171–182
25. Sivashanker S, Bag A (2001) Kink-band propagation in a multidirectional carbon fibre-polymer composite. Metall Mater Trans A: Phys Metall Mater Sci 32:3157–3160

26. Sivashanker S, Fleck NA, Sutcliffe MPF (1996) Microbuckle propagation in a unidirectional carbon fibre-epoxy matrix composite. Acta Mater 44:2581–2590
27. Sluys LJ, de Borst R (1992) Wave propagation and localization in a rate-dependent cracked medium-model formulation and one-dimensional examples. Int J Solids Struct 29:2945–2958
28. Soutis C, Curtis PT, Fleck NA (1993) Compressive failure of notched carbon-fibre composites. Proc Royal Soc Lond Series A: Math Phys Eng Sci 440:241–256
29. Soutis C, Spearing SM (2002) Compressive response of notched, woven fabric, face sheet honeycomb sandwich panels. Plast Rubber Compos 31:392–397
30. Sutcliffe MPF, Fleck NA (1994) Microbuckle propagation in carbon fibre-epoxy composites. Acta Metall Mater 42:2219–2231
31. Williams KV, Vaziri R, Poursartip A (2003) A physically-based continuum damage mechanics model for thin laminated composite structures. Int J Solids Struct 40:2267–2300
32. Zobeiry N (2004) Progressive damage modeling of composite materials under compressive loads. M.A.Sc. thesis, Department of Civil Engineering, The University of British Columbia, Vancouver, BC, Canada
33. Zobeiry N, McGregor C, Vaziri R, Poursartip A (2005) Simulation of the Nonlinear Compressive Response and Failure of Fibre Reinforced Composites. CANCOM, Vancouver, Canada

Chapter 10
Elastoplastic Modeling of Multi-phase Metal Matrix Composite with Void Growth Using the Transformation Field Analysis and Governing Parameter Method

Ernest T.Y. Ng and Afzal Suleman

Abstract In this paper, we employ the combined *Transformation Field Analysis* (TFA) method and the *Governing Parameter Method* (GPM) to predict the overall elastoplastic behavior of multi-phase fibrous composite materials using Gurson-Tvergaard yield criterion in order to account for the effect of void growth in the matrix phase. For the homogenization scheme, we employ the TFA method with concentration factors determined by the Eshelby-Mori-Tanaka (EMT) theory. Regarding to the stress integration of the governing TFA equations, we employ an implicit integration scheme, namely the GPM. Furthermore, a necessary condition for the possible ranges of the governing parameters based on the GPM integration scheme is derived in a more general setting by including the rate of nucleation and coalescence within the context of writing the expression of the rate of change of porosity. To validate our proposed approach, we compare our results to both numerical and experimental results provided in the existing literature.

10.1 Introduction

A metal matrix fiber-reinforced composite has many advantages over conventional engineering materials because of its light-weight and good formability under fabrication. However, the intrinsic inhomogeneities of fibrous composite materials has made the prediction of the mechanical behavior of such a material a great challenge over the past three decades. As described in the preceding paper by Ng and Suleman [19], the combined TFA-GPM provided a good approximation of determining the

Ernest T.Y. Ng
Department of Mechanical Engineering, University of Victoria, British Columbia, Canada, e-mail: eng@me.uvic.ca

A. Suleman
Instituto de Engenharia Mecánica, Instituto Superior Técnico (IDMEC-IST), Instituto Superior Técnico, Lisbon, Portugal, e-mail: suleman@ist.utl.pt

overall elastoplastic behavior of multi-phase fiber-reinforced composite materials based on the von-Mises yield criterion. In this paper, we will employ the combined TFA-GPM approach but with Gurson-Tvergaard yield criterion instead of von-Mises yield criterion to predict the overall elastoplastic behavior of n-phase fiber-reinforced composites with isotropic strain hardening.

Elastoplastic modelling of n-phase fiber-reinforced composites (advanced hybrid composites) has been proposed by many researchers. One elegant method, namely, the *Transformation Field Analysis* (TFA) [7] proposed by Dvorak has shown to have many advantages over the other models within the context of computational micromechanics. For instance, the algorithm can take account of the microgeometry of the fiber phase and is suitable for modelling multi-phase fibrous composites; it can accommodate with any inelastic constitutive relation, micromechanical model and uniform overall loading path. More importantly, it is also suitable for 3D modelling of multi-phase fiber-reinforced composite structures within the finite element method framework. To determine the concentration factors needed by the governing TFA equations, we invoke the Eshelby-Mori-Tanaka (EMT) theory [3, 8, 17]. However, the integration scheme employed in the original paper written by Wafa et al. is explicit [1]. Over the past years, implicit integration has shown to have more advantages over explicit integration in integrating the constitutive equation within the context of finite element analysis. Moreover, explicit integration even has complicated the numerical procedures for analyzing multi-phase fibrous composite material as discussed in the preceding paper. In this paper, the TFA method is used to predict the overall elastoplastic behavior of n-phase fiber-reinforced composites using Gurson-Tvergaard yield criterion. In order to integrate the overall TFA governing equations, an implicit stress integration scheme called the *Governing Parameter Method* (GPM) [15, 16] is used to replace the explicit integration scheme employed in the original paper by Wafa et al. In short, this paper has the following contributions:

1. Extend the widely used von-Mises yield criterion to a more general Gurson-Tvergaard yield criterion in order to account for the effects of void growth in the matrix phase;
2. Perform the mathematical analysis to obtain the necessary conditions for the ranges of the change of the mean plastic strain Δe_m^P and the change of the effective plastic strain $\Delta \bar{e}^P$ of the matrix phase within the context of the iterative algorithm based on the GPM and the Gurson-Tvergaard model;
3. Use the proposed approach to simulate a 4-phase fibrous composite material.

The layout of the paper is as follow: Sect. 10.2 presents the micromechanics of elastoplastic analysis of multi-phase fiber-reinforced composite materials, this includes the governing TFA equations and the EMT equations; Sect. 10.3 outlines the stress integration scheme, this includes a general description to the GPM algorithm, the procedure to apply the GPM to solving the governing TFA equations; Sect. 10.4 includes the formulation of Gurson-Tvergaard plasticity within the context of GPM. More importantly, a necessary condition for the ranges of the change of the mean plastic strain Δe_m^P and the change of the effective plastic strain $\Delta \bar{e}^P$

have also been formulated; Sect. 10.5 carries out the evaluation and verification of the developed computational framework and the results are compared with experimental and computational results presented in the literature. The paper concludes with closing remarks.

10.2 Micromechanics

10.2.1 Setting the Stage

Consider a composite medium $\Omega \subseteq \mathbb{R}^3$ which consists of a single matrix phase Ω_0 (the subscript '0' denotes the matrix phase henceforth) and n phases of ellipsoidal fiber phases Ω_r where the index 'r' running from 1 to n with a total of $n+1$ phases. Also, we define the fiber volume fraction as

$$c_r \equiv \frac{\mathscr{V}(\Omega_r)}{\mathscr{V}(\Omega)} \tag{10.1}$$

where $\mathscr{V}(\Omega_r)$ and $\mathscr{V}(\Omega)$ are the volume of the r-th phase material and the volume of the composite medium, respectively. Thus, we have

$$\sum_{r=0}^{n} c_r = 1 \tag{10.2}$$

Before delving into any analysis, we assume the following:

1. All phases are assumed to be isotropic and homogeneous
2. The fiber's shape is assumed to be ellipsoidal
3. The interfaces between the matrix and fibers are assumed to be perfectly bonded

Furthermore, the composite medium that is of interest is assumed to be *statistically homogeneous* and the longitudinal axis of the fibers are aligned in the x_3 direction of the x_1-x_2-x_3 Cartesian coordinate system which are randomly distributed over the entire composite domain. Consequently, we can choose a *Representation Volume Element* (RVE) to evaluate both the local and the overall fields [10]. By assuming a statistically homogeneous composite medium Ω, we have

$$\langle \boldsymbol{\sigma}_r \rangle = \frac{1}{\mathscr{V}(\Omega)} \int_{\Omega} \boldsymbol{\sigma}_r(\boldsymbol{x}) dV \tag{10.3}$$

$$\langle \boldsymbol{\varepsilon}_r \rangle = \frac{1}{\mathscr{V}(\Omega)} \int_{\Omega} \boldsymbol{\varepsilon}_r(\boldsymbol{x}) dV \tag{10.4}$$

for the average of the local stress field and strain field of the r-th phase material. The main reason for considering the average field is because it is almost impossible to know the exact nonuniform local field, therefore, it is more natural to consider the average local field. This rationale is applied freely in the field of micromechanics.

To simplify, the bracket '$\langle\rangle$' is dropped henceforth. That is, we will denote the exact local tensor field as $\boldsymbol{T}_r(\boldsymbol{x})$ and the average local tensor field as $\boldsymbol{T}_r$ by dropping out the '$(\boldsymbol{x})$' for any tensor field unless needed for further clarification. As usual in micromechanics theory, one can write the overall stress field $\bar{\boldsymbol{\sigma}}$ (or strain field $\bar{\boldsymbol{\varepsilon}}$) as a linear combination of its relevant local fields as follow:

$$\bar{\boldsymbol{\sigma}} = \sum_{r=0}^{n} c_r \boldsymbol{\sigma}_r \tag{10.5}$$

$$\bar{\boldsymbol{\varepsilon}} = \sum_{r=0}^{n} c_r \boldsymbol{\varepsilon}_r \tag{10.6}$$

The above two sets of equations are jointly referred to as the *homogenization equations*.

10.2.2 Governing TFA Equations

In this section, a summary of the governing TFA equations and the EMT equations is given. For the details in the formulation of the TFA equations and its relevant issues, we refer to [1,4,6,7]. Generally speaking, the framework of the TFA method provides three sets of equations, which include the global equations, local equations and localization equations. These three sets of equations constitute the foundation of inelastic analysis of n-phase fiber-reinforced composites within the context of the TFA method. On the other hand, the EMT theory provides the overall elastic stiffness matrix $\boldsymbol{L}$ (or overall compliance matrix $\boldsymbol{M}$) in terms of the phase elastic stiffness matrix $\boldsymbol{L}_r$ (or phase compliance matrix $\boldsymbol{M}_r$) and the relevant mechanical concentration factors $\boldsymbol{A}_r$ (or $\boldsymbol{B}_r$) respectively. That is, we have

$$\boldsymbol{L} = \sum_{r=0}^{n} c_r \boldsymbol{L}_r \boldsymbol{A}_r \tag{10.7}$$

$$\boldsymbol{M} = \sum_{r=0}^{n} c_r \boldsymbol{M}_r \boldsymbol{B}_r \tag{10.8}$$

and their relevant mechanical concentration factors

$$\boldsymbol{A}_r = \boldsymbol{A}_r^{dil} \boldsymbol{A}_0 \tag{10.9}$$

$$\boldsymbol{B}_r = \boldsymbol{B}_r^{dil} \boldsymbol{B}_0 \tag{10.10}$$

with

$$\boldsymbol{A}_r^{dil} = [\boldsymbol{I} + \boldsymbol{S}_r^{Esh} \boldsymbol{M}_0 (\boldsymbol{L}_r - \boldsymbol{L}_0)]^{-1} \tag{10.11}$$

$$\boldsymbol{A}_0 = [c_0 \boldsymbol{I} + c_r \boldsymbol{A}_r^{dil}]^{-1} \tag{10.12}$$

$$\boldsymbol{A}_r \equiv \boldsymbol{A}_r^{dil} \boldsymbol{A}_0 \tag{10.13}$$

and

$$\boldsymbol{B}_r^{dil} = \boldsymbol{L}_r \boldsymbol{A}_r^{dil} \boldsymbol{M}_0 \tag{10.14}$$

$$\boldsymbol{B}_0 = \left[c_0 \boldsymbol{I} + \sum_{r=1}^{n} c_r \boldsymbol{B}_r^{dil} \right]^{-1} \tag{10.15}$$

$$\boldsymbol{B}_r = \boldsymbol{B}_r^{dil} \boldsymbol{B}_0 \tag{10.16}$$

where $\boldsymbol{S}_r^{Esh}$ is the Eshelby tensor of the r-th phase material and $\boldsymbol{I}$ is the 6×6 identity matrix. Note that $\boldsymbol{A}_0^{dil} = \boldsymbol{A}_0 = \boldsymbol{B}_0^{dil} = \boldsymbol{B}_0 = \boldsymbol{I}$.

In the context of TFA method, the localization rules with only elastic-plastic deformation are given by

$$\boldsymbol{\varepsilon}_r = \boldsymbol{A}_r \bar{\boldsymbol{\varepsilon}} - \sum_{s=0}^{n} \boldsymbol{D}_{rs} \boldsymbol{M}_s \boldsymbol{\lambda}_s^p \tag{10.17}$$

$$\boldsymbol{\sigma}_r = \boldsymbol{B}_r \bar{\boldsymbol{\sigma}} - \sum_{s=0}^{n} \boldsymbol{F}_{rs} \boldsymbol{L}_s \boldsymbol{\mu}_s^p \tag{10.18}$$

where $\boldsymbol{\lambda}_r^p$ and $\boldsymbol{\mu}_r^p$ are the local eigenstress and eigenstrain fields regarding to plastic deformation respectively. According to the terminology used in Dvorak's papers, the eigenstrain and eigenstress fields described above are jointly called the *transformation fields*. The main assumption made by Dvorak and Benveniste is the piecewise uniform distribution of the eigenfields over the phases. This assumption is based on the premise of the existence of uniform fields in heterogeneous media [6]. Moreover, $\boldsymbol{D}_{rs}$ and $\boldsymbol{F}_{rs}$ are the corresponding *transformation concentration factors* which are given as follows:

$$\boldsymbol{D}_{rs} = (\boldsymbol{I} - \boldsymbol{A}_r)(\boldsymbol{L}_r - \boldsymbol{L})^{-1} (\delta_{rs} \boldsymbol{I} - c_s \boldsymbol{A}_s^T) \boldsymbol{L}_s \tag{10.19}$$

$$\boldsymbol{F}_{rs} = (\boldsymbol{I} - \boldsymbol{B}_r)(\boldsymbol{M}_r - \boldsymbol{M})^{-1} (\delta_{rs} \boldsymbol{I} - c_s \boldsymbol{B}_s^T) \boldsymbol{M}_s \tag{10.20}$$

for any multi-phase system. Here δ_{rs} is the Kronecker delta and $\boldsymbol{A}_r^T$ and $\boldsymbol{B}_r^T$ are the transpose of $\boldsymbol{A}_r$ and $\boldsymbol{B}_r$ respectively. The global equations within the context of the TFA are given as follows:

$$\bar{\boldsymbol{\varepsilon}} = \boldsymbol{M} \bar{\boldsymbol{\sigma}} + \bar{\boldsymbol{\mu}}^p \tag{10.21}$$

$$\bar{\boldsymbol{\sigma}} = \boldsymbol{L} \bar{\boldsymbol{\varepsilon}} + \bar{\boldsymbol{\lambda}}^p \tag{10.22}$$

where $\bar{\boldsymbol{\lambda}}$ and $\bar{\boldsymbol{\mu}}$ are the overall eigenstress and eigenstrain corresponding to plastic deformation, respectively. Likewise, the local equations are given as follows:

$$\boldsymbol{\varepsilon}_r = \boldsymbol{M}_r \boldsymbol{\sigma}_r + \boldsymbol{\mu}_r^p \tag{10.23}$$

$$\boldsymbol{\sigma}_r = \boldsymbol{L}_r \boldsymbol{\varepsilon}_r + \boldsymbol{\lambda}_r^p \tag{10.24}$$

with $\boldsymbol{\lambda}_r^p$ and $\boldsymbol{\mu}_r^p$ denote the volume-averaged phase eigenstress and eigenstrain, corresponding to phase r, respectively. Moreover, the piecewise approximation of the

overall eigenstress $\bar{\boldsymbol{\lambda}}^p$ and eigenstrain $\bar{\boldsymbol{\mu}}^p$ are given as follow:

$$\bar{\boldsymbol{\lambda}} = \sum_{r=0}^{n} c_r \boldsymbol{A}_r^T \boldsymbol{\lambda}_r^p \tag{10.25}$$

$$\bar{\boldsymbol{\mu}} = \sum_{r=0}^{n} c_r \boldsymbol{B}_r^T \boldsymbol{\mu}_r^p \tag{10.26}$$

In this paper, the only eigenstrain is the plastic strain for the matrix phase. Customary, we write $\boldsymbol{\mu}_0^p = \boldsymbol{\varepsilon}_0^p$ and note that $\boldsymbol{\mu}_r^p = \boldsymbol{\lambda}_r^p = \mathbf{0}$ for $r = 1,2,\ldots,n$. Consequently, we have

$$\bar{\boldsymbol{\lambda}}^p = c_0 \boldsymbol{\lambda}_0^p \tag{10.27}$$

$$\bar{\boldsymbol{\varepsilon}}^p = \bar{\boldsymbol{\mu}}^p = c_0 \boldsymbol{\mu}_0^p = c_0 \boldsymbol{\varepsilon}_0^p \tag{10.28}$$

10.3 GPM Algorithm

In this section, a description of the GPM to integrate the governing TFA equations is presented. The basic idea of the governing parameter method is to set up a governing nonlinear equation in terms of one variable (i.e. the governing parameter). For more details in the general procedures of the GPM, see references [15] and [2]. The general steps of the GPM include the following:

Step 1 Select a governing parameter p
Step 2 Express all the unknown quantities in terms of the governing parameter p
Step 3 Solve $g(p) = 0$
Step 4 Update all the quantities
Step 5 Evaluate the consistent tangent moduli as needed

In the following, we provide the general structure of the computational algorithm for the GPM. Since all the stress integration schemes are mostly designed for use within the context of finite element method, all quantities at time step t are assumed to be known in *a priori* before starting the stress integration algorithm in time step $t + \Delta t$. We also have to invoke the governing TFA equations to convert between the global and local fields. When analyzing multi-phase fiber-reinforced composites, the governing TFA equation are invoked twice. The first time, the TFA equations are used to convert the given global elastic trial stress ${}^{t+\Delta t}\bar{\boldsymbol{\sigma}}^E$ into the local elastic trial stress ${}^{t+\Delta t}\boldsymbol{\sigma}_0^E$ for the matrix phase. If the yield function is greater than zero under this elastic trial stress, then the local stress integration reverts the updated matrix stress ${}^{t+\Delta t}\boldsymbol{\sigma}_0$ back to the updated yield surface. In addition, all other internal variables have to be updated at the end of the time step $t + \Delta t$. With this updated local stress, the governing TFA equations is invoked again to obtain the updated fiber stress ${}^{t+\Delta t}\boldsymbol{\sigma}_r$. Finally, the basic micromechanics equations are used to determine the updated overall stress ${}^{t+\Delta t}\bar{\boldsymbol{\sigma}}$ or strain ${}^{t+\Delta t}\bar{\boldsymbol{\varepsilon}}$, as needed. In addition, since our analysis assumes that solely the matrix phase undergoes plastic deformation, all the

stress fields, strain fields and internal variables are referred to the matrix phase when dealing with the stress integration algorithm.[1]

10.4 Gurson-Tvergaard Model in GPM

In this section, a detailed formulation of the Gurson-Tvergaard plasticity within the framework of GPM is presented.[2]

10.4.1 Gurson-Tvergaard Yield Criterion

In order to account for voids inside the matrix phase, Gurson provided a yield criterion that takes care of the porosity effect. Later on, Tvergaard modified the original Gurson yield criterion which gave a more general form of yield criterion for modelling porous rate-independent plasticity [22, 23]. Further developments based on the Gurson-Tvergaard model have been reported by Niemi and Zhang [20]. For a numerical formulation of Gurson-Tvergaard model using the GPM, we refer to [16]. The yield function $\mathscr{F}$ of the Gurson-Tvergaard model is given by

$$\mathscr{F}(J_2, \sigma_m) = \frac{1}{2}\boldsymbol{S} : \boldsymbol{S} - \frac{1}{3}\left[2f^* q_1 \cosh\left(\frac{3q_2\sigma_m}{2\hat{\sigma}_y}\right) - 1 - q_3^2(f^*)^2\right]\hat{\sigma}_y^2 \tag{10.29}$$

where f^* is the porosity parameter, σ_m is the mean stress, $\boldsymbol{S}$ is the deviator stress tensor, $\hat{\sigma}_y$ is the yield stress and q_1, q_2, q_3 are material parameters. Note that the symbol ':' represents a double contraction of $\boldsymbol{S}$, that is $\boldsymbol{S} : \boldsymbol{S} = S_{ij}S_{ij}$. Also, when $f^* = 0$, this yield criterion becomes the von-Mises yield criterion. Furthermore, f^* is a function of the void volume fraction f, critical void volume fraction f_c and f_f which is the value of f at material failure. Therefore, f^* is given by

$$f^* = \begin{cases} f & \text{if } f \le f_c \\ f_c + K_f(f - f_c) & \text{if } f_c < f \le f_F \\ f_F & \text{if } f > f_f \end{cases} \tag{10.30}$$

where

$$K_f = \frac{1/q_1 - f_c}{f_f - f_c} \tag{10.31}$$

[1] The subscript '0' for the matrix phase will be dropped henceforth for the sake of clarity in this section.

[2] In the following formulation, '$\boldsymbol{e}$' will be used instead of '$\boldsymbol{\varepsilon}$' to denote all strain relative fields such as plastic strain so as to keep the symbols consistent with the original GPM formulation by Kojić.

$$f_F = \frac{q_1 + \sqrt{q_1^2 - q_3}}{q_3} \tag{10.32}$$

In this paper, we restrict the damage analysis by only considering the rate of void growth $\dot{f}_G$, consequently, the rate of change of porosity is equal to the rate of void growth, that is $\dot{f} = \dot{f}_G$ where

$$\dot{f}_G = (1-f)\dot{e}_V^P \tag{10.33}$$

Moreover, $\dot{e}_V^P$ is the rate of plastic volumetric strain and $\dot{\bar{e}}^P$ is the rate of effective plastic strain. In this paper, we only consider $\dot{f}_G$. Next, we divide the stress tensor at time $t+\Delta t$ into trial deviator stress $\boldsymbol{S}^E$ and the trial mean stress σ_m^E.

$$^{t+\Delta t}\boldsymbol{S}^E = 2G^{t+\Delta t}\boldsymbol{e}'^E \tag{10.34}$$

$$^{t+\Delta t}\sigma_m^E = c_m{}^{t+\Delta t}e_m^E \tag{10.35}$$

where G is the shear modulus and $\boldsymbol{e}'^E$ is the trial deviator strain tensor. On the other hand

$$c_m = \frac{E}{(1-2\nu)} \tag{10.36}$$

with E be the elastic modulus and ν be the Poisson's ratio and e_m^E is merely the elastic counterpart of the total mean strain e_m where

$$e_m = \frac{1}{3}e_V \tag{10.37}$$

and e_V is the volumetric strain and it is sometimes called the first invariant of strain tensor.

Next, we write the total deviatoric stress and the total mean stress in terms of plastic strain and mean plastic strain:

$$^{t+\Delta t}\boldsymbol{S} = {}^{t+\Delta t}\boldsymbol{S}^E - 2G^{t+\Delta t}\Delta\boldsymbol{e}'^P \tag{10.38}$$

$$^{t+\Delta t}\sigma_m = {}^{t+\Delta t}\sigma_m^E - c_m\Delta e_m^P \tag{10.39}$$

By using the flow rule, we have

$$^{t+\Delta t}e_{ij}'^P = \Delta\lambda^{t+\Delta t}S_{ij} \tag{10.40}$$

$$\Delta e_m^P = \frac{\Delta\lambda}{3}{}^{t+\Delta t}\mathscr{F}' \tag{10.41}$$

where

$$^{t+\Delta t}\mathscr{F}' \equiv {}^{t+\Delta t}\left(\frac{\partial\mathscr{F}}{\partial\sigma_m}\right) = q_1q_2{}^{t+\Delta t}\hat{\sigma}_y{}^{t+\Delta t}f^*\sinh\left(\frac{3q_2{}^{t+\Delta t}\sigma_m}{2^{t+\Delta t}\hat{\sigma}_y}\right) \tag{10.42}$$

and $\Delta\lambda$ is the plastic multiplier. Substituting $e_{ij}'^P$ into the deviatoric stress-strain relation and obtain

$$^{t+\Delta t}\boldsymbol{S} = \frac{^{t+\Delta t}\boldsymbol{S}^E}{1+2G\Delta\lambda} \tag{10.43}$$

Also, by writing the rate of change of porosity equation into the incremental form, we obtain

$$\Delta f = 3(1-{}^{t+\Delta t}f)\Delta e_m^P + A\Delta\bar{e}^P \tag{10.44}$$

where $A = A_1 + A_2$. Likewise, for the equivalence of plastic work, we have

$$\boldsymbol{\sigma} : \Delta\boldsymbol{e}^P = (1-f)\hat{\sigma}_y\Delta\bar{\boldsymbol{e}}^P \tag{10.45}$$

with

$$^{t+\Delta t}\hat{\sigma}_y = {}^{t+\Delta t}\hat{\sigma}_y({}^t\bar{e}^P + \Delta\bar{e}^P) \tag{10.46}$$

After expanding the term $\boldsymbol{\sigma} : \Delta\boldsymbol{e}^P$, we rewrite the equivalence of plastic work at the end of the time step as

$$\Delta\lambda\,{}^{t+\Delta t}\boldsymbol{S} : {}^{t+\Delta t}\boldsymbol{S} + 3{}^{t+\Delta t}\sigma_m\,{}^{t+\Delta t}e_m^P = (1-{}^{t+\Delta t}f)^{t+\Delta t}\hat{\sigma}_y\Delta\bar{e}^P = 0 \tag{10.47}$$

Then, defining the functional $\mathscr{P}$ as

$$^{t+\Delta t}\mathscr{P} \equiv \Delta\lambda\,{}^{t+\Delta t}\boldsymbol{S} : {}^{t+\Delta t}\boldsymbol{S} + 3{}^{t+\Delta t}\sigma_m\,{}^{t+\Delta t}e_m^P - (1-{}^{t+\Delta t}f)^{t+\Delta t}\hat{\sigma}_y\Delta\bar{e}^P \tag{10.48}$$

Clearly, $\mathscr{P} = 0$ has to be satisfied at the end of all time steps by definition. Likewise, the yield function has to be equal to zero at the end of all time steps for plastic loading, that is $^{t+\Delta t}\mathscr{F}({}^{t+\Delta t}\boldsymbol{S}, {}^{t+\Delta t}\sigma_m, {}^{t+\Delta t}\hat{\sigma}_y, {}^{t+\Delta t}f) = 0$ or explicitly,

$$\frac{1}{2}{}^{t+\Delta t}\boldsymbol{S} : {}^{t+\Delta t}\boldsymbol{S} - \frac{^{t+\Delta t}\hat{\sigma}_y^2}{3}\left[2^{t+\Delta t}f^* q_1\cosh\left(\frac{3q_2{}^{t+\Delta t}\sigma_m}{2^{t+\Delta t}\hat{\sigma}_y}\right) - 1 - q_3^2({}^{t+\Delta t}f^*)^2\right] = 0 \tag{10.49}$$

Up to this point, we have presented all the relevant equations for the Gurson-Tvergaard model. In summary, we have to solve two nonlinear algebraic equations for every time step.

$$^{t+\Delta t}\mathscr{P}(\Delta\bar{e}^P, \Delta e_m^P) = 0$$
$$^{t+\Delta t}\mathscr{F}(\Delta\bar{e}^P, \Delta e_m^P) = 0$$

where $\Delta\bar{e}^P$ and Δe_m^P are the two unknowns (where $\Delta\bar{e}^P$ is the governing parameter). After solving for $\Delta\bar{e}^P$ and Δe_m^P, we can determine Δf and then f^*. Furthermore, we can obtain $\mathscr{F}'$, $\Delta\lambda$, $\boldsymbol{S}$ and σ_m. With these variables determined, one can obtain the updated local stress for all phases using the TFA equations.

10.4.2 Newton's Method

For the Gurson-Tvergaard model, there is a system of two nonlinear equations, namely $^{t+\Delta t}\mathscr{P} = 0$ and $^{t+\Delta t}\mathscr{F} = 0$. That is, we have two unknowns at the end of

each time step, namely Δe_m^P and $\Delta \bar{e}^P$. There are many techniques to solve such a system. Here, we employ the Newton's method. Note that in the original Kojić's paper, the author uses the bisection method to solve for the system of equations. Although Newton's method is more computational demanding since it needs to evaluate the Jacobian matrix at every iteration, it does converge with a quadratic convergence rate provided that good initial values are given. Next we rewrite the two governing equations in the form that is ready for applying Newton's method algorithm.

$$\begin{Bmatrix} \Delta e_m^{P(i+1)} \\ \Delta \bar{e}^{P(i+1)} \end{Bmatrix} = \begin{Bmatrix} \Delta e_m^{P(i)} \\ \Delta \bar{e}^{P(i)} \end{Bmatrix} - \begin{bmatrix} \dfrac{\partial \mathscr{P}}{\partial(\Delta e_m^P)} & \dfrac{\partial \mathscr{P}}{\partial(\Delta \bar{e}^P)} \\ \dfrac{\partial \mathscr{F}}{\partial(\Delta e_m^P)} & \dfrac{\partial \mathscr{F}}{\partial(\Delta \bar{e}^P)} \end{bmatrix}^{-1} \begin{Bmatrix} \mathscr{P}(\Delta e_m^{P(i)}, \Delta \bar{e}^{P(i)}) \\ \mathscr{F}(\Delta e_m^{P(i)}, \Delta \bar{e}^{P(i)}) \end{Bmatrix} \tag{10.50}$$

In order to start the iterations, we need to determine the four partial derivatives, namely $\frac{\partial \mathscr{P}}{\partial(\Delta e_m^P)}$, $\frac{\partial \mathscr{P}}{\partial(\Delta \bar{e}^P)}$, $\frac{\partial \mathscr{F}}{\partial(\Delta e_m^P)}$ and $\frac{\partial \mathscr{F}}{\partial(\Delta \bar{e}^P)}$ at every step 'i' and are given in the appendix.

10.4.3 Ranges of Δe_m^P and $\Delta \bar{e}^P$

The bisection method and the Newton's method need an initial approximation in order to start the iteration. However, if we are able to narrow the possible range of the initial guess, it will definitely save both time and effort. In this section, we will try to minimize the possible range of Δe_m^P and $\Delta \bar{e}^P$. In principle, both Δe_m^P and $\Delta \bar{e}^P$ can be any real number. However, in order to make physical sense, these two variables are subject to some restrictions. The most obvious one is $\Delta \bar{e}^P \geq 0$ by definition. On the other hand, we need to determine the range of Δe_m^P which is less obvious.

In the following argument, our discussion is based on the loading phase, that is $\Delta\lambda > 0$. According to Kojić's paper [16], the rate of change of porosity is written as

$$\dot{f} = \dot{f}_G + \dot{f}_N + \dot{f}_C \tag{10.51}$$

which is sum of the rate of void growth $\dot{f}_G$, nucleation $\dot{f}_N$ and coalescence $\dot{f}_C$.

$$\dot{f}_G = (1-f)\dot{e}_V^P \tag{10.52}$$

$$\dot{f}_N = A_1 \dot{\bar{e}}^P \tag{10.53}$$

$$\dot{f}_C = A_2 \dot{\bar{e}}^P \tag{10.54}$$

where A_1 and A_2 are material parameters and can be functions of internal variables. If we let $A = A_1 + A_2$, then we have

$$\dot{f} = (1-f)\dot{e}_V^P + A\dot{\bar{e}}^P \tag{10.55}$$

First of all, the increment of porosity Δf has to be nonnegative, that is

$$\Delta f = \frac{3(1-{}^t f)\Delta e_m^P + A\Delta\bar{e}^P}{1+3\Delta e_m^P} \geq 0$$

From this inequality, it follows immediately that $\Delta e_m^P \neq -\frac{1}{3}$ in any event. Also, recall the following important relations:

$$\Delta\lambda = \frac{3\Delta e_m^P}{q_1 q_2 {}^{t+\Delta t}\hat{\sigma}_y {}^{t+\Delta t} f^* \sinh\left(\frac{3q_2 {}^{t+\Delta t}\sigma_m}{2^{t+\Delta t}\hat{\sigma}_y}\right)} > 0$$

$${}^{t+\Delta t}\sigma_m = {}^{t+\Delta t}\sigma_m^E - c_m \Delta e_m^P$$

Since $\Delta\lambda$ has to be greater than zero, it implies that Δe_m^P and ${}^{t+\Delta t}\mathscr{F}'$ must have the same sign. But this further implies that Δe_m^P and ${}^{t+\Delta t}\sigma_m$ must have the same sign. Up to this point, $\Delta\bar{e}^P$ and Δe_m^P are subject to the following constraints:

1. $\Delta\bar{e}^P \geq 0$
2. $\Delta e_m^P \neq -\frac{1}{3}$
3. Δe_m^P and ${}^{t+\Delta t}\sigma_m$ must have the same sign
4. $\Delta f = \frac{3(1-{}^t f)\Delta e_m^P + A\Delta\bar{e}^P}{1+3\Delta e_m^P} \geq 0$
5. ${}^{t+\Delta t}\sigma_m = {}^{t+\Delta t}\sigma_m^E - c_m\Delta e_m^P$

Before we start examining the possible values of $\Delta\bar{e}^P$ and Δe_m^P, let us pick out the known quantities since these are the known values before entering the iterations. The known quantities are ${}^t f$, A, ${}^{t+\Delta t}\sigma_m^E$ and c_m. In general, ${}^t f \geq 0$, $A \geq 0$ and $c_m > 0$. However, ${}^{t+\Delta t}\sigma_m^E$ can be negative, zero or positive depending on the type of loading. So, let us examine ${}^{t+\Delta t}\sigma_m^E$ first since the sign of ${}^{t+\Delta t}\sigma_m^E$ will put further restrictions on Δe_m^P.

The first case is $\sigma_m^E > 0$ and will lead to the following theorem:

Theorem 10.1. *Suppose that $\sigma_m^E > 0$, then there exists $\Delta e_m^P > 0$ such that $\sigma_m > 0$. Moreover, we have the following inequality:*

$$0 < \Delta e_m^P < \frac{\sigma_m^E}{c_m} \tag{10.56}$$

Proof. Follow the properties of real numbers and the fact that $\Delta\lambda > 0$. That is, $\Delta\lambda > 0$ implies that both σ_m and Δe_m^P must have the same sign. Since $\sigma_m^E > 0$ and Δe_m^P cannot be negative or equal to zero, or otherwise we have $\Delta\lambda \leq 0$. Consequently, both σ_m and Δe_m^P have to be positive. The existence of such a Δe_m^P is because of the completeness of real numbers [24]. This theorem simply states that our initial guess for Δe_m^P has to lie in between 0 and $\frac{\sigma_m^E}{c_m}$ in order to enable a solution if $\sigma_m^E > 0$. ■

The second case is $\sigma_m^E = 0$ which are usually consequences of applying pure shear loading on an isotropic materials. In this case, we have $\sigma_m = -c_m\Delta e_m^P$. Since

$\Delta\lambda$ has to be positive for plastic loading, therefore the only choice is $\Delta e_m^P = 0$, which implies $\sigma_m = 0$. In this case, we have $\Delta f = A\Delta\bar{e}^P$. But then we have arrived an undetermined form for $\Delta\lambda$ which is $\Delta\lambda \to \frac{0}{0}$. Thus, the formula $\Delta\lambda = \frac{3\Delta e_m^P}{\mathscr{F}'}$ is no longer valid in this case. Therefore, we expect $\Delta\lambda$ is no longer a function of Δe_m^P and hence, $\Delta\lambda = \Delta\lambda(\Delta\bar{e}^P)$. Thus, we have the following theorem:

Theorem 10.2. *Suppose that $\sigma_m^E = 0$, then we have the following form for $\mathscr{P}$ and $\mathscr{F}$:*

$$^{t+\Delta t}\mathscr{P} = \Delta\lambda\, {}^{t+\Delta t}\boldsymbol{S} : {}^{t+\Delta t}\boldsymbol{S} - (1 - {}^{t+\Delta t}f)^{t+\Delta t}\hat{\sigma}_y \Delta\bar{e}^P \tag{10.57}$$

$$^{t+\Delta t}\mathscr{F} = \frac{1}{2}{}^{t+\Delta t}\boldsymbol{S} : {}^{t+\Delta t}\boldsymbol{S} + \frac{{}^{t+\Delta t}\hat{\sigma}_y^2}{3}[2q_1{}^{t+\Delta t}f^* - 1 - (q_3{}^{t+\Delta t}f^*)^2] \tag{10.58}$$

Moreover, we have

$$\Delta\lambda = \mathscr{R}\frac{\Delta\bar{e}^P}{{}^{t+\Delta t}\hat{\sigma}_y} \tag{10.59}$$

where

$$\mathscr{R} = \frac{3(1 - {}^{t+\Delta t}f)}{2[1 + (q_3{}^{t+\Delta t}f^*)^2 - 2q_1{}^{t+\Delta t}f^*]} \tag{10.60}$$

Proof. Since $\sigma_m = 0$, therefore $\cosh\left(\frac{3q_2{}^{t+\Delta t}\sigma_m}{2^{t+\Delta t}\hat{\sigma}_y}\right) = 1$. Substitute these two relations into the expressions of $\mathscr{P}$ and $\mathscr{F}$ of Gurson-Tvergaard model to obtain the results. To show that $\Delta\lambda = \mathscr{R}\frac{\Delta\bar{e}^P}{{}^{t+\Delta t}\hat{\sigma}_y}$, simply set the expressions for $\mathscr{P}$ and $\mathscr{F}$ equal to zero and combine the two expressions. That is, we have

$${}^{t+\Delta t}\boldsymbol{S} : {}^{t+\Delta t}\boldsymbol{S} = \frac{2^{t+\Delta t}\hat{\sigma}_y^2}{3}[1 + (q_3{}^{t+\Delta t}f^*)^2 - 2q_1{}^{t+\Delta t}f^*]$$

follow from the expression $\mathscr{F} = 0$. Then substitute ${}^{t+\Delta t}\boldsymbol{S} : {}^{t+\Delta t}\boldsymbol{S}$ into the expression $\mathscr{P} = 0$ to solve for $\Delta\lambda$. ■

However, if ${}^t f = 0$ and $A = 0$, then $\Delta f = \frac{3\Delta e_m^P}{1+3\Delta e_m^P}$ and we have back to von-Mises case and this leads to the following corollary of the above theorem:

Corollary 10.1. *Suppose that ${}^t f = 0$, $A = 0$ and $\sigma_m^E = 0$, then we have the following form for $\mathscr{P}$ and $\mathscr{F}$:*

$$^{t+\Delta t}\mathscr{P} = \Delta\lambda\, {}^{t+\Delta t}\boldsymbol{S} : {}^{t+\Delta t}\boldsymbol{S} - {}^{t+\Delta t}\hat{\sigma}_y \Delta\bar{e}^P \tag{10.61}$$

$$^{t+\Delta t}\mathscr{F} = \frac{1}{2}{}^{t+\Delta t}\boldsymbol{S} : {}^{t+\Delta t}\boldsymbol{S} + \frac{1}{3}{}^{t+\Delta t}\hat{\sigma}_y^2 \tag{10.62}$$

Moreover, we have

$$\Delta\lambda = \frac{3\Delta\bar{e}^P}{2^{t+\Delta t}\hat{\sigma}_y} \tag{10.63}$$

Proof. The proof is by setting ${}^{t+\Delta t}f$ and ${}^{t+\Delta t}f^*$ equal to zero in the expression of R. ■

The last case is $\sigma_m^E < 0$. In this situation, we must have $\Delta e_m^P < 0$ or otherwise σ_m and Δe_m^P will have different signs which lead to $\Delta\lambda < 0$. But this simply implies that $\sigma_m^E < c_m \Delta e_m^P$. Then have the following theorem.

Theorem 10.3. *Suppose that $\sigma_m^E < 0$, then there exists $\Delta e_m^P < 0$ such that $\sigma_m < 0$. Moreover, we have the following inequality:*

$$\frac{\sigma_m^E}{c_m} < \Delta e_m^P < 0 \tag{10.64}$$

Proof. The proof follows from previous inequality. ■

This further leads to an important theorem:

Theorem 10.4. *Suppose that $\sigma_m^E \neq 0$, then there exists Δe_m^P such that the following inequality holds.*

$$0 < |\Delta e_m^P| < \frac{|\sigma_m^E|}{c_m} \tag{10.65}$$

Proof. The proof follows directly from the consequences of Theorems 3.1 and 3.3. ■

Now we have the following preliminary conclusion: σ_m and Δe_m^P must have the same sign as σ_m^E. Next we try to examine how the range of Δe_m^P affects the range of $\Delta \bar{e}^P$. Since $\Delta e_m^P \neq -\frac{1}{3}$, we can divide into four different cases, which are $\Delta e_m^P < -\frac{1}{3}$, $-\frac{1}{3} < \Delta e_m^P < 0$, $\Delta e_m^P = 0$ and $0 < \Delta e_m^P$.

For the case that $\Delta e_m^P < -\frac{1}{3}$, then $1 + 3\Delta e_m^P$ and $3(1 - {}^t f)\Delta e_m^P$ are both less than zero which further implies

$$\begin{aligned} & 3(1 - {}^t f)\Delta e_m^P + A\Delta \bar{e}^P \leq 0 \\ \Rightarrow \quad & 3(1 - {}^t f)|\Delta e_m^P| \geq A\Delta \bar{e}^P \end{aligned}$$

If $A > 0$, then

$$\Delta \bar{e}^P \leq \frac{3(1 - {}^t f)|\Delta e_m^P|}{A} \tag{10.66}$$

For the case that $-\frac{1}{3} < \Delta e_m^P < 0$, then $1 + 3\Delta e_m^P > 0$ and $3(1 - {}^t f)\Delta e_m^P < 0$. Hence, we have

$$\begin{aligned} & 3(1 - {}^t f)\Delta e_m^P + A\Delta \bar{e}^P \geq 0 \\ \Rightarrow \quad & 3(1 - {}^t f)|\Delta e_m^P| \leq A\Delta \bar{e}^P \end{aligned}$$

If $A > 0$, then

$$\frac{3(1 - {}^t f)|\Delta e_m^P|}{A} \leq \Delta \bar{e}^P \tag{10.67}$$

However, if $A = 0$, then the expression $3(1 - {}^t f)|\Delta e_m^P| \leq A\Delta \bar{e}^P$ is not valid, which implies that we cannot choose such an Δe_m^P between $-\frac{1}{3}$ and 0. For $0 \leq \Delta e_m^P$, we have $3(1 - {}^t f)\Delta e_m^P + A\Delta \bar{e}^P \geq 0$. Consequently, $\Delta f \geq 0$ is automatically satisfied for $0 \leq \Delta e_m^P$.

In summary, the range of Δe_m^P is strongly depended on the sign of σ_m^E. Based on the restriction on Δe_m^P, the range of $\Delta \bar{e}^P$, is then further restricted by the criterion $\Delta f \geq 0$. Thus, we obtain the range of Δe_m^P and $\Delta \bar{e}^P$ for the Gurson-Tvergaard model in the governing parameter method algorithm.

10.5 Verifications and Examples

10.5.1 Test Cases

In this section, an evaluation and verification of the modelling framework is performed. The accuracy of the model is compared to results in the literature. Moreover, the yield curve for the models employed here has the form:

$$\hat{\sigma}_y = \sigma_{yv} + h(\bar{e}^P)^q \tag{10.68}$$

where σ_{yv} is the yield stress of the matrix phase at the original state. Also, h and q represent the *strength coefficient* and the *work-hardening exponent*, respectively. From the definition of the plastic modulus E_P, we have

$$E_P = \frac{d\hat{\sigma}_y}{d\bar{e}^P} = qh(\bar{e}^P)^{q-1} \tag{10.69}$$

for the proposed test cases. Note that Gurson yield criterion is a special case of the Gurson-Tvergaard yield criterion with $q_1 = q_2 = q_3 = 1.0$. Moreover, the critical void volume fraction is assumed to be $f_c = 0.05$ and the failure void volume fraction is taken as $f_f = 0.315$.

In Table 10.1, four different fiber-reinforced composite materials are shown. The numerical values for the properties of composite materials have been taken from the literature. For the abbreviations used in Table 10.1, the first letter (or the first two letters with the second letter in lower case) relates to the authors. For instance, 'JLS' represents the paper written by three authors Ju et al.; 'Ll' represents the paper written by Llorca. With reference to the shapes, the following abbreviations, 'S', and 'PS' represent sphere and prolate spheroid, respectively. In addition, 'ζ' denotes the aspect ratio.

10.5.1.1 Ju and Lee 2000

According to the paper by Ju and Lee [11], the predicted the overall yield criterion for the fiber-reinforced composite is based on the ensemble-volume averaging process. As a results of this approach, they used the classical plasticity theory to predict the overall elastoplastic response of the composite material as an effective yield criterion is obtained. This is certainly different from our approach which only

Table 10.1 Properties table

	JLS	PA	JL1	JL2	Ll
E_m [GPa]	70	73	55.8	68.3	71.8
ν_m	0.3	0.33	0.32	0.33	0.33
E_f [GPa]	450	485	397	490	450
ν_f	0.2	0.2	0.2	0.17	0.17
σ_{yv} [MPa]	300	220	87.8	250	169
h [GPa]	1,000	370	972	137	463.24
q	0.5	0.3	0.55	0.55	0.39252
c_f	0.15	0.20	0.20	0.20	0.06,0.13
Shape	PS	S	S	S	S
ζ	3	1	1	1	1

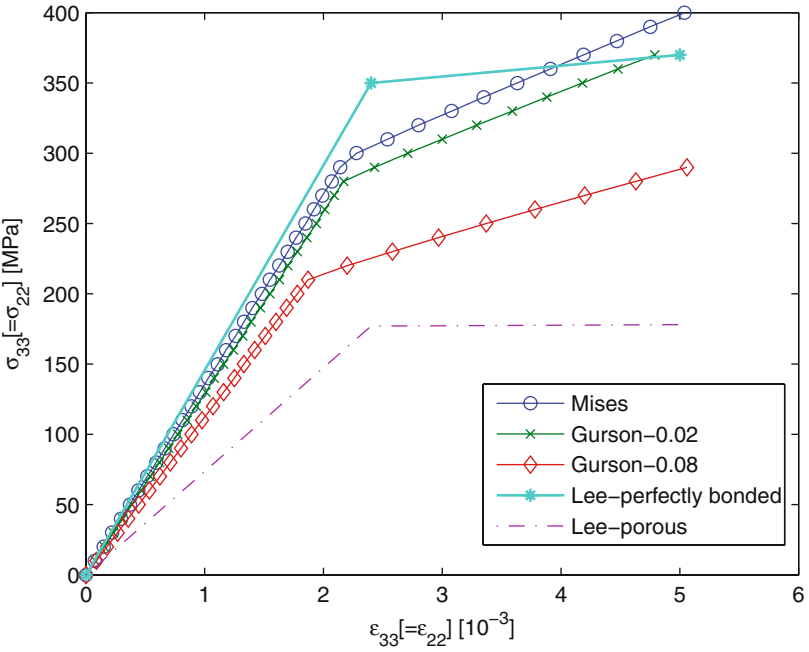

Fig. 10.1 Results: Biaxial Loading, Ju and Lee 2000

requires the matrix phase to satisfy the classical plasticity theory. Also, Ju and Lee proposed an interfacial debonding process which is governed by the mean stress of the matrix phase while the damage evolution is governed by the Weibull interfacial strength parameter [9, 18]. Also, they present a comparison with an experimental study documented by Llorca in 1991. We compare our results to both Ju and Lee's results (Fig. 10.1) and Llorca's results (Fig. 10.2).

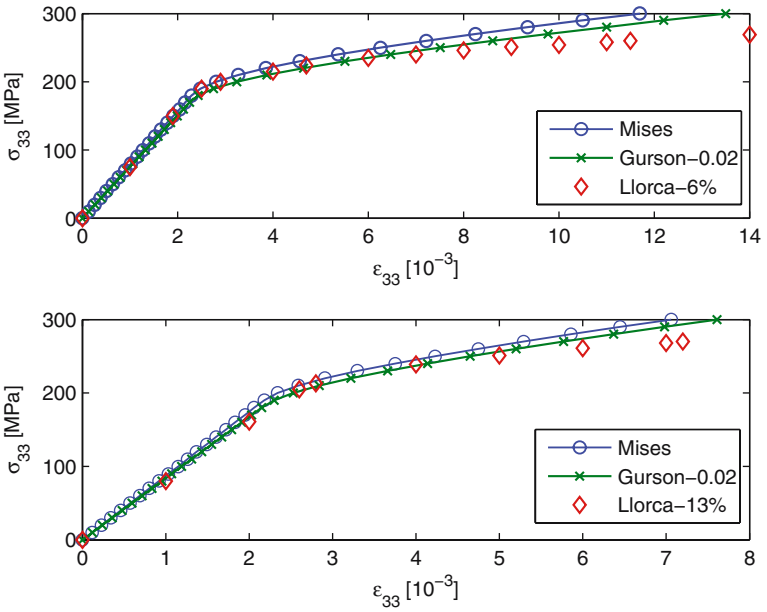

Fig. 10.2 Results: Llorca 91 (experimental)

10.5.1.2 Denda, Weng and Zheng 2003

Denda et al. proposed a method that combined the homogenization scheme with the finite element analysis to examine the influence of the debonding angle to the overall elastoplastic behavior of fiber-reinforced composites. According to the paper, the debonding angle is the half-angle of the entire debonding measured from the axis of symmetry [5]. Furthermore, the authors assumed the entire composite to consist of three phases, namely, the fibers, cracks and matrix. Recalling the micromechanics theory, one can relate the local strain of the fibers to the local strain of the matrix using the strain concentration factors. In this case, their model proposed two strain concentration factors, namely the fiber strain concentration factor and the damaged zone (cracks) strain concentration factor. These strain concentration factors are approximated by a complex-variable solution proposed by Toya [21]. Note that the solution obtained from Toya is restricted to a circular inclusion embedded within an infinite matrix medium. On the other hand, the overall nonlinear behavior of the composites is predicted by the secant-modulus approach. In addition, the authors used ANSYS finite element software to study the effect of the debonding angle to the material properties of the composites. The material properties of this model are given in Table 10.1 and the results are plotted in Fig. 10.3.

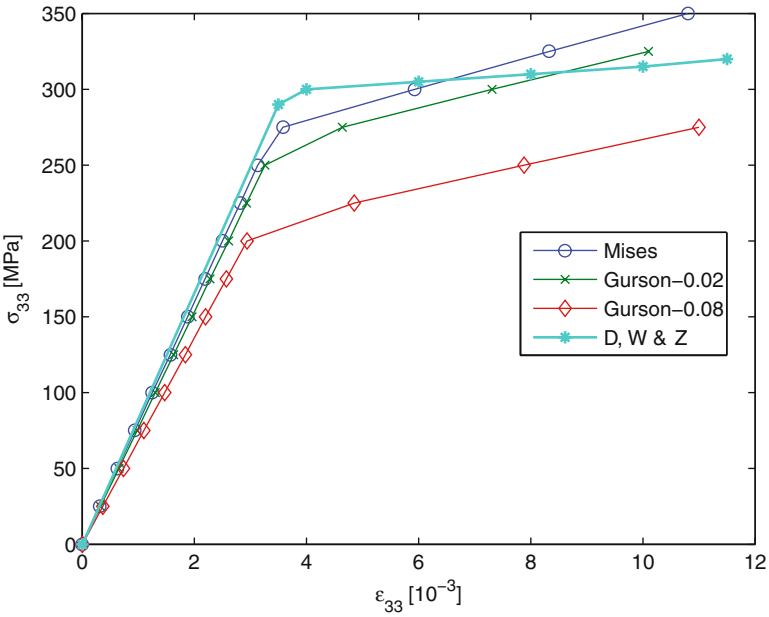

Fig. 10.3 Results: Denda, Weng and Zheng 2003

10.5.1.3 Ju, Liu and Sun 2003

Here, we compare two material models with our proposed model. The first material is an aluminum alloy particle-reinforced composite. The fibers are prolate spheroids with aspect ratio equal to 3.0 (i.e. $\zeta = 3.0$). In this paper, the authors proposed an elastoplastic damage model to predict the partial debonding process of metal matrix composites under elastoplastic deformation [12]. The governing parameter of the damage process is the average particle stress. That is, once the average particle stress attained to a certain level, the evolution of damage starts. Note that the only difference between the model in Ju and Lee's and Ju, Liu and Sun's papers is the consideration of the partial debonding evolution. However, the damage evolution is governed by the Weibull statistics in both cases. In addition, Ju, Liu and Sun also compared their model to experimental data provided in Papazian and Adler's paper. In this simulation, we will employ the GPM algorithm to integrate the governing TFA equations using both the von-Mises and Gurson's yield criterion. Only the isotropic hardening rule is considered. The material properties of the composite are given in Table 10.1 and the results are presented in Fig. 10.4.

The second material is a SiC particulate-reinforced 5456 aluminum alloy composite used in Papazian and Adler's experimental results. The inclusion shape is assumed to be spherical. The material properties of the composites are given in Table 10.1 and the results are plotted in Fig. 10.5.

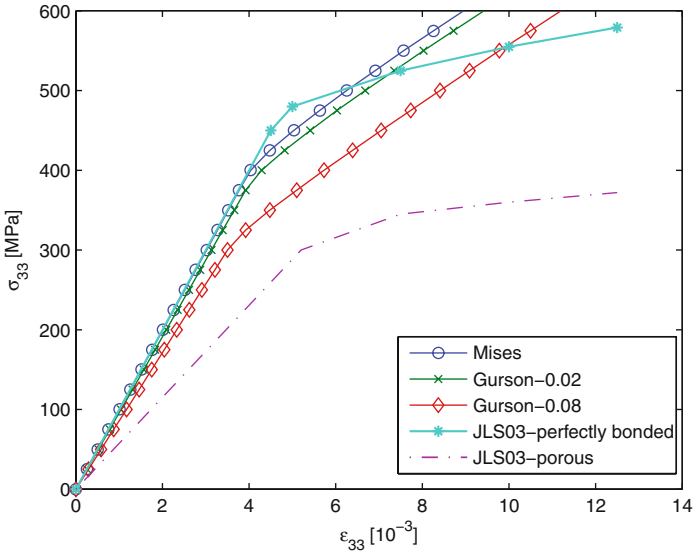

Fig. 10.4 Results: Ju, Liu and Sun 2003

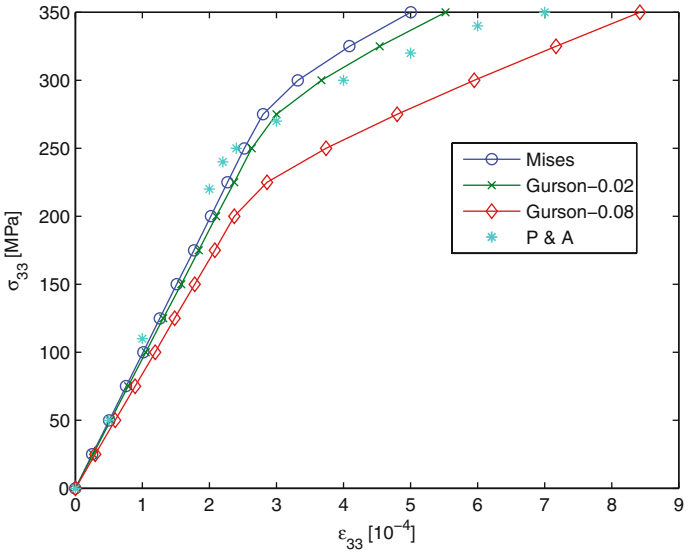

Fig. 10.5 Results: Papazian and Alder 1990

10.5.1.4 Ju, Liu and Sun 2006

The material considered in this section is the same as in the case of Ju and Lee's, however, the inclusion shape is spherical. In the paper by Ju, Liu and Sun 2006, the authors proposed a new particle-matrix interfacial debonding model to predict the

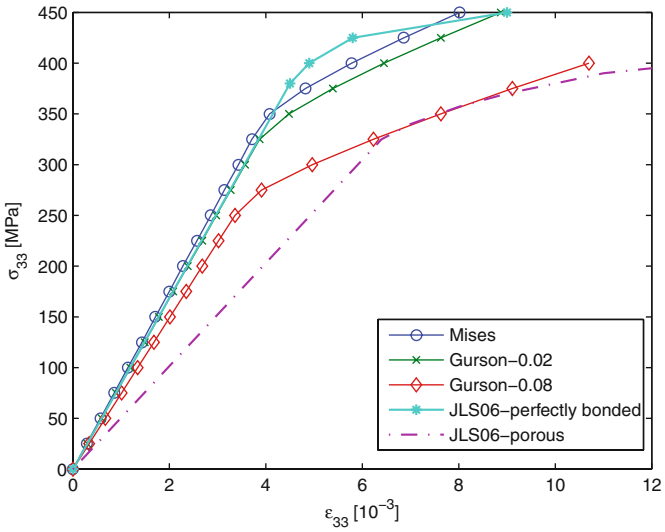

Fig. 10.6 Results: Ju, Liu and Sun 2006

partially debonding process of metal matrix composites under elastoplastic deformation [13, 14]. The governing damage parameters are based on four different debonding modes while the damage evolution is based on the Weibull statistics. These modes are governed by the so-called "interfacial damage parameters". According to the authors, the interfacial damage parameter measures the reduction of elastic stiffness in certain directions. Quantitatively speaking, it is the ratio of the projected damaged area to the original interface area in a certain direction. For results, see Fig. 10.6.

10.5.2 Discussion on the Evaluation Process

The combined TFA-GPM method framework provides good agreement with the results presented in the literature. More importantly, the evaluation and verification procedure demonstrated the versatility, capability and flexibility of the proposed elastoplastic modelling framework formulated and implemented in this paper.

In the paper by Ju and Lee 2000, the authors compared their model to Zhao and Weng's model under uniaxial and biaxial loading. In addition, Ju and Lee also compared the results produced by their model to an experimental result given by Llorca in 1991. In the above simulation, we compared our model to Ju and Lee's results, Zhao and Weng's results and Llorca's experimental results. As shown in Fig. 10.4, our results for the von-Mises case and Gurson-0.02 case lie between the Ju and Lee's perfectly bonded curve and Zhao and Weng's perfectly bonded curve. On the other hand, the Gurson-0.08 curve lies between the upper bound and lower

bound of Zhao and Weng's results. Note that in any event, our results have shown to be stiffer when compared to Ju and Lee and Zhao and Weng's numerical models for the same reasons as described previously. However, as shown in Fig. 10.2, our results show good agreement when compared to Llorca's experimental result.

When compared to Denda, Weng and Zheng's secant model, our results (von-Mises, Gurson-0.02 and Gurson-0.08) have shown that we have a lower overall yield stress on the composite. Also, the overall stress-strain curve predicted by our models are stiffer than Denda, Weng and Zheng's secant model.

In the case of Ju, Liu and Sun's model, we compared our results using prolate spheroidal shape fibers with $\zeta = 3.0$ and spherical shape fibers. In general, our results lie between their upper bound (perfectly bonded case) and lower bounded (porous case). Again, our results show a stiffer overall stress-strain curve. Note that the only difference between Ju, Liu and Sun's model and Ju and Lee's model is the interfacial damage model and they both employed the Weibull statistics governing equation for the evolutionary damage process. Consequently, it is expected that they have similar results. On the other hand, our results have shown a good agreement between our models and Papzian and Alder's experimental results.

In summary, we have the following observations from the model validation and verification.

1. The TFA-GPM model tends to give stiffer overall stress-strain curves. The possible reason is the approximation of the continuous plastic strain fields by piecewise uniform plastic strain fields and the Mori-Tanaka scheme.
2. The TFA-GPM in combination with Gurson yield criterion with initial porosity of 2% reduces the overall stiffness of the elastoplastic curves in the uniaxial tension case. This clearly confirms that porosity and the evolutionary damage due to porosity are significant factors that affect the overall elastoplastic behavior of the composite.
3. Initial yielding of the overall composite materials is sandwiched between the perfectly bonded case and the porous case in the case of Ju and Lee, Denda, Weng and Zheng and Ju, Liu and Sun regardless of the yield criteria used.

10.5.3 4-phase Composite Material

In this section, we will consider a more complex model in order to show the full capabilities of the proposed model to simulate a 4-phase Carbon/Glass Fibrous composite. For simplicity, we assume the following holds true for this analysis:

1. The total fiber volume fraction is assumed to be 40%.
2. The graphite fibers occupy 60% of the total fiber volume fraction.

The initial distribution of the percentage of different phases given are shown in Table 10.2.

Table 10.2 Initial phase volume fraction

Phase	2% Void	8% Void
Epoxy	58%	52%
Graphite fibers	24%	24%
E-glass fibers	16%	16%

Table 10.3 Phase properties of epoxy/e-glass/graphite composite

Phase property	Epoxy	E-glass	Graphite
E [GPa]	3.0	72	275.6
ν	0.35	0.17	0.2
σ_{yv} [MPa]	150	–	–
h [GPa]	400	–	–
q	0.5	–	–

Table 10.4 Overall properties: $\zeta = 1$

Parameters	2% Void	8% Void
E [GPa]	6.47	5.65
ν	0.307	0.287
G [GPa]	2.47	2.19
$\bar{\sigma}_{yv}$ [MPa]	208.2	166.9

Table 10.5 Overall properties: $\zeta = 5$

Parameters	2% Void	8% Void
$E_{11} = E_{22}$ [GPa]	6.14	5.31
E_{33} [GPa]	14.8	13.4
$\nu_{12} = \nu_{21}$	0.412	0.388
$\nu_{13} = \nu_{23}$	0.128	0.103
$\nu_{31} = \nu_{32}$	0.321	0.307
G_{12} [GPa]	2.17	1.91
$G_{13} = G_{23}$ [GPa]	2.45	2.17
$\bar{\sigma}_{yv}$ [MPa]	507.7	421.1

In this analysis, we tested for both the carbon fiber phase and the glass fiber phase with aspect ratio 1 and 5. The mechanical properties of the epoxy are obtained from Benzeggagh and Mergahni's experimental results which are given in Table 10.3.

From the analysis, the overall properties for the Epoxy/E-Glass/Graphite composite are obtained and these are recorded in Tables 10.4 for $\zeta = 1$ (spherical shape) and 10.5 for $\zeta = 5$ (spheroidal shape). The final distribution of the percentage between epoxy and void for all the cases are given in Table 10.6. In addition, for the cases where $\zeta = 1$, we apply a monotone loading up to 400 MPa while for the

Table 10.6 Final phase volume fraction

Phase	2%, $\zeta = 1$	8%, $\zeta = 1$	2%, $\zeta = 5$	8%, $\zeta = 5$
Epoxy	57.893%	49.952%	57.996%	51.888%
Void	2.107%	10.048%	2.004%	8.112%

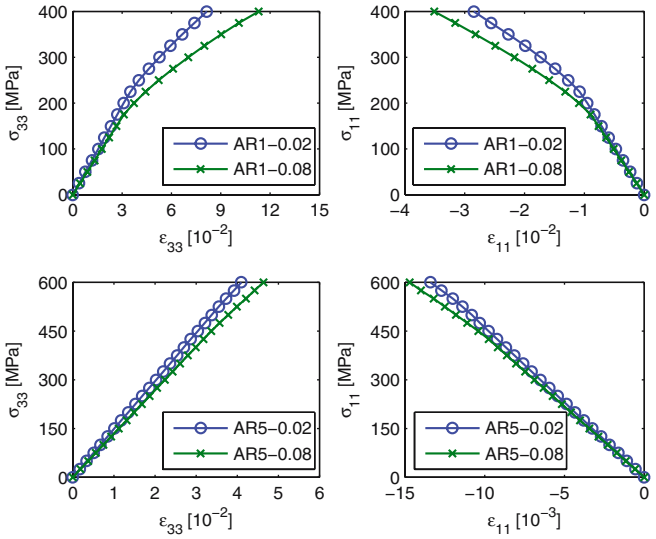

Fig. 10.7 Overall curves for epoxy/e-glass/graphite composite

cases where $\zeta = 5$, we load up to 600 MPa in the 33-direction. For the plots of stress - strain curves, see Fig. 10.7.

Based on the results of the analysis, we can draw the following conclusions:

1. For $\zeta = 5$ cases, the overall composites are transversely isotropic.
2. As aspect ratio increases, the composite becomes stiffer.
3. The overall initial yielding is strongly affected by the combination of the aspect ratio and the initial void volume fraction. For instance, in the case of 2% initial void, we have $\bar{\sigma}_{yy} = 208.2$ MPa for $\zeta = 1$ whereas we have $\bar{\sigma}_{yy} = 507.7$ MPa for $\zeta = 5$.
4. Both the initial void volume fraction and the geometry of the fiber significantly affect the final void volume fraction. As shown in Table 10.6, for the case where initial void is 2% and $\zeta = 1$, we have 2.11% final void percentage. However, if the initial void is 8%, then the final void percentage is 10.05%.

10.6 Closing Remarks

In this paper, the combined TFA-GPM approach is implemented to predict the overall elastoplastic behavior of n-phase fiber-reinforced composites. The localization rule is based on the TFA method while the prediction of the mechanical concentration factors is estimated by the EMT theory. The yield criterion of the matrix phase is extended from the von-Mises yield criterion to the Gurson-Tvergaard yield criterion so as to take into account the effects of void growth under plastic deformation. The results show that the Gurson-Tvergaard yield criterion does provide a better approximation in the prediction of overall elastoplastic behavior of different types of 2-phase fiber-reinforced composites. Furthermore, simulation of a 4-phase fiber-reinforced composite is also provided, this certainly demonstrates the power of the existing model. More importantly, a rigorous mathematical analysis of the possible ranges of Δe_m^P and $\Delta \bar{e}^P$ has been provided. This certainly reduces the computational effort for guessing the possible values of Δe_m^P and $\Delta \bar{e}^P$. In Sect. 10.5, the evaluation and verification of the proposed TFA-GPM model under different cases have been accomplished. This assures the validity of the proposed model and it provides a level of confidence for other applications.

In summary, the two significant contributions in this research work include:

1. The Gurson-Tvergaard yield criterion gives better results compared to the von-Mises yield criterion since the effect of void growth has been considered in the analysis.
2. A rigorous mathematical analysis was performed to obtain the necessary conditions within the ranges for the change of the mean plastic strain Δe_m^P and the change of the effective plastic strain $\Delta \bar{e}^P$. This certainly provides a better start for the iteration of the algorithm.

Appendix – The Four Partial Derivatives

$$\frac{\partial \mathscr{P}}{\partial(\Delta e_m^P)} = \frac{\boldsymbol{S}^E : \boldsymbol{S}^E}{(1+2G\Delta\lambda)^2}\left[1 - \frac{4G\Delta\lambda}{1+2G\Delta\lambda}\right]\frac{\partial(\Delta\lambda)}{\partial(\Delta e_m^P)} + 3(\sigma_m^E - 2c_m\Delta e_m^P) + \hat{\sigma}_y\Delta\bar{e}^P\frac{\partial(\Delta f)}{\partial(\Delta e_m^P)} \tag{10.70}$$

$$\frac{\partial \mathscr{F}}{\partial(\Delta e_m^P)} = -\frac{2G\boldsymbol{S}^E : \boldsymbol{S}^E}{(1+2G\Delta\lambda)^3}\frac{\partial(\Delta\lambda)}{\partial(\Delta e_m^P)} - \frac{2q_3^2\hat{\sigma}_y^2 f^*}{3}\frac{\partial f^*}{\partial(\Delta e_m^P)} + \frac{2q_1\hat{\sigma}_y^2}{3}\left[\frac{\partial f^*}{\partial(\Delta e_m^P)}\cosh\left(\frac{3q_2\sigma_m}{2\hat{\sigma}_y}\right) - \frac{3q_2c_m f^*}{2\hat{\sigma}_y}\sinh\left(\frac{3q_2\sigma_m}{2\hat{\sigma}_y}\right)\right] \tag{10.71}$$

$$\frac{\partial \mathscr{P}}{\partial(\Delta\bar{e}^P)} = \frac{\boldsymbol{S}^E : \boldsymbol{S}^E}{(1+2G\Delta\lambda)^2}\frac{\partial(\Delta\lambda)}{\partial(\Delta\bar{e}^P)}\left(1-\frac{4G\Delta\lambda}{1+2G\Delta\lambda}\right) - (1-f)\left(\hat{\sigma}_y - \frac{\partial\hat{\sigma}_y}{\partial(\Delta\bar{e}^P)}\Delta\bar{e}^P\right) \tag{10.72}$$

$$\frac{\partial \mathscr{F}}{\partial(\Delta\bar{e}^P)} = -2G\frac{\boldsymbol{S}^E : \boldsymbol{S}^E}{(1+2G\Delta\lambda)^3}\frac{\partial(\Delta\lambda)}{\partial(\Delta\bar{e}^P)} + \frac{2\hat{\sigma}_y}{3}\frac{\partial\hat{\sigma}_y}{\partial(\Delta\bar{e}^P)} \left\{q_1 f^* \left[2\cosh\left(\frac{3q_2\sigma_m}{2\hat{\sigma}_y}\right) - \frac{3q_2\sigma_m}{2\hat{\sigma}_y}\sinh\left(\frac{3q_2\sigma_m}{2\hat{\sigma}_y}\right)\right] - [1+(q_3 f^*)^2]\right\} \tag{10.73}$$

References

1. Bahei-El-Din YA, Dvorak GJ, Wafa AM (1994) Implementation of transformation field analysis for inelastic composite materials. Comput Mech 14:201–228
2. Bathe KJ, Kojić M (2005) Inelastic Analysis of Solids and Structures. Computational Fluid and Solid Mechanics. Springer, Berlin
3. Benveniste Y (1987) A new approach to the application of Mori-Tanaka's theory in composite materials. Mech Mater 6:147–157
4. Benveniste Y, Dvorak GJ (1992) On transformation strains and uniform fields in multiphase elastic media. Proc Royal Soc Lond A437:291–310
5. Denda M, Weng GJ, Zheng SF (2003) Overall elastic and elastoplastic behavior of a partially debonded fiber-reinforced composite. J Compos Mater 37:741–758
6. Dvorak GJ (1990) On uniform fields in heterogeneous media. Proc Royal Soc Lond A431: 89–110
7. Dvorak GJ (1992) Transformation field analysis of inelastic composite materials. Proc Royal Soc Lond A437:311–327
8. Eshelby JD (1957) The determination of the elastic field of an ellipsoidal inclusion, and related problems. Proc Royal Soc Lond A241:376–396
9. Freiman SW, Fuller ER, White GS (2002) Mechanical Reliability and Life Prediction for Brittle Materials. In: Kutz M (ed) Handbook of Materials Selection, pp 809–828. Wiley, New York
10. Hori M, Nemat-Nasser S (1999) Micromechanics: Overall Properties of Heterogeneous Materials. North-Holland, New York, 2nd edition
11. Ju JW, Lee HK (2000) A micromechanical damage model for effective elastoplastic behavior of ductile matrix composites considering evolutionary complete particle debonding. Comput Methods Appl Mech Eng 183:201–222
12. Ju JW, Liu HT, Sun LZ (2003) Elastoplastic modeling of metal matrix composites with evolutionary particle debonding. Mech Mater 35:559–569
13. Ju JW, Liu HT, Sun LZ (2004) An interfacial debonding model for particle-reinforced composites. Int J Damage Mech 13:163–185
14. Ju JW, Liu HT, Sun LZ (2006) Elastoplastic modeling of progressive interfacial debonding for particle-reinforced metal-matrix composites. Acta Mech 181:1–17
15. Kojić M (2002) Stress integration procedures for inelastic material models within the finite element method. Appl Mech Rev 55:389–414
16. Kojić M, Vlastelica I, Zivkovic M (2002) Implicit stress integration procedure for small and large strains of the Gurson model. Int J Numer Methods Eng 53:2701–2720

17. Mori T, Tanaka K (1973) Average stress in matrix and average elastic energy of materials with misfitting inclusions. Acta Metall 21:571–574
18. Munz D (2002) Failure Modes: Performance and Service Requirements for Ceramics. In: Kutz M (ed) Handbook of Materials Selection, pp 787–808. Wiley, New York
19. Ng ETY, Suleman A (2007) Implicit stress integration in elastoplasticity of *n*-phase fiber-reinforced composites. Mech Adv Mater Struct 14:633–641
20. Niemi E, Zhang ZL (1995) A new failure criterion for the Gurson-Tvergaard dilational constitutive model. Int J Fract 70:321–334
21. Toya M (1974) A crack along the interface of a circular inclusion embedded in an infinite solid. J Mech Phys Solids 22:325–348
22. Tvergaard V (1981) Influence of voids on shear band instabilities under plane strain conditions. Int J Fract 17:389–407
23. Tvergaard V (1982) On localization in ductile materials containing spherical voids. Int J Fract 18:237–252
24. Wade WR (2003) An Introduction to Analysis, 3rd edn. Prentice-Hall

Chapter 11
Prediction of Mechanical Properties of Composite Materials by Asymptotic Expansion Homogenisation

J.A. Oliveira, J. Pinho-da-Cruz, and F. Teixeira-Dias

Abstract Finite element (FE) simulation plays a crucial role in the analysis of the mechanical behaviour of structural elements built with complex microstructure composite materials. In order to define microstructural details, finite element analysis (FEA) often leads to the need for unstructured meshes and large numbers of finite elements. This fact frequently makes it impossible to perform numerical analyses on the mechanical behaviour of such structural components, due to the large amounts of required memory and CPU time. In this particular context, homogenisation methodologies lead to significant computational benefits.

One of these homogenisation methods is the asymptotic expansion homogenisation (AEH). Following this approach, overall material properties can be derived from the mechanical behaviour of selected microscale representative volumes, also known as representative unit-cells (RUC). Nevertheless, unit-cell based models require the control of several parameters. Additionally, the unstructured tetrahedral finite element meshes frequently required by the complexity of RUC involve the control of specific periodic boundary conditions.

This work shows the mathematical formulation and implementation details of a dedicated three-dimensional FEA platform developed by the authors, which enables the modelling of the elastic behaviour of structural components built from composite materials. Automatic representative unit-cell generation procedures are also developed with control over relevant geometrical parameters. Additionally, in order to enforce the periodicity of boundary conditions, specific algorithms for the association of degrees of freedom are implemented.

J.A. Oliveira, J. Pinho-da-Cruz, and F. Teixeira-Dias
Departamento de Engenharia Mecânica, Universidade de Aveiro, Campus Universitário de Santiago, 3810-193 Aveiro, Portugal, e-mail: {jalex,jpc,ftd}@ua.pt

11.1 Introduction

When numerically simulating the behaviour of metal matrix composites (MMC) it is often necessary to use unstructured finite element meshes. The need for significant memory and CPU time resources leads to the use of dedicated optimisation methodologies. Numerical models that predict the behaviour of these materials are developed with these methodologies. One of these methods is the asymptotic expansion homogenisation (AEH). Applying the AEH, overall material properties can be derived from the mechanical behaviour of selected microscale representative unit-cells (RUC). Nevertheless, unit-cell based modelling requires the control of parameters such as reinforcement volume fractions, geometries and distributions within the matrix material. This leads to the development of automatic geometry generation algorithms. Additionally, unstructured tetrahedral meshes required by complex RUC involve the control of specific periodic boundary conditions.

11.2 Asymptotic Expansion Homogenisation

The asymptotic expansion homogenisation (AEH) method is used to solve problems that involve physical phenomena on continuous media with periodic microstructures. It is a useful technique to study the behaviour of structural components built from composite materials. The main advantages of this methodology lie on the fact that (i) it allows a significant reduction of the problem size and (ii) it has the capability to characterise stress and deformation microfields. AEH leads to specific equations that characterise these fields in a process called localisation, not found on most homogenisation methods. The localisation process is essentially the inverse of the homogenisation process.

11.2.1 AEH in Linear Elasticity

Consider a homogenenous linear elastic material associated to a material body Ω. Its microstructure is made from the spatially periodic distribution of a representative unit-cell, associated with a body Y, as shown in Fig. 11.1. Most heterogeneous materials have a small relation ε between the characteristic dimensions of the micro- and macroscale ($\varepsilon \ll 1$). Applying loads to these materials results in periodic oscillations of the resulting displacement, stress or deformation fields. These oscillations derive from the periodicity of the microstructural heterogeneities and are evident on a boundary of dimension ε of any point in Ω. Accordingly, it is usual to assume the existence of two separate dimensional scales, $\mathbf{x}$ and $\mathbf{y}$, linked to material behaviour phenomena at the macroscale Ω and microscale Y levels, respectively (see Fig. 11.1). Therefore, variables related to these fields functionally depend on both $\mathbf{x}$ and $\mathbf{y}$, where

$$\mathbf{y} = \mathbf{x}/\varepsilon \tag{11.1}$$

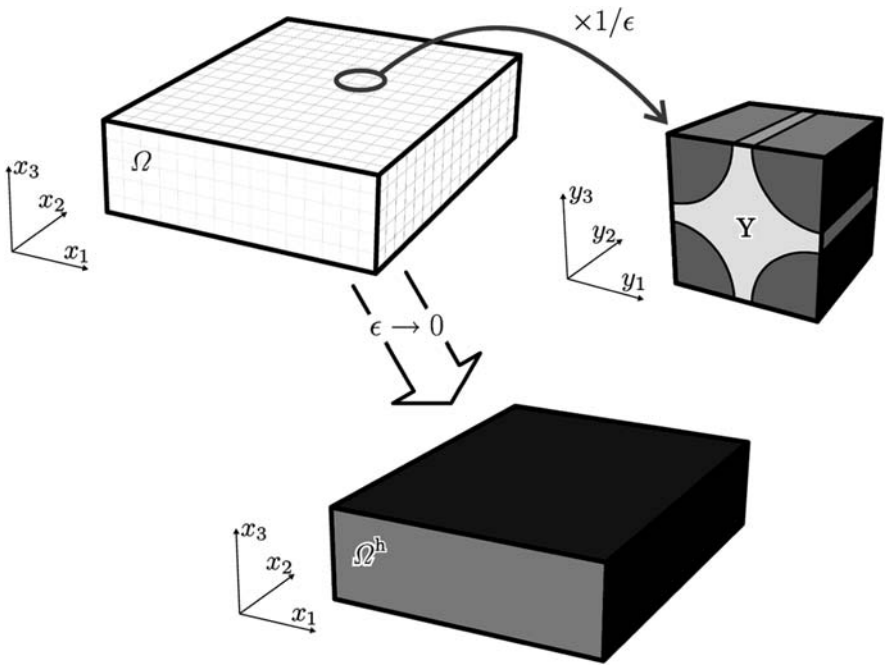

Fig. 11.1 Schematic representation of the heterogeneous elastic material body Ω and the unit-cell Y, representative of the microscale, used in the AEH, which results, with $\varepsilon \to 0$, in the homogenous material Ω^{h}

As a result, the dependence in $\mathbf{y}$ is periodic in the domain Y. This property is designated Y-periodicity.

In terms of elastic properties, the microstructural Y-periodicity is reflected on the fact that the elasticity tensor $\mathbf{D}$ is Y-periodic in $\mathbf{y}$. On the other hand, the homogeneity of the material at the macroscale level results on the indirect dependence of the elasticity tensor on the macroscale coordinate system, $\mathbf{x}$. Hence, in terms of the components of the elasticity tensor,

$$D_{ijkl} = D_{ijkl}(\mathbf{y}) \tag{11.2}$$

However, in the macroscale coordinate system $\mathbf{x}$, the microstructural heterogeneities are noticeable on a period ε^{-1} times smaller than the characteristic dimension of the domain Y. According to Eq. (11.1), this fact is denoted by

$$D^{\varepsilon}_{ijkl}(\mathbf{x}) = D_{ijkl}(\mathbf{x}/\varepsilon) \tag{11.3}$$

where the index ε stands for the fact that $\mathbf{D}$ is εY-periodic on the macroscale coordinate system, $\mathbf{x}$. Assuming infinitesimal deformations and a static equilibrium, and using Einstein's tensor notation, the linear elasticity problem is described by equilibrium equations, deformation-displacement relations and constitutive relations,

written as [7]

$$\frac{\partial \sigma_{ij}^{\varepsilon}}{\partial x_j^{\varepsilon}} + f_i = 0 \quad \text{in} \quad \Omega \tag{11.4}$$

$$\varepsilon_{ij}^{\varepsilon} = \frac{1}{2}\left(\frac{\partial u_i^{\varepsilon}}{\partial x_j^{\varepsilon}} + \frac{\partial u_j^{\varepsilon}}{\partial x_i^{\varepsilon}}\right) \quad \text{in} \quad \Omega \quad \text{and} \tag{11.5}$$

$$\sigma_{ij}^{\varepsilon} = D_{ijkl}^{\varepsilon}\varepsilon_{kl}^{\varepsilon} \quad \text{in} \quad \Omega \tag{11.6}$$

respectively, for $i,j,k,l = 1,...,3$. σ_{ij} and ε_{ij} are the components of the Cauchy stress and deformation tensors, respectively. f_i and u_i are the components of the volume loads and displacement vectors, respectively.

The boundary of Ω is defined by the disjoint surfaces Γ_{u} and Γ_{t}. These surfaces are related to the Dirichlet and Neumann boundary conditions, defined by

$$u_i^{\varepsilon} = \bar{\mathrm{u}}_i \quad \text{in} \quad \Gamma_{\mathrm{u}} \quad \text{and} \tag{11.7}$$

$$\sigma_{ij}^{\varepsilon} n_j = \bar{\mathrm{t}}_i \quad \text{in} \quad \Gamma_{\mathrm{t}} \tag{11.8}$$

respectively, with $\Gamma_{\mathrm{u}} \cup \Gamma_{\mathrm{t}} = \Gamma$ and $\Gamma_{\mathrm{u}} \cap \Gamma_{\mathrm{t}} = \emptyset$. $\bar{\mathrm{u}}_i$ and $\bar{\mathrm{t}}_i$ are prescribed displacement and surface load values, respectively. n_j are the components of the normal versor external to the surface Γ_{t}.

The resolution of the elasticity problem consists on the determination of the displacement field corresponding to the solution $\mathbf{u}^{\varepsilon} \in \mathrm{V}_{\Omega}^{0}$ of the variational problem

$$\int_{\Omega} D_{ijkl}^{\varepsilon} \frac{\partial u_k^{\varepsilon}}{\partial x_l^{\varepsilon}} \frac{\partial v_i}{\partial x_j^{\varepsilon}} \mathrm{d}\Omega = \int_{\Omega} f_i v_i \mathrm{d}\Omega + \int_{\Gamma_{\mathrm{Nu}}} \bar{t}_i v_i \mathrm{d}\Gamma, \quad \forall \mathbf{v} \in \mathrm{V}_{\Omega}^{0} \tag{11.9}$$

where V_{Ω}^{0} is the set of continuous and sufficiently regular functions, zero-valued in Γ_{u}.

Considering that the heterogenous material is made of $n > 1$ homogenous materials, the elasticity problem consists of n equations analogous to Eq. (11.4), associated to the continuity conditions of the displacements and surface loads in any of the subdomain interfaces. The displacement field can be approximated with the following asymptotic expansion in ε:

$$u_i^{\varepsilon}(\mathbf{x}) = u_i^{(0)}(\mathbf{x},\mathbf{y}) + \varepsilon u_i^{(1)}(\mathbf{x},\mathbf{y}) + \varepsilon^2 u_i^{(2)}(\mathbf{x},\mathbf{y}) + \cdots \tag{11.10}$$

where $u_i^{(r)}(\mathbf{x},\mathbf{y})$, with $r \in \mathbb{N}_0$, are Y-periodic functions in $\mathbf{y}$ and are called correctors of order r of the displacement field. With $\mathbf{y} = \mathbf{x}/\varepsilon$ and according to the differentiation chain rule,

$$\frac{\partial \cdot}{\partial x_i^{\varepsilon}} = \frac{\partial \cdot}{\partial x_i} + \frac{1}{\varepsilon}\frac{\partial \cdot}{\partial y_i} \tag{11.11}$$

Replacing the displacement asymptotic expansion (Eq. (11.10)) in the deformation-displacement relations 11.5 and using Eq. (11.11), a microscale problem is obtained, which is associated to the definition of the characteristic displacement field tensor $\boldsymbol{\chi}$.

The components of $\boldsymbol{\chi}$ are the solutions $\chi_i^{kl} \in \widetilde{\mathrm{V}}_{\mathrm{Y}}$ of the auxiliary variational problem

$$\int_{\mathrm{Y}} D_{ijkl} \frac{\partial \chi_k^{mn}}{\partial y_l} \frac{\partial v_i}{\partial y_j} \mathrm{d}Y = \int_{\mathrm{Y}} D_{ijmn} \frac{\partial v_i}{\partial y_j} \mathrm{d}Y, \quad \forall v_i \in \widetilde{\mathrm{V}}_{\mathrm{Y}} \tag{11.12}$$

where $\widetilde{\mathrm{V}}_{\mathrm{Y}}$ is the set of Y-periodic continuous and sufficiently regular functions with zero average value in Y. On the macroscale Ω the displacement field $u_i^{(0)}$ is the solution of the homogenised elasticity problem

$$\frac{\partial \Sigma_{ij}}{\partial x_j} + f_i = 0 \quad \text{in } \Omega \tag{11.13}$$

$$u_i^{(0)} = \bar{\mathrm{u}}_i \quad \text{in } \Gamma_{\mathrm{u}} \tag{11.14}$$

$$\Sigma_{ij} n_j = \bar{\mathrm{t}}_i \quad \text{in } \Gamma_{\mathrm{t}} \quad \text{with} \tag{11.15}$$

$$\Sigma_{ij} = D^{\mathrm{h}}_{ijkl} \frac{\partial u_k^{(0)}}{\partial x_l} \quad \text{in } \Omega \tag{11.16}$$

where the components D^{h}_{ijkl} of the homogenised elasticity tensor correspond to

$$D^{\mathrm{h}}_{ijmn} = \frac{1}{|\mathrm{Y}|} \int_{\mathrm{Y}} D_{ijkl}(\mathbf{y}) \left[\mathrm{I}^{mn}_{kl} - \frac{\partial \chi_k^{mn}}{\partial y_l} \right] \mathrm{d}Y \tag{11.17}$$

The analysis of the **x** and **y** scales comes from the possibility that the resulting displacement fields exhibit periodic oscillations. These oscillations are superimposed on macroscopic fields that do not consider the influence of microstructural details. Thus, these oscillations can be interpreted as fluctuations around an average macroscopic value (see Fig. 11.2). The methodology here presented allows the definition of a first order approximation $\widetilde{u}_i^{\varepsilon}(\mathbf{x})$, linear in relation to ε, for the displacement

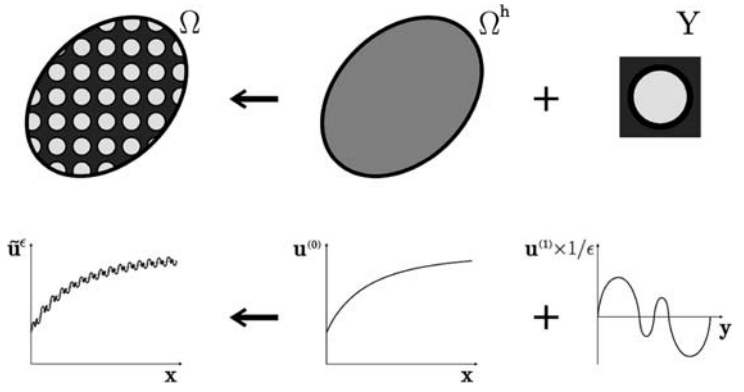

Fig. 11.2 First order approximation of the asymptotic expansion of the displacement field, for a one-dimensional case: the displacement field, in Ω, is approximated by the overlapping of the macroscale homogenised field, in Ω^{h}, with the oscillations that result from the Y-periodicity of the microscale field, in Y

asymptotic expansion, $u_i^\varepsilon(\mathbf{x})$ (see Fig. 11.2), resulting, for null integration constants for the term $u_i^{(1)}$ of the asymptotic expansion of the displacement field (Eq. (11.10)), in

$$u_i^\varepsilon(\mathbf{x}) \approx \widetilde{u}_i^\varepsilon(\mathbf{x}) = u_i^{(0)}(\mathbf{x}) + \varepsilon u_i^{(1)}(\mathbf{x},\mathbf{y}) \tag{11.18}$$

A significant part of structural engineering applications that use heterogeneous materials of periodic microstructure is based on values of $\varepsilon \ll 1$. This being the case, a first order approximation for the displacement field is adequate to represent u_i^ε. Not considering the higher-order terms simplifies the AEH, resulting in the conventional homogenisation methodology [10, 21]. For the elasticity problem, this consists on an exact mathematical technique, through which one can solve a problem associated with a differential partial operator with high frequency periodic variations of its coefficients (Eqs. (11.4)–(11.8)) in a simpler fashion, solving a problem associated with a differential operator with constant coefficients (Eqs. (11.13)–(11.16)), which is called the homogenised elasticity problem. The coefficients of the homogenised problem are determined from the solution of a problem defined on the microscale RUC, enforcing periodic constraints on its boundaries (Eqs. (11.12) and (11.17)).

11.2.2 Localisation Methodology

Another advantage of the AEH method is that it allows the characterisation of the microstructural deformation and stress fields. This process, often called localisation, is the inverse process of the homogenisation (see Fig. 11.3).

In a conventional homogenisation approach, a first order approximation in ε is considered. For the localisation procedure, zero-order approximations in ε, $\widetilde{\sigma}_{ij}^\varepsilon$ and $\widetilde{\varepsilon}_{ij}^\varepsilon$, are considered for the stress and deformation microstructural fields, respectively. Hence, the microstructural stress field is

$$\sigma_{ij}^{(1)}(\mathbf{x},\mathbf{y}) = D_{ijkl}(\mathbf{y})\left(\mathrm{I}_{kl}^{mn} - \frac{\partial \chi_k^{mn}}{\partial y_l}\right)\frac{\partial u_m^{(0)}}{\partial x_n} \tag{11.19}$$

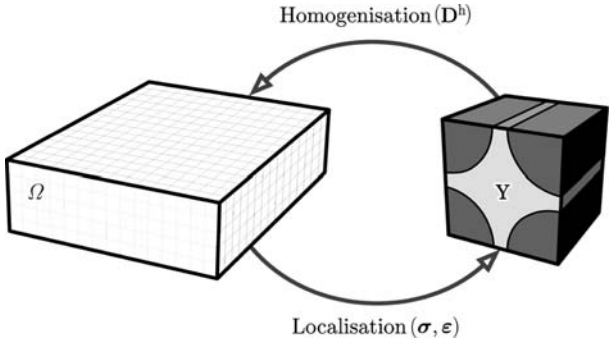

Fig. 11.3 Schematic illustration of the information flow in homogenisation and localisation procedures, between the macroscale Ω and the microscale Y

Moreover, the deformation microstructural field is defined by

$$\varepsilon_{ij}^{(1)}(\mathbf{x},\mathbf{y}) = \mathrm{T}_{ij}^{kl}\left(\mathrm{I}_{kl}^{mn} - \frac{\partial \chi_k^{mn}}{\partial y_l}\right)\frac{\partial u_m^{(0)}}{\partial x_n} \tag{11.20}$$

where

$$\mathrm{T}_{ij}^{kl} = \frac{1}{2}\left(\delta_{ik}\delta_{jl} + \delta_{il}\delta_{jk}\right) \tag{11.21}$$

δ_{ij} is the Kronecker delta. For a given point on the macroscale $\mathbf{x}$, Eqs. (11.19)–(11.20) are used to calculate approximate values of the stress and deformation fields, respectively, within the heterogeneous material. In contrast, the homogenised stress field, as it is the average value of the microstructural stresses $\sigma_{ij}^{(1)}$ in Y, is unable to represent any microstructural fluctuations of the stress field.

11.3 Finite Element Method in AEH

11.3.1 Corrector $\boldsymbol{\chi}$

The solution of Eq. (11.12) is called corrector ($\boldsymbol{\chi}$) and contains the eigendeformations of the representative periodic geometry [5]. The element strain and stress matrices are $\varepsilon = \mathbf{Bu}$ and $\sigma = \mathbf{DBu}$, respectively, where all the variables belong to the microscale problem, i.e. are relative to the geometry and material of the RUC. Therefore, the finite element approach to Eq. (11.12) results in

$$\int_{\mathrm{Y^e}} \mathbf{B}^{\mathrm{T}}\mathbf{DB}\mathrm{d}Y\,\boldsymbol{\chi} = \int_{\mathrm{Y^e}} \mathbf{B}^{\mathrm{T}}\mathbf{D}\mathrm{d}Y = \mathbf{F}^{\mathrm{D}} \tag{11.22}$$

where the index e denotes element quantities from the meshed unit-cell domain (body Y) [6]. It is worthwhile to note that the corrector $\boldsymbol{\chi}$ is a matrix, not a vector. The second term of Eq. (11.22) consists on the columns of the matrix $\mathbf{F}^{\mathrm{D}}$ [6], which consist on six load vectors, leading to the same number of systems of equations to solve. The results are solutions that make up the corrector, each one defining an eigendeformation mode. Moreover, the definition of matrix $\mathbf{F}^{\mathrm{D}}$ shows that the force vectors appear from the integration of the gradient of elastic properties of the material components that form the composite material.

11.3.2 Periodicity Boundary Conditions

Periodicity boundary conditions are imposed over the surface boundaries of the RUC. For a hexahedral unit-cell in $y_1 \in [0, y_1^0]$, $y_2 \in [0, y_2^0]$ and $y_3 \in [0, y_3^0]$, the boundary conditions can be defined as follows:

$$\begin{aligned}
\chi_i^{jk}(0,y_2,y_3) &= \chi_i^{jk}(y_1^0,y_2,y_3) \\
\chi_i^{jk}(y_1,0,y_3) &= \chi_i^{jk}(y_1,y_2^0,y_3) \quad \text{and} \\
\chi_i^{jk}(y_1,y_2,0) &= \chi_i^{jk}(y_1,y_2,y_3^0)
\end{aligned} \tag{11.23}$$

In order to prevent rigid body motion, displacements and rotations of an arbitrary point of the unit-cell must be locked. In this work, this restriction is created acting only on the translation degrees of freedom of one of the vertices of the RUC. Rigid body motion is avoided by the periodicity constraints, which, as shown in relations 11.23, force the restriction to act equally over all other vertices.

11.3.3 Homogenised Elasticity Matrix D^h

The homogenised elasticity matrix $\mathbf{D}^{\mathrm{h}}$ is obtained from Eq. (11.17), resulting in

$$\mathbf{D}^{\mathrm{h}} = \sum_{k=1}^{n_{\mathrm{e}}} \frac{Y^k}{Y} \mathbf{D}^k (\mathbf{I} - \mathbf{B}^k \boldsymbol{\chi}^k) \tag{11.24}$$

where Y^k is the volume of element k, Y the total geometry volume and $\mathbf{I}$ the identity matrix. Note that if $\boldsymbol{\chi} = \mathbf{0}$, this equation becomes the classical volume average of the elastic properties of the microscale elements.

11.4 Numerical Procedures

The numerical tools developed by the authors are based on the finite element method (FEM) [13, 15, 25] and use tetrahedral and hexahedral finite elements. The main focus of this section is on the auxiliary algorithms for RUC generation and periodicity boundary condition management.

11.4.1 The Main Program

The finite element code is developed for structural linear elastic computations [13]. It solves 3-D problems using tetrahedral or hexahedral (linear or quadratic) finite elements.

Since the FEM analyses considered in this work often lead to sparse coefficient matrices, using the complete matrix on the numerical calculations greatly reduces the efficiency of the matrix operations involved. This may become critical with the increase of the size of the problem, as the number of zero coefficients tends to increase, leading to a waste of computational effort. This limitation can be overcome

identifying the zero values and ignoring subsequent operations. In this context, the chosen storage scheme was the Compressed Row Storage (CRS) [2].

When performing numerical simulations, most of the computational time is spent solving the system of equations [22], thus requiring a careful selection of an efficient method. In this work, the authors opted for a non-stationary iterative method based on Krylov subspaces [22]. This choice is based on the properties of the matrix of coefficients, leading to the conjugate gradient method (CG) [9, 11]. The CG method is further improved with the use of preconditioning techniques, as the convergence rate of the method greatly depends on the conditioning of the matrices [2].

Having to account for multi-freedom constraints (MFC) [8] in order to ensure the periodicity of deformed RUC, the chosen method to impose essential boundary constraints (prescribed displacements) was the penalty method.

11.4.2 Representative Unit-Cell Generation

RUC modelling requires accurate control of some geometric parameters, such as (i) component volume fractions, (ii) reinforcement geometry and dimensions, (iii) its distribution and (iv) geometric periodicity [14, 17]. The features of the developed program can be fit within three main groups: (i) standard models: cubic RUC with predefined distributions of spherical particles, controlling volume or mass reinforcement fractions; (ii) random distribution and/or sizes: the position of spherical reinforcement particles or their dimensions (or both) are randomly calculated for RUC with different properties, with or without interference between particles and (iii) RUC reinforced with continuous fibres: the distribution may be random or confined to specific regions within the RUC. Additionally, geometric periodicity must be guaranteed. For each reinforcement element that intersects the boundaries of the cell, a set of matching geometries is created in order to guarantee cell-to-cell continuity (see Fig. 11.4).

11.4.3 Automatic Association of Degrees of Freedom

To ensure that a unit-cell is representative of a periodic material, it is not only necessary to guarantee geometric periodicity but also to enforce periodic deformations through specific boundary conditions. There must be cell-to-cell continuity, meaning that opposite geometrical boundaries of a given cell have to be identical, both for the original and deformed states [3] (see Fig. 11.5). Deformed periodicity depends on periodicity boundary conditions (see Eq. (11.23)). Thus, finite element nodes on the geometry boundaries must be connected in order to ensure that displacements are compatible with those of neighbouring cells. To make this task user-independent and automatic, the matching degrees-of-freedom are found and associated.

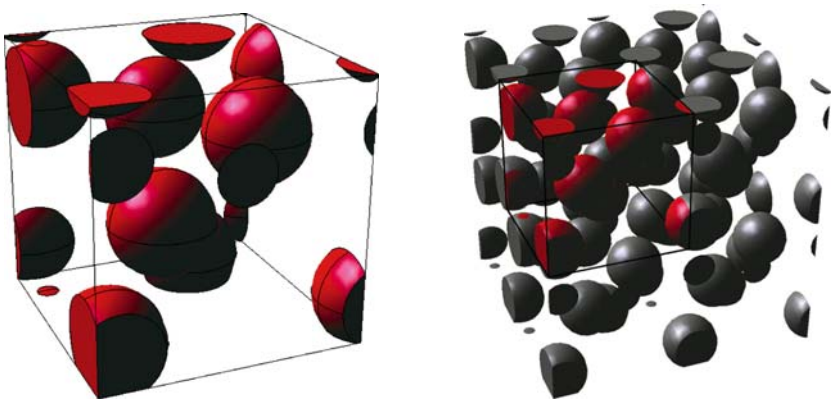

Fig. 11.4 Particle generation scheme for periodical RUC: (**a**) random representative unit-cell and (**b**) unit-cell periodicity

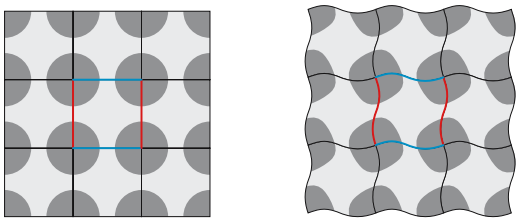

Fig. 11.5 RUC periodicity: (**a**) original and (**b**) deformed geometries

Node association procedures are divided in three different stages: on corners, edges and faces. Cell corners are linked since, in terms of periodicity/continuity, they all represent the same point in neighbouring cells. The same is done between parallel edges and parallel faces of the RUC. Afterwards, nodes are separated according to the region where they belong and boundary nodes are separated between master and slave nodes. Finally, for each node on a slave region, the program looks for the ideal node on the master region to control the slave and creates indexes that connect both nodes. Based on these indexes, it is then possible to impose the periodicity boundary constraints which are a special case of multi-freedom constraints.

When working with structured finite element meshes, it is always possible to find a master node that matches the place of a given slave. However, this is not true for unstructured meshes. In this case, the mesh is often not periodic, meaning that the node distribution on a master boundary may not be the same as in the matching slave. Thus, it is necessary to check which master node is closer to where the slave is and, by association, the master is expected to be.

11.5 Numerical Applications

One of the main objectives of this work is to validate both the use of the asymptotic expansion homogenisation method and the use of unstructured finite element meshes. The AEH is applied to the prediction of the mechanical properties of composite materials with continuous fibre reinforcement. The results are obtained for structured and unstructured finite element meshes and compared with analytical and experimental results in order to validate the implemented procedures. The authors start by evaluating the applicability of the use of unstructured tetrahedral finite element meshes within the AEH method. The continuous parallel fibre reinforcement composite material studied is schematically illustrated in Fig. 11.6, along with the adopted RUC. The composite material is made of an aluminium (Al) matrix and boron (B) reinforcement. The mechanical properties of these materials are listed in Table 11.1 [12]. The homogenised elastic properties of the composite material are calculated for a reinforcement volume fraction $f_r = 47\%$. Several numerical simulations are done using two types of finite element: (i) linear tetrahedra and (ii) linear hexahedra. For each finite element type, the authors performed a convergence analysis [16] for the homogenised elasticity matrix $\mathbf{D}^h$ that results from the homogenisation procedure applied to the representative unit-cell (see Fig. 11.6). Six different mesh refinement levels were considered for each finite element type. Numerical simulation results show that the homogenised elasticity matrices $\mathbf{D}^h$ are orthotropic. The orthotropic character of the composite material lies on the

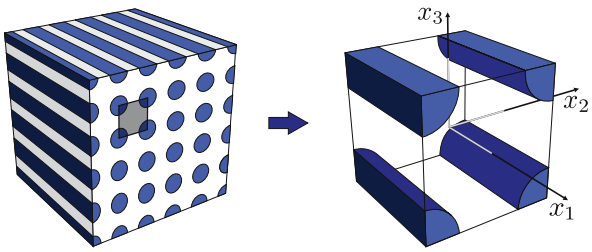

Fig. 11.6 Schematic representation of (**a**) the continuous parallel fibre reinforcement composite material and (**b**) the adopted representative unit-cell

Table 11.1 Elastic properties of the matrix (m) and reinforcement (r) materials of the aluminium matrix composite reinforced with boron fibres

Property	Value
Matrix elastic modulus, E_m [GPa]	68.3
Matrix Poisson coefficient, ν_m [-]	0.3
Reinforcement elastic modulus, E_r [GPa]	379.3
Reinforcement Poisson coefficient, ν_r [-]	0.1

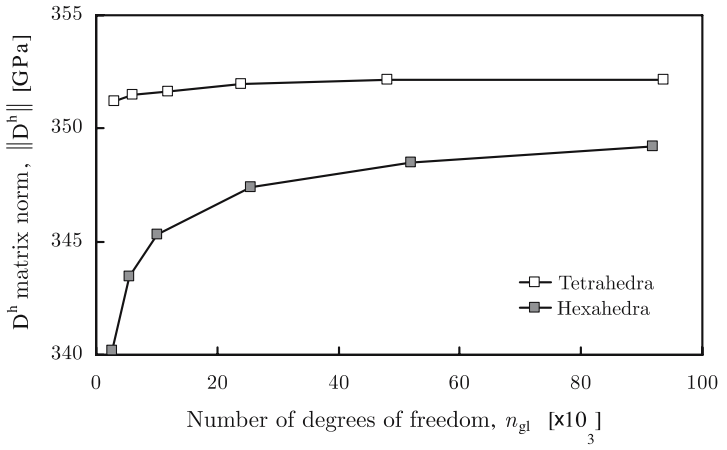

Fig. 11.7 Evolution of the norm of $\mathbf{D}^{\mathrm{h}}$ with the number of degrees of freedom

fact that it has three orthogonal material symmetry planes – x_1Ox_2, x_2Ox_3 and x_1Ox_3 (see Fig. 11.6). In fact, the elasticity matrices $\mathbf{D}^{\mathrm{h}}$ define a special case of the orthotropic material – the tetragonal structure material[1] [1] – defined by the following homogenised elasticity matrix:

$$\mathbf{D}^{\mathrm{h}} = \begin{bmatrix} D^{\mathrm{h}}_{11} & D^{\mathrm{h}}_{12} & D^{\mathrm{h}}_{12} & 0 & 0 & 0 \\ D^{\mathrm{h}}_{12} & D^{\mathrm{h}}_{22} & D^{\mathrm{h}}_{23} & 0 & 0 & 0 \\ D^{\mathrm{h}}_{12} & D^{\mathrm{h}}_{23} & D^{\mathrm{h}}_{22} & 0 & 0 & 0 \\ 0 & 0 & 0 & D^{\mathrm{h}}_{44} & 0 & 0 \\ 0 & 0 & 0 & 0 & D^{\mathrm{h}}_{55} & 0 \\ 0 & 0 & 0 & 0 & 0 & D^{\mathrm{h}}_{44} \end{bmatrix} \tag{11.25}$$

The convergence study showed that there is a simultaneous convergence of all the $\mathbf{D}^{\mathrm{h}}$ matrix components, where very little variations are observed. From this, in order to simplify the presentation of the results, the main analysis is shown considering the evolution of the Frobenius norm[2] of matrix $\mathbf{D}^{\mathrm{h}}$, $\|\mathbf{D}^{\mathrm{h}}\|$, with the number of degrees of freedom. These results are shown in Fig. 11.7. The evolution of the norm of $\mathbf{D}^{\mathrm{h}}$ with the number of degrees of freedom, n_{gl}, for the presented finite elements does not show evidence of numerical instability (numerical oscillation or divergence phenomena). On the other hand, in the AEH method, the convergence of the results depends not only on the number of degrees of freedom but also on the number of finite elements. In fact, while the convergence of a conventional finite

[1] The fact that $D^{\mathrm{h}}_{55} \neq \frac{D^{\mathrm{h}}_{22} - D^{\mathrm{h}}_{23}}{2}$ excludes the transverselly isotropic material.

[2] The convergence of the Frobenius norm of a matrix is a necessary, but not sufficient, condition for the convergence of all its components.

element analysis depends only on the number of degrees of freedom [16], in the AEH the $\mathbf{D}^{\mathrm{h}}$ matrix is calculated by a volume average of the microscale properties, corrected by the gradients of the characteristic displacement fields of the RUC over all elements (Eq. (11.24)). Thus, this method also requires a number of elements large enough to allow for this averaging process to reach asymptotic convergence. The convergence may be further improved using quadratic elements, which better represent the referred gradients and allow for the use of a lower number of elements [15]. Figure 11.8 represents the evolution of the norm of $\mathbf{D}^{\mathrm{h}}$ with the number of finite elements, n_{el}, used in each finite element mesh. Each mesh refinement step led to approximations with relative variations always lower than 1%. The linear hexahedra had a gradual approximation to the convergence limit, while both types of finite element resulted in good approximations. The mesh refinement process led to improvements under 0.5% for mesh refinements with over 41,140 tetrahedral elements (8,006 nodes) and 6,860 hexahedral elements (8,520 nodes), thus associated to converged solutions [16]. These finite element meshes are shown in Fig. 11.9, along with the original geometries. The constitutive matrices $\mathbf{D}^{\mathrm{h}}$ resulting from the

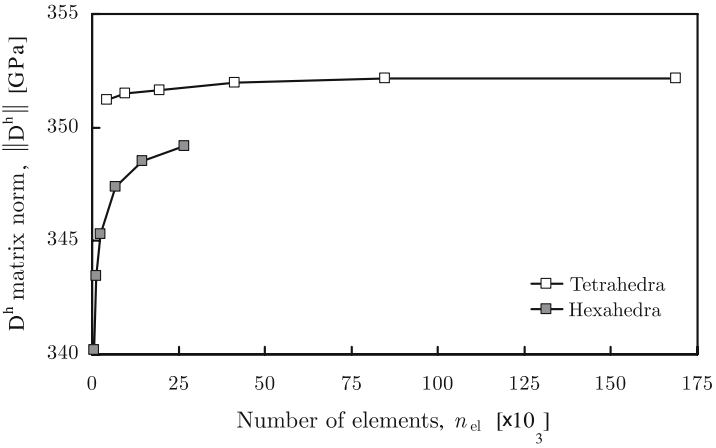

Fig. 11.8 Evolution of the norm of $\mathbf{D}^{\mathrm{h}}$ with the number of finite elements

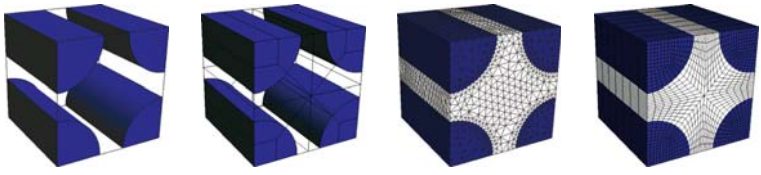

Fig. 11.9 Representative unit-cell for an aluminium matrix composite material reinforced with continuous boron fibres (47% vol.): (**a**) and (**b**) geometry; (**c**) unstructured tetrahedral mesh and (**d**) structured hexahedral mesh

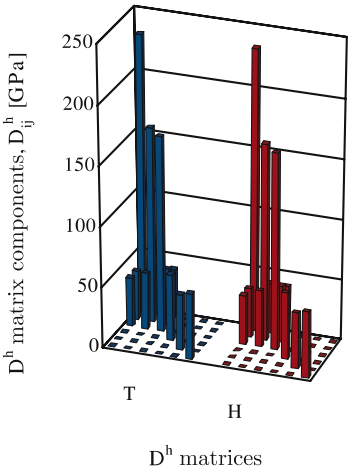

Fig. 11.10 Representation of the components of the constitutive material matrix $\mathbf{D}^h$ calculated with tetrahedra (T) and hexahedra (H) finite element meshes, for an aluminium matrix composite material reinforced with boron continuous cylindrical fibres (47% vol.)

Table 11.2 Numerical (N), analytical (A) and experimental (E) elastic properties of an aluminium matrix composite material reinforced with boron fibres (47% vol.)

Results	E_{11} [GPa]	E_{22} [GPa]	G_{12} [GPa]	G_{23} [GPa]	ν_{12} [-]	ν_{23} [-]
N – AEH	214.6	144.5	54.7	46.2	0.19	0.25
N – Xia et al.	214	143	54.2	45.7	0.195	0.253
N – Sun and Vaidya	215	144	57.2	45.9	0.19	0.29
A – Sun and Chen	214	135	51.1	–	0.19	–
A – Chamis	214	156	62.6	43.6	0.20	0.31
A – Whitney and Riley	215	123	53.9	–	0.19	–
E – Kenaga et al.	216	140	52	–	0.29	–

use of these finite element meshes are represented in Fig. 11.10, where, according to Eq. (11.25), the tetragonal character of the composite material is observed. The manipulation of the homogenised flexibility matrix components associated to the numerical analysis using the tetrahedral finite element mesh allows the calculation of the elastic properties of the composite material. These properties are shown in Table 11.2, along with results taken from numerical (N) and analytical (A) predictions, and experimental results (E) [12]. In what concerns the numerical prediction results, Xia et al. [24] presented values achieved through a combination of the finite element method with explicit periodicity conditions based on the micromechanical models developed by Suquet [20]. Sun and Vaidya [19] presented numerical results based on the conjugation of principles of equivalent deformation energy with the finite element method. The analytical prediction results of Whitney and Riley [23] are based on energy weighting methods derived from the classical theory of elasticity. The analytical prediction results presented by Sun and Chen [18] and Chamis [4] are based on micromechanical models involving continuity and load equilibrium conditions. The numerical values were obtained by the inversion of the elasticity

matrix $\mathbf{D}^{\mathrm{h}}$, resulting in the homogenised flexibility matrix[3]

$$\mathbf{S}^{\mathrm{h}} = \begin{bmatrix} \frac{1}{E_{11}} & \frac{-\nu_{12}}{E_{11}} & \frac{-\nu_{12}}{E_{11}} & 0 & 0 & 0 \\ \frac{-\nu_{12}}{E_{11}} & \frac{1}{E_{22}} & \frac{-\nu_{23}}{E_{22}} & 0 & 0 & 0 \\ \frac{-\nu_{12}}{E_{11}} & \frac{-\nu_{23}}{E_{22}} & \frac{1}{E_{22}} & 0 & 0 & 0 \\ 0 & 0 & 0 & \frac{1}{G_{12}} & 0 & 0 \\ 0 & 0 & 0 & 0 & \frac{1}{G_{23}} & 0 \\ 0 & 0 & 0 & 0 & 0 & \frac{1}{G_{12}} \end{bmatrix} \tag{11.26}$$

where E_{11} and E_{22} are the elasticity moduli, regarding the fibre longitudinal and transverse directions, respectivelly. G_{12}, ν_{12}, G_{23} and ν_{23} are the shear moduli and the Poisson ratios associated with directions 1 and 2, and 2 and 3, respectively. The results of the AEH are good approximations for the experimental results. In fact, the values obtained for E_{11}, E_{22} and G_{12} only differ by 0.6%, 3.2% and 5.2% from the experimental ones, respectivelly. Although a 34.5% deviation appears for ν_{12} in comparison with the experimental value, the best approximation (Chamis) still differs by 31%. The differences between the AEH results and experimental results can be related to the fact that the numerical modelling doesn't consider the irregular distribution of the reinforcement fibres, defects within the composite material, imperfect adhesion between the material components, etc. Even so, the numerical results are considered as valid estimations for the mechanical properties of the composite material. In comparison to the rest of the prediction methods, the AEH gives the best overall approximations.

Another relevant aspect is the fact that AEH homogenised properties are calculated using the corrector $\boldsymbol{\chi}$ of the displacement field (Eq. (11.24)). The characteristic displacements (i.e. eigendeformations) defined by the corrector are a measure of the microstructural composite material heterogeneity [5]. The six characteristic displacement fields are shown in Fig. 11.11, for the RUC meshed with tetrahedra and hexahedra. The displacements defined in the columns of matrix $\boldsymbol{\chi}$ are the (six) solutions of a system of equations where the load vectors are the (six) columns of the matrix $\mathbf{F}^{\mathrm{D}}$ (Eq. (11.22)), designated characteristic load vectors (see Fig. 11.12). The differences in terms of the type of elements and the fact that only the structured meshes are periodical (in spite of being a discretisation of the same periodical geometry), through the use of the degree of freedom association, do not compromise the results. Furthermore, the fact that the homogenised elastic properties converge to the same values shows that the AEH leads to correctors $\boldsymbol{\chi}$ representative of the same heterogeneity. The deformed periodicity is also guaranteed, as may be seen for the shear mode $\boldsymbol{\chi}_{23}$ in Fig. 11.13, using eight tiled RUC.

After the validation of the AEH procedure for non-periodical/unstructured meshes, there is still the need to evaluate the procedure analysing the dependence on the choice of a given unit-cell as truly representative of the material geometry and

[3] Note that for a tetragonal material $E_{33} = E_{22}$, $G_{13} = G_{12}$ and $\nu_{13} = \nu_{12}$, requiring only six independent properties for its definition: E_{11}, E_{22}, G_{12}, G_{23}, ν_{12} and ν_{23}.

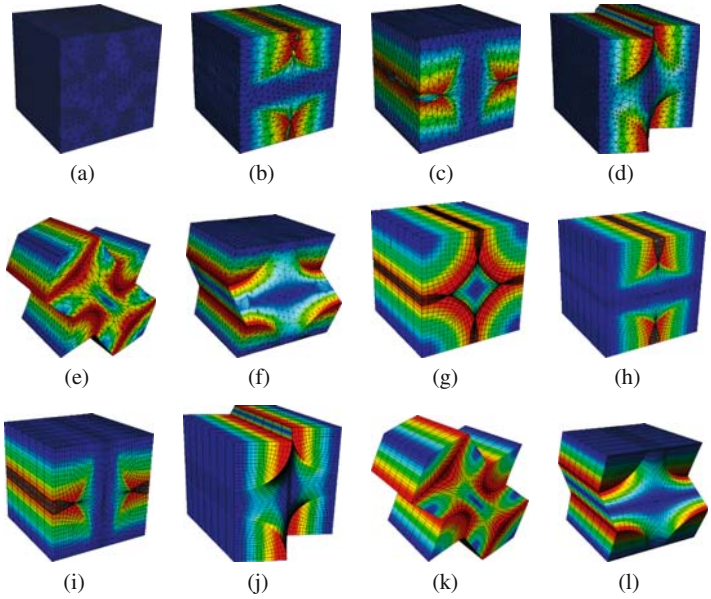

Fig. 11.11 Characteristic displacements for a RUC of a fibre reinforced composite material, meshed with (**a–f**) tetrahedra and (**g–l**) hexahedra – axial modes (**a**, **g**) $\boldsymbol{\chi}_{11}$, (**b**, **h**) $\boldsymbol{\chi}_{22}$ and (**c**, **i**) $\boldsymbol{\chi}_{33}$, and shear modes (**d**, **j**) $\boldsymbol{\chi}_{12}$, (**e**, **k**) $\boldsymbol{\chi}_{23}$ and (**f**, **l**) $\boldsymbol{\chi}_{13}$

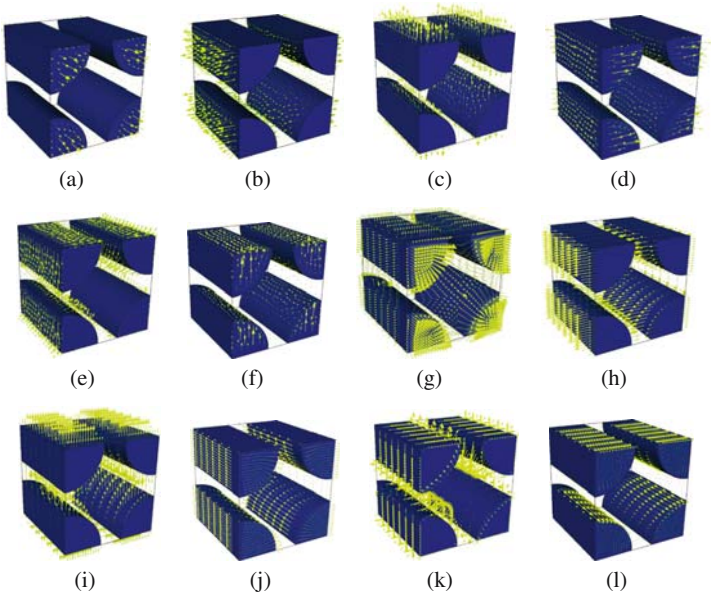

Fig. 11.12 Characteristic load vectors for a RUC of a fibre reinforced composite material, meshed with (**a–f**) tetrahedra and (**g–l**) hexahedra – axial modes (**a**, **g**) $\mathbf{F}^{\mathrm{D}}_{11}$, (**b**, **h**) $\mathbf{F}^{\mathrm{D}}_{22}$ and (**c**, **i**) $\mathbf{F}^{\mathrm{D}}_{33}$, and shear modes (**d**, **j**) $\mathbf{F}^{\mathrm{D}}_{12}$, (**e**, **k**) $\mathbf{F}^{\mathrm{D}}_{23}$ and (**f**, **l**) $\mathbf{F}^{\mathrm{D}}_{13}$

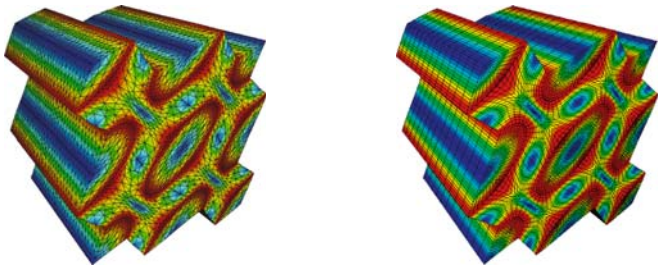

(a) (b)

Fig. 11.13 Y-periodicity of the characteristic displacements – illustration of the shear mode $\boldsymbol{\chi}_{23}$ using eight RUC meshed with (**a**) tetrahedra and (**b**) hexahedra

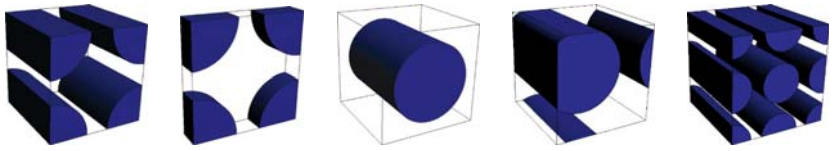

(a) (b) (c) (d) (e)

Fig. 11.14 Alternative RUC for a fibre reinforced composite material ($f_r = 47\%$): (**a**) reference RUC, (**b**) C1, (**c**) C2, (**d**) C3 and (**e**) C4

Table 11.3 Absolute value of the relative error of the homogenised elasticity matrix, in comparison to the reference RUC

RUC	C1	C2	C3	C4
|REN| [%]	0.14	0.47	0.0072	0.38

mechanical behaviour. Thus, a numerical study was done using different RUC, all related to the same composite material. These geometries are shown in Fig. 11.14, as well as the reference RUC studied in the previous section. Note that cell C4 has twice the size of the others and is equal to eight tiled reference unit-cells.

The results are listed in Table 11.3, in terms of the modulus of the relative error of the norm (|REN|) of the homogenised elasticity matrix, in comparison to the reference RUC. Approximations of the same order are determined for the components of homogenised elasticity matrices, showing that the AEH method is accurate enough to represent the behaviour of a given periodic microstructure composite material as long as the chosen volume element is representative of the distribution of the microscale material. The fact that the method does not require cubic cells, as shown with the representative unit-cell C1, is also relevant. In this case, the RUC size can be reduced along the longitudinal axis of the fibres, as the effective properties of the composite material along this direction are coincident with the law of mixtures for a parallel association of material components. On the other hand, observing RUC C4 and its results, becomes clear that, in this case, the dimension factor ε between

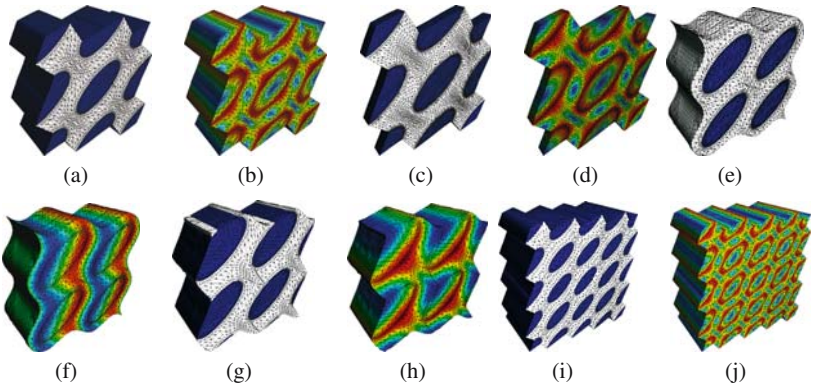

Fig. 11.15 Y-periodicity of the characteristic displacements – shear mode $\boldsymbol{\chi}_{23}$ using alternative RUC: (**a–b**) reference RUC, (**c–d**) C1, (**e–f**) C2, (**g–h**) C3 and (**i–j**) C4

scales is not numerically relevant. In fact, ε does not even appear in the explicit formulation of the method for a first order approximation (i.e. the conventional AEH method), as considered in this work.

Tiles of four RUC are shown in Fig. 11.15 in order to illustrate the fact the correctors are indeed representative of the microscale heterogeneities. It is now easier to see that the correctors exactly represent the same deformed geometry of the overall composite material, even if obtained from different representative volumes. Note that the displacement values shown in Figs. 11.15f, h seem to represent a different deformed geometry when compared to the other results. Nevertheless, as seen in Figs. 11.15e, g, it is exactly the same. The differences in terms of displacement are derived from the fact that the fixed points used to avoid rigid motion are located at different places within the material microstructure.

11.6 Final Remarks

The main conclusion of this work is the validation of the use of the AEH approach, both in terms of global finite element simulation applications and prediction of effective material properties for periodic microstructure composite materials.

The numerical simulation results show that the homogenised elasticity matrices $\mathbf{D}^{\mathrm{h}}$ of the fibre reinforced composite material define a particular case of orthotropic material: the tetragonal structure material.

The convergence study showed the simultaneous convergence of all $\mathbf{D}^{\mathrm{h}}$ matrix components, as well as of the Frobenius norm, for structured and unstructured/non-periodical meshes. Moreover, in the AEH the convergence of the results depends not only on the number of degrees of freedom but also on the number of finite elements.

The AEH proved to be accurate enough to represent the behaviour of a given periodic microstructure composite material as long as the chosen volume element is representative of the microscale material distribution. Additionally, the fact that the homogenised elastic properties converge to the same values shows that the AEH procedure leads to correctors $\boldsymbol{\chi}$ that are representative of the same heterogeneities.

The obtained numerical results indicate that the tools that were developed allow the use of non-periodical meshes within a finite element homogenisation approach for periodic microstructures. The results of the AEH method are good approximations for the experimental results. In comparison to the rest of the prediction methods used, the AEH gives the best global approximations.

References

1. Banks-Sills L, Leiderman V, Fang D (1997) On the effect of particle shape and orientation on elastic properties of metal matrix composites. Compos Part B 28:465–481
2. Barrett R, Berry M, Chan TF et al. (1994) Templates for the solution of linear systems: Building blocks for iterative methods. SIAM, Philadelphia. PA
3. Böhm HJ (1998) A short introduction to basic aspects of continuum micromechanics, CDL-FMD-Report, TU Wien, Wien
4. Chamis CC (1984) Simplified Composite Micromechanical Equations for Hygral, Thermal, and Mechanical Properties. Sampe Quartely 15:14–23
5. Chung PW (1999) Computational methods for multi-scale/multi-physics problems in heterogenous/composite structures. Ph.D. thesis, University of Minesota, Minesota
6. Chung PW, Tamma KK, Namburu RR (2001) Asymptotic expansion homogenization for heterogeneous media: Computational issues and applications. Compos Part A 32:1291–1301
7. Cioranescu D, Donato P (1999) An introduction to homogenization. Oxford University Press, Oxford
8. Felippa C (2004) Introduction to finite element methods. University of Colorado, Boulder, CO
9. Golub GH, O'Leary DP (1989) Some history of the conjugate gradient and lanczos algorithms: 1948–1976. SIAM Rev 31:50–102
10. Guedes JM, Kikuchi N (1990) Preprocessing and postprocessing for materials based on the homogenization method with adaptive finite element methods. Comput Methods Appl Mech Eng 83:143–198
11. Hestenes MR, Stiefel EL (1952) J Res Natl Bur Stand 49:409–436
12. Kenaga D, Doyle JF, Sun CT (1987) The characterization of boron/aluminum composite in the nonlinear range as an orthotropic elastic-plastic material. J Compos Mater 21:516–531
13. Oliveira JA (2006) Micromechanical modelling of the behaviour of aluminium matrix composites. M.Sc. thesis (in portuguese), Aveiro University, Aveiro
14. Oliveira JA, Pinho-da-Cruz J, Andrade-Campos A, Teixeira-Dias F (2004) On the modelling of representative unit-cell geometries with GiD. In: 2nd Conference on Advances and Applications of GiD. SEMNI, Barcelona
15. Pinho-da-Cruz J (2007) Thermomechanical characterisation of multiphasic materials using homogenisation procedures. Ph.D. thesis (in portuguese), Aveiro University, Aveiro
16. Rizzo AR (1991) Estimating errors in FE analyses. Mech Eng 113:61–63
17. Segurado J, Llorca J (2002) A numerical approximation to the elastic properties of sphere-reinforced composites. J Mech Phys Solids 50:2107–2121
18. Sun CT, Chen JL (1991) A micromechanical model for plastic behavior of fibrous composites. Compos Sci Technol 40:115–129
19. Sun CT, Vaidya RS (1996) Prediction of composite properties from a representative volume element. Compos Sci Technol 56:171–179

20. Suquet PM (1987) Elements of homogenization theory for inelastic solid mechanics. In: Sanchez-Palenzia E, Zaoui A (eds) Homogenization techniques for composite media. Lecture Notes in Physics. Springer, Berlin
21. Terada K (1996) Global-local modeling for composites by the homogenization method. Ph.D. thesis, Michigan University, Michigan
22. van der Vorst HA (2003) Iterative Krylov methods for large linear systems. Cambridge University Press, Cambridge
23. Whitney JM, Riley MB (1966) Elastic properties of fiber reinforced composite materials. AIAA J 4:1537–1542
24. Xia Z, Zhang Y, Ellyin F (2003) A unified periodical boundary conditions for representative volume elements of composites and applications. Int J Solids Struct 40:1907–1921
25. Zienkiewicz OC, Taylor RL (1989) The finite element method, Vol. I. McGraw-Hill, London

Chapter 12
On Buckling Optimization of a Wind Turbine Blade

Erik Lund and Leon S. Johansen

Abstract The design of composite structures such as wind turbine blades is a challenging problem due to the need for pushing the material utilization to the limit in order to obtain light and cost effective structures. As a consequence of the minimum material design strategy the structures are becoming thin-walled, such that buckling problems must be addressed, and in this work the aim is to obtain buckling optimized multi-material designs of wind turbine blades. The design problem consists of distributing multiple materials within a given design domain, and the candidate materials may be fiber-reinforced materials, oriented at given discrete fiber angles, together with isotropic materials like foam materials used for sandwich structures. The discrete design optimization problem is converted to a continuous problem using the so-called Discrete Material Optimization (DMO) approach based on ideas from multi-phase topology optimization where interpolation functions with penalization are introduced. In this way traditional gradient based optimization techniques including efficient methods for design sensitivity analysis and mathematical programming can be used for solving the multi-material distribution problem. The multi-material topology optimization approach is demonstrated for buckling optimization of a 9 m generic wind turbine blade test section.

12.1 Introduction

Fiber-reinforced composite laminates are popular because of high stiffness-to-weight and strength-to-weight ratios compared with isotropic materials, and they are, for example, used in naval, aerospace, automobile and other mechanical applications. Such composite laminates consist of layers of one or more materials stacked at different orientation angles, and they permit the designer to tailor the structure or component to achieve the specified objectives.

E. Lund and L.S. Johansen
Department of Mechanical Engineering, Aalborg University, Pontoppidanstraede 101, DK-9220 Aalborg East, Denmark, e-mail: el@ime.aau.dk

In the design optimization of composite laminates, ply angles and layer thicknesses are often employed as continuous design variables. However, in practice the layer thickness for each material is usually fixed and fiber orientation angles of the fiber-reinforced materials, e.g. Glass and Carbon Fiber Reinforced Polymers (GFRP/CFRP), are often limited to a discrete set such as 0°, $\pm 45^\circ$, and 90° in order to obtain a cost-effective design. Occasionally ply angles which have 15° increments between 0° and 90° may be used. Thus, the design of such structures is often considered as a discrete optimization problem involving the specification of material type and orientation of ply layers in the stacking sequence. Such optimization problems are considered in this paper with focus on buckling design of wind turbine rotor blades.

Laminate design is an area of major importance, as shown in the book [15] that contains extensive references. A survey of optimal design of laminated plates and shells can be found in, e.g., Abrate [1]. A major challenge for optimizing composite structures is the non-convexity of the design space, i.e. the risk of ending up with a local optimum solution is high.

For composite laminates made of a single FRP material one approach is to use continuous design variables and introduce the lamination parameter method by [36] used by e.g. [24] and [17] for orientational stiffness optimization of plates. Introduction of lamination parameters is efficient for stiffness optimization because the stiffness components of laminated composites are expressed as linear functions with respect to lamination parameters. However, the lamination parameter method requires closed-form analytical formulation of appropriate lamination parameters which has so far only been achieved for relatively simple geometries, i.e., not in case of general shell structures. [12] studied buckling optimization of orthotropic laminated cylindrical shells under combined loadings using lamination parameters and a mathematical programming method. [11] studied buckling optimization of plates and cylindrical shells taking thermal effects into account. In [10] a general approach of forcing convexity of ply angle optimization of single material composite laminates based on lamination parameters is presented. However, lamination parameters do not allow for design with multiple materials and material properties that vary spatially over the structure and convexity is lost for problems with multiple design criteria.

The problem of combined design for orientation and topology has been studied using several different approaches. Varying the fiber volume fraction and changing the fibers orientation at each point of the structure result in a variable stiffness composite, see e.g. different approaches in [9, 22, 34, 35]. Combined topology and fiber path design of composite laminae has been studied by [27] using the SIMP (Solid Isotropic Material Penalization) approach of topology design, see [7], in a cellular automata framework.

In [2] laminated hybrid composites consisting of CFRP in the outer layers and GFRP in the inner layers are optimized for maximum buckling load and minimum cost with only a discrete set of available ply orientations. When the composite laminate design problem is considered as a discrete optimization problem where ply angles are limited to a discrete set, most approaches use evolutionary algorithms

such as genetic algorithms, see [15] and references therein. In such evolutionary algorithms the performance of each design has to be evaluated, for example using finite element methods like in this work, and in case of large real life structures with many design variables such approaches thus become very computationally expensive, see e.g. [3].

In this paper the design problem is formulated using the so-called Discrete Material Optimization (DMO) approach based on ideas from multi-phase topology optimization (see Sigmund and co-workers [13, 29]) where the material stiffness (or density) is computed as a weighted sum of candidate materials. In this way the discrete problem of choosing the best material (with the right orientation) for each ply with fixed thickness is converted to a continuous formulation where the design variables are the scaling factors (or weight functions) on each candidate material. The method has been successfully applied for maximum stiffness design, eigenfrequency design, and buckling design using as many as 12 candidate materials at each point and several hundred thousands of design variables in total, see [20, 21, 31]. In [20] the DMO method is applied for buckling design of laminated multi-material shell structures, and in the current work the approach is investigated for buckling design of a wind turbine blade test section.

In Sect. 12.2 the DMO approach is described followed by details about the finite element based analysis and design sensitivity analysis in Sect. 12.3. The optimization problem is solved using mathematical programming as described in Sect. 12.4, and finally the design optimization approach is demonstrated for buckling design of a wind turbine blade test section in Sect. 12.5.

12.2 Discrete Material Optimization (DMO) Approach

The design problem is posed as to optimize a general laminated multi-material composite structure where each of the plies have fixed thickness and the ply angles of FRP materials are limited to a discrete set such as $0°$, $\pm 45°$, and $90°$. The candidate materials to choose between may be FRP materials (with a given fiber angle) together with isotropic materials like foam materials.

The discrete optimization problem is converted to a continuous problem in the DMO approach by introducing continuous weight functions, such that the materials stiffness (or density) is computed as a weighted sum of candidate materials, see [20, 21, 31]. Weight functions are introduced for this interpolation, and it is the aim of the optimization to yield a distinct choice of candidate material as in traditional topology optimization where the material distribution of a single material within a given design domain is typically investigated. The continuous formulation allows the use of efficient gradient based optimization techniques for the multi-material topology optimization problem considered while reducing the risk of obtaining a local optimum solution (see, e.g., minimum compliance examples in [32] with provably good objective functions and compare with DMO results in [21]).

12.2.1 Parametrization for Single Layered Laminate Structures

As in traditional topology optimization the parametrization of the DMO formulation is invoked at the finite element level. The element constitutive matrix, $\mathbf{C}^e$, for a single layered laminate structure may in general be expressed as a sum over the element number of candidate material configurations, n^e:

$$\mathbf{C}^e = \sum_{i=1}^{n^e} w_i \mathbf{C}_i = w_1\mathbf{C}_1 + w_2\mathbf{C}_2 + \cdots + w_{n^e}\mathbf{C}_{n^e}, \qquad 0 \le w_i \le 1 \tag{12.1}$$

where each candidate material is characterized by a constitutive matrix $\mathbf{C}_i$. The weight functions w_i must all have values between 0 and 1 in order to be physically allowable. Furthermore, in case of solving buckling problems or having a mass constraint as in the optimization problems studied here, it is necessary that the sum of the weight functions is 1.0, i.e., $\sum_{i=1}^{n^e} w_i = 1.0$. If this demand is not fulfilled, physically meaningless results will be obtained for the buckling load factor for intermediate values of the weight functions. Similarly, the mass density ρ is computed using the weight functions, and if the sum of the weight functions does not add up to unity, the computed mass M cannot be compared to the prescribed mass constraint $\overline{M}$.

For details about different parametrization schemes the reader is referred to [30, 31], and only the most effective implementation is briefly outlined here.

For each element a number of design variables x_i^e, $i = 1,\ldots,n^e$ is introduced, and the weight functions w_i used are defined as

$$w_i = \frac{\hat{w}_i}{\sum_{k=1}^{n^e} \hat{w}_k}, \quad i = 1,\ldots,n^e \qquad \text{where} \quad \hat{w}_i = (x_i^e)^p \prod_{j=1;\ j\neq i}^{n^e} \left(1-(x_j^e)^p\right) \tag{12.2}$$

As an example, in case of four candidate materials the weight functions $\hat{w}_i$ are given as

$$\begin{aligned}
\hat{w}_1 &= (x_1^e)^p\,(1-(x_2^e)^p)\,(1-(x_3^e)^p)\,(1-(x_4^e)^p)\\
\hat{w}_2 &= (x_2^e)^p\,(1-(x_1^e)^p)\,(1-(x_3^e)^p)\,(1-(x_4^e)^p)\\
\hat{w}_3 &= (x_3^e)^p\,(1-(x_1^e)^p)\,(1-(x_2^e)^p)\,(1-(x_4^e)^p)\\
\hat{w}_4 &= (x_4^e)^p\,(1-(x_1^e)^p)\,(1-(x_2^e)^p)\,(1-(x_3^e)^p)
\end{aligned} \tag{12.3}$$

The SIMP method known from topology optimization has been adopted by introducing the power, p, to penalize intermediate values of x_i^e, such that the design variables x_i^e are pushed towards 0 or 1. The power p is typically set to 1 or 2 in the beginning of the optimization process and then increased by 1 for every 10 design iterations until p is 3 or 4. Moreover, the term $(1-x_j^e)_{j\neq i}$ is introduced such that an increase in x_i^e results in a decrease of all other weight functions. Finally, the weights have been normalized in order to satisfy the constraint that the sum of the weight functions is 1.0 (this is in general not the case for the weight functions $\hat{w}_i$).

The initial values of the design variables, x_i, may in principle be any set of numbers between 0 and 1 but in general the values should be chosen such that the initial weighting is uniform, i.e. $w_i = w_j$ for all $i, j = 1, \ldots, n^e$. In this way no candidate material is favored a priori.

12.2.2 Parametrization for Multi Layered Laminate Structures

The only difference between single and multi layered laminate structures is that the interpolation given above has to be used for all layers, i.e., the layer constitutive matrix $\mathbf{C}_k^l$ for layer k is computed as

$$\mathbf{C}_k^l = \sum_{i=1}^{n^l} w_i \mathbf{C}_i \tag{12.4}$$

where n^l is the number of candidate materials for the layer.

12.2.3 Patch Design Variables

The design variables x_i may be associated with each finite element of the model or the number of design variables may be reduced by introducing patches, covering larger areas of the structure. This is a valid approach for practical design problems since laminates are typically made using fiber mats covering larger areas.

12.2.4 DMO Convergence

In order to describe whether the optimization has converged to a satisfactory result, i.e. whether a single candidate material has been chosen in all layers and all other materials have been discarded, a DMO convergence measure is defined. For each layer in each element the following inequality is evaluated for all n^l weight factors, w_i:

$$w_i \geq \varepsilon \sqrt{w_1^2 + w_2^2 + \cdots + w_{n^l}^2} \tag{12.5}$$

where ε is a tolerance level, typically 95–99.5%. If the inequality 12.5 is satisfied for one of the weight factors w_i in the layer it is flagged as converged. The DMO convergence measure, h_ε, is then defined as the ratio of converged layers in all elements $N_c^{l,tot}$ to the total number of layers in all elements $N^{l,tot}$:

$$h_\varepsilon = \frac{N_c^{l,tot}}{N^{l,tot}} \tag{12.6}$$

The DMO convergence measure is denoted $h_{99.5}$ if the tolerance level is 99.5% (and so forth) and full convergence, i.e. $h_{99.5} = 1$, simply means that all layers in all elements have a single weight factor contributing more than 99.5% to the Euclidian norm of the weight factors.

12.3 Analysis and Design Sensitivity Analysis

The analysis of the general laminated composite structure is in this work based on nine node isoparametric shell finite elements. All materials are assumed to behave linearly elastic and the structural behavior of the laminate is described using an equivalent single layer theory where the layers are assumed to be perfectly bonded together such that displacements and strains will be continuous across the thickness. Such theories are known to be sufficiently accurate for modeling of the structural stiffness. The shell elements used are derived using the degenerated solid approach and are thus based on first order shear deformation theory, see, e.g., [5].

The analyses involved are static stress analysis and linear buckling analysis in order to determine the buckling load factor, i.e., the structure is assumed to be perfect with no geometrical imperfections and the buckling load found will typically be an upper limit for the real value. Thus, the analyses performed are

$$\mathbf{KD} = \mathbf{F} \quad \text{and} \quad (\mathbf{K} + \lambda_j \mathbf{K}_\sigma)\,\boldsymbol{\Phi}_j = \mathbf{0}, \qquad j = 1, 2, \ldots \tag{12.7}$$

Here $\mathbf{K}$ is the global stiffness matrix, $\mathbf{D}$ is the global displacement vector and $\mathbf{F}$ the global load vector. In the buckling analysis problem $\mathbf{K}_\sigma$ is the global stress stiffness matrix, the eigenvalues λ_j are assumed ordered by magnitude, such that λ_1 is the lowest eigenvalue, i.e., buckling load factor, and $\boldsymbol{\Phi}_1$ is the corresponding eigenvector.

In order to optimize the structure using the DMO approach gradients must be made available. The design variables are termed $x_i, i = 1, \ldots, I$, and the design sensitivity analysis is based on the direct differentiation approach. In case of a simple, i.e. distinct, eigenvalue λ_j in the buckling analysis, the eigenvalue sensitivity is given as [8, 14, 16, 23, 37]

$$\frac{d\lambda_j}{dx_i} = -\boldsymbol{\Phi}_j^T \left(\frac{d\mathbf{K}}{dx_i} + \lambda_j \frac{d\mathbf{K}_\sigma}{dx_i} \right) \boldsymbol{\Phi}_j \tag{12.8}$$

where it has been assumed that the eigenvectors have been $\mathbf{K}_\sigma$-orthonormalized, such that $\boldsymbol{\Phi}_j^T \mathbf{K}_\sigma \boldsymbol{\Phi}_j = 1$.

In case of multiple eigenvalues the eigenvectors are not unique, which complicates the sensitivity analysis and optimization due to the non-differentiability of the eigenvalues. In such situations the sensitivity analysis described in [28], see also [20], is used together with the optimization algorithm developed in [19]. The details are omitted here for brevity.

For the DMO material parametrization used in this work where the geometry is fixed and only the material is changed, the stiffness matrix derivative $d\mathbf{K}/dx_i$ only involves the derivative of the element layer constitute matrix $\mathbf{C}_k^l$ with respect to x_i, which is easily done analytically by differentiating the interpolation, see Eqs. (12.1) and (12.2).

The stress stiffness matrix is an implicit function of the displacement field, i.e. $\mathbf{K}_\sigma = \mathbf{K}_\sigma(\mathbf{D}(\mathbf{x}), \mathbf{x})$, which must be taken into account. The displacement sensitivities $d\mathbf{D}/dx_i$ are computed using the direct differentiation approach, i.e., the static equilibrium equation is differentiated with respect to a design variable x_i

$$\mathbf{K}\frac{d\mathbf{D}}{dx_i} = \frac{d\mathbf{F}}{dx_i} - \frac{d\mathbf{K}}{dx_i}\mathbf{D} \tag{12.9}$$

where the load sensitivity $d\mathbf{F}/dx_i$ is zero for the DMO material design variables used, unless volume forces are considered. The displacement sensitivity is computed analytically by solving Eq. (12.9) for each design variable x_i, reusing the factorized global stiffness matrix $\mathbf{K}$ from the analysis in case of using a direct solver. The stress stiffness matrix sensitivity $d\mathbf{K}_\sigma/dx_i$ in Eq. (12.8) is computed by a central difference approximation at the element level, i.e.

$$\frac{d\mathbf{K}_\sigma}{dx_i} \approx \frac{\mathbf{K}_\sigma(\mathbf{x}+\Delta x_i, \mathbf{D}+\Delta\mathbf{D}) - \mathbf{K}_\sigma(\mathbf{x}-\Delta x_i, \mathbf{D}-\Delta\mathbf{D})}{2\Delta x_i} \tag{12.10}$$

where $\Delta\mathbf{D} \approx \frac{d\mathbf{D}}{dx_i}\Delta x_i$. Thus, a semi-analytical design sensitivity analysis is applied. The perturbation Δx_i of the DMO design variable x_i is set to 0.001. The well-known inaccuracy problem associated with semi-analytical design sensitivity analysis of slender beam, plate and shell structures only appears in case of shape design variables (see [4, 26] for details) and no inaccuracy problems have been observed for the central difference approximation of element stress stiffness matrix sensitivities in case of DMO material design variables.

Alternatively, the element stress stiffness matrix sensitivities can be computed using

$$\frac{d\mathbf{K}_\sigma}{dx_i} = \frac{\partial\mathbf{K}_\sigma}{\partial x_i} + \frac{\partial\mathbf{K}_\sigma}{\partial\mathbf{D}}\frac{d\mathbf{D}}{dx_i} \tag{12.11}$$

but this requires quite a lot of additional derivations and programming to implement which is the main reason for using Eq. (12.10).

12.4 The Optimization Problem

The optimization problem of maximizing the buckling load factor λ_1 with a mass constraint is formulated using a bound formulation, see [6], as

$$\text{Objective: } \max_{\mathbf{x},\beta} \ \beta$$

$$\begin{aligned} \text{Subject to: } & \lambda_j \geq \beta, \quad j = 1,\ldots,N_\lambda \\ & (\mathbf{K} + \lambda_j \mathbf{K}_\sigma)\,\boldsymbol{\Phi}_j = \mathbf{0}, \qquad j = 1,2,\ldots \\ & M \leq \overline{M} \\ & \underline{x_i} \leq x_i \leq \overline{x_i},\ i = 1,\ldots,I \end{aligned} \tag{12.12}$$

where $\overline{M}$ is the upper limit on the mass M of the structure. By introducing the bound parameter β the lowest N_λ eigenvalues are considered when solving the minimax problem of maximizing the buckling load factor, and the possibility of crossing eigenvalues (mode switching) and creation of multiple eigenvalues is taken into account during the optimization process.

The derivative of the mass constraint in Eq. (12.12) is also computed analytically, and having obtained all the necessary design sensitivities, the mathematical programming problem is solved using the Method of Moving Asymptotes by Svanberg [33]. A nested approach is used, i.e., the state equations added as equality constraint in Eq. (12.12) are not included in the mathematical programming problem as they are solved a priori using the inhouse finite element code MUST [25]. The closed loop of analysis, design sensitivity analysis and optimization is repeated until convergence in terms of no change of the design variables is reached or until a prescribed maximum number of design iterations has been performed.

12.5 Buckling Optimization of Wind Turbine Blade Test Section

The design of wind turbines blades is a challenging problem due to the need for pushing the material utilization to the limit in order to obtain light and cost effective structures. As a consequence of the minimum material design strategy the structures are becoming thin-walled, such that buckling problems must be addressed, and in this work the aim is to obtain buckling optimized designs of a 9 m generic wind turbine blade test section using the multi-material topology optimization approach presented.

The generic 9 m wind turbine blade test section has been studied numerically and experimentally in the Ph.D. thesis by Kühlmeier [18], see Fig. 12.1. The test section is used for technology demonstration projects and conceptual studies. The 9 m section is un-tapered and non twisting, i.e. it is an extruded 2D section. The test setup in which the 9 m section is normally tested is in a 4-point flap-wise bending configuration where the middle 2 m of the 9 m section is loaded with a constant bending moment as seen in Fig. 12.1.

The structural instability behavior of the test section in pure bending has been investigated both experimentally and using finite element models for linear buckling analysis and geometrically non-linear analysis. The conclusion from [18] is that a linear buckling analysis may underestimate the buckling load factor significantly as imperfections are thus neglected but the buckling mode obtained from the linear buckling analysis is quite similar to the deformation mode observed experimentally and also obtained from a geometrically non-linear analysis. Thus, from an

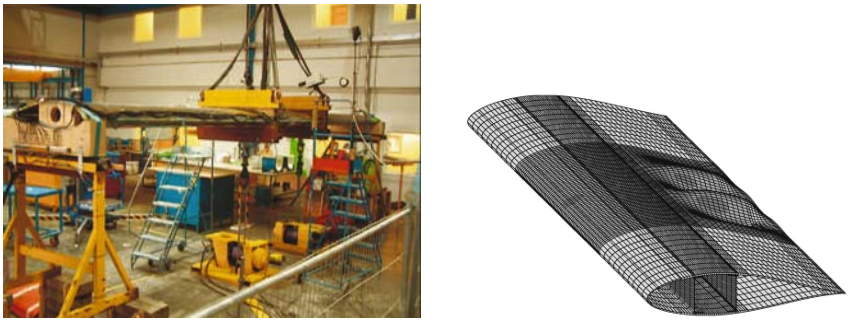

(A) (B)

Fig. 12.1 **A**: 9 m generic wind turbine blade test section in four point bending, see details in [18]. **B**: An example of linear buckling analysis of a generic wind turbine blade using a solid shell finite element model

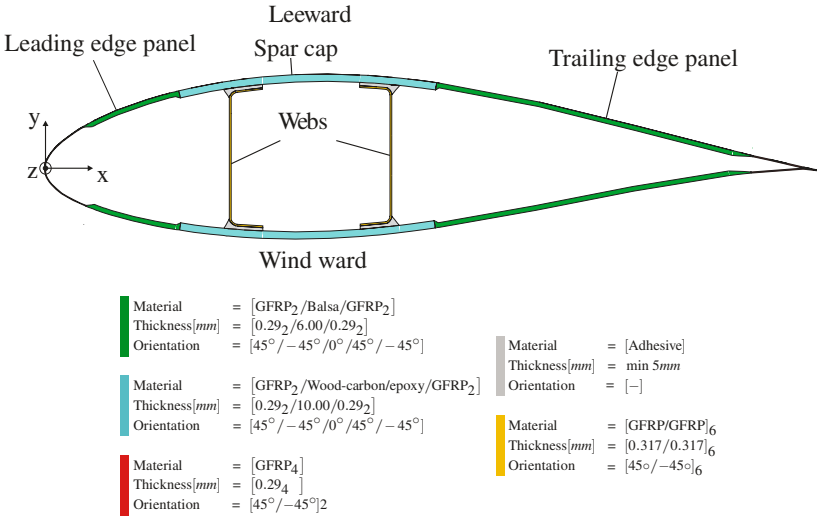

Fig. 12.2 Cross section and layup of NACA 63_4 - 421 wind turbine blade test section studied in [18]. The fiber angles are given with respect to the length direction (z)

optimization point of view, a linearized buckling analysis may constitute a sufficiently accurate analysis model as starting point when the objective is to solve the material distribution problem for maximizing the buckling resistance of the blade.

The cross section of the 9 m section is a NACA 63_4 - 421 profile with a chord of 1.17 m. It is close to being symmetric as it only has a 4% chamber, and in this paper the cross section is considered symmetric in order to reduce the size of the computational model. The cross section and the layup can be seen in Fig. 12.2.

The materials used for the test section can be seen in Table 12.1.

Typically there is a design constraint on the global bending stiffness of the blade since fatigue issues often drive the design. Hence the maximum strain of the material

Table 12.1 Material properties for wind turbine blade

Material property	GFRP	Wood-carbon/epoxy	Adhesive	Balsa	Foam
E_1 [MPa]	30,600	57,500	3,000	352	2,000
E_2 [MPa]	8,700	620	–	352	–
E_3 [MPa]	8,700	620	–	3,920	–
ν_{12}	0.29	0.45	0.37	0.3	0.47
ν_{23}	0.30	0.3	–	0.1	–
ν_{13}	0.30	0.3	–	0.1	–
G_{12} [MPa]	3,240	1,200	1,095	15.7	680
G_{23} [MPa]	2,900	1,100	–	157	–
G_{13} [MPa]	3,240	1,200	–	157	–
Density [kg/m^3]	1,686	1,079	1,200	80	200

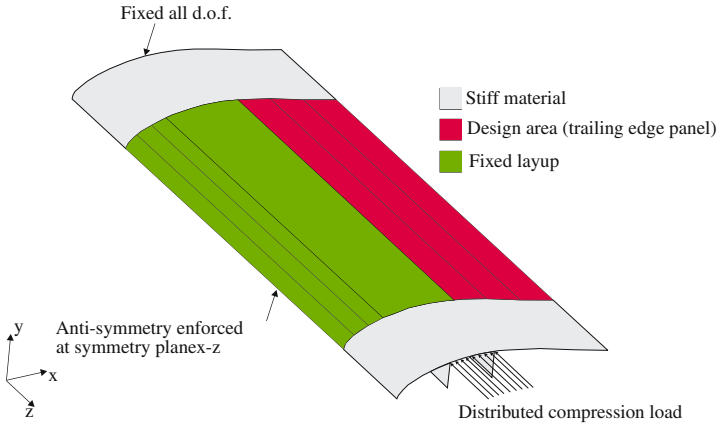

Fig. 12.3 Simplified model of the NACA 63_4 - 421 airfoil test section. The design domain is the trailing edge panel. Antisymmetric boundary conditions are assumed

is a constraining factor. Today's carbon fibre materials have excellent fatigue properties and thus the material is strained still harder to gain the maximum utilization of the expensive carbon fibre. Thus the structure should be buckling stably at the highest possible strain. Because of the constraint on the global stiffness the expensive wood-carbon/epoxy material is used in the spar cap and remains fixed during the optimization in the example considered.

In the analysis model used the middle 2 m of the test section is extended with areas consisting of stiff material (10 times stiffer than the test section) in order to simulate the boundary conditions in the test. Furthermore symmetry of the cross section is assumed for simplicity, and this results in antisymmetric boundary conditions as illustrated in Fig. 12.3.

The total axial load is $166 \cdot 10^3$ N distributed as a compression load on the spar cap as illustrated in Fig. 12.3, giving a total moment of 47.5 kNm. The analysis model consists of 1,642 nine node isoparametric shell finite elements.

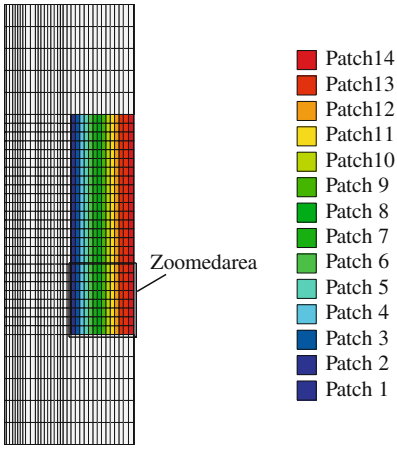

Fig. 12.4 The design area (the trailing edge sandwich panel) is divided into 14 patches. Results of the topology optimization will be presented for the zoomed area

The whole trailing edge panel is allowed to change in the design optimization (including the part close to the trailing edge marked with the color red in Fig. 12.2), and it is divided into 14 patches as illustrated in Fig. 12.4. Each patch has 12 layers of equal thickness 0.5 mm, i.e., the total thickness is 6 mm everywhere in the design area. The buckling modes of the lowest eigenvalues are local modes of the trailing edge panel (see also Fig. 12.1B).

First the candidate materials are GFRP unidirectional material oriented at 0°, +45°, −45°, and 90° for the two outer layers whereas the foam material also can be selected together with the four GFRP candidate materials for the 10 inner layers. The mass constraint $\overline{M}$ is set to 24.9 kg which corresponds to 2/3 of the design domain being filled with foam material.

When solving the optimization problem given by Eq. (12.12) the three lowest eigenvalues are taken into account in all design iterations. The penalization power p used in the weight functions in Eq. (12.2) is initially set to 1 and increased by 1 for every 10 design iterations until p equals 3. The move limit used on all DMO design variables is 5%, i.e. each design variable may change up to 5% in every design iteration.

The result of the optimization can be seen in Fig. 12.5. If the GFRP material has been selected, then the material orientation is shown for each finite element, whereas white means that the foam material has been selected. The results of the optimization are shown for the zoomed area defined in Fig. 12.4.

The DMO convergence measure, see Eq. (12.6), is $h_{95} = 0.89$ and $h_{99.5} = 0.84$. Thus, in 5/6 of the domain a distinct choice of material is obtained. The convergence of the lowest eigenvalue is monotonic and is increased from $\lambda_1 = 1.05$ for the initial design where all weight factors on the candidate materials have equal values to $\lambda_1 = 2.23$ for the optimized design where the mass constraint is active.

It is seen that the GFRP material at the left part of the trailing edge part (at the transition to the spar cap) should be oriented at 0°, and the overall distribution of foam material through the thickness seems reasonable. However, the GFRP material

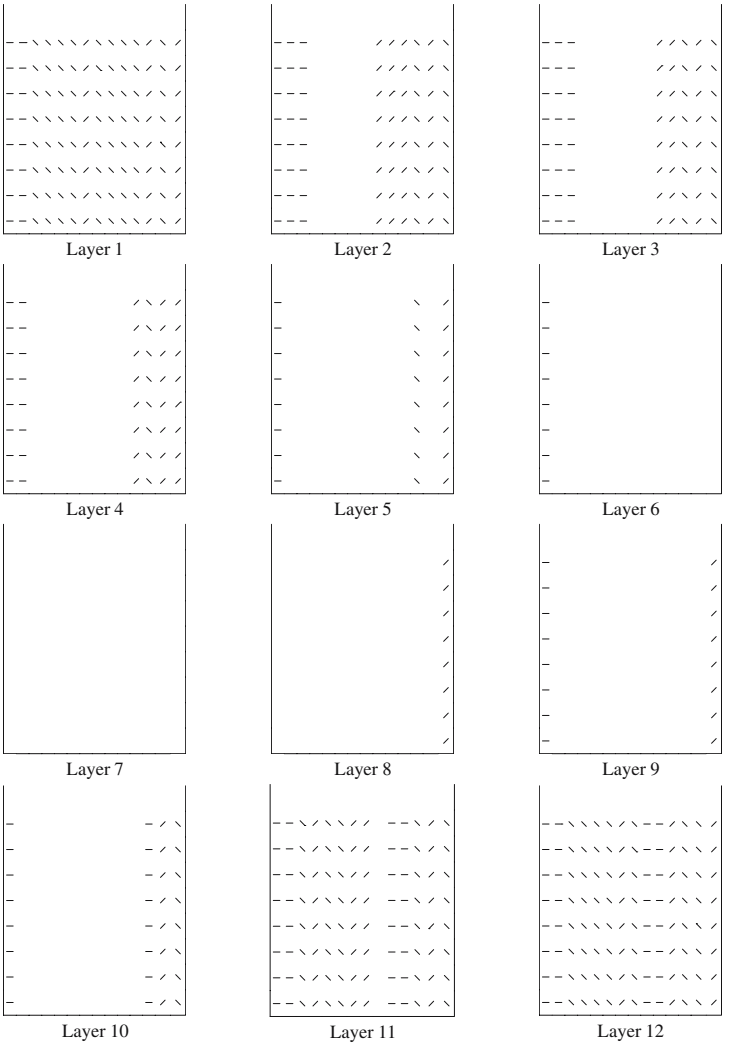

Fig. 12.5 Case 1: Optimized material directions (fiber angles) for maximum buckling load factor design of 12-layer trailing edge panel of the test section when five DMO variables per patch are used (foam material together with unidirectional GFRP material oriented at 0°, +45°, −45°, and 90°). In all elements the candidate material with the largest weight factor is shown. White means that the isotropic foam material has been selected. *Layer 1* is the lower layer and *layer 12* is the top (outer) layer. The results are shown for the zoomed area defined in Fig. 12.4

orientations in the middle of the panel and at the right part at the trailing edge vary between 0°, +45°, and −45° in the patches in a somewhat random way, judged by engineering intuition. This may indicate that the unidirectional GFRP used is not well suited for giving good resistance against the local buckling modes of the panel.

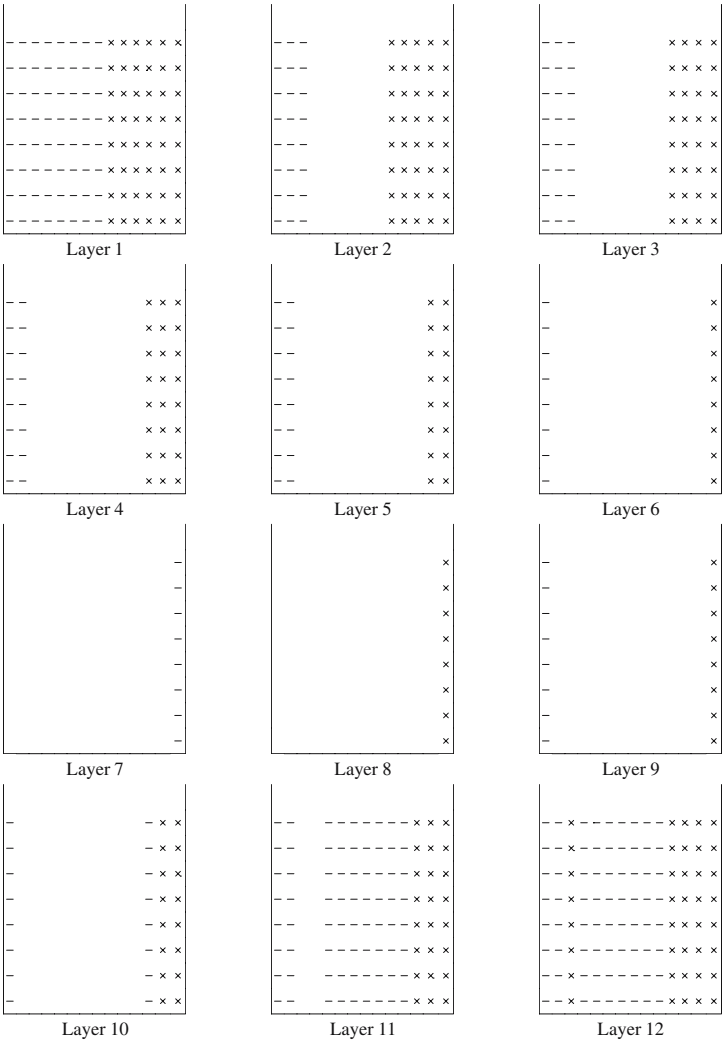

Fig. 12.6 Case 2: Optimized material directions (fiber angles) for maximum buckling load factor design of 12-layer trailing edge panel of the test section when 4 DMO variables per patch are used (foam material together with GFRP unidirectional material oriented at 0° and 90° and GFRP ± 45° angle-ply). White means that the isotropic foam material has been selected. *Layer 1* is the lower layer and *layer 12* is the top (outer) layer. The results are shown for the zoomed area defined in Fig. 12.4

Thus, the parametrization is changed such that the unidirectional GFRP material is either oriented at 0° or 90°, and then a GFRP ± 45° angle-ply candidate material is introduced. The mass constraint and the other specifications of the optimization problem are unchanged, and the results of this second case of optimization are shown in Fig. 12.6.

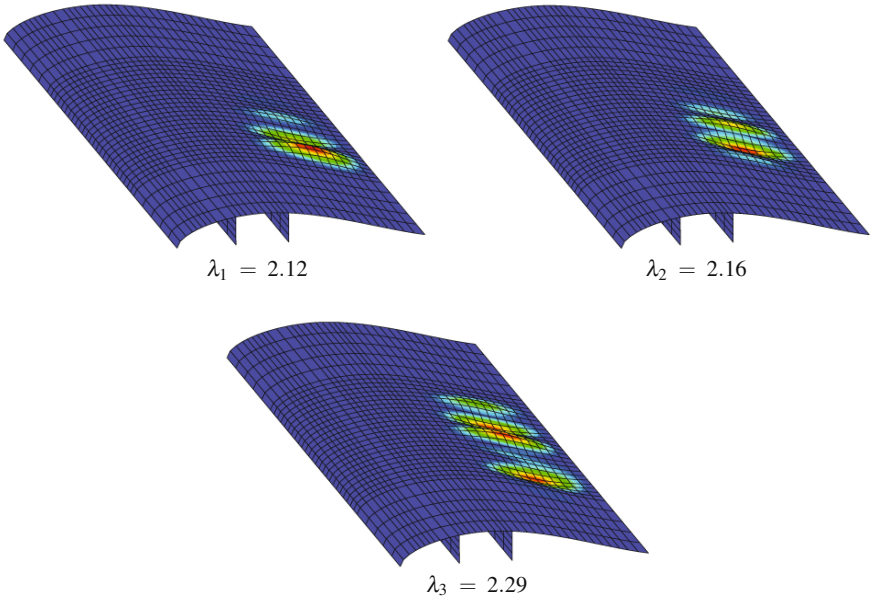

Fig. 12.7 The three lowest buckling modes for the optimized design (case 2)

In this second case the DMO convergence measure is $h_{95} = 0.98$ and $h_{99.5} = 0.96$. Thus, a distinct choice of material is obtained nearly everywhere in the design domain which is better than in case 1. Furthermore, the selected GFRP candidate materials are in better agreement with engineering intuition now.

Again it is seen that the GFRP material at the left part of the trailing edge part should be oriented at 0°, but due to the removal of $+45^\circ$ and -45° unidirectional GFRP as candidate materials, the region of 0° GFRP is extended to the middle of the panel. The distribution of foam material through the thickness is approximately as before. In comparison to case 1, a much more clear distinct spatial distribution of the GFRP material is obtained, and it is clear that the $\pm 45^\circ$ angle-ply should be used at the trailing edge. The selection of $\pm 45^\circ$ angle-ply GFRP has also been observed for compliance optimization problems in shear dominated areas of the design domain, and looking at the buckling modes of the optimized design in Fig. 12.7, the material distributions seem very reasonable.

The 0° GFRP material at the left part of the trailing edge part gives a stiff connection to the stiff spar cap section, and the $\pm 45^\circ$ angle-ply dominated layup at the trailing edge yields good resistance against the local buckling modes.

The convergence of the lowest eigenvalue is again monotonic and is increased from $\lambda_1 = 0.93$ for the initial design where all weight factors on the candidate materials have uniform values to $\lambda_1 = 2.12$ for the optimized design where the mass constraint is active. The buckling load factor in case 1 where only unidirectional GFRP is used together with foam material is actually a little higher, but this is

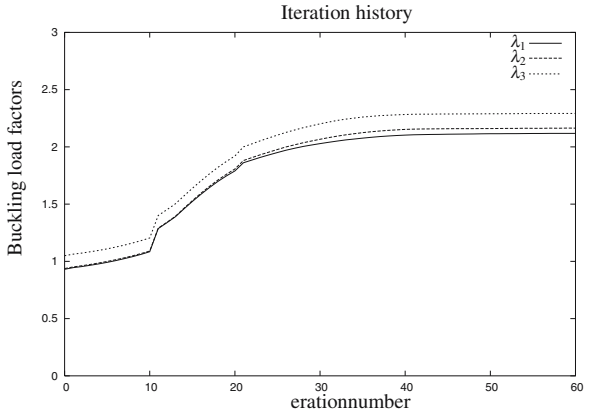

Fig. 12.8 Iteration history for the three lowest buckling load factors for case 2

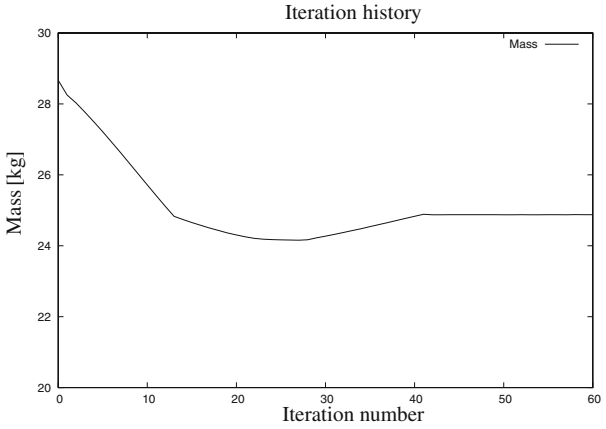

Fig. 12.9 Iteration history for the mass constraint for case 2

mainly because of a non-converged solution in 1/6 of the design domain in case 1. In these non-converged areas the material used is a mixture of several candidate materials which typically yields a better performance than the $\pm 45^\circ$ angle-ply used in case 2.

The iteration history for the three lowest eigenvalues is shown in Fig. 12.8 and for the mass constraint in Fig. 12.9.

The mass constraint $\overline{M}$ of 24.9 kg for the trailing edge panel is violated for the initial design where all weight factors on the candidate materials have equal values in order not to favor any of the candidate materials, and it becomes active after 42 iterations where the design optimization process more or less has converged. A larger move limit on the design variables could be used in order to reduce the number of iterations, but this might give some oscillations in the iteration history for the objective function.

12.6 Conclusion

The problem of multi-material topology design of composite laminated structures has been investigated using the so-called Discrete Material Optimization (DMO) approach. The design problem is initially stated as a discrete optimization problem involving the specification of material type and orientation of ply layers in the stacking sequence where the ply angles are limited to a discrete set such as $0°$, $\pm 45°$, and $90°$. The candidate materials may be FRP materials (with given orientations) together with isotropic materials like foam, and the multi-material design problem is converted to a continuous problem by introducing weight factors that interpolate between candidate materials. Penalization techniques together with gradient based optimization methods are used to obtain a distinct choice of material everywhere in the design domain.

The DMO method has been used for buckling multi-material topology optimization of a wind turbine blade test section. The test section is modeled using a shell finite element model, and the trailing edge part has been redesigned with the objective of maximizing the buckling load factor of the test section, taking a weight constraint into account. The trailing edge part has been topology optimized using 2/3 of foam material and 1/3 of GFRP material. The material distribution results and the convergence history of the design optimization demonstrate, that the DMO approach can be a strong preprocessing tool for multi-material topology optimization of composite structures in the early design phase, where the general topology design of structures should be decided before more detailed designs are investigated.

Acknowledgements Thanks to our former colleague, Assistant. Professor. Jan Stegmann, for our joint work on development of the Discrete Material Optimization (DMO) approach.

References

1. Abrate S (1994) Optimal design of laminated plates and shells. Compos Struct 29:269–286
2. Adali S, Richter A, Verijenko VE, Summers EB (1995) Optimal design of hybrid laminates with discrete ply angles for maximum buckling load and minimum cost. Compos Struct 32:409–415
3. Adams DB, Watson LT, Seresta O, Gürdal Z (2007) Global/local iteration for blended composite laminate panel structure optimization subproblems. Mech Adv Mater Struct 14:139–150
4. Barthelemy B, Haftka RT (1990) Accuracy analysis of the semi-analytical method for shape sensitivity analysis. Mech Struct Mach 18:407–432
5. Bathe KJ (1996) Finite Element Procedures. Prentice-Hall, Englewood Cliffs, NJ
6. Bendsøe MP, Olhoff N, Taylor JE (1983) A variational formulation for multicriteria structural optimization. J Struct Mech 11:523–544
7. Bendsøe MP, Sigmund O (2003) Topology optimization – theory, methods and applications, 2nd edn. Springer, New York
8. Courant R, Hilbert D (1953) Methods of Mathematical Physics, Volume 1. Interscience Publishers, New York

9. Duvaut G, Terrel G, Léné F, Verijenko VE (2000) Optimization of fiber reinforced composites. Compos Struct 48:83–89
10. Foldager J, Hansen JS, Olhoff N (1998) A general approach forcing convexity of ply angle optimization in composite laminates. Struct Optim 16:201–211
11. Foldager J, Hansen JS, Olhoff N (2001) Optimization of the buckling load for composite structures taking thermal effects into account. Struct Multidiscip Optim 21:14–31
12. Fukunaga H, Vanderplaats GN (1991) Stiffness optimization of orthotropic laminated composites using lamination parameters. AIAA J 29:641–646
13. Gibiansky LV, Sigmund O (2000) Multiphase composites with extremal bulk modulus. J Mech Phys Solids 48:461–498
14. Gu YX, Zhao GZ, Zhang HW et al. (2000) Buckling design optimization of complex built-up structures with shape and size variables. Struct Multidiscip Optim 19:183–191
15. Gürdal Z, Haftka RT, Hajela P (1999) Design and Optimization of Laminated Composite Materials. Wiley, New York
16. Haftka RT, Adelman HM (1989) Recent developments in structural sensitivity analysis. Struct Optim 1:137–151
17. Hammer VB, Bendsøe MP, Lipton R, Pedersen P (1997) Parametrization in laminate design for optimal compliance. Int J Solids Struct 34:415–434
18. Kühlmeier L (2007) Buckling of Wind Turbine Rotor Blades - Analysis, Design and Experimental Validation. Ph.D. thesis, Department of Mechanical Engineering, Aalborg University, Denmark
19. Lund E (1994) Finite element based design sensitivity analysis and optimization. Ph.D. thesis, Institute of Mechanical Engineering, Aalborg University, Denmark. Special report No. 23, available at www.ime.aau.dk/˜el
20. Lund E (2007) Buckling topology optimization of laminated multi-material composite shell structures. Compos Struct. To appear. Also available as DCAMM Report No. 721, October 2006, 12 pages, www.dcamm.dk
21. Lund E, Stegmann J (2005) On structural optimization of composite shell structures using a discrete constitutive parametrization. Wind Energy 8:109–124
22. Martin AF, Leissa AW (1989) Application of Ritz method to plane elasticity problems for composite sheets with variable fiber spacing. Int J Numer Methods Eng 28:1813–1825
23. Mateus HC, Mota Soares CM, Mota Soares CA (1997) Buckling sensitivity analysis and optimal design of thin laminated structures. Comput Struct 64:461–472
24. Miki M, Sugiyama Y (1993) Optimum design of laminated composite plates using lamination parameters. AIAA J 31:921–922
25. MUST (2007) Department of Mechanical Engineering, Aalborg University, Denmark. www.ime.aau.dk/must
26. Olhoff N, Rasmussen J, Lund E (1993) "Exact" numerical differentiation for error elimination in finite element based semi-analytical shape sensitivity analysis. Mech Struct Mach 21:1–61
27. Setoodeh S, Abdalla MM, Gürdal Z (2005) Combined topology and fiber path design of composite layers using cellular automata. Struct Multidiscip Optim 30:413–421
28. Seyranian AP, Lund E, Olhoff N (1994) Multiple eigenvalues in structural optimization problems. Struct Optim 8:207–227
29. Sigmund O, Torquato S (1997) Design of materials with extreme thermal expansion using a three-phase topology optimization method. J Mech Phys Solids 45:1037–1067
30. Stegmann J (2004) Analysis and optimization of laminated composite shell structures. Ph.D. thesis, Institute of Mechanical Engineering, Aalborg University, Denmark. Special report No. 54, available at www.ime.aau.dk/˜js
31. Stegmann J, Lund E (2005) Discrete material optimization of general composite shell structures. Int J Numer Methods Eng 62:2009–2027
32. Stolpe M, Stegmann J (2007) A Newton method for solving continuous multiple material minimum compliance problems. Struct Multidiscip Optim 35:93–106
33. Svanberg K (1987) The method of moving asymptotes - a new method for structural optimization. Numer Methods Eng 24:359–373

34. Thomsen J (1991) Optimization of composite discs. Struct Optim 3:89–98
35. Thomsen J, Olhoff N (1990) Optimization of fiber orientation and concentration in composites. Control Cybern 19:327–341
36. Tsai SW, Pagano NJ (1968) Invariant properties of composite materials. In: Tsai SW et al. (ed) Composite Materials Workshop, Volume 1 of Progress in Material Science, pp 233–253, Technomic Publishing, Stamfort, CT
37. Wittrick WH (1962) Rates of change of eigenvalues, with reference to buckling and vibration problems. J Royal Aeronaut Soc 66:590–591

Chapter 13
Computation of Effective Stiffness Properties for Textile-Reinforced Composites Using X-FEM

M. Kästner, G. Haasemann, J. Brummund, and V. Ulbricht

Abstract The macroscopic material behaviour of novel textile-reinforced composites is defined by its constituents (micro-level) and the design of the textile reinforcement (meso-level). Consequently, a multi-scale approach to the prediction of the material behaviour is necessary because only in this vein the adaptability of the textile reinforcement can be used to develop materials whose features can be adjusted precisely to certain applications.

Due to the difference in size between the macroscopic component and the fine-scale material structure a direct modelling of the reinforcement in a structural analysis is not reasonable.

Therefore, a decoupled computational homogenization procedure is applied. Based on a representative volume element (RVE) of the reinforcing architecture effective material properties $\bar{C}_{ijkl}$ for a macroscopically homogeneous continuum are computed. These properties are used to characterize the effective linear elastic material behaviour of the composite in a structural analysis and allow for efficient component analysis and design.

In the process of generating numerical models for RVE of textile-reinforced composites the extended finite element method (X-FEM) is applied and an automated modelling procedure is developed. The computed effective stiffness values are compared to experimental data from ultrasonic and standard tensile tests.

13.1 Homogenization

The macroscopic mechanical behaviour of textile-reinforced composite structures is mainly governed by its constituents on the meso- and micro-scale. In this hierarchical structure the micro-level represents the smallest scale with explicit consideration of single fibres and matrix that form the reinforcement on the meso-level (Fig. 13.1).

M. Kästner, G. Haasemann, J. Brummund, and V. Ulbricht
Technische Universität Dresden, Institute of Solid Mechanics, D-01062 Dresden, Germany,
e-mail: Markus.Kaestner@tu-dresden.de

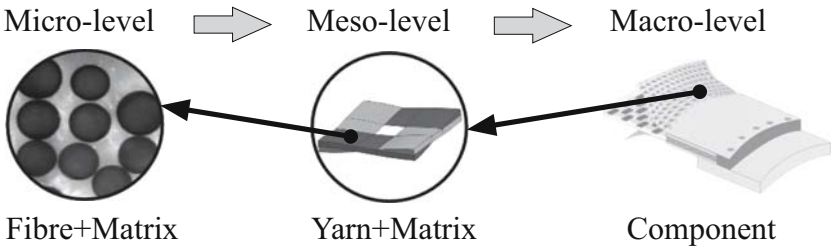

Fig. 13.1 Multi-scale approach to modelling of composite structures

Together with pure matrix fractions the reinforcing architecture – modelled as homogeneous yarn – is the most important feature of a meso-scale RVE.

In order to motivate the idea of homogenization consider the mechanical boundary value problem given by the static equilibrium

$$\sigma_{ij,i} + f_j = 0; \;\; \sigma_{ij} = \sigma_{ji} \;\; \forall\, x_i \in \Omega \;\; (i,j = 1 \ldots 3) \tag{13.1}$$

with the symmetric stress tensor σ_{ij} and the body force vector f_j; the linear strain-displacement relations

$$\varepsilon_{ij} = \frac{1}{2}\left(u_{i,j} + u_{j,i}\right) \;\; \forall\, x_i \in \Omega \tag{13.2}$$

with the symmetric strain tensor ε_{ij} and the displacement vector u_i as well as HOOKE's law

$$\sigma_{ij} = C_{ijkl}\varepsilon_{kl} \;\; \forall\, x_i \in \Omega \tag{13.3}$$

with the fourth order elasticity tensor C_{ijkl}. In addition to the governing equations suitable boundary displacements $\tilde{u}_j$

$$u_j = \tilde{u}_j \;\; \forall\, x_i \in \partial\Omega_u \tag{13.4}$$

or tractions $\tilde{t}_m$

$$\sigma_{lm} n_l = \tilde{t}_m \;\; \forall\, x_i \in \partial\Omega_t \tag{13.5}$$

have to be applied to the boundary $\partial\Omega$ of the structure Ω (Fig. 13.2) where $\partial\Omega_u \cup \partial\Omega_t = \partial\Omega$ and $\partial\Omega_u \cap \partial\Omega_t = \varnothing$.

For heterogeneous media the elasticity tensor C_{ijkl} will depend on the location. In combination with a pronounced material structure on the micro- and meso-level this will result in an extensive modelling effort and unfavourable fine meshes if the local heterogeneity is to be modelled explicitly in the structural analysis.

However, the hierachical character of the problem with clearly separated length scales is predestinated for the application of computational homogenization techniques.

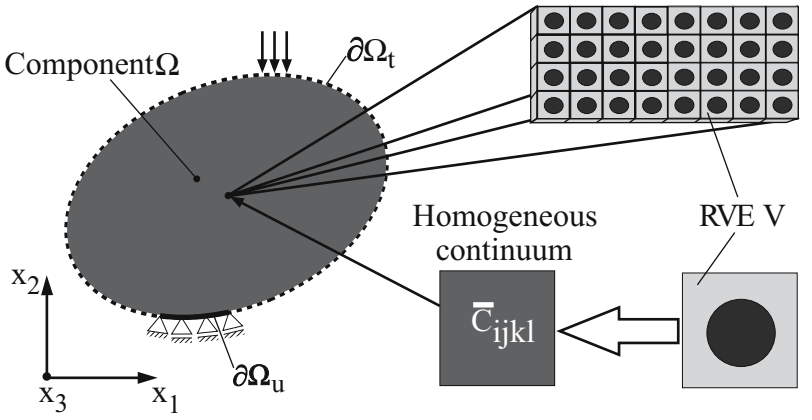

Fig. 13.2 Computation of effective macroscopic properties $\bar{C}_{ijkl}$ for a locally heterogeneous material

Using the homogenization approach for periodic media the original locally heterogeneous material is replaced by a homogeneous medium with an effective elasticity tensor $\bar{C}_{ijkl}$ (Fig. 13.2). The original problem in Eqs. (13.1)–(13.3) will then be approximated by

$$\left.\begin{aligned} \bar{\sigma}_{ij,i} + \bar{f}_j = 0; \quad \bar{\sigma}_{ij} = \bar{\sigma}_{ji} \\ \bar{\varepsilon}_{ij} = \tfrac{1}{2}\left(\bar{u}_{i,j} + \bar{u}_{j,i}\right) \\ \bar{\sigma}_{ij} = \bar{C}_{ijkl}\bar{\varepsilon}_{kl} \end{aligned}\right\} \quad \forall\, x_i \in \Omega \tag{13.6}$$

and boundary conditions according to Eqs. (13.4) and (13.5)

$$\bar{u}_j = \tilde{u}_j \quad \forall\, x_i \in \partial\Omega_u \tag{13.7}$$

$$\bar{\sigma}_{lm} n_l = \tilde{t}_m \quad \forall\, x_i \in \partial\Omega_t \tag{13.8}$$

where $\bar{\sigma}_{ij}$ and $\bar{\varepsilon}_{ij}$ are the associated macroscopic stress and strain fields. In order to obtain a sufficient approximation of the original solution it has to be ensured that the characteristic dimensions or wavelengths of two consecutive scales satisfy

$$\frac{l_{n+1}}{l_n} \gg 1 \tag{13.9}$$

There are different theoretical foundations for the prediction of effective properties $\bar{C}_{ijkl}$ based on a RVE entirely typical for the heterogeneous fine-scale material structure, e.g. asymptotic expansion of field quantities [10, 14] or energy averaging theorems [7]. Here the latter, namely the equivalence of the volume average of

elastic strain energy density $\{U\}$ in the RVE V and in the homogeneous macroscopic continuum $\bar{U}$

$$\{U\} = \bar{U} \tag{13.10}$$

$$\{U\} = \frac{1}{2}\{\sigma_{ij}\varepsilon_{ij}\}; \quad \{\ldots\} = \frac{1}{V}\int_V \ldots dV \tag{13.11}$$

$$\bar{U} = \frac{1}{2}\bar{\sigma}_{ij}\bar{\varepsilon}_{ij}, \tag{13.12}$$

will be focused.

13.1.1 Boundary Conditions and Deformation Modes

Assuming that a RVE for the considered reinforcing structure has been identified, the determination of effective material properties requires the equivalence criterion to be evaluated numerically. To this end suitable boundary conditions are applied to the RVE defining deformation modes with either prescribed average stress $\{\sigma_{ij}\} = \bar{\sigma}_{ij}$ or average strain $\{\varepsilon_{ij}\} = \bar{\varepsilon}_{ij}$.

The applied boundary conditions are chosen to fulfill the identity

$$\{\sigma_{ij}\varepsilon_{ij}\} = \{\sigma_{ij}\}\{\varepsilon_{ij}\} = \bar{\sigma}_{ij}\bar{\varepsilon}_{ij} \tag{13.13}$$

also known as HILL-MANDEL-Lemma. In general there are three different boundary conditions for which Eq. (13.13) is satisfied:

- Constant tractions

$$t_j = \bar{\sigma}_{ij} n_i(x_k) \quad \forall\, x_i \in \partial V \tag{13.14}$$

- Linear displacements

$$u_i = \bar{\varepsilon}_{ij} x_j \quad \forall\, x_i \in \partial V \tag{13.15}$$

- Periodic displacements in conjunction with antiperiodic tractions

$$\left.\begin{array}{l} u_i = \bar{\varepsilon}_{ij} x_j + u_i^P \\ u_i^P \text{ periodic} \\ t_i \text{ anti-periodic} \end{array}\right\} \forall\, x_i \in \partial V \tag{13.16}$$

where n_i is the outward normal and t_i is the traction vector on the boundary ∂V of the RVE.

While one of the average values in Eq. (13.13) is well-defined by the applied boundary conditions 13.14–13.16, the second average is obtained from the numerical solution of prescribed deformation modes. A sufficient number of such deformation modes has to be evaluated in order to be able to compute the desired effective material properties using the macroscopic constitutive relations

$$\bar{\sigma}_{ij} = \bar{C}_{ijkl}\bar{\varepsilon}_{kl} \quad \text{or} \quad \bar{\varepsilon}_{kl} = \bar{S}_{ijkl}\bar{\sigma}_{ij} \tag{13.17}$$

where $\bar{S}_{ijkl}$ is the macroscopic compliance tensor.

13.1.1.1 Periodic Deformation Modes

Here periodic displacement boundary conditions 13.16 are applied to generate the aforementioned deformation modes. These boundary conditions consist of a linear part which is equivalent to Eq. (13.15) and creates an average strain

$$\bar{\varepsilon}_{ij} = \{\varepsilon_{ij}\} = \frac{1}{V}\int_V \varepsilon_{ij}\, dV \tag{13.18}$$

in the RVE. Furthermore, they allow for a periodic deviation u_i^P from the linear boundary displacement which does not affect the average strain.

For being able to compute the effective material properties easily, six deformation modes $\bar{\boldsymbol{\varepsilon}}^{(kl)}$ with only one non-zero component in the effective strain tensor are used. They are given by

$$\bar{\boldsymbol{\varepsilon}}^{(kl)} = \frac{1}{2}\bar{\varepsilon}\left(\delta_{pk}\delta_{ql} + \delta_{pl}\delta_{qk}\right)\mathbf{e}_p \otimes \mathbf{e}_q \tag{13.19}$$

where $\bar{\varepsilon}$ is a scalar defining the magnitude of the non-zero strain component. The resulting deformation modes for linear and periodic displacement boundary conditions are illustrated in Fig. 13.3.

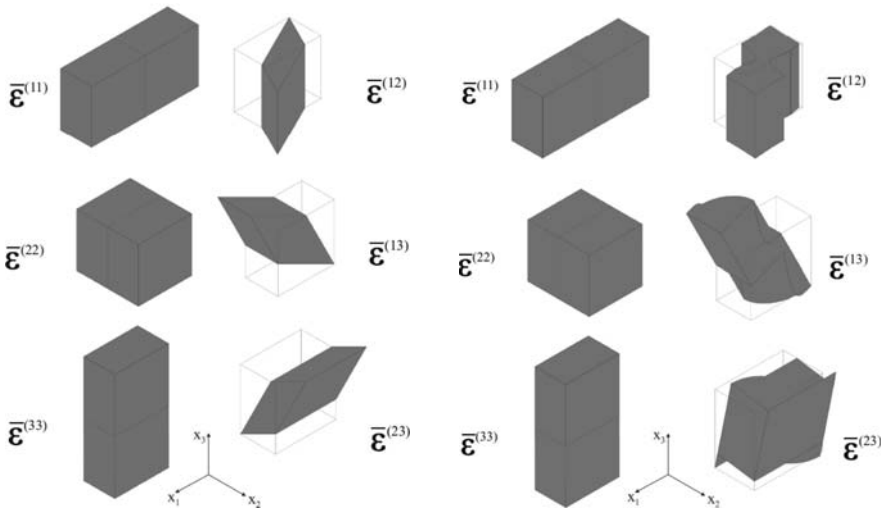

(a) Linear boundary conditions (b) Periodic boundary conditions

Fig. 13.3 Deformation modes resulting from linear and periodic displacement boundary conditions

13.1.1.2 Periodic Boundary Conditions for Symmetric RVE

RVE of textile-reinforced composites often exhibit symmetries that can be employed to improve the efficiency of homogenization techniques. Compared to well-known symmetry boundary conditions in structural analysis the periodicity requirements of the solution have to be taken into account here.

Consider the following rectangular solid RVE with a single symmetry plane at $x_1 = 0$, dimensions $\Delta x_1 = 2x_R$, Δx_2, Δx_3, volume V and surface ∂V. Two mirrored coordinate systems $\hat{x}_i$ and $\tilde{x}_i$ are introduced to formulate the symmetry requirements on displacements and material properties (Fig. 13.4).

Starting from a decomposition of the virtual displacement field into a symmetric ($\delta\mathbf{u}^S$) and an anti-symmetric ($\delta\mathbf{u}^A$) part

$$\delta\mathbf{u} = \delta\mathbf{u}^S + \delta\mathbf{u}^A \quad \text{with} \quad \left.\begin{array}{rl} \delta\tilde{\mathbf{u}}^S(\tilde{x}_m) = & \delta\hat{\mathbf{u}}^S(\hat{x}_m) \\ \delta\tilde{\mathbf{u}}^A(\tilde{x}_m) = & -\delta\hat{\mathbf{u}}^A(\hat{x}_m) \end{array}\right\} \quad \tilde{x}_m = \hat{x}_m \tag{13.20}$$

and assuming a symmetric material structure in the RVE (Fig. 13.4)

$$\tilde{C}_{ijkl}(\tilde{x}_m) = \hat{C}_{ijkl}(\hat{x}_m); \quad \tilde{x}_m = \hat{x}_m \tag{13.21}$$

it can be shown that the virtual work in equilibrium, neglecting all body forces,

$$\delta W = \int_V \sigma_{lm}\delta\varepsilon_{lm}\, dV - \oint_{\partial V} t_m \delta u_m\, dO = 0 \tag{13.22}$$

can be separated into two parts associated with the symmetric (S) und anti-symmetric (A) boundary value problem respectively

$$\delta W = \delta W^S + \delta W^A = 0 \tag{13.23}$$

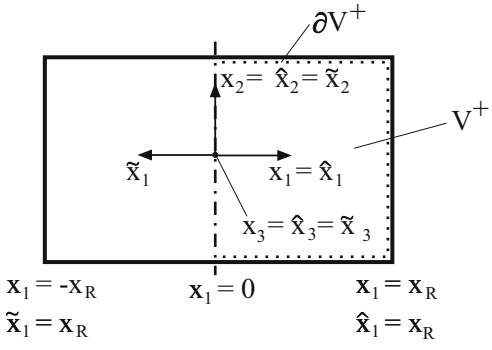

Fig. 13.4 RVE with a single symmetry plane at $x_1 = 0$

Additionally, the calculations show that it is completely sufficient to examine one half of the RVE as

$$\int_V \sigma_{lm}\delta\varepsilon_{lm}\,dV = 2\int_{V^+}\left(\sigma^S_{lm}\delta\varepsilon^S_{lm}+\sigma^A_{lm}\delta\varepsilon^A_{lm}\right)dV \quad \text{and} \tag{13.24}$$

$$\oint_{\partial V} t_m\delta u_m\,dO = 2\int_{\partial V^+}\left(t^S_l\delta u^S_l + t^A_l\delta u^A_l\right)dO \tag{13.25}$$

where V^+ is the part of the RVE between $x_1 = 0$ and $x_1 = x_R$. ∂V^+ is the surface of V^+ excluding the symmetry plane $x_1 = 0$ (Fig. 13.4). After the application of GAUSS' theorem to Eq. (13.24) the local equilibrium and the symmetry boundary conditions at $x_1 = 0$ can be obtained from Eq. (13.23). It has to be mentioned that the boundary conditions depend on whether the deformation mode is symmetric or anti-symmetric with respect to the considered symmetry plane ($i, j = 1\ldots3$; α, $\beta = 2,\ 3$):

- Deformation mode *symmetric* with respect to $x_1 = 0$

$$\sigma^S_{ij,i} = 0 \ \ \forall\, x_i \in V^+ \tag{13.26}$$

$$u^S_1(x_1 = 0, x_\alpha) = 0 \quad \sigma^S_{1\beta}(x_1 = 0, x_\alpha) = 0 \tag{13.27}$$

- Deformation mode *anti-symmetric* with respect to $x_1 = 0$

$$\sigma^A_{ij,i} = 0 \ \ \forall\, x_i \in V^+ \tag{13.28}$$

$$u^A_\beta(x_1 = 0, x_\alpha) = 0 \quad \sigma^A_{11}(x_1 = 0, x_\alpha) = 0 \tag{13.29}$$

By combining the required periodicity of u^P_i resulting from the boundary conditions 13.16

$$u^P_i(-x_R, x_\alpha) = u^P_i(x_R, x_\alpha) \tag{13.30}$$

with the required symmetry or anti-symmetry of the displacement field in the RVE, the following boundary conditons for $x_1 = x_R$ can be derived:

- Deformation mode *symmetric* with respect to $x_1 = 0$

$$u^P_1(x_1 = x_R, x_\alpha) = 0 \tag{13.31}$$

- Deformation-mode *anti-symmetric* with respect to $x_1 = 0$

$$u^P_\beta(x_1 = x_R, x_\alpha) = 0 \tag{13.32}$$

The results for a simply symmetric RVE can be extended to RVE with multiple symmetry planes. Hence, for a RVE symmetric to $x_1 = 0$, $x_2 = 0$ and $x_3 = 0$ it is sufficient to model and to compute only one eighth of the original problem.

13.1.2 Effective Properties

After the application of boundary conditions the deformation modes mentioned above are solved numerically using finite element analysis. Two different approaches to the determination of the required effective material properties of the homogeneous medium will be outlined in brief.

13.1.2.1 Averaging Local Stress Distributions

Considering the applied deformation modes 13.19 it is found that the effective stiffness properties of the homogeneous macroscopic continuum can be computed by

$$\bar{C}_{ijkl} = \frac{1}{\bar{\varepsilon}} \left\{ \sigma_{ij} \left(\bar{\boldsymbol{\varepsilon}}^{kl} \right) \right\} = \frac{1}{\bar{\varepsilon} V} \int_V \sigma_{ij} \left(\bar{\boldsymbol{\varepsilon}}^{kl} \right) dV \tag{13.33}$$

where $\sigma_{ij}\left(\bar{\varepsilon}_{pq}\right)$ are the local stress distributions in the RVE for deformation mode $\bar{\boldsymbol{\varepsilon}}^{(kl)}$. The integration in Eq. (13.33) is done numerically with respect to the used element type and element geometry. Altogether the solution and evaluation of six deformation modes is sufficient for the computation of all 21 independent elements of $\bar{C}_{ijkl}$.

13.1.2.2 Reaction Forces at Master Nodes

Because the evaluation of local stress distributations in the RVE has to be done with respect to the used element type and geometry of every single element, a more efficient procedure using only reaction forces and applied displacements at a set of master nodes has been developed (Fig. 13.5).

The master nodes $M^{x_1^+}$, $M^{x_2^+}$ and $M^{x_3^+}$ are used to apply the displacement boundary conditions described above. The associated reaction forces $\mathbf{F}^{x_1^+}$, $\mathbf{F}^{x_2^+}$, $\mathbf{F}^{x_3^+}$ at the surfaces x_1^+, x_2^+, x_3^+ of the RVE can be used to compute the effective properties without averaging the local stress fields.

After converting the volume average of stress into a surface integral

$$\bar{\sigma}_{ij} = \{\sigma_{ij}\} = \frac{1}{V} \int_V \sigma_{ij} dV = \frac{1}{V} \int_{\partial V} t_j x_i dO \tag{13.34}$$

and the evaluation of Eq. (13.34) assuming a rectangular solid RVE a relation between stress average and reaction forces can be derived and the effective properties are found to be

$$\bar{C}_{ijkl} = \frac{1}{A^{x_i^+} \bar{\varepsilon}} F_j^{x_i^+} \left(\bar{\boldsymbol{\varepsilon}}^{kl} \right) \tag{13.35}$$

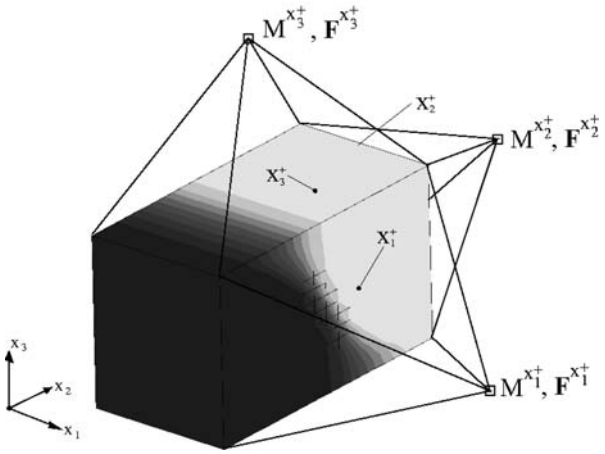

Fig. 13.5 Computation of effective properties from reaction forces

with the areas of the associated surfaces

$$A^{x_1^+} = \Delta x_2 \Delta x_3; \quad A^{x_2^+} = \Delta x_1 \Delta x_3; \quad A^{x_3^+} = \Delta x_1 \Delta x_2 \tag{13.36}$$

whereat Δx_1, Δx_2 and Δx_3 are the dimensions of the RVE.

Hence, the effective properties can be computed independently from element type and geometry which is very efficient and flexible.

13.1.3 Summary

As a summary an outline of the general homogenization procedure is given below.

1. Identification and modelling of RVE
2. Application of suitable boundary conditions to generate characteristic deformation modes
3. Numerical solution to the deformation modes
4. Computation of effective properties from averaging of local field quantities (Eq. (13.33)) or evaluation of reaction forces (Eq. (13.35))

13.2 Application of the eXtended Finite Element Method (X-FEM) to Modelling of Textile-Reinforced Composites

As a result of the complex geometry of the textile reinforcing architecture, generating a finite element (FE) model of the RVE is a particular problem. The application of common FE methods tends to result in an extensive modelling and meshing effort

including problems related to distorted element shapes and poor numerical condition of the system of equations to be solved.

In order to improve flexibility and efficiency of the homogenization technique an alternative modelling strategy is examined. For this purpose X-FEM – whose major benefits such as regular meshes and reduced meshing effort while retaining all advantages of the classical finite element approach have been demonstrated recently [1, 6, 9, 12, 13, 16] – is applied to modelling of composite materials here.

13.2.1 Fundamentals

Based on the partition of unity technique [11] X-FEM offers the possibility to model arbitrary discontinuities using regular finite element meshes that do not need to match interfaces, a fact that is very advantageous in modelling of cracks. Various extensions include enrichment functions for the crack tip [19], the application of higher order elements [15], geometrically nonlinear formulations [3], as well as the simulation of 3D [4, 5, 18] and bi-material cracks [17].

Refering to textile-reinforced composites the indepence of mesh geometry and internal discontinuities implies that element boundaries do not conform to a material interface. Instead, the mechanical behaviour which is characterized by a discontinuity of strain perpendicular to the interface ∂G (Fig. 13.6)

$$\begin{matrix}\left[\tilde{\varepsilon}_{1j}\right] = \left[\tilde{\varepsilon}_{j1}\right] \neq 0 \\ \left[\tilde{\varepsilon}_{\alpha\beta}\right] \quad = 0\end{matrix} \quad i,\ j = 1,2,3; \quad \alpha,\ \beta = 2,3 \tag{13.37}$$

with $\tilde{\varepsilon}_{ij} = c_{ik}c_{jl}\varepsilon_{kl}$; $c_{ij} = \tilde{\mathbf{e}}_i \cdot \mathbf{e}_j$; $\tilde{\mathbf{e}}_1 = \mathbf{n}$; $[a] = a^+ - a^-$ is represented by a *local* enrichment of the FE displacement approximation within the element

$$\mathbf{u}^{\text{X-FEM}} = \underbrace{\sum_i N_i \mathbf{u}_i}_{\text{FEM}} + \underbrace{\sum_{j\in\mathscr{E}} N_j \mathbf{a}_j F}_{\text{Enrichment}} \tag{13.38}$$

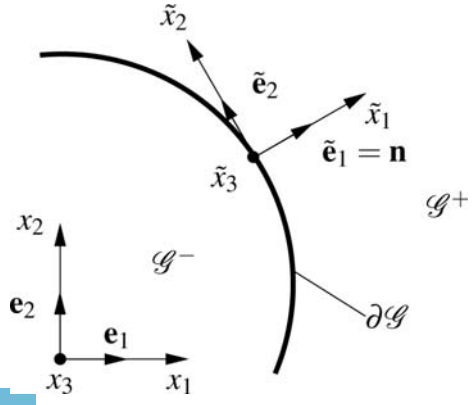

Fig. 13.6 Interface with strain discontinuity

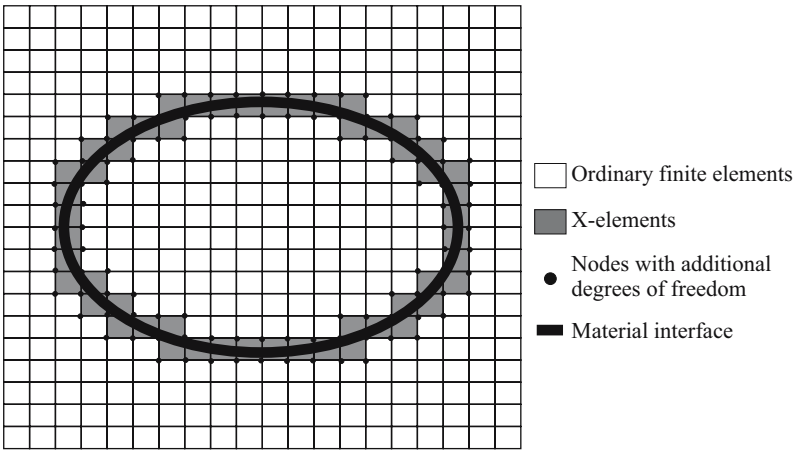

Fig. 13.7 Material interface with X-elements and nodes with additional degrees of freedom

The first summation corresponds to the known approximation of the displacement field $\mathbf{u}$ as product of shape functions N_i and a vector of degrees of freedom $\mathbf{u}_i$ at node i. The enrichment of the original FE approximation consists of additional degrees of freedom $\mathbf{a}_j$ as well as an enrichment function F which accounts for the character of the interface. $\mathscr{E}$ is the set of nodes with additional degrees of freedom. From Fig. 13.7 it can be observed that additional degrees of freedom are only introduced at nodes whose support is intersected by a material interface. A suitable choice of the enrichment function F allows for modelling of strong (discontinuous displacements) and weak (discontinuous strains) discontinuities at an interface [1].

The practical realization of this idea is accomplished by defining a new element type called X-element which replaces the original finite elements intersected by a material interface (compare Fig. 13.7). The implementation is realized using the user-subroutine feature of the commerical FE-code MARC [9]. The user-subroutine defining the element type is called during the assembly of the global stiffness matrix and computes element stiffness matrices for all X-elements in the mesh. In addition, the routine performs stress and strain recovery as well as the determination of element reaction forces which are needed for the computational homogenization procedure (Eq. (13.35)).

13.2.2 Definition of X-elements

Based on the enriched displacement approximation (Eq. (13.38)) an element stiffness matrix has to be derived. Computing this matrix requires a suitable enrichment function as well as an algorithm for locating the material interface within the regular non-conforming finite element mesh.

In order to locate a given interface in the domain of the X-element the signed distance φ_i between the interface and node i is computed whereat the sign of φ_i depends on the position of the node with respect to the interface [16].

The distribution $\varphi(\mathbf{x})$ in the element can be interpolated using the standard shape functions

$$\varphi(\mathbf{x}) = \sum_i N_i \varphi_i \tag{13.39}$$

The position of a material interface Γ is then given by $\varphi(\mathbf{x}) = 0$.

Due to the interpolation which limits the accuracy of the interface approximation the mesh has to be sufficiently refined in order to locate an interface precisely.

The interpolated distance function $\varphi(\mathbf{x})$ is of particular importance for the formulation of enrichment functions. At a material interface a sudden change of coefficients of the partial differential equations occurs. This implicates a discontinuity of strain fields perpendicular to the interface as described in equation (Eq. (13.37)).

Looking at the interpolated values of the distance function $\varphi(\mathbf{x})$ it can be seen that the function itself and its first partial derivatives are continuous over the interface.

Using the absolute value of the interpolation (Eq. (13.39)) is a smart way to introduce the desired discontinuity [16]

$$\tilde{F}(\varphi(\mathbf{x})) = \left| \sum_i N_i \varphi_i \right| \tag{13.40}$$

On the other hand the influence of the enrichment function $\tilde{F}$ is not limited to the region of a single element which is unfavorable for the definition of a special X-element that is to be used together with standard elements in the same mesh. In this case an enrichment function that is zero at element boundaries connected to standard elements is desired. As suggested in [12] this can be ensured by choosing the enrichment function

$$F(\varphi(\mathbf{x})) = \sum_i N_i |\varphi_i| - \left| \sum_i N_i \varphi_i \right| \tag{13.41}$$

which is plotted for a straight interface intersecting a 2D plane element in Fig. 13.8.

After all essential data such as material properties, the location of the interface in each element defined by the distance function values φ_i at nodes, etc. are obtained during pre-processing, the integration of the element stiffness matrix

$$\mathbf{K}^e = \int_{\Omega^e} \mathbf{B}^T \mathbf{D} \mathbf{B} \, d\Omega^e \tag{13.42}$$

is performed where $\mathbf{D}$ is a matrix representation of C_{ijkl}.

Due to the enrichment the matrix $\mathbf{B}$ contains partial derivatives of the enrichment function which are discontinuous over the interface as well as different material properties. In order to handle the discontinuous integrand, the element domain Ω^e is

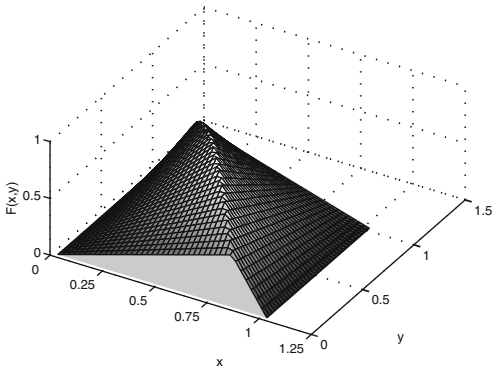

Fig. 13.8 Plot of the enrichment function $F(\varphi(\mathbf{x}))$ over a 2D plane element domain

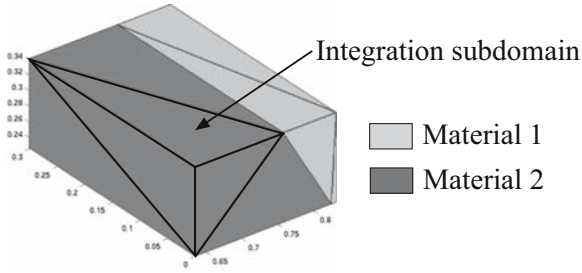

Fig. 13.9 Integration subdomains

divided into n_s integration subdomains Ω_i^s applying DELAUNAY hex-tet subdivision in three dimensions

$$\int d\Omega^e \;\Rightarrow\; \sum_{i=1}^{n_s} \int d\Omega_i^s \tag{13.43}$$

as shown in Fig. 13.9.

After the decomposition each subdomain is assigned with the right material properties and the integration of the element stiffness matrix is carried out using standard GAUSS quadrature rules. Finally, the element stiffness matrix is passed into the commerical FE-code where the global stiffness matrix is assembled.

When modelling textile-reinforced composites – mainly due to the combination of high fibre volume fractions and complex reinforcing architectures – the problem of branching material interfaces is observed. As shown in Fig. 13.10a the material interface between warp and weft yarn opens into two yarn-matrix interfaces.

Therefore, a second new element type called 2X-element is introduced which can handle two branching material interfaces in a single element domain. Numerically the case of two material interfaces in a single element is treated by introducing another set of additional degrees of freedom $\mathbf{b}_i$ at nodes whose support is cut by both interfaces leading to a further enrichment of the displacement approximation

$$\mathbf{u}^{\text{X-FEM}} = \sum_i N_i \mathbf{u}_i + \sum_j N_j \mathbf{a}_j F_1(\varphi_1(\mathbf{x})) + \sum_k N_k \mathbf{b}_k F_2(\varphi_2(\mathbf{x})). \tag{13.44}$$

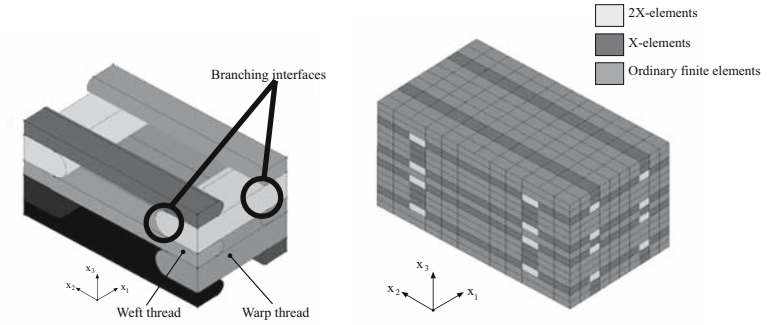

(a) Geometry model of reinforcement with branching interfaces

(b) X-FEM mesh with 2X-elements

Fig. 13.10 Modelling branching interfaces

This is a consistent extension to Eq. (13.38) and therefore the same procedures as for X-elements with a single interface can be applied. The particular enrichment functions F_1 and F_2 correspond to Eq. (13.41) but they now depend on two different distance functions – one for each interface

$$F_1 = F_1\left(\varphi_1\left(\mathbf{x}\right)\right) \quad \text{and} \quad F_2 = F_2\left(\varphi_2\left(\mathbf{x}\right)\right). \tag{13.45}$$

This approach is similar to techniques proposed for branching and intersecting cracks [1, 2]. During the assembly of the global stiffness matrix one has to deal with a different number of degrees of freedom at a single node. If both, X- and 2X-elements, are present in the mesh, this problem is handled by constraint equations to ensure the continuity of the displacement approximation. They are applied during an automated model generation procedure which is briefly outlined in the following.

13.2.3 Automated Model Generation

In order to allow for an efficient simulation strategy for textile-reinforced composites the modelling process has to be automated to large extent. For that purpose a modelling procedure has been developed that automatically converts the geometry of the reinforcing structure into a X-FEM mesh of the RVE. Starting from a 3D geometric model a rectangular solid RVE domain is filled with finite elements layer by layer (Fig. 13.11). Depending on the number of interfaces in the generated elements they become ordinary finite elements, X-elements or 2X-elements. Details of the procedure can be found in [6].

In addition to the element formulation, routines that accomplish the automatic detection and location of material interfaces, perform the element subdivision, assign material properties, determine the orientation of anisotropic material

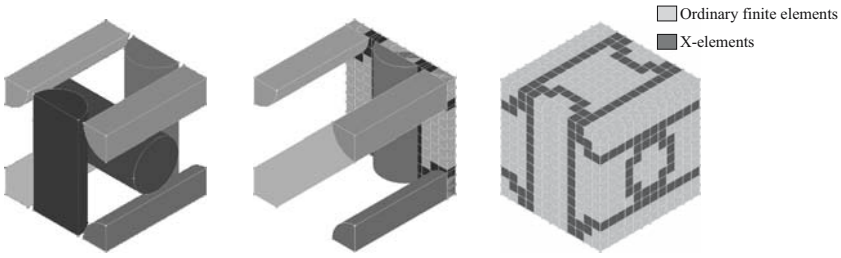

(a) 3D geometry (b) Model generation (c) X-FEM RVE-model

Fig. 13.11 Generation of numerical X-FEM RVE-model in layers

Table 13.1 Material properties of glass fibre (GF) and polypropelene (PP) matrix

Material	E[GPa]	ν[−]
GF	73	0.25
PP	1.22	0.4

properties in the integration subdomain and compute the values of the enrichment function at each integration point are required.

The particular challenge of these automatic procedures is to cover all possible geometric configurations of material interfaces in the RVE, to assign additional degrees of freedom to the correct interfaces as well as to accurately assemble the global stiffness matrix.

13.3 Effective Material Properties of GF-PP Woven Fabric

As illustrated in Fig. 13.1 the considered composites feature a hierarchical material structure with three different length scales. In order to find effective macroscopic material properties two homogenization steps are performed. While in the first step – the micro-meso homogenization – the effective stiffness of the yarn is determined, the meso-macro homogenization in step two provides the effective macroscopic stiffness. The necessary input data consist of the material properties of glass fibre (GF) and polypropelene (PP) matrix listed in Table 13.1 as well as two idealized geometry models for yarn and reinforcing architecture which are derived from polished micrograph sections.

13.3.1 Effective Yarn Properties

As stated above, the assumption of a homogeneous yarn forming the texile reinforcing structure on the meso-scale is an idealization. Especially for composites

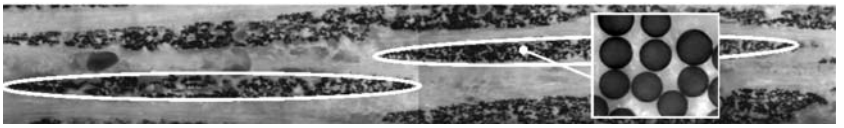

Fig. 13.12 Identification of yarn cross-sections in a micrograph of a GF-PP woven fabric (meso-scale) and fibre arrangement (micro-scale)

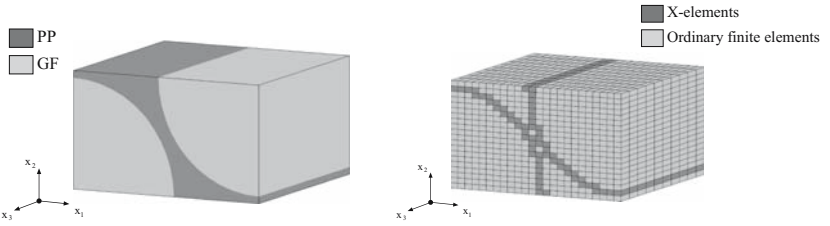

(a) Numerical model using symmetry boundary conditions

(b) X-FEM mesh

Fig. 13.13 Idealized fibre arrangement and numerical model for micro-meso homogenization

Table 13.2 Nonzero coordinates of $\bar{C}^{\text{yarn}}_{ijkl}$[GPa] (fibre volume fraction $v_F^{\text{yarn}} = 0.8$)

Stiffness [GPa]	$\bar{C}_{1111}$	$\bar{C}_{2222}$	$\bar{C}_{3333}$	$\bar{C}_{1122}$	$\bar{C}_{1133}$	$\bar{C}_{2233}$	$\bar{C}_{2323}$	$\bar{C}_{1313}$	$\bar{C}_{1212}$
FEM	15.82	15.82	61.85	6.43	6.12	6.12	3.72	3.72	4.70
X-FEM	15.82	15.82	61.85	6.52	6.12	6.12	3.80	3.80	4.70

consolidated from commingled glass-thermoplastic hybrid yarns no pure fibre domains can be identified. Instead the mesoscopic yarn represents a fibre-matrix mixture with a considerably high fibre volume fraction (Fig. 13.12).

Using the idealization of a hexagonal array with equally spaced fibres on the micro-scale effective meso-scale properties have to be computed for the yarn, resulting in a transversly isotropic material behaviour. Modelling of the fibre array is performed applying X-FEM and symmetry boundary conditions during the homogenization process (Fig. 13.13).

The results of the micro-meso homogenization are listed in Table 13.2. The comparison to a conventional FE model demonstrates a very good agreement of both modelling approaches.

13.3.2 Effective Properties of Plain Weave Fabric

The geometric model of the woven reinforcement is deduced from different micrographs. The mathematical description of cross-section as well as the arrangement of yarns in the RVE is defined by trigonometric functions. In order to form a solid

RVE, the textile reinforcement illustrated in Fig. 13.14 is enclosed in a cubic matrix box resulting in an overall volume fraction of $v_F = 0.35$ and a lamina thickness of 0.34 mm.

Based on the given geometry, an X-FEM model is created using the automatic modelling strategy. In this process special attention has to be drawn to the orientation of the material prefered direction which is determined from the geometry model for each element containing a yarn fraction. Figure 13.15 shows the resulting mesh with ordinary finite elements, X- and 2X-elements.

Due to the application of symmetry boundary conditions only one quater of the original RVE has to be modelled. Table 13.3 presents a comparison of the numerically determined effective stiffness properties to those obtained from ultrasonic measurements [8].

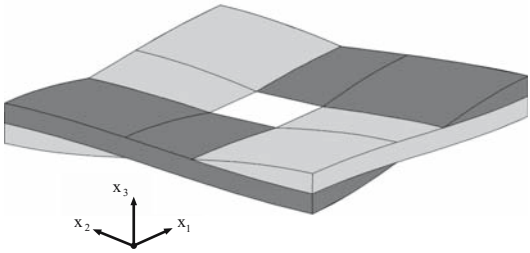

Fig. 13.14 Idealized geometry model of a woven fabric with branching interfaces

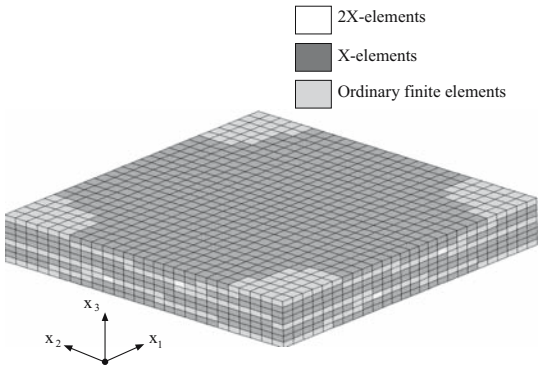

Fig. 13.15 X-FEM RVE model for woven fabric

Table 13.3 Comparison of effective stiffness properties $\bar{C}_{ijkl}$ for a woven GF-PP composite obtained from homogenization and ultrasonic tests (unlisted $\bar{C}_{ijkl} = 0$)

Stiffness [GPa]	$\bar{C}_{1111}$	$\bar{C}_{2222}$	$\bar{C}_{3333}$	$\bar{C}_{1122}$	$\bar{C}_{1133}$	$\bar{C}_{2233}$	$\bar{C}_{2323}$	$\bar{C}_{1313}$	$\bar{C}_{1212}$
Homogenization	15.8	15.8	4.5	2.9	2.4	2.4	0.8	0.8	1.5
Ultrasonic test	15.5	15.5	9.0	–[a]	3.7	4.0	2.6	2.6	–[a]

[a] Stiffness property incapable of measurement

Table 13.4 Comparison of engineering constants computed from numerical and experimental effective stiffness properties $\bar{C}_{ijkl}$ with results from standard tensile tests

Property	$\bar{E}_{11}$[GPa]	$\bar{G}_{12}$[GPa]	$\bar{\nu}_{12}$[-]
Homogenization	14.37	1.50	0.11
Ultrasonic test	13.45[a]	–[b]	0.38[a]
Tensile test	13.05	1.11	0.09

[a] Results for assumed stiffness property value $\bar{C}_{1122} = 4.0$ GPa
[b] Arbitrary as $\bar{G}_{12} = \bar{C}_{1212}$

13.3.3 Experimental Verification

The comparison of numerically determined effective stiffness properties to those measured by ultrasonic tests in Table 13.3 demonstrates a very good agreement of the tensile stiffness $\bar{C}_{1111}$ and $\bar{C}_{2222}$.

On the other hand a quite significant difference is observed for the transverse and shear properties which are subject to further investigation on the influence of scatter in the input data as well as the geometric assumptions made.

In addition, the effective stiffness properties obtained from homogenization and ultrasonic testing have been converted into the well-known engineering constants. In order to be able to invert the stiffness matrix a reasonable estimate for $\bar{C}_{1122}$ in Table 13.3 has been made. The properties characterizing the in-plane material behaviour are given in Table 13.4. They are compared to results from tensile testing. This comparison reveals a general correlation between experimental and numerical results. On the other hand a fairly large deviation of the two experimental testing methods can be observed.

13.4 Conclusion

In this work an efficient modelling strategy for textile-reinforced composites has been proposed. A computational homogenization technique based on the equivalence of strain energy in a locally heterogeneous material and an effective homogeneous medium is applied. In addtion an X-FEM approach to handle the complexity of textile reinforcement is developed, resulting in an algorithm for automated modelling of RVE based on a 3D geometric model.

As it was demonstrated in the previous section, the main advantage of simulation over experimental tests is that all stiffness properties required for a structural analysis can be quantified more efficiently. In contrast to procedures that identify parameters of an assumed constitutive relation from experiments the material behaviour is predicted using geometrical and physical characteristics of two different length scales.

In order to improve the flexibility of the approach it has to be extended to more complex weft-knitted fabrics. Furthermore, the combination of X-FEM and non-linear material behaviour will be adressed in the future.

Acknowledgements Financial support for this research project from the German Research Fundation (DFG) in the framework of the Collaborative Research Centre (SFB) 639 is gratefully acknowledged. Additionally, the authors thank the Institute of Lightweight Construction and Polymer Technology (ILK) at TU Dresden for providing experimental data obtained from ultrasonic and tensile tests.

References

1. Belytschko T, Moës N, Usui S, Parimi C (2001) Arbitrary discontinuities in finite elements. Int J Numer Meth Eng 50:993–1013
2. Daux C, Moës N, Dolbow J et al (2000) Arbitrary branched and intersecting cracks with the extended finite element method. Int J Numer Meth Eng 48:1741–1760
3. Fagerström M, Larsson R (2006) Theory and numerics for finite deformation fracture modelling using strong discontinuities. Int J Numer Meth Eng 66:911–948
4. Gravouil A, Moës N, Belytschko T (2002) Non-planar 3D crack growth by the extended finite element and level sets – Part I: mechanical model. Int J Numer Meth Eng 53:2549–2568
5. Gravouil A, Moës N, Belytschko T (2002) Non-planar 3D crack growth by the extended finite element and level sets – Part II: level set update. Int J Numer Meth Eng 53:2569–2586
6. Haasemann G, Kästner M, Ulbricht V (2006) Multi-Scale modelling and simulation of textile-reinforced materials. CMC 3:131–146
7. Hill R (1963) Elastic properties of reinforced solids: some theoretical principles. J Mech Phys Solids 11:357–372
8. Hufenbach W, Böhm R, Langkamp A, Kroll L, Ritschel T (2006) Ultrasonic evaluation of anisotropic damage in textile multi-axial reinforced thermoplastic composites made from hybrid yarns. Mech Compos Mater 42:221–234
9. Kästner M, Ulbricht V (2006) Homogenization of fibre-reinforced composites using X-FEM. Proc Appl Math Mech 6:489–490
10. Lukkassen D, Persson LE, Wall P (1995) Some engineering and mathematical aspects on the homogenization method. Compos Eng 5:519–531
11. Melenk JM, Babuška I (1996) The partition of unity finite element method: basic theory and applications. Research Report
12. Moës N, Cloirec M, Cartraud P, Remacle J (2003) A computational approach to handle complex microstructure geometries. Comput Methods Appl Mech Eng 192:3163–3177
13. Moës N, Dolbow J, Belytschko T (1999) A finite element method for crack growth without remeshing. Int J Numer Meth Eng 46:131–150
14. Sanchez-Palencia E, Zaoui E (1987) Homogenization techniques for composite media. Lecture Notes in Physics 272. Springer, Berlin
15. Stazi L, Budyn E, Chessa J, Belytschko T (2003) An extended finite element method with higher-order elements for curved cracks. Comput Mech 31:38–48
16. Sukumar N, Chopp D, Moës N, Belytschko T (2001) Modeling holes and inclusions by level sets in the extended finite element method. Comput Methods Appl Mech Eng 190:6183–6200
17. Sukumar N, Huang ZY, Prévost J, Suo Z (2004) Partition of unity enrichment for bimaterial interface cracks. Int J Numer Meth Eng 59:1075–1102
18. Sukumar N, Moës N, Moran B, Belytschko T (2000) Extended finite element method for three-dimensional crack modelling. Int J Numer Meth Eng 48:1549–1570
19. Zi G, Belytschko T (2003) New crack-tip elements for XFEM and applications to cohesive cracks. Int J Numer Meth Eng 57:2221–2240

Chapter 14
Development of Domain Superposition Technique for the Modelling of Woven Fabric Composites

Wen-Guang Jiang, Stephen R. Hallett, and Michael R. Wisnom

Abstract A Domain Superposition Technique (DST) is proposed for the simulation of woven fabric composites. Instead of modelling the tows and the likely degenerated resin pocket regions among tows explicitly, DST separately models the tow domain and the global domain which are both non-degenerated, and can thus be easily discretised using the traditional solid elements. During the solution process, the two domains are superimposed by coupling them together to produce the exact results. Numerical simulation shows that the results of DST correlate very well with the results of conventional finite element analysis.

14.1 Introduction

Woven fabric composites (WFC) present various attractive aspects such as light weight, low fabrication costs, ease of handing and high adaptability when compared to tape laminates and more traditional engineering materials. With these cost and performance advantages, WFC have received increased attention and popularity in many structural applications in recent years.

Literature reviews [2, 8] show that finite element (FE) and theoretical analysis methods are powerful tools for studying the mechanical properties of WFC. The micro-structure is, however, complex in nature and the parameters controlling the mechanical properties are numerous. Various finite element techniques and assumptions have been proposed for simplifying the analysis. Most of the models for WFCs are based on the definition of a unit cell geometry and include the major architectural

W.-G. Jiang, S.R. Hallett, and M.R. Wisnom
Advanced Composites Centre for Innovation & Sciences, Queens Building, University of Bristol, Bristol, BS8 1TR, United Kingdom, e-mail: {stephen.hallett,m.wisnom}@bristol.ac.uk

W.-G. Jiang (currently at)
Department of Engineering, University of Leicester, Leicester LE1 7RH, United Kingdom, e-mail: wgj1@leicester.ac.uk

parameters in predicting the mechanical properties. One of the fundamental difficulties faced in modelling the detailed unit cell using solid elements is to build a geometry free from interpenetration at tow crossovers. Furthermore, a very fine FE mesh is required to deal with some "not-quite-relevant" details, i.e. the degenerated volumes of the resin pockets. This can lead to very large FE models exceeding a million of degrees of freedom to model a single unit cell, which is only a very small part of the WFC structure. Cox et al. [1, 7, 9, 10] developed a FE method, known as the 'binary model', for simulating woven textile composites. In this model, the axial properties of tows were represented by two-noded line elements possessing axial rigidity, while the transverse stiffness, shear stiffness, and Poisson's effect of the composite were represented by 8-node solid 'effective medium' elements. Due to the simplified assumptions, a complex parameter calibration is needed to yield good correlation which could still be mesh size dependent. Another significant simplification is that the detailed tow geometric features are omitted, making the actual stress calculation process quite complex.

In this paper a Domain Superposition Technique (DST) proposed by the first author [5] is presented. Instead of modelling the tows and the likely degenerated resin pockets explicitly, DST meshes the tow domain and the global domain separately, which are both non-degenerated. Both domains are modelled using solid elements and the final result is simply the superposition of the two domains using coupling equations. In contrast to other mesh superposition methods which require iterative procedures [3, 4, 11], DST is conceptually concise and much simpler to implement.

14.2 Domain Superposition Technique

A typical DST FE mesh for a representative volume element (RVE) is shown in Fig. 14.1. The implementation of DST requires two essential technical strategies. The first is the derivation of the correct material property configurations of the two domains; the second is the establishment of the coupling relationships between the two domains. For the material models, the actual matrix material properties are used for the elements of the global domain and the elements in the tow domains use a modified mechanical model, i.e. the constitutive stiffness matrix is based on the difference between the actual tow material and that of the matrix material. The independent tow FE meshes need to be coupled onto the global FE mesh and this is implemented by a constraint equation coupling technique. This ensures that the two phases of the superimposed materials in the tow space have the equivalent mechanical properties of the actual tows; the remaining matrix material domain has the unchanged matrix material properties. Compared with the traditional FE models of WFC, the DST has the following advantages:

- Every tow may be independently discretised using the traditional eight-noded solid element geometry by simply dragging a cross-sectional area pattern along the centre line of the tow. Each element has edges parallel to the centre line of the tow which can be conveniently used for material orientation.

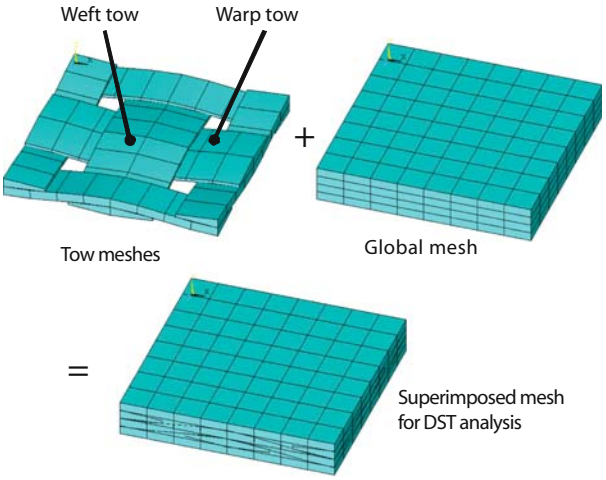

Fig. 14.1 An example of DST meshes for a RVE of a plain weave composite

- The global space can be easily meshed using solid elements without the need to consider the very complex material distributions within the domain.
- The actual matrix material space is not modeled explicitly, in contrast to the traditional FE analysis, which requires significant computational resources to handle this.
- Defects in the geometric model, e.g. the difficult-to-avoid interpenetrations at tow crossovers from the creation of the geometric models, can be tolerated in DST.
- Model size can be reduced.

14.2.1 Coupling Technique

The first essential numerical technique related to the implementation of DST is the coupling of the global matrix FE mesh with the reinforcement tow mesh to ensure that the coincident points between the two phases of materials can have the same displacement during deformation [5]. This is the continuity/compatibility condition of DST, which must be correctly dealt with in order to establish an accurate numerical model.

Considering a general three-dimensional solid element, the coordinate interpolations of a given point (x, y, z) inside the element are

$$x = \sum_{i=1}^{m} N_i x_i; \qquad y = \sum_{i=1}^{m} N_i y_i; \qquad z = \sum_{i=1}^{m} N_i z_i \tag{14.1}$$

where x_i, y_i, z_i are the coordinates of the m element nodes in global Cartesian coordinate system. The interpolation functions $N_i(\xi, \eta, \zeta)$ are defined in the natural

coordinate system of the element, which has variables ξ, η, ζ that each vary from -1 to $+1$. The fundamental property of the interpolation function N_i is that its value in the natural coordinate system is unity at node i and zero at all other nodes.

To enhance the continuity between the two material domains, it is preferable that the same element formulation be used for both domains. In this paper, conventional eight-noded three-dimensional linear isoparametric solid brick elements are used for the structural discretisation to establish the DST model.

An important advantage of using isoparametric elements is that in the isoparametric formulation, the displacements are interpolated in the same way as the geometry; i.e.

$$u = \sum_{i=1}^{m} N_i u_i; \qquad v = \sum_{i=1}^{m} N_i v_i; \qquad w = \sum_{i=1}^{m} N_i w_i \tag{14.2}$$

where u_i, v_i, w_i are the displacement components of the m element nodes.

To establish the coupling relationship between the two sets of FE meshes for DST, for each node of the tow meshes, $n(x,y,z)$, we need to first find the specific global solid element inside which the tow node is located, and determine the local coordinates (ξ, η, ζ) of this tow nodal location within this global solid element by Eq. (14.1), and then the coupling equations to be established for this tow node will be in the form of the displacement interpolation functions, i.e. Eq. (14.2).

14.2.2 Material Models

Through the implementation of the coupling technique discussed above, the independent tow FE meshes can be coupled into the global FE mesh. As all the elements in the global mesh use the actual matrix material properties, to ensure that the two phases of the superimposed materials in the tow space have the equivalent mechanical properties of the actual tows, the "material properties" used in the tow elements should be adjusted to reflect this scenario [5].

An isotropic elastic material model is used for the matrix material which forms the global domain in DST. The stress-strain matrix in three dimensions is given by

$$[\mathbf{D}]_{matrix} = \frac{E(1-\nu)}{(1+\nu)(1-2\nu)} \begin{bmatrix} 1 & \frac{\nu}{1-\nu} & \frac{\nu}{1-\nu} & 0 & 0 & 0 \\ \frac{\nu}{1-\nu} & 1 & \frac{\nu}{1-\nu} & 0 & 0 & 0 \\ \frac{\nu}{1-\nu} & \frac{\nu}{1-\nu} & 1 & 0 & 0 & 0 \\ 0 & 0 & 0 & \frac{1-2\nu}{2(1-\nu)} & 0 & 0 \\ 0 & 0 & 0 & 0 & \frac{1-2\nu}{2(1-\nu)} & 0 \\ 0 & 0 & 0 & 0 & 0 & \frac{1-2\nu}{2(1-\nu)} \end{bmatrix} \tag{14.3}$$

where E and ν are the elastic modulus and Poisson ratio of the matrix material.

For the actual tows, an orthotropic elastic model is used, and its stress-strain matrix in three dimensions is given by

$$[\mathbf{D}]_{tow} = \begin{bmatrix} \frac{1}{E_1} & \frac{-\nu_{21}}{E_2} & \frac{\nu_{31}}{E_3} & 0 & 0 & 0 \\ \frac{-\nu_{12}}{E_1} & \frac{1}{E_2} & \frac{-\nu_{32}}{E_3} & 0 & 0 & 0 \\ \frac{-\nu_{13}}{E_1} & \frac{-\nu_{23}}{E_2} & \frac{1}{E_3} & 0 & 0 & 0 \\ 0 & 0 & 0 & \frac{1}{G_{12}} & 0 & 0 \\ 0 & 0 & 0 & 0 & \frac{1}{G_{23}} & 0 \\ 0 & 0 & 0 & 0 & 0 & \frac{1}{G_{13}} \end{bmatrix}^{-1} \tag{14.4}$$

where E_1, E_2, E_3 are elastic moduli; ν_{12}, ν_{13}, etc. are Poisson ratios; and G_{12}, G_{13}, G_{23} are elastic shear moduli.

The constitutive stress-strain matrix used for the tow element in DST analysis is based on the difference between that of the actual tow material and the matrix material, i.e.

$$[\mathbf{D}]_{modeled\ tow} = [\mathbf{D}]_{tow} - [\mathbf{D}]_{matrix} \tag{14.5}$$

14.3 Numerical Analysis Results

To fully understand and validate the domain superposition technique, both DST and traditional analyses were performed on a plain weave composite plate structure. A commercial finite element analysis program (ANSYS) was used. The geometry of the representative volume element (RVE) analyzed is given in Fig. 14.2. The warp tows and the weft tows should touch at tow crossovers for a realistic composite material, i.e. $a = 0$. For the sake of easy generation of the conventional FE meshes, it is common practice to create an arbitrarily small resin gap between the crossing tows in the geometric model. For example, the dimension $a = t/10$ is used in this paper (Fig. 14.4). For all the analyses performed, an average unit tension load is applied in the warp direction on the two ends of the RVE as shown in Fig. 14.2. Periodic boundary conditions are implemented in the loading direction [6]. Eight noded brick elements are used throughout for the structural discretisation in the DST models. The material elastic constants used for the numerical analysis are $E = 3.5$ GPa and $\nu = 0.35$ for the matrix material, and $E_1 = 138$ GPa, $E_2 = E_3 = 9$ GPa, $\nu_{12} = \nu_{13} = \nu_{23} = 0.3$ and $G_{12} = G_{13} = G_{23} = 6.9$ GPa for the tow material. The numerical analysis results are discussed in detail in Sects. 14.3.1–14.3.1.2.

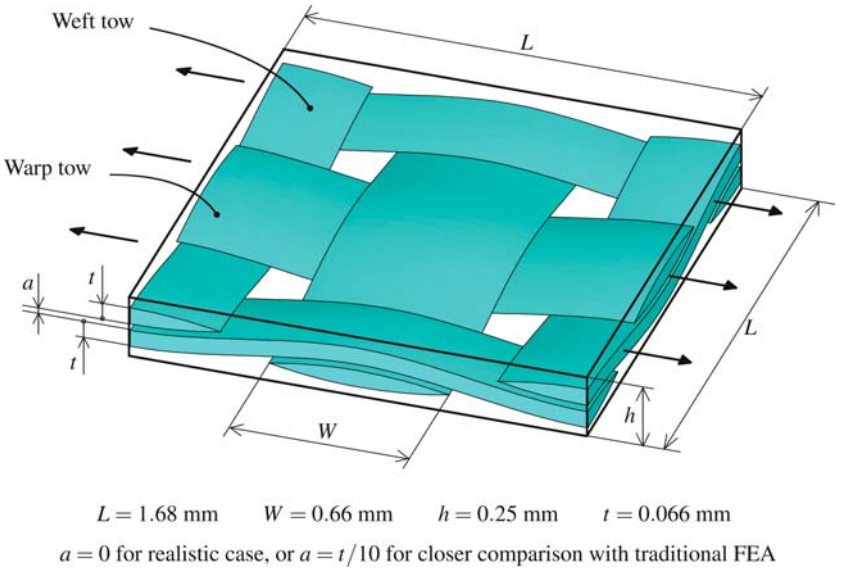

Fig. 14.2 Geometric parameters for a RVE of a plain weave composite

14.3.1 Convergence Study of DST

Although the technique of embedding two-noded beams into solid elements such as the "binary model" [1, 7, 9, 10] has the benefit of substantially smaller model size, these models are mesh size dependent. That is to say, when the FE mesh is refined further, the results will change continuously rather than converge to the real state as the modelled structure should behave. In contrast, DST is mesh density objective, i.e. the simulation results will converge if the meshes are fine enough. To understand the performance of DST, a mesh sensitivity study has been performed. In order to simulate a more realistic woven geometry, the gap size at the crossing tows in the model used for the analysis is set to zero ($a = 0$). It would be extremely difficult to build a proper FE mesh for this special case with touching tows at the crossover. However this is no longer an issue for DST analysis.

14.3.1.1 Mesh Refining Scheme 1

In the first mesh refining scheme, both global and tow meshes are re-fined simultaneously. Typical DST finite element meshes used for the mesh effect study are depicted in Fig. 14.3. The analysis results are given in Table 14.1. As desired, it can be seen from this table that both stiffness and stress converge as the FE meshes are refined.

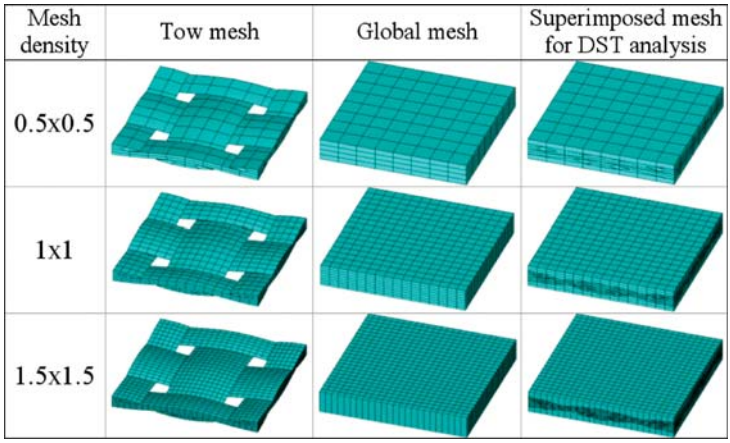

Fig. 14.3 DST finite element meshes (mesh refining scheme 1: refining both global and tow meshes simultaneously, the gap size between crossing tows is $a = 0$)

Table 14.1 Convergence study of DST (mesh refining scheme 1: refining both global and tow meshes simultaneously, the gap size between crossing tows is $a = 0$)

Mesh Density	Tow mesh		Global mesh		Tensile modulus (GPa)	Normalized maximum stress in tow
(Global) × (Tow)	N° of node	N° of element	N° of node	N° of element		
0.5 × 0.5	450	192	405	256	19.31	8.20
1 × 1	2,480	1,536	2,048	5,387	19.80	7.82
1.5 × 1.5	7,184	5,184	6,912	15,959	19.83	7.80
2 × 2	15,736	12,288	16,384	35,371	19.84	7.80

14.3.1.2 Mesh Refining Scheme 2

To study the effects of relative mesh density, in the second mesh refining scheme, we keep the global mesh the same (of course, this mesh should be fine enough), and only refine the tow meshes. The analysis results are given in Table 14.2. Once again we can see that both stiffness and stress converge as the tow finite element meshes are refined. This means that DST is not sensitive to the relative mesh refinement between the global and the tow meshes. As long as the global and tow meshes are both fine enough, the analysis results will converge. As a simple guideline for establishing the DST model, the tow element size used should be comparable or smaller than that of the global mesh.

Table 14.2 Convergence study of DST (mesh refining scheme 2: global mesh re-mains the same, only tow meshes refined, the gap size between crossing tows is $a = 0$)

Mesh Density	Tow mesh		Global mesh		Tensile modulus (GPa)	Normalized maximum stress in tow
(Global) × (Tow)	N° of node	N° of element	N° of node	N° of element		
1 × 0.5	450	192	2,048	5,387	19.64	8.08
1 × 1	2,480	1,536	2,048	5,387	19.80	7.82
1 × 1.5	7,184	5,184	2,084	5,387	19.83	7.80
1 × 2	15,736	12,288	2,084	5,387	19.84	7.80

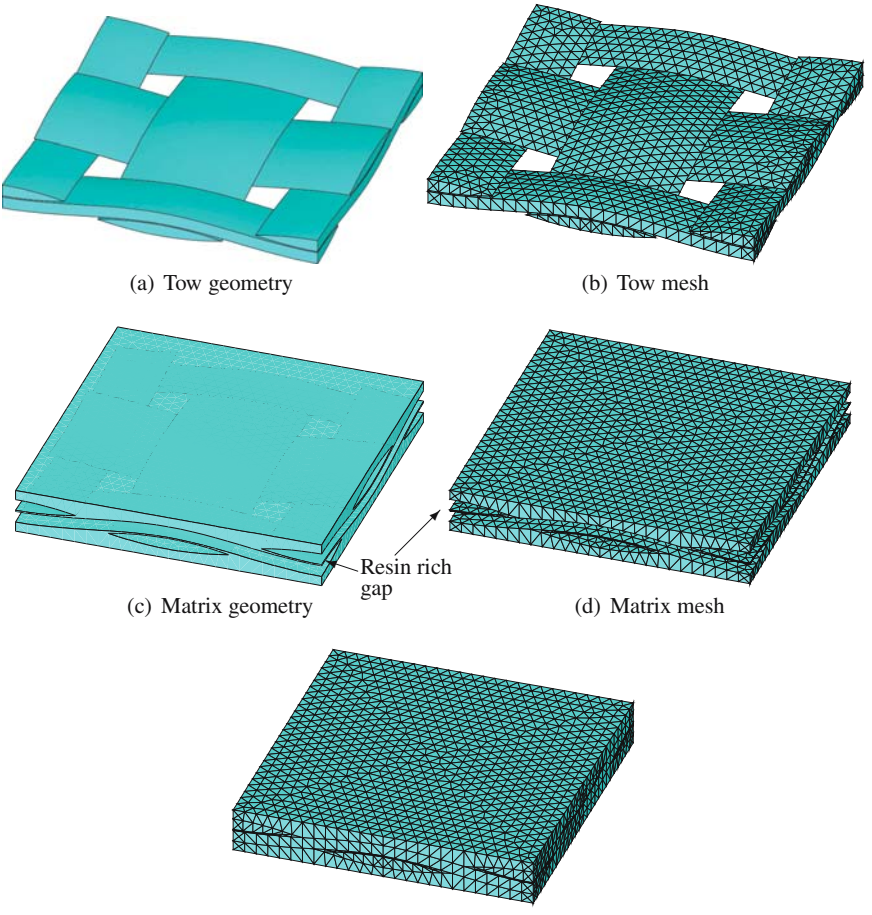

Fig. 14.4 Unit cell geometry showing the resin rich gap between crossing tows $a = t/10$ and traditional finite element meshes using 10-noded tetrahedral elements

14.3.2 Comparison Between DST and Conventional FE Analysis

To further validate the domain superposition technique, both DST and traditional FE analyses were performed based on a RVE geometry with a finite gap size of $a = t/10$ to allow the standard FE model to be easily established (Fig. 14.4). DST can easily use brick elements to discretise the woven composite geometry, whilst tetrahedral elements have to be used to allow the commercial FE analysis program to build a conventional FE mesh. Selected contour plots of the analysis results under unit tension load are compared in detail in Fig. 14.5 for the two methods. The FE mesh information for the two approaches and the results predicted are compared in Table 14.3. It can be seen that both stiffness and local stress predicted from DST correlate extremely well with those from the traditional FE analysis. It is also worth noting that even using a very coarse mesh (855 nodes, see Table 14.3), DST still predicts reasonable results (only 1.8% error in stiffness, 3.7% error in stress) compared with a traditional FE analysis (15,766 nodes). The number of nodes used in the DST is as little as 5% of the traditional FE analysis.

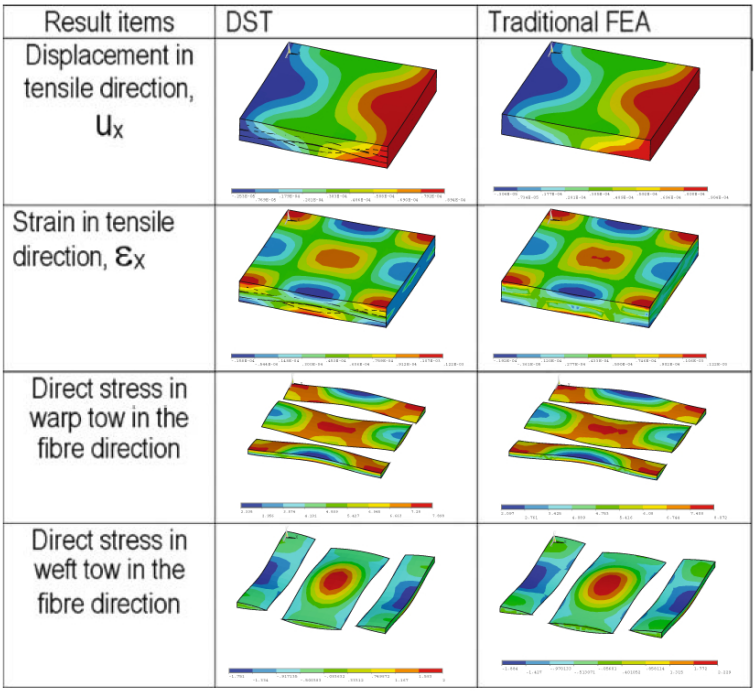

Fig. 14.5 Comparison of results between DST and traditional FEA (same geometry is used for both methods)

Table 14.3 Comparison between DST and conventional FEA (the gap size between crossing tows is $a = t/10$ to allow conventional FEA to work)

Model type	Element type used	Mesh density (global) × (tow)	N° of node	N° of elements	Tensile modulus (GPa)	Normalized maximum stress in tow
DST	8-noded brick	0.5×0.5	855	448	18.87	8.3
DST	8-noded brick	1×1	4,528	6,923	19.29	7.9
Conventional FEA	10-noded Tetrahedral	–	15,766	23,430	19.21	8.0

14.4 Conclusions

A novel domain superposition technique (DST) has been proposed to analyze complex woven fabric composites. DST can avoid explicitly modelling the degenerated volumes of resin rich regions between crossing tows and thus ease the requirement of high quality geometric models. A mesh density effect study on the newly proposed DST has been performed, and the numerical analyses show that the DST analysis converges when the FE mesh is refined just as the traditional FE analysis does. DST compares well with traditional FE analysis in terms of global stiffness and stress distribution. It is easier to set up than conventional FE models and the required model size to generate accurate results can be significantly smaller.

Acknowledgements This work has been funded under the DTI Technology Programme (Project No. TP/3/dsm/6/1/16666): Simulation and Modelling of 3D Woven Fabrics for Structural Composites (3D SIMCOMS), project partners: Rolls-Royce Plc, Advanced Composites Group, BAE Systems, Deep Sea Engineering, Dowty Propellers, Sigmatex, University of Bristol, University of Nottingham, and University of Ulster.

References

1. Cox BN, Carter WC, Fleck NA (1994) A binary model of textile composites-I Formulation. Acta Metall Mater 42:3463–3479
2. Crookston JJ, Long AC, Jones IA (2005) A summary review of mechanical properties prediction methods for textile reinforced polymer composites. Proc IMechE, Part L: J Mater: Des Appl 219:91–109
3. Fish J, Yu Q, Shek K (1999) Computational damage mechanics for composite materials based on mathematical homogenization. Int J Numer Methods Eng 45:1657–1679
4. Fisher J, Markolefas S, Guttal R, Nayak P (1994) On adaptive multilevel superposition of finite element meshes for linear elastostatics. Appl Numer Math 14:135–164
5. Jiang WG (2007) A computer and a method of modeling a woven composite material, UK patent application No: 0706600.4, Applicant: Rolls-Royce Plc, 27th March 2007

6. Jiang WG, Henshall JL (2006) Analysis of composite laminate beams using coupling cross-section finite element method. Appl Math Mech 27:1709–1718
7. McGlockton MA, Cox BN, McMeeking RM (2003) A binary model of textile composites: III high failure strain and work of fracture in 3D weaves. J Mech Phys Solids 51:1573–1600
8. Tan P, Tong L, Steven GP (1997) Modelling for predicting the mechanical properties of textile composites – A review. Compos Part A 28:903–922
9. Xu J, Cox BN, McGlockton MA, Carter WC (1995) A binary model of textile composites-II. The elastic regime. Acta Metall Mater 43:3511–3524
10. Yang QD, Cox BN (2003) Spatially averaged local strains in textile composites via the binary model formulation Source. Journal of Engineering Materials and Technology - Trans ASME 125:418–425
11. Zako M, Kurashiki T, Nakai H, Imura M (2007) A multiscale analysis for textile composite materials to evaluate the mechanical properties. Sixteenth International Conference on Composite Materials, July 8–13, Kyoto, Japan

Chapter 15
Numerical Simulation of Fiber Orientation and Resulting Thermo-Elastic Behavior in Reinforced Thermo-Plastics

H. Miled, L. Silva, J.F. Agassant, and T. Coupez

Abstract In this work, we describe a numerical technique to predict fiber orientation during injection moulding of fiber reinforced polymers, and how the resulting part behaves regarding this process induced orientation. The orientation state of a set of fibers is described by a second order tensor. Its evolution is given by the Folgar and Tucker tensorial hyperbolic equation. Even if this equation contains a fourth order term, it may be expressed as a function of the second order tensor using a closure approximation. The resolution of Folgar and Tucker's equation is carried out by a continuous approach based on the Standard Galerkin method, with stabilisation. The results are compared with experimental orientation measurements on an injected plate. Once the part solidifies it is considered as a biphasic material, composed by the fibers and the polymer matrix, where each phase has a linear elastic behaviour. The thermo-elastic properties of the composite material are linked to the fiber orientation and the properties of each phase using a homogenisation technique. Finally, to validate the previous study on the prediction of the thermo-elastic properties at the solid state, a three-dimensional industrial case is deeply analysed.

15.1 Introduction

Fiber reinforced thermoplastics are currently applied in injection moulding due to the enhancement of the part's rigidity and resistance when subjected to mechanical and thermal solicitations. The injection process induces an oriented layered structure

H. Miled, L. Silva (currently at), J.F. Agassant, and T. Coupez
Ecole des Mines de Paris; Centre de Mise en Forme des Matériaux, 1, Rue Claude Daunesse, F-06904 Sophia Antipolis Cedex, UMR CNRS N° 7635, France,
e-mail: {houssem.miled, jean-francois.agassant, thierry.coupez}@ensmp.fr

L. Silva
DEMEGI, Faculdade de Engenharia, Universidade do Porto, Rua Dr. Roberto Frias, 4200-465, Porto, Portugal, e-mail: luisa.silva@ensmp.fr

for this type of composites and several studies [27, 28] have shown that orientation depends on the flow characteristics. For example, in the vicinity of the injection gate, the material's flow front adopts a radial flow extension which is divergent and one gets a transverse orientation compared to the flow direction. Far from the gate, the shear rate is weaker and fibers preserve a state of orientation close to the initial one. Solidification occurring near the wall contributes to the formation of a frozen-in oriented layer. Near this layer, the shear rate is very important and fibers orient in the flow direction. Beyond the ones referred, other parameters influence the orientation state such as the injection speed or the holding pressure.

The most general descriptor of an oriented state is the probability distribution function $\psi\left(\underline{p},t\right)$ of orientation that represents the probability to find, at time t, a fiber with axis oriented in the direction of the unit vector $\underline{p}$. Computation of ψ can be performed using the Fokker and Plank equation. However, the quantity ψ is difficult to handle numerically, and thus not commonly used; Hand [21] introduced the second order (and more) orientation tensors, expressed as a function of ψ and $\underline{p}$, as a quantitative measure of the orientation state. Lipscomb et al. [31] combined Jeffery [25] and Fokker and Plank equations to represent the evolution of the second order orientation tensor by a convection-reaction equation, containing also a fourth order tensor, which can be expressed as a function of the second order one using a closure approximation. Folgar and Tucker [16] extended Lipscomb et al. equation [31] by taking into account the interaction between fibers.

Orientation induced during processing will give rise to anisotropic mechanical properties at the solid state. The macroscopic behaviour of unidirectional composites has been widely studied and we find several homogenisation models like the *Halpin-Tsai model* [19, 20] the *Auto-Coherent model* [22], Eshelby model [13, 14] and the Mori-Tanaka model [35]. These models consider that the reinforced thermoplastic is a biphasic material, composed by the fibers and the polymer matrix, where each phase has a linear elastic behaviour. Nevertheless, few studies take into account the orientation of the reinforcement, and mainly for isotropic distributions reinforcements [6, 10, 39, 40]. Ashton et al. [3], Tsai et al. [41] and Fu et al. [17] used the theory of laminates to predict mechanical properties for a two-dimensional orientation distribution. Other authors [1, 18, 22] suggested a two level procedure to determine the effective properties of the composite: firstly the unidirectional properties are evaluated, and then these properties are weighted by the probability density function and then averaged for all fibers directions. This method was exploited by [24, 30, 34] and required the computation of the probability density distribution. Advani and Tucker [1] proposed an extension of the laminates theory by expressing directly the stiffness tensor as a function of both the unidirectional properties of the composite and the second order orientation tensor.

In this paper, we propose to predict the thermo-mechanical properties of fiber reinforced thermoplastics injection moulded. Fiber orientation formulation and its numerical resolution are presented in Sect. 15.2. The model considered was proposed by Folgar and Tucker [16] and its numerical resolution is carried out using the Standard Galerkin method. The Results are compared to those obtained using

the Space-Time Discontinuous Galerkin method, applied by Redjeb et al. [36], and the experimental ones, on an industrial test case. Once the part solidifies, we consider an anisotropic elastic behaviour, described in Sect. 15.3. The goal is to determine the effective elastic properties of the composite, for a given orientation state (which is supposed not to be modified after the filling step of the injection cycle). As proposed in the literature, our approach proceeds in two steps: first, using homogenisation techniques, the unidirectional properties are determined; secondly, the Advani and Tucker model [1] is used to compute the anisotropic mechanical properties as a function of the unidirectional ones and of the second order orientation tensor. In Sect. 15.4, an industrial example is considered to show the feasibility of this methodology for the prediction of the thermo-elastic properties in the solid state.

15.2 Modelling Flow-Induced Fiber Orientation

15.2.1 Evolution Equation of Fiber Orientation

For a single fiber, the orientation can be classically described by a unit vector $\underline{p}$ which indicates the direction of the fiber axis (Fig. 15.1):

The evolution of $\underline{p}$ for a single fiber in a Newtonian fluid was given by Jeffery [25]:

$$\frac{\partial \underline{p}}{\partial t} + \underline{v}.\nabla \underline{p} = \underline{\underline{\Omega}}.\underline{p} + \lambda \left(\underline{\underline{\dot{\varepsilon}}}\,\underline{p} - \left(\underline{\underline{\dot{\varepsilon}}} : \underline{p} \otimes \underline{p} \right) \underline{p} \right) \tag{15.1}$$

where $\underline{v}$ is the local velocity of the fluid, $\underline{\underline{\Omega}} = (\nabla \underline{v} - \nabla \underline{v}^t)/2$ is the rotation tensor, $\underline{\underline{\dot{\varepsilon}}} = (\nabla \underline{v} + \nabla \underline{v}^t)/2$ is the strain rate tensor and λ is a function of the fiber aspect ratio β:

$$\lambda = \frac{\beta^2 - 1}{\beta^2 + 1}; \qquad \beta = \frac{l}{D} \tag{15.2}$$

In this expression, l is the length of the fiber and D its diameter, supposed constants. For a set of fibers, it is hard to follow each fiber but it is feasible to consider the orientation distribution, given by a continuous function $\psi(\underline{p}, t)$, which represents

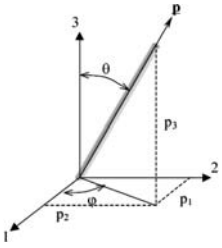

Fig. 15.1 Definition of the vector $\underline{p}$ which characterizes the orientation of a single fiber [1]

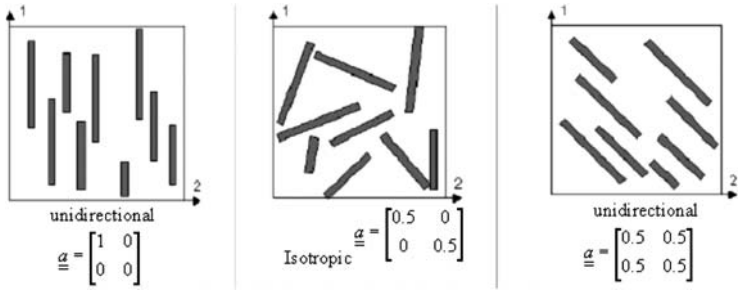

Fig. 15.2 Different values second order orientation tensor for a given set of fibers

the probability to find, at time t, a fiber which is oriented along $\underline{p}$. The evolution of this function is given by the Fokker and Plank equation:

$$\frac{\partial \psi}{\partial t} + \frac{\partial}{\partial \underline{p}} \left[\psi \frac{d\underline{p}}{dt} \right] = D_r \frac{\partial^2 \psi}{\partial \underline{p}^2} \tag{15.3}$$

where $d\underline{p}/dt$ is the material derivative of $\underline{p}$ and D_r is the Brownian diffusivity. However, the resolution of Eq. 15.3 needs an accurate computation of $d\underline{p}/dt$ (which is expressed as a function of the mean velocities) and requires important computational resources. Hand [21] introduced the second and fourth order orientation tensors, defined respectively as:

$$\underline{\underline{a}} = \int (\underline{p} \otimes \underline{p}) \, \psi(\underline{p}) \, dp = \langle \underline{p} \otimes \underline{p} \rangle \tag{15.4}$$

$$\underline{\underline{\underline{a}}} = \int (\underline{p} \otimes \underline{p} \otimes \underline{p} \otimes \underline{p}) \, \psi(\underline{p}) \, dp = \langle \underline{p} \otimes \underline{p} \otimes \underline{p} \otimes \underline{p} \rangle \tag{15.5}$$

These tensors are symmetric and with unitary trace. Figure 15.2 shows the values of the second order tensor, in 2D, for different orientation states.

Folgar and Tucker [16] modified Eq. 15.1 by introducing a Brownian term which expresses the interaction between fibers. Adopting the same approach for the second order orientation tensor equation, we obtain the following expression:

$$\frac{\partial \underline{\underline{a}}}{\partial t} + v.\nabla \underline{\underline{a}} = (\underline{\underline{\Omega}}\,\underline{\underline{a}} - \underline{\underline{a}}\,\underline{\underline{\Omega}}) + \lambda \left(\underline{\underline{\dot{\varepsilon}}}\,\underline{\underline{a}} + \underline{\underline{a}}\,\underline{\underline{\dot{\varepsilon}}} - 2\underline{\underline{\dot{\varepsilon}}} : \underline{\underline{\underline{a}}} \right) + 2dC_I \dot{\bar{\varepsilon}} \left(\underline{\underline{a}} - \frac{\underline{\underline{1}}}{d} \right) \tag{15.6}$$

where d is the space dimension, $\dot{\bar{\varepsilon}}$ is the magnitude of the strain rate tensor, C_I is a dimensionless coefficient introduced by Folgar and Tucker [16] which is a measure of the intensity of fiber interactions in the suspension. Prediction of the interaction coefficient is hard to predict since orientation distribution must be known. Via simulations, Folgar and Tucker found that a range of C_I between 10^{-2} and 10^{-3} provides a good fit to experimental data.

Equation 15.6 has a solution if the fourth order orientation tensor is known. The fourth order tensor is the result of the resolution of a convection-reaction equation in which there is a sixth order tensor, and so on. The problem can be simplified by

using an adequate closure approximation which expresses the fourth order tensor as a function of the second order tensor. Many closure approximations are proposed in the literature [2, 11, 23, 32] and its choice depends on the strain rate and fiber orientation. We consider in this paper the quadratic approximation:

$$\underline{\underline{\underline{\underline{a}}}} = \underline{\underline{a}} \otimes \underline{\underline{a}} \tag{15.7}$$

This approximation is exact for flows with high strain rate and where all fibers are uniformly aligned in one direction [12].

15.2.2 Numerical Resolution of Folgar and Tucker's Equation

The numerical resolution of Folgar and Tucker's equation has been performed by Kabanemi and Hétu [26] using the fourth order Runge-Kutta method, by Martinéz [33] with the method of characteristics, and Redjeb et al. [36] with a Space-Time Discontinuous Galerkin scheme.

We present a different numerical approach based on a stabilised Galerkin method, using a continuous approximation of the orientation tensor. The *Folgar and Tucker* equation's can be re-written:

$$\frac{\partial \underline{\underline{\underline{\underline{a}}}}}{\partial t} + \underline{v}.\nabla \underline{\underline{\underline{\underline{a}}}} + \underline{\underline{B}}_1.\underline{\underline{\underline{\underline{a}}}} + \underline{\underline{\underline{\underline{a}}}}.\underline{\underline{B}}_2 + 2\lambda \left(\underline{\underline{\underline{\underline{a}}}} : \nabla \underline{v}\right) \underline{\underline{\underline{\underline{a}}}} + \frac{1}{\theta}\left(\underline{\underline{\underline{\underline{a}}}} - \frac{\underline{\underline{\underline{\underline{1}}}}}{d}\right) = 0, \quad \Omega \times]0,\tau[\tag{15.8}$$

where τ is the simulation time and Ω denotes the spatial computational domain, we denote also by $\partial\Omega$ the border and $\partial\Omega^l$ is the reentrant flow border. We note P the functional space of symmetric tensors with components in $L^2(\Omega)$, and V the functional space of symmetric tensors for which the derivative is in $L^2(\Omega)$.

For the temporal term in Eq. 15.8, we use an implicit Euler scheme. Because of the term $(\underline{\underline{\underline{\underline{a}}}} : \nabla \underline{v})\underline{\underline{\underline{\underline{a}}}}$, Eq. 15.8 is non linear. The following approximation is then considered:

$$\left(\underline{\underline{\underline{\underline{a}}}} : \nabla \underline{v}\right) \underline{\underline{\underline{\underline{a}}}} \approx \left(\underline{\underline{\underline{\underline{a}}}}^{t-\Delta t} : \nabla \underline{v}\right) \underline{\underline{\underline{\underline{a}}}}^t \tag{15.9}$$

Using this approximation and the temporal scheme, the problem can be rewritten as shown in the following expression:

$$\underbrace{\frac{1}{\Delta t}\underline{\underline{\underline{\underline{a}}}}^t + \underline{v}.\nabla \underline{\underline{\underline{\underline{a}}}}^t}_{\text{transport term}} + \underbrace{\underline{\underline{B}}_1.\underline{\underline{\underline{\underline{a}}}}^t + \underline{\underline{\underline{\underline{a}}}}^t.\underline{\underline{B}}_2}_{\text{rotation term}} + \underbrace{\left(2\left(\underline{\underline{\underline{\underline{a}}}}^{t-\Delta t} : \nabla \underline{v}\right) + \frac{1}{\theta}\right)\underline{\underline{\underline{\underline{a}}}}^t}_{\text{reaction term}} = \underbrace{\frac{\underline{\underline{\underline{\underline{1}}}}}{3\theta} + \frac{1}{\Delta t}\underline{\underline{\underline{\underline{a}}}}^{t-\Delta t}}_{\text{second member}} \quad \text{on } \Omega \tag{15.10}$$

with initial and boundary conditions:

$$\begin{aligned} &\underline{\underline{\underline{\underline{a}}}}(x, t=0) = \underline{\underline{\underline{\underline{F}}}}(x) \\ &\underline{\underline{\underline{\underline{a}}}} \text{ is known on } \partial\Omega^l \subset \partial\Omega \text{ at each instant } t \end{aligned} \tag{15.11}$$

Each member of Eq. 15.10 is multiplied by a test function $\underline{\underline{a}}^*$ chosen in V and integrated on the domain Ω which leads to the weak formulation. The hyperbolic character of the orientation equation provides well known oscillating solutions when the Standard Galerkin method is used. Stabilization techniques have been developed to overcome this problem. Residual Free bubble (RFB) and Streamline Upwind Petrov-Galerkin (SUPG) methods have been implemented and are used in this paper.

The Streamline Upwind Petrov-Galerkin method (SUPG) [8] consists in replacing the test function $\underline{\underline{a}}^*$ by another function $\tilde{\underline{\underline{a}}}^*$ defined as:

$$\tilde{\underline{\underline{a}}}^* = \underline{\underline{a}}^* + \zeta \underline{v}.\nabla \underline{\underline{a}}^* \tag{15.12}$$

where ζ is a perturbation coefficient. For the consistency of the solution, ζ is taken equal to $h_m / \|2\underline{v}\|$ where h_m is the mean mesh size. Since the main cause of oscillations is a dominant convection term, the perturbation of the original $\underline{\underline{a}}^*$ function decreases the effect of convection by adding a diffusive term. This scheme stabilizes the solution and is also consistent.

The Residual Free Bubble method (RFB) is inspired by a class of multi-scale methods using functional spaces enriched by bubble functions [7]. Its principle consists in finding the solution of the weak problem on the functional space V^{RFB}, such that:

$$V^{RFB} = V \oplus V_B \tag{15.13}$$

where V_B is the bubble space. Each element $\underline{\underline{a}}_h \in V^{RFB}$ is then the sum of a linear quantity $\underline{\underline{a}}_L \in V$ and a bubble function $\underline{\underline{a}}_B \in V_B$.

$$\underline{\underline{a}}_h = \underline{\underline{a}}_L + \underline{\underline{a}}_B \tag{15.14}$$

Brezzi et al. [7] showed that for convection equations, SUPG and RFB methods are equivalents if the bubble function is condensed. These two methods were compared to the Galerkin method for the flow of fiber reinforced Newtonian fluid between parallel plates (Fig. 15.3).

η denotes the viscosity of the polymer which is supposed constant and equal to 1,000 Pa.s. Profile of local velocity of the polymer is considered parabolic; we suppose that orientation is initially isotropic and that the orientation tensor is maintained isotropic at the entry. Results obtained by the Galerkin Standard method are compared to the ones obtained using stabilization methods for the computation of the first orientation tensor component a_{11} (Fig. 15.4).

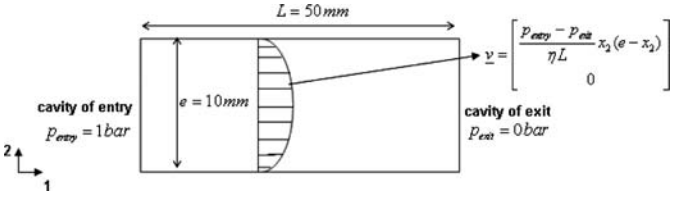

Fig. 15.3 Two-dimensional Poiseuille flow

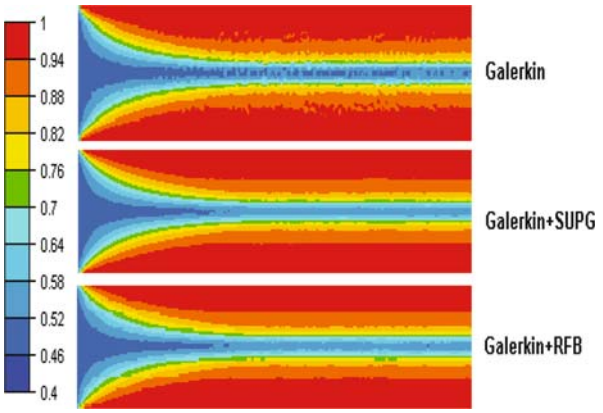

Fig. 15.4 Distribution of the first orientation tensor component a_{11} with Galerkin method, Galerkin associated with RFB method and Galerkin associated with SUPG method

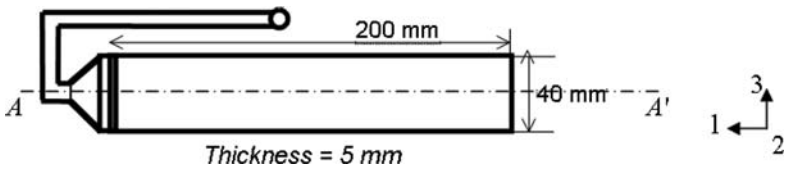

Fig. 15.5 Mould schematic view

Profiles of a_{11} obtained by the Galerkin method, the SUPG method and the RFB method are very similar. However, the use of stabilisation methods reduces oscillations generated by the Galerkin method and gives a more regular profile.

15.2.3 Validation on an Industrial Part

The approach presented previously was implemented on the injection moulding software Rem3D, developed at the Center for Material Forming of the Ecole des Mines de Paris.

We consider the injection moulding of a three-dimensional plate, and in particular we study the orientation development near the injection gate. Dimensions of the plate are given in Fig. 15.5. Only half of the plate will be considered in the simulation, since the geometry presents a symmetry plane.

The polymer is a polyarylamide (Solvay Ixef 1022) reinforced with 50% weight (31.6% volume) glass fibers. The fiber aspect ratio is considered constant and equal to 10, and the interaction coefficient is equal to 10^{-2}. The injection is done at a flow rate of $20\,\mathrm{cm}^3/\mathrm{s}$ and the initial polymer temperature is 270°C. The mould

temperature is kept constant to 130°C. The temperature balance equation is:

$$\rho C_p \left(\frac{\partial T}{\partial t} + \underline{v}.\nabla T \right) = div\,(k\nabla T) + \dot{w} \tag{15.15}$$

ρ is the volume density, C_p is specific heat, k is the thermal conductivity and $\dot{w}$ is the viscous dissipation. These properties are considered not dependant from the induced flow anisotropy.

For short fiber reinforced materials, the flow becomes viscoelastic and the stress tensor is expressed as a function of the fourth order orientation tensor [5]:

$$\underline{\underline{\sigma}} = 2\eta\left(\dot{\bar{\varepsilon}}, T\right)\left[\underline{\underline{\dot{\varepsilon}}} + N_p\left(\underline{\underline{\underline{\underline{a}}}} : \underline{\underline{\dot{\varepsilon}}}\right)\right] - p\underline{\underline{1}} \tag{15.16}$$

where $\eta(\dot{\bar{\varepsilon}}, T)$ is the temperature-dependent viscosity due to both the polymer matrix and fibers. The induced anisotropy is represented by the parameter N_p which depends on the fiber concentration and on the fiber aspect ratio, and is difficult to be predicted. Thus, its contribution to the material's rheology is not taken into account in this work. As a consequence, the problem is considered governed by the Navier and Stokes equations:

$$\begin{gathered} \rho\left(\frac{\partial \underline{v}}{\partial t} + (\underline{v}.\nabla)\,\underline{v}\right) = -\nabla p + \nabla.\left(2\eta\underline{\underline{\dot{\varepsilon}}}\right) + \underline{f} \\ \nabla.\underline{v} = 0 \end{gathered} \tag{15.17}$$

p is the polymer's pressure and $\underline{f}$ are the body forces (such as gravity). We suppose that the viscosity is given by the Carreau-Yasuda law [9,43]:

$$\eta(\dot{\bar{\varepsilon}}, T) = \eta_0(T)\left[1 + \left(\eta_0(T)\frac{\dot{\bar{\varepsilon}}}{\tau_s}\right)^{\alpha}\right]^{\frac{m-1}{\alpha}} \tag{15.18}$$

where α and m are constant parameters, and $\eta_0(T)$ represents the temperature dependency, following the Arrhenius law:

$$\eta_0\,(\mathrm{T}) = \eta_0\,(\mathrm{T_{ref}})\,.\exp\left[\beta\left(\frac{1}{\mathrm{T}} - \frac{1}{\mathrm{T_{ref}}}\right)\right] \tag{15.19}$$

The velocity-pressure mechanical problem is solved using the mixed finite element method with the P1+/P1 element and the thermal problem using a classical Galerkin formulation. Both problems are weakly coupled: at each time increment, the temperature-dependant viscosity used is the one computed at time $t - \Delta t$. Furthermore, the position of the flow front is advected using a Level set technique [4]. Parameters used in Eqs. 15.15, 15.18 and 15.19 are given in Table 15.1.

Table 15.1 Parameters used in Eqs. 15.15, 15.18 and 15.19

τ_s	8.18 10^{-2} MPa
η_0 (T_{ref})	270 Pa.s
α	0.55
m	0.4
T_{ref}	549 K
β	7,764 K
k	0.3 W/m.K
Cp	1,766 J/Kg.K
ρ	1,522 Kg/m^3

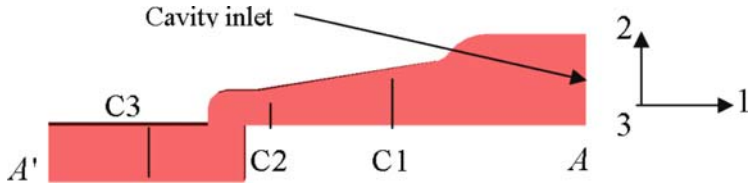

Fig. 15.6 Sensors on the plate symmetry plan

Table 15.2 Computation time for discontinuous and continuous approaches

	Assembly time	Resolution time	Computation time
Continuous approach	2 days, 12 hours, 42 minutes	15 hours, 17 minutes	3 days, 3 hours
Discontinuous approach	8 hours, 29 minutes	3 days, 5 hours, 15 minutes	3 days, 13 hours, 44 minutes

The experimental measurements [42] of the orientation gives, for example, the distribution of the first component, a_{11}, of the orientation tensor on three sensors (see Figs. 15.5 and 15.6).

In what concerns simulation data, orientation is supposed isotropic at the cavity inlet. The orientation problem is solved after the thermal and the mechanical problems. All computations are carried out on an anisotropic mesh of 165,000 nodes and 902,000 elements. Computations were launched on 12 processors; each one has 2.4 GHz frequency and 2 GB RAM, with a time step equal to 10^{-4} s. Resolution, assembly and computation times are shown in Table 15.2. In this case, continuous versus discontinuous approaches are compared.

If a discontinuous approximation of the orientation tensor is considered [36], the orientation tensor is approximated per element P0, whereas in the continuous case P1 (nodal) approximation is used. The number of nodes is 5.5 times lower than the number of elements for a three-dimensional mesh, and thus the memory space is then less important with the second approach.

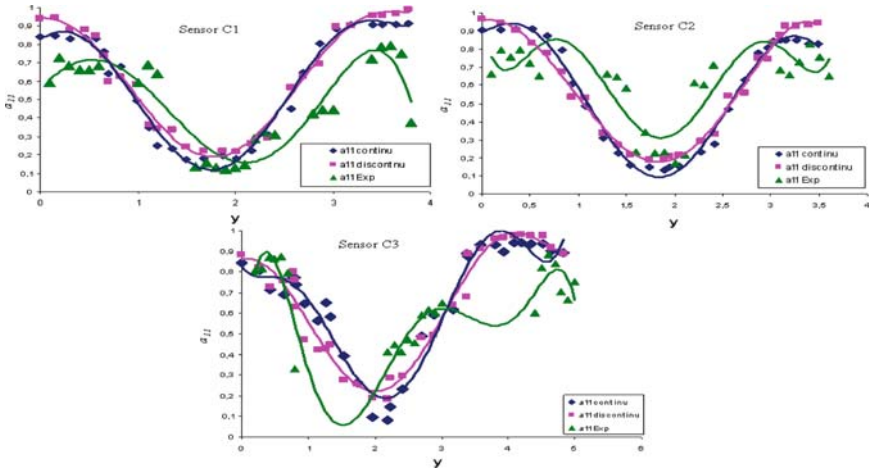

Fig. 15.7 Comparisons between experimental and numerical results on sensors C1, C2 and C3

The number of unknowns is 902,000 for a discontinuous approach whereas it is only 165,000 for the discontinuous one. This difference can explain the time saving of the resolution process. In the continuous approach, the size of the local matrix is equal to the one of the discontinuous approach times the square of the number of nodes per elements. Therefore the assembly time is much more important for the continuous approach.

The experimental and numerical results are plotted for the first component of the orientation tensor (Fig. 15.7).

The comparison between the two numerical results shows that the orientation profile is better captured on the center of the mould with the continuous approach than with the discontinuous one.

The experimental results do not match quantitatively with the numerical ones. A possible explanation lies with the choice of the interaction term C_I, the other with the choice of the closure approximation. In fact, this approximation is not exact since a range of fibers, especially in the center of the mould, are not aligned in a single direction.

15.3 Predicting Thermo-Elastic Properties of the Composite

In this section, a two levels approach is proposed to determine the thermo-mechanical properties of the composite as a function of the local fiber orientation. This approach consists, first, on determining the properties of the composite having the fibers aligned in a single direction (unidirectional properties), and then the average of these properties with the fiber orientation distribution is performed.

The thermo-elastic behaviour law is:

$$\underline{\underline{\sigma}} = \underline{\underline{\underline{\underline{C}}}}^c(T) : \left(\underline{\underline{\varepsilon}} - \underline{\underline{\alpha}}^c(T)\Delta T\right) \tag{15.20}$$

where T denotes the temperature of the composite, $\underline{\underline{\underline{\underline{C}}}}^c$ is the fourth order stiffness tensor of the composite, $\underline{\underline{\alpha}}^c$ is the thermal expansion tensor and ΔT is the difference between initial and final temperature distributions.

In what follows we will predict $\underline{\underline{\underline{\underline{C}}}}^c$ and $\underline{\underline{\alpha}}^c$. Fibers and polymer matrix are supposed to have, each one, an isotropic linear elastic behaviour with respectively Young Modulus E_f and E_m, and Poisson ration ν_f and ν_m. These properties may be temperature dependent.

15.3.1 Unidirectional Properties

This step is achieved by means of micromechanical models, fibers are assumed aligned in the 1-direction. The determination of the stiffness tensor for unidirectional properties is equivalent to find five independent elastic constants: the longitudinal Young modulus E_1, the transverse young modulus E_2, the in-plane $(1,2)$ shear modulus G_{12} and the Poisson ratios ν_{12} and ν_{23}. For the expansion tensor, only two coefficients are needed: the longitudinal thermal expansion coefficient α_1 and the transverse thermal expansion coefficient α_2.

Fibers are considered as ellipsoidal inclusions where the revolution axis is supposed to be the 1-axis (Fig. 15.8). Ellipsoid parameters are s_1, s_2 and s_3 such that: $s_1 = s_2 \leq s_3$. The fiber aspect ratio can be defined as: $\beta = \frac{s_3}{s_1}$.

Many micromechanical models in the literature are based on this representation for fibers. In this paper, three micromechanical models are presented to estimate the elastic properties:

- The Halpin-Tsai model [19, 20]

The computation of an elastic property M, is performed by means of the following equation:

$$\frac{M}{M_m} = \frac{1 + \zeta_r \eta V_f}{1 - \eta V_f}; \quad \eta = \frac{M_r - 1}{M_r + \zeta_r} \tag{15.21}$$

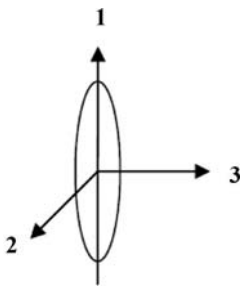

Fig. 15.8 Fiber can be assimilated to an ellipsoidal inclusion

Table 15.3 Property M (Eq. (15.21)) with empirical parameter

M	M_f	M_m	ζ_r
E_1	E_f	E_m	2β
E_2	E_f	E_m	2
G_{12}	G_f	G_m	1
G_{23}	G_f	G_m	$\frac{K_m}{G_m}/\left(\frac{K_m}{G_m}+2\right)$

ζ_r is an empirical parameter, $M_r = M_f/M_m$ where M_f and M_m are respectively the fibers and the matrix used for the computation of the property M. These parameters are listed in Table 15.3.

Where K_m is the matrix bulk modulus, G_m and G_f are respectively the matrix and fiber shear modulus. The Poisson ratio is expressed by means of the transverse Young modulus E_2 and the in-plane (*2,3*) shear modulus G_{23}:

$$\nu_{23} = \frac{E_2}{2G_{23}} - 1 \tag{15.22}$$

ν_{12} is computed using a mixture law:

$$\nu_{12} = V_f \nu_f + \left(1 - V_f\right) \nu_m \tag{15.23}$$

V_f denotes the volume fraction of fibers.

- The Eshelby model [13, 14]

This model supposes that each reinforcement is surrounded by an infinite domain with properties similar to those of the polymer matrix, and that no interaction exists between the reinforcements. The unidirectional stiffness tensor is given by:

$$\underline{\underline{\underline{\underline{C}}}}^{UD} = \underline{\underline{\underline{\underline{C}}}}^{m} - V_f \left(\underline{\underline{\underline{\underline{C}}}}^{f} - \underline{\underline{\underline{\underline{C}}}}^{m}\right) \underline{\underline{\underline{\underline{A}}}}^{Eshelby} \tag{15.24}$$

$\underline{\underline{\underline{\underline{C}}}}^{m}$ and $\underline{\underline{\underline{\underline{C}}}}^{f}$ are respectively the matrix and fibers stiffness tensors. $\underline{\underline{\underline{\underline{A}}}}^{Eshelby}$ is the strain concentration tensor obtained from the Eshelby Tensor $\underline{\underline{\underline{\underline{E}}}}$ [13]:

$$\underline{\underline{\underline{\underline{A}}}}^{Eshelby} = \left[\underline{\underline{\underline{\underline{1}}}} + \underline{\underline{\underline{\underline{E}}}}.\underline{\underline{\underline{\underline{C}}}}^{m^{-1}} . \left(\underline{\underline{\underline{\underline{C}}}}^{f} - \underline{\underline{\underline{\underline{C}}}}^{m}\right)\right]^{-1} \tag{15.25}$$

- The Mori-Tanaka model [35]

The unidirectional stiffness tensor is given by:

$$\underline{\underline{\underline{\underline{C}}}}^{UD} = \underline{\underline{\underline{\underline{C}}}}^{m} - V_f \left(\underline{\underline{\underline{\underline{C}}}}^{f} - \underline{\underline{\underline{\underline{C}}}}^{m}\right) \underline{\underline{\underline{\underline{A}}}}^{MT} \tag{15.26}$$

where the strain concentration tensor $\underline{\underline{\underline{\underline{A}}}}^{MT}$ is expressed by means of $\underline{\underline{\underline{\underline{A}}}}^{Eshelby}$:

$$\underline{\underline{\underline{\underline{A}}}}^{MT} = \underline{\underline{\underline{\underline{A}}}}^{Eshelby} \cdot \left[\left(1 - V_f\right) \underline{\underline{\underline{\underline{1}}}} + V_f \underline{\underline{\underline{\underline{A}}}}^{Eshelby} \right]^{-1} \tag{15.27}$$

This model is more efficient than the Eshelby model because it takes into account the interaction between fibers and so it is able to account for a large number of fibers.

The estimation of the thermal properties is done after determining the mechanical properties. Levin [29] expressed the thermal expansion tensor as a function of respectively compliance tensor and thermal expansion tensors of fibers and matrix, and the effective compliance tensor of the composite. This approach can be used to predict directly the anisotropic thermal properties if the anisotropic compliance tensor is known. Scharpery [37] evaluated the longitudinal and transverse thermal expansion coefficients by means of fibers and matrix thermo-elastic properties, fiber concentration and the Poisson ratio ν_{12}.

15.3.2 Anisotropic Properties

For an unidirectional composite with fibers aligned in the direction of $\underline{p}$, each component of the stiffness tensor can be written as:

$$\begin{aligned} C_{ijkl}^{UD}\left(\underline{p}\right) = {} & b_1 p_i p_j p_k p_l + b_2 \left(p_i p_j \delta_{kl} + p_k p_l \delta_{ij}\right) + b_3 \left(p_i p_k \delta_{jl} + p_i p_l \delta_{jk} \right. \\ & \left. + a_{jk} \delta_{il} + p_j p_l \delta_{ik}\right) + b_4 (\delta_{ij} \delta_{kl}) + b_5 \left(\delta_{ik} \delta_{jl} + \delta_{il} \delta_{jk}\right) \end{aligned} \tag{15.28}$$

where δ_{ij} is the Kronecker symbol, and the five constants $b_1, \ldots, b_5$ are related to the standard components of the stiffness tensor with fibers oriented along the 1-axis:

$$\begin{aligned} b_1 &= C_{1111}^{UD} - 2C_{1122}^{UD} - 4C_{1212}^{UD} + C_{2222}^{UD} \\ b_2 &= C_{1122}^{UD} - C_{2233}^{UD} \\ b_3 &= C_{1212}^{UD} - \frac{1}{2}\left(C_{2222}^{UD} - C_{2233}^{UD}\right) \\ b_4 &= C_{2233}^{UD} \\ b_5 &= \frac{1}{2}\left(C_{2222}^{UD} - C_{2233}^{UD}\right) \end{aligned} \tag{15.29}$$

For the more general case of a composite with anisotropic fiber distribution, the effective stiffness of the composites is given by:

$$\underline{\underline{\underline{\underline{C}}}}^{c} = \int_{\Omega} \underline{\underline{\underline{\underline{C}}}}^{UD}\left(\underline{p}\right) \psi\left(\underline{p}\right) d\Omega \tag{15.30}$$

Eqs. 15.28 and 15.30 lead to the Advani and Tucker model [1] which expresses the effective stiffness tensor as a function of the second and fourth orientation tensors:

$$C^c_{ijkl}\left(\underline{p}\right) = b_1 a_{ijkl} + b_2\left(a_{ij}\delta_{kl} + a_{kl}\delta_{ij}\right) + b_3\left(a_{ik}\delta_{jl} + a_{il}\delta_{jk} + a_{jk}\delta_{il} + a_{jl}\delta_{ik}\right) + b_4\left(\delta_{ij}\delta_{kl}\right) + b_5\left(\delta_{ik}\delta_{jl} + \delta_{il}\delta_{jk}\right) \tag{15.31}$$

An averaging on the compliance tensor gives an expression of the anisotropic tensor which is similar to Eq. 15.31, with five constants $m_1, ..., m_5$:

$$S^c_{ijkl} = m_1 a_{ijkl} + m_2\left(a_{ij}\delta_{kl} + a_{kl}\delta_{ij}\right) + m_3\left(a_{ik}\delta_{jl} + a_{il}\delta_{jk} + a_{jk}\delta_{il} + a_{jl}\delta_{ik}\right) + m_4\left(\delta_{ij}\delta_{kl}\right) + m_5\left(\delta_{ik}\delta_{jl} + \delta_{il}\delta_{jk}\right) \tag{15.32}$$

In spite of $\underline{\underline{\underline{\underline{S}}}}^{UD}$ being the inverse of $\underline{\underline{\underline{\underline{C}}}}^{UD}$, the effective compliance tensor is not the inverse of the stiffness tensor given by Eq. 15.31. This represents the weakness of the two levels approach. Many authors [18, 34], prefer to use the stiffness tensor to describe the anisotropic properties because of his better agreement with experiments.

The effective thermal expansion tensor can be also expressed as a function of the second order orientation tensor [1]

$$\underline{\underline{\alpha}}^c = P_1\underline{\underline{a}} + P_2\underline{\underline{1}} \tag{15.33}$$

P_1 and P_2 are two constants related to the unidirectional thermal properties:

$$\begin{aligned} P_1 &= \alpha_1 - \alpha_2 \\ P_2 &= \alpha_2 \end{aligned} \tag{15.34}$$

15.4 Results and Discussion

15.4.1 Choice of a Micromechanical Model for the Unidirectional Properties

In order to compare the three models listed in Sect. 15.3, a composite reinforced by spherical inclusions is considered ($\beta = 1$). The predicted longitudinal Young modulus is compared to experimental measurements conducted by Simth [38]. The Young's modulus of the matrix and particles are respectively $E_m = 3$ GPa, $\nu_m = 0.4$, $E_f = 76$ GPa, and $\nu_f = 0.23$. The comparison between predicted and effective longitudinal Young modulus is done for increasing fiber volume fractions (Fig. 15.9).

Figure 15.9 shows that Mori-Tanaka model gives the better prediction of the longitudinal Young modulus for volume fraction going up to 20–30%.

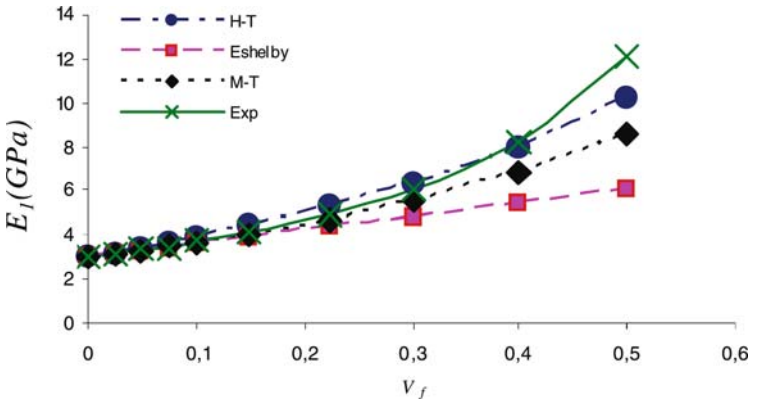

Fig. 15.9 Longitudinal Young modulus given by experimental and micromechanical models for spherical inclusions [38]

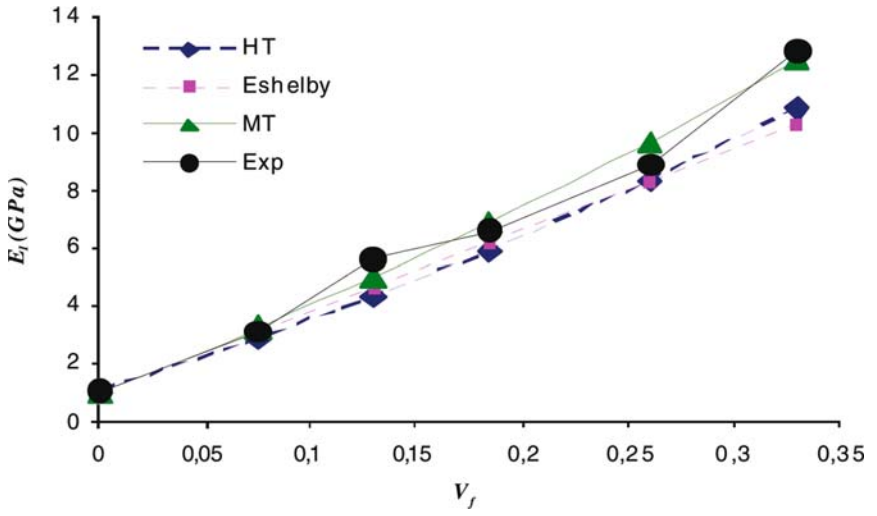

Fig. 15.10 Longitudinal Young modulus given by experiment and micromechanical models for ellipsoidal inclusions [15]

Another comparison is done on the high-density polyethylene (HDPE) reinforced by glass fibers. The Young's modulus and the Poisson ratio of the matrix and particles are, respectively, $E_m = 1.04$ GPa, $\nu_m = 0.34$, $E_f = 72.5$ GPa, and $\nu_f = 0.2$. The fiber aspect ratio is supposed constant and equal to 16 (ellipsoidal inclusions). Figure 15.10 shows a comparison between prediction and experimental data [15] for the longitudinal Young modulus.

In that case, the better prediction of the longitudinal Young modulus is given by the Mori-Tanaka model. As a consequence, this model will be used for the prediction of the unidirectional properties.

15.4.2 Effective Properties of a Three-Dimensional Plate

Simulations were performed on the example presented in Sect. 15.2.3. After prediction of the second order orientation tensor, we propose to compute the mechanical properties distribution on the plate of the Solvay Ixef 1022, once the part ejected. Influence of temperature is neglected in this study as well as the dilatation coefficients. The Young modulus and the Poisson ratio of the matrix and fibers, at the ambient temperature, are respectively $E_m = 4$ GPa, $\nu_m = 0.36$, $E_f = 74$ GPa, and $\nu_f = 0.25$.

The five mechanical constants of the unidirectional composite are computed using the Mori-Tanaka model, and are found equal to: $E_1 = 20.78$ GPa, $E_2 = 7.15$ GPa, $\nu_{12} = 0.33$, $\nu_{23} = 0.46$, and $G_{12} = 3.52$ GPa.

The unidirectional stiffness tensor is determined as a function of these five elastic constants and then using Eqs. 15.29 and 15.31, the effective stiffness tensor of the composite is predicted. Components S^c_{ijkl} of the effective tensor can be computed by inversing the obtained stiffness tensor. We can then define the elastic modulus E_{11}, E_{22} and E_{33} as:

$$E_{11} = \frac{1}{S^c_{1111}}; \quad E_{22} = \frac{1}{S^c_{2222}}; \quad E_{33} = \frac{1}{S^c_{3333}} \tag{15.35}$$

Figure 15.11 shows the anisotropic Young modulus E_{11}, E_{22} and E_{33} in directions 1, 2 and 3, respectively. In the vicinity of the plate walls, fibers are oriented in the flow direction (1-direction), this orientation induces a maximum value of E_{11}, which is close to the Young modulus E_1. The minimum of E_{11} is reached at the center of the part (since a_{11} is weak in this area). We infer that the rigidity of the composite in the 1-direction is stronger in the vicinity of the plate walls than at its center. Young

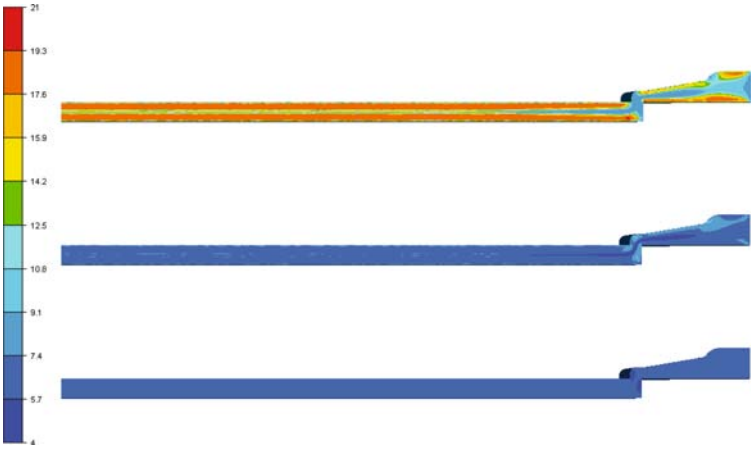

Fig. 15.11 Distribution of the elastic modulus E_{11}, E_{22}, and E_{33}

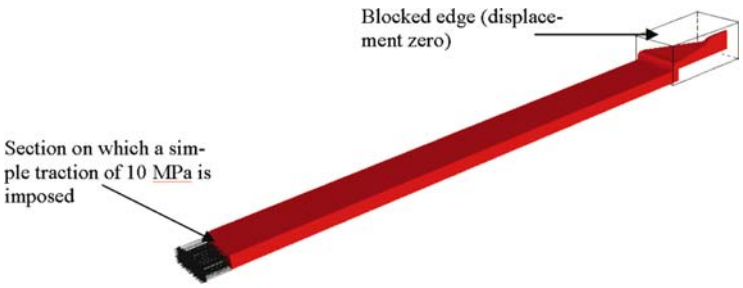

Fig. 15.12 Conditions imposed on the plate for a static deformation test

modulus E_{22} and E_{33} are weak compared to E_{11}, which means that an important rigidity was added in the flow direction.

The plate is now subjected to a simple traction in the 1-direction, as shown in Fig. 15.12. The plate is fixed at the other extremity, near the injection gate.

To solve the mechanical problem, the behaviour law is rewritten as following:

$$\underline{\underline{\sigma}} = \underline{\underline{\underline{\underline{C}}}}^{c} : \underline{\underline{\varepsilon}} - (q + \xi \nabla . \underline{u})\,\underline{\underline{1}} \tag{15.36}$$

where $\underline{u}$ denotes the displacement and q and ξ are a scalar numbers taken such as:

$$q + \xi \nabla . \underline{u} = 0 \tag{15.37}$$

The mechanical problem to be solved is then:

$$\begin{aligned} &\nabla . \left(\underline{\underline{\underline{\underline{C}}}}^{c} : \underline{\underline{\varepsilon}}(\underline{u}) - \xi\,(\nabla . \underline{u})\,\underline{\underline{1}} \right) - \nabla q + \underline{f_v} = 0 \\ &\nabla . \underline{u} + \frac{1}{\xi} q = 0 \end{aligned} \tag{15.38}$$

where $\underline{f_v}$ are the body forces.

Equation 15.38 takes the advantage to deal with the isotropic case when the material is incompressible. In fact, for an isotropic material, Eq. 15.38 is rewritten as:

$$\begin{aligned} &\nabla . \left(2\mu \underline{\underline{\varepsilon}}(\underline{u}) + (\lambda - \xi) \nabla . \underline{u} \underline{\underline{1}} \right) - \nabla q + \underline{f_v} = 0 \\ &\nabla . \underline{u} + \frac{1}{\xi} q = 0 \end{aligned} \tag{15.39}$$

where λ and μ are the Lame coefficients, defined as a function of the Young modulus and the Poisson ratio:

$$\mu = \frac{E}{2(1+\nu)}; \quad \lambda = \frac{\nu E}{(1-2\nu)(1+\nu)} \tag{15.40}$$

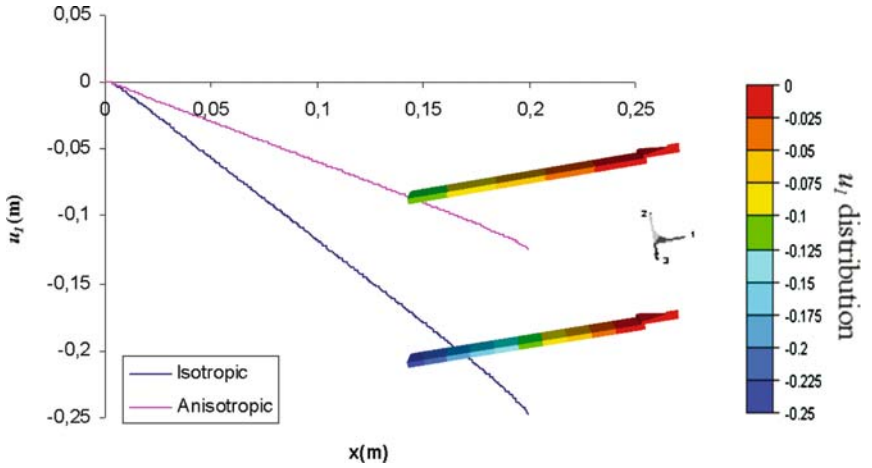

Fig. 15.13 Comparisons between isotropic and anisotropic fiber distribution on the first displacement component

Incompressibility is defined by a Poisson ratio close to 0.5 which is equivalent ton an infinite value for the Lame coefficient λ. The coefficient ξ is then taken as following:

$$\xi = \frac{d.\lambda + 2\mu}{d} \tag{15.41}$$

For isotropic incompressible case, Eq. 15.39 becomes:

$$\begin{aligned} &\nabla.\left(2\mu\underline{\underline{\varepsilon}}(\underline{u}) - \frac{2\mu}{d}\nabla.\underline{u}\,\underline{\underline{1}}\right) - \nabla q + \underline{f_v} = 0 \\ &\nabla.\underline{u} = 0 \end{aligned} \tag{15.42}$$

The general case (Eq. 15.38), the problem is solved using the mixed finite element method with the element P1+/P1 for $(\underline{u}, q)$.

The computed displacements were compared for isotropic and anisotropic oriented fibers. Comparisons were done on the first displacement component, u_1, measured along the one-axis of the plate, at the symmetry plane. Figure 15.13 confirms that fibers increase the plate rigidity in the flow direction: in the anisotropic case, the displacement is lower than in the isotropic case.

15.5 Conclusion

In this work, an approach for prediction of the thermo-elastic properties of fiber reinforced thermoplastics is presented. Fiber orientation is described by a second order orientation tensor which is the solution of a tensorial convection-reaction equation. Its resolution is carried out by a continuous approach based on the Galerkin Standard

method. To overcome the instabilities generated by this method, because of the dominant convection term, two stabilisation methods were used: SUPG and RFB. These methods were tested on a three-dimensional injection plate and compared to a discontinuous approach and the experimental results. Once the orientation shape is computed at the end of the filling step, the prediction of the mechanical properties is performed. A two levels approach was proposed; first the unidirectional properties are carried out by mean of micromechanical models, and second, these properties are averaged to give the effective properties as a function of the orientation distribution. Three micromechanical models were compared with experimental data on the prediction of the longitudinal Young modulus: Halpin-Tsai, Eshelby and Mori-Tanaka models for spherical and ellipsoidal particles. Results given by the Mori-Tanaka model were the more consistent with experimental data.

Simulations were done on the three-dimensional injection plate, for which the orientation tensor distribution was predicted. The Advani and Tucker model was combined with the Mori-Tanaka model for the prediction of the mechanical behaviour which takes into account the orientation distribution. Results show clearly that the part becomes more rigid in the direction of fiber orientation.

Next developments, in the Rem3D project, will deal with the coupling between rheology and fiber orientation in the filling step. The prediction of the thermo-elastic properties will be carried out by Finite Elements methods. In fact, for a given fiber orientation, the stiffness tensor is then computed by mean of numerical solicitations.

Acknowledgements The authors acknowledge The Rem3D consortium which includes: Cemef, Schneider Electrics, Arkema, Snecma Porpulsion Solide, Dow Chemical, Rhodia and Transvalor for its financial support. They thank also M. Vincent for experimental results done on the measure of the orientation tensor which were used to validate the numerical approach.

References

1. Advani SG, Tucker III CL (1987) The use of tensors to describe and predict fiber orientation in short fiber composites. J Rheol 31:751–784
2. Advani SG, Tucker CL (1990) Closure approximations for three-dimensional structure tensors. J Rheol 34:367–386
3. Ashton JE, Halpin JC, Petit PH (1969) Primer on Composite Analysis. Technomic Publishing, Stamford, CT
4. Basset O, Digonnet H, Guillard H, Coupez T (2005) Multi-phase flow calculation with interface tracking coupled solution. Int Conf on Computational Methods for Coupled Problems in Science and Engineering, CIMNE, Barcelona
5. Batchelor GK (1970) The stress generated in a non dilute suspension of elongated particles by pure straining motion. J Fluid Mech 46:813–829
6. Benveniste Y (1987) A new approach to the application of Mori-Tanaka's theory in composite materials. Mech Mater 6:147–157
7. Brezzi F, Franca LP, Russo A (1998) Further considerations on residual free bubbles for advective-diffusive equations. Comput Methods Appl Mech 166:25–33
8. Brooks AN and Hughes TJR (1982) Streamline Upwind/Petrov Galerkin formulations for convection dominated flows with particular emphasis on the incompressible Navier-Stokes equations. Comput Methods Appl Mech Eng 32:199–259

9. Carreau P, DeKee D, Daroux M (1979) An analysis of the behaviour of polymeric solutions. Can J Chem Eng 57:135–140
10. Christensen RM, Waals FM (1972) Effective stiffness of randomly oriented fiber composites. J Compos Mater 6:518–532
11. Cintra JS, Tucker CL (1995) Orthotropic closure approximations for flow induced fiber orientation. J Rheol 39:1095–1122
12. Doi M (1981) Molecular Dynamics and rheological properties of concentrated solutions of rodlike polymers in isotropic and liquid crystalline phases. J Polymer Sci: Polymer Phys Edn 19:229
13. Eshelby JD (1957) The determination of the elastic field of an ellipsoidal inclusion and related problems. Proc Royal Soc 241:376–396
14. Eshelby JD (1961) Elastic inclusions and inhomogeneities. In: Sneddon IN, Hill R (eds) Progress in Solid Mechanics, Vol. 2, pp. 89–140
15. Facca G, Kortschot T, Yan N (2006) Predicting the elastic modulus of natural fibre reinforced thermoplastics. Compos Part A 37:1660–1671
16. Folgar FP, Tucker CL (1984) Orientation behavior of fibers in concentrated suspensions. J Reinf Plast Compos 3:98–119
17. Fu SY, Lauke B (1998) The elastic modulus of misaligned short fibre reinforced polymers. Compos Sci Technol 58:389–400
18. Gupta M, Wang KK (1993) Fibre orientation and mechanical properties of short-fibre-reinforced injection-molded composites: simulation and experimental results. Polym Compos 14:367–382
19. Halpin JC (1969) Stiffness and expansion estimates for oriented short fiber composites. J Compos Mater 3:732–734
20. Halpin JC, Kardos JL (1976) The Halpin-Tsai equations: a review. Polym Eng Sci 16:732–352
21. Hand GL (1962) A theory of anisotropic fluids. J Fluid Mech 13:33–46
22. Hershey AV (1954) The elasticity of an isotropic aggregate of anisotropic cubic crystals. J Appl Mech 21:236–241
23. Hinch EJ, Leal LG (1976) Constitutive equations in suspension mechanics. Part 2. Approximate forms for a suspension of rigid particles affected by Brownian rotations. J Fluid Mech 76:187–208
24. Huang JH (2001) Some closed-form solutions for effective moduli of composites containing randomly oriented short fibers. Mater Sci Eng 315:11–20
25. Jeffery G (1922) The motion of ellipsoidal particles immersed in viscous fluid. Proc Royal Soc Lond A 102:161
26. Kabanemi KK, Hétu JF (1999) Modelling and simulation of nonisothermal effects in injection moulding of rigid fibers suspensions. J Inject Mould Technol 3:80–87
27. Kamal MR, Singh P (1975) The extend to which fibre breakdown can be influenced when injection moulding glass fibre reinforced thermoplastics. Plaste U Kaut 22:739–746
28. Karpov V, Kaufman M (1965) Injection moulding of glass reinforced nylon 66. Br Plast 38:498–506
29. Levin VM (1967) Thermal expansion coefficients of heterogeneous materials. Mekhanika Tverdogo Tela 2:88–94
30. Lielens G, Pirotte P, Couniot A et al. (1998) Prediction of thermo-mechanical properties of compression-moulded composites. Compos Part A 29:63–70
31. Lipscomb GG, Keunings R, Marucci G, Denn MM (1984) A continuum theory for fiber suspensions. Proc IX Int Congress on Rheology 2:497–499
32. Lipscomb GG, Denn MM, Hur DU, Boger DV (1988) The flow of fiber suspensions in complex geometries. J Non-Newtonian Fluid Mech 26:297–325
33. Martinéz MA, Cueto E, Doblaré M, Chinesta F (2003) Natural element meshless simulation of flows involving short fiber suspensions. J Non-Newtonian Fluid Mech 115:51–78
34. Mlekush B (1999) Thermoelastic properties of short-fiber-reinforced thermoplastics. Compos Sci Technol 59:911–923
35. Mori T, Tanaka K (1973) Average stress in matrix and average elastic energy of material with misfitting inclusions. Acta Metall 21:571–574

36. Redjeb A, Laure P, Silva L, Vincent M, Coupez T (2005) Simulation numérique de l'orientation de fibres en injection de thermoplastique renforcé. 17éme Congrès Français de Mécanique, Troyes, France
37. Scharpery RA (1968) Thermal expansion coefficients of composite materials based on energy principles. J Compos Mater 2:380–404
38. Simth JC (1976) Experiment values for elastic constants of a particulate-filled flassy polymer. J Res Natl Inst Stand Technol 80:45–49
39. Tandon GP, Weng GJ (1986) Average stress in the matrix and effective moduli of randomly oriented composites. Compos Sci Technol 27:111–132
40. Taya M, Dunn ML, Derby B, Walker J (1990) Thermal residual stress in a two-dimensional in-plane misoriented short fiber composite. Appl Mech 43:294–303
41. Tsai SW, Pagano NJ (1969) Invariant properties of composite materials. In: Tsai SW, Halpin JC, Pagano NJ (eds) Composite Materials Workshop. Technomic Publishing, Stamford, CT
42. Vincent M, Redjeb A, Laure P, Coupez T (2006) Injection moulding of short fiber reinforced thermoplastics: a comparison between experimental results and numerical simulation. ECCM 12, Biarritz, France
43. Yasuda K, Armstrong R, Cohen R (1981) Shear-flow properties of concentrated solutions of linear and star branched polystyrenes. Rheol. Acta 20:163–178